MECHANICAL AND ELECTROMECHANICAL CHARACTERIZATION OF A NOVEL COMPOSITE CELLULAR SOLID FOR ORTHOPAEDIC APPLICATIONS: A FEASIBILITY STUDY

BY

Nicolas Jaumard
Mechanical Engineering
University of Kansas

Submitted to the School of Engineering
and the Graduate Faculty of the University of Kansas
in partial fulfillment of the requirements for the degree of
Doctor of Philosophy

Dr. Elizabeth A. Friis, Chair

Dr. Ronald M. Barrett-Gonzalez

Dr. Terry N. Faddis

Dr. Kenneth J. Fischer

Dr. Carl W. Luchies

Date defended: December 15, 2008

The Dissertation Committee for Nicolas V. Jaumard certifies
that this is the approved version of the following dissertation:

MECHANICAL AND ELECTROMECHANICAL CHARACTERIZATION OF A NOVEL COMPOSITE CELLULAR SOLID FOR ORTHOPAEDIC APPLICATIONS: A FEASIBILITY STUDY

Committee

_____
Dr. Elizabeth A. Friis, Chair

_____
Dr. Ronald M. Barrett-Gonzalez

_____
Dr. Terry N. Faddis

_____
Dr. Kenneth J. Fischer

_____
Dr. Carl W. Luchies

Date approved: December 17, 2008

Acknowledgements

I would like to express my gratitude to my advisor, Dr. Elizabeth A. Friis, for giving me the opportunity to collaborate with her on many projects. I learned a lot through our interactive partnership. I would also like to thank Dr. Stuart R. Bell, the Dean of the School of Engineering and Dr. Ronald L. Dougherty, Chair of the Mechanical Engineering Department at the University of Kansas for welcoming me, supporting me, and providing a favorable environment for the development and enhancement of the gifts that were bestowed on me.

As ever, I am infinitely thankful to my parents and family for their constant supportive love despite the disheartening distance between us. I also wish to thank my wife, Emily, as well as my friends and colleagues for their physical, moral, and spiritual support. They have always trusted me to be successful in this endeavor that I hope will lead me to greater achievements for the good of everyone.

Abstract

This document presents investigations concerning the feasibility of manufacturing a novel active composite cellular structure to be used in surgical applications such as spinal fusion. The development of a biomimetic spinal fusion implant was motivated by two main factors. The population of patients whose metabolic conditions jeopardize the success of this surgical operation keeps increasing. Current implants and techniques present financial, technical, and health drawbacks. The new medical device would feature enhanced mechanical and electromechanical properties that would overcome these issues and could accelerate bone healing.

A simple one-dimensional piezoelectric re-entrant structure was created from piezoceramic plates positioned between metallic bowtie open cells. Various sizes of this structure were prepared by hand and by a solid free-form process. These ductile cellular solids were tested to verify if they presented a nonlinear mechanical behavior at small strains along with mechanical parameters and an electromechanical behavior that could be tailored for orthopaedic applications. The tensile strength of a gradual composition material used as an interface between the metallic and ceramic elements of the structure was also evaluated.

Despite the small number of specimens and limitations in the current manufacturing process, the investigations showed that the mechanical and electromechanical properties of the re-entrant structure can be controlled and tailored via their relative density. Also, the gradual composition interfacing material presented a linear change in tensile strength that could eliminate the problems of stress

concentration in the structure. This work provides base data for future finite element analyses of such and evolved versions of the piezoelectric re-entrant structure.

Table of Contents

List of Figures

List of Tables

List of Symbols and Acronyms

σ_{pl}*	Plastic collapse stress of the cellular solid
σ_{pl}*/σ_{ys}	Relative plastic collapse stress
σ_{ys}	Yield strength of the material composing the cellular solid
3D	Three- Dimensional
3DP	Three Dimensional Printing
AC	Alternating Current
ANOVA	Analysis of variance
Ba	Barium
$BaTiO_3$	Barium titanate
BMP	Bone Morphogenic Protein
CCD	Charge-Coupled Device
CSR	Compressive Strain Ratio
CW2400	Circuit Works 2400
D	Electric displacement or charge density
DC	Direct Current
d_{ij}	Piezoelectric charge coefficient
E	Electric field
E	Modulus of elasticity
E*	Modulus of elasticity of the cellular solid
E*/ E_s	Relative modulus of elasticity
EBRD	Extrusion-Based Robotic Deposition
$E_{composite}$	Modulus of elasticity of a composite material
$E_{material\ i}$	Modulus of elasticity of material *i*
E_s	Modulus of elasticity of the material employed in the cellular solid
F	Mechanical force
G	Shear modulus
g_{ij}	Piezoelectric voltage coefficient
I	Electric current
I_{exp}	Experimental electric current
I_{theo}	Theoretical electric current
JEOL	Japan Electron Optics Laboratory
K	Bulk modulus
k^2	Coupling coefficient
KU	University of Kansas
kV	Kilovolt
L	Length or thickness of a cylindrical specimen
L	Large
LVDT	Linear Voltage Displacement Transducer
M	Medium
mm	Millimeter
MPa	MegaPascal

MTI	Mechanical Technology Incorporated
MTS	Materials Testing Systems
N	Newton
n	Number of specimens
nA	NanoAmp
Ni	Nickel
nm	Nanometer
NPR	Negative Poisson's Ratio
OSU	Oklahoma State University
P	Mechanical load to fracture a cylindrical specimen
Pb	Lead
pC	PicoCoulomb
PEEK	Polyetheretherketone
pL	Piezoelectric Large
pm	Picometer
PVC	Polyvinyl chloride
PVDF	Polyvinylidene fluoride
pXL	Piezoelectric Extra-large
pXXL	Piezoelectric Extra-extra-large
Q	Electric charge
R	Radius of a cylindrical specimen
R^2	Coefficient of determination
S	Small
s^D	Elastic compliance at constant electric displacement
s^E	Elastic compliance at constant electric field
SEM	Scanning Electron Microscope
SFF	Solid Free Form
TGF	Transforming Growth Factor
Ti	Titanium
$V_{material\ i}$ or $VF_{material\ i}$	Volume fraction of material *i*
x	Strain
X	Stress
x	Distance from the vertical plane of symmetry of the cylindrical specimen
XL	Extra-large
XXL	Extra-extra-large
Zr	Zirconium
ε_{ys}	Yield strain of the material composing the cellular solid
ε	Engineering strain
$\varepsilon_{long.}$	Longitudinal (or axial) strain
$\varepsilon_{trans.}$	Transverse strain
ε^X	Permittivity under constant stress
μA	MicroAmp
μm	Micrometer
ν	Poisson's ratio

π	Number Pi
ρ^*	Density of the cellular solid
ρ^*/ρ_s	Relative density of the cellular solid
ρ_s	Density of the material employed in the cellular solid
σ	Engineering stress
σ_{el}^*	Elastic collapse stress
σ_{el}^*/E_s	Relative elastic collapse stress
σ_{UTS}	Ultimate tensile strength
σ_x	Stress in the x-direction (tensile)
σ_y	Stress in the y-direction (compressive)

I Chapter 1: Introduction

The goal of this study was to investigate the feasibility of manufacturing a novel active composite cellular structure which uses piezoelectric ceramic plates and metallic open bowtie cells. This new material could be used in surgical applications such as spinal fusion to accelerate bone healing, thus overcoming financial and health drawbacks faced by current implants.

I.1 Presentation of the problem

Advances in implant designs have been tremendous over the past fifty years in orthopaedics. The devices employed in the surgical reconstruction of hips, knees, shoulders or the spine present features obtained through decades of research. Those features, following constantly-refined design criteria, address the needs that will ensure successful healing in the majority of the cases. The principal design criteria are that the implant must support the physiological loads and share them with the surrounding tissues, remain in place once implemented and be biocompatible.

The devices need to be as adaptable as possible to fit the unique characteristics of each patient while meeting the above global requirements. This explains why there is so much variety among orthopaedic products. Cementless implants are devices impacted into bone instead of being “glued” with polymeric cement to bone. Cement-less implants such as spine spacers, hip stems, tibial plateau, artificial discs, screws

and plates share one particular characteristic. They all present external porous surfaces or macro texturing [1]. As it will be detailed in the following chapter, it was found that the surfaces of cement-less implants in contact with bone should offer more contact area to the living tissue to favor their mutual bonding. The outer surface of those implants first evolved from being smooth to be roughened. It was found that a network of pores was more efficient for the bonding with bone so implants were coated with layers of small beads or even mesh. By mimicking the trabecular bone architecture that surrounds the implant, the porous structure actually favors bony ingrowth and increases the chances of a long-term fixation of the device [1]. This feature alone does not guarantee the success of the implantation for every patient. There are still reports of failures that have led to painful and expensive revision surgeries despite the enhanced efficiency of porous coated implants in terms of implant stability overtime [2-4].

In 2004, 350,000 spinal fusions were performed in the United States and 600,000 annually are estimated by 2010 [5]. The number of fusions keeps increasing despite limitations and a success rate that ranges between 54% and 95% depending on the patient condition and the associated treatments [6-15]. Metabolic deficiencies caused by obesity, smoking, diabetes and spondylolysthesis jeopardize the success of spinal fusion. For the high-risk patient population presenting those deficiencies, a failed fusion can result in the formation of pseudoarthrosis, calcified fibrous tissues, instead of bone. The implant and tissues are consequently loosely bonded, which

endangers their stability and the patient's health. A delayed or non-existing fusion also increases the risks of medical device migration and subsidence, which present painful and dangerous consequences.

The pioneering works of Yasuda, Fukada and others helped to address this problem [16-19]. Those investigators demonstrated the existence and role of bioelectric phenomena (piezoelectricity and streaming potentials) in the maintenance of skeletal integrity [16- 24]. Two clinical techniques, electrical and electromagnetic stimulations, are now used to enhance the chances for osteogenesis (formation of bone) to occur at the surgical implantation site. Biochemical methods such as the injection of Bone Morphogenic Proteins (BMPs) have also been shown to enhance the success of fusion [25-26]. In ideal situations the synergetic roles of these bone growth stimulation techniques result in a very high spinal fusion success rate even for high-risk patients but also present drawbacks. First, they are not widely available because of their costs ($3,000 to $10,000) [31]. Health care insurance does not always cover the charges associated with the purchase and implementation of an electrical stimulator, which is in addition to the average $34,000 spinal fusion surgery bill [32,33]. Those devices also lengthen the time of surgery (implementation and removal), they increase the risk of infection, and they eventually induce aesthetic and comfort problems [2-4].

Since 32.2% of the US population over 20 is obese [34] and 21% of the US population over 60 presents a form of diabetes [35] the high-risk patient population is

non-negligible. It would be beneficial to develop a spinal implant material that could have the same stimulating capabilities as the electrical devices and chemical agents without their surgical and financial disadvantages [32].

In addition to being osteoconductive (favoring the development of bone), a key function of an orthopaedic implant is to provide mechanical stability and to transfer part of the load to the adjacent bone. This is needed if the device has to re-establish the functionality and, if sought, mobility of the defective joint it replaces as well as to stimulate bone formation. However, this goal cannot be completely fulfilled by current implants, which sometime fail because they induce stress shielding and subside. Stress shielding is a phenomenon that causes bone to locally resorb around the implant because the device supports the entire load and there is not enough mechanical stimulation of the bone. This is caused by the difference in mechanical properties, mainly stiffness, between the bone and the implant material. It is thus very important that the device should support but also gradually transfer a portion of the load to the surrounding living tissues so that their mechanical stimulation is maintained. Another problem caused by the difference in stiffness is the potential subsidence of the implant into bone. This causes a malfunction and further complications for the health of the patient. For instance, the subsiding of a spinal fusion cage could cause the reduction of the foramen hole between two vertebral bodies, which could lead to the pinching of nerves, a source of handicapping back pain. Finally, the longer it takes for new bone to form, the higher the risk of migration

of the implant. A device such as a cage, positioned between two vertebral bodies can move and clog the spinal canal, or compress nerves.

In summary, the population of candidates to spinal fusion who present high-risk of non-fusion keeps growing. Treatments and devices meant to increase the success rate of the surgical procedure present drawbacks and limitations that can be addressed by the design and development of new medical devices.

I.2 Solutions to overcome limitations

From an engineering perspective, improvements of the spinal fusion implants can be made at the mechanical and electromechanical levels. These would eliminate the drawbacks of and enhance the current techniques employed to provide mechanical and electrical stimulation of bone formation.

I.2.1 Piezoelectricity

Electrical stimulation is appropriate to enhance bone healing but its implementation is problematic and needs improvement. To address the limitations associated with electrical stimulation, it was hypothesized that the implant itself could integrate the stimulation system. With the development of piezoelectric films, ideas of transforming the mechanical energy produced while walking into electric energy emerged. In the 1980's several studies focused on the fabrication and testing of "piezoelectric" implants that no longer required an external battery pack and the necessary surgery to implement it [36-44]. Those devices auto-generated the current required for electrical stimulation on-site. Several patents and patent applications have been filed since then, proving that the interest is still important and the potential benefits appealing [45-48]. Despite the positive results obtained and the improvements in piezoelectric processes, no recent (last decade) peer-reviewed article on piezoelectric implants could be found. The fact that no orthopaedic company

manufactures such a device might indicate that there are still challenges and limitations to overcome. Some of the patented devices and their limitations are presented in more detail in the following chapter.

I.2.2 New materials and structures

The mechanical problems of stress shielding, subsidence, migration [49-56], and nonlinear behavior at small strains can be addressed by developing different materials and structures. Discoveries in the field of materials sciences have resulted in the fabrication of new plastics such as PEEK that can be as inert as ceramic and as strong as steel but with a stiffness close to that of bone. Another solution consists in modifying the structure of a material that is already satisfying. This technique has been exploited to create tantalum foam, titanium mesh, and cobalt-chromium sponge to serve as an osteoconductive spacer in spinal fusion procedures [57-59]. These biocompatible orthopaedic porous structures present mechanical properties close to those of trabecular bone that prevent the risks of stress shielding and subsidence. They thus have a positive influence on the healing rate and success of spinal fusion [57, 60, 61]. However, these current implants have only been developed to present porous surfaces and match certain mechanical parameters (modulus of elasticity, compressive strength) of the biologic tissue they interface with. The implants do not present an appropriate mechanical behavior at small strains that is critical to reduce crack formation and damage in bone. Studies showed that the bone formation, adaptation and repair are triggered by very small mechanical strains [62]. New

material and new structure could be combined to create a new cellular solid whose mechanical properties (parameters and behavior at small strains) could be tailored to match even more those of trabecular bone. It was hypothesized that this closer match in mechanical properties would enhance the mechanotransduction process and lead to a faster formation of bone thus reducing the risks of migration of the implant.

I.2.3 Need for improvement

Despite the positive reports concerning the efficacy of current implants, failures are still reported, highlighting some of their limitations. Also, more and more people turn towards surgery to alleviate their impairment caused by trauma or degeneration [63]. An enlarged patient population comprises younger persons who are active and want to remain so. The implants have therefore to last longer while being subjected to more strenuous loading conditions such as jogging and playing tennis. Consequently, the design inputs have changed and orthopaedic manufacturers have to make modifications in order for their products to meet the demands of the customers. These facts explain and support the need for a novel spinal fusion device to be developed. This new implant should be less expensive, widely available, and more efficient for both the active and the high-risk patients.

I.3 Proposal

I.3.1 Next generation of implants: combined stimulations

The design of the new device should build on what has been done so far. On the mechanical level, a phenomenological look at all the improvements achieved reveals that a porous material is beneficial to a successful healing and that the mechanical properties of the material are controlled by its porosity and structure. In this project, it was hypothesized that the mechanical properties of the novel implant (modulus of elasticity, yield strength, ultimate strength, resilience, stress-strain behavior at small strains) could be tailored via its structure. From experience, electrical stimulation has shown positive influence on bone healing and this could be implemented by embedding piezoelectric elements in the novel structure. A biomimetic implant should thus present a modulus of elasticity and strength similar to that of trabecular bone, a nonlinear stress-strain behavior at small strains, as well as electromechanical potential. It was hypothesized that these complementary properties would simulate even more the natural environment and could intensify cellular development and accelerate bone formation.

I.3.2 The project

The main objective of this project was to create a ductile cellular solid featuring a nonlinear mechanical behavior at small strains along with mechanical

parameters and an electromechanical behavior that could be tailored for orthopaedic applications.

As was demonstrated by Friis et *al.* [64], a re-entrant structure presents a nonlinear load-displacement relationship at small strains (up to 5%). A re-entrant structure, also called an auxetic structure, is a structure that has an apparent negative Poisson's ratio [65-70]. A bowtie cell (Figure 1-1) illustrates the re-entrant mechanism very clearly. A patent filled by Smith presents a composite structure consisting of piezoelectric ceramic rods compressed by a re-entrant polymeric foam [70]. Based on this invention, the concept of a biocompatible ductile and electroactive cellular solid could be created by combining a ferroelectric ceramic (for example barium titanate [40, 71, 72]) and a metal (titanium [73-77]). This novel structure could be prepared from a composite metal/ceramic material or from interfacing metallic and ceramic parts.

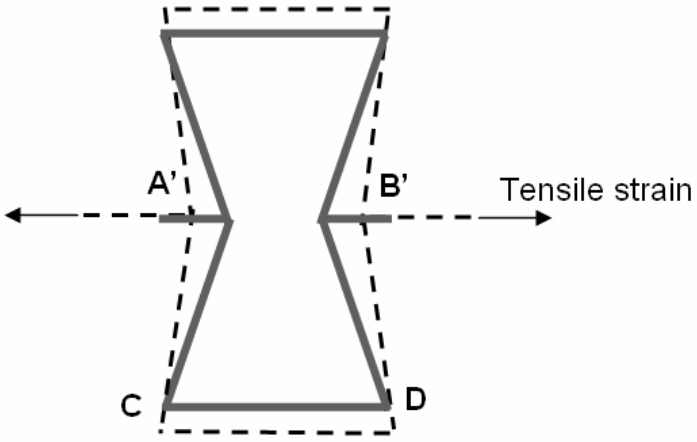

Figure 1-1. Schematic of a re-entrant open bowtie cell and illustration of its deformation under tensile strain (the shape of deformed cell is dashed)

The goal of this study was to provide proof that this conceptual novel structure can be fabricated. The principal challenges were the design of the porous re-entrant structure, the choice of materials and the testing of the targeted mechanical and electromechanical properties. Preliminary research revealed that a composite metal/ceramic material was not suitable because of its brittleness conferred by the ceramic inclusions. The focus was thus placed on a composite structure featuring metallic and ceramic parts. This implied that the properties of the interface between the different materials should be investigated because it could be a potential weak point, jeopardizing the integrity of the structure. Even though the main motivation for such a study was biomedical applications, the novel structure could be of interest to other engineering fields. Therefore, prototypes of various sizes were prepared to investigate if and how their properties could be controlled.

The overall hypothesis was that this new composite structure could be created and would display both controllable nonlinear mechanical behavior at small strains and piezoelectric properties. The first specific aim was then to verify if a re-entrant structure could be created and investigate its mechanical properties. The second specific aim was to study the effect of adding ceramic parts to the structure on its mechanical and electromechanical behaviors. Finally, the third specific aim examined the mechanical properties of a potential interfacing material. A thorough research of the literature provided evidence and support concerning the materials and methods

that could be employed to manufacture the novel composite structure. This is presented in the second chapter of this document. Chapter three to five develop in depth the investigations of specific aims one to three, respectively. Concluding remarks and appendices can be found after chapter five.

References

1. Martz E.O., Goel V.K., Pope M.H., Park J.B., Materials and Design of Spinal Implants—A Review, J. Biomed. Mater. Res. (Appl. Biomater.), Vol.38: 267–288, 1997
2. Österman H., Sund R., Seitsalo S., Keskimäki I., Risk of multiple reoperations after lumbar discectomy: a population-based study. Spine , Vol.28, No.6:621-627, 2003
3. Kane W.J., Facilitation of lumbosacral fusions by means of electronic bone growth stimulation. Presented at the Scoliosis Research Society, Seattle, 1979
4. Kucharzyk D., A controlled prospective outcome study of implantable electrical stimulation with spinal instrumentation in a high-risk spinal fusion population. Spine, Vol.5:465-469, 1999
5. Clemow A.J.T., Market Potential for an Artificial Disc Implant, Nexgen Spine Inc., http://www.nexgenspine.com/Market.htm (accessed 01/30/2008)
6. Meril A.J., Direct Current (DC) Stimulation of Allograft in Anterior and Posterior Lumbar Interbody Fusions. Spine, Vol.19:2393-2397, 1994
7. Kane W.J., Direct current electrical bone growth stimulation for spinal fusion. Spine, Vol.24:363-365, 1988
8. Rogozinski A., Rogozinski C., Efficacy of implantable bone growth stimulation in instrumented lumbosacral spinal fusion, Spine,Vol.21, No.21:2479-2483, 1996
9. Kucharzyk D., A controlled prospective outcome study of implantable electrical stimulation with spinal instrumentation in a high-risk spinal fusion population. Spine 5:465-469, 1999
10. Goodwin C.B., Brighton C.T., Guyer R.D., A double blind study of capacitively coupled electrical stimulation as an adjunct to lumbar spinal fusions. Spine, Vol.4, No.13:1349-1357, 1999
11. Mooney V., A randomized double-blind prospective study of the efficacy of pulsed electromagnetic fields for interbody lumbar fusions. Spine, Vol.15, No.7:708-712, 1990
12. Patient Demographics: Information about Orthopaedic Patients and Conditions, American Association of Orthopaedic Surgeons. http://www.aaos.org/Research/stats/Total%20Number%20of%20Spinal%20Fusion%20Patients%20Chart.pdf (accessed 01/30/08)
13. Patient Demographics: Information about Orthopaedic Patients and Conditions, American Association of Orthopaedic Surgeons. http://www.aaos.org/Research/stats/patientstats.asp (accessed 01/30/08)
14. Facts on Spinal Fusion, American Association of Orthopaedic Surgeons. http://www.aaos.org/Research/stats/Facts%20on%20Spinal%20Fusions.pdf (accessed 01/30/08)
15. Future Directions in musculoskeletal Research: A summary report of the AAOS Research Committee Panel Studies, p61, 2003.

http://www.aaos.org/Research/documents/panel_future_directions.pdf. (accessed 01/30/08)
16. Fukada E., Yasuda I., On the Piezoelectric Effect of bone, Journal of the Physical Society of Japan, Vol.12, No.10:1158-1162, 1957
17. McElhaney J.H., The charge distribution on the human femur due to load, Journal of Bone Joint Surgery, Vol.49A:1561, 1967
18. Marino A.A., Becker R.O., Piezoelectric effect and growth control in bone, Nature Vol.228:473, 1970
19. Bur A.J., Measurements of the dynamic piezoelectric properties of bone as a function of temperature and humidity, J. Biomechanics, Vol.9:495-507, 1976
20. Shamos M.H., Piezoelectric effect in bone, Nature, No.4862:81, 1963
21. Gu W.Y., Mao X.G., Rawlins B.A., Iatridis J.C., Foster R.J., Sun D.N., Weidenbaum M., Mow V.C., Streaming potential of human lumbar annulus fibrosus is anisotropic and affected by disc degeneration, J. Biomech., Vol.32, No.11:1177-1182, 1999
22. Friedenberg Z.B., Brighton C.T., Bioelectric potentials in bone, Journal of Bone and Joint Surgery, Vol.48A, No.5:915-923, 1966
23. Gross D., Williams W.S., Streaming potential and the electromechanical response of physiologically-moist bone. J. Biomech., Vol.15, No.4:277-95, 1982
24. Guzelsu N., Walsh W.R., Streaming potential of intact wet bone, J. Biomech. Vol.23, No.7:673-85, 1990
25. Wang J.C., Walsh M.C., BMP Improves Spinal Fusion http://www.spineuniverse.com/displayarticle.php/article1711.html (accessed 01/30/08)
26. Burkus, K.J., Clinical and Radiographic Outcomes of Anterior Lumbar Interbody Fusion Using Recombinant Human Bone Morphogenetic Protein-2. Total Spine Pre-Course Symposium. 2002.
27. Patel N., Can Bone Morphogenic Proteins Make a Positive and Sustained Impact on the U.S. and European Spinal Fusion Markets?, http://www.frost.com/prod/servlet/market-insight-top.pag?docid=21764169, 2004 (accessed 01/30/2008)
28. Polly D.W. Jr, Ackerman S.J., Shaffrey C.I., Ogilvie J.W., Wang J.C., Stralka S.W., Mafilios M.S., Heim S.E., Sandhu H.S., A cost analysis of bone morphogenetic protein versus autogenous iliac crest bone graft in single-level anterior lumbar fusion., Orthopedics, Vol.26, No.10:1027-37, 2003
29. Hodges S.D., Eck J.C., Humphreys S.C., Use of electrical bone stimulation in spinal fusion, J Am Acad Orthop Surg., Vol.11, No.2:81-88, 2003
30. M.A. Morone, H. Feuer, The use of electrical stimulation to enhance spinal fusion, Neurosurg Focus, Vol.13, No.6, Article 5:1-7, 2002
31. Bridwell K.H., Anderson P.A., Boden S.D., Vaccaro A. R., Wang J.C., What's new in Spine Surgery, J. Bone Joint Surgery Am., Vol.89:1654-1663, 2007

32. Deyo R.A., Nachemson A., Mirza S.K., Spinal-Fusion Surgery – The Case for Restraint, The New England Journal of Medicine, Vol.350, No.7:722, 2004
33. Deyo R.A., Gray D.T., Kreuter W., Mirza S., Martin B.I., United States trends in lumbar fusion surgery for degenerative conditions, Spine, Vol.30, No.12:1441-1445, 2005
34. Ogden C.L., Carroll M.D., Curtin L.R., McDowell M.A., Tabak C.J., Flegal K.M., "Prevalence of overweight and obesity in the United States, 1999-2004". JAMA, Vol.295, No.13:1549-1555, 2006
35. National Diabetes Information Clearinghouse, Statistics. http://diabetes.niddk.nih.gov/dm/pubs/statistics/index.htm#7 (accessed 12/05/07)
36. Park J.B., von Recum A.F., Kenner G.H., Kelly B.J., Coffeen W.W., Grether M.F., Piezoelectric ceramic implants: a feasibility study, Journal of Biomedical Materials Research, Vol.14, No.3:269-277, 1980
37. Park J.B., Kelly B.J., Kenner G.H., von Recum A.F., Grether M.F., Coffeen W.W., Piezoelectric ceramic implants: in vivo results, Journal of Biomedical Materials Research, Vol.15, No.1:103-110, 1981
38. Cochran G.V., Johnson M.W., Kadaba M.P., Palmieri V.R., Mahaffey G., Design considerations in development of a prototype, piezoelectric internal fixation plate: a preliminary report, Journal of Rehabilitation Research and Development, Vol.24, No.2:39-50, 1987
39. Manouel M., Pearlman H.S., Belakhlef A., Brown T.D., A miniature piezoelectric polymer transducer for in vitro measurement of the dynamic contact stress distribution, J. Biomech., Vol.25, No.6:627-635, 1992
40. Jianqing F., Huipin Y., Xingdong Z., Promotion of osteogenesis by a piezoelectric biological ceramic, Biomaterials, Vol.18, No.23:1531-1534, 1997
41. Willner I., Willner B., Biomaterials integrated with electronic elements: en route to bioelectronics, TRENDS in Biotechnology, Vol.19, No.6:222-230, 2001
42. Gobin P.F., Jayet Y., Guy P., Godin N., Morin M., Gauthier C., Kleber X., Reynaud P., Courbon J., Cavaille J-Y., Smart materials group at the national institute of applied science: Recent data and trends, Materials Transactions, Vol.45, No.2:166-172, 2004
43. Cochran G.V., Kadaba M.P., Palmieri V.R., External ultrasound can generate microampere direct currents in vivo from implanted piezoelectric materials, Journal of Orthopaedic Research, Vol.6, No.1:145-147, 1988
44. US Patent 5,032,129 Active Implant, Kurze P., Krysmann W., Knoefler W., Graf H-L., Bethmann W., Horst H., 1991
45. US Patent 5,298,602 Polymeric Piezoelectric Material, Shikinami Y., Hata K., 1994
46. US Patent 5,684,061 Bone Inducing Material, Ohnishi T., Moriyama N., 1997
47. US Patent 6,143,035 Implanted Bone Stimulator and Prosthesis System and Method of Enhancing Bone Growth, McDowell C.S., 1999

48. US Patent 6,571,130 B1 Medical Implant with Piezoelectric Material in Contact with Body Tissue, Ljungstrom K., Nilsson K., Lidman J., Kjellman C., 2003
49. Tsantrizos A., Baramki H.G., Zeidman S., Steffen T., Segmental Stability and Compressive Strength of Posterior Lumbar Interbody Fusion Implants, Spine, Vol.25, No.15:1899–1907, 2000
50. Martz E.O., et al., Materials and Design of Spinal Implants: a review, J Biomed Mater Res (Appl Biomater), Vol.38:267-288, 1997
51. Wilke H.J, Kettler A., Goetz C., Claes L., Subsidence Resulting From Simulated Postoperative Neck Movements: An In Vitro Investigation With a New Cervical Fusion Cage, Spine, Vol.25, No.21:2762–2770, 2000
52. Thébault M-A., Moreau S., Assad M., Rivard C-H., Leroux, M.A., Cervical Interbody Fusion Devices: A Load-Induced Subsidence Resistance Evaluation, Proceedings of the 7th world biomaterials congress, Sydney, Australia, 17–21 May, 2004
53. McAfee P.C., Cunningham B.W., Lee G.A., Orbegoso C.M., Haggerty C.J., Fedder I.L., Griffith S.L., Revision strategies for salvaging or improving failed cylindrical cages, Spine.Vol.24, No.20:2147-53, 1999
54. Chen L., Yang H., Tang T., Cage Migration in Spondylolisthesis Treated With Posterior Lumbar Interbody Fusion Using BAK Cages, Spine, Vol.30, No.19:2171–2175, 2005
55. Uzi E.A., Dabby D., Tolessa E., Finkelstein J.A., Early Retropulsion of Titanium-Threaded Cages After Posterior Lumbar Interbody Fusion: A Report of Two Cases, Spine, Vol.26, No.9:1073–1075, 2001
56. Elias W.J., Simmons N.E., Kaptain G.J., Chadduck J.B., Whitehill R., Complications of posterior lumbar interbody fusion when using a titanium threaded cage device, J. Neurosurg (Spine 1) Vol.93: 45-52, 2000
57. Zardiackas L.D., Structure, Metallurgy, and Mechanical properties of a porous Tantalum foam, Journal of Biomedical Material Research, Vol.58, No.2, pp: 180-187, 2001
58. Rao G., Titanium foams fabricated for bone-tissue engineering applications, Research/Researchers MRS bulletin, p940, 2002 [www.mrs.org/publications/bulletin] (accessed 11/18/08)
59. Waisbrod H., Treatment of metastatic disease of the spine with anterior resection and stabilization by means of a new cancellous metal construct: a preliminary report, Arch. Orthop. Trauma Surg., Vol.107:222-225, 1988
60. Shimko D.A., et al., Effects of porosity on the fluid flow characteristics and mechanical properties of tantalum scaffolds, Journal of biomedical Materials Research Part B, Vol.73B, No.2: 315-324, 2005
61. Toth J.M., Turner A.S., Kabo J.M., Linda E.A., Porous Tantalum metal as a biologically advantageous spinal fixation material, October 24, 1996, [http://www. Spine.org/conf_abstracts_10_20_96/338-Toth.html]
62. Morgan E.F., Yeh O.C., Chang W.C., Keaveny T.M., Nonlinear behavior of trabecular bone at small strains, J Biomech Eng. 2001 Feb;123(1):1-9

63. Clemow A.J.T., Challenges in spinal repair and regeneration, Presentation at the Society For Biomaterials, Chicago 2007
64. Friis E.A., Lakes R.S., Park J.B., Negative Poisson's ratio polymeric and metallic materials, Journal of Materials Science, Vol.23:4406-4414, 1988
65. Lakes R.S., Foam structures with a negative Poisson's ratio, Science, Vol.235:1038-1040, 1987
66. Yang W., Zhong-Ming L., Shi W., Xie B.-H., and Yang W.-B., Review on auxetic materials, Journal of Materials Science, Vol.39:3269-3279, 2004
67. Caddock B.D., Evans K.E., Microporous materials with negative Poisson's ratios: I. Microstructure and mechanical properties, J. Phys. D: Appl. Phys., Vol.22: 1877-1882, 1989
68. Caddock B.D., Evans K.E., Microporous materials with negative Poisson's ratios: II. Mechanisms and interpretations, J. Phys. D: Appl. Phys., Vol.22: 1883-1887, 1989
69. Smith F.C., Scarpa F., Chambers B., The electromagnetic properties of re-entrant dielectric honeycombs, IEEE microwave and guided wave letters, Vol.10, No.11: 451-453, 2000
70. US Patent 5334903 Composite piezoelectrics utilizing a negative Poisson ratio polymer, Smith W.A., 1994
71. Park Y.J., Hwang K.S., Song J.E., Ong J.L., Rawls H.R., Growth of calcium phosphate on poling treated ferroelectric $BaTiO_3$ ceramics. Biomaterials, Vol.23:3859-3864, 2002
72. Park J.B., et al., Piezoelectric ceramic implants: in vivo results, Journal of Biomedical Materials Research, Vol.15, pp:103-110, 1981
73. Giavaresi G., Giardino R., Ambrosio L., Battiston G., Gerbasi R., Fini M., Rimondini L., Torricelli P., In vitro biocompatibility of titanium oxide for prosthetic devices nanostructured by low pressure metal-organic chemical vapor deposition, Int. J. Artif. Organs., Vol.26, No.8:774-80, 2003
74. Simon M., Lagneau C., Moreno J., Lissac M., Dalard F., Grosgogeat B., Corrosion resistance and biocompatibility of a new porous surface for titanium implants, Eur. J. Oral. Sci., Vol.113, No.6:537-545, 2005
75. Carlsson L., Röstlund T., Albrektsson B., Albrektsson T., Brånemark P.I., Osseointegration of titanium implants, Acta Orthop. Scand., Vol.57, No.4:285-289, 1986
76. Kasemo B., Biocompatibility of titanium implants: surface science aspects, J. Prosthet. Dent., Vol.49, No.6:832–837, 1983
77. Huang N., Yang P., Leng Y.X., Chen J.Y., Sun H., Wang J., Wang G.J., Ding P.D., Xi T.F., Leng Y. Hemocompatibility of titanium oxide films, Biomaterials, Vol.24: 2177–2187, 2003

II Chapter 2: Background

This chapter presents in more detail the concepts and statements that were introduced in the first chapter to explain the motivation of the present project. Basic concepts of piezoelectricity and auxeticity are first described then the requirements for orthopaedic implants, their status and limitations are presented. Finally, a brief overview of electronic-based robotic deposition technique is given.

II.1 Piezoelectricity

II.1.1 History and description

In 1880, Pierre and Jacques Curie demonstrated a remarkable feature of some materials: the ability to generate electric charges when mechanically loaded. This phenomenon was later coined the piezoelectric effect from the Greek word “piezin” which means “to press”. It concerns a group of dielectric materials called ferroelectrics, by analogy to magnetism, whose domain structure can be modified by an electric field. Out of the 32 crystal classes, 11 are centro-symmetric and 21 non-centro-symmetric. The centro-symmetric crystals have a symmetrical repartition of cations and anions so they cannot present a dipole moment and cannot be piezoelectric. Twenty of the 21 non-centro-symmetric crystals are piezoelectric and 10 are polar. Those 10 polar crystals are both pyroelectric and piezoelectric since electric charges are created when they are heated and squeezed, respectively. These

characteristics are intrinsic to the structure of the crystal and can be altered by several parameters such as temperature and pressure [1,2]. The most common piezoelectric crystal structure is the perovskite structure ABO3 displayed on Figure 2-1.

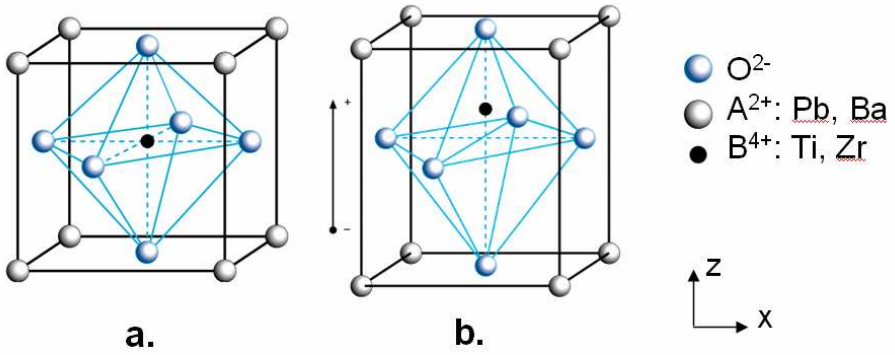

Figure 2-1. Example of a perovskite structure: (a) above and (b) below the Curie temperature. The cubic lattice (a) presents a symmetrical arrangement of positive and negative charges. The tetragonal lattice (b) has an electric dipole moment because the symmetry between the charges is broken [2]

A polar crystal naturally displays a dipole moment. Non-centro-symmetric crystals will also become polarized or will undergo a change in polarization when stressed. This is actually known as the direct piezoelectric effect. But the same crystal can be strained when subjected to an electric field, which is known as the converse piezoelectric effect. As mentioned above, temperature considerably influences the piezoelectric characteristic of ferroelectric crystals. Above a certain value called the Curie temperature, the crystals have a symmetrical cubic structure (Figure 2-1a) which does not allow for the existence of a dipole moment. Below the Curie temperature, crystals present a tetragonal or rhombohedral structure. The central B^{4+}

atom is no longer at the intersection of the plans of symmetry (the center of the structure). Therefore the centers of the positive and negative charges do no longer coincide. This lack of symmetry shown in Figure 2-1b generates an electric dipole moment.

barium titanate presents such a structure and since it features a natural polarization, this material is classified as a ferroelectric. It appears obvious that the piezoelectric effect of ferroelectric materials depends on their atomic structure. Consequently, applying a stress in one or the other direction of the unit cell can thus have different results. For instance, if the unit cell is compressed in the X-direction, the atom B^{4+} will move up even more thus increasing the dipole moment (Figure 2-1b). On the other hand, if it is compressed in the Z-direction, this atom will move down thus decreasing the dipole moment. There exist directions of compression that will result in no change at all in the dipole moment [3].

Each unit cell in the crystal presents a local dipole moment and adjoining dipoles that are aligned form a Weiss domain. Each domain presents a net dipole moment and a net polarization. Most of polycrystalline materials consist of crystallites (small single crystals) held together by thin layers of amorphous solid. Within and between the crystallites, the neighboring Weiss domains are randomly oriented so that there is no overall polarization of the crystal (Figure 2-2, Figure 2-3a). Nevertheless, it is possible to alter the direction of polarization in the crystallites to give the crystal an overall polarization. This process is called poling. The domain

structure is generated by the minimization of internal energy by local charge displacement. If sufficient time is allowed for wall mobility, an equilibrium configuration is established. To balance the domain wall energy, 90° and 180° domains are created through cooperative twinning in adjacent grains and are maintained by high internal stresses. Poling consists of subjecting the material to a very high DC electric field at a temperature slightly below the Curie one to rotate and reverse the 90° and 180° domains respectively. Application of a mechanical stress only results in the 90° domains rotation because of the anisotropy of the tetragonal structure that requires a change in shape.

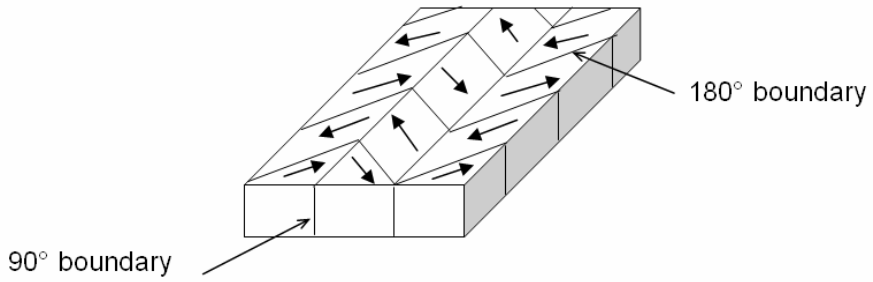

Figure 2-2. Schematic diagram of 90° and 180° domains [2]

The change in orientation is caused by ionic movement in specific crystallographic directions. Through the poling treatment, the domains most nearly aligned with the electric field expand so the crystal lengthens in the direction of the field while contracts in the transversal directions (Figure 2-3b). The dipoles are locked into a configuration of near alignment and remain so when the electric field is removed and the crystal cooled (Figure 2-3c). The dipole alignment is not perfect and

total because the polarization is only allowed along preferential directions depending on the crystallographic class. For instance, the orthorombic and rhombohedral structures present six and eight spontaneous polarization direction, respectively. The ferroelectric material that was thus poled, becomes piezoelectric [1, 4, 5].

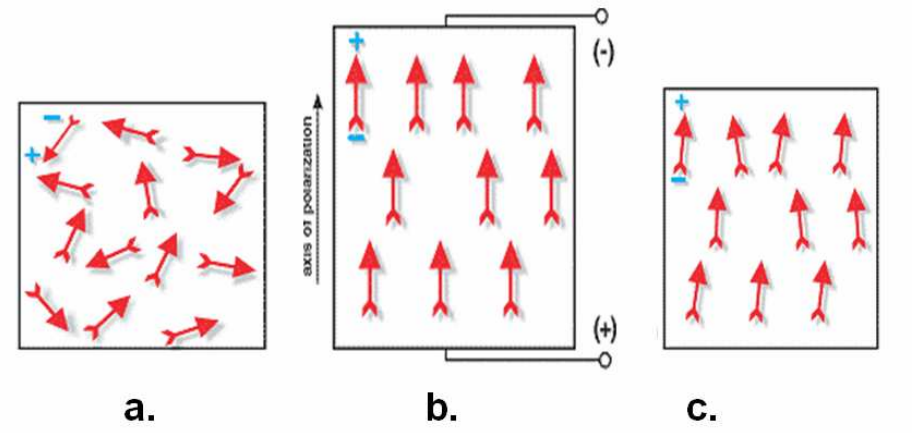

Figure 2-3. Poling treatment of a ferroelectric material, (a) random orientation of polar domains prior to polarization, (b) Polarization in DC electric field, the specimen changes dimensions and shape (c) Remanent polarization and modified shape and dimensions after removal of electric field [2]

Changes in the polarization, caused by the direct effect, manifest themselves in the appearance of electric charges on the crystal surface and, in the case of a closed circuit, in a current. However, because of the dielectric constant of the material and the resistance of the circuit compared to the smallness of the charges produced, the current is very low even if the voltage is very high. Tension and compression generate voltages of opposite polarity and in proportion to the applied force. But the relationship is linearly proportional only up to a material-specific stress. On the other hand, when an electric voltage is applied to a poled piezoelectric material, the Weiss

domains increase their alignment proportional to the voltage. The result is a change in dimensions (expansion, contraction) of the material. By using an alternative signal, a crystal can thus be made to vibrate as it is the case for quartz crystals in a digital watch. When operated far below the resonant frequency, a piezoelectric material behaves as a capacitor where displacement is proportional to charge (first order magnitude).

II.1.2 Scientific explanation

The electromechanical properties of piezoelectric materials can be theoretically demonstrated with equations derived from mechanical and electrical laws [6-9]. The notations employ a great number of symbols and parameters, some of which are characteristic of and permit us to distinguish piezoelectric materials. The electromechanical relationship is simply explained in mathematical terms in equations {2-1} to {2-4}. The electrical parameters such as the electric field E, and electric displacement D, are linked to the stress and strain via various factors such as the piezoelectric coefficients (d, g), the dielectric constant (εX), and the stress (X) .

The electric displacement is induced by an electric field and is also linearly related to any applied stress so that both effects can add up to yield:

$$D = d \,.\, X + \varepsilon^{X} \,.\, E \qquad \{2\text{-}1\}$$

Where D = electric displacement or charge density [C/m^2]
d = piezoelectric charge coefficient [C/N]
X = stress [N/m^2]
ε^X = permittivity under constant stress [F/m]
E = electric field [V/m]

The mechanical strain is related to the mechanical stress by the compliance (inverse of the elastic modulus) and is also induced when a polar crystal deforms under the influence of an electric field. Thus, both effects also add up as follows:

$$x = s^E . X + d . E \quad \{2\text{-}2\}$$

Where x = strain
s^E = elastic compliance at constant electric field [m^2/N]

Those two equations can be manipulated to yield other useful expressions involving different factors.

$$E = -g . X + D/ \varepsilon^X \quad \{2\text{-}3\}$$

$$x = s^D . X + g . D \quad \{2\text{-}4\}$$

Where g = piezoelectric voltage coefficient [V.m/N]
s^D = elastic compliance at constant electric displacement [m^2/N]

An additional equation can be derived from those above to yield the relationship between the two piezoelectric coefficients.

$$d = g \cdot \varepsilon_r \cdot \varepsilon_0 = g \cdot \varepsilon^X \qquad \{2\text{-}5\}$$

Where ε_r = relative permittivity (dielectric constant)
ε_0 = permittivity of free space (8.85x10-12) [F/m]

Finally, the direct piezoelectric effect is simply a transformation of mechanical energy into electrical energy while the electrical-to-mechanical transformation is termed the inverse – or converse – piezoelectric effect. Another set of equations was then written to express the outcome of such a transformation. The symbol for the outcome was chosen as 'k^2' and is known as the coupling coefficient. Its mathematical expression can be derived from the above equations as shown in equations {2-6) and {2-7}.

$$s^D = s^E \cdot (1 - k^2) \qquad \{2\text{-}6\}$$

$$k^2 = d^2 / (s^E \cdot \varepsilon^X) \qquad \{2\text{-}7\}$$

The coupling coefficient 'k2' indicates the efficiency of the energy conversion in the material. For an electrically stressed component, 'k2' is the mechanical energy restituted over the total energy stored. For a mechanically stressed component, 'k2' is the electrical energy restituted over the total energy stored. Since there cannot be a perfect conversion of energy, there are losses. Those losses, which can be measured,

are intrinsic to the very nature of the piezoelectric material. So the loss and the quality factors are often reported along with the piezoelectric and the coupling coefficients.

II.1.2.1 Direction dependence

Since a poled piezoelectric material is anisotropic, the piezoelectric coefficients d and g relate to both the direction of the applied mechanical or electrical force and the directions perpendicular to the applied force. Consequently, the constants are not scalars but tensors and have two subscripts. The first subscript indicates the poling (or the applied field) direction. The second subscript is the direction of the applied stress (or the induced strain). Subscripts 1, 2 and 3 represent the X, Y and Z directions respectively, while subscripts 4, 5 and 6 represent the shear about these axes. By convention the poling axis is taken as the Z-direction (Figure 2-4). On Figure 2-5, for configuration (a), the piezoelectric coefficients will bear the subscripts 33 while for configuration (b), the subscripts will be 32 (or equivalently 31).

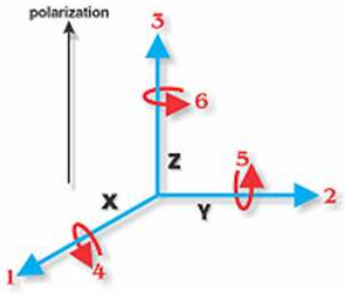

Figure 2-4. Directions of forces affecting a piezoelectric element [9] www.americanpiezo.com

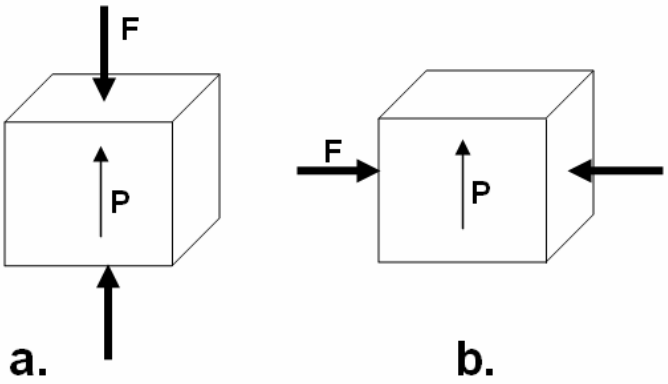

Figure 2-5. Examples of mechanical loading F parallel (a) or perpendicular (b) to the poling direction (P) of a piezoelectric element

II.1.3 Applications

Polycrystalline materials displaying piezoelectric properties such as ceramics (quartz) are widely used because they are physically strong, chemically inert, inexpensive to manufacture and their composition, shape and dimensions can be

tailored. Nowadays, they are grown artificially and are the principal components of sensors and transducers. Force and displacement sensors (accelerometers, sonar), ultrasound-generating and control positioning devices, laser optics, spark ignitors and valves actuators are a few examples. Quartz, metal-oxide-based ceramics such as PZT (lead zirconium titanate) and $BaTiO_3$ (barium titanate) are the primary piezoceramics [6-8]. But the range of applications of piezoelectric materials has been broadened thanks to piezopolymers. These are more ductile than their ceramic counterparts and so can be employed in situations where the shape and geometry of the actuator is intricate. For instance, a thin film of piezopolymer controls the zooming motion of a digital camera and electrets were wrapped around fractured bones to enhance their healing [10].

II.2 Negative Poisson's Ratio – Auxeticity

As mentioned earlier, an artificial structure displaying a nonlinear mechanical behavior at small strains to mimic that of the living tissue is sought. It is possible to prepare such a structure with existing and employed biomaterials by conferring an apparent negative Poisson's ratio on it, and thus making it auxetic (or re-entrant). The first part of this sub-chapter defines the Poisson's ratio and how it is measured. The second part is dedicated to defining auxeticity and its advantages.

II.2.1 Definition of Poisson's ratio

Poisson's ratio, named after Simeon-Denis Poisson (French mathematician, engineer and physicist) is defined as the opposite of the transverse strain divided by the longitudinal strain (equation {2-8}).

$$\nu = -\frac{\varepsilon_{trans.}}{\varepsilon_{long.}} \qquad \{2\text{-}8\}$$

Where ν = Poisson's ratio
$\varepsilon_{trans.}$ = transverse strain
$\varepsilon_{long.}$ = longitudinal (or axial) strain

It is thus a material property that relates the modulus of elasticity (*E*), the shear modulus (*G*) and the bulk modulus (*K*).

$$G = \frac{E}{2.(1+\nu)} \qquad \{2\text{-}9\}$$

$$K = \frac{E}{3.(1-2.\nu)} \qquad \{2\text{-}10\}$$

These equations show that Poisson's ratio affects the material's response to shear, linear strain and change in volume. In other words, it plays a role in the control of the material's mechanical behavior. Homogeneous isotropic elastic materials experience a transversal shrinking when stretched (Figure 2-6a) and a transversal widening when compressed longitudinally (Figure 2-6b). The most common materials such as metals and polymers have a positive Poisson's ratio around 0.3 and 0.4, respectively. But this parameter does not need to be positive. In order to respect the conservation of energy, it has been shown that the Poisson's ratio of isotropic elastic materials has to take a value between -1 and +0.5 [11].

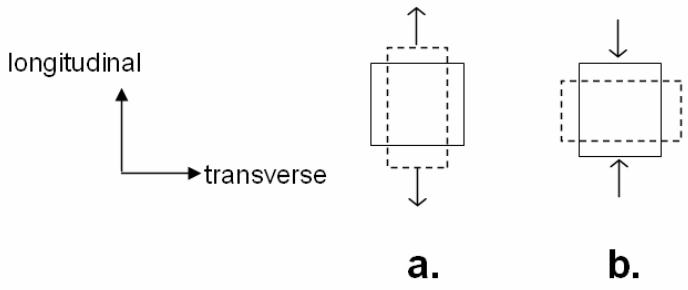

Figure 2-6. Illustration of the effects of a positive Poisson's ratio under tension (a) and compression (b) (The shape of the deformed object is dashed)

II.2.1.1 Measurement of Poisson's ratio

As defined in the above paragraph, the Poisson's ratio cannot be directly measured. It requires the determination of measurable quantities. For instance,

measuring the axial and transverse displacements of a specimen subjected to uni-axial tension or compression yields the corresponding strains and their ratio. However, since the Poisson's ratio is an intrinsic property of every structure, it can be found in many equations involving mechanical properties and can thus be deduced from the measurement of other parameters yielded by ultrasonic sound wave tests or interferometric stress pattern analysis, for instance. The preferred mode of determination remains the measurement of strains. But, there are numerous ways of determining strains, which can be classified in two broad categories, contacting and non-contacting methods.

II.2.1.2 Contacting methods

The oldest contacting method consists in affixing a transverse extensometer to the specimen to measure the transverse displacement during the test. Another extensometer, usually built in the testing system, permits to measure the axial displacement. The extensometers, often LVDTs (Linear Voltage Displacement Transducers) are linked to a data acquisition system. This method requires the accurate measurement of the specimen's dimensions prior to the test, so that the strains can be calculated.

Another contacting method consists in implementing strain gauges (uniaxial, 90-rosette or rosette) on the specimen. The strain gauges are hooked to a Wheatstone bridge module and a data acquisition system. This technique does not demand any calculation and is very useful for evaluating the strains locally.

Finally, an original technique employed by Krause et *al.* [12] consisted in measuring the volume change of liquid mercury surrounding the object while it is being compressed. The researchers reported that the Poisson's ratio could be estimated within an error of 0.005. However ingenious it is, this technique requires the submersion of the specimen in a toxic substance and was mainly developed for materials undergoing large strains. In addition, piezoelectric measurement would not be possible in this method since the conductive mercury would shunt all connections.

II.2.1.3 Non-contacting methods

The non-contacting methods were made possible by technological improvement and were motivated by the basic need to avoid any influence of the results caused by the presence of the measuring device. Those technological improvements were in the field of optics and yielded optical methods to measure the Poisson's ratio. Indeed, light is weightless and does not induce any extra mechanical load when pointed at an object. With the development of laser techniques and equipment, it was possible to point a focused beam of known wavelength onto the specimens under test. The procedure is very simple in theory: a light of known wavelength is emitted by a source, reflected by the object under test and received by captors. The displacement or deformation of the object under test is derived from the measurement of the traveling time of light between emission and reception. This was,

until recently, too intricate to implement because of the cost and complexity constraints of the light source and the data acquisition system required.

Another method was based on cinematographic techniques, in which images of the specimen are taken at several time intervals and analyzed to evaluate the movement of the specimen. The displacement can thus be calculated from frame to frame. This technique can be enhanced by the use of a speckle pattern, instead of a dot or stripes, “painted” on the object under test, and high-speed CCD cameras. Then a software program is employed for image analysis.

Interferometry as well as photoelasticity techniques have also been employed. Those techniques are identical to the one described above except that the speckle pattern is replaced by interferometric fringes or stress contours, respectively.

II.2.1.4 Limitations of contacting and non-contacting methods

Each and every one of those techniques has limitations. The sensitivity and resolution as well as the cost and ease of use are intrinsic to each piece of equipment and associated process. However, the methods will be more or less affected by the characteristics of the object under test. For instance, it might not be possible to use an extensometer if the specimen is too small. Also, strain gauges and speckle patterns may not be able to be implemented on an object with no continuous external surface (foam). This is also a problem if the specimen has no surface to reflect the incident light employed with the laser technique. Furthermore, even if a method seems to be

adequate, the measurements can still be biased because of calibration or implementation errors. For example, strain gauge data are influenced by a gauge misalignment and the presence of bending moments in addition to the axial force.

Finally, certain of those techniques are not suitable because of the type of mechanical test associated with them (vibration or bending instead of uni-axial compression). Despite their advantages and drawbacks, every method will be the best in given particular conditions. It is up to the researchers to figure which technique is the most suitable for their needs. The methods described above are applicable whether the Poisson's ratio to measure is positive or negative. However, this just illustrates how important it is to fully characterize the structure under test to choose the most appropriate technique.

II.2.2 Definition of Auxeticity

The term 'auxetic' comes from the greek word "auxesis" which means "increase, growth". It was used by Evans to designate materials that were experiencing a transversal expansion when stretched longitudinally. This behavior is contrary to that of an ordinary rubbery material that is why auxetic materials are also called dilatational or anti-rubber. Dr. Roderic Lakes was the first to show evidence of such a behavior in polymeric foam structures [13]. Through diverse theoretical and experimental studies, Lakes et al. [14,15] showed that the Poisson's ratio is governed by three parameters:

- The presence of rotational degrees of freedom
- Non-affine deformation kinematics
- The anisotropy of the structure

The present work is concerned only with non-affine deformations resulting in a structure having a negative Poisson's ratio, which provides the structure with a non-linear mechanical behavior. Non-affine deformation refers to an inequal deformation of a structure, i.e. parts of the structure distort more than others when the whole structure is subjected to a homogeneous global strain. A negative Poisson's ratio (NPR) finds its roots in the type of structure. This point can be illustrated by considering the two structures provided on Figures 2-7 and 2-8. Figure 2-7 represents the basic unit cell of standard honeycomb structures, a hexagon. On Figure 2-8 the schematic cell, referred to as a bowtie structure, is simply obtained by protruding four of the hexagon cell struts inward; hence the adjective "re-entrant" which is synonymous with auxetic. When a tensile strain is applied to two opposite nods, the other nods of the hexagon get closer to one another (Figure 2-7-b). The exact contrary occurs to the bowtie cell as shown on Figure 2-8-b. The non-affine deformation becomes evident when considering what happens to the distances A-B and C-D; the distance A-B becomes the longer open segment A'-B' while the segment C-D remains unchanged.

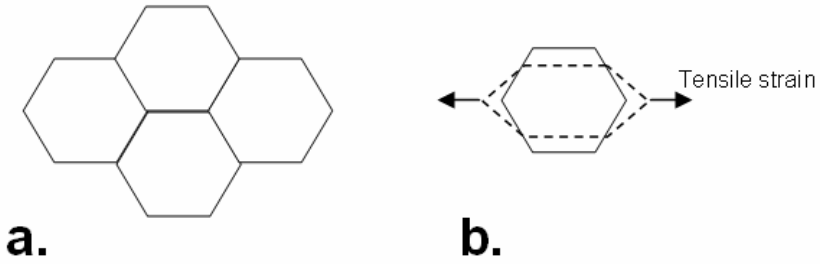

Figure 2-7. (a) Hexagonal cells forming a honeycomb structure and (b) illustration of the deformation of a cell subjected to a tensile strain (the shape of deformed cell is dashed)

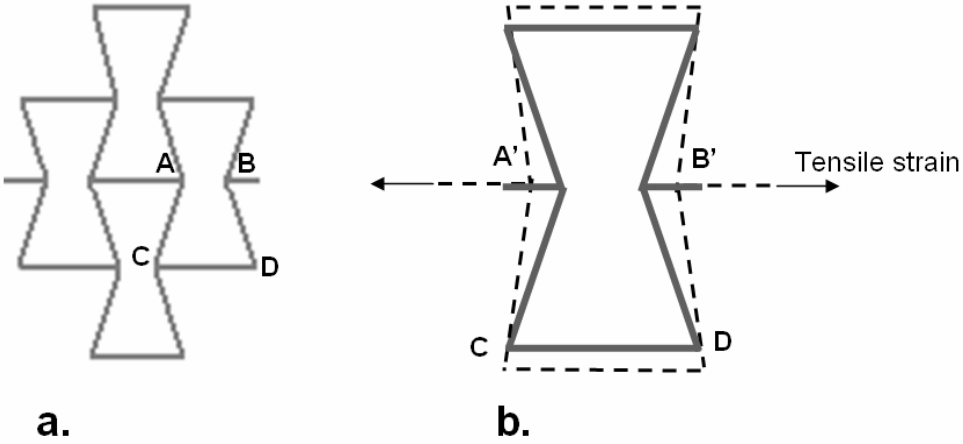

Figure 2-8. (a) Re-entrant structure formed of bowtie cells and (b) illustration of the deformation of a bowtie cell subjected to a tensile strain (the shape of deformed cell is dashed)

One can clearly understand that the principles illustrated in Figures 2-7 and 2-8 remain the same regardless the size of the unit cell. This is so because the theory of elasticity contains no characteristic length scale. Moreover, since the negative Poisson's ratio of the cells of Figure 2-8 is a result of their bowtie arrangement, they

could be made of a material such as copper or titanium, which presents a positive Poisson's ratio.

Cellular re-entrant structures can be obtained from existing conventional ones. Dr. Lakes elaborated on this observation and thought of two processes to prepare auxetic structures from standard cellular materials, depending on the nature of the base material (metallic or polymeric). In both cases the goal of the process is to deform partially the basic unit cells that compose the structure so that some ribs (or struts or segments) protrude permanently inward as was done to produce a bowtie from a hexagon. The two processes investigated by Dr. Lakes are:

- Triaxial compression in a heated mold for thermoplastic foams
- Progressive plastic deformation (compression) in the three orthogonal directions for metallic foams.

There is of course an interest to manipulate materials this way. Several studies [13] have investigated the properties and potential applications of such modified structures. Auxetic (or re-entrant) foams were found to have enhanced mechanical properties:

- Resilience
- Plane strain
- Fracture toughness
- Shear modulus

- Indentation resistance
- Acoustic response

Despite a decrease in modulus of elasticity, those superior properties were obtained with re-entrant foams presenting a completely random structure. In theory, controlling the structure would result in a higher control of such properties. However, despite their not-yet-demonstrated advantages, re-entrant structures remain an abstraction because they are very intricate to manufacture. The honeycomb making process could be modified to produce a bowtie panel but manufacturers have not taken the step most likely because of the monetary investment required. Progresses in solid free form printing allow preparing prototypes of complex three-dimensional (3D) re-entrant structures. The following section describes the novel 3D-printing process developed by Dr. James Smay at Oklahoma State University.

II.3 Electronic-Based Robotic Deposition

II.3.1 Definition

Extrusion-Based Robotic Deposition or EBRD, is one of many solid free form fabrication (SFF) techniques. SFF refers to the assembly of three-dimensional objects without the need for tools to remove mater or molds to shape it. EBRD falls into the category of additive SFF, which means that only the material required for the construction of the desired object is used. This material is selectively deposited in a controlled manner via the computer programming of the pattern.

Other additive SFF methods such as stereo lithography [16], selective laser sintering [17, 18], 3-D printing (3DP) [19-30], laminated object manufacturing [31, 32], ink jet printing [33], and laser engineered net shaping have been successful in the preparation of scaffolds. However, progresses in those techniques and more particularly in the combination of the materials employed can give them an edge over conventional manufacturing techniques.

EBRD consists of extruding a continuous filament of mater through a deposition nozzle. The extruded material or ink is deposited on a two-dimensional fashion. Then the deposition nozzle is moved up before starting the deposition of a new layer. This takes place in a bath of neutral synthetic oil. The oil protects the slurry materials (ink) from oxidation. Once the deposition has been completed, the green body is cured and sintered in a furnace to solidify. The last enhancements in

this SFF technique come mainly from the development of colloidal inks employed as the base material. The formulation of the ink has to be such that it remains viscous enough to be extruded but it has to solidify enough in a short time to provide support for the other layers (Figure 2-9). This rapid partial solidification allows printing compact solids (Figure 2-9a) and cellular solids of staked (Figure 2-9b) or crossed layers (Figure 2-9c). The use of colloidal inks presents several advantages over the other techniques. Metals, ceramics, and polymers can be employed in their powder form to prepare colloidal inks. This is appealing for the processing of nanomaterials. The ink formulation also grants the EBRD method other advantages such as near room temperature processing and near neutral pH. Finally, advances in machining techniques and tools permitted the production of very small deposition nozzles (200 micron diameter) and mixing chambers. Colloidal inks of different materials, a metal and a ceramic for instance, can thus be injected into a mixing chamber before the composite is extruded. This confers a great potential for in-situ blending that can be employed for a three-dimensional grading of materials and properties.

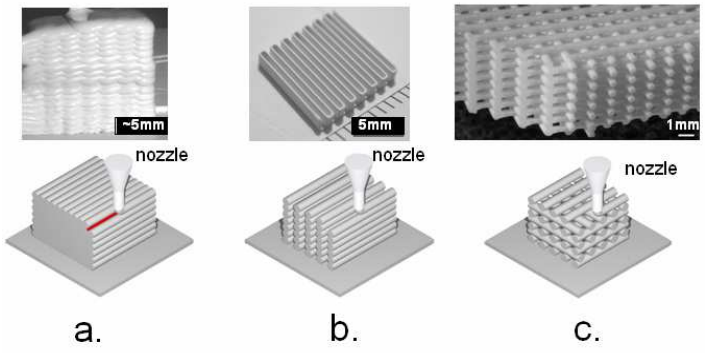

Figure 2-9. Structures fabricated by Dr. Smay from $Pb(Zr,Ti)O_3$: (a) solid block from space filling layers, (b) as-dried high aspect ratio wall structure, and (c) crossed layers structure

II.3.2 Interest

When it comes to tissue scaffold preparation, EBRD thus appears as the most appropriate technique [34]. It yields a precise reconstruction of intricate three-dimensional scaffolds that can match the architecture of biologic tissues. The process gives a complete control over the structure and thus over the mechanical properties of the scaffold. The porosity of the structure and the struts dimensions can be tailored to promote the colonization and growth of biologic cells. Finally, the colloidal inks can be made of entirely biocompatible materials.

II.4 Mechanical behavior of trabecular bone

In reconstructive surgery, almost all the cement-less orthopaedic implants interface with trabecular bone. It is the interest of this study to propose a structural material that will present mechanical properties as close as possible to those of the biological tissue. This matching is hypothesized to be of prime importance to enhance the mechanical stimulation of osteogenic cells. The resulting positive consequences of an early and rapid bone formation would be a better anchoring of the implant, a stronger interface less sensitive to fatigue and the possibility for the patient to recover faster from the operation. As technologies evolve, refinements can be performed to yield products with better qualities. Current implants present an overall stiffness and yield strength that can match that of cancellous bone. However adequate this mechanical similitude is, it could be enhanced to reach a higher degree and feature a similar mechanical behavior as trabecular bone at small strains. In order to tailor the properties of a novel cellular structure, the literature was searched for information concerning the mechanical behavior of trabecular bone.

II.4.1 Description

Trabecular bone is a porous cellular solid that is generally found at the extremities of long bones and in the vertebral bodies of mammals. Figure 2-10 shows the trabecular network and the cortical bone shell of a vertebral body. The porosity

can reach 85 % in a healthy person. Platelets of the base material are deposited to create the struts of a porous solid so that fat, proteins and bone marrow can be stored. The struts are oriented along the stress lines to be more resistant. Although the base material is the same as that of cortical bone (collagen, hydroxyapatite, proteins, water), its architecture makes it more fragile. Degeneration caused by aging and illnesses can lower its density and render bone more susceptible to fracture.

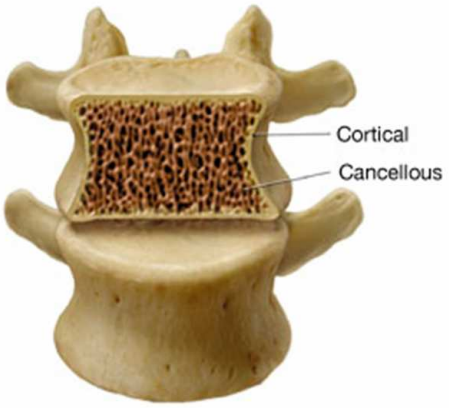

Figure 2-10. Photograph of human trabecular and cortical bone in a vertebral body (permission to use requested)
http://www.ama-cmeonline.com/osteo_mgmt/module03/images/m3_02path_02.jpg

II.4.2 Mechanical behavior at small strains

Many studies have been conducted to investigate the properties of trabecular bone from various species. Ranges of values have been found for the stiffness, ultimate strength, yield strength and strain, and resilience. However, those tremendously vary between species but also between individuals of a same species

and even within anatomic location in each individual [35]. The loading history, architecture, and density, among others, are parameters that influence bone properties.

In 1987 Linde and Hvid [36] demonstrated the dependence of stiffness on the strain rate. They tested human tibial epiphyses that yielded a non-linear strain-stress relationship. They concluded that the modulus of elasticity of cancellous bone could only be accurately determined at very low strain rates, which is almost impractical to do. Later on Morgan et *al.* [37] tested the trabecular bone obtained from human vertebrae, tibias and femurs in compression up to 1.2% strain. Their strain-stress graphs featured a subtle concave upward curve that did not agree with previous findings by other scientists. They considered that the concave downward "toe" or even initial linear curves presented by their peers were caused by an end-artifact due to the test set-up.

In 2003, Bredbenner and Davy [38] presented a model to facilitate the finite element modeling of human vertebral trabecular bone. Their study focused on the strains below 1.2 % and the experimental curves they used for comparison to their model also presented a concave upward trend. On the other hand Sierpowska et *al.* [39] obtained concave downward strain-stress graphs from human trabecular bone samples (tibia, femur) tested to 5% strain. The trend was the same for the load-deformation curves of pig vertebral trabecular bone obtained by Mosekilde et *al.* [40]. Finally, even if the strain-stress curves Guedes et *al.* [41] derived were from the test of bovine femurs, they presented two interesting features for this project. The curves

displayed an initial concave downward region and then behaved like certain cellular solids tested by Gibson and Ashby [42]. This supported the conclusion of Hvid who 18 years earlier, had suggested that the foam-like structure of trabecular bone enabled it to absorb a large quantity of energy [43].

The small size, the tremendous variations in material properties, and the numerous influencing parameters result in great discrepancies in the mechanical properties of trabecular bone and disagreement between researchers. However, several results of previous studies are of major interest for the present one. For instance, focus should be placed on the mechanical behavior at small strains where most of the mechanical stimulation and/or micro-damage occur [37]. Also, the boundary conditions of the test set-up must be considered to take into consideration all the bias they might introduce [37, 44]. In the present study, it was considered that trabecular bone displays a nonlinear behavior under certain conditions and it was hypothesized that such a behavior should be replicated by the novel structural implant to enhance mechanical stimulation and accelerate bone formation. More details on the motivations and justification for these hypotheses will be provided in the following chapter.

II.5 Potential application for novel structure: Orthopaedic Implants

In life sciences man tries to imitate nature and more knowledge about natural processes allows their replication. In orthopaedics, a more complete characterization of bone, which is a living material, results in new ways to repair it when needed. Since the demonstration of the existence and importance of bioelectricity for the normal life of living tissues, scientists have tried to use this information in orthopaedic applications. Many experiments and theoretical analysis have shown that the natural electrical activity of the human body helps to maintain the skeleton in shape. Whether the source of electricity is piezoelectric or due to streaming potentials [45-55], such a stimulus partakes in the degradation/regeneration cycles of bone throughout the life of a person. More recently, mechanical stimuli were found to affect cell differentiation and osteogenesis (bone production) [55-59].

Through the process of mechanotransduction, the mechanical stresses experienced by the living tissues are transformed into chemical signals that influence the evolution of cells involved in the repairing of micro- and macro-defects of bones. The fact that bone repairs itself is not new. As far back as 1892, Wolff had made the observation that became a law: bone is deposited and resorbed in accordance with the stresses placed upon it. This is unnoticeably experienced by everybody everyday but in a more painful way by those patients with an implant who suffer from the consequences of implant loosening, stress-shielding or subsidence.

Acrylic adhesives such as bone cement were developed to connect bone with the implant and reduce these problems. Bone cement is liquid when prepared and poured into the bony cavity just instants before the implant, and then it hardens. It thus can flow through the trabecular network on one side and secure the implant on the other side, allowing a better repartition of the loading forces and a decrease in the stress concentration. But this material also presents disadvantages: the polymerizing reaction is exothermic and release chemical products. The increase in temperature in such a confine volume can induce necrosis of the surrounding tissue while the chemical residues can migrate in the body and sicken the patient. Air bubble can also be trapped thus increasing the risk of failure through crack initiation and propagation.

Because of those drawbacks cementless methods are also employed for implant fixation. Instead of having a material filling the pores of the trabecular bone, the native bone is invited to grow into intimate attachment with the external surface of the implant [60]. In order to do so, internal medical devices were designed so that they presented a porous structure or external porous surfaces to reflect that of the cancellous bone. The introductory chapter also mentioned electrical stimulating techniques to get bone to grow faster at the surgical site. The following chapters detail the potentials and limitations of porous structures and electrical stimulation.

II.5.1 Porous Structures

A porous surface is synonymous with a greater surface of contact between the bone and the implant. This was first achieved by increasing the roughness of the implants' surfaces instead of polishing them. However, this posed a health hazard since microscopic metallic particles were loosened from the roughened surfaces because of the mechanical loading (at implantation or caused by fatigue) and entered the fluid systems. This could result in tissue necrosis (metallosis), clogging of the lymphatic system and even death of the patient. But another way of roughening the external surfaces of the implants was through chemical processes such as Chemical Vapor Deposition (CVD) and porous plasma spray coating. These techniques are employed to deposit layers of small beads or fibers onto the implants' external surface (Figure 2-11). This results in the formation of a somewhat controlled and simple to manufacture porous network. Figure 2-12 shows the porous surfaces of an artificial disc. These methods also allow the combination of hydroxyapatite, a natural constituent of bone, to the metallic alloy to be sprayed. Implants featuring this type of coating yielded higher degree and quality of osteointegration than non-coated ones [61-63].

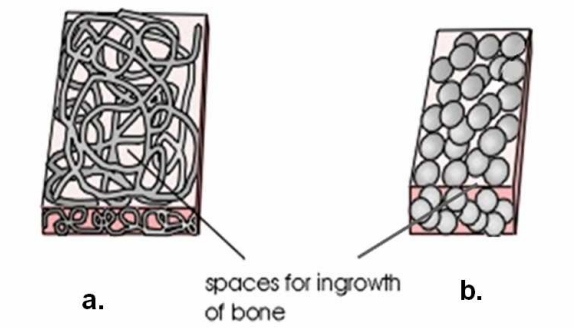

Figure 2-11. Illustrations of titanium porous coatings (a) mesh), (b) sintered balls (permission to use requested)
http://www.totaljoints.info/AllTHporouscoating1.jpg

In other applications such as spinal fusion implants, a unique material, Trabecular Metal™ can be used. It is a tantalum sponge with porosity close to 80%. Figure 2-13 shows various spinal fusion implants of various sizes and shapes made of tantalum. Many mechanical characterizations and in-vivo experiments have proven that this material is very well suited for spinal fusion [64-67]. It is then a material worth considering as the basis for the next generation of spinal implants. The most successful porous implants (tantalum and titanium meshes) could also match the mechanical behavior of bone at small strains, a property they do not feature yet.

Figure 2-12. Photographs of an artificial intervertebral disc with porous tantalum surfaces (permission to use requested)
http://biomed.brown.edu/Courses/BI108/BI108_2002_Groups/discs/Prodisc.htm

Figure 2-13. Photographs of Tantalum spacers of various sizes and shapes (permission to use requested)
http://www.zimmer.co.nz/web/images/products/spine/spinetrabmetal01.gif

Porous materials also present other advantages. In order to boost or simply spark osteogenesis, the pores can be filled with chemicals inducing bone growth such as Bone Morphogenic Protein (BMP) or Transforming Growth Factor proteins (TGF-β) that control the development and proliferation of cells. The surface roughness promotes a tight fit against bone which strengthens the fixation of the implant by mechanical interlocking as well as direct contact with the living tissue and fluid, ideal for bone cells invasion and proliferation. This eventually permits the patient to resume physical therapy earlier since the risk of implant loosening is lowered, thus reducing the total financial costs of surgery.

II.5.1.1 Limitations of porous structures

Despite all their advantages, current porous structures and materials present limitations. They have been quite successful in promoting bony ingrowth but failures have occurred [68, 69].

Their overall porosity and pores interconnectivity are still low in comparison with that of the natural trabecular bone. The sprayed layers of beads and wires present a porosity of up to 45% only which is barely more than half that of trabecular bone [70]. Also, because of the processes and the geometry of the layers' basic elements, beads or wires, the interconnectivity of pores is lower than what is found in the living tissue. Another drawback with the plasma spray technique is that the required heating of both the implant and the coating to extreme temperature affect their superficial chemical composition and reduce the fatigue strength of the assembly. A second factor also negatively influences fatigue strength: the interfacial geometry between the porous coating and the implant produces stress concentrations at the interface [72]. This lack of resistance to fatigue is likely to result in the loosening of the implant and the need for revision surgeries that cannot be as conservative as the first one. Indeed, retrieving an implant that was impacted into bone and in which bone has grown will inevitably damage the surgical site thus reducing the amount of natural material available for a second implantation. From a mechanical standpoint, the cellular structure presenting a greater surface area is a positive feature. But from a chemical standpoint, a weaker porous layer is a negative feature since it increases the chances of metallic ion and debris release in the body fluids [72]. These circulating

residues have been shown to sicken patients and jeopardize their healing and health [72-76].

II.5.2 Bone growth stimulation: electricity and therapeutic agents

Electrical bone growth stimulation techniques such as direct current, pulse electromagnetic field, and capacitively coupling can be classified as invasive, external or semi-invasive. Even though they rely on different physics principle they all result in exposing living tissues to electric fields or currents. The effects of some techniques are still mitigated but overall, it has been shown that the stimulation is effective in helping with tissue repair in different situations (e.g. spinal fusion, fracture non-union, pseudoarthrodesis). In the same way, BMPs have shown a tremendous potential in the stimulation of bone growth and the enhancement of fusion [77, 78]. This simple method consists in injecting a dose of BMPs at the surgical site either directly or by loading the porous implant.

II.5.2.1 Limitations of stimulating techniques

Despite the advantage of electrical stimulation on bone regeneration no current implant features any kind of embedded electrical stimulating system. Subcutaneous and small external battery packs have been developed for

implementation along with an implant. But their use is principally reserved to high-risk patients who need extra-stimulation to increase their chances of healing. These patients often suffer from metabolic impairments caused by obesity and/or smoking or because they have another physical (spondilolysthesis) that reduces the ability of their body to heal properly. The main issue with electrical stimulator is that their reimbursement was granted only a few years ago and is not covered completely by all insurance companies [79, 80].

The lack of implants featuring an embedded electrical stimulation system does not however mean that they have not been investigated or even prototyped through academic or industrial research. The very first trials started by modifying an implant to connect it to an energy source. For instance, Weinstein et al. prototyped porous Al_2O_3 implants whose hollow core was filled with a stainless steel electrode connected to an implanted power supply [81]. Scientists intended to insert a battery into the implant but because of geometrical and dimension limitations, this was not feasible. Either a battery that would last long enough was too bulky to fit in the implant or the battery could be implemented in the implant but could not last long enough. Then, it was thought that the mechanical energy developed during walking or moving could be transformed into electrical energy. This energy transformation was made possible by advances in piezoelectricity that could address the problems posed by batteries. However, the implementation of piezoelectric elements into implants proved troublesome. It required that these elements be embedded and isolated from

any body fluid that could severely alter its functionality (shunting, charge dissipation). Electronics were also needed to transform the raw alternating (AC) signal into a continuous (DC) one. As explained by Cochran et *al.* electronic components must also be implemented to switch, rectify, filter, and control the alternative current generated by the piezoelectric elements and transform it into a direct current [82]. Finally, wires also had to be positioned nearby to serve as electrodes. These technical issues complicated the surgery and raised concerns about potential infections.

In the 1980's, investigations on piezoelectric implants were conducted but no other public investigation has benefited from the results of those early trials since. Park et *al.* implanted poled barium titanate implants in the cortex of dogs' femurs and reported the generation of 0.01 microamperes currents along with bone formation [82, 83]. On the other hand, many patents have been issued on that topic. Before going further in the presentation of the various ways employed to generate electricity in-situ, we should answer the following questions. Why is electrical stimulation really advantageous and why is it employed? This technique is not attractive because it stimulates the production of more bone but because it stimulates a faster production of bone [84, 85]. A faster osteogenesis helps to stabilize the implant earlier in the recovery phase and thus reduces any risk of its moving and getting out of proper position, which could be detrimental. For instance McAfee et *al.* reported failures of lumbar spine fusion caused by the migration of implanted cylindrical cages. In one

case, the cage had retropulsed into the spinal canal four weeks after surgery, provoking back pain, bilateral leg pain and causing an infection [69].

Another advantage is that the properties of bone whose formation was electrically stimulated are not different because of its faster development rate [85]. Numerous comparative experiments showed that stimulation-generated bone had the same mineral content and properties as naturally formed bone. These investigations also found that both types of bone, stimulated and non-stimulated, eventually mend any defect as well overtime [63, 64]. So the goal of electrical stimulation is to accelerate osteogenesis by providing the body with an additional stimulus. That could explain why this technique does not always result in a successful healing in complex situations in which it was thought to balance the negative effects of a damaged metabolism. Electrical stimulation alone could not compensate for deficient natural chemical and mechanical stimuli to foster bone formation.

II.5.3 Combining a porous structure and electrical stimulation

The different materials investigated to induce bioactive processes and promote osteogenesis are piezoelectrically active substances [83, 86, 87]. Some are ceramic such as dihydrogene phosphates, zirconates, and titanates. Others are polymeric electrets such as polyvinyl chloride (a.k.a. PVC) and ferroelectric materials such as polyvinylidene fluoride (a.k.a. PVDF) [88]. Polymeric ferroelectric materials do not necessarily require a poling treatment to exhibit piezoelectric-like properties. The

mere presence of electric charges, not current, can directly affected the living tissues in-situ just as streaming potentials and biopiezoelectricity do. As shown by Yasuda [89], Teflon™ films formed into electrets, simply applied against or wrapped around a rabbit bone led to callus formation in four weeks. With such medical materials there is no need for any embedded AC-DC current transformation circuitry.

Progresses in the processing of materials make it possible to create an ideal implant that would combine the advantages of a porous structure and an electrical stimulation system. The cellular structure could be tailored to mimic the topological environment of the hosting tissues to enhance the bonding with the implant but also to display a similar nonlinear mechanical behavior at small strains. Recent studies showed that the size of the pores, in the cancellous bone, has a significant effect on bone cells migration, differentiation, and bone generation [90-94]. Other investigations demonstrated the stimulating role of mechanotransduction on cells activity [56-59, 95,96]. An enhanced medical device would also feature a modulus of elasticity and strength close to that of bone, which would lead to a better sharing of the mechanical loading at the interface. This would reduce the risks of stress-shielding and subsidence while improving the mechanical stimulation of the living tissues. Finally, inclusion of a ferroelectric phase as part of the structure would confer the whole assembly piezoelectric properties that could lead to electrical stimulation under varying loading conditions. The synergetic combination of these mechanical

and electromechanical characteristics could eventually favor a greater osteogenesis than each characteristic separately as illustrated on Figure 2-14.

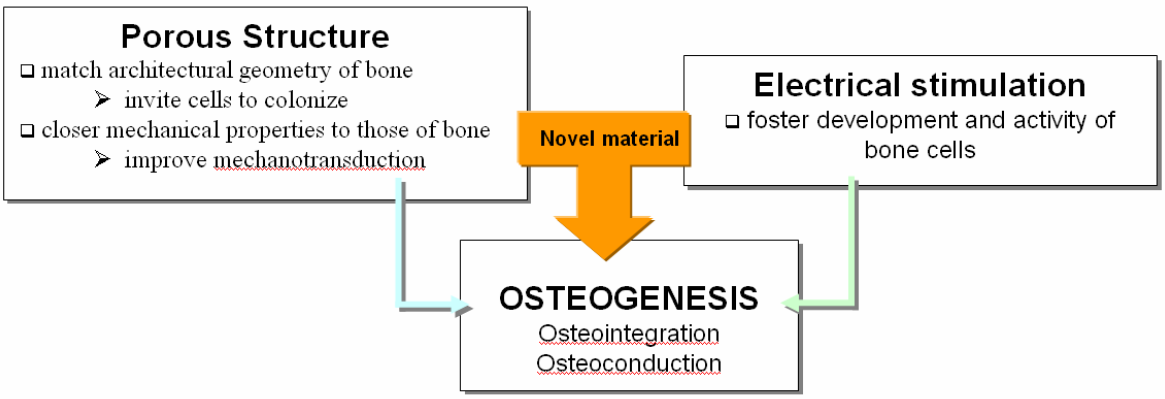

Figure 2-14. Diagram illustrating the diverse and combined influences of porous coating and electrical stimulation leading to osteogenesis

References

1. Jaffe B., Cook W.R. Jr., Jaffe H.L., Piezoelectric ceramics, London, New York, Academic Press, 1971
2. Fundamentals of Piezoelectricity and Piezoelectric Actuators, Physik Instrumente (PI) GmbH & Co., http://www.physikinstrumente.com/tutorial/4_15.html (accessed 01/18/2008)
3. The piezoelectric dipole moment, Department of Materials Science and Metallurgy, University of Cambridge, http://www.doitpoms.ac.uk/tlplib/piezoelectrics/dipole.php (accessed 01/18/2008)
4. Bill B., Measuring with Crystals: Principles and applications of the piezoelectric measuring technique, verlag moderne industrie, D-86895 Landsberg/Lech, 2002 (http://www.mi-verlag.de)
5. Martin R.M., Piezoelectricity, Physical Review B, Vol.5, No.4, pp.1607-1613, 1972
6. Moulson A.J., Herbert J.M., Electroceramics: Materials, Properties, Applications, 2nd Ed.
7. Jordan T.L., Ounaies Z., Piezoelectric Ceramics Characterization, NASA/CR-2001-211225, ICASE Report No.2001-28, 2001
8. Li J-F., Takagi K., Terakubo N., Watanabe R., Electrical and mechanical properties of piezoelectric ceramic/metal composites in the Pb(Zr, Ti)O3/Pt system, Applied Physics Letters, Vol.79, No.15, pp.2441-2443, 2001
9. Piezoelectricity, APC International, Ltd (http://www.americanpiezo.com) (accessed 01/18/2008)
10. Fukada E., Piezoelectricity of biopolymers, Biorheology, Vol.32, No.6,pp:593-609, 1995
11. Fung Y.C., Foundations of solid mechanics, p353, (Prentice Hall, 1968)
12. Krause I., Segreto A.J., Mach R.L., Przirembel H., The measurement of Poisson's Ratio for Viscoelastic Materials in Uniaxial Compression, American Society of Mechanical Engineers Papers, 65-WA/RP-8, 1965
13. Lakes R.S., Foam structures with a negative Poisson's ratio, science, Vol.235:1038-1040, 1987
14. Choi J.B., Lakes R.S., Nonlinear properties of metallic cellular materials with a negative Poisson's ratio, Journal of Materials Science, Vol.27, pp: 5373-5381, 1992
15. Friis E.A., et al., Negative Poisson's ratio polymeric and metallic materials, Journal of Materials Science, Vol.23, pp:4406-4414, 1988
16. Griffith M.L., Halloran J.W., Freeform fabrication of ceramics via stereolithography, Journal of the America Ceramic Society, Vol.79, No.10:2601-2608, 1996
17. Bourell, D.L., Marcus, H.L., Barlow, J.W., Beaman, J.J., Selective Laser Sintering of Metals and Ceramics, International Journal of Powder Metallurgy, Vol.28, No.4:369-381., 1992

18. Marcus, H.L., Beaman, J.J., Barlow, J.W., Bourell, D.L., Solid Freeform Fabrication - Powder Processing, American Ceramic Society Bulletin, Vol.69, No.6:1030-1031, 1990
19. Giordano R.A., Wu B.M., Borland S.W., Cima L.G., Sachs E.M., Cima M.J., Mechanical properties of dense polylactic acid structures fabricated by three dimensional printing, Journal of Biomaterials Science-Polymer Edition, Vol.8, No.1:63-75, 1996
20. Grau J.E., Uhland S.A., Moon J., Cima M.J., Sachs E.M., Controlled cracking of multilayer ceramic bodies, Journal of the American Ceramic Society, Vol.82, No.8:2080-2086, 1999
21. Holman R.K., Uhland S.A., Cima M.J., Sachs E.M., Surface adsorption effects in the inkjet printing of an aqueous polymer solution on a porous oxide ceramic substrate, Journal of Colloid and Interface Science, Vol.247, No.2:266-274, 2002
22. Holman R.K., Cima M.J., Uhland S.A., Sachs E.M., Spreading and infiltration of inkjet-printed polymer solution droplets on a porous substrate, Journal of Colloid and Interface Science, Vol.249, No.2:432-440, 2002
23. Jackson T.R., Liu H., Partikalakis N.M., Sachs E.M., Cima M.J., Modeling and designing functionally graded material components for fabrication with local composition control, Materials & Design, Vol.20, No.2-3:63-75, 1999
24. Moon J., Grau J.E., Knezevic V., Cima M.J., Sachs E.M., Ink-jet printing of binders for ceramic components, Journal of the American Ceramic Society, Vol.85, No.4:755-762, 2002
25. Moon, J., Grau, J.E., Cima, M.J., Sachs, E.M., Slurry chemistry control to produce easily redispersible ceramic powder compacts, Journal of the American Ceramic Society, Vol.83, No.10:2401-2408, 2000
26. Sachs E.M., Wylonis E., Allen S.,Cima M.J., Honglin G., Production of injection molding tooling with conformal cooling channels using the three dimensional printing process, Polymer Engineering and Science, Vol.40, No.5:1232-1247, 2000
27. Sachs E.M., Cima M.J., Williams P., Brancazio D., Cornie J., 3-Dimensional Printing - Rapid Tooling and Prototypes Directly from a Cad Model, Journal of Engineering for Industry-Transactions of the ASME, Vol.114, No.4:481-488, 1992
28. Seerden K.A.M., Reis N., Evans J.R.G., Grant P.S., Halloran J.W., Derby B., Ink-Jet Printing of Wax-Based Alumina Suspensions, Journal of the American Ceramic Society, Vol.84, No.11:2514-20, 2001
29. Uhland S.A., Holman R.K., Morissette S., Cima M.J., Sachs E.M., Strength of green ceramics with low binder content, Journal of the American Ceramic Society, Vol.84, No.12:2809-2818, 2001
30. Wu B.M., Borland S.W., Giordano R.A., Cima L.G., Sachs E.M., Cima M.J., Solid free-form fabrication of drug delivery devices, Journal of Controlled Release, Vol.40, No.1-2:77-87, 1996

31. Cawley J.D., Heuer A.H., Newman W.S., Mathewson B.B., Computer-aided manufacturing of laminated engineering materials, American Ceramic Society Bulletin, Vol.75, No.5:75-79, 1996
32. Griffin E.A., Mumm D.R., Marshall D.B., Rapid prototyping of functional ceramic composites, American Ceramic Society Bulletin, Vol.75, No.7:65-68, 1996
33. Alper J., Biology and the Inkjets, Science, Vol.305:1895, 2004
34. Woodfield T.B., Malda J., de Wijn J., Péters F., Riesle J., van Blitterswijk C.A., Design of porous scaffolds for cartilage tissue engineering using a three-dimensional fiber-deposition technique, Biomaterials, Vol.25, No.18:4149-4161, 2004
35. Goldstein S.A., The mechanical properties of trabecular bone: dependence on anatomic location and function, J. Biomech., Vol.20, No.11-12, pp:1055-1061, 1987
36. Linde F., Hvid I., Madsen F., The effect of specimen geometry on the mechanical behaviour of trabecular bone specimens, J. Biomechanics, Vol.25, No.4:359-368, 1992
37. Morgan E.F., Yeh O.C., Chang W.C., Keaveny T.M., Nonlinear behavior of trabecular bone at small strains, J Biomech Eng., Vol.123, No.1:1-9, 2001
38. Bredbenner T.L., Davy D.T., A damaging-viscoelastic-viscoplastic constitutive model for human vertebral trabecular bone applied to experimental specimen response, Summer Bioengineering Conference, Sonesta Beach Resort, Key Biscayne, Florida, 2003
39. Sierpowska J., Hakulinen M.A., Töyräs J., Day J.S., Weinans H., Jurvelin J.S., Lappalainen R., Prediction of mechanical properties of human trabecular bone by electrical measurements, Physiolo. Meas. Vol.26:S119-S131, 2005
40. Mosekilde L., Kragstrup J., Richards A., Compressive strength, ash weight, and volume of vertebral trabecular bone in experimental fluorosis in pigs, Calcif. Tissue Int., Vol.40:318-322, 1987
41. Guedes R.M., Simoes J.A., Morais J.L., Viscoelastic behaviour and failure of bovine cancellous bone under constant strain rate, Journal of Biomechanics, Vol.39:9-60, 2006
42. Gibson L.J., Ashby M.F., Cellular solids, structure and properties (2nd Ed.), Cambridge University Press, 1997 (ISBN 0 521 49560 1)
43. Hvid I. Mechanical strength of trabecular bone at the knee, Dan. Med. Bull., Vol.35, No.4:345365, 1988
44. Keaveny T.M., Guo X.E., Wachtel E.F., McMahon T.A., Hayes W.C., Trabecular bone exhibits fully linear elastic behavior and yields at low strains, J Biomech.,Vol.27, No.9:1127-1136, 1994
45. Gu W.Y., Mao X.G., Rawlins B.A., Iatridis J.C., Foster R.J., Sun D.N., Weidenbaum M., Mow V.C., Streaming potential of human lumbar annulus fibrosus is anisotropic and affected by disc degeneration, J. Biomech., Vol.32, No.11:1177-1182, 1999

46. Friedenberg Z.B., et al., Bioelectric potentials in bone, Journal of Bone and Joint Surgery, Vol.48A, No.5:915-923, 1966
47. Gross D., Williams W.S., Streaming potential and the electromechanical response of physiologically-moist bone, J Biomech, Vol.15, No.4:277-295, 1982
48. Guzelsu N., Walsh W.R., Streaming potential of intact wet bone, J Biomech, Vol.23, No.7:673-685, 1990
49. Beck B.R., Qin Y.X., McLeod K.J., Otter M.W., On the relationship between streaming potential and strain in an in vivo bone preparation, Calcif Tissue Int, Vol.71, No.4:335-343, 2002
50. Becker R.O., Electrical behavior of cartilage during loading, Science, Vol.178:982-983, 1961
51. Becker R.O., The significance of bioelectric potentials, Bioelectrochemistry and Bioenergetics, Vol.1:187-199, 1974
52. Gross D., Williams W.S., Streaming potential and the electromechanical response of physiologically-moist bone, J Biomech, Vol.5, No.4:277-295, 1982
53. Hastings G.W., ElMessiery M.A., Rakowski S., Mechano-electrical properties of bone, Biomaterials, Vol.2, No.4:225-233, 1981
54. Hastings G.W., Mahmud F.A., Electrical effects in bone, Review , J Biomed Eng, Vol.10, No.6:515-521, 1988
55. Marino A.A., Becker R.O., Soderholm S.C., Origin of the piezoelectric effect in bone, Calcified Tissue Research, Vol.8, No.2:177-180, 1971
56. Butler D.L., Juncosa-Melvin N., Boivin G.P., Galloway M.T., Shearn J.T., Gooch C., Awad H., Functional tissue engineering for tendon repair: A multidisciplinary strategy using mesenchymal stem cells, bioscaffolds, and mechanical stimulation, J Orthop Res., Vol.26, No.1:1-9, 2007
57. Juncosa-Melvin N., Shearn J.T., Boivin G.P., Gooch C., Galloway M.T., West J.R., Nirmalanandhan V.S., Bradica G., Butler D.L., Effects of mechanical stimulation on the biomechanics and histology of stem cell-collagen sponge constructs for rabbit patellar tendon repair, Tissue Eng., Vol.12, No.8:2291-2300, 2006
58. Juncosa-Melvin N., Matlin K.S., Holdcraft R.W., Nirmalanandhan V.S., Butler D.L., Mechanical Stimulation Increases Collagen Type I and Collagen Type III Gene Expression of Stem Cell–Collagen Sponge Constructs for Patellar Tendon Repair, Tissue Engineering, Vol.13, No.6:1219-1226, 2007
59. Butler D.L., Goldstein S.A., Guilak F., Functional tissue engineering: the role of biomechanics, J Biomech Eng.,Vol.122, No.6:570-575, 2000
60. US Patent 6,610,096 Prosthetic Implant Having Enhanced Utility, McDonald S.G., 2003
61. Landor I., Vavrik P., Sosna A., Jahoda D., Hahn H., Daniel M., Hydroxyapatite porous coating and the osteointegration of the total hip replacement, Arch Orthop Trauma Surg.,Vol.127, No.2:81-89, 2007

62. Thanner J., The acetabular component in total hip arthroplasty. Evaluation of different fixation principles, Acta Orthop Scand Suppl., Vol.286:1-41, 1999
63. Kusakabe H., Sakamaki T., Nihei K., Oyama Y., Yanagimoto S., Ichimiya M., Kimura J., Toyama Y., Osseointegration of a hydroxyapatite-coated multilayered mesh stem, Biomaterials, Vol.25, No.15:2957-2969, 2004
64. Ong J.L., Calcium Phosphate Coatings and Scaffolds, University of Missouri – Kansas City Seminar, May 16, 2007
65. Shimko D.A., Shimko V.F., Sander E.A., Dickson K.F., Nauman E.A., Effects of porosity on the fluid flow characteristics and mechanical properties of tantalum scaffolds, Journal of biomedical Materials Research Part B, Vol.73B, No.2:315-324, 2005
66. Toth J.M., Turner A.S., Kabo J.M., Linda E.A., Porous Tantalum metal as a biologically advantageous spinal fixation material, [http://www. Spine.org/conf_abstracts_10_20_96/338-Toth.html], October 24, 1996
67. Zardiackas L.D., Structure, Metallurgy, and Mechanical properties of a porous Tantalum foam, Journal of Biomedical Material Research, Vol.58, No.2:180-187, 2001
68. McAfee P.C., Cunningham B.W., Lee G.A., Orbegoso C.M., Haggerty C.J., Fedder I.L., Griffith S.L., Revision strategies for salvaging or improving failed cylindrical cages, Spine, Vol.24, No.20:2147-2153, 1999
69. Schiffman M., Brau S.A., Henderson R., Gimmestad G., Bilateral implantation of low-profile interbody fusion cages: subsidence, lordosis, and fusion analysis, Spine J., Vol.3, No.5:377-387, 2003
70. Karageorgiou V., Kaplan D., Porosity of 3D biomaterial scaffolds and osteogenesis, Biomaterials, Vol.26, No.27:5474-5491, 2005
71. US Patent 5,258,030 Porous coated implants, Wolfarth D., Ducheyne P., 1993
72. Martz E.O., Goel V.K., Pope M.H., Park J.B., Materials and Design of Spinal Implants—A Review, J. Biomed. Mater. Res. (Appl. Biomater.), Vol.38: 267–288, 1997
73. Papageorgiou I., Brown C., Schins R., Singh S., Newson R., Davis S., Fisher J., Ingham E., Case C.P., The effect of nano- and micron-sized particles of cobalt-chromium alloy on human fibroblasts in vitro, Biomaterials, Vol.28, No.19:2946-2958, 2007
74. Ingham E., Fisher J., Biological reactions to wear debris in total joint replacement, Proc Instn Mech Engrs, Vol.214,Part H, 2000
75. Catelas I., Bobyn J.D., Medley J.B., Krygier J.J., Zukor D.J., Huk O.L., Size, shape, and composition of wear particles from metal–metal hip simulator testing: Effects of alloy and number of loading cycles, J Biomed Mater Res A.,Vol.67, No.1:312-327, 2003
76. Catelas I, Campbell PA, Bobyn JD, Medley JB, Huk OL., Wear particles from metal-on-metal total hip replacements: effects of implant design and implantation time, Proc Inst Mech Eng [H], Vol.220, No.2:195-208, 2006

77. Wang J.C., Walsh M.C., BMP Improves Spinal Fusion http://www.spineuniverse.com/displayarticle.php/article1711.html
78. Burkus K.J., Clinical and Radiographic Outcomes of Anterior Lumbar Interbody Fusion Using Recombinant Human Bone Morphogenetic Protein-2. Total Spine Pre-Course Symposium. March 2002.
79. Blue Cross of California Medical Policies, Electrical stimulation devices reimbursement. http://medpolicy.bluecrossca.com/policies/DME/elect_bone_grwth_stim.html
80. Gardner S.E., Frantz R.A., Schmidt F.L., Effect of electrical stimulation on chronic wound healing: a meta-analysis, Wound Repair and Regeneration, Vol.7, No.6:495-503, 1999.
81. Weinstein A.M., Klawitter J.J., Cleveland T.W., Amoss D.C., Electrical stimulation of bone growth into porous Al2O3, J. Biomed. Mater. Res., Vol.10: 231-247, 1976
82. Cochran G.V., Johnson M.W., Kadaba M.P., Palmieri V.R., Mahaffey G., Design considerations in development of a prototype, piezoelectric internal fixation plate: a preliminary report, Journal of rehabilitation Research and Development, Vol.24, No.2:39-50, 1987
83. Park J.B., von Recum A.F., Kenner G.H., Kelly B.J., Coffeen W.W., Grether M.F., Piezoelectric ceramic implants: a feasibility study, Journal of Biomedical Materials Research, Vol.14, No.3:269-277, 1980
84. Park J.B., Kelly B.J., Kenner G.H., von Recum A.F., Grether M.F., Coffeen W.W., Piezoelectric ceramic implants: in vivo results, Journal of Biomedical Materials Research, Vol.15, No.1:103-110, 1981
85. Park J.B., Kenner G.H., Effect of electrical stimulation on the tensile strength of the porous implant and bone interface, Biomater Med Devices Artif Organs, Vol.3, No.2:233-243, 1975
86. Colella S.M., Miller A.G., Stang R.G., Stoebe T.G., Spengler D.M., Fixation of porous titanium implants in cortical bone enhanced by electrical stimulation, Journal of Biomedical Material Research, Vol.15:37-49, 1981
87. US Patent 5,032,129 Active Implant, Kurze P., Krysmann W., Knoefler W., Graf H-L., Bethmann W., Horst H., 1991
88. Jianqing F., Huipin Y., Xingdong Z., Promotion of osteogenesis by a piezoelectric biological ceramics, Biomaterials, Vol. 18, pp: 1531-1534, 1997
89. US Patent 5,298,602 Polymeric Piezoelectric Material, Shikinami Y., Hata K., 1994
90. Yasuda I., Electrical Callus and Callus Formation by Electret, Clinical Orthopaedics and Related Research, No.124:53-56, 1977
91. Rao G., Titanium foams fabricated for bone-tissue engineering applications, Research/Researchers MRS bulletin, P940, 2002 [www.mrs.org/publications/bulletin]
92. Uchida A., Nade S.M., McCartney E.R., Ching W., The use of ceramics for bone replacement. A comparative study of three different porous ceramics, Vol.66-B, No.2:269-275, 1984

93. Zeltinger J., Sherwood J.K., Graham D.A., Müeller R., Griffith L.G., Effect of Pore Size and Void Fraction on Cellular Adhesion, Proliferation, and Matrix Deposition, Tissue Engineering, Vol.7, No.5:557-572, 2001
94. Clemow A.J.T., Weinstein A.M., Klawitter J.J., Koeneman J., Anderson J., Interface mechanics of porous titanium implants, Journal of Biomedical Materials Research, Vol.15, No.1: 73-82, 1981
95. Hastings G.W., ElMessiery M.A., Rakowski S., Mechano-electrical properties of bone. Biomaterials, Vol.2, No.4:225-233, 1981
96. Moss M.L., The functional matrix hypothesis revisited:1.The role of mechanotransduction, Am J Orthod Dentofacial Orthop, Vol.112, No.1:8-11, 1997
97. Moss M.L., The functional matrix hypothesis revisited: 2.The role of an osseous connected cellular network, Am J Orthod Dentofacial Orthop, Vol.112, No.2:221-226, 1997

III Chapter 3: Mechanical properties of one-dimensional porous bowtie structure

III.1 Introduction

This study presents the investigation of the mechanical properties of porous bowtie re-entrant structures. An open bowtie cell is similar to a hexagonal cell with inverted segments. Based on previous experimental observations [1], this type of structure was hypothesized to display a nonlinear load-deformation behavior at small strains. A second hypothesis was that such a nonlinear mechanical behavior could be predicted and thus tailored. The works of Gibson and Ashby [2] supported this second hypothesis and provided an extensive background on the behavior of cellular solids, particularly honeycombs. It thus seemed obvious to study the re-entrant structure as a particular case of a hexagonal structure, at least with regards to the mechanical parameters.

The mechanical parameters and behavior constitute what is referred to as the "mechanical properties" in this document. Gibson and Ashby focused on the mechanical parameters of cellular solids, such as the relative modulus of elasticity and the relative strength. In the present study, those parameters were also investigated as well as the compressive strain ratio (CSR) and the mechanical behavior, i.e. how the stress relates to the strain. As explained in the introductory chapter, the main hypothesis was that the similarity of mechanical behavior between the implant and the surrounding bone tissue would enhance the mechanotransduction process in bone

and thus its healing. Predictions of the mechanical properties of the novel structure were based on the theory developed by Gibson and Ashby combined with experimental results as presented in the following sub-section.

III.2 Materials and Methods

III.2.1 Theory

III.2.1.1 Theory of cellular solids for the prediction of the mechanical parameters

Cellular solids, or foams, are found all around us in nature at different scales. Cellular solids are generally optimized structures in terms of mechanical properties and weight. For instance, the trunk of trees as well as human bone can support tremendous loads while remaining light and allowing for development. But cellular structures present other advantages such as thermal insulation, fluid transport or storage and energy absorption. There are thus countless potential applications for cellular materials in our industrialized societies. Man has then mimicked nature to design and develop artificial porous materials. Packaging, shock absorption and fluid storage are a few examples of applications. With the recent progresses in the processing of materials, it has become easier to manufacture more intricate cellular structures at different scales. But understanding their behavior increases design efficiency to meet the demands for given applications.

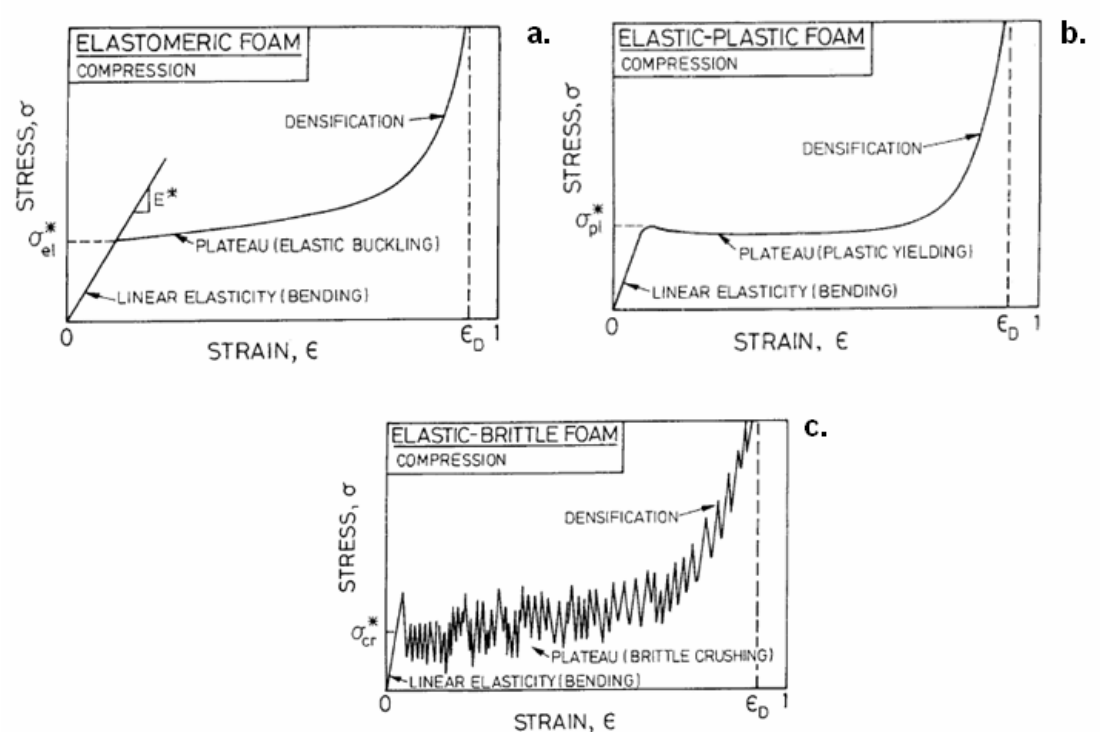

Figure 3-1. Schematic compressive stress-strain curves for foams, showing the three regimes of linear elasticity, collapse and densification: (a) elastomeric foam, (b) elastic-plastic foam, (c) elastic-brittle foam [2] (reproduced with permission from Canterbury Press)

In their investigation of the mechanical properties of cellular solids, Gibson and Ashby [2] showed that those properties are strongly dependent on the type of pores (open or closed) and on the relative density. As illustrated on Figure 3-1, they identified the principal deformation mechanisms of various foams in compression. The stress-strain curve usually presents an initial “linear” elasticity portion followed by a plateau region during which strain increases while the stress remains somewhat constant until reaching a densification regime during which the stress rises steeply.

The “linear” portion is actually not truly linear. The deformation is initially caused by bending but as the load increases, this creates an additional moment which lowers the modulus E*. If the axial load reaches a critical value, the struts also buckle, thus altering the modulus. Therefore, the stress-strain curve is not linear but concave downwards (or nonlinear) [2]. The stress plateau is associated with the collapse of the cells via the formation of plastic hinges at the connection between struts. When the struts of the cells have completely collapsed and are bent so that they touch each other, further deformation induces a rapid increase of stress. The large amount of evidence produced by their research attested that the relative mechanical parameters of the cellular solid could be expressed as a power function of its relative density. Those relationships are mathematically presented in equations {3-1} to {3-4} below for open cell foams.

$$\frac{E^*}{E_s} = C_1 \cdot \left(\frac{\rho^*}{\rho_s}\right)^2 \qquad \text{with } 0 < C_1 < 1 \qquad \{3\text{-}1\}$$

$$\frac{\sigma_{el}^*}{E_s} = C_4 \cdot \left(\frac{\rho^*}{\rho_s}\right)^2 \quad \text{or} \quad \frac{\sigma_{el}^*}{E_s} = C_4' \cdot \left(\frac{\rho^*}{\rho_s}\right)^2 \cdot \left(1 + \left(\frac{\rho^*}{\rho_s}\right)^{1/2}\right)^2 \quad \text{with } 0 < C_4 < 1 \quad \{3\text{-}2\}$$

Where E* is the modulus of elasticity of the cellular solid

E_s is the modulus of elasticity of the material employed in the cellular solid

σ^*_{el} is the elastic collapse stress

ρ^* is the density of the cellular solid

ρ_s is the density of the material employed in the cellular solid

ρ^*/ρ_s is the relative density of the cellular solid

For metals the ratio of the yield strength over the modulus of elasticity is so small that the conditions of equilibrium state that the elastic collapse stress is greater than the plastic collapse stress (equation {3-3}). This means that plastic collapse dominates over elastic collapse at all densities for the metallic foams. The relative plastic collapse stress (plastic collapse stress over the yield strength of the bulk material) is also a power function of the relative density (equation {3-4}).

$$\frac{\sigma_{ys}}{E_s} \approx \frac{1}{300} \quad \text{thus} \quad \frac{\rho^*}{\rho_s} \geq 36.\left(\frac{\sigma_{ys}}{E_s}\right)^2 \quad \text{which implies that } \sigma_{el}^* \geq \sigma_{pl}^* \qquad \{3\text{-}3\}$$

$$\frac{\sigma_{pl}^*}{\sigma_{ys}} = C_5.\left(\frac{\rho^*}{\rho_s}\right)^{3/2} \quad \text{or} \quad \frac{\sigma_{pl}^*}{\sigma_{ys}} = C_5.\left(\frac{\rho^*}{\rho_s}\right)^{3/2}.\left(1+\left(\frac{\rho^*}{\rho_s}\right)^{1/2}\right) \quad \text{where } 0< C5 < 1 \quad \{3\text{-}4\}$$

Where σ_{pl}^* is the plastic collapse stress of the cellular solid
σ_{ys} is the yield strength of the material

The relative density of the bowtie re-entrant structure is a function of the ratio between the length and the thickness of the cell members as shown by equations {3-5} to {3-7} and Figure {3-2}.

$$\left(\frac{\rho^*}{\rho_s}\right) = \frac{occupied\ area}{total\ area} \qquad \{3\text{-}5\}$$

$$\left(\frac{\rho^*}{\rho_s}\right)=\frac{2\times h\times t+4\times l\times\frac{t}{2}}{2\times\left[\left(h+(h-2\times l\times\sin(\theta))\times\left(l\times\frac{\cos(\theta)}{2}\right)\right]}=\frac{\left(\frac{h}{l}+1\right)\times\frac{t}{l}}{\left(\frac{h}{l}-\sin(\theta)\right)\times\cos(\theta)} \quad \{3\text{-}6\}$$

$$\left(\frac{\rho^*}{\rho_s}\right)\approx\frac{4}{\sqrt{3}}\times\left(\frac{t}{l}\right) \text{ for } \theta \text{ equal to } 60° \quad \{3\text{-}7\}$$

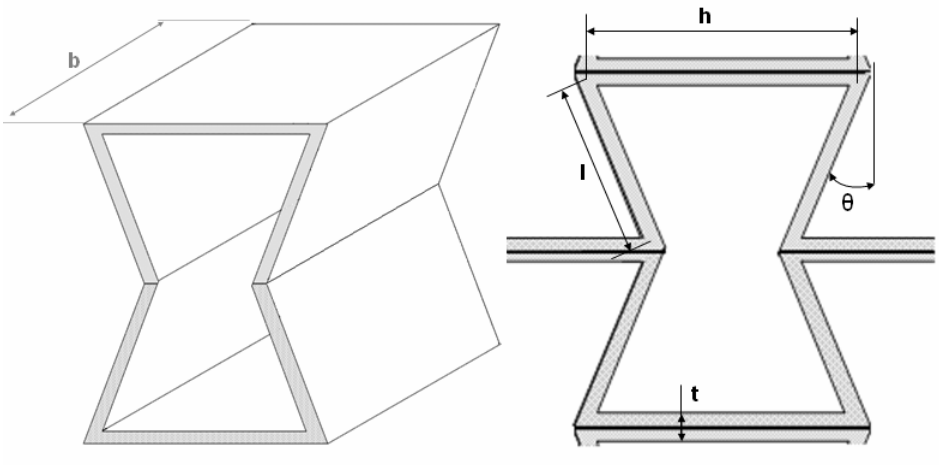

Figure 3-2. Schematic of the open bowtie cell and the nomenclature for its dimensions (**l** length**, h** width, **t** thickness, **θ** angle, and **b** depth)

III.2.1.2 The mechanical behavior of trabecular bone

Gibson and Ashby extended their investigations to cellular solids found in nature such as trabecular bone. Their experiments demonstrated that human trabecular bone presents the same relationships between its mechanical parameters and relative density. These equations and the derived engineering stress-strain curves

agree with those of many other researchers [3-5] who investigated the overall mechanical behavior of the biological structure. When the samples are strained up to 60% to 80%, the stress-strain curve presents three main regions: an initial linear elastic portion, a plateau, and a nonlinear densification rise.

Over the past twenty years, contradictory results have however been published concerning the stress-strain behavior of human trabecular bone at small strains (up to 5% strain). Several researchers [4, 6-11] have pointed out artifactual errors that can arise in the measurement of the modulus and strength during unconfined compression tests. The errors associated with the conventional compression test of trabecular bone come from three main sources: friction, damage, and testing equipment compliance [7-9]. The friction artifact comes from friction between the specimen and the compressive platens. It causes stress inhomogeneity at the specimen's ends that induces overestimation of the modulus. The damage artifact is caused by the sudden interruption of the natural trabecular network. Vertical trabeculae, nearest to the surface, are unstable because they lack horizontal support. Finally, measuring the force and displacement of the specimen indirectly through the load frame leads to an underestimation of the modulus since strains are so small. Keaveny et *al.* [9-11] developed a test method to get rid of those artifacts to measure the mechanical properties of trabecular bone more accurately. They demonstrated that the nonlinear J-shaped stress-strain curve ("toe" region) as reported by several researchers [8, 12] was an artifact. While the work and value of the investigations and conclusions made

by Keaveny and others should be acknowledged, the end-artifact-free testing method described [10] was not employed in the present work. As Keaveny himself recognized, the use of this technique depends on the objectives of a particular study.

The research detailed in this document deals with the mechanical properties of an artificial structure in series with trabecular bone, which implies the presence of boundary conditions within the system under investigation. This system is not a continuous undamaged cellular solid like the trabecular bone specimens characterized previously by those researchers. In other words, no matter the implant considered for spinal fusion (bone graft dowel, cage, and metallic cellular solid), the problems of friction, damage, and compliance are real for an implant placed between two vertebral bodies. For instance, the removal of a degenerated intervertebral disc, even well performed, exposes the non-even trabecular structure of the vertebral bodies. Some struts are cracked or bent and pieces of broken ones might be stuck in some pores. Several researchers have also shown the regional variability of the mechanical properties in the trabecular network of the vertebral bodies [8, 10, 13, 14-18], which could be linked to a difference in regional porosity. In addition, there is an uneven phenomenon of settling and progressive yielding of the exposed trabeculae at the interface. When the spinal implant features grooves, beads, prongs, holes, or simply presents a different porosity, the contact with trabecular bone is not uniform. All of these details create friction and a non-uniform loading of the implant and the subjacent trabecular bone.

Therefore, the mechanical behavior to emulate in a novel implant is not that of trabecular bone tested under ideal conditions but that of trabecular bone tested in implant-interfacing conditions as described above for which the nonlinear behavior is a reality to be mimicked. The focus was placed on reproducing the mechanical behavior at small strains because it was shown [11, 19] that microdamage, mechanical degradation, and biological repair response occur at strains below 0.5% in trabecular bone.

III.2.1.3 Theory for the nonlinear mechanical behavior of the novel structure

Friis and Lakes [1] investigated the mechanical properties of standard and re-entrant metallic open cell foams. They reported a nonlinear stress-strain relationship at small strains for re-entrant copper foam. Such cellular solids were obtained via a sequenced tri-axial compression of standard foam followed by annealing. This manufacturing process did not provide control over the pores that remained randomly organized. From these results and the works of Gibson and Ashby [2], it was hypothesized that a more controlled re-entrant architecture would yield a more controllable nonlinear mechanical behavior. The findings of Morgan et al. on the mechanical behavior at small strains [11] and Rabkin and Hsu [20] on the stress-stain relationship of biological tissues supported the hypothesis that the stress-stain relationship to be mimicked was a quadratic polynomial expression or a power function as illustrated by equations {3-8} and {3-9}. In these expressions, the

coefficients A, B, D, and p would present a linear or power relationship with the relative density of the re-entrant structure.

$$\sigma = A \times \varepsilon^2 + B \times \varepsilon \qquad \{3\text{-}8\}$$

$$\sigma = D \times \varepsilon^p \qquad \{3\text{-}9\}$$

Where σ is the engineering stress
ε is the engineering strain
A, B, D, p are coefficients that can depend on other parameters

The objective of this study was to investigate the mechanical behavior of a novel porous re-entrant structure at small strains. The first specific aim was to design and build prototypes of a controlled porous re-entrant structure. The second specific aim was to subject these novel structures to compressive tests to obtain their mechanical behavior and verify the nonlinearity at small strains.

III.2.2 Experiment

Different one-dimensional porous bowtie structures were manufactured by hand and via the Electronic-Based Robotic Deposition process and subjected to quasi-static and cyclic compression. The test set-up permitted simultaneous measurements of the mechanical behavior and of the Poisson's ratio.

III.2.2.1 Design and development of the bowtie (re-entrant) structure

The first step of the project was to design a structure made of porous re-entrant cells. The following sub-section presents the steps of the design process that led to the study of a one-dimensional porous bowtie structure.

Considering a tetrakaidecahedron unit cell, Lakes [21] proposed an idealized unit cell for a three-dimensional re-entrant structure (Figure 3-3). From this original idea, the Universities of Kansas (KU) and Oklahoma State (OSU) worked together to create the unit cell of a three-dimensional (3D) re-entrant structure (Figure 3-4). Once the shape was achieved, the focus was put on the materials selection. The structure had to consist of biocompatible materials, metal and ferroelectric ceramic, since it was destined to orthopaedic applications (spinal fusion implant). Other requirements such as mechanical integrity, electromechanical properties, chemical processing, and availability were also considered.

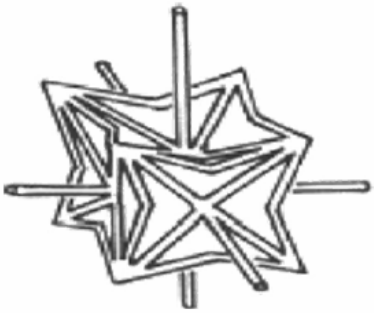

Figure 3-3. Idealized re-entrant three-dimensional cell, Lakes, *Science*, 1987 [22] (printed with permission from author)
http://silver.neep.wisc.edu/~lakes/sci87.html

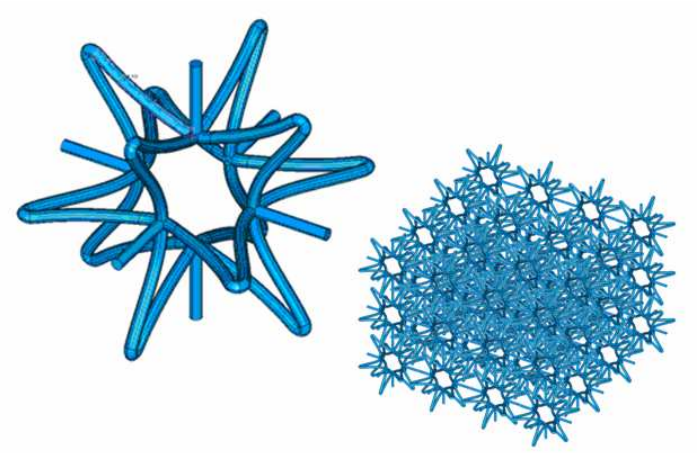

Figure 3-4. Modeling image of part of the 3D re-entrant specimen and one unit cell

Many of the scaffolds developed and investigated in tissue engineering studies provided useful information for this choice. The currently applied 3D scaffolding materials include ceramics, metals, natural and synthetic polymers and processed organic materials (collagen, HA). Despite their advantages, these materials are not all suitable for trabecular bone osteogenesis. For instance, biodegradable polymers (PGA, PLA) might weaken too fast for new bone to form, and fuse, in which case no structural network (bone or degraded implant) can provide support for the loads. Polymeric composites such as the carbon fiber/PEEK cage from Ultrapek® present appropriate mechanical properties that decrease the risk of stress shielding [22]. However, as ceramic inserts (Calcium–Phosphate, Hydroxyapatite) they do not deform significantly enough to provide the proper mechanical stimulation at small strains. As several studies showed [23-29], one of the best materials for bone in-growth is titanium. It has been successfully used in surgical practice (orthopaedic

implants) in a bulk form because of its excellent mechanical properties, biocompatibility, and ease of use in the clinical setting (MRI compatible) [29]. Furthermore, it can be made into a porous fiber mesh, which provides the scaffold with elasticity while keeping enough strength for load-bearing applications. Titanium is well known among orthopedic surgeons and engineers for its high biocompatibility and its osteo-inductive capacities as demonstrated in several studies [24-30]. Barium titanate has been employed in conjunction with different calcium-phosphates for the realization of porous bone implants [31-34]. It is biocompatible, it has been shown to bond well with titanium alloys [29-30] and it is available in micro- and nano-sized particles. Titanium and barium titanate ($BaTiO_3$) were thus initially selected for the research project presented. However, nano-meter sized titanium powder was too expensive to purchase so it was replaced with nickel powder for the initial investigations detailed in this document.

The development of the appropriate robocasting process to manufacture the three-dimensional structure proved very challenging for the OSU collaborators. A simpler one-dimensional structure was thus designed for the proof of concept. One of the simplest one-dimensional re-entrant unit cells is the bowtie, a modified hexagon, which was thus chosen to create the structure shown on Figure 3-5. The adjective ‘one-dimensional’ refers to the orientation of the bowtie-based cylinders in only one direction in the structure.

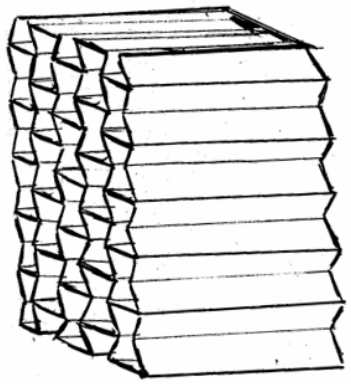

Figure 3-5. Sketch of the one-dimensional bowtie structure to be tested

III.2.2.2 Specimens

Small (S) and Medium (M) sized bowtie structures were prepared from nickel powder via the EBRD process at Oklahoma State University. The open bowtie cells were built upward along their long axis by staking a filament of extruded colloidal ink on top of a previous one partially solidified. After sintering, the stacked filaments are still visible as shown on Figure 3-6. Large (L), extra-large (XL) and extra-extra-large (XXL) versions of the same structure were handcrafted at the University of Kansas from various thicknesses Grade 302 stainless steel shim stock strips. One inch-wide strips were cut, periodically bent at 90 degrees with a mini press-brake and over-bent into half-bowties rows by hand. The strips were placed in a convective oven at 650 degrees Fahrenheit (343°C) [35] for two hours and left in the oven to cool down to ambient temperature, before bending. This stress-relief annealing procedure took place a second time; the 90 degree-bent strips were positioned between aluminum plates with weight put on them. A final manual bending transformed the 90 degree-

bent strips into half-bowties strips by matching a template. Once those half-bowties strips were ready, the structure was assembled and maintained by clipping the strips on top of each other with flat metal pieces and bulldog clips. This assembly was then put in the oven with weight on it for an ultimate annealing. The surfaces of those smooth bent strips were then roughened with 80-grit sandpaper, cleaned with rubbing alcohol and assembled with epoxy glue. Wooden pieces and bulldog clips were employed to maintain the proper alignment of the strips while the epoxy glue was curing. A total of five different structure types were prepared – eight Small 200μm-thick nickel, six Medium 200μm-thick nickel, three Large 100μm-thick stainless steel, three Extra-large 100μm-thick stainless steel and three Extra-extra-large 200μm-thick stainless steel. The dimensions of the structures displayed on Figure 3-7 are provided in Table 3-1.

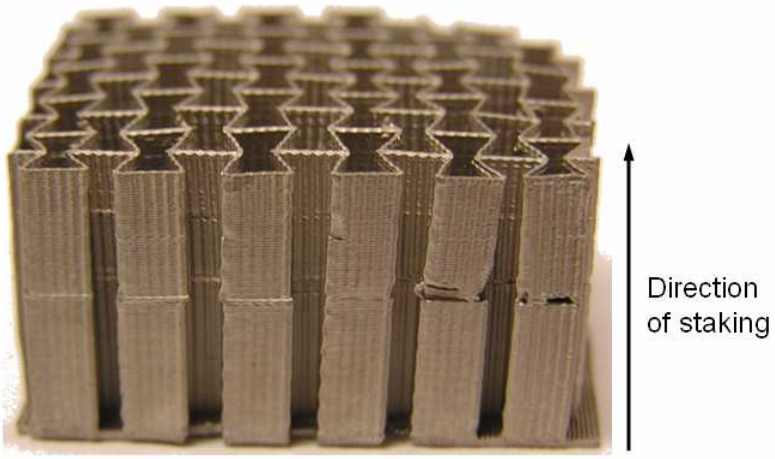

Figure 3-6. Photograph of a medium EBRD-made bowtie structure. The sintered filaments of colloidal ink can be seen in the plane perpendicular to the direction of staking

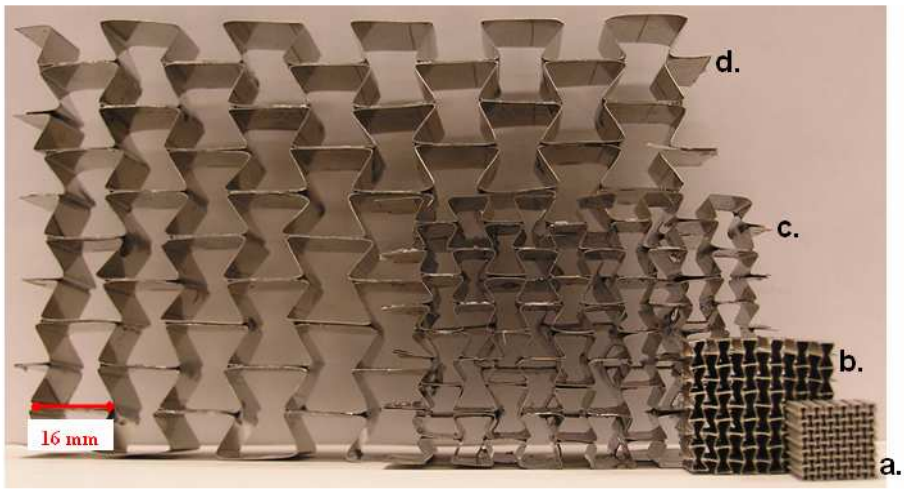

Figure 3-7. Photograph of the (a) small, (b) medium, (c) large, and (d) extra-large EBRD-made and handcrafted bowtie structures. The extra-extra-large is not shown because it resembles the extra-large but features a greater thickness

Table 3-1. Dimensions of the bowtie structures (mm)

Specimen Type	Plain Nickel		Plain Stainless Steel		
	S	**M**	**L**	**XL**	**XXL**
Width	1.3	3	7.5	16.5	16.5
Length	1.2	1.2	4	8	8
Thickness	0.203	0.203	0.102	0.102	0.203
Slenderness ratio (l/t)	5.9	5.9	39.2	78.4	39.4
Relative density	0.551	0.274	0.059	0.028	0.055

III.2.2.3 Test set-up and protocol(s)

The structures were subjected to cyclic and quasi-static compressive tests in a servo-hydraulic MTS system (Mini Bionic 858, MTS, Eden Prairie, MN). Extended platens were manufactured and adapted to the self-aligning compressive platens of the MTS to accommodate for the different sizes of the bowtie structures. In order to investigate the effect of friction on the mechanical behavior of the structures, tests were performed with and without lubricant spread on the top and bottom surfaces of the bowtie structures in contact with the compressive platens. The cyclic tests consisted of subjecting the structure to triangular compressive cycles up to a certain specified strain level at 0.04 mm/sec after ramping to a nominative value that ensured the specimen was always under compression. Four different axial strain levels (0.5%, 0.6%, 0.75%, and 1.0%) served for the evaluation of the mechanical behavior of the bowtie structures. Table 3-2 summarizes the various test configurations employed. One to three runs of the same test were performed consecutively with a repositioning and manual preconditioning of the specimen and a rest period between runs. The small and medium structures were tested only to 0.5% and 0.6% strain because a specimen of each type broke when tested at the next strain level. For the quasi-static tests, employing the exact same set-up, the specimens were slowly compressed (0.4233 mm/min) to failure. These displacement-controlled tests were initiated after ten manual preconditioning cycles (compression between -1 and -10 N) had been performed and the specimen was under a compressive load of 10 N.

MTI fiber optic probes (MTI Instruments Inc, Albany, NY) faced reflective targets mounted on opposite sides of the specimen to measure its transverse displacement. The targets, silver reflective tape implemented on a thin flat plastic sheet, were "glued" to the specimen with a jelly lubricant. This set-up allowed the targets to move with the specimen's sides without being deformed. Validation of this protocol is provided in Appendix 1. Semi-automated calibration of the probes followed preconditioning with the specimen still under a 10 N compressive load.

Table 3-2. Various test configurations employed in the test of the bowtie structures

Test	#1	#2	#3	#4	#5
Absolute end strain	0.5%	0.5%	0.6%	0.75%	1.0%
Lubricant	No	Yes	Yes	Yes	Yes

III.2.3 Analysis

The cyclic and quasi-static tests aimed at the determination of different mechanical properties. The quasi-static tests gave an idea of the overall mechanical behavior of the bowtie structures and permitted the calculation of various mechanical parameters such as the Young's modulus, plastic collapse stress, yield stress, yield strain, and resilience. Figure 3-8 depicts how the various mechanical parameters were

derived from the quasi-static stress-strain curve. The maximum stress reached before the stress plateau was measured as the plastic collapse stress. For the brittle structures (S and M), the maximum stress corresponded to the fracture stress. The modulus of elasticity was calculated as the slope of the region comprised between stresses equal to 45% and 60% of the maximum stress determined previously, as described by Sierpowska et al. [12]. For the non-brittle specimens (stainless steel L, XL, and XXL) a 0.2% strain offset was employed to estimate the yield stress and strain. Finally, the resilience was calculated as the area under the stress-strain curve up to the yield point. Comparisons of the relative modulus and plastic collapse stress to theoretical values were also established. Scanning Electron Microscope (SEM) pictures of the fractured surfaces of the specimens were taken with a JEOL 6380 (10 kV, sizepoint 28) to observe the internal microstructure of the EBRD-made nickel structures.

The cyclic tests were focused on the mechanical behavior at small strains and the apparent Poisson's ratio, or Compressive Strain Ratio (CSR). Quadratic polynomial and power function fittings were compared to the experimental nonlinear stress-strain curves. The CSR was obtained from the conversion of axial and transverse deformations into their respective strains. The measurement of the CSR was performed to demonstrate the re-entrant behavior of the structures. These combined results provided the researchers with a more complete description of the mechanical properties of the porous bowtie structure. To complete the investigation, the effect of lubrication on the mechanical behavior of the structures was also evaluated via the comparison of the CSR values obtained at the 0.5% strain level with

and without lubricant between the structures and the self-aligning metallic compressive platens.

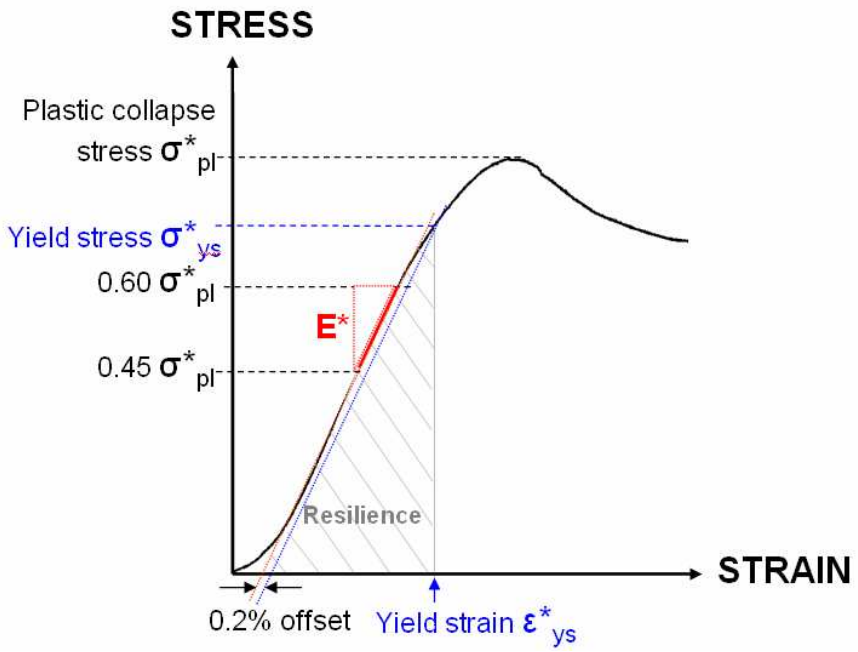

Figure 3-8. Schematic of a stress-strain curve displayed by the bowtie structures and the related mechanical parameters. The actual curves are displayed in Appendix 3-A

III.3 Results

III.3.1 Quasi-static strain-stress parameters

The strain-stress curves were derived from the axial deformation and force values measured during the compression tests. The general shape of these curves was evaluated first, followed by the estimation of mechanical parameters: modulus of elasticity, plastic collapse stress, yield strength, yield strain, and resilience, via custom made Matlab programs (The MathWorks Inc., Natick, MA). The experimental values of these parameters are presented for each of the L, XL, and XXL structures while average values are provided for the S and M structures since more specimens of these types were tested.

III.3.1.1 Mechanical behavior

The Small and Medium nickel structures prepared via the EBRD process displayed a very brittle behavior that was not expected for this material, as shown on Figure 3-9. On the contrary, all the handmade stainless steel specimens displayed the load-deformation relationship expected for cellular solids. The stress-strain curves clearly presented specific features: a linear increase followed by a plateau stress region and a final nonlinear increase in stress (densification), as illustrated on Figure 3-1. These curves also featured an initial “toe-region” preceding the linear region.

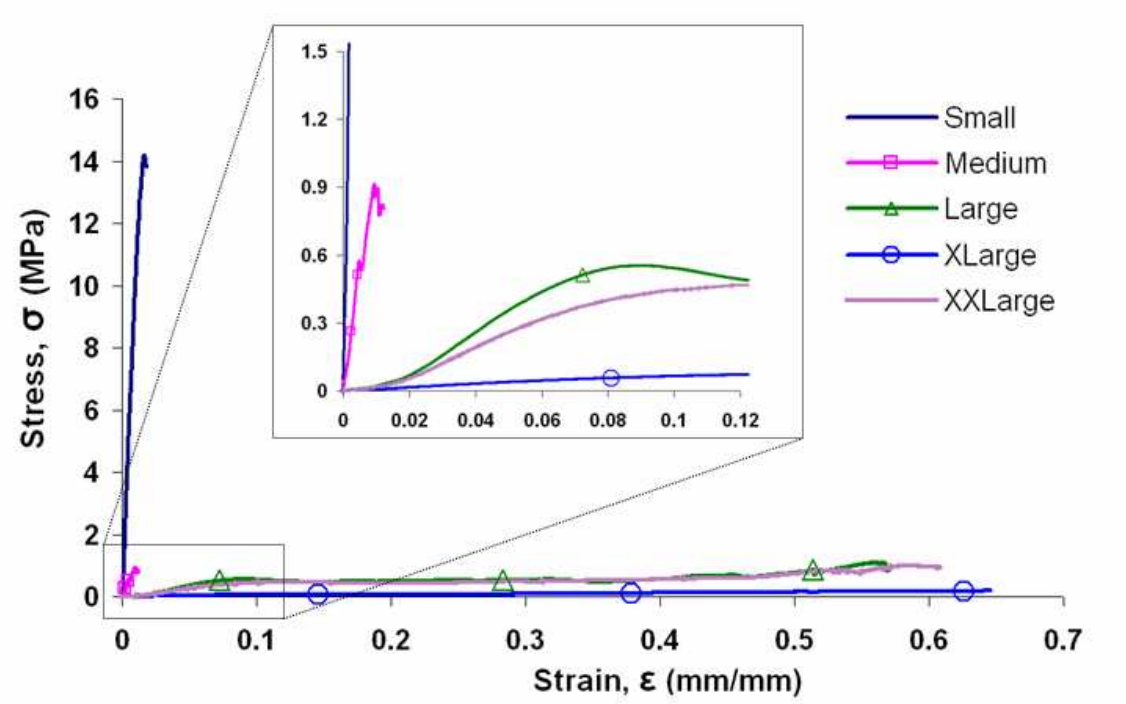

Figure 3-9. Stress-strain curves of the porous bowtie structures subjected to quasi-static compression at a rate of 25.4mm/minute. A zoom at small strains shows the nonlinear behavior of the L, XL, and XXL structures

III.3.1.2 Mechanical parameters

The average and standard deviation values of the five parameters are displayed in Table 3-3 for each type of structure along with their estimated average relative density. The relative collapse stress and relative modulus were calculated by dividing the plastic collapse stress and modulus values of the structure by the yield strength and modulus of elasticity of the base material, respectively. The relative modulus of elasticity and plastic collapse stress were calculated to investigate their relationship with the relative density at different powers. Those allowed verifying if

the relationship agreed with the cellular solid theory developed by Gibson and Ashby (equations {3-1} and {3-4}).

Table 3-3. Mechanical parameters and relative density of the five different porous bowtie structures tested in quasi-static compression [average (standard deviation)] ** fracture stress for the S and M structures, and to the plastic collapse stress for the L, XL, and XXL structures

Specimen Type	S (n=7)	M (n=5)	L (n=3)	XL (n=3)	XXL (n=3)
Elastic modulus (MPa)	1434 (1082)	158 (33)	8.4 10.1 10.6	0.6 0.7 0.6	6.4 6.9 6.8
Maximum Stress (MPa)**	14.7 (2.42)	1.2 (0.97)	0.51 0.56 0.56	0.07 0.08 0.09	0.46 0.53 0.52
Yield Strength (MPa)	-	-	0.36 0.43 0.42	0.04 0.05 0.06	0.34 0.35 0.36
Yield Strain	-	-	0.06 0.06 0.05	0.07 0.07 0.09	0.06 0.07 0.07
Resilience (MPa)	-	-	0.009 0.010 0.010	0.002 0.002 0.003	0.011 0.010 0.010
Relative density	0.551	0.274	0.059	0.028	0.055

Both the elastic modulus and the maximum stress (plastic collapse stress) of the stainless steel structures were one and three orders of magnitude smaller than those of the Medium and Small nickel structures, respectively. Overall, the modulus of elasticity increased with the relative density. The yield strength, yield strain, and resilience values obtained for the stainless steel specimens demonstrated that the mechanical properties are all dependent on the relative density. The Large and Extra-

extra-large structures that featured similar relative densities (0.059 and 0.055, respectively) yielded similar mechanical parameters. For instance, their respective yield strengths were around 0.40 MPa and 0.35 MPa and their respective resilience values were both around 0.010 MPa. The extra-large structure whose relative density was 50% smaller, the yield strength and resilience were seven and four times smaller, respectively, than those of the other two structures. These results coincided with the greater deformation of the XL structure in comparison to the deformation of the L and XXL structures, at the plastic collapse stress (around 0.18, 0.09, and 0.12, respectively) as shown by the curves in Appendix 3-A. Comparisons with theory were enabled by calculating the relative modulus of elasticity (experimental modulus divided by the modulus of elasticity of the base material) and the relative plastic collapse stress.

III.3.1.3 Experimental vs. theoretical

The relative modulus was calculated for the five different structures. The relative parameter values were plotted against the relative density to the power two. Figures 3-10 and 3-11 illustrate the linear proportionality between the relative modulus and the square of the relative density. The data points fit well the dashed theoretical line obtained from equation {3-1} with a coefficient C_1 equal to 0.0116. Table 3-4 shows that this coefficient matched the ratio of the relative modulus over the square of the relative density for all but the XL structure. The least-square fitting yielded an overall coefficient of determination R^2 equal to 0.9989. The ratio for the

XL type was three to four times smaller than those of the other structures and the C_1 coefficient.

Since the S and M structures were brittle, the relative plastic collapse stress was calculated for the L, XL, and XXL types only. A plot of these values against the relative density to the power 3/2 showed the linear correlation (Figure 3-12). The data points fit well the dashed theoretical line obtained from equation {3-4} with a coefficient C_5 equal to 0.038. Table 3-4 details more precisely that this coefficient matched the ratio of the relative plastic collapse stress over the relative density to the power 3/2 for the L and XXL structures. But the ratio obtained for the XL structure was more than two times smaller than this coefficient C_5.

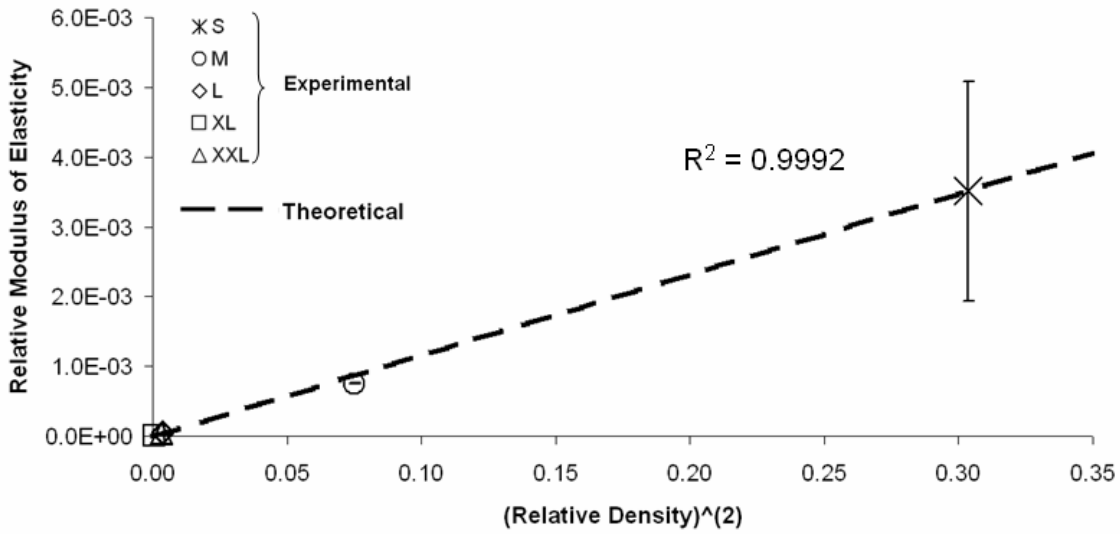

Figure 3-10. Theoretical and experimental values of the Relative Modulus of Elasticity vs. (Relative Density)^(2) for the S (x), M (o), L (◇), XL (□), and XXL (△) bowtie structures

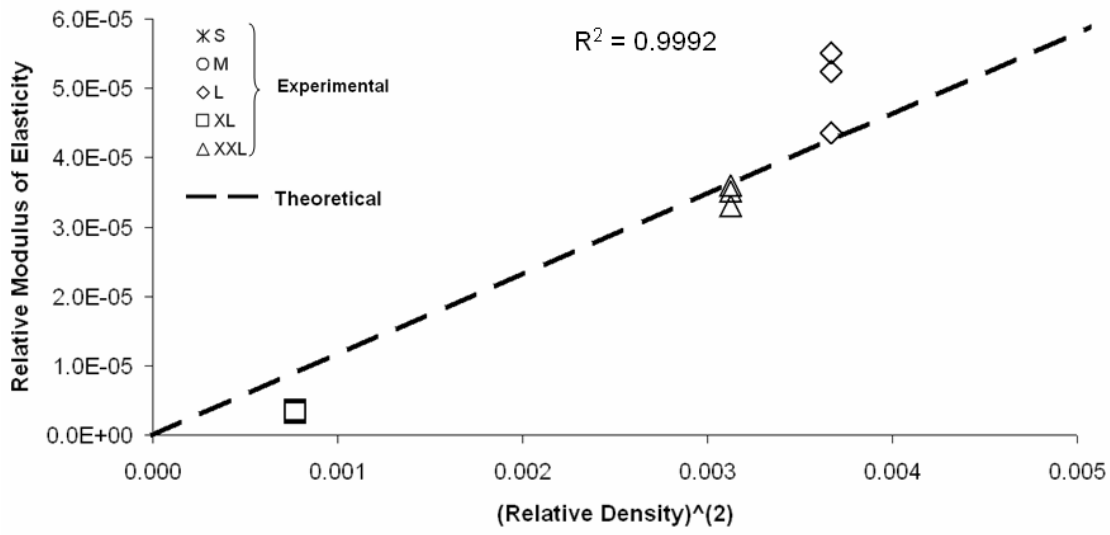

Figure 3-11. Theoretical and experimental values of the Relative Modulus of Elasticity vs. (Relative Density)^(2). Zoom showing the relationship for the L (◇), XL (□), and XXL (△) bowtie structures

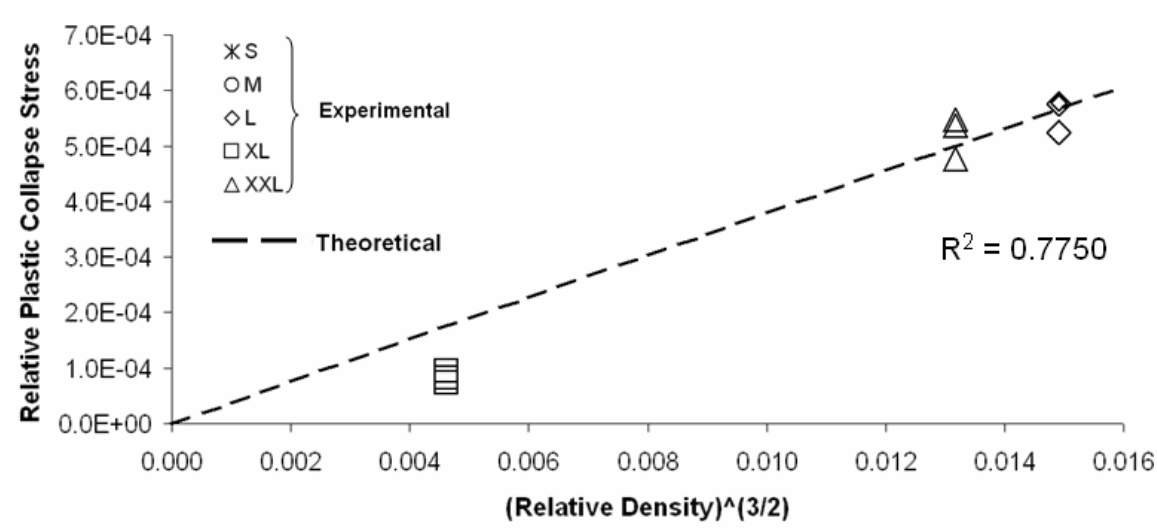

Figure 3-12. Relative Plastic Collapse Stress vs. (Relative Density)^(3/2) for the L (◇) , XL (□), and XXL (△) bowtie structures

Table 3-4. Experimental values corresponding to coefficients C_1 and C_5 of equations {3-1} and {3-4}, respectively, for the five types of bowtie structures [average (standard deviation)]

Coefficients	S (n=7)	M (n=5)	L (n=3)	XL (n=3)	XXL (n=3)
C1	0.012 (0.005)	0.010 (0.000)	0.011 0.015 0.016	0.004 0.005 0.004	0.010 0.012 0.011
C5	-	-	0.034 0.040 0.040	0.016 0.017 0.020	0.035 0.042 0.041

III.3.2 Cyclic stress-strain behavior

All the structures were subjected to cyclic compression tests at different strain levels. The analysis of the recorded axial deformation and force yielded a relationship between the strain and stress, which served for the analysis of the mechanical behavior at small strains. This behavior was identified as being a function of the relative density of each structure. Compressive Strain Ratio evaluation permitted the verification that the structures displayed a re-entrant behavior.

III.3.2.1 Mechanical behavior

All the structures displayed a repeatable behavior at all the various strain levels they were tested since the hysteresis was very small and the cycle loops of the stress-strain curves were overlapping each other (Figure 3-13, Appendix 3-B). This proved that no macro-scale plasticity was taking place, but friction was probably occurring despite the presence of lubricant between the structure and the compressive

platens. Attention was focused on the shape of the loading portion of the cycles. Those were best fitted by a second-order polynomial as expressed in equation {3-8}. Coefficients A and B of this mathematical expression were evaluated for each cycle, averaged for each test run, and correlated with the relative density. From the works of Gibson and Ashby [2], the relationship between the polynomial coefficients and the relative density was first compared to power functions. Eventually, the trends shown on Figures 3-14 and 3-15 (and Appendices 3-C and 3-D) for coefficients A and B resembled expressions such as those described by equations {3-10} and {3-11}. Experimental data were employed to evaluate the various constants of these equations.

$$A = D_A \times \left(\frac{\rho^*}{\rho_s} \right)^{C_A} \qquad \{3\text{-}10\}$$

$$B = -\mathrm{e}^{\left(C_B \times \left(\frac{\rho^*}{\rho_s} \right) + D_B\right)} \qquad \{3\text{-}11\}$$

where ρ^* is the density of the structure
ρ_s is the density of the base material of the structure
ρ^*/ρ_s is the relative density of the structure
C_A, C_B, D_A, D_B are constants

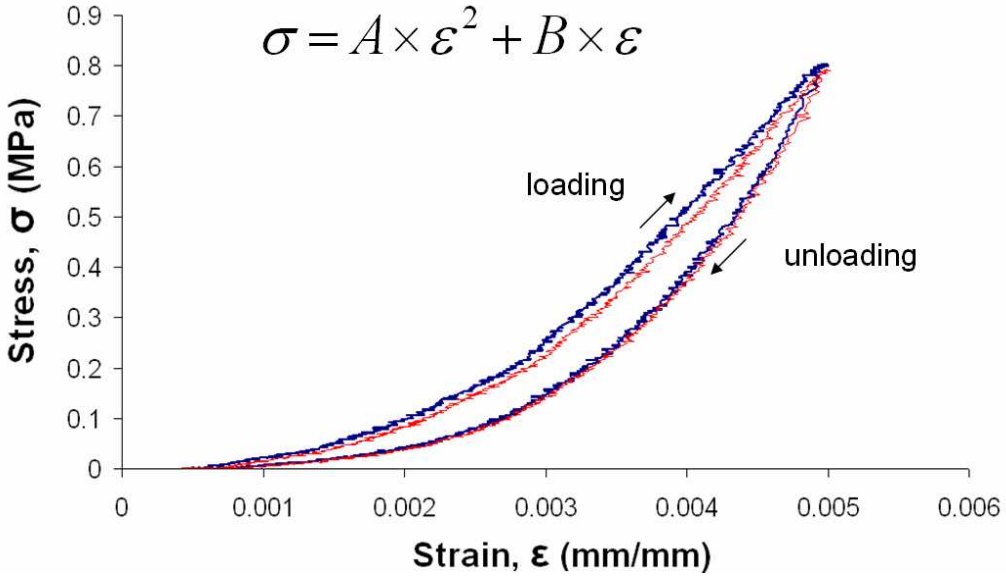

Figure 3-13. Nonlinearity of the stress-strain behavior observed during the first two (as shown) and subsequent loading-unloading cycles of the five bowtie structures after preconditioning. All the curves are provided in Appendix 3-B

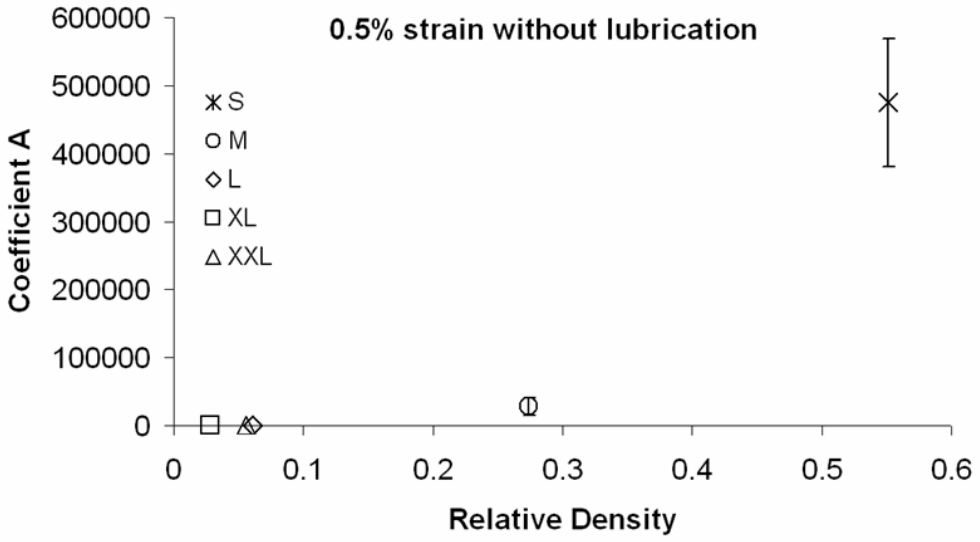

Figure 3-14. Plot of coefficient A values versus the relative density for the five structures at 0.5% strain without lubrication. Identical plots at the other strain levels are provided in Appendix 3-C

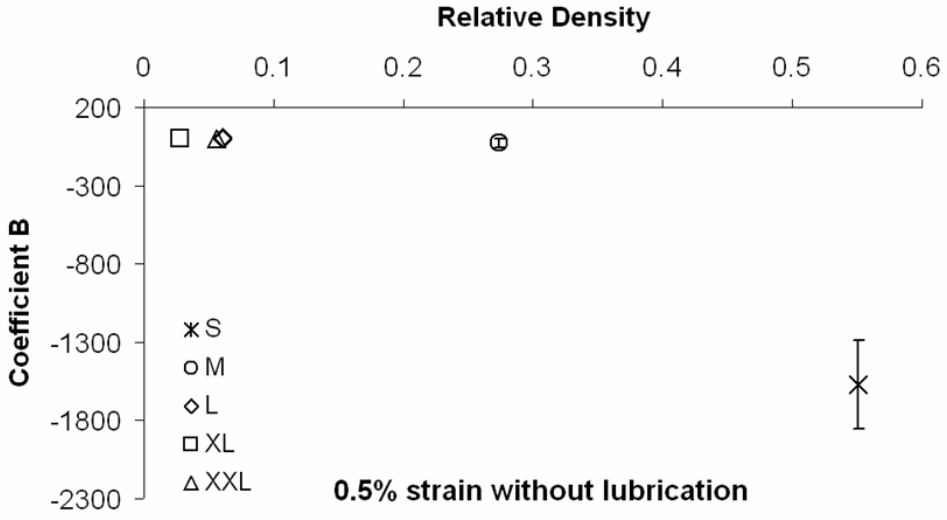

Figure 3-15. Plot of coefficient B values versus the relative density for the five structures at 0.5% strain without lubrication. Identical plots at the other strain levels are provided in Appendix 3-D

Determination of equation {3-10} from experimental data

The logarithmic values (base 10) of the average A values were calculated and plotted against the relative density (Figure 3-16 and Appendix 3-E). The data points fit the following logarithmic expression (equation {3-12}) appropriately.

$$\log_{10}(A) = \beta_A \times \log_e\left(\frac{\rho^*}{\rho_s}\right) + \delta_A \qquad \{3\text{-}12\}$$

A change of logarithmic base was required to obtain the power relationship between the polynomial coefficient and the relative density. A step-wise derivation of equation {3-10} from equation {3-12} is provided below.

$$\log_e(A) = \frac{\beta_A}{\log_{10}(e)}.\log_e\left(\frac{\rho^*}{\rho_s}\right) + \frac{\delta_A}{\log_{10}(e)} \quad \{3\text{-}13\}$$

$$\log_e(A) = C_A \times \log_e\left(\frac{\rho^*}{\rho_s}\right) + \log_e(D_A) \quad \{3\text{-}14\}$$

$$\log_e(A) = \log_e\left(\left(\frac{\rho^*}{\rho_s}\right)^{C_A}\right) + \log_e(D_A) \quad \{3\text{-}15\}$$

$$\log_e(A) = \log_e\left(D_A \times \left(\frac{\rho^*}{\rho_s}\right)^{C_A}\right) \quad \{3\text{-}16\}$$

$$A = D_A \times \left[\left(\frac{\rho^*}{\rho_s}\right)^{C_A}\right] \quad \{3\text{-}10\}$$

Where β_A, δ_A, C_A, D_A are constants

Coefficients C_A and D_A were estimated at each strain level for each relative density.

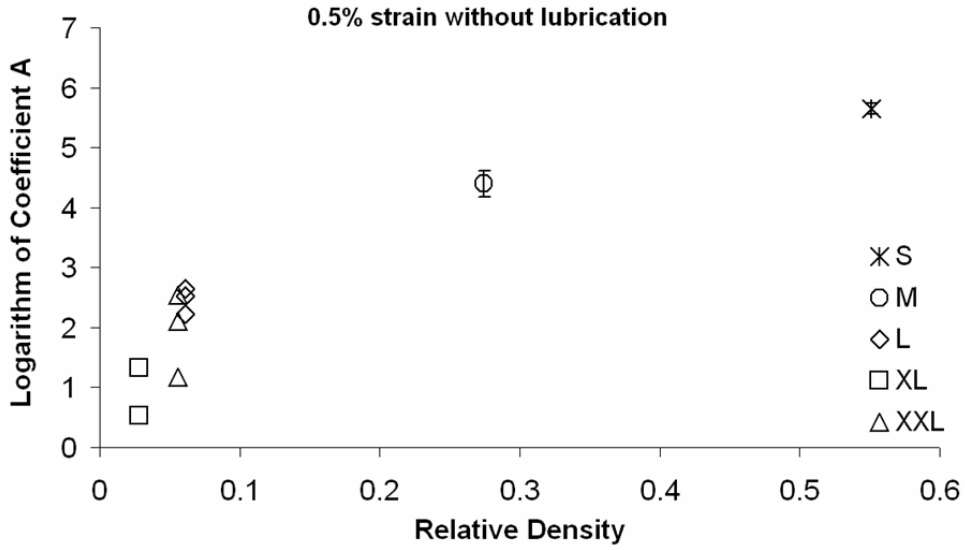

Figure 3-16. Plot of the logarithm of coefficient A versus the relative density for the five structures at 0.5% strain without lubrication. Identical plots at the other strain levels are provided in Appendix 3-E

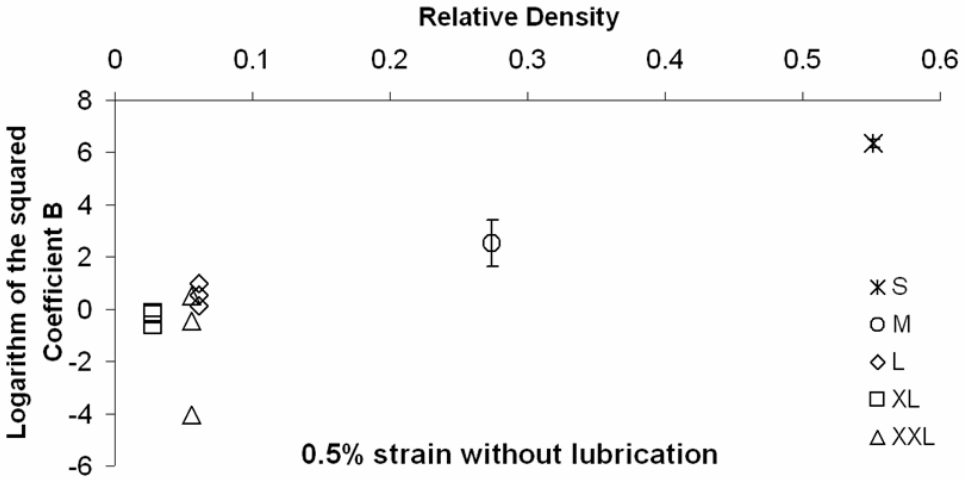

Figure 3-17. Plot of the logarithm of coefficient B versus the relative density for the five structures at 0.5% strain without lubrication. Identical plots at the other strain levels are provided in Appendix 3-F

Determination of equation {3-11} from experimental data

The values of coefficient B obtained for the S and M structures were negatives so all the coefficient B values were squared before their logarithm was calculated. A plot of the logarithm of the squared B values against the relative density yielded a linear correlation at the first three test levels as displayed in Figure 3-17 and Appendix 3-F. This correlation allowed evaluating coefficients C_B and D_B of equation {3-11} as explained below. The linear correlation was not considered at test levels 4 and 5 because there were only three data points to interpolate, which biased the slope of the fitting line. A step-wise derivation of equation {3-11} is provided below.

$$\log_{10}\left(B^2\right)=\alpha_{B}\times\left(\frac{\rho^*}{\rho_s}\right)-\delta_B \qquad \{3\text{-}17\}$$

$$2\times\log_{10}\left(B\right)=\alpha_{B}\times\left(\frac{\rho^*}{\rho_s}\right)-\delta_B \qquad \{3\text{-}18\}$$

$$\log_{e}\left(B\right)=\frac{\alpha_{B}}{2\times\log_{10}(e)}\times\left(\frac{\rho^*}{\rho_s}\right)-\frac{\delta_B}{2\times\log_{10}(e)} \qquad \{3\text{-}19\}$$

$$\log_{e}\left(B\right)=C_B\times\left(\frac{\rho^*}{\rho_s}\right)+D_B \qquad \{3\text{-}20\}$$

$$B=-e^{\left(C_B\times\left(\frac{\rho^*}{\rho_s}\right)+D_B\right)} \qquad \{3\text{-}11\}$$

Where $\alpha_{\mathbf{B}}$, δ_B, C_B, D_B are constants

The minus sign in equation {3-11} was added in accordance with the negative values of coefficient B at high densities. Coefficients C_B and D_B were estimated at each strain level and then averaged to yield an average B coefficient for each relative density. From a global prospective the theoretical data points fit the experimental ones points nicely especially at the highest densities, regardless of the strain level. However, the discrepancy was significant between the experimental and theoretical values at small densities. Replacing A and B in equation {3-8} yielded expressions of the stress as a function of both the strain and the relative density (equation {3-19}). Tables 3-5 and 3-6 display the values of the experimental polynomial coefficients obtained from the data analysis and plotted on Figures 3-14 and 3-15.

$$\sigma = \left(D_A . \left(\frac{\rho^*}{\rho_s} \right)^{C_A} \right) . \varepsilon^2 - \left(e^{\left(C_B . \left(\frac{\rho^*}{\rho_s} \right) + D_B \right)} \right) . \varepsilon \qquad \{3\text{-}21\}$$

Table 3-5. Average experimental polynomial values of **coefficient A** for the five bowtie structures at each strain level. All structures were tested with lubrication unless noted otherwise

Structure type	Relative Density	Experimental				
		0.5% without lubrication	0.5%	0.6%	0.75%	1.0%
S	0.551	474932 (94385)	410892 (264680)	280372 (265626)	-	-
M	0.274	27909 (12396)	22539 (9895)	29232 (6336)	-	-
L	0.059	262	4	139	123	156
		335	230	405	327	219
		444	439	310	259	183
XL	0.028	21	-14	-8	0	1
		-3	-22	-8	6	37
		3	-21	-13	22	28
XXL	0.055	126	68	93	101	153
		349	312	274	234	190
		15	8	20	21	20

Table 3-6. Average experimental polynomial values of **coefficient B** for the five bowtie structures at each strain level. All structures were tested with lubrication unless noted otherwise

Structure type	Relative Density	Experimental				
		0.5% without lubrication	0.5%	0.6%	0.75%	1.0%
S	0.551	-1569 (283)	-960 (688)	-1019 (850)	-	-
M	0.274	-29 (30)	-19 (37)	-82 (43)	-	-
L	0.059	3.1	3.6	3.4	4.0	3.9
		1.2	1.9	0.9	1.6	2.4
		1.9	2.1	3.0	3.0	3.6
XL	0.028	0.5	0.6	0.5	0.5	0.5
		0.8	1.0	0.9	0.8	0.6
		0.8	1.0	0.9	0.7	0.7
XXL	0.055	1.8	2.0	2.0	1.8	1.6
		0.0	0.3	0.3	0.6	0.9
		0.6	0.6	0.6	0.6	0.6

III.3.2.2 Compressive Strain Ratio

The Compressive Strain Ratio was evaluated for each cycle of each run, averaged over the runs and then averaged for each strain level for each structure type. As shown in Figures 3-18 and 3-19, the test average CSR values were all negative as expected and confirmed the re-entrant behavior observed during the quasi-static and cyclic tests. Regardless of the strain level and the lubrication condition, the average bar graphs and the data point in Figure 3-18 illustrated that the small structures displayed the smallest average CSR values, followed by the medium, extra-extra-large, and large structures. The extra-large structures displayed the lowest average CSR values whose magnitude was two to six times greater than those of the other structures. Figure 3-19 enabled comparing the average CSR values obtained at the 0.5% strain level with and without lubrication.

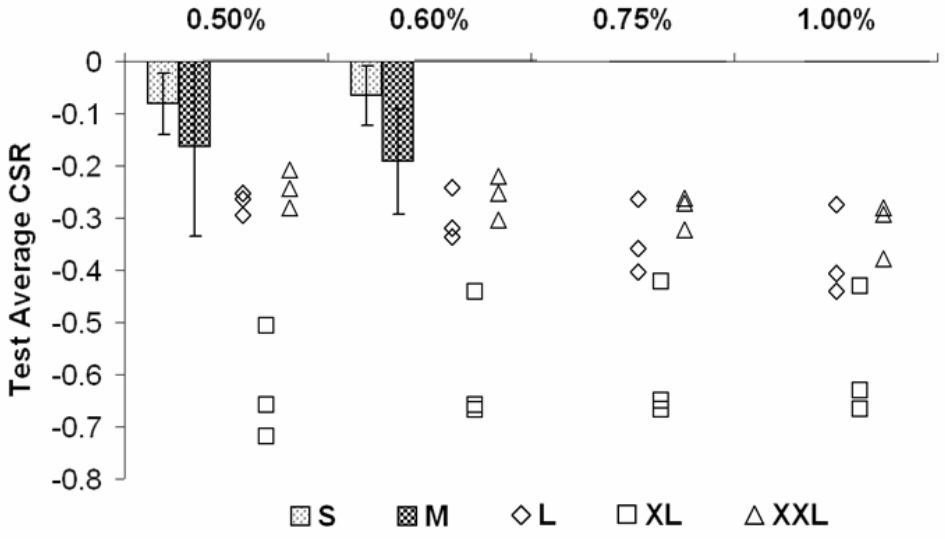

Figure 3-18. Average CSR values of the five bowtie structures tested at four different strain levels with lubricant at the interface with the compressive platens

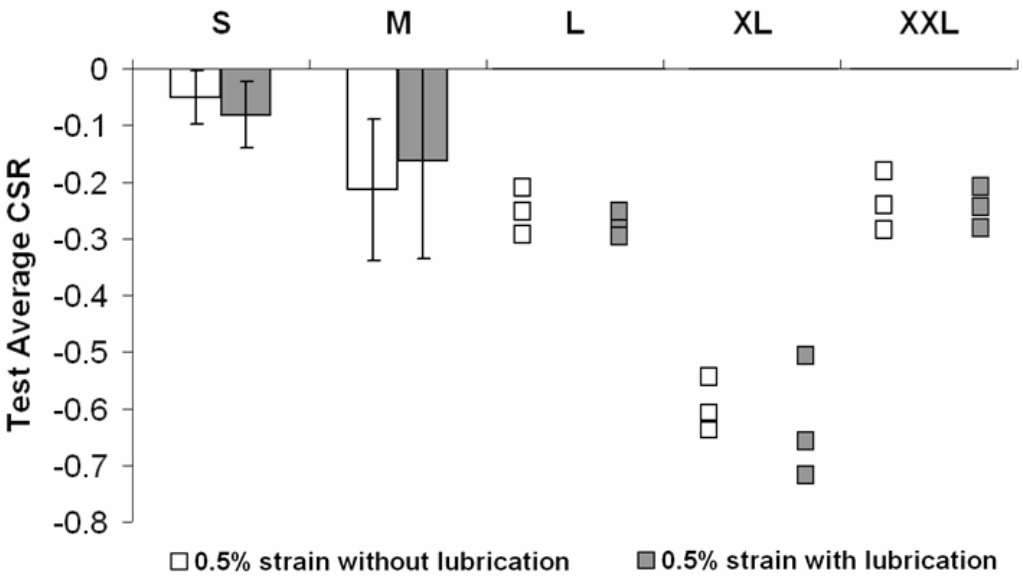

Figure 3-19. Average CSR values of the five bowtie structures compressed down to 0.5% strain with and without lubrication at the interface with the compressive platens

The average CSR values were also compared between strain levels with lubrication for each structure separately. The standard deviations were very large with-respect-to the average CSR values for the small and medium structures. As can be seen on Figures 3-20 and 3-21, the average CSR values were similar at the 0.5%, and 0.6% strain levels for the small and the medium structures. The p-values obtained via the analysis of variance (ANOVA) for these average values revealed that they were not significantly different for the small structure but significantly different for the medium one (p-value <0.05). This significant difference for the medium structure was validated by a statistical power of 100% whereas the power was about 20% for the small structure.

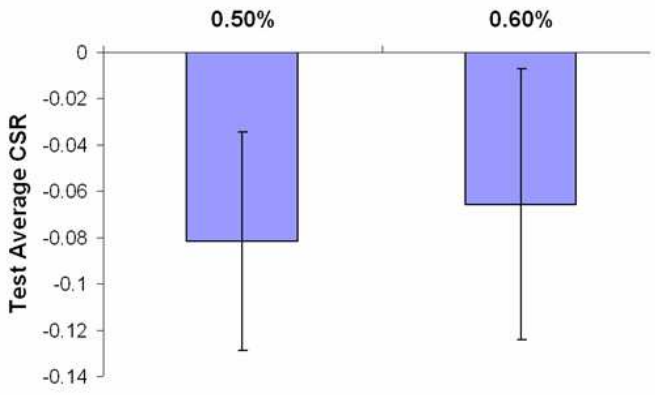

Figure 3-20. Average CSR values of the **small** bowtie structures tested at two different strain levels with lubrication at the interface with the compressive platens

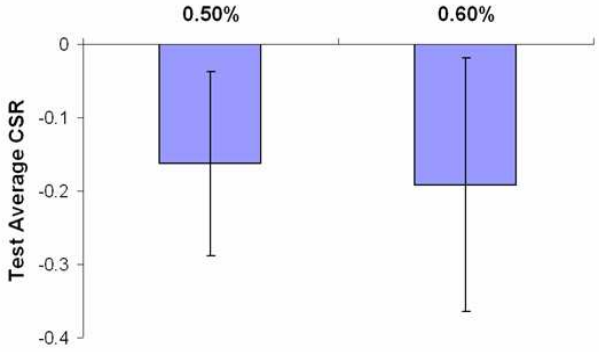

Figure 3-21. Average CSR values of the **medium** bowtie structures tested at two different strain levels with lubrication at the interface with the compressive platens

For the large, extra-large, and extra-extra-large structures the small number of specimens led to a lack of statistical power (less than 20%) that did not allow statistical analyses. Figures 3-22 and 3-24 revealed that the magnitude of the average CSR tended to increase with the strain level. The increase in CSR magnitude from 0.5% to 0.6%, 0.6% to 0.75%, and 0.75% to 1.0% was on average 10.5%, 13.2%, and

9.0%, respectively, for the large structure. For the extra-extra-large structure, the magnitude increase was on average 6.1%, 8.9% and 10.7%, respectively. As shown in Figure 3-23, there was an average decrease of 6.2%, 2.2%, and 0.5%, respectively, between these strain levels for the extra-large structure.

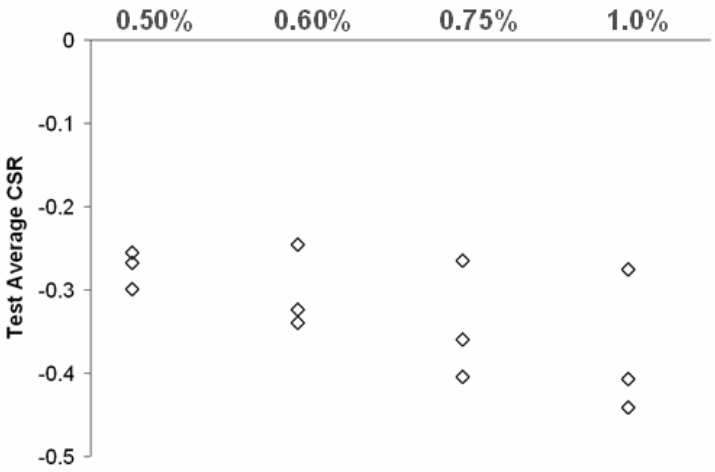

Figure 3-22. Average CSR values of the large bowtie structures tested at four different strain levels with lubrication at the interface with the compressive platens

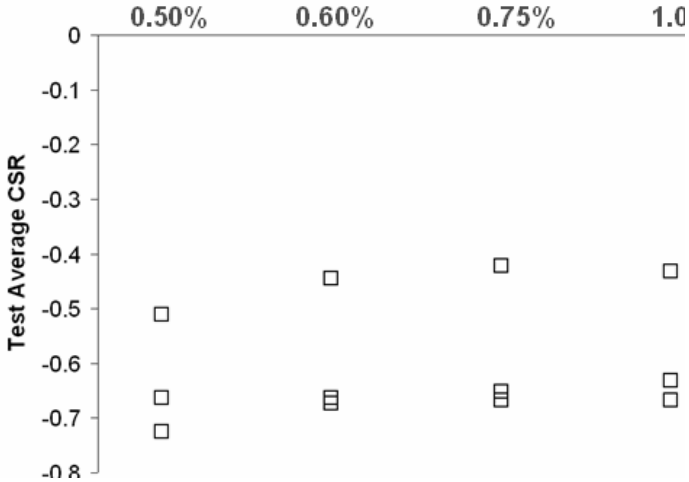

Figure 3-23. Average CSR values of the extra-large bowtie structures tested at four different strain levels with lubrication at the interface with the compressive platens

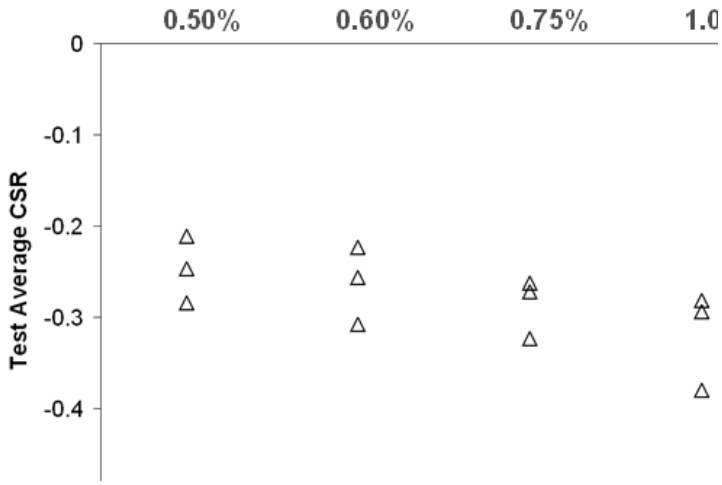

Figure 3-24. Average CSR values of the extra-extra-large bowtie structures tested at four different strain levels with lubrication at the interface with the compressive platens

III.3.2.3 SEM pictures

Scanning Electron Microscope (SEM) pictures were taken as part of the post-failure analysis. Pieces of open bowtie cells that had broken as illustrated in Figure 3-25 were observed at two different locations. Figure 3-26 shows the 500x and 1000x enhanced SEM pictures of the external and fractured surfaces of a bowtie open cell from a small structure. Similar pictures are presented in Figure 3-27 for a bowtie open cell from a medium structure. The pictures showed that the nickel particles were not fused. In addition, the pictures of the fractured surfaces illustrated the dispersion of the particles in a darker homogeneous matrix material. The dispersion of the nickel particles was greater in the small bowtie (Figure 3-26a and b) while the medium bowtie contained more nickel particles (Figures 3-27a and b). The enhanced pictures of the external surfaces showed that a sintered filament of colloidal ink consisted of

agglomerated five to ten micron-wide polyhedral nickel particles. A closer observation of Figures 3-26c and d showed the presence of micro-pores and the dark material also on the external surface of the sintered colloidal filaments of the small bowtie. This dark material was not observed on the external surface of the medium bowtie but Figures 3-27c and d highlighted the presence of micro-pores.

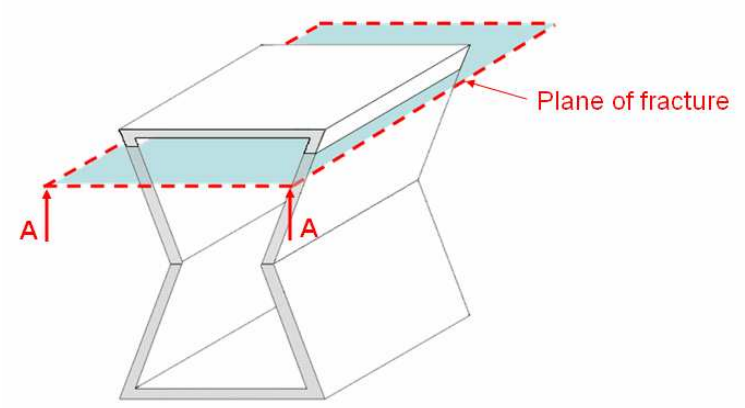

Figure 3-25. Schematic of an open bowtie cell and the plane of fracture explaining the central photographs in Figures 3-26 and 3-27

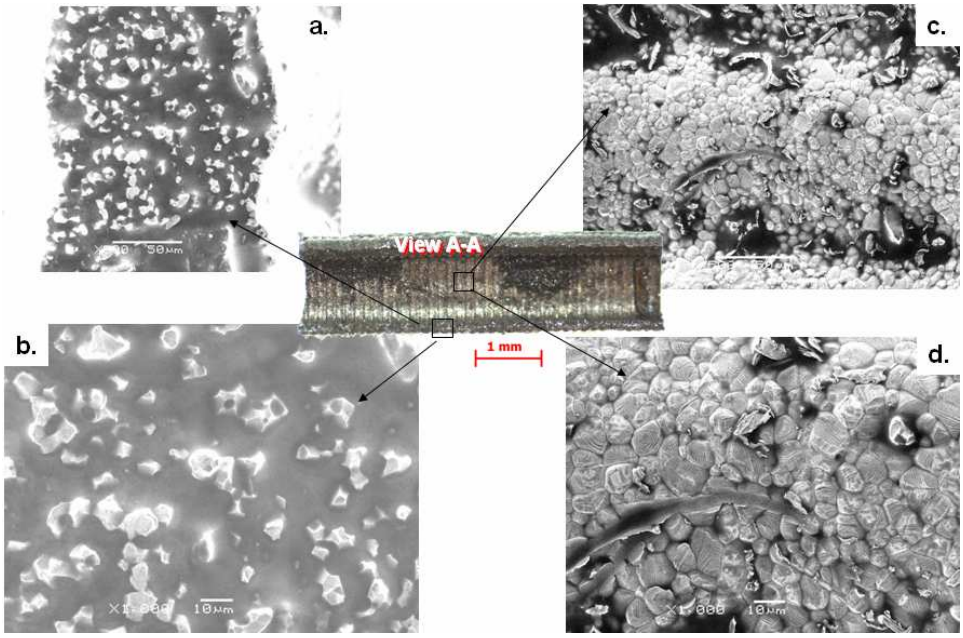

Figure 3-26. SEM pictures of the fractured surface x500 (a), x1000 (b), and of the external surface x500 (c), x1000 (d) of a failed small bowtie cell

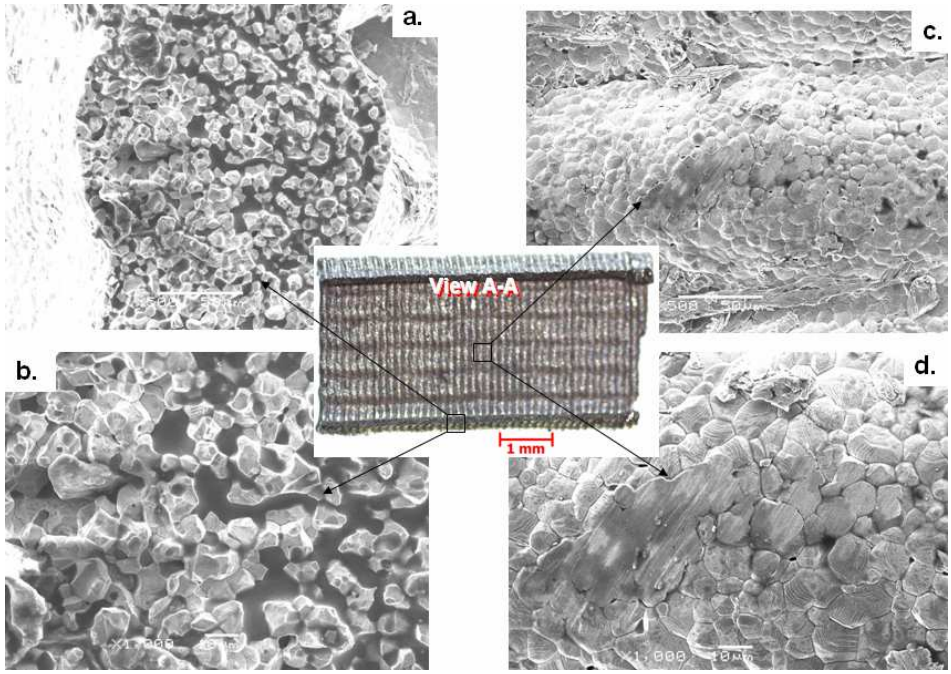

Figure 3-27. SEM pictures of the fractured surface x500 (a), x1000 (b), and of the external surface x500 (c), x1000 (d) of a failed medium bowtie cell

III.4 Discussion

This section discusses the results and provides insight on the general mechanical behavior and parameters of the bowtie structures tested. Comparisons also permitted the understanding of the effect of the base material and aspect ratio of the structures on their mechanical properties. This chapter was partitioned to discuss the results of the quasi-static and cyclic compressive tests, respectively, in that order.

III.4.1 Quasi-static compression tests

The contrast between the different bowtie structures showed the effect of the relative density, unit cell's dimensions, and base material. Comparisons to trabecular bone were also performed to complete the analysis and check if the research was heading in the right direction.

III.4.1.1 Mechanical behavior

Unexpectedly, the plain nickel small and medium EBRD structures displayed a very brittle behavior uncharacteristic of this ductile material. SEM pictures confirmed the presence of micro-pores in the open bowtie cell walls. Some of the holes might have been caused by micro air bubbles entrapped during the filling of the deposition syringe. A parallel study on discs obtained from the same nickel colloidal ink revealed the high porosity (20%-25%) present in the sintered nickel colloidal ink

but not the presence of another material beside the nickel particles. The dark homogeneous material was likely a fused nickel oxide. The presence of nickel oxide and the lack of particles fusion caused discontinuities in the microstructure that led to a brittle behavior. Despite sharing this defect, the modulus of the small structure was an order of magnitude greater than that of the medium ones. This was explained by considering the dimensions of the open bowtie cells in the small and medium structures. The longer re-entrant members of the medium bowtie cells presented was more cantilever potential than the shorter members of the small bowtie cells that bent and buckled less easily. The sturdier small bowtie cells therefore requiring more mechanical energy to deform displayed a greater average modulus.

For the larger stainless steel structures, the differences in modulus and plastic collapse stress values can be linked to the aspect ratio of the unit cells. With respect to the XL structure, the L and XXL structures presented shorter and thicker non-horizontal struts, respectively. These modifications affected the slenderness ratio (length of the non-horizontal strut over thickness), which controls the second moment of inertia of the open bowtie cells. Decreasing the length or increasing the thickness of the struts increased their bending stiffness and resistance to buckling. That explains why the mechanical properties of the L and XXL structures were similar to each other and dissimilar from that of the XL structure. But this difference demonstrated that the mechanical behavior can be tailored by modifying the dimensions of the unit cells. For the L and XXL structures, the strain-stress graphs (zoomed view in Figure 3-8) presented a “toe-region” up to 0.025 strain before rising linearly and then

transitioning to a convex upward curve just before reaching the plastic collapse stress. This initial concave downward portion defined the nonlinear character of the stress-strain behavior.

III.4.1.2 Mechanical parameters

Strain-stress curves were analyzed more specifically to evaluate the values of mechanical parameters related to the initial non-plastic region of the curve. The apparent modulus of elasticity of each structure was normalized to that of the base material to allow comparing the effect of relative density. The relationship was linear between the relative modulus and the square of the relative density; this agreed well with the theory for cellular solids. However, the experimental coefficient of proportionality 0.0116 was different from coefficient C_1 in equation {3-1}, equal to one for open cell cellular solids according to Gibson and Ashby [2]. In the same way, the experimental coefficient of proportionality between the relative plastic collapse and the relative density to the power 3/2 was equal to 0.038 that did not match the C_5 coefficient (0.23 – 0.3) found for open cell cellular solids in the equations developed by these researchers. The mismatch between those coefficients and the C_1 and C_5 coefficients obtained by Gibson and Ashby was easily explained. The main reason was that the bowtie structure under test was porous in only one direction. It was not a 3D-structure with fully open or closed cells as in the works of the previous researchers.

The relationship between the relative modulus and the relative density was the same as the relationship between the modulus of elasticity and the relative density that was evidenced by the values in Table 3-3. This conservation of trend was explained by the fact that nickel and stainless steel have similar moduli of elasticity (207 and 193 GPa, respectively). Therefore, normalizing the modulus of elasticity by those of these materials accordingly for each structure did not modify their ranking with respect to their relative density. This proved that the parameter that controlled the mechanical parameter was the unit cells' dimensions and more precisely the relative density. The S and M structures whose relative densities were five to ten times greater than those of the L, XL, and XXL structures, displayed moduli of elasticity two to three orders of magnitude greater. The reported values of yield strength, yield strain and resilience confirmed this dependence of the mechanical parameters on the relative density. For instance, the values of the mechanical parameters were very similar for the L and XXL structures that also featured close relative densities (0.061 and 0.056, respectively) and slenderness ratios (39.2 and 39.4, respectively).

III.4.1.3 Comparison to trabecular bone

The concrete application of the novel structure under investigation is orthopedic implants. To remain consistent with this long-term goal, a direct comparison was established between strain-stress graphs obtained from the

compressive tests of the bowtie structure and of trabecular bone. The biological tissues (pigs, cows) tested by Moselkide, Hvid and Guedes et *al.* [36-38] displayed a more pronounced nonlinearity at strains below 5%. Even if the behavior of the EBRD structures tested was much more brittle and less nonlinear, Figure 3-28 shows that more ductile bowtie structures of intermediary size could yield a behavior close to that of trabecular bone. Therefore, these preliminary results were very encouraging even if nickel was used instead of the biocompatible titanium. It meant that the mechanical properties of the structure could be tailored to match that of cancellous bone by modifying the bowtie unit cell's dimensions such as length, width, thickness or angle.

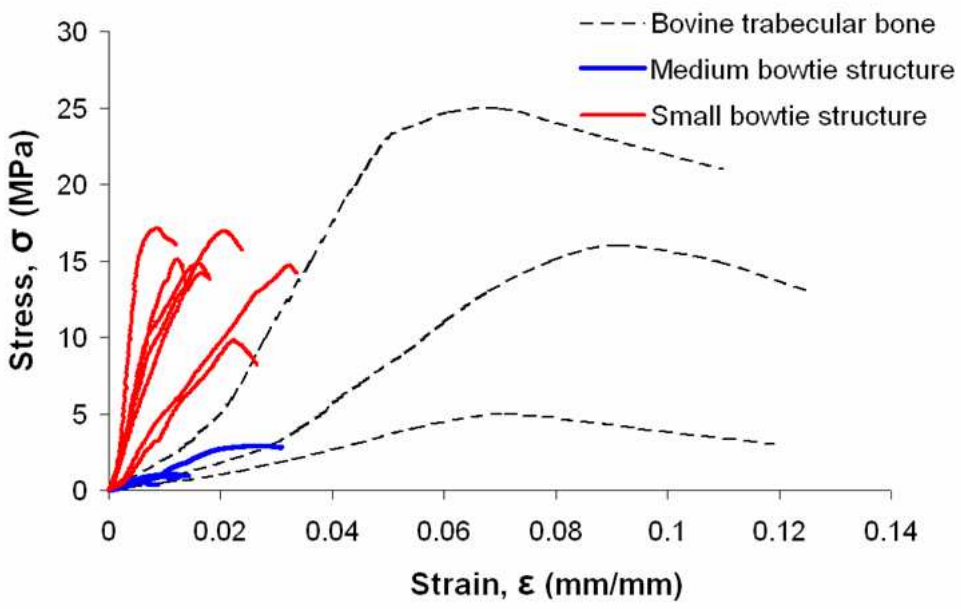

Figure 3-28. Comparison of the strain-stress behavior of the EBRD-made bowtie structure and bovine trabecular bone adapted from Guedes et *al.*, 2006 [37]

III.4.2 Cyclic compression tests

III.4.2.1 Mechanical behavior

As in the analysis of the quasi-static compression tests, the mechanical behavior, or trend of the strain-stress curve, was scrutinized to verify the hypothesis of a nonlinear relationship at small strains. The strain-stress hysteretic cycles displayed a repeatable nonlinearity. Part of the initial nonlinearity response was caused by the loading protocol at the onset of the tests and the boundary conditions. The top and bottom rows of open bowtie cells were free to move in the horizontal plane because of the lubricated contact with the compressive platens. However, the open bowtie cells of the top and bottom rows were not uniformly in contact with the self-aligning metallic compressive platens. As the compression of the structure increased the platens came in contact with the open bowtie cells they were not initially touching. The load was therefore shared by more open bowtie cells, which modified the stresses in the whole structure. This load evolution was reversed as the structure was decompressed. In summary, the very beginning of the nonlinear curve was probably caused by these varying boundary conditions and not by the mechanical behavior of the structure itself only. This would happen also if such a structure was implemented between two vertebral bodies, in non-uniform contact with the trabecular bone network.

The varying initial local boundary conditions also explained why there were great differences between the average values of coefficients A and B of the stress-

strain equation from test to test. Test 1 and test 2 (0.5% strain compression) were exactly the same except for the presence of lubricant at the interface between the structures and the compressive platens. The differences in the polynomial coefficient values and thus in the mechanical behavior were attributed to friction of the structure with the compressive platens. This agrees with the findings of Keaveny and others [4, 9-11] about the artifactual effect. This also implies that friction, which takes place between a medical device and the trabecular bone network, should be considered when designing and testing an orthopaedic implant with a targeted mechanical behavior.

III.4.2.2 CSR Analysis

The Compressive Strain Ratio (CSR) was estimated from the transverse deformation of the structure measured with the MTI photonic probes during cyclic compressive tests. These probes had a very small measurement range (300 micrometers) that was adapted to the repeatable transverse dimensional changes of the structures during the cyclic compressive tests. Implementation of reflective targets on the structure with petroleum jelly was found to be the best way to reflect the MTI-emitted light and measure the transverse deformation [39]. However, this set-up was subject to variability as demonstrated by the variations in CSR values, especially for the small and medium nickel structures. This was explained by the fact that the targets had to be implemented directly onto the sides of these structures unlike for the

L, XL, and XXL structures. The external surfaces of the S and M structures could not be trimmed precisely enough to eliminate their defects and to provide an even contact of the flat targets with all the bowtie cells rows. Therefore, the reflective targets did not always remain orthogonal to the photonic probes during the deformation of the structure, which altered the measurements of the transverse deformation. In addition, unequal deformation of the bowtie cells rows combined to the size of the reflective target biased the measurements and thus the estimations of the CSR.

Another factor could explain partly the large standard deviations and the smaller magnitude of the CSR values for the S and M structures (Figures 3-20 and 3-21) compared to those of the other structures. During the fabrication process, the stacked colloidal ink filaments bent because of their weight, thus disrupting the parallelism of the external surfaces as shown on Figure 3-29. This lack of parallelism prevented the alignment of the MTI photonic probes that therefore did not measure a true transverse deformation. For the large, extra-large and extra-extra-large stainless steel handmade bowtie structures the reflective targets were implemented on supports attached to the middle bowtie rows of the structure. They were thus representing the transverse deformation of one or two middle rows instead of the average transverse deformation of the whole structure. But, as mentioned above and reported by other researchers [2], the rows of cellular solids do not deform equally, so the notion of ‘average’ transverse deformation is very subjective.

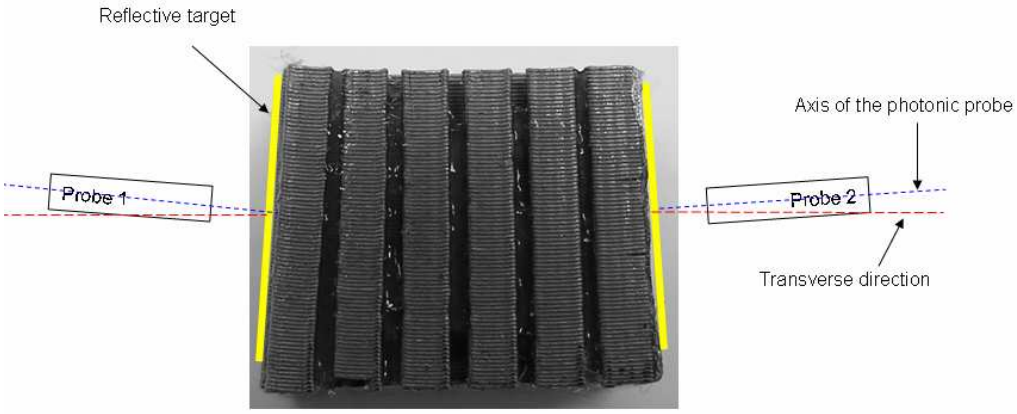

Figure 3-29. Top view of a small bowtie structure showing the lack of parallelism of the external surfaces. The additional schematic illustrate the misalignment between the axis of the photonic probes and the transverse direction. Note that the photonic probes were positioned orthogonal to the reflective targets

Comparisons of the average CSR values agreed with dimensional differences between the structures and their other mechanical properties. For instance, the length of the non-horizontal open bowtie cell members was increasing from small to medium to large to extra-large and extra-extra-large types. Therefore, the critical load to induce their bending or buckling was decreasing in the same order. The length of the re-entrant struts of the open bowtie cells was the same in the XL and XXL structures but the thickness of the struts was twice greater in the XXL structure (Table 3-1). In other words, a given axial deformation, or force, induced a greater transverse deformation in the extra-large than in the extra-extra-large structures because the latter had a greater stiffness. The slenderness ratio was almost identical for the large

and extra-extra-large structures so it was expected that they would feature similar average CSR values since their other mechanical properties were also similar.

The works of Choi and Lakes [40] showed that the Poisson's ratio of conventional and re-entrant metallic foams is nonlinear and depends on the strain level. It was thus expected that the CSR values measured would be different for each structure at the four different strain levels. Figures 3-22 and 3-24 showed that the CSR values of the L and XXL structures tended to increase with the strain level. However, no trend could be evidenced for the small and medium structures that had only been tested at the 0.5% and 0.6% strain levels. At this point, no explanation can be given to explain why the average CSR values of the XL structures yielded a trend opposite to those of the L and XXL structures. The relationship between the average CSR values and the strain levels for the L and XXL structures could support their nonlinear mechanical behavior in the given test conditions. The change from 0.5% to 0.6%, 0.6% to 0.75%, and 0.75% to 1.0% strain corresponded to a strain increase of 0.1%, 0.15%, and 0.25% strain, respectively. The magnitude increase per 0.1% strain increase ratios were therefore 6%, 6%, and 4.4% for the L structure and 10.5%, 8.8%, and 3.6% for the XXL structure. The magnitude increase per 0.1% strain level increment was not constant as it should be for a linear behavior. This lack of constancy of this ratio was likely caused by the fact that the transverse strain increased faster than the axial strain from one strain level to the other.

Finally, lubrication cannot be presented as an influential factor of the mechanical behavior of the bowtie structures at small strains. This was caused by the

lack of statistical significance in the differences between the values of coefficients A, B and the CSR obtained in lubricated and non-lubricated conditions. Friction might influence the mechanical behavior once large deformations have taken place and the bowtie structure is fully in contact with the compressive platens unlike at 0.5% strain.

III.4.3 Limitations

The large standard deviations reflected the limitations in preparing perfectly similar structures with reproducible mechanical properties. A close look at the data presented would show that the discrepancies were found in both the handcrafted and the EBRD-made structures. The manufacturing irregularities for the stainless steel structures concerned the bending into half bowtie cells and the assembly. Despite the use of a template, the re-entrant angles were not sharp but rounded (Figure 3-30), which affected the dimensions of the open bowtie cells. The length ‘l’ and width ‘h’ differed by up to half a millimeter from cell to cell. Therefore, two assembled half-bowtie strips were either not perfectly aligned or they were forcefully aligned, which introduced internal stresses in the structure. Automation of the small and medium bowtie structures manufacturing via the EBRD process was also a source of defects in these structures. As shown on Figure 3-31, the colloidal ink distribution was not uniform and the angles of the open bowtie cells were also rounded. In the bowtie unit cells of the small structure, the struts were thicker at the “corner” than in the middle of the strut. This was likely caused by a change in the ratio between the speed of

displacement of the tip and the volume of deposition of colloidal ink during the change from going in a straight line to 'turning' 120 degrees. Other defects such as holes, indented or broken struts, and deformations presented in Figure 3-32 proved the challenging task of manufacturing such fine structures. Finally, the micro-porosity and lack of fusion revealed by the SEM pictures highlighted the limitations of the current colloidal inks. The weakening effect of the solidified colloidal inks caused by these two defects was shown by further investigations described in the fifth chapter of this document.

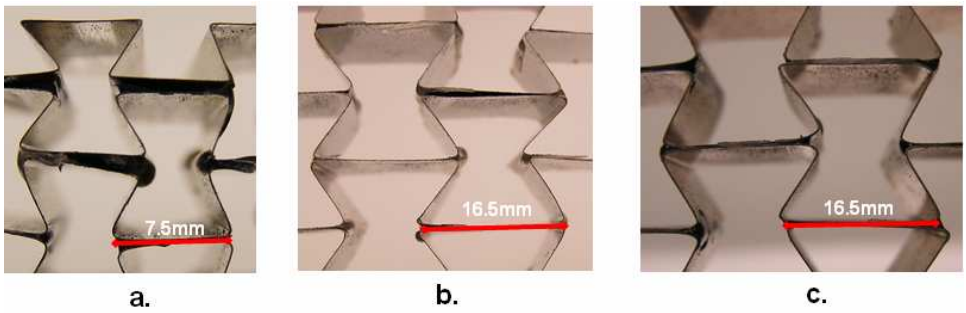

Figure 3-30. Close-up pictures of the handcrafted bowtie structures showing the rounded angles (a) L, (b) XL, (c) XXL

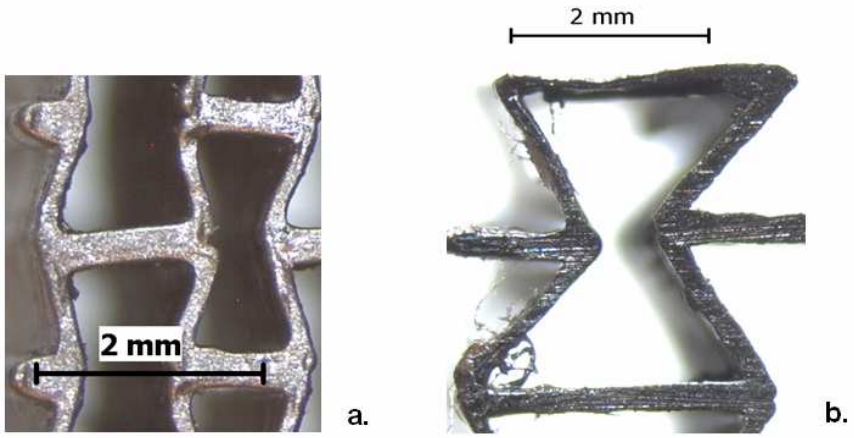

Figure 3-31. Microscopic photographs of the small (a) and medium (b) open bowtie cells

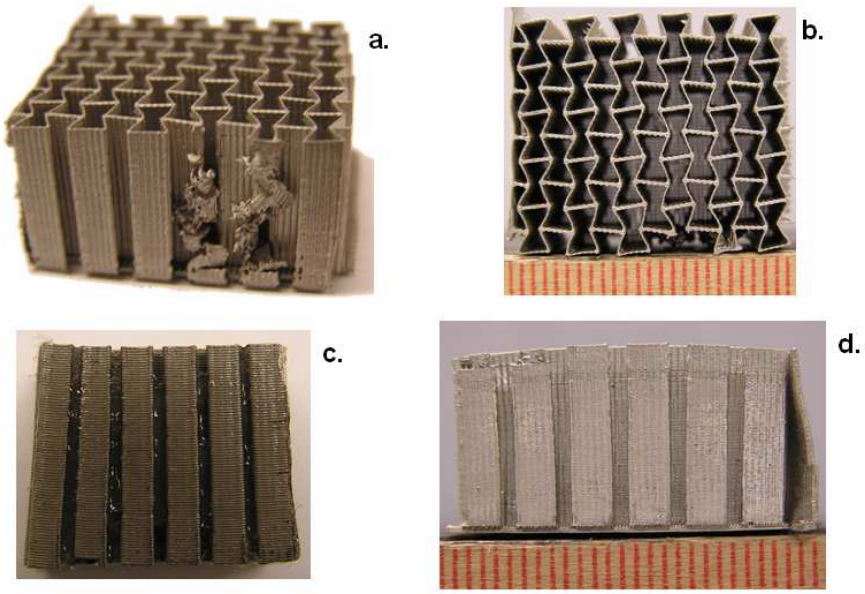

Figure 3-32. Photographs of the various defects introduced in the small and medium bowtie structures during their manufacturing, (a) shredded half bowtie cells, (b) inclination of the bowtie cells, (c) lack of parallelism of external surfaces, (d) bend of the whole structure

III.5 Conclusion

Cyclic and quasi-static compression tests permitted the investigation of the mechanical properties of porous bowtie structures of various relative densities. The cyclic tests demonstrated the repeatability of a nonlinear mechanical behavior at small strains. This nonlinear stress-strain relationship was described as a function of the relative density as hypothesized. The polynomial relationship found between stress and strain, as a function of the relative density at small strains, was a first step and should be considered in relation with the described boundary conditions only. More testing on similar structures featuring different relative densities should be performed to provide statistical significance to the experimental equations derived.

Time and cost constraints did not allow a complementary finite element analysis to be performed at this time but it will be done in a future study.

A new non-contact method for measuring the transverse deformation was developed and employed to estimate the compressive strain ratio of the structures. The CSR analysis confirmed the re-entrant behavior of the bowtie structures. The comparison of the negative CSR values also supported the nonlinear behavior of some bowtie structures under the given test conditions. The quasi-static tests demonstrated that the stainless steel bowtie structures displayed the overall stress-strain behavior expected of cellular solids unlike the brittle EBRD structures. Their brittleness was likely caused by the presence of micro-pores, nickel oxides and lack of fusion between the nickel particles as suggested by the SEM pictures. These limitations of the colloidal ink and associated sintering process need to be addressed to ensure the preparation of fine ductile re-entrant structures for orthopaedic applications. The results obtained supported the hypothesis that the mechanical properties of such a structure can be controlled via the relative density. They could be tailored to match the mechanical properties of trabecular bone if the structure were to be used as a spinal fusion device. Future works should focus on creating similar structures with intermediary relative densities and with a biocompatible material such as titanium.

References

1. Friis E.A., Lakes R.S., Park J.B., Negative Poisson's ratio polymeric and metallic materials, Journal of Materials Science, Vol.23:4406-4414, 1988
2. Gibson L.J., Ashby M.F., Cellular solids, structure and properties (2nd Ed.), Cambridge University Press, 1997 (ISBN 0 521 49560 1)
3. Goldstein S.A., The mechanical properties of trabecular bone: dependence on anatomic location and function, J. Biomechanics, Vol.20, No.11/12:1055-1061, 1987
4. Kopperdahl D.L., Keaveny T.M., Yield strain behavior of trabecular bone, J. Biomechanics, Vol.31:601-608, 1998
5. Morgan E.F., Bayraktar H. H., Keaveny T.M., Trabecular bone modulus-density relationships depend on anatomic site, J. Biomechanics, Vol.36:897-904, 2003
6. Rohl L., Larsen E., Linde F., Odgaard A. Jorgensen J., Tensile and compressive properties of cancellous bone, J. Biomechanics, Vol.24, No.12:1143-1149, 1991
7. Odgaard A., Linde F., The underestimation of Young's modulus in compressive testing of cancellous bone specimens, J. Biomechanics, Vol.24, No.8:691-698, 1991
8. Linde F., Hvid I., Madsen F., The effect of specimen geometry on the mechanical behaviour of trabecular bone specimens, J. Biomechanics, Vol.25, No.4:359-368, 1992
9. Keaveny T.M., Borchers R.E., Gibson L.J., Hayes W.C., Theoretical analysis of the experimental artifact in trabecular bone compressive modulus, J. Biomechanics, Vol.26, No.4/5:599-607, 1993
10. Keaveny T.M., Guo X.E., Wachtel E.F., McMahon T.A., Hayes W.C., Trabecular bone exhibits fully linear elastic behavior and yields at low strains, J. Biomechanics, Vol.27, No.9:1127-1136, 1994
11. Morgan E.F., Yeh O.C., Chang W.C., Keaveny T.M., Nonlinear behavior of trabecular bone at small strains, Journal of Biomechanical Engineering, Vol.123:1-9, 2001
12. Sierpowska J., Hakulinen M.A., Töyräs J., Day J.S., Weinans H., Jurvelin J.S., Lappalainen R., Prediction of mechanical properties of human trabecular bone by electrical measurements, Physiol. Meas., Vol.26: S119-S131, 2005
13. Keaveny T.M., Morgan E.F., Niebur G.L., Yeh O.C., Biomechanics of trabecular bone, Annu. Rev. Biomed. Eng., Vol.3:307-333, 2001
14. Kim D-G., Hunt C.A., Zauel R., Fyhrie D.P., Yeni Y.N., The effect of regional variations of the trabecular bone properties on the compressive strength of human vertebral bodies, Annals of Biomedical Engineering, Vol.35, No.11:1907-1913, 2007
15. Hulme P.A., Boyd S.K., Ferguson S.J., Regional variation in vertebral bone morphology and its contribution to vertebral fracture strength, Bone, Vol.41:946-957, 2007

16. Banse X., Devogelaer J.P., Munting E., Delloye C., Cornu O., Grympas M., Inhomogeneity of human vertebral cancellous bone: systematic density and structure patterns inside the vertebral body, Bone, Vol.28, No.5:563-571, 2001
17. Cvijanovic O., Bobinac D., Zoricic S., Otojic Z., Maric I., Crncevic-Orlic Z., Kristofic I., Ostojic L., Age- and region-dependent changes in human lumbar vertebral bone: A histomorphometric study, Spine, Vol.29, No.21:2370-2375, 2004
18. Simpson E.K., Parkinson I.H., Manthey B., Fazzalari N.L., Intervertebral disc disorganization is related to trabecular bone architecture in the lumbar spine, Journal of Bone and Mineral Research, Vol.16, No.4:681-687
19. Morgan E.F., Yeh O.C., Keaveny T.M., Damage in trabecular bone at small strains, European Journal of Morphology, Vol.42, No.1/2:13-21, 2005
20. Rabkin S.W., Hsu P.H., Mathematical and mechanical modeling of stress-strain relationship of pericardium, Amer Journal of Physiology, Vol.229, No.4:896-900, 1975
21. Lakes R.S., Foam structures with a negative Poisson's ratio, science, Vol.235:1038-1040, 1987
22. Martz E.O., Goel V.K., Pope M.H., Park J.B., Materials and Design of Spinal Implants—A Review, J. Biomed. Mater. Res. (Appl. Biomater.), Vol.38: 267–288, 1997
23. Rao G., Titanium foams fabricated for bone-tissue engineering applications, Research/Researchers MRS bulletin, p940, 2002 [www.mrs.org/publications/bulletin] (accessed 11/18/08)
24. Van den Dolder J., Vehof J.W.M., Spauwen P.H. M., Jansen J.A., Bone formation by rat bone marrow cells cultured on titanium fiber mesh: Effect of in vitro culture time. J. Biomed. Mater. Res., Vol.62:350–358, 2002
25. Shalabi M.M., Walboomers X.F., Jansen J.A., The influence of bone formation on anchoring percutaneous devices with titanium fiber mesh flanges. Journal of materials science: materials in medicine, Vol.15:809-816, 2004
26. Van den Dolder J., Farber E., Spauwen P.H.M., Jansen J.A., Bone tissue reconstruction using titanium fiber mesh combined with rat bone marrow stromal cells. Biomaterials, Vol.24:1745–1750, 2003
27. Van den Dolder J., Bancroft G.N., Sika Vitsas V.I.,Spauwen P.H.M., Mikos A.G., Jansen J.A., Effect of Fibronectin- and Collagen I-coated titanium fiber mesh on proliferation and differentiation of osteogenic cells. Tissue Engineering, Vol.9, No.3., 2003
28. Vehof J.W.M., Haus M.T.U., De Ruijter A.E., Spauwen P.H.M, Jansen J.A., Bone formation in transforming growth factor beta-I-loaded titanium fiber mesh implants. Clin. Oral Impl. Res., Vol.13:94-102, 2002
29. Vehof J. W. M., Van den Dolder J., De Ruijter J. E., Spauwen P. H. M., Jansen J. A., Bone formation in CaP-coated and noncoated titanium fiber mesh. J. Biomed Mater. Res., Vol.64A: 417–426, 2003

30. Vehof J.W.M., Spauwen P.H.M., Jansen J.A., Bone formation in calcium-phosphate-coated titanium mesh. Biomaterials, Vol.21:2003-2009, 2000
31. Jianqing F., Huipin Y., Xingdong Z., Promotion of osteogenesis by a piezoelectric biological ceramic, Biomaterials, Vol.18, No.23:1531-1534, 1997
32. Park Y.J., Hwang K.S., Song J.E., Ong J.L., Rawls H.R., Growth of calcium phosphate on poling treated ferroelectric $BaTiO_3$ ceramics. Biomaterials, Vol.23:3859-3864, 2002
33. Baxter F.R., Turner I.G., Bowen C.R., Gittings J.P., Chaudhuri J.B., Lewis R.W.C., The structure and properties of electroceramics for bone graft substitution, Key Emgineering Materials, Vols.361-363:99-102, 2008
34. Chen L, Chen Z, Zhang M., An experimental study on the implantation of a biomaterial with electro-activity for replacement of hard tissue in bone, Journal of West China University of Medical Sciences, Vol.32, No.4:526-528, 554, 2001
35. Bhonsle, S.R, Van Karsen, C.D., Mechanical and fatigue properties of stress relieved type 302 stainless steel wire, Journal of Materials Engineering and Performance, Vol.1, No.3:363-370, 1992
36. Moselkide L., Kragstrup J., Richards A., Compressive strength, ash weight, and volume of vertebral trabecular bone in experimental fluorisis in pigs, Calcif. Tissue Int., Vol.40: 318-322, 1987
37. Guedes R.M., Simoes J.A., Morais J.L., Viscoelastic behaviour and failure of bovine cancellous bone under constant strain rate, Journal of Biomechanics, Vol.39:49-60, 2006
38. Hvid I., Mechanical strength of trabecular bone at the knee, Dan. Med. Bull., Vol.35, No.4:345365, 1988
39. Jaumard N.V., Friis E.A., Non-contact method for the measurement of transverse deformation. Submitted to the Research in Nondestructive Evaluation – Journal of the American Society for Nondestructive Testing, May 2008
40. Choi, J. B. and Lakes, R. S., "Nonlinear properties of metallic cellular materials with a negative Poisson's ratio", adapted from J. Materials Science, Vol.27:5373-5381, 1992

IV Chapter 4: Electromechanical properties of piezocomposite bowtie units

IV.1 Introduction

With the discovery of bioelectricity and its effects on bone maintenance [1-3], electrical stimulation was shown to favor healing of patients who had spinal fusion or any other major orthopaedic surgery. Electrical stimulators have thus been implemented to enhance bone growth in patients who are at higher risks of failed bone fusion. However, the use of such medical devices is not always efficient and there are associated drawbacks such as additional surgery, higher risk of infection, greater costs and aesthetics issues. Failure sometime occurs either because the stimulation is too low to support or trigger bone formation or too high, leading to the formation of osteophytes or resorption of allograft material [4]. These drawbacks can cause further complications such as stenosis or nerve impairment.

Electrical stimulation is an adequate treatment but its implementation is challenging as reported in the second chapter, and it could be better controlled to adjust to the needs of patients and to avoid any adverse effects. Natural electrical stimulation occurs in the form of bioelectricity that finds its origins within the bony matrix. The constitutive materials of bone and the physiological mechanical activities cooperate in such a way that piezoelectric behavior and streaming potentials are triggered in the skeletal structure itself. Embedding the stimulation system in the

implant and making it dependent on the mechanical loading was thus envisioned as a way to replicate the natural phenomena. Moreover, an embedded stimulation would reduce or even eliminate all the drawbacks associated with the implementation of an external or internal electrical stimulator.

The re-entrant bowtie structure presented in the previous chapter showed the potential to provide a more appropriate mechanical stimulation of trabecular bone at small strains. As mentioned in the first two chapters of this document, piezoelectricity was chosen to create the required local electrical stimulation to stimulate and support osteogenesis. The bowtie structure was considered suitable for the integration of piezoelectric elements, so that the composite structure would feature both mechanical and electromechanical stimulations that could accelerate bone formation and healing.

Poled ferroelectric ceramic plates were implemented between rows of metallic bowties to transform the re-entrant bowtie structure into a stacked array capacitor. These plates were implemented in such a way that they would be mainly subjected to compression and not to tension, a stress mode that ceramics cannot tolerate. Elementary electric considerations showed that the current running in the struts of an open bowtie cell is the same in each cell. It was hypothesized that this current would vary with the mechanical loading and could be tailored to fall in the range of suitable values that would promote bone formation. The main interest was to create local electrical stimulation in each open bowtie cell hosting osteoblasts, the bone forming

cells. In order to prove this concept, it thus appeared that focus should be placed on the most fundamental unit level, the open bowtie cell. Tests could be performed on simple units consisting of a piezoelectric ceramic plate positioned between two metallic bowtie open cells.

It was hypothesized that a metallic re-entrant bowtie structure featuring piezoelectric plates between every second bowtie cell would present a similar mechanical behavior at small strains. The mechanical nonlinearity at small strains and auxeticity would be maintained since they would be dictated by the more ductile metallic bowtie cells rather than by the stiffer ceramic plates. However, focus was placed on simple composite structural bowtie units instead of the whole structure. Therefore, it was anticipated that the relationship between the stress, strain, and relative density would differ for these structural units from that presented in the previous chapter. The aim of this study was thus the investigation of the electromechanical properties of composite structural bowtie units. It was hypothesized that the composite structural units would generate an electric current when mechanically deformed. The experimental current values were hypothesized to match the theoretical ones. The objective of this study was thus twofold. First, piezoelectric composite bowtie units of various relative densities were manufactured and subjected to cyclic compression tests at different levels of strain. The experimental and theoretical current values were then calculated and compared.

IV.2 Materials and Methods

IV.2.1 Materials

IV.2.1.1 Theory for theoretical current

From the description of piezoelectricity in the second chapter of this document, one can understand how alternating current is created when a piezoelectric plate is cyclically compressed. Current is defined as the change of charge over time. When a piezoelectric plate is compressed in the direction it is poled, an electric dipole is created implying that one side of the plate is positively charged while the other side is negatively charged. Figure 4-1a depicts a piezoelectric composite structural unit in which all the ceramic plates have been implemented in the same direction between metallic bowtie open cells. The top and bottom surfaces of the bowtie cells in contact with the piezoelectric plates are thus charged differently. This imbalance of charges (or voltage potential) is unstable and electric equilibrium is reestablished naturally by a flow of charges from one side of the bowtie cell to the other when electrical connections are complete (Figure 4-1b). This flow, or change of charge over time dQ/dt, is the current I. The charge Q generated by the mechanical force F is calculated via the piezoelectric coefficient d_{33} as shown by equation {4-1}. Therefore, the current can be theoretically evaluated by equation {4-2}.

$$Q = d_{33} \cdot F \qquad \{4\text{-}1\}$$

$$I = \frac{dQ}{dt} = d_{33} \cdot \frac{dF}{dt} \qquad \{4\text{-}2\}$$

Where Q is the charge [C]

d_{33} is a piezoelectric coefficient [pC/N]

F is the axial mechanical force applied to the structure [N]

I is the current generated by the cyclic compression of the piezoelectric plates [A]

dQ/dt is the change of charge over time

dF/dt is the change of force over time

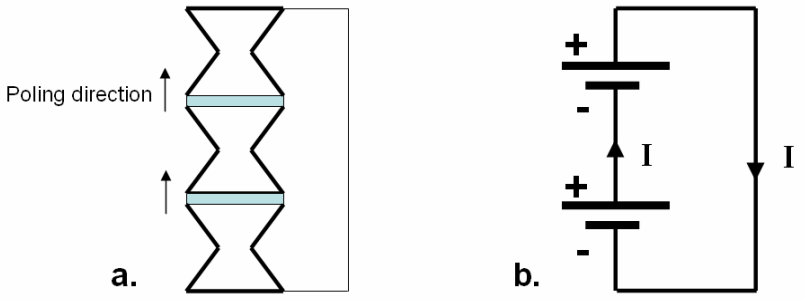

Figure 4-1. Schematic of a simple composite bowtie structural unit (a) and its equivalent electric diagram (b). In this version, the piezoelectric ceramic plates are implemented between the metallic bowtie open cells with their poling direction in the same orientation

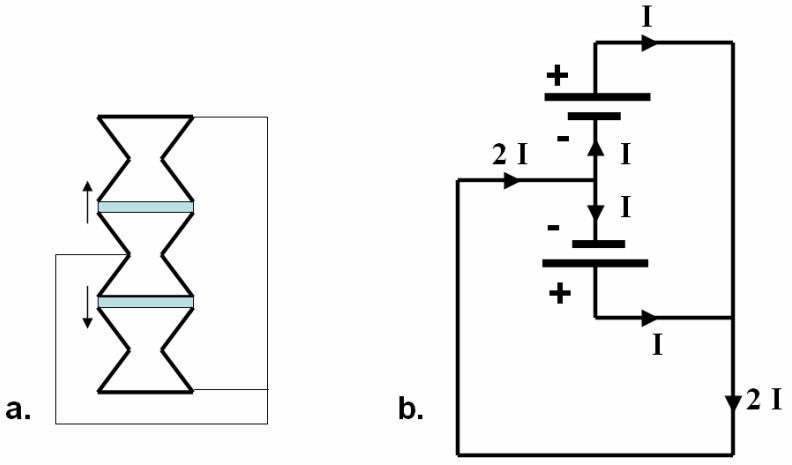

Figure 4-2. Schematic of a simple composite bowtie structural unit (a) and its equivalent electric diagram (b). In this version, the piezoelectric ceramic plates are implemented between the metallic bowtie open cells with their poling direction in opposite orientations

IV.2.1.2 Full piezocomposite structure to structural units

The ultimate goal of the project is to develop a piezoelectric composite re-entrant structure featuring biomimetic properties. The Electronic-Based Robotic Deposition (EBRD) technique is the only process that currently allows the manufacturing of such structures at the required small scale. The ferroelectric ceramic has to be transformed into a colloidal ink to be implemented as ceramic plate elements within the re-entrant structure. Therefore, post-manufacturing poling is necessary to align the electric dipoles of the ferroelectric ceramic crystals and make the ceramic piezoelectric. This poling treatment can be performed in two ways that will result in the electric arrangement illustrated in Figure 4-1a and 4-2a. In order to obtain a unique direction of poling, an electric field has to be applied across the whole structure vertically by using the top and bottom metallic bowtie cells as the two electrodes. In order to obtain alternated poling directions, an electric field has to be applied vertically by using every other metallic bowtie cell as the anode or the cathode.

In either electric configuration, the top and bottom surfaces of a metallic bowtie cell carry different charges. This is the case whether the piezoelectric plates are implemented or poled in the same direction (with their poling orientation both up or both down, Figure 4-1a) or not. As shown on Figures 4-1b and 4-2b The same current I will flow in the struts of the bowtie cell regardless the relative orientation of the ceramic plates from cell to cell (poling orientation up or down). This is the case whether the structure under test presents piezoelectric plates implemented in between

only two or 65 bowtie open cells, as in the structure in the previous chapter. The stacking of an open bowtie cell/piezoceramic plate/open bowtie cell presented in Figure 4-1a and 4-2a resembled a slender column that would buckle under axial compression. To increase structural rigidity and reduce the risk of buckling that would subject the piezoelectric plate to shear, the composite structural units that were investigated consisted of two piezoelectric ceramic plates sandwiched by two linked rows of two metallic bowties (Figure 4-3).

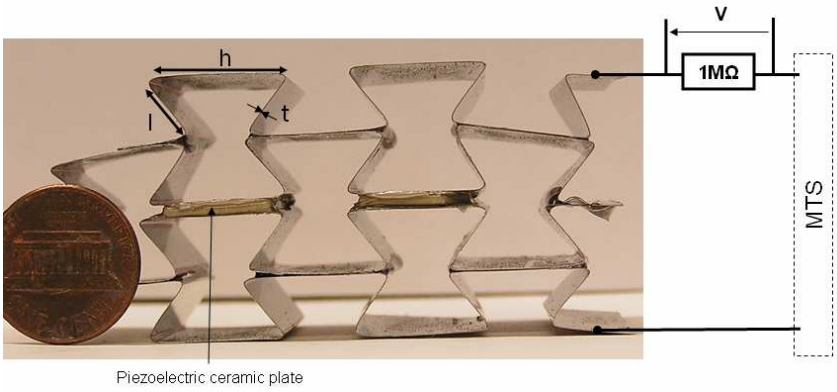

Figure 4-3. Photograph of the handcrafted piezocomposite bowtie structure and electric diagram

IV.2.1.3 Three specimens, three relative densities

Three composite piezoelectric structural units, one large (pL), one extra-large (pXL), and one extra-extra-large (pXXL), were prepared from Grade 302 stainless steel shim stock and poled barium titanate ($BaTiO_3$) plates. The metallic bowtie cells were obtained via the exact same procedure as that described in the previous chapter to create the mechanically tested bowtie structures. The ‘p’ stands for ‘piezoelectric’

to differentiate these structures from the mechanically tested ones. The fabrication process of these partial structures required two steps. A picture of a composite bowtie structural unit is presented in Figure 4-3.

The first step was the preparation of the metallic bowtie rows, as described in the previous chapter. The second step was the gluing of one-millimeter-thick, solid $BaTiO_3$ plates between rows of metallic bowties with silver conductive epoxy glue CW2400 [ITW Chemtronics, Kennesaw, GA]. This implementation technique was identical as that used by Kahn et *al.* [5] and Siivola and Saarinen [6] to create piezoelectric transducers. The ceramic plates were cut and implemented in the same orientation (poling direction) between the rows of bowties. They were prepared and poled at SANDIA National Laboratories. Prior to their implementation silicone was sprayed on the vertical sides of the ceramic plates to prevent any electric short circuit to form between the electroded top and bottom surfaces via epoxy bridging. Non-conductive epoxy was also applied between the remaining incomplete metallic cells, at the extremities of the strips, to prevent direct metal-to-metal contact that would have shunted the piezoelectric plates. Two strain gage wires, one featuring a one MegaOhm resistor, were soldered to the top and bottom metallic bowtie rows for voltage measurements. Limited ceramic plate availability permitted the preparation of only three additional composite bowtie structural units (two pL, one pXL).

IV.2.2 Methods

IV.2.2.1 Test set-up and protocol

Three composite bowtie structural units (one of each type) were subjected to cyclic compressions. The voltage change caused by the direct piezoelectric effect was monitored along with the axial deformation and force. Additionally, the voltage drop across the one MegaOhm resistor placed in series in the electric circuit provided an indirect measure of the current created by the cyclic compression of the piezoelectric plates. The three different aspect ratio structures featuring identical piezoplate elements were tested to identify the effect of their relative density on the mechanical and electromechanical properties.

Lubricant (petroleum jelly) was applied on the top and bottom surfaces of the specimen before it was positioned between the self-aligning metallic compressive platens of the mechanical testing system (MTS Mini Bionix 858, MTS, Eden Prairie, MN). One millimeter-thick Plexiglas™ plates were placed between the structure and the metallic compressive platens to avoid electric charge leakage from the specimen through these platens. Ten preconditioning cycles (-1 to –10 N) insured that the viscoelastic effects of the lubricant would be minimized. Cyclic displacement-controlled tests, consisting of 11 cycles, were performed at five different strain levels (0.5%, 0.6%, 0.75%, 1.0%, and 1.5%). The same test was consecutively run three times with a minute of rest in-between each time. After a one second ramp down to the starting point of the 11 cycles (-0.01 mm), the displacement followed a triangular wave at a frequency of 1 Hz. Data were collected at a frequency of 100 Hz.

IV.2.3 Electromechanical analysis

A custom-made Matlab program (The MathWorks Inc., Natick, MA) permitted the computation of the experimental and theoretical current developed during each loading portion of the 11 compressive cycles. The first and last cycles were discarded to eliminate ramping artifacts. As indicated by equations {4-1} and {4-2}, the charge is a function of the compressive force applied to the piezoelectric ceramic plates, which thus had to be measured. However, the current is a function of the change of force over time that can be derived from the force signal. The force signal recorded by the MTS system was similar to the triangular wave displacement signal used as a command. The change of force over time dF/dt was thus approximated as $\Delta F/\Delta t$ in equation {4-3} to calculate the theoretical current I_{theo}. As shown in Figure 4-4, the change of force and of time between the starting and ending points of the loading portion of a cycle were calculated and their ratio was multiplied by the known d_{33} coefficients to yield the theoretical current values. Given the small strain levels at which the structural units were tested; the actual deformation of the ductile bowtie cells did not require high compressive forces (20 N maximum). The load cell had a sensitivity of plus/minus one Newton. Therefore, the force cycles were not perfectly identical to each other. As a consequence there was some slight variation in the $\Delta F/\Delta t$ coefficient that introduced variation among the nine theoretical values of the current obtained for each test run. Since three runs were performed at each strain level, the theoretical current was the average of the 27 calculated values (nine cycles for each of the three test runs at a given strain level).

The voltage change across the resistor divided by the resistance yielded the experimental current I_{exp}. From equation {4-4} and the triangular shape of the force signal, the current signal was expected to resemble a square wave, as shown in Figure 4-4. Despite the filtering of the voltage signal to get rid of the ambient 60 Hz noise, the current signal fluctuated between the starting and ending time points of the loading portion of each cycle. The experimental current was thus calculated as the mean value of the current between these time points. There was therefore one average I_{exp} and one average I_{theo} value at each strain level for each of the three composite bowtie structural units tested.

$$I = d_{33} \cdot \frac{\Delta F}{\Delta t} \qquad \{4\text{-}3\}$$

Where I is the current [A]
d_{33} is a piezoelectric coefficient [pC/N]
$\Delta F/\Delta t$ is the change of force over time [N/sec]

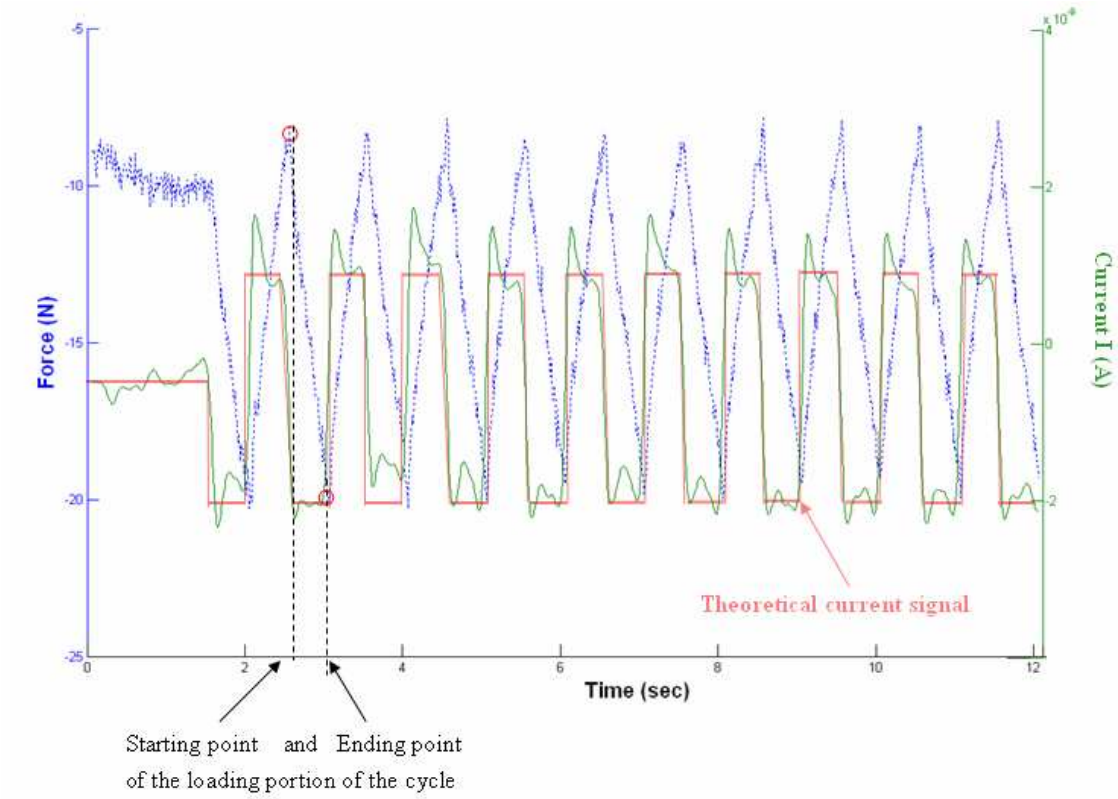

Figure 4-4. Graph of the force and current versus time with the starting and ending points of the loading portion of a cycle

IV.3 Results

The data recorded during the cyclic compression tests performed on the three different composite bowtie structural units allowed electromechanical investigations. The voltage developed across the resistor during the cyclic loading of the structural units permitted the calculation of the experimental current provided by the compressed piezoelectric plates. The force/current versus time graphs are provided in Appendix 4-A. Comparisons with the theoretical current values were performed showing the dependence of the current values on the strain level and the relative density of the bowtie structural units.

IV.3.1 Electromechanical behavior as a function of the strain level and the relative density

Figures 4-5a, 4-5b, and 4-5c present the theoretical and experimental currents calculated from the voltage, axial displacement and force recorded during the cyclic tests. The first noticeable feature of these graphs was that the magnitude of the theoretical currents did not increase similarly for the three types of structural units. For the pL structural unit the magnitude of both the experimental and theoretical currents increased with the strain level (Figure 4-5a). For the pXL structural unit the experimental and theoretical currents followed different trends. As shown in Figure 4-5b, the magnitude of the experimental currents slightly increased with the strain level but changed sign (passed 0.75% strain) while the theoretical currents increased but

remained negative. Finally, the experimental currents of the pXXL structural unit were negative but of equivalent magnitude at all but 1.5% strain level at which its negative magnitude increased (Figure 4-5c).

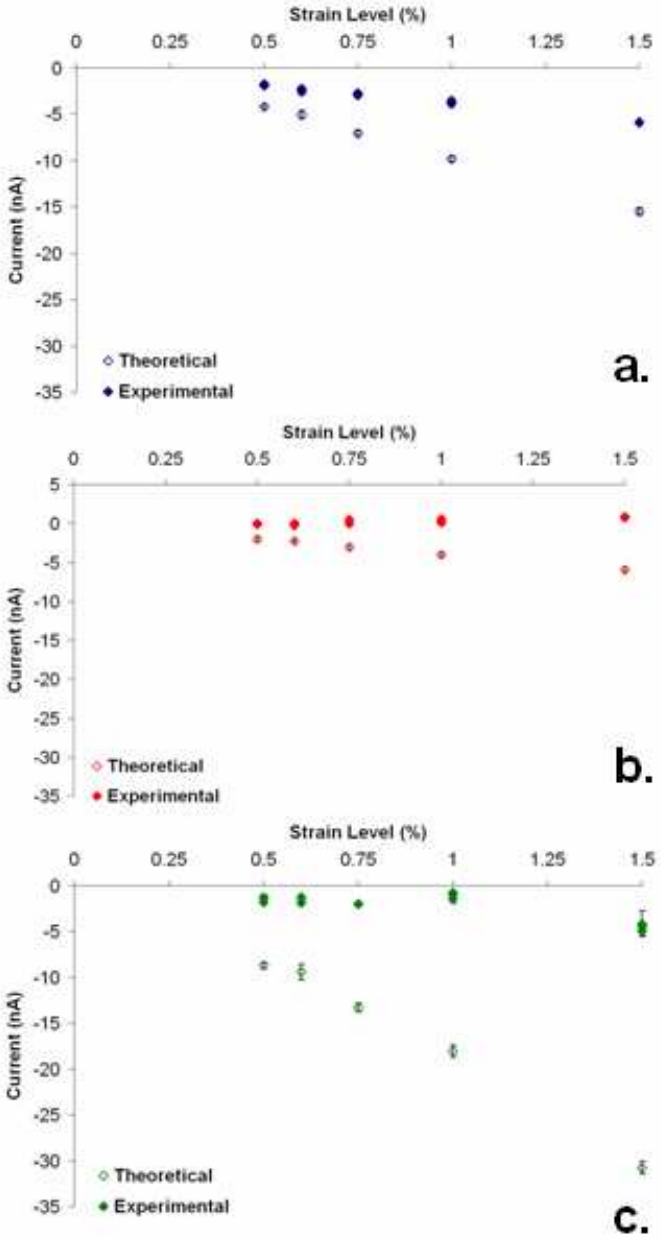

Figure 4-5. Graph of the theoretical and experimental current values versus the strain level for the three types of specimens (a) pL, (b) pXL, and (c) pXXL

From these figures was derived the ratio of the experimental to the theoretical current values. The plots of the experimental-to-theoretical current ratio versus the relative density are provided in Figure 4-6 and Appendix 4-B. These plots showed that the current ratio was different for each structural unit, i.e. at each relative density. The pL and pXL structural units, which featured the highest and lowest relative density, respectively, yielded the highest and lowest current ratio, respectively. The second noticeable feature of these plots was the low values of the current ratios. The overall maximum value reached was 48% for the pL structural unit while the maximum values reached by the pXL and pXXL structural units were 13% and 20%, respectively. Even if the mismatch between the experimental and theoretical currents was large, the trend appearing on the plots signaled that the current ratio increased with the relative density of the structural unit. A similar trend was displayed on the graph of the experimental current against the relative density (Figure 4-7 and Appendix 4-C). The experimental current values were negative but their magnitude increased with the relative density, regardless of the strain level. For example, the pXL structural unit that had the lowest relative density yielded the lowest current (between -0.29 and 0.89 nA) while the pL structural unit whose relative density was the highest yielded currents of the greatest magnitudes, between -5.89 and -1.73 nA. Finally, the experimental currents of the pXXL structural unit (between -4.89 and -0.73 nA) were comparable to those of the pL structural units as expected since their relative densities were similar (0.060 and 0.056, respectively).

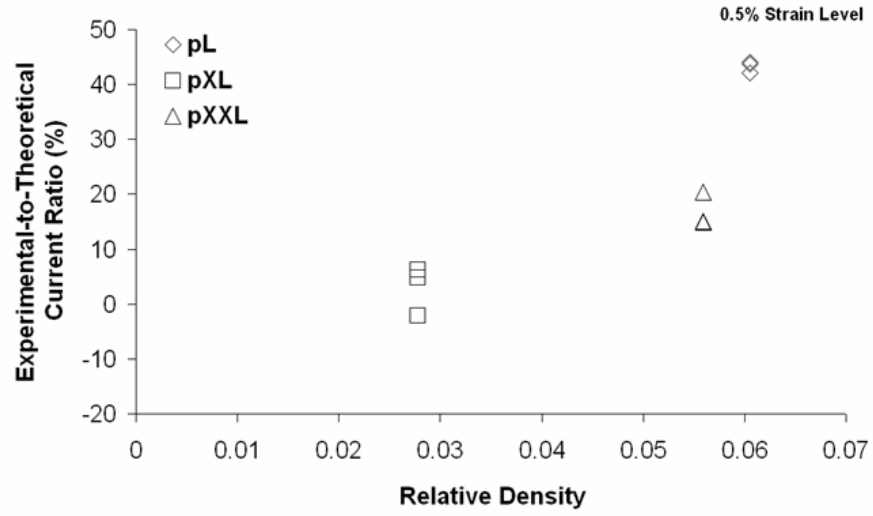

Figure 4-6. Graph of the experimental-to-theoretical current ratio versus the relative density at all strain levels

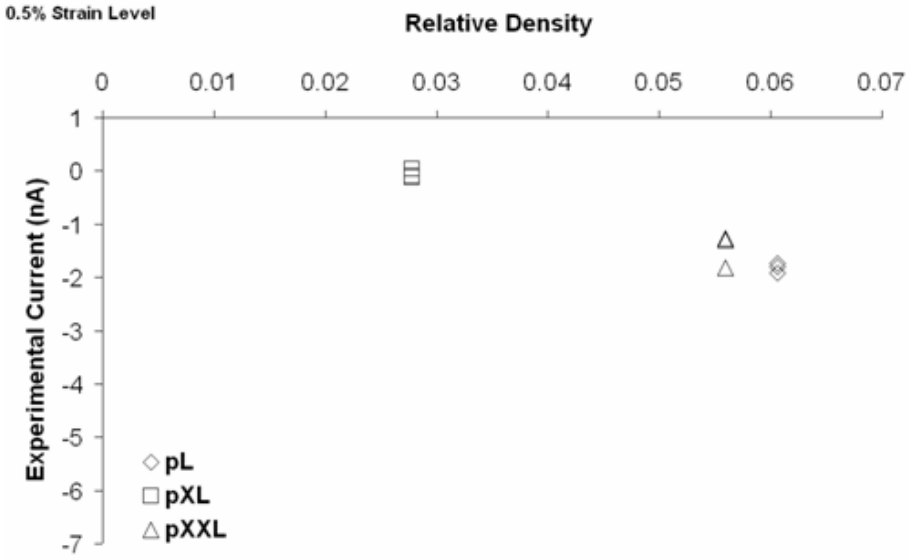

Figure 4-7. Graph of the experimental current values versus the relative density at all strain levels

IV.4 Discussion

The three different composite bowtie structural units that were tested displayed promising electromechanical trends that confirmed most of the hypotheses. Explanations were proposed to clarify some of the discrepancies between experimental and theoretical current values. These differences highlighted some limitations related to the materials and the manufacturing process.

IV.4.1 Electromechanical results

IV.4.1.1 Electromechanical behavior as a function of the strain level

The principle of piezoelectricity states that the magnitude of the generated current (or outcome voltage) varies with the force applied to the piezoelectric element. The variation of force implies a variation of strain, or deformation of the piezoelectric crystal. When the deformation of the piezoelectric element is increased in the dipole direction, the electric dipole varies and so is the amount of charge developed at the poles of the piezoelectric element. This principle has been evidenced in this study as by many other researchers [7, 8, 9]. Figure 4-8 showed that a greater force was applied as the strain level increased. As stated by equations 4-1, 4-2, and 4-3, the increase in force applied to the piezoelectric element over a certain period of time, should have caused a greater current to be generated in the electric circuit. The experimental current values obtained for the pL structural unit increased for the strain

level thus agreeing with the theory and proving that the composite structure truly displayed piezoelectric properties as hypothesized (Figure 4-5a). However, this was not the case for the pXL and pXXL structural unit (Figure 4-5b and 4-5c). The fact that the current became positive at the 0.75%, 1.0%, and 1.5% strain levels in the pXL structural units could theoretically be explained by a reversing of the polarization of the piezoceramic plates. But the ceramic plates were not subjected to the type of mechanical forces or electric field required for this reversal to take place. One potential explanation was that silver cations migrated within the conductive epoxy glue, which could have led to an artifactual reversal of the current.

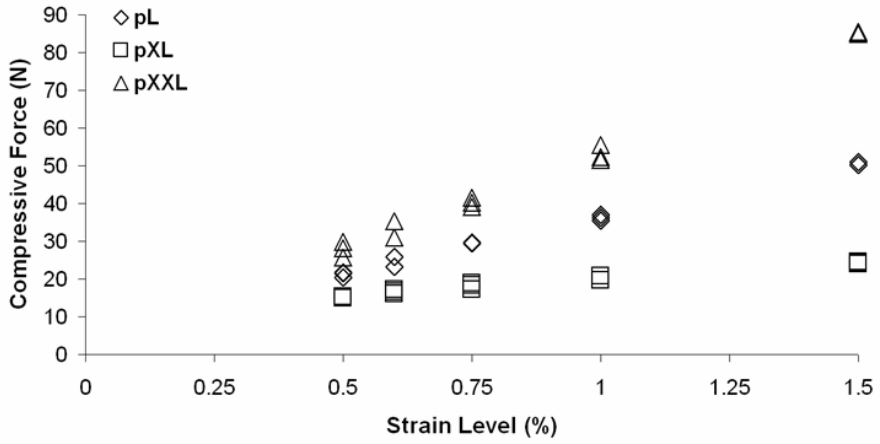

Figure 4-8. Overall averaged coefficient A values versus the relative density of the three piezocomposite bowtie units

IV.4.1.2 Electromechanical outcome as a function of the relative density

As shown in Figure 4-7 the magnitude of the experimental current developed in the composite structural units increased with the relative density. Structures pL and

pXXL had a greater relative density and were sturdier/stiffer than the highly deformable pXL structure. A greater stiffness implied that less of the mechanical energy was employed to deform the structure. Instead, more mechanical energy was transferred through the stiffer bowtie struts to compress the piezoelectric ceramic plates. In other words, the mechanical-to-electric energy conversion was greater at higher relative densities. However, the structural units were still highly deformable meant that the varying orientation of their re-entrant struts modified the type of load transferred to the piezoelectric plates. First, because of the open bowtie cell geometry, the piezoceramic plates were not uniformly loaded across their width but instead loaded more at the edges than in the center. Secondly, they were possibly subjected to multiple types of loads. Compression in the vertical direction and tension in the horizontal directions, via the d_{33} and d_{31} coefficient, respectively, would have counteracting piezoelectric effects, as presented in the second chapter. Smith addressed this well-known problem by implementing piezoelectric rods in a re-entrant foam [10]. The non-vertical compression portion of the load thus decreased the overall piezoelectric response in the structure. These non-uniform and varying loading conditions most likely contributed to the mismatch between experimental and theoretical current values in the pL and pXL structural units. This could explain the smaller increase in magnitude for the pL structural unit and the change of sign of the current for the pXL structural unit. However, this phenomenon could not explain the trend observed for the pXXL structural unit. In this last case, the fact that the current magnitude was equivalent at the 0.5%, 0.6%, 0.75%, and 1.0% to suddenly increase

at 1.5% strain suggested that the problem was linked to the bonding of the piezoceramic plates to the metallic bowtie cells. At the highest strain level, the electric contact was eventually properly established as the elements were compressed against each other.

The very low magnitudes of the theoretical current values suggested that a deficient electromechanical bonding and charge leaking in the silver conductive epoxy glue could tremendously reduce the magnitude of the experimental currents. The low magnitude of the experimental and theoretical current values (smaller than 10 nA, Figure 4-5) compared well with those obtained by Cochran et *al.* [7] and Park et al. [11] who tested $BaTiO_3$ piezoelectric implants. These researchers reported that the generated currents were not successful in increasing the strength of fixation of the implants in bone. The hypothesized cause of failure was that the piezoelectric implant generated a low density of electric charge. However, Baranowski et *al.* [12] had found that direct currents as low as 75 nA could promote osteogenesis. The piezocomposite structural units tested in this study delivered experimental currents whose magnitudes were far from this value. However, this could be imputed to the value of the one centimeter-long resistor connected to the piezoelectric structural units. This impedance of 1 MegaOhm was much greater than the equivalent 80 kiloOhm impedance reported for a one centimeter-long piece of human trabecular bone [11]. From Ohm's law, for a given voltage, the current is higher for lower resistance/impedance. Matching impedance calculations would thus show that at this lower impedance, the currents yielded by the piezoelectric structural units would be

higher. As displayed in Figure 4-7 and Appendix 4-C, the relationship between the relative density and the current suggested that the structure could be tailored to attain desired current values for targeted applications. The coefficient of proportionality (slope) of this linear relationship increased with the strain level. From the results of the previous chapter, it was hypothesized that this linear relationship could be extended to higher relative densities for each strain level. Estimates of experimental currents were thus calculated for the relative densities of the small and medium bowtie structures investigated previously, and for a 80 kiloOhm instead of a one MegaOhm resistance. As displayed in Table 4-1, small and medium piezoelectric structures strained between 0.5% and 1.5% would generate currents whose magnitudes would range between 343 and 1279 nA and 162 and 597 nA, respectively. Large, extra-large and extra-extra-large structures would generate -23 nA, -1 nA, and -18 nA at 0.5% strain, which is a physiologic loading. The currents generated by the pL, pXL, and pXXL could not promote osteogenesis, but the estimated ones for the small and medium structures could according to the standards empirically established by Cochran et *al.* [7]. However, such piezoelectric-generated currents would be alternating instead of direct, and thus might not affect the biologic tissues as reported by Cochran et *al.* [7].

Table 4-1. Average current values (μA) at different strain levels for structures of various relative densities with a matching impedance of 80 kOhms. The values highlighted in gray are the average of corrected experimental measures at each strain level. The values for the two highest relative densities were estimates based on a linear relationship between the corrected average experimental current values and the relative densities of the pL, pXL, and pXXL structures

Structure	Relative Density	Strain Level				
		0.5	0.6	0.75	1	1.5
pSmall	0.551	-0.343	-0.421	-0.562	-0.619	-1.279
pMedium	0.274	-0.162	-0.199	-0.263	-0.288	-0.597
pL	0.061	-0.023	-0.030	-0.035	-0.046	-0.073
pXL	0.028	-0.001	-0.001	0.002	0.004	0.010
pXXL	0.056	-0.018	-0.020	-0.025	-0.013	-0.056

IV.4.1.3 Current as a function of the material

From these past and present data, using barium titanate was also considered as a factor leading to low current values. This was confirmed by equation {4-2} from which one could deduce that a material with a higher piezoelectric coefficient d33 would create higher currents. A concrete application of this law is the replacement of barium titanate by lead-based ceramics such as lead zirconium titanate (PZT) in many applications requiring a piezoelectric transducer. PZT features a range of higher piezoelectric d_{33} coefficients than barium titanate, 240 to 505 pC/N compared to 200 pC/N or lower, respectively [13]. However, researchers have been reluctant to using lead-based piezoelectric ceramics for biomechanical applications because of the toxicity potential of this material [14]. This toxicity issue of PZT and the proven

biocompatibility of barium titanate [7, 8, 11, 15] led the present research to investigate this accepted ceramic material for orthopaedic applications. However, a recent study demonstrated that PZT is also biocompatible in certain conditions [16] and thus could be used instead of barium titanate. Other materials such as piezoelectric polyvinylidene fluoride (PVDF) film could also be used in the composite bowtie structure. However, this polymer is not compatible with the Electronic-Based Robotic Deposition (EBRD) technique that was envisioned as the manufacturing process for the piezoelectric composite re-entrant structure aimed at bony fusion as described in the first chapter. On the other hand, barium titanate colloidal ink can be prepared and deposited while retaining its ferroelectric properties. Then the structure can be poled to confer the barium titanate elements piezoelectric properties.

IV.4.2 Limitations

The difference in dependence of current on the strain level and the mismatch between the experimental and theoretical current values for the pL, pXL, and pXXL structural units highlighted issues with the quality control of the specimens. Improper mechanical and electrical bonding between the metallic bowtie open cells and the choice of the ceramic for these piezoelectric plates could partly explain these discrepancies.

The problems were correlated to the use of silver epoxy glue to implement the piezoelectric plate. Two pL and one pXL additional structural units were prepared and tested. The current signal derived from the voltage recordings presented random spurious spikes instead of the square-like wave pattern that was expected and observed with the other three specimens. The random spurious spikes in the signal were attributed to a defective conductivity of the interfacing material most likely caused by a combination of two factors. First the degraded quality of the epoxy material involved in the preparation of the silver epoxy glue. Secondly the mixing of the silver filler in the epoxy matrix might not have been homogeneous for all the implemented ceramic plates. However, there was no method to verify the homogeneity of the silver particles mixing within the epoxy matrix before application because the curing time was short. These problems explained the potential improper electrical bonding between the metallic bowtie open cells and the ceramic plates.

In addition, an uneven spreading of the silver epoxy glue during the implementation of the ceramic plates between the metallic bowtie open cells could have jeopardized their mechanical bonding. The same quantity of silver epoxy glue was prepared and spread on each side of the ceramic plates positioned between two metallic bowtie open cells. More glue was placed in the middle of the plate than on the edges so that it would flow outward when the ceramic plate was pressed closer to the metallic bowtie cell surface. This technique was necessary to ensure that the areas of the ceramic plate and the bowtie cell were both totally impregnated with silver epoxy glue. However, this technique was more likely to entrap air bubbles in the glue,

thus creating zones of disconnection and weak mechanical bonding. Also, cured silver epoxy glue is softer than metal and ceramic; therefore a part of the compressive energy was employed to squeeze it instead of being transferred completely from the metallic bowtie cells to compress the piezoelectric plates. These mechanical bonding issues could partly explain why the experimental current values were lower than the theoretical ones. The imperfect mechanical bonding would have lowered even more the already incomplete mechanical-to-electrical energy conversion. In other words, mechanical and electrical energy could be lost in the silver epoxy interface.

Despite all these limitations, silver epoxy glue was the chosen material to interface the metallic and ceramic element of the composite structural units because two main advantages. It cures at room temperature without any exothermic effect and in a short time (four hours at room temperature). The cold curing was an extremely important aspect considering the implementation of the piezoelectric ceramic plates. As presented in the section on piezoelectricity in the second chapter, ferroelectric materials are subjected to an atomic rearrangement at the Curie temperature. For barium titanate, this Curie temperature is very low (120°Celcius). Other conductive gluing media did not present the limitations of silver epoxy glue but required heating above that specific temperature. However, silver epoxy glue is not a biocompatible material so it would not be used in the manufacturing of the piezoelectric composite re-entrant structures. Moreover, the bonding of the different elements of the structure via a gluing medium is inherently weak because of the mechanical and chemical discontinuity at the interfaces. Therefore, these limitations justify the use of the

Electronic-Based Robotic Deposition technique and the development of an interfacing material that would provide an adequate mechanical and electromechanical bonding of the ceramic and metallic elements of the novel structure.

Finally, problems of material availability limited the preparation of a greater number of specimens. Six 1” x 1” x 0.04” poled barium titanate plates were prepared by Dr. Clem at SANDIA National Laboratories and used to manufacture the present structural units. In three of these, the degraded quality of the epoxy glue led to poor bonding and the discarding of the collected data. But the piezoceramic plates of the discarded structural units could not be scavenged for re-implementation, without being damaged. Furthermore, lack of proper equipment did not allow Oklahoma State University to manufacture and pole additional barium titanate plates identical to the ones from SANDIA to create more structural units.

IV.5 Conclusion

In conclusion, the investigation performed on piezoelectric composite re-entrant structural units permitted the confirmation of certain hypotheses and highlighted some issues. The electromechanical results confirmed that the composite structural units displayed piezoelectric properties. These electromechanical properties could be tailored by choosing both the unit cell dimensions and the piezoelectric ceramic that would lead to a most efficient mechanical-to-electric energy transformation in given loading conditions. However, the problems caused by the silver conductive epoxy glue used to bond the piezoelectric ceramic elements to the metallic bowtie cells demonstrated that special attention has to be given to the interface between these elements to enhance their mechanical and electromechanical bonding.

In finer composite structural units prepared via the EBRD process, the interface between the metallic and ceramic parts of a piezocomposite bowtie structure would not present the limitations of silver epoxy glue. Indeed, the colloidal inks of the biocompatible metal and ceramic would be deposited on top of each other and blend upon contact. This more intimate contact in the pre-cured configuration would lead to a more continuous and homogeneous bonding than what the silver conductive epoxy glue can achieve. However, this interface could be jeopardized by thermal stresses that would develop during sintering and lead to internal cracks because of the difference in properties of the two materials. A solution would then consist in gradually mixing the metal and ceramic colloidal inks and depositing this mixture,

thus creating a gradual composite material to transition smoothly from one to the other. The next chapter presents the investigation of the mechanical properties of such a gradual composite interfacing material hypothesized to provide a gradual stress transition between the metallic and ceramic parts of the composite structure.

The limitations related to material availability and quality control of the hand-manufactured specimens justified the need for an automated process such as the Electronic-Based Robotic Deposition (EBRD) process to build this type of one-dimensional re-entrant structure in a reproducible manner. The EBRD technique would actually allow the preparation of more complex three-dimensional re-entrant structures, such as the one presented in the introductory chapter, with ceramic elements at precise locations. Despite the limitations, the trends shown supported the general hypothesis and idea that a piezoelectric composite re-entrant structure can be manufactured and that its electromechanical properties can be controlled.

These results can be used as a basic experimental comparative model from which finite element studies can be derived. The composite structural units investigated in this work will be modeled in Abaqus Multiphysics (SIMULIA, Providence, RI) to provide a canvas for multiple analyses. For instance, the materials and their properties could be modified to meet the demands of the final orthopaedic applications targeted by the project. Nickel could thus be replaced by titanium and barium titanate by another material with higher piezoelectric properties.

References

1. Fukada E., Yasuda I., On the Piezoelectric Effect of bone, Journal of the Physical Society of Japan, Vol.12, No.10, pp:1158-1162, 1957
2. McElhaney J.H., The charge distribution on the human femur due to load, Journal of Bone Joint Surgery, Vol.49A, p1561, 1967
3. Marino A.A., Becker R.O., Piezoelectric effect and growth control in bone, Nature Vol.228, p473, 1970
4. Bridwell K.H., Anderson P.A., Boden S.D., Vaccaro A. R., Wang J.C., What's new in Spine Surgery, J. Bone Joint Surgery Am., Vol.89:1654-1663, 2007
5. Kahn M., Chase M., Lewis D., PiezogranTM structure for large area transduction, Proceedings of the Tenth IEEE International Symposium on Applications of Ferroelectrics,Vol.1:535-538 http://ieeexplore.ieee.org/stamp/stamp.jsp?arnumber=00602807, (accessed 11/21/2008)
6. Siivola J., Saarinen A., Piezoelectric film transducer for recording of oculography in electro-encephalogram-polygraphy, Medical and Biological Engineering and Computing, Vol.40, No.4:469-470, 2002
7. Cochran G.V.B., Johnson M.W., Kadaba M.P., Palmieri V.R., Mahaffey G., Design considerations in development of a prototype, piezoelectric internal fixation plate: a preliminary report, Journal of rehabilitation Research and Development, Vol.24, No.2, pp:39-50, 1987
8. Park J.B., Kelly B.J., Kenner G.H., von Recum A.F., Grether M.F., Coffeen W.W., Piezoelectric ceramic implants: in vivo results, Journal of Biomedical Materials Research, Vol.15, No.1:103-110, 1981
9. Platt, Electrical power generation within orthopaedic implants using piezoelectric ceramics, Master Thesis
10. US Patent 5334903 Composite piezoelectrics utilizing a negative Poisson ratio polymer, Smith W.A., 1994
11. Park J.B., von Recum A.F., Kenner G.H., Kelly B.J., Coffeen W.W., Grether M.F., Piezoelectric ceramic implants: a feasibility study, Journal of Biomedical Materials Research, Vol.14, No.3:269-277, 1980
12. Baranowski Jr. T. J., Black J., Brighton C.T., Friedenberg Z.B., Electrical osteogenesis by low direct current, Journal of Orthopaedic Research, Vol. 1, No.2:120-128, 1984
13. www.matweb.com (accessed 09/23/08)
14. PCT/US2001/006744, Avrahami Y. Tuller H.L., Rhombohedral-phase barium titanate as a piezoelectric transducer, 2001 http://www.wipo.int/pctdb/en/wo.jsp?IA=US2001006744&DISPLAY=DESC (accessed 11/24/2008)
15. Jianqing F., Huipin Y., Xingdong Z., Promotion of osteogenesis by a piezoelectric biological ceramic, Biomaterials, Vol.18, No.23:1531-1534, 1997

16. Sakai T., Hoshiai S., Nakamachi E., Biochemical compatibility of PZT piezoelectric ceramics covered with titanium thin film, Journal of Optoelectronics and Advanced Materials Vol. 8, No. 4:1435 – 1437, 2006

V Chapter 5: Mechanical Properties of Interfacing Material (Diametral Compression Test)

V.1 Introduction

As highlighted in the discussion section of the previous chapter, the interface between different elements of a composite structure is often the weak point. It is where structural, material, and mechanical discontinuities lead to damaging consequences. For instance, the difference in mechanical properties between metallic and ceramic elements gives rise to stress concentrations.

A composite bowtie structure such as that investigated in the previous chapter but at a smaller size and comprising as many bowtie cells as the small specimens tested in the second chapter is the goal of the overall project. Such small structures would be prepared via the Electronic-Based Robotic Deposition (EBRD) technique described in this document. The theoretical capabilities of the EBRD process promise the preparation of a composite structure with a gradually changing composition interfacing material to link the nickel bowtie cells to the barium titanate plates (Figure 5-1). The overall hypothesis was that a gradual composite material would present mechanical properties that would gradually change with the volume content of the two phases (metal and ceramic) thus reducing stress concentrations at the interface, and their detrimental consequences.

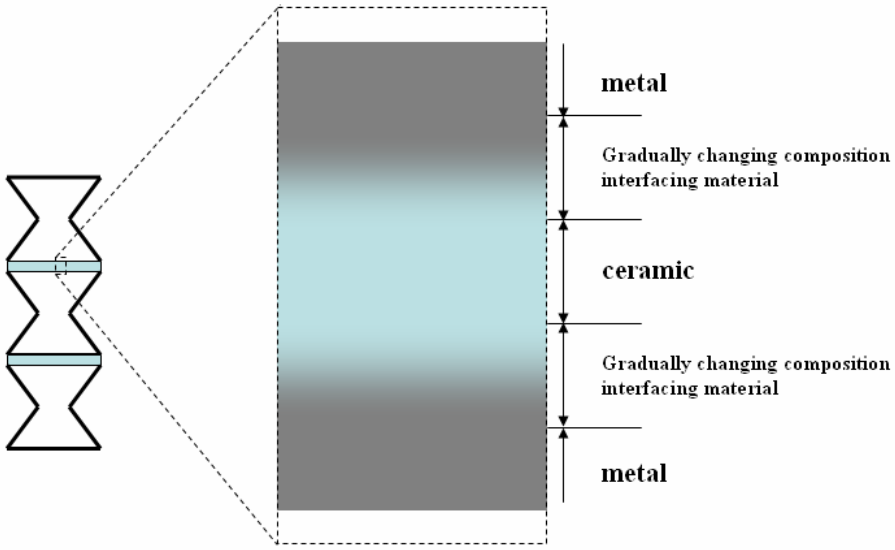

Figure 5-1. Illustration of the gradual composition material linking the metallic bowties to the ceramic piezoelectric plates

Before trying to create and test a gradual composite material, corresponding intermediate compositions should be prepared and tested. A specific hypothesis was that the mechanical properties of the varying composition interfacing material could be known from those of materials of intermediate compositions. The objective of this study was thus to investigate the mechanical properties of various compositions of nickel (Ni) and barium titanate ($BaTiO_3$) composites prepared via colloidal inks. Barium titanate and nickel powders were mixed in controlled weight ratios to prepare the various compositions. As shown in the following section, the properties of composite materials are estimated from the properties of the base materials and their interactions. Another hypothesis thus considered that the mechanical properties of the varying composition interfacing material and of the various intermediate compositions could be estimated from the theory of mixture.

Compression and tension are the two major stress modes to which the interfacing material will be subjected. From the mechanical tests reported in the third chapter, and the compressive properties of nickel and barium titanate, the compressive strength of the interfacing material was not an issue. However, ceramics are not usually strong in tension so the tensile properties of the composite interfacing material were investigated. Limited material availability and manufacturing challenges prevented the collaborative researchers from preparing standard tensile test specimens. Three-point or four-point bending tests are usually alternative options to obtain tensile properties, but the dimensional requirements for the specimens associated with these tests were also too challenging to meet. The tensile and bending specimens necessitate too much material for their preparation via colloidal inks. Even if enough colloidal ink could be prepared and poured in the required shapes, these would not remain within dimensional tolerances because of bending, warping and cracking during the curing and sintering processes. Diametral compression testing was thus considered the most suitable mode of testing. The diametral compression test consists in subjecting a cylindrical specimen to compression along its diameter to obtain the tensile strength at failure.

V.2 Materials and Methods

V.2.1 Theory

V.2.1.1 Presentation of the diametral compression test

During a diametral compression test a cylindrical specimen, disc or rod (depending on the value of L, thickness or length) of radius R is subjected to pure compression along its diameter (Figure 5-2, [1]). The load P, the radius R and the thickness (or length) L are employed to calculate the stress in the horizontal and vertical directions (X and Y, respectively) as a function of the 'x' position. The compression in the vertical direction gives rise to tensile stresses in the horizontal direction.

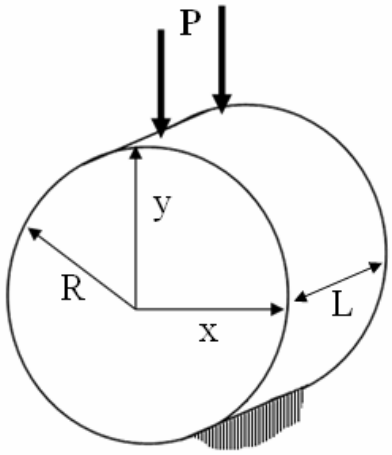

Figure 5-2. Schematic of the diametral compression test. A load ***P*** is applied to a cylindrical specimen of diameter ***R*** and thickness ***L***

Equations {5-1} and {5-2} are used to calculate the stresses in the diametral specimen [1]. The maximum stresses are located in the central vertical plane (x =0). The ultimate tensile stress was experimentally computed by replacing 'P' with the maximum force measured (at failure of the disc) in equation {5-1} for a value of 'x' equal to zero. The dimensions 'R' and 'L' were measured with a digital caliper (±0.01 mm), prior to testing.

$$\sigma_x = \frac{P}{\pi \times R \times L} \times \left[1 - \frac{4 \times R^2 \times x^2}{\left(R^2 + x^2 \right)^2} \right] \qquad \{5\text{-}1\}$$

$$\sigma_y = \frac{P}{\pi \times R \times L} \times \left[1 - \frac{4 \times R^4}{\left(R^2 + x^2 \right)^2} \right] \qquad \{5\text{-}2\}$$

V.2.1.2 Theory of mixture applied to 0-3 composites

The theory of mixture first developed by Woltman in 1794 and then by Fick, Darcy and Stefan, states that the properties of a composite are a function of the properties of the basic materials and their volume fraction. Depending on the homogeneity and the structural relationship of the two materials (in series, in parallel, or a combination of both), equations can be employed to derive the properties of a composite. For materials in parallel (Voigt model) or in series (Reuss model), expressions {5-3} and {5-4} yield estimated values for the modulus of elasticity.

$$E_{composite} = V_{material1} \times E_{material1} + V_{material2} \times E_{material2}$$

Voigt model {5-3}

$$\frac{1}{E_{composite}} = \frac{V_{material1}}{E_{material1}} + \frac{V_{material2}}{E_{material2}}$$

Reuss model {5-4}

$$V_{material1} + V_{material2} = 1 \qquad \{5\text{-}5\}$$

Where $E_{composite}$ = modulus of elasticity of the composite
$E_{material\ i}$ = modulus of elasticity of material *i*
$V_{material\ i}$ = volume fraction of material *i*

It was experimentally shown that these models are not adequate in all situations to predict the modulus [2]. However, the series and parallel models served as a basis for and were combined in later models. For instance, Pauer developed a cube model to extrapolate the properties of 0-3 composites. A 0-3 composite is a composite in which one of the materials does not present a continuous connectivity between its smallest building blocks, in any direction. Micron-sized ceramic powder particles homogeneously dispersed in a polymer matrix is an example of a 0-3 composite. The model representing the smallest composite block is a unit cube of the matrix material containing an m x m x m cube of the particle material [3-5]. Banno [3, 6], Wenger and Das-Gupta [4, 7], as well as Hashin and Shtrikman [8] proposed modified versions of the Pauer cube model that provided better estimates for the

properties of the 0-3 composite.(Figure 5-3). In these models, the volume fraction of the second basic material is expressed as a function of parameters m and n.

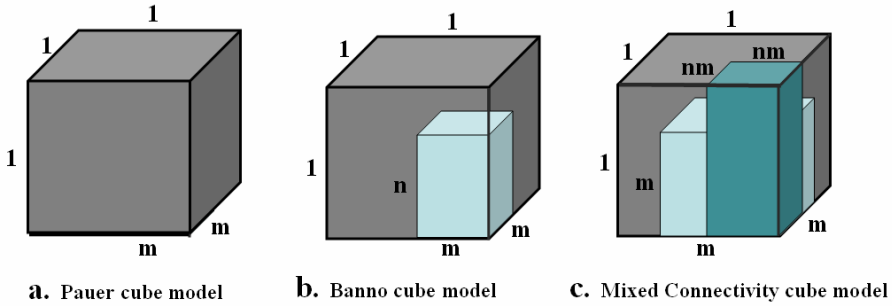

Figure 5-3. Different cube models for the 0-3 composites [4] (permission to reproduce requested)

The expression for the modulus of elasticity E was derived from Banno's model (equations {5-6} to {5-8}) and the Mixed Connectivity model (equations {5-9} to {5-11}) proposed by Wenger and Das-Gupta [4,7] as follows. In both models materials 1 and 2 referred to the base materials. Since the volume fraction of barium titanate was varied it was considered as material 2 while nickel was considered as material 1. In Banno's model, the unit cube is considered as an assembly of two substructures, a truncated unit cube of material 1 (substructure I) in parallel with a composite (materials 1 and 2) parallelepiped (substructure II). The parallelepiped of dimensions m x m x 1 consists of a smaller material 1 parallelepiped in series with a material 2 parallelepiped of dimensions m x m x (n-1) and m x m x n, respectively (Figure 5-4).

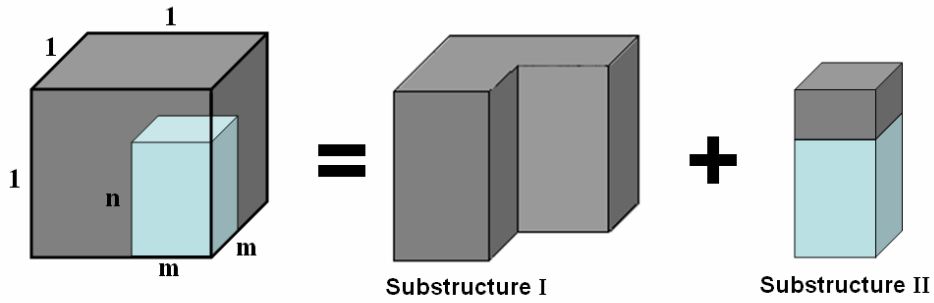

Figure 5-4. Schematic decomposition of Banno's cube model

$$E = V_I \times E_I + V_{II} \times E_{II} \qquad \{5\text{-}6\}$$

$$E = V_{I,1} \times E_1 + V_{II} \times \left(\frac{1}{\frac{V_{II,1}}{E_1} + \frac{V_{II,2}}{E_2}} \right) \qquad \{5\text{-}7\}$$

$$E = (1-m^2) \times E_1 + m^2 \times \left(\frac{1}{\frac{(1-n)}{E_1} + \frac{n}{E_2}} \right) \qquad \{5\text{-}8\}$$

In the Mixed Connectivity model, the unit cube is considered as an assembly of three substructures, a truncated unit cube of material 1 (substructure I) in parallel with a truncated composite (materials 1 and 2) parallelepiped (substructure II) and a smaller parallelepiped of material 2 (substructure III). The truncated composite parallelepiped consists of a smaller material 1 parallelepiped in series with a material 2 parallelepiped (Figure 5-5). The third substructure accounts for potential local 1-3 arrangements within the matrix caused by particle clotting.

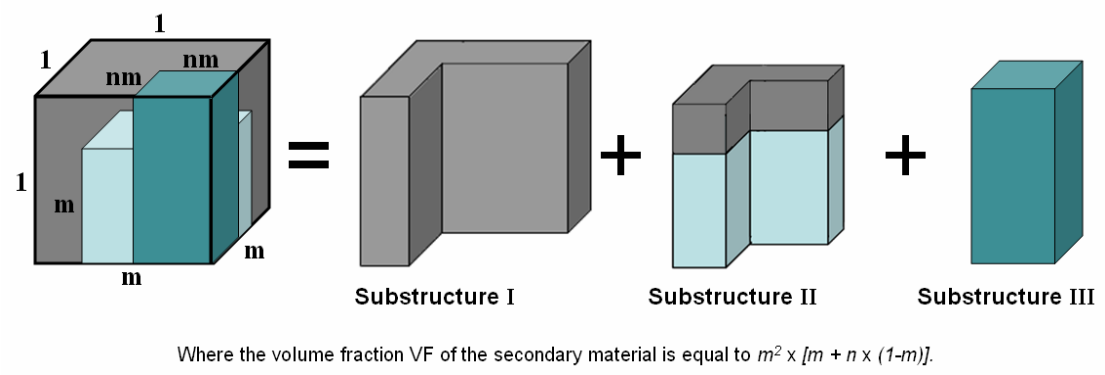

Figure 5-5. Schematic decomposition of the Mixed Connectivity cube model

$$E = V_I \times E_I + V_{II} \times E_{II} + V_{III} \times E_{III} \quad \{5\text{-}9\}$$

$$E = V_{I,1} \times E_1 + V_{II} \times \left(\frac{1}{\frac{V_{II,1}}{E_1} + \frac{V_{II,2}}{E_2}} \right) + V_{III,2} \times E_2 \quad \{5\text{-}10\}$$

$$E = (1-m^2) \times E_1 + m^2(1-n^2) \times \left(\frac{1}{\frac{(1-m)}{E_1} + \frac{m}{E_2}} \right) + n^2 m^2 \times E_2 \quad \{5\text{-}11\}$$

All of these models have limitations when the particle size (that determines values m and n) to composite thickness ratio approaches one or when the volume fraction of the second material becomes too large. But, under certain conditions, the models allow the estimation of the dielectric, elastic, and electromechanical properties of composites. Theoretical expressions yield evaluated values of the main mechanical properties such as the modulus of elasticity (or compliance) and the

Poisson's ratio. Several researchers [3, 5, 6] have derived similar expressions to calculate the values of electromechanical properties (dielectric constants, piezoelectric coefficients) of composites. It was thus hypothesized that a comparable mathematical expression could be developed and used to evaluate the ultimate tensile strength of the composite materials to be tested. Similar equations to those used in Banno's model and the Mixed Connectivity model were employed to estimate the ultimate tensile strength of the composite materials from the experimental ultimate tensile strength values (σ_{UTS}) of the pure nickel and pure $BaTiO_3$ specimens. As shown in equations {5-12} and {5-13}, the parameter E was simply replaced by the ultimate tensile strength parameter σ_{UTS}.

For Banno's model:

$$\sigma_{UTS,composite} = (1-m^2)\times\sigma_{UTS,1} + m^2 \times \left(\frac{1}{\frac{(1-n)}{\sigma_{UTS,1}} + \frac{n}{\sigma_{UTS,2}}} \right) \qquad \{5\text{-}12\}$$

For the Mixed Connectivity model:

$$\sigma_{UTS,composite} = (1-m^2)\times\sigma_{UTS,1} + m^2(1-n^2)\times \left(\frac{1}{\frac{(1-m)}{\sigma_{UTS,1}} + \frac{m}{\sigma_{UTS,1}}} \right) + n^2 m^2 \times \sigma_{UTS,2} \qquad \{5\text{-}13\}$$

As stated earlier, the Banno's model and the Mixed Connectivity model were initially developed to provide more accurate estimates than the simple Voigt and Reuss models. Therefore, a similar replacement of the modulus of elasticity by the ultimate tensile strength in these simpler models to obtain theoretical data was not performed.

V.2.2 Experiment

V.2.2.1 Specimens, set-up and protocol

Two different micron-size powders, nickel (ENP 800, Umicore, Canada) and barium titanate (Ticon HPB, Ferro Inc., NY) served for the preparation of seven colloidal inks at Oklahoma State University (OSU). Plain and chemically modified nickel, $BaTiO_3$, and nickel/ $BaTiO_3$ colloidal inks of different compositions were prepared. The powder was mixed with various chemical compounds and mixed in a planetary centrifuge machine to create a colloidal ink. The paste was then poured into a 3-cubic-centimeter-syringe until it cured and became a more rigid green body. This green body was taken out of the syringe shaft and sintered in a furnace at a high temperature (1600°Celcius) in a neutral atmosphere (hydrogen/ nitrogen mix). The sintering process aimed at fusing the cohesive particles together. After eight hours in the furnace, the green bodies became fully solid rods that were shipped to the University of Kansas (KU). Rods that were 10mm to 16mm-long and 7.5mm in diameter were created out of the following seven compositions:

- pure Ni

- pure $BaTiO_3$
- Ni 95w% - $BaTiO_3$5w%
- Ni 80w% - $BaTiO_3$ 20w%
- Ni 60w% - $BaTiO_3$ 40w%
- Ni 40w% - $BaTiO_3$ 60w%
- Ni 20w% - $BaTiO_3$ 80w%

The rods were cut into discs of different thicknesses with a precision diamond saw (Buehler Ltd, Lake Bluff, IL). As summarized in Table 5-1, six 2mm-thick discs of each composition were machined. In order to verify the effect of the disc thickness on the ultimate tensile strength, as reported in other studies [9, 10], six 5mm-thick and six 10mm-thick discs of pure nickel and pure barium titanate were also cut. Figure 5-6 shows pure nickel and barium titanate specimens of the three thicknesses. The specimens' thickness was significantly larger (two millimeters minimum) in comparison to the size of the powder particles employed to prepare them (five to ten microns). In the composite specimens, the particles of the secondary material were assumed to be uniformly distributed in the matrix of the primary material, so that the composite material was considered homogeneous and isotropic. In a similar experiment, Chisholm et *al.* [9] had tested 6mm-diameter discs with thicknesses between 2mm and 30mm. The three thicknesses (2, 5, and 10mm) were chosen to show significant differences while complying with the limited availability of colloidal inks used in the rods preparation. Thinner discs were not prepared because they

would have required a more accurate alignment and they could have been subjected to buckling.

Table 5-1. Number of specimens of each material and thickness

L / Specimen	2 mm	5 mm	10 mm
Pure Ni	6	6	6
Ni 95w% - $BaTiO_3$ 5w%	6	0	0
Ni 80w% - $BaTiO_3$ 20w%	6	0	0
Ni 60w% - $BaTiO_3$ 40w%	6	0	0
Ni 40w% - $BaTiO_3$ 60w%	6	0	0
Ni 20w% - $BaTiO_3$ 80w%	6	0	0
Pure $BaTiO_3$	6	6	6

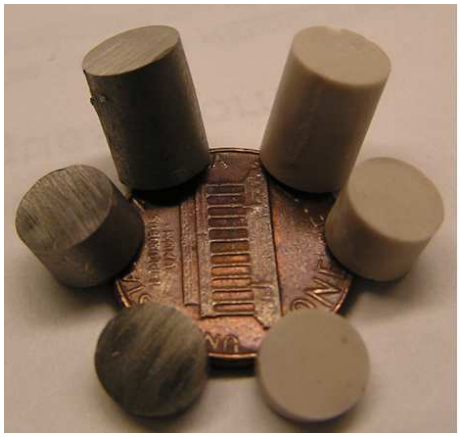

Figure 5-6. Photograph of the pure Ni (dark) and pure $BaTiO_3$ (white) specimens of different thicknesses (2mm, 5mm, 10mm)

For the diametral test, a disc was positioned at the center of a leveled self-aligning compressive jig. The upper metallic compressive platen was lowered to come in contact with the specimen. A displacement-controlled configuration allowed the compression of the disc at a constant rate (0.42 mm/sec) until complete failure. This displacement rate was the same as that used to compress the bowtie structures to failure (Chapter 2). The MTS system (MTS, Eden Prairie, MN) recorded the axial force and displacement while a video camera recorded specimen failure. The recorded videos (24 images/second) were slowed down and watched frame by frame to identify the type of fracture that took place and thus determine the validity of the results for each specimen.

A custom Matlab program analyzed the data and retrieved the maximum load P that led to the specimen's fracture. This maximum load value and the dimensions of the specimen were plugged into equation {5-1}, for 'x' equal to zero, to yield the ultimate tensile stress withstood by the specimen. The Matlab program also provided stiffness values. Stiffness was directly calculated from the measured data. But this parameter was not equal to the modulus of elasticity in the present investigation. The modulus of elasticity E is a property of the material whereas stiffness is a property of a solid body that depends on its constituting material(s), its shape, and on the boundary conditions of testing. In this study, stiffness was defined as the change of force over a displacement. Stiffness was computed as the slope of the linear portion of the axial load-deformation curve prior to failure; between 45% and 60% of the peak load (Figure 5-7) as was done for the modulus of elasticity in chapter three.

Given this definition, meaningful comparisons between the different composites could only be made by normalizing this parameter. The experimental stiffness values were divided by the value obtained for pure $BaTiO_3$.

A digital caliper (±0.01 mm) was used to measure the thickness and diameter of all the specimens. Six measures were performed to calculate an average value. The specimens were also weighed on a digital scale (0.01 gram precision). Their experimental density was estimated from their average dimensions as the weight over the volume for comparison to theoretical values. SEM pictures of the fractured surfaces of the specimens were taken with a JEOL 6380 (10 kV, sizepoint 28) to observe the microstructure of the composite materials.

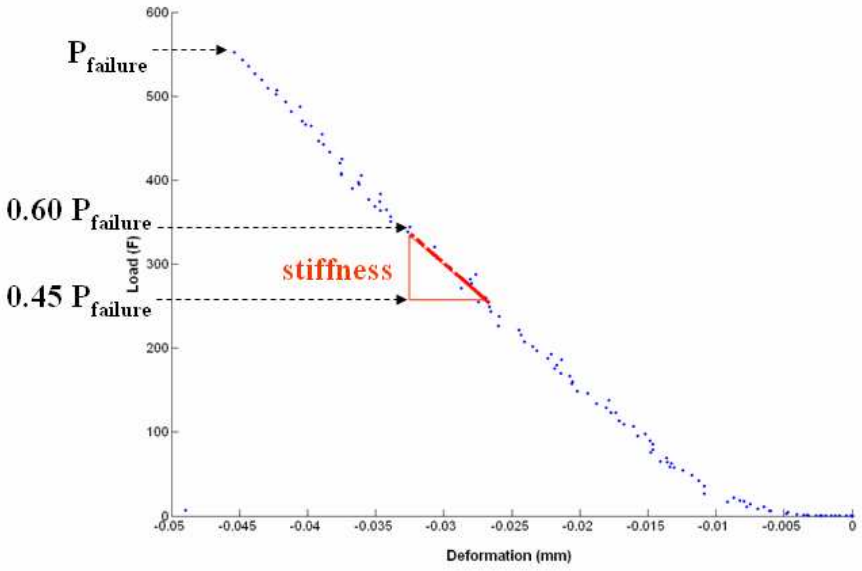

Figure 5-7. Illustration of the stiffness calculation from the load-deformation graph

V.2.3 Theoretical calculations

V.2.3.1 Ultimate tensile strength σ_{UTS}

The various compositions tested in this study spanned from one pure material to the other. Calculations of the theoretical ultimate tensile strength values were thus adequately performed by considering nickel as material ***1*** and barium titanate as material ***2***. The minimum and maximum standard ultimate tensile strength values provided by the literature [11] 45-317 MPa for $\sigma_{UTS,Nickel}$ and 21-59 MPa for $\sigma_{UTS,BaTiO3}$ were used in the equations as $\sigma_{UTS,1}$ and $\sigma_{UTS,2}$, respectively, for both Banno's model and the Mixed Connectivity model. Since volume fraction was the only known parameter, the theoretical ultimate tensile strengths were calculated for all the possible combinations of 'm' and 'n' (both ranging from 0 to 1). The range of standard ultimate strength values and the m-n combinations explain why several figures of the ultimate tensile strength against the volume fraction of $BaTiO_3$ were plotted and they contain a decade of theoretical curves.

Ceramics are brittle and do not display any yielding before failure that occurs at the ultimate tensile strength they can withstand. But if particles of ductile material are added, then it provides the composite with a potential for some yielding before failure. This increase in ductility is not linearly proportional to the increase in volume fraction of nickel in the ceramic. The crystallographic arrangement of nickel atoms and the potential for dislocation motion to occur (causing strain hardening) depends on the surrounding atomic structure. Because of energy considerations, dislocations will move more easily between planes of nickel atoms than between a plane of nickel

atoms and a plane of $BaTiO_3$. For this reason, it is difficult to estimate the influence of the composition on the ultimate tensile strength. This potentially explains any mismatch between theoretical and experimental values. The fact that the modulus of elasticity and the strength are related but not controlled by the same physical phenomena could also explain any mismatch. Therefore, the addition of a coefficient 'K' was justified to take into consideration the change of post-linear elastic behavior caused by the composition. Adjustments of the theoretical models were thus performed as expressed in equations {5-14} and {5-15}. A coefficient of proportionality K was added to equations {5-12} and {5-13}. This coefficient K was first considered as a function of the volume fraction (equations {5-16}) and then as a constant.

$$\sigma_{UTS,composite} = K \cdot \left[(1-m^2) \times \sigma_{UTS,1} + m^2 \times \left(\frac{1}{\frac{(1-n)}{\sigma_{UTS,1}} + \frac{n}{\sigma_{UTS,2}}} \right) \right] \quad \{5\text{-}14\}$$

$$\sigma_{UTS,composite} = K \cdot \left[(1-m^2) \times \sigma_{UTS,1} + m^2 (1-n^2) \times \left(\frac{1}{\frac{(1-m)}{\sigma_{UTS,1}} + \frac{m}{\sigma_{UTS,1}}} \right) + n^2 m^2 \times \sigma_{UTS,2} \right] \quad \{5\text{-}15\}$$

$$K = 1 + VF_{Nickel} \quad \{5\text{-}16\}$$

Where VF_{Nickel} is the volume fraction of nickel

V.2.3.2 Porosity

The theoretical density was calculated from the theory of mixture as the sum of the density of the base materials multiplied by their respective volume fraction (equation{5-18}). Comparing the experimental to the theoretical density provided an estimation of the porosity of the specimens. The percentage of porosity was equal to the percentage difference between the experimental and theoretical densities.

$$\rho_{composite} = \rho_{Ni} \cdot VF_{Ni} + \rho_{BaTiO_3} \cdot VF_{BaTiO_3} \qquad \{5\text{-}18\}$$

where ρ_{Ni}, is the density of nickel
ρ_{BaTiO3} is the density of $BaTiO_3$
VF_{Ni} is the volume fraction of nickel
VF_{BaTiO3} is the volume fraction of $BaTiO_3$

V.3 Results

The failure load was obtained from the collected data and used to calculate the ultimate tensile strength (σ_{UTS}) of each disc. The average and standard deviation values were computed to first check the effect of the disc thickness. Then comparisons of these average values were established between the different compositions for the 2mm-thick discs. These average ultimate tensile strengths were also compared to theoretical values obtained from the theory of mixture. Normalized stiffness values were calculated from the recorded data to establish a comparison between the different compositions. In parallel, comparisons of the experimental and theoretical density values yielded estimates of the porosity of the specimens.

V.3.1 Average ultimate tensile strength

As displayed on Figure 5-8 the average theoretical ultimate tensile strength significantly decreased when the specimen thickness increased for pure nickel and pure barium titanate (p-values < 0.05, ANOVA). The larger value obtained for the 2mm-thick was 32% and 48% greater than for the 5mm- and 10mm-thick discs, respectively for the pure barium titanate. These results agreed with the trend observed by other investigators [9, 10]. For the pure nickel, the larger value obtained for the 2mm-thick was 15% and 18% greater than for the 5mm- and 10mm-thick discs, respectively. The 2mm thickness was chosen to test discs of intermediate compositions for four reasons. First, as was reported by other researchers, the

ultimate tensile strength value derived from the diametral test tends to be underestimated because the specimen is in a biaxial stress configuration [10, 12]. Therefore, the largest value obtained is the less underestimated. Secondly, the values obtained for the 2mm-thick discs were closer to the standard values [11]. Three, the impact of specimen variability on the standard deviation is reduced when considering the largest average value. Four, they require less material to be made.

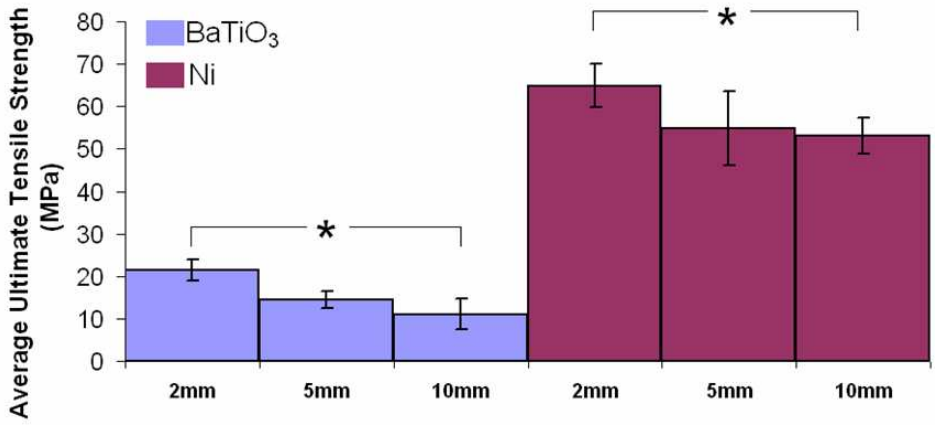

Figure 5-8. Average ultimate tensile strength values for the pure Barium Titanate and pure Nickel specimens for various thicknesses. (* significant difference, $p < 0.05$, ANOVA)

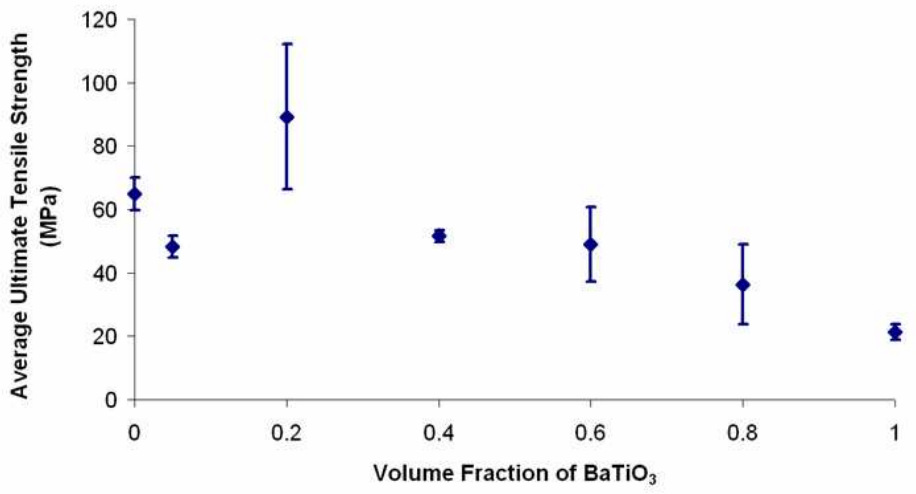

Figure 5-9. Experimental average ultimate tensile strength values for the 2mm-thick specimens of the seven different materials

Figure 5-9 presents a comparison of the average ultimate tensile strength as a function of the volume fraction of barium titanate for the 2mm-thick discs of the seven compositions. The pure $BaTiO_3$ discs yielded the lowest σUTS while the highest value was measured for the Ni 80w% - $BaTiO_3$ 20w% specimens instead of the pure nickel specimens as expected. There was a significant difference (ANOVA, $p < 0.00001$) between the σ_{UTS} of all the Ni-$BaTiO_3$ composites. The lack of hierarchy among the values obtained from the discs containing 100vol%, 95vol%, and 80vol% of nickel signaled a potential problem with these composite materials, the diametral test, or both. Image analysis from the video recordings showed that plastic deformation had taken place in discs of these compositions prior to failure. Figures 5-10a and 5-10b illustrate the plastic deformation and the brittle failure caused by shear instead of tensile stresses for the pure, and 95vol% nickel discs,

respectively. In the specimens containing 80vol% of nickel, plastic zones first developed at the contact with the compressive platens then a vertical crack appeared as shown in Figure 5-10c immediately followed by additional side fractures as shown in Figures 5-10a and 5-10b. The failure modes of these three composite materials were not associated with the pure tensile failure pattern expected and required to validate the results of the diametral compressive test. The large plastic deformation zones formed at the contact with the compressive platens and the failure due to shear stresses invalidated the results for these three composites.

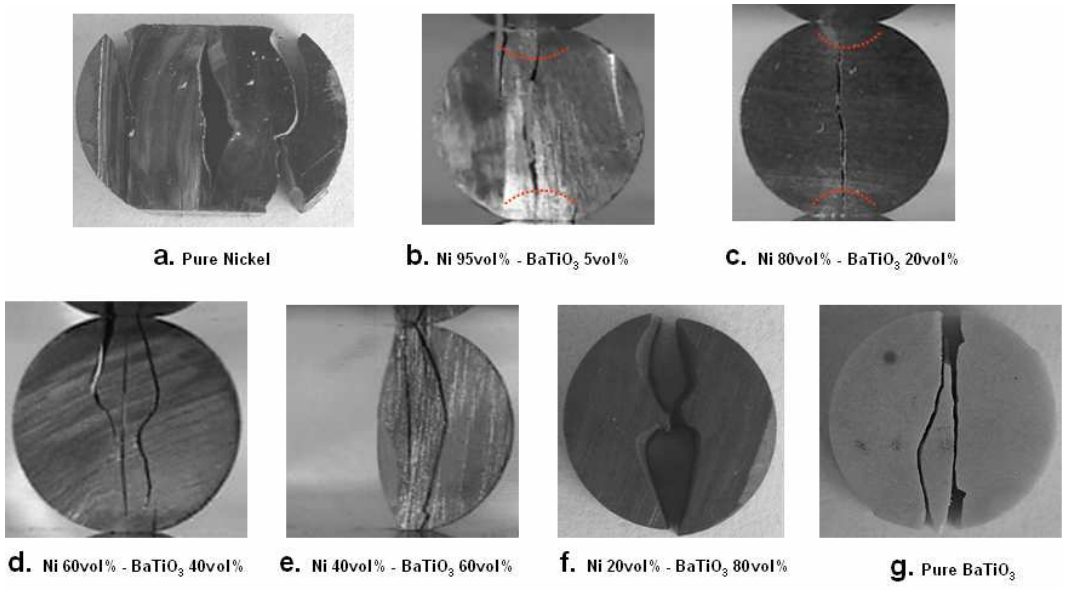

Figure 5-10. Photographs of the fracture mode in all the diametral compression specimens. Labels a)-g) are provided underneath the pictures. The dashed curves on figures b) and c) delimit the plastic zones that formed prior to failure

For the composites containing over 40vol% of barium titanate, the “triple clef” failure shown in Figures 5-10d to 5-10g took place. As demonstrated by Rudnick et al. [1], this mode of failure was truly triggered by tensile stress and was considered valid. Therefore, the results of the diametral test for the specimens containing 100vol%, 95vol%, and 80vol% of nickel were discarded. From this point on, only the results of the remaining composites (those with a volume fraction of barium titanate superior or equal to 0.4) are presented. An inter-experimental comparative statistical analysis was performed for the specimens containing 40, 60, 80, and 100 vol% of $BaTiO_3$. Analysis of variance (ANOVA, alpha equal to 0.05) revealed that the σ_{UTS} values of those four compositions were significantly different ($p < 0.00001$). The difference was also significant ($p=0.039$) between the values of these first three compositions. However, Student T-tests (alpha equal to 0.05) concluded that there was no significant difference between the σ_{UTS} values of the 40 vol% and 60 vol% and between those of the 60 vol% and 80 vol% $BaTiO_3$ composites (p-values of 0.61 and 0.10, respectively).

V.3.1.1 Experimental-Theoretical comparisons

The theoretical values from Banno’s model and the Mixed Connectivity model followed a similar trend as the experimental ones: a decrease in ultimate tensile strength with an increase of $BaTiO_3$ volume fraction. For the theoretical calculations from Banno’s model and the Mixed Connectivity model, standard σ_{UTS} values were employed for pure nickel because the diametral experimental value was

obtained from an invalidated diametral compression test. Nickel can be subjected to various treatments such as annealing or cold working that affect its mechanical properties. Since, the EBRD process (colloidal ink preparation, curing, and sintering) could not be related to any particular material treatment, both extreme σ_{UTS} values (45 MPa and 317 MPa) were considered for nickel in the calculations. For barium titanate, the experimental σ_{UTS} value was equal to the lower end of the range of standard values for this material. Therefore, this lower value only (21 MPa) was employed in the theoretical calculations. Figures 5-11a and 5-11b show that the theoretical ultimate strength were underestimated in both models when taking $\sigma_{UTS,Nickel}$ equal to 45 MPa. However, when this parameter was fixed at 317 MPa, both models greatly overestimated the values. As shown in Figure 5-12a this overestimation yielded a broader range of values at all volume fractions in Banno's model while the Mixed Connectivity model yielded a narrower range of overestimated values (Figure 5-12b). Because of this overestimation, which was caused by the large value of $\sigma_{UTS,Nickel}$ further theoretical estimates were calculated with $\sigma_{UTS,Nickel}$ equal to 45 MPa only. Graphs obtained from the other theoretical calculations with $\sigma_{UTS,Nickel}$ equal to 317 MPa are however provided in Appendix 5-A.

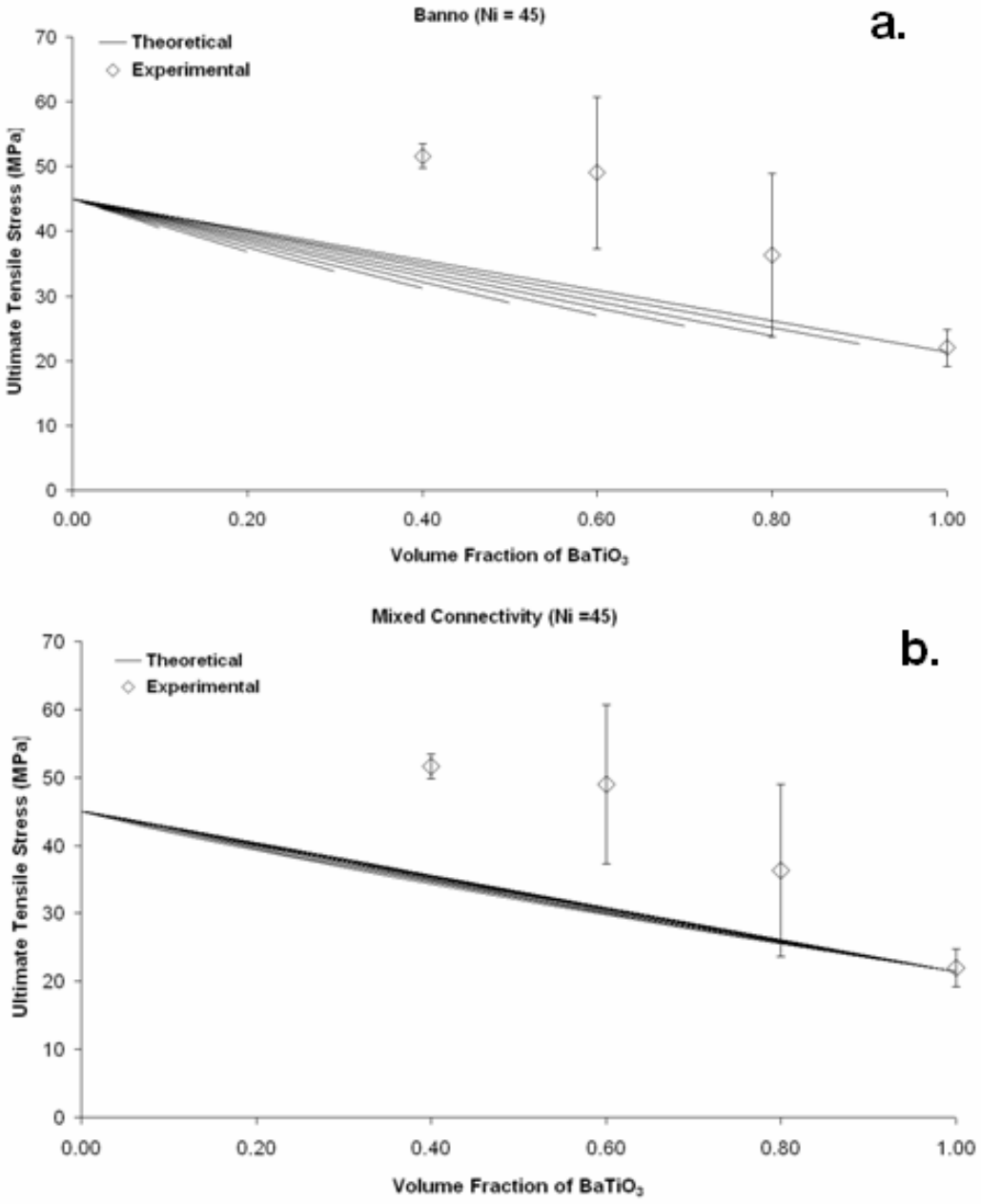

Figure 5-11. Experimental (symbols) and theoretical (lines) average ultimate tensile strength values from a) Banno's model and b) the Mixed Connectivity model for the 2mm-thick specimens. Theoretical values obtained from equations 5-12, 5-13 with $\sigma_{UTS,Nickel}$ = 45 MPa and $\sigma_{UTS,\ BaTiO3}$ = 21 MPa

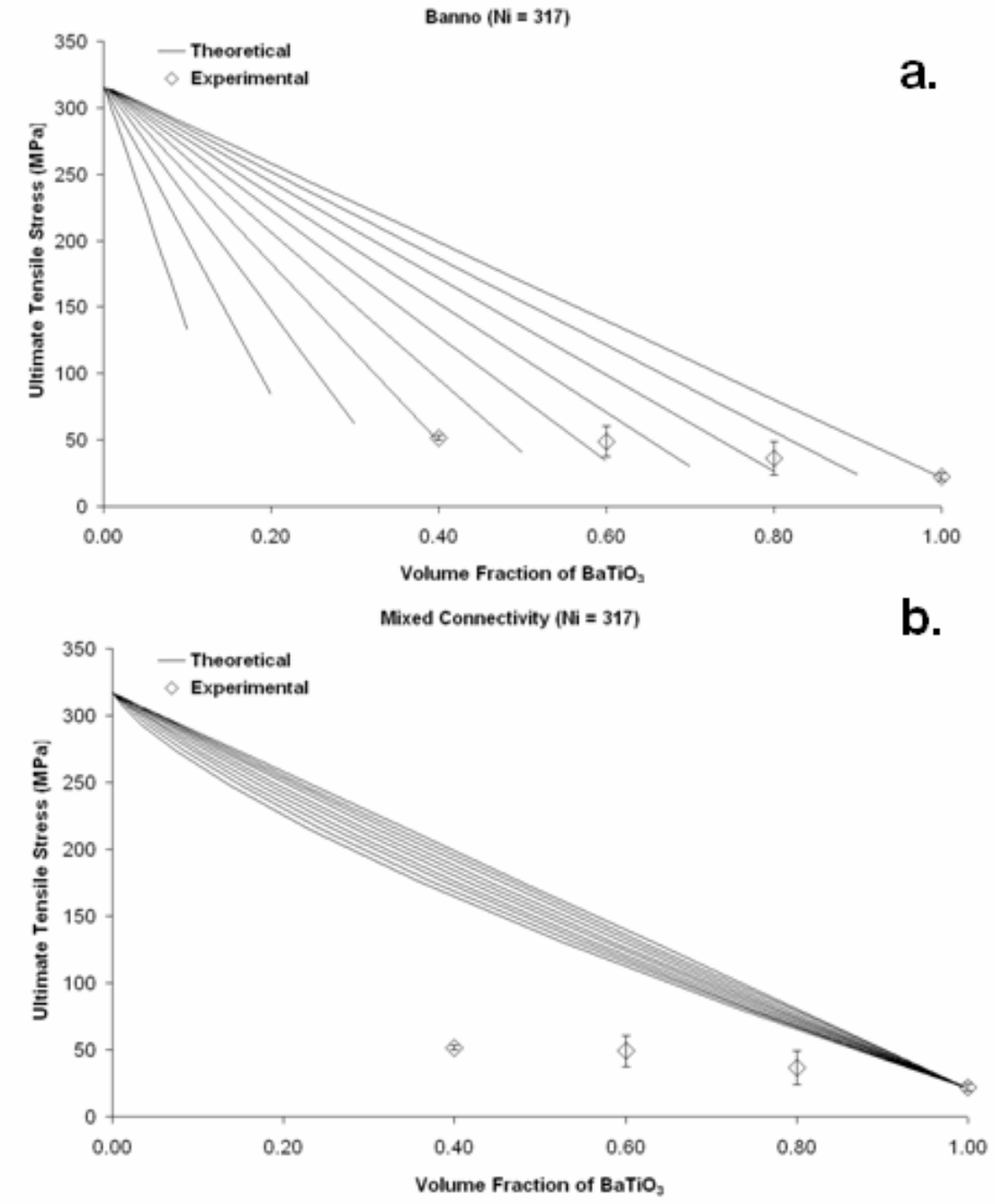

Figure 5-12. Experimental (symbols) and theoretical (lines) average ultimate tensile strength values from a) Banno's model and b) the Mixed Connectivity model for the 2mm-thick specimens. Theoretical values obtained from equations 5-12, 5-13 with $\sigma_{UTS,Nickel}$ = 317 MPa and $\sigma_{UTS,\ BaTiO3}$ = 21 MPa

The over- and under-estimation of the theoretical σ_{UTS} values led to additional theoretical calculations performed from modified equations based on the two models. Two modifications, consisted in adding a coefficient of proportionality K to the initial theoretical expressions (equations {5-12} and {5-13}). In the first case, the coefficient K was a function of the volume fraction of nickel as expressed in equation {5-18}. In the second case, the coefficient K was a constant based on the average experimental-to-theoretical ultimate tensile strength ratio. The theoretical values obtained from both the Banno's model and the Mixed Connectivity model, at volume fractions of $BaTiO_3$ equal to 0.4, 0.6, 0.8, and 1, were employed in the calculation of this constant coefficient. Figures 5-13 and 5-14 compare the theoretical ultimate strength values obtained from the first and second modifications, respectively, to the experimental values. For volume fractions of $BaTiO_3$ between 0.4 and 0.8, the experimental values were within one standard deviation of the theoretical ones except at 0.4 for the second-modification (K function of the volume fraction of nickel) Mixed Connectivity model (Figure 5-13b). In figures 5-14a and 5-14b, the constant K of the second-modification theoretical models led to a linear decrease of the ultimate tensile strength values with an increase of the volume fraction of $BaTiO_3$. The matching of the theoretical and experimental values was increased for volume fractions of $BaTiO_3$ of 0.6 and 0.8 in the second-modification Banno's model. The matching of the theoretical and experimental values was increased for volume fractions of $BaTiO_3$ of 0.4, 0.6, and 0.8 in the second-modification Mixed

Connectivity model. However, in both these models, the experimental value was 32% smaller than the theoretical one.

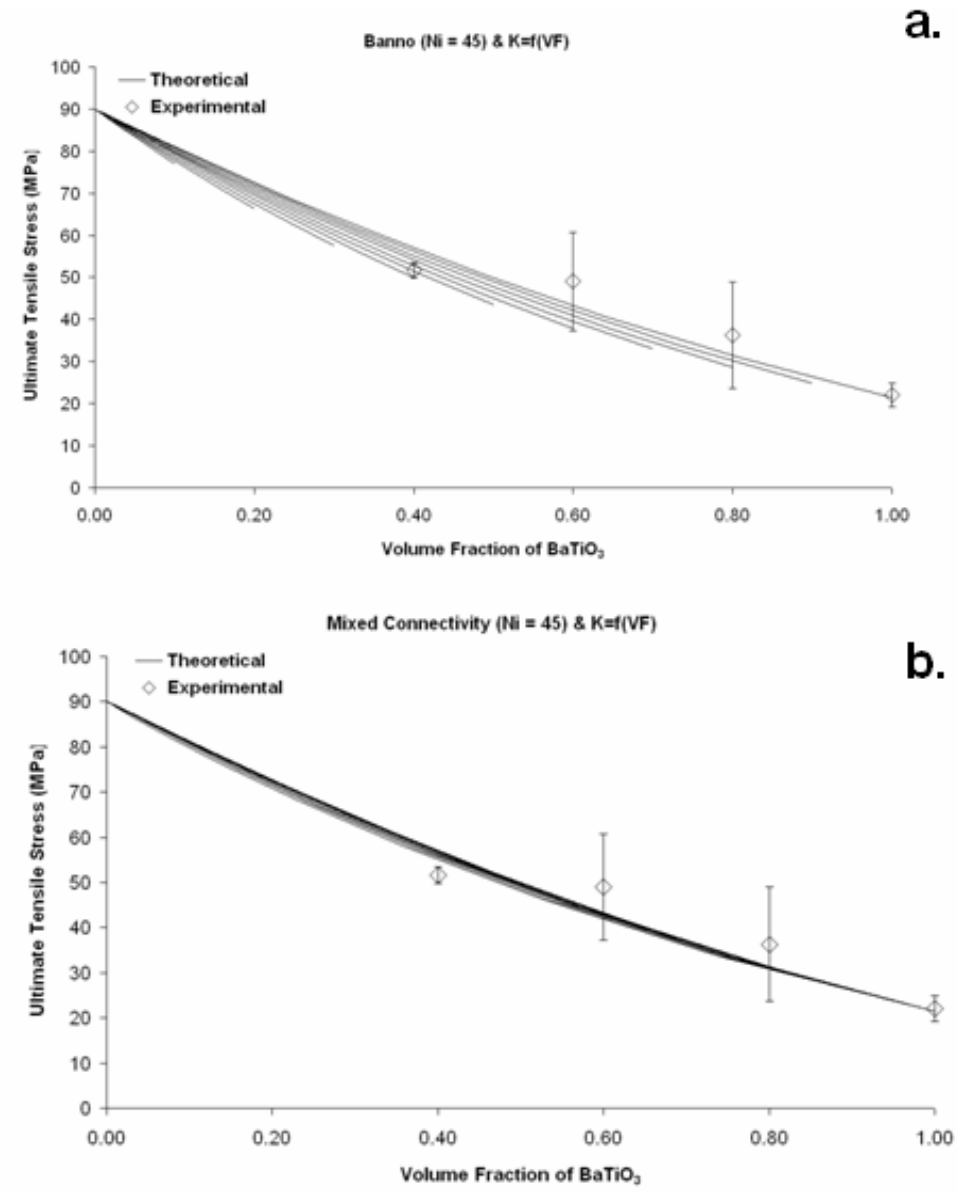

Figure 5-13. Experimental (symbols) and theoretical (lines) average ultimate tensile strength values from a) Banno's model and b) the Mixed Connectivity model for the 2mm-thick specimens. Theoretical values obtained from equations 5-15, 5-16 with $\sigma_{UTS,Nickel}$ = 45 MPa and $\sigma_{UTS,\ BaTiO3}$ = 21 MPa and K as function of the volume fraction of nickel

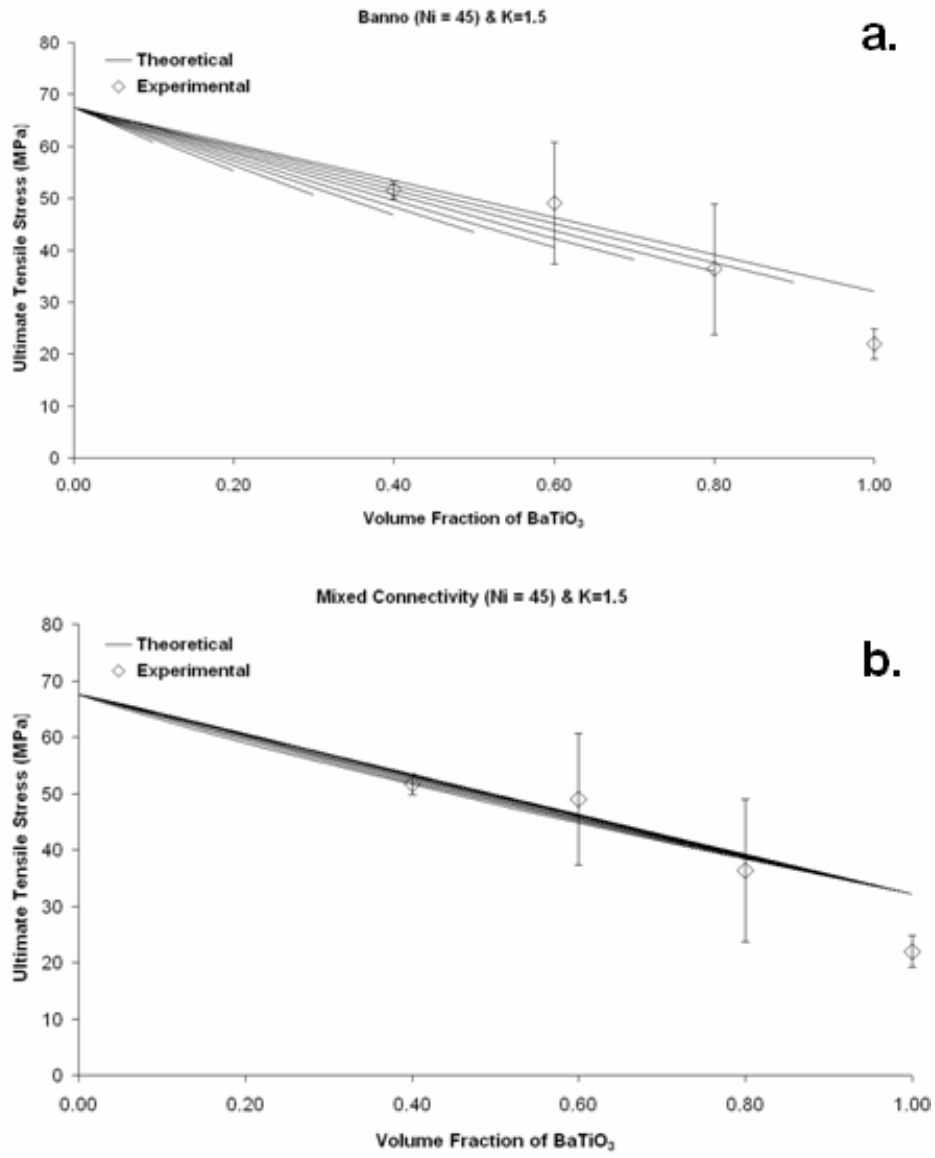

Figure 5-14. Experimental (symbols) and theoretical (lines) average ultimate tensile strength values from a) Banno's model and b) the Mixed Connectivity model for the 2mm-thick specimens. Theoretical values obtained from equations 5-15, 5-16 with $\sigma_{UTS,Nickel}$ = 45 MPa and $\sigma_{UTS,\ BaTiO3}$ = 21 MPa and K as a constant equal to 1.5

The theoretical and experimental ultimate tensile strength values and their percentage differences corresponding to the graphs in Figures 5-13 and 5-14, at these four compositions, are provided in Table 5-2. In the first-modification models, the percent differences between the theoretical and experimental values were greater at 0.6 and 0.8 volume fraction of $BaTiO_3$ for the modified Banno's model (29% and 27%, respectively) than for the modified Mixed Connectivity model (14% and 16%, respectively). But it was the contrary at a volume fraction of 0.4 with 3% difference for the modified Banno's model and -8% difference for the modified Mixed Connectivity model. In the second-modified models, the percent differences between the theoretical and experimental values were greater at 0.4 and 0.6 volume fraction of $BaTiO_3$ for the modified Banno's model (10% and 21%, respectively) than for the modified Mixed Connectivity model (6% and -7%, respectively). But it was the contrary at a volume fraction of 0.8 with 1% difference for the modified Banno's model and -7% difference for the modified Mixed Connectivity model.

Table 5-2. Experimental and theoretical ultimate tensile strength values from the modified Banno's model and Mixed Connectivity models. The table also indicates the percentage differences between the experimental and theoretical values

UTS Nickel = 45 MPa	Experimental UTS (MPa)	Theoretical UTS (MPa)				% difference			
		K = f(VF_{Nickel})		K = 1.5		K = f(VF_{Nickel})		K = 1.5	
		Banno's model	Mixed Connectivity model	Banno's model	Mixed Connectivity model	Banno's model	Mixed Connectivity model	Banno's model	Mixed Connectivity model
Pure $BaTiO_3$	22	21	21	32	32	3	3	-32	-32
Ni 20vol%- $BaTiO_3$ 80 vol%	36	29	31	36	39	27	16	1	-7
Ni 40vol%- $BaTiO_3$ 60 vol%	49	38	43	41	46	29	14	21	6
Ni 20vol%- $BaTiO_3$ 40 vol%	52	50	56	47	53	3	-8	10	-2

V.3.1.2 Average normalized stiffness

Figure 5-15 shows that the normalized stiffness of the composites with volume fractions of $BaTiO_3$ of 0.4, 0.6, and 0.8 were respectively 33%, 49%, and 27% larger than that of pure barium titanate. Analysis of variance showed that there was a significant difference (p-value < 0.05) between the average normalized stiffness values of the specimens with volume fraction of $BaTiO_3$ of 0.4, 0.6, 0.8, and 1.0. However, there was no significant difference between the average normalized stiffness values of the specimens with volume fraction of $BaTiO_3$ of 0.4, 0.6, and 0.8 (p-value of 0.480). This was confirmed by Student T-tests comparisons (0.4 vs. 0.6, 0.6 vs. 0.8, 0.8 vs.1.0 volume fraction of $BaTiO_3$) that yielded p-values of 0.16, 0.50, and 0.07, respectively.

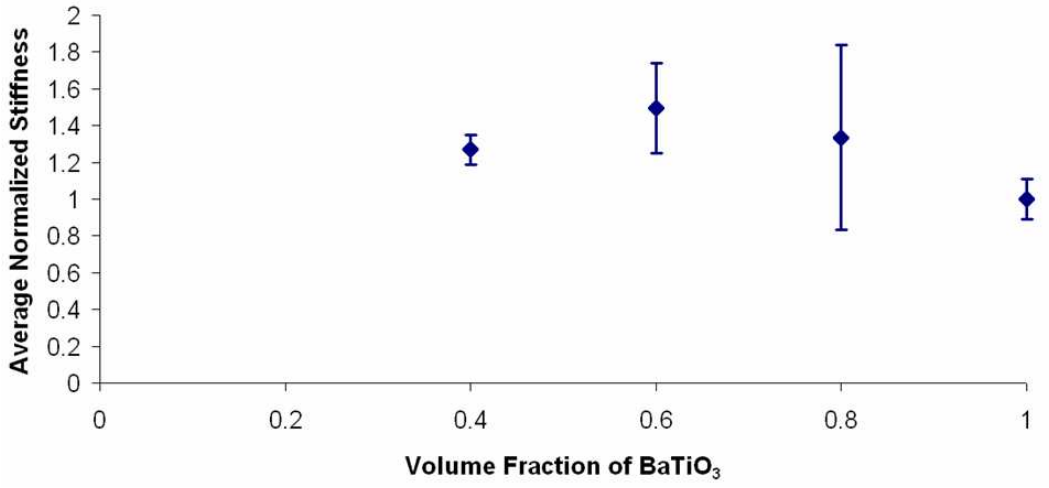

Figure 5-15. Average stiffness for the 2mm-thick specimens of pure and composite materials

V.3.1.3 Average porosity and SEM pictures

Experimental densities were smaller than the theoretical ones at all compositions. Their difference was divided by the theoretical density to provide an estimate of the porosity of each 2mm-thick disc. The specimens with volume fractions of nickel of 0.95 and 1.0 presented the highest average porosities of 21% and 18%, respectively. The disc containing 80vol% of nickel had the smallest average porosity of all, 4%. The discs of the other four compositions displayed similar average porosities ranging from 11% to 14% as reported in Table 5-3.

Table 5-3. Estimated porosities of the tested specimens of the seven compositions

Composition	100% Nickel	95%Ni-5%$BaTiO_3$	80%Ni-20%$BaTiO_3$	60%Ni-40%$BaTiO_3$	40%Ni-60%$BaTiO_3$	20%Ni-80%$BaTiO_3$	100% $BaTiO_3$
Average Porosity (%)	18 (±2)	21 (±2)	4 (±2)	14 (±1)	12 (±2)	11 (±2)	11 (±1)

SEM pictures of the fractured surfaces (Figures 5-16 to 5-22) revealed the differences and similarities of the microstructures of these composite materials. All of them presented identical features such as a rough surface of non-fused particles and presence of micro-pores. However, the pictures also demonstrated the great differences in particle shape and interaction between compositions. Figure 5-16b showed that the nickel particles were five to ten micron polyhedrons in the 100vol% nickel specimens whereas they were five microns or smaller in the 95vol% nickel composites Figure 5-17b and two microns or smaller in the other composites. The same trend applied to the barium titanate particles that reduced from 20-30 microns in

the pure $BaTiO_3$ (Figure 5-22a) specimens to about one micron in the other composites, more particularly in those containing 40vol% and 60vol% of nickel (Figures 5-20b and 5-19b, respectively). Finally, the nickel particles were compacted together (Figure 5-16b and 5-17b) but still distinct from one another in all the composites except in the one containing 80vol% of nickel. In this particular composite the metallic particles were flatter and better fused (Figure 5-18b). In the same way, the edges of the barium titanate particles displayed in Figure 5-21b and 5-22a were not as distinct because partially fused.

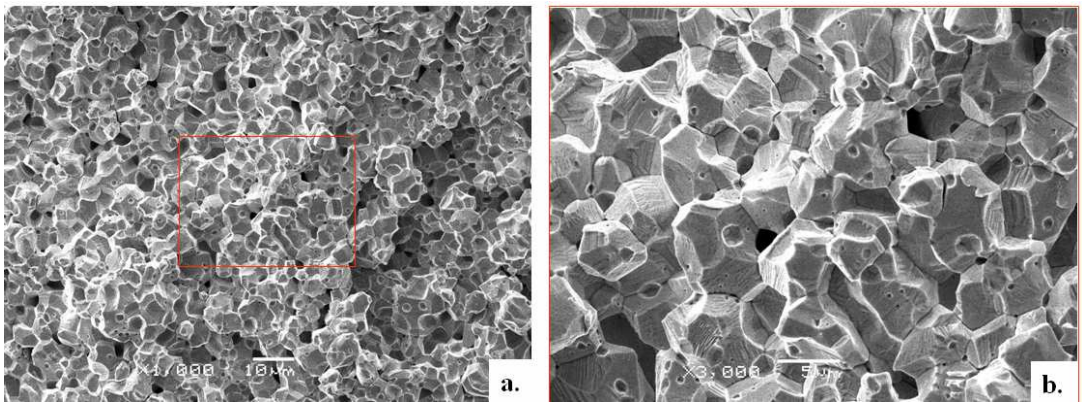

Figure 5-16. SEM pictures of the fracture surface of a pure Nickel specimen, (a) 1,000x magnification, (b) 3,000x magnification

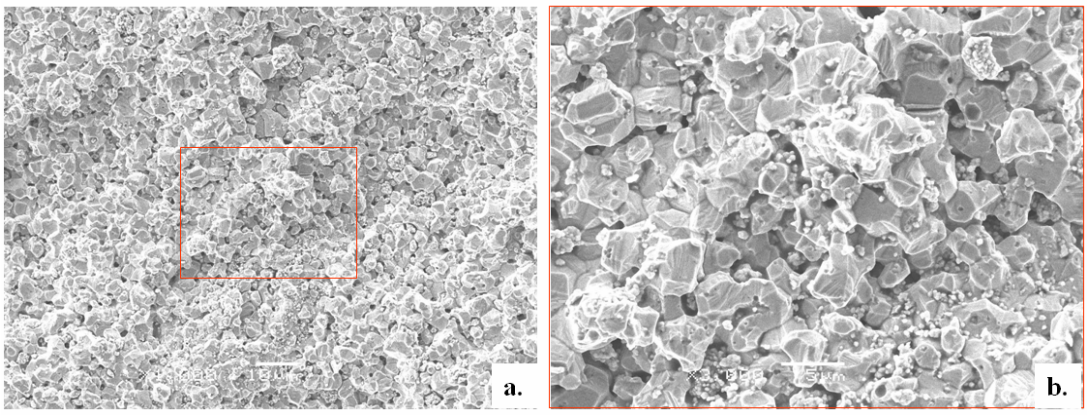

Figure 5-17. SEM pictures of the fracture surface of a Ni 95vol% - $BaTiO_3$ 5vol% specimen, (a) 1,000x magnification, (b) 3,000x magnification

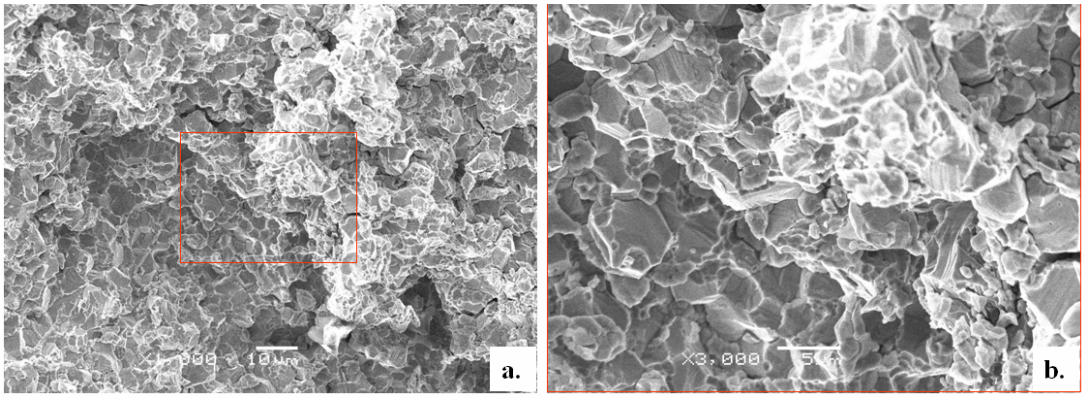

Figure 5-18. SEM pictures of the fracture surface of a Ni 80vol% - $BaTiO_3$ 20vol% specimen, (a) 1,000x magnification, (b) 3,000x magnification

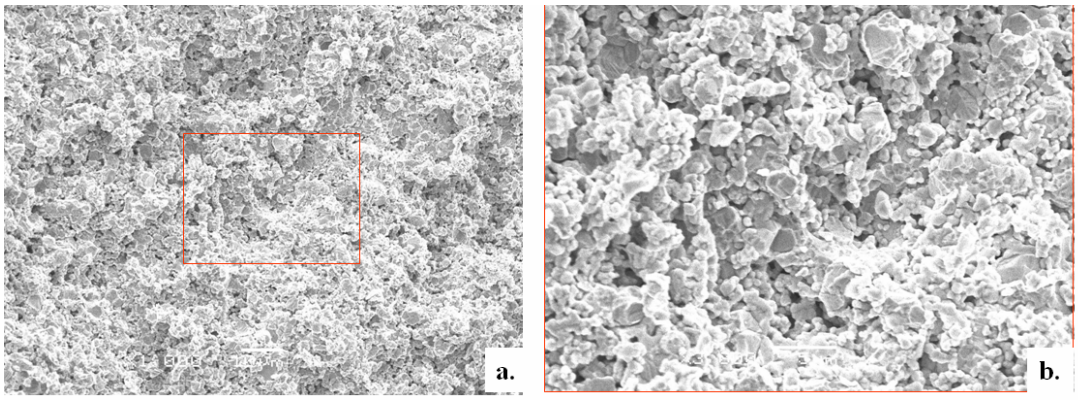

Figure 5-19. SEM pictures of the fracture surface of a Ni 60vol% - $BaTiO_3$ 40vol% specimen, (a) 1,000x magnification, (b) 3,000x magnification

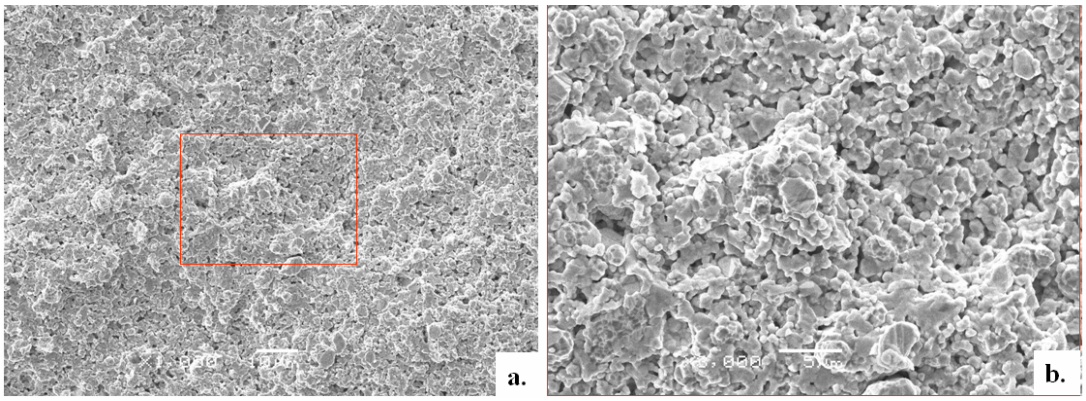

Figure 5-20. SEM pictures of the fracture surface of a Ni 40vol% - $BaTiO_3$ 60vol% specimen, (a) 1,000x magnification, (b) 3,000x magnification

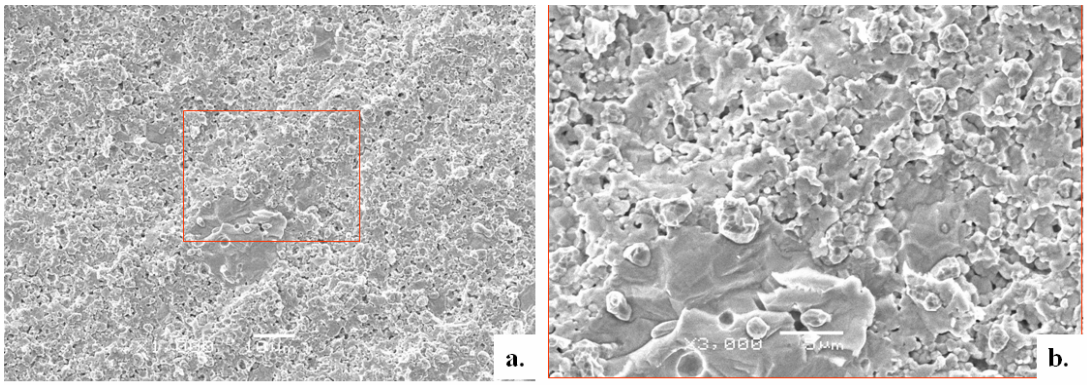

Figure 5-21. SEM pictures of the fracture surface of a Ni 20vol% - $BaTiO_3$ 80vol% specimen, (a)

Figure 5-21. SEM pictures of the fracture surface of a Ni 20vol% - $BaTiO_3$ 80vol% specimen, (a) 1,000x magnification, (b) 3,000x magnification

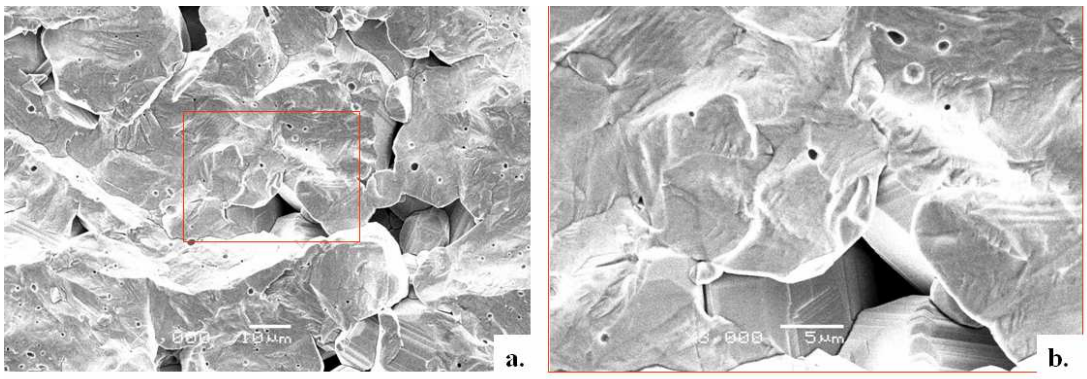

Figure 5-22. SEM pictures of the fracture surface of a pure $BaTiO_3$ specimen, (a) 1,000x

Figure 5-22. SEM pictures of the fracture surface of a pure $BaTiO_3$ specimen, (a) 1,000x magnification, (b) 3,000x magnification

V.4 Discussion

The results obtained were subjected to a careful examination to provide explanations concerning the trends displayed by the data points on Figures 5-9 and 5-15. Analysis of these figures and the SEM pictures allowed analyzing the validity of the theoretical expressions for estimating the ultimate tensile strength and of the diametral compression test for ductile materials.

V.4.1 Average ultimate tensile strength

V.4.1.1 Theoretical models

As presented in the results section, the initial Banno's model and Mixed Connectivity models under- and over-estimated the ultimate tensile strength values when $\sigma_{UTS,Nickel}$ was equal to 45 MPa and 317 MPa, respectively. The addition of a coefficient of proportionality in the equations of these models showed that the experimental values could be well estimated by the models for volume fractions of $BaTiO_3$ between 0.4 and 1. The differences between the experimental and theoretical values reported in Table 5-2 can appear to be large but should be considered with respect to the standard deviation of the experimental values. Indeed, Figures 5-13 and 5-14 demonstrate that the theoretical values were within one standard deviation of the experimental one except at a volume fraction of 0.4 for the first-modification Mixed Connectivity model (Figure 5-13b). Since the theoretical values were calculated for all the combinations of the m and n parameters, a range of estimates were obtained at

each volume fraction. The range of theoretical values was broader in the modified Banno's model (Figures 5-13a and 5-14a) than in the modified Mixed Connectivity model (Figures 5-13b and 5-14b). This explained the better match at 0.4 volume fraction of $BaTiO_3$ for the first-modification Banno's model.

The experimental-to-theoretical ratio values presented in Table 5-4 allowed discerning which of the four modified theoretical models (list below) was the most appropriate.

- Banno's model with K as a function of the volume fraction of nickel
- Mixed Connectivity model with K as a function of the volume fraction of nickel
- Banno's model with K equal to 1.5
- Mixed Connectivity model with K equal to 1.5

For each model, an average experimental-to-theoretical ratio was computed from the values obtained for the four compositions of interest (volume fraction of $BaTiO_3$ equal to 0.4, 0.6, 0.8, and 1). These average ratio values were 1.2, 1.1, 1.0, and 0.9 for the four models as listed above, respectively. This suggested that the modified Banno's model including a coefficient of proportionality K equal to 1.5 was the most suitable to evaluate the ultimate tensile strength of the nickel/barium titanate interfacing material.

Table 5-4. Experimental and theoretical ultimate tensile strength values from the modified Banno's model and Mixed Connectivity models. The table also indicates the experimental-to-theoretical ultimate tensile strength ratio

UTS Nickel = 45 MPa	Experimental UTS (MPa)	Theoretical UTS (MPa)				Experimental-to-Theoretical UTS ratio			
		$K = f(VF_{Nickel})$		K = 1.5		$K = f(VF_{Nickel})$		K = 1.5	
		Banno's model	Mixed Connectivity model	Banno's model	Mixed Connectivity model	Banno's model	Mixed Connectivity model	Banno's model	Mixed Connectivity model
Pure $BaTiO_3$	22	21	21	32	32	1.0	1.0	0.7	0.7
Ni 20vol%- $BaTiO_3$ 80 vol%	36	29	31	36	39	1.3	1.2	1.0	0.9
Ni 40vol%- $BaTiO_3$ 60 vol%	49	38	43	41	46	1.3	1.1	1.2	1.1
Ni 20vol%- $BaTiO_3$ 40 vol%	52	50	56	47	53	1.0	0.9	1.1	1.0

V.4.1.2 Influence of disc thickness

The significant difference between the ultimate tensile strength values of the 2mm, 5mm, and 10mm-thick discs of pure materials can be explained as follows. As the thickness of the specimen decreases, the non-uniformity of the load distribution also decreases. The 5mm and 10mm-thick discs, rather cylinders, presented a greater outer surface than the 2mm-thick discs. Diametral changes and rough spots increased as the cylinder lengthened. These defects prevented the specimen from being uniformly loaded in the vertical plane. Therefore, the 5mm and 10mm-thick specimens were not purely in a state of plane stress as were the 2mm-thick discs. This non-uniform loading led to the fracturing of the thicker specimens at lower loads.

V.4.1.3 Influence of composition

As illustrated on Figure 5-9 the ultimate tensile strength (σ_{UTS}) decreased linearly with increasing volume fractions of $BaTiO_3$. This decrease was expected because the ductility conferred on the composite by the nickel particles diminished as the volume fraction of metallic particles was reduced and replaced by more brittle ceramic particles. It was interesting to note that the discarded experimental σUTS value obtained from the pure nickel specimens (65 MPa) fell in the range of standard values and was greater than that of pure $BaTiO_3$ as it should be. The experimental 22 MPa average ultimate tensile strength obtained via the diametral compression test for pure $BaTiO_3$ was on the low end of reported standard range, 21 MPa to 59 MPa [9]. This experimental average value was also on the low end of the range reported for the compressive strength of titanium mesh [13] that compared well with that of trabecular bone. The fact that the present experimental value was on the low end of these ranges was not a concern because the small bowtie structures presented in the third chapter never reached that level of stress even when tested to failure. Therefore, barium titanate plates implemented in a bowtie structure via the EBRD process would not be stressed beyond their failure point.

V.4.1.4 Influence of microstructure

A lower average ultimate tensile strength value could be attributed to defects in the structure, such as pores caused by air bubbles or a non-homogeneous

repartition particles. Since the Ni 80vol% composites yielded a greater average ultimate strength even if they contained more $BaTiO_3$ particles than the Ni 95vol% composite and the pure nickel specimens. The discrepancies between the average σ_{UTS} values obtained for the specimens containing 100vol%, 95vol%, and 80vol% of nickel were unexpected. Indeed, the composite with the highest volume fraction of $BaTiO_3$ (80vol% Ni- 20vol% $BaTiO_3$) yielded the highest average σ_{UTS} value. The discrepancies and large standard deviations between the normalized stiffness values of the other four composite materials (40vol% to 100vol% of $BaTiO_3$) were also intriguing. The video recordings of the tests revealed that the discs with 100vol%, 95vol%, and 80vol% of nickel displayed noticeable plastic deformation before brittle failure occurred. The video recordings of the other four composites revealed that they had all displayed a “triple clef” fracture. The failure mode being identical within each group, the source of the discrepancies was linked to materials problems as suggested by the porosity calculations and the SEM pictures.

As shown in Table 5-3 the estimated porosity of the 80vol% nickel discs was five and four times smaller than that of the 100vol% and 95vol% nickel discs, respectively. This alone could explain the discrepancies between these three composites. But for the other four composites, the estimated porosities were too similar to account for the differences in the average σ_{UTS} values. The SEM pictures of the fractured surfaces (Figures 5-16 to 5-22) confirmed the porosity calculations by showing the numerous micro-pores present in the microstructures. These pictures also showed the great differences in particle shape and interaction that could be imparted

to material treatment, primarily the mixing and sintering processes. Mixing of the powders was performed with a planetary centrifuge machine that uses high rotating speeds in different directions to ensure homogeneous repartition of particles in the colloidal inks. In the composite materials, the smaller but denser nickel particles collided with the bigger barium titanate particles thus breaking them down. The dissipation of kinetic energy of the particles was such that the nickel particles also broke down. The size reduction of the particles probably increased their packing factor but could not prevent the presence of micro-pores between them. For this reason, no 1-3 connections form as evidenced by the SEM pictures. This confirmed the hypothesis of a 0-3 connectivity and supported further that the modified Banno's model should be considered over the Mixed Connectivity model. The effect of the sintering temperature (1600° Celcius) became more evident when comparing the interaction and cohesion of the particles between compositions. The flatter layered nickel particles of the 80vol%-Ni composite (Figure 5-18) and the partially fused edges of the barium titanate particles displayed on Figure 5-21b and 5-22a suggested that partial recrystallization and growth had taken place.

Finally, the smaller porosity of and better particle interaction in the 80vol% nickel composite led to a more cohesive structure and explained why the average σ_{UTS} value was higher for this composition. The particle interaction, which is also a function of the particle size, can explain the experimental discrepancies between the stiffness values of the containing 40vol%, 60vol%, 80vol%, and 100vol% of $BaTiO_3$. The pure barium titanate discs presented bigger $BaTiO_3$ particles than the other three

composites materials. For this pure material, bigger particles implied that there were less particle boundaries for dislocations to go through. Less particle boundaries implied that less energy was needed for a crack to propagate and thus explained why the stiffness of the pure barium titanate was smaller than that of the other three composite materials

V.4.1.5 Influence of poling

The effects of the compositions and the microstructure are critical to consider for the manufacturing of the composite piezoelectric re-entrant structure via the EBRD process because they also influence the piezoelectric properties of the structure. In order for the structure to display piezoelectric properties, the ferroelectric ceramic elements will have to be poled after manufacturing because they are made by the deposition of $BaTiO_3$ colloidal ink filaments. The poling process, which consists in aligning the electric dipoles present in the ferroelectric ceramic crystals in the same direction, can therefore alter the mechanical properties of the composite interface that contains such crystals. The re-orientation of the dipoles implies crystallographic plane re-orientation and structure elongation that modify the compliance of the ceramic material and can create internal stresses and cracks in a composite. This is expressed mathematically in equation {2-6} that links the compliance of the ferroelectric ceramic before poling to that after poling via the coupling coefficient. This equation states that the compliance of the poled material is greater than when it is not poled. In

other words, the modulus of elasticity, which is the inverse of the compliance, decreases when the material is poled. However, no study has quantified the change in the mechanical properties caused by the poling process. Costa et *al.* [14] demonstrated an anisotropic influence of poling on the mechanical properties of a piezoelectric polymer. Tanimoto and Okazaki [15] showed that specific strength of the poling electric field and temperature can improve the electrical and mechanical properties (mainly resistance to fatigue) of barium titanate.

Another problem concerns the consistency of poling throughout the interfacing composite material because of the particles dispersion. . Baxter et *al.*, Bowen et *al.* [16, 17] showed that a minimum of 70 vol% of ferroelectric ceramic is required to create a composite material that can be poled to feature a piezoelectric behavior. Therefore, the interfacing material would not be subjected to the effects of poling homogeneously throughout its thickness. This could raise issue concerning the mechanical and electromechanical integrity of the interface and of the whole structure

V.4.2 Average normalized stiffness

The differences in the microstructure, the particle size and cohesion and the micro-porosity also explained the discrepancies in the stiffness values. According to figure 5-15 the standard deviations were larger for the composite materials that contained a ceramic volume fraction greater than 0.5. This could indicate that the $BaTiO_3$ particles lead to greater discrepancies in the microstructure that counteract the increase in stiffness that should arise from the greater amount of ceramic in the

composite material. The lack of fusion between the various particles and the effect on stiffness was evidenced by the non-significant differences in the normalized values. This result could mean that the loading of the gradual composition interfacing material would be homogeneous throughout its thickness, which supports the previous findings of a smooth stress transition. Therefore, the load would be homogeneously transmitted from the metallic open bowtie cells to the piezoelectric ceramic plates.

V.5 Conclusion

The analysis demonstrated that the diametral compression test was not suitable for a ductile material and that the theory of mixture could be employed to estimate the ultimate tensile strength of composites. But the main conclusion of this study was that a gradual composite interfacing material (from pure nickel to pure $BaTiO_3$) could provide a physical support for the transmission of, sharing of, and resistance to tensile stresses, which is important to reduce internal stress concentration and maintain the mechanical integrity of the whole structure.

The results of the diametral compression tests were satisfactory in terms of showing that a gradual interfacing material would feature a gradient of ultimate tensile strength values. The data analysis proved that the ultimate tensile strength decreases smoothly as the volume fraction of $BaTiO_3$ increases. This smooth stress transition could alleviate the problem of stress concentration that usually plagues and weakens composite structures. The micro-porosity and particle interactions revealed by the SEM pictures demonstrated that there was no 1-3 connectivity of the particles in any of the intermediary composite materials. Therefore, the modified Banno's model including a constant coefficient K of 1.5 (and with $\sigma_{UTS,Nickel}$ equal to 45 MPa) was considered as the most accurate model to estimate the ultimate tensile strength of nickel/ $BaTiO_3$ composites containing 40vol% or more of $BaTiO_3$. The microstructural differences revealed by the SEM pictures led to the conclusion that the current processing of materials needs better control to decrease porosity and

ensure fusion of the particles since the affect the mechanical properties. Despite micro-structural imperfections, the σ_{UTS} values of the composites containing more than 40vol% of $BaTiO_3$ were high (over 21 MPa) for the targeted biomedical applications.

The porous nickel bowtie/ $BaTiO_3$ plate composite structure described in previous chapters was designed as an electromechanical active device. This implied that the $BaTiO_3$ plates would require poling to display piezoelectric properties. Therefore, the gradual composition interfacing material will also be subjected to the poling electric field, which would modify its mechanical and electromechanical properties. The exact same seven composite materials should thus be tested to investigate the effect of poling on their mechanical properties. Finally, this work could also be taken a step further into the development of a new biomaterial structure. A similar study can investigate the mechanical properties of composite materials in which titanium replaces nickel.

References

1. Rudnick A., Hunter A.R., Holden F.C., An analysis of the diametral compression test, Materials Research & Standards, 283-289, 1963
2. Hossack J.A., Auld B.A., Improved Modeling of 0:3 Composite Materials, IEEE Ultrasonics Symposium, 945-949, 1995
3. Banno H., Effects of Shape and Volume Fraction of Closed Pores on Dielectric, Elastic, and Electromechanical Properties of Dielectric and Piezoelectric Ceramics – A Theoretical Approach, Ceramic bulletin, Vol. 66, No. 9: 1332-1337, 1987
4. Wenger M.P., Das-Gupta D.K., Mixed Connectivity Composite Material Characterization for Electroactive Sensors, Polymer Engineering and Science, Vol. 39, No. 7:11761188, 1999
5. Hajeeraeh S., Muensit S., Theory and measurements for 0-3 $BaTiO_3$/PVDF composites, Songklanakarin J. Sci. Technol., Suppl.2: 413-418, May 2007
6. Banno H., Effects of Porosity on Dielectric, Elastic, and Electromechanical Properties of Pb(Zr,Ti)O3 Ceramics with Open Pores: A Theoretical Approach, Jpn. J. Appl. Phys. Vol.32: 4214-4217, 1993
7. Dias C.J., Das-Gupta D.K., Electroactive Polymer-Ceramic Composites, Proceedings of the 4th International Conference on Properties and Applications of Dielectric Materials, 175-178, 1994
8. Hashin Z., Shtrikman S., A variational approach to the theory of the elastic behaviour of multiphase materials, J. Mech. Phys. Solids, Vol. 11: 127-140, 1963
9. Chisholm J.M., Hahn H.T., Williams J.G., Diametral compression of pultruded composite rods as a quality control test, Composites 20 (6): 553-558, 1989
10. Fahad M.K., Stresses and failure in the diametral compression test, Journal of Materials Science 31: 3723-3729, 1996
11. www.matweb.com (accessed 09/23/08)
12. Wright P.J.F., Comments on indirect tensile test on concrete cylinders, Mag. Concr. Res. Vol.7, No.20:87-96, 1955
13. Rao G., Titanium foams fabricated for bone-tissue engineering applications, Research/Researchers MRS bulletin, P940, 2002 [www.mrs.org/publications/bulletin]
14. Costa C.M., Sencadas V., Mano J.F., Lanceros-Méndez S., Effect if poling on the mechanical properties of β-poly(vinylidene fluoride), Materials Science Forum, Vols.514-516:951-956, 2006
15. Tanimoto T., Okazaki K., Electrical degradation process and mechanical performance of piezoelectric ceramics for different poling conditions, Proceedings of the Eighth IEEE International Symposium on Application of Ferroelectrics, pp504-507, 1992

16. Bowen C.R., Gittings J., Turner I.G., Baxter F., Chaudhuri J.B., Dielectric and piezoelectric properties of hydroxyapatite- $BaTiO_3$ composites, Applied Physics Letters, Vol.89 (132906), 2006
17. Baxter F.R., Turner I.G., Bowen C.R., Gittings J.P., Chaudhuri J.B., Lewis R.W.C., The structure and properties of electroceramics for bone graft substitution, Key Engineering Materials, Vols.361-363: 99-102, 2008

VI Chapter 6: Conclusion

The increasing need for bioactive orthopaedic implants and the limitations of the current ones call for the design and development of biomimetic medical devices. Benefiting from the progresses achieved in various engineering fields and the successes and failures of previous devices, new materials and structures can be engineered to respond to the demand while improving the outcome. In the NSF-funded project of which this study is a part, the focus was placed on a spinal fusion implant that could be more readily available due to reduced cost, less risky in terms of infection, and with better outcomes for patients at high risk of non-fusion. This could later be extended for use in every candidate requiring bony fusion. The long-term objective of the project is to develop a mechanical and electromechanical active structure that would favor, support, and accelerate bone formation. This would eventually reduce the surgical time and costs associated with the surgery and would allow the patient to resume a normal life earlier. The first step of the project was thus to prove that a material/structure could be developed for use in such medical devices. This study presented the investigation of three key issues towards this goal. The prime research aimed at demonstrating that a re-entrant metallic structure could be tailored to replicate the mechanical behavior displayed by the loaded trabecular network at small strains. A composite piezoelectric re-entrant structure was then shown to possess controllable piezoelectric properties. Finally, the composite re-entrant structure required the study of a potential interfacial material that would

provide a strong mechanical and electromechanical bonding between its metallic and piezoelectric ceramic elements.

The data analysis showed that the mechanical behavior at small strains presented nonlinearity similar to that of trabecular bone as reported in the literature. In the given testing conditions, this nonlinear behavior of the novel structure was a function of its relative density, which implied that this behavior could be controlled. The electromechanical tests demonstrated that the piezoelectric properties of the ceramic plates were conferred on to the whole re-entrant structure. More specifically, these properties were a function of the ceramic material and the relative density of the structure and could thus be controlled and tailored for specific applications. Finally, the diametral compression tests of various metal-ceramic composites demonstrated the linear variation of their tensile strength with the volume fraction of ceramic. This led to the conclusion that a gradually changing composition material would provide a suitable interface with gradient mechanical strength and thus reduce the negative effects of stress concentrations.

Some of the results and trends observed lacked statistical significance because of the small number of specimens tested. The studies also revealed current limitations in the manufacturing process of the novel structure. These limitations suggested that similar investigations should be performed using additional specimens to show statistical significance. However, time and resources could be dedicated to complementary studies such as a finite element analyses, especially for the

electromechanical behavior of the piezoelectric composite structure. These future investigations could use the results of the present study as a basis for initial comparison.

VI.1 Future Works

The results of the three key investigations presented in the chapters of this document opened access to a great variety of potential future studies. The trends displayed could lead into new developments and more focused refining studies, which could be performed in parallel. It was hypothesized that this biomimetic device would enhance the mechanotransduction process that takes part in bone formation and maintenance, as well as provide in-situ electrical stimulation of bone cells. Consequently, these enhancements would accelerate bone fusion. The risks of subsidence or migration of the implant would thus be reduced and the patient could resume physical activities earlier in the post-surgery phase. Some further investigations should thus focus on in-vitro biological tests of this composite piezoelectric re-entrant structure to verify this hypothesis. But before these take place, many technical questions remain to be addressed.

The one-dimensional re-entrant structures presented in this study would not be suitable as such for in-vitro tests because they lack an essential feature of successful cellular solid implants: interconnectivity of the cells. A modified version of these

tested structures could consist of layers of one-dimensional re-entrant cells stacked such that the long-axis of each layer is at 90° from that of the adjacent layers. The struts of the re-entrant cells would need to present regularly spaced holes to interconnect with the cells of the adjacent layers. Another design of a three-dimensional re-entrant structure, presented in the third chapter, could also be considered. The capability of the Electronic-Based Robotic Deposition (EBRD) process theoretically enables the preparation of such complex structures in which ferroelectric elements are created at specific locations. However, the programming of the layer-printing pattern that would allow the printing f these complex three-dimensional structures will require several trials. And once many of these three-dimensional structures are produced, their mechanical and electromechanical properties need to be investigated to verify their reproducibility and appropriateness for orthopaedic applications.

With the biological tests in mind, small and medium composite re-entrant structures should be prepared from a biocompatible metal such as titanium instead of nickel. This will first require the development of titanium colloidal inks that, once sintered, would present fewer micro-pores and be more ductile than the nickel structures tested in this study. Parallel studies could focus on the mechanical and electromechanical behaviors of these fine structures. Since they would be manufactured via the EBRD process they would necessitate poling to display piezoelectric properties. Therefore, the effects of poling on the integrity and the

mechanical performance of the structures should be investigated. Another axis of research in the preparation of colloidal inks would concern the preparation as well as the mechanical and electromechanical characterization of a gradual composition interfacing material from mixed titanium and barium titanate colloidal inks.

Finally, when all these investigations have provided enough supportive data, such composite structures could be tested in a biologic solution to verify if they stimulate biologic cells. Then, additional studies could investigate the effect of the ionic biologic solution on the electromechanical properties of the composite structure. For instance, shielding of the piezoelectric elements from the ionic solution will probably be required to prevent short circuits and to direct the electric energy to the metallic re-entrant cells intended to host the biologic cells. Therefore, a study will have to be performed to find an appropriate biocompatible protecting material that is stable overtime and does not affect the manufacturing process of the structures.

Many more investigations can spring from the results and conclusions of the present study as suggested above. It is expected that this work, as another step in the field of orthopaedic implant development, will help other researchers to advance further towards the understanding of how new devices and techniques can be utilized to improve patients' care.

Appendix-1. Non-contact method for the measurement of transverse deformation

Abstract

Common methods for measuring strain and deformation are not adequate for use on all structural materials. A novel non-contact technique was developed to determine the transverse deformation of cellular structures used in calculating apparent Poisson's ratio. This method uses fiber optic probes that monitor the intensity of the light reflected by the illuminated object under test. The variation in light intensity is linearly correlated to the change in distance between the fixed probe and the specimen. Results using this new technique were compared to data collected using the strain gage method for the measurement of the transverse deformation of a solid specimen subjected to cyclic compression. It was hypothesized that if the two methods yielded comparable results for the plain solid, the new method could then be used with confidence with cellular structures. Constrained and unconstrained reflective targets were implemented on the specimen to reflect the probes light. The transverse deformation values measured by the non-contact method (with unconstrained targets) were not significantly different from the values obtained using a strain gage, thus validating the novel technique.

Introduction

Extensometers and strain gages are the most common transducers used to measure deformation or strain. However, these transducers are not appropriate for use on all materials or specimen types. For example, the specimen may be so small and low in rigidity that presence of a contact type measuring transducer would bias the results. In structural materials such as cellular solids, the surface texture does not allow the implementation of these commons tools. In such cases, the measurement of deformation must be performed using a non-contact technique that will not interfere with specimen behavior. Several non-contact deformation methods, such as lasers, CCD cameras, interferometry and photoelasticity, have been described in the literature. These methods all use optic principles to quantify deformation. Each technique has limitations including overall test set-up cost, resolution, and appropriateness for material and specimen type.

The non-contact method described in this paper was developed to address the need of measuring transverse deformation in compression of a structural material with three-dimensional and surface porosity. This novel metallic structural material was developed for eventual use in medical device applications. This structure was cellular and its geometry was tailored so that it would display an overall negative apparent Poisson's ratio. The apparent Poisson's ratio or compressive strain ratio (CSR) of objects under compression is defined as the opposite of the transverse strain over the axial strain. In order to evaluate the CSR, both the axial and transverse

deformations must be measured to yield the axial and transverse strain, respectively. Axial strain could be ascertained from the axial deformation values output from transducers integrated in the mechanical test system. Accurate transverse deformation measurement on these metallic cellular structures was more challenging due to specimen surface irregularities. To resolve this need, we developed and validated a new technique employing the MTI 2100 Fotonic™ sensor (MTI Instruments, Albany, NY); validation of the technique is the focus of this paper.

Experiments

The novel technique to evaluate transverse specimen deformation described in this paper utilized two MTI fiber optic probes facing opposing lateral sides of the specimen (Figure A-1-1). The probe technology uses a bundle of fiber optics with half light-emitting, half light-receiving fibers. Each probe tip was positioned perpendicular to and at a calibrated distance from the side of the specimen. As the distance between the probe tip and the specimen changed, reflected light intensity measured by the probe was altered. The average change in reflected light intensity measured by the two probes could then be correlated to overall transverse deformation of the specimen. A requirement of this technique is that either the specimen surfaces or reflective targets mounted on the specimen surface reflected the incident light evenly [1-4].

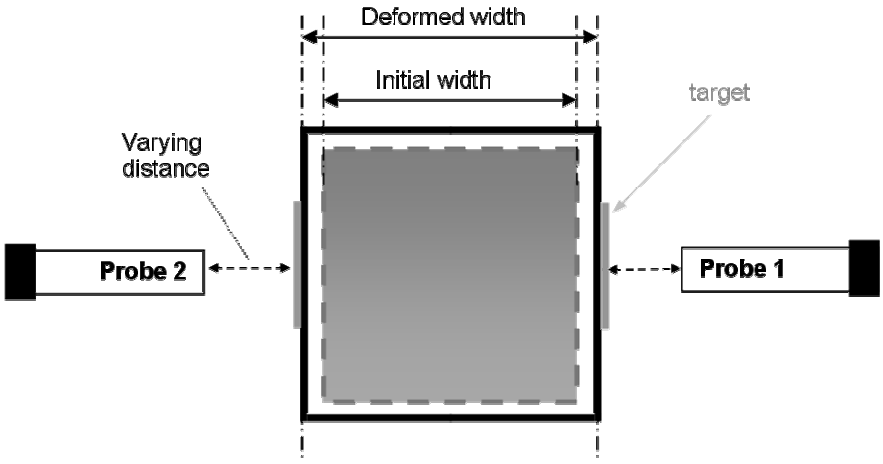

Figure A-1-1. Schematic of the top view of the CSR specimen and MTI probes set-up before (dashed contour) and after (solid contour) deformation

It was hypothesized that if this new technique provided an accurate measurement of the deformation of plain solid specimens, it would perform equally with cellular solids. For validation purposes, results obtained using the non-contact probe method were compared to those from the well-established strain gage technique on solid materials. Validation of the probe method was assumed if the transverse deformation values obtained from both methods at the same time were not significantly different (alpha = 0.05). A uniaxial strain gage (UW500-06-120, Vishay Micro Measurements, Raleigh, NC) was mounted transversely on the side of a 1.9 cm x 1.9 cm x 4.1 cm piece of polyvinyl chloride (PVC). Reflective targets were required for the non-contact method since the PVC was dark gray. As advised by the probe manufacturer, silver reflective tape (No.850 Scotch Brand, 3M, St Paul, MN) was used to prepare two types of reflective targets. The first target type, "Type 1", consisted of the silver tape directly applied onto the two specimen sides facing the MTI probes. The second

target type, “Type 2”, consisted of the silver tape first applied on thin flat plastic sheets, then loosely mounted onto the specimen using a thin layer of Vaseline® to create a low-friction adhesion between the specimen and the plastic sheet. Type 2 allowed for free movement of the target on the specimen during deformation; this feature was required for use on specimens with porous surfaces.

The effect of the quantity of low-friction adhesive on target kinematic with respect to the specimen was also investigated. Three levels of low-friction adhesive thickness were employed to test influence of this thickness on Type 2 target performance. The target was removed and reapplied in each test and deformations were measured using identical test methods. Results were compared and statistically analyzed. The analysis revealed that the change in transverse deformation for different amounts of low-friction adhesive employed to “glue” the Type 2 targets on the specimen were insignificant (p-value range: 0.07 to 0.86). Therefore, further experimentation with Type 2 targets did not include extreme measures to control the thickness of the low-friction adhesive layer.

The test assembly, as shown in Figure A-1-2, was then positioned between self-aligning compressive platens on a mechanical test system with load cell resolution of one Newton (858 MiniBionix, MTS Corp., Eden Prairie, MN). Tests were conducted using both target types. The specimen was preconditioned manually for ten cycles to a maximum compressive load of 25 N. In order to avoid specimen translation in the

transverse plane during the MTI probes calibration, a preload of 25 N was maintained on the specimen until the onset of the test. Eleven cycles of triangular loading displacement-control deformations at 1 Hz to approximate axial compressive strains of 0.01% to 0.49% were then applied to the specimen. Transverse strains from the strain gage signals were processed to the MTS system via a custom-made LabVIEW program (LabVIEW 8.0, National Instruments, Austin, TX). They were thus recorded along with the MTS actuator displacements and loads at a rate of 100 Hz. The entire test sequence was repeated a minimum of six times, with a rest period of at least one minute between repetitions. In order to compensate for possible slight temperature fluctuations and specimen placement differences, the test sequence was repeated over a period of ten days. A total of 40 and 25 tests with Type 1 and 2 targets, respectively, were performed.

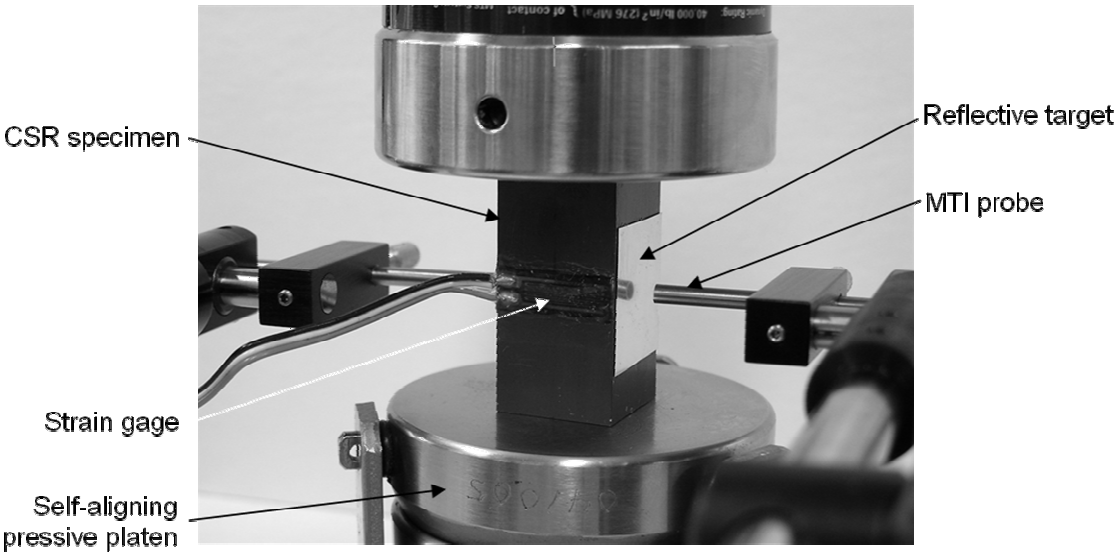

Figure A-1-2. Angled view of the test set-up implemented to measure the transverse deformation of the CSR specimen with the MTI Fotonic™ probes. Note the reflection image of the probe tip on the reflective target

Data Analysis

The MTI Fotonic™ sensor emitted voltage signals that were recorded by the MTS system along with the axial force and displacement. Those voltages were converted into a transverse displacement/deformation. The MTS system also captured the voltage signal coming from the strain gage, which was also converted into transverse deformation. The first and last cycles (of the eleven cycles applied in each test) were discarded to eliminate potential loading and unloading artifacts. The time of maximum and minimum axial displacements were identified and used to identify the corresponding maximum and minimum values from the MTI probes and strain gage signals. Differences between the maximum and minimum transverse deformation values were calculated for each cycle and averages and standard deviations computed.

Results

Transverse deformation values obtained from the MTI probes and the strain gage were compared for each target type. As displayed in Figure A-1-3, the transverse deformations measured with the MTI probes were greater than those calculated from strain gage data, regardless of the target type. As expected, average deformations calculated from strain gage data in both target configurations were not significantly different. However, average transverse deformations yielded by the MTI probes were different for the two target configurations. Type 1 target MTI measured deformations were significantly different from strain gage inferred values ($p = 0.011$). Type 2 target

MTI measured deformations were not significantly different from strain gage inferred values ($p = 0.15$; paired, double-sided Student's t-test).

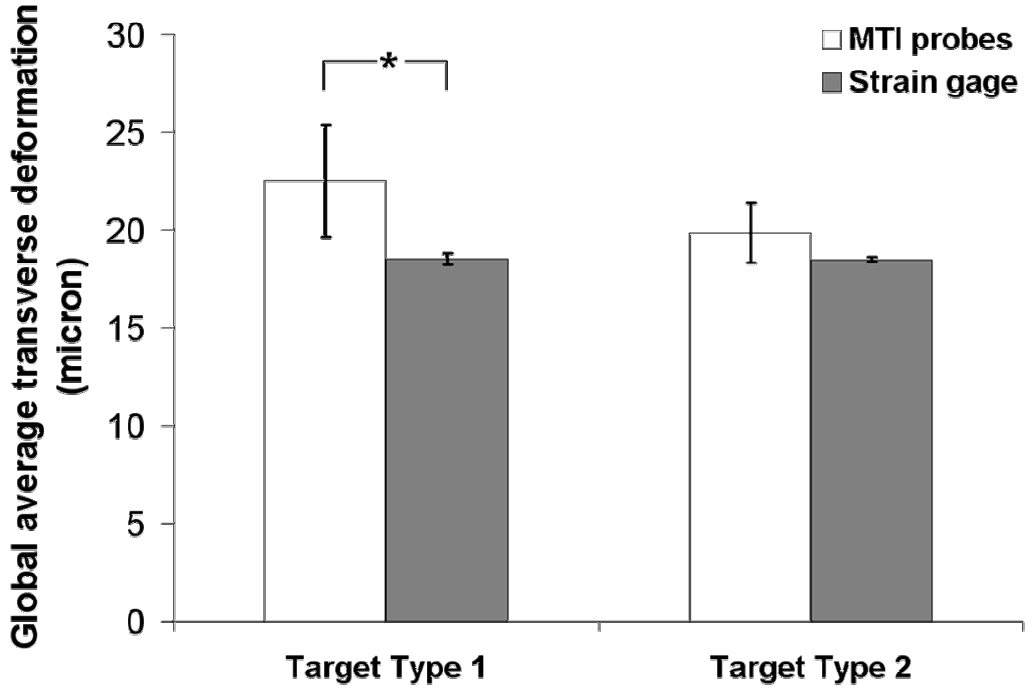

Figure 3. Global average transverse deformation values (μm) yielded by the MTI Fotonic™ sensor probes and the strain gage with each target type. (* significant difference)

Figure A-1-3. Global average transverse deformation values (μm) yielded by the MTI Fotonic™ sensor probes and the strain gage with each type of target (* significant difference)

Discussion

Theories to explain the discrepancies between the transverse deformation values measured with the MTI techniques and the strain gage are presented.

Theories for discrepancies

Two main reasons explain the noticeable differences between the transverse deformation values obtained from the MTI probes and the strain gage. First, as the specimen was compressed, it moved in the transverse plane; the MTI probes thus measured both specimen displacement and deformation. This issue was addressed by the use of two MTI probes facing opposite sides of the specimen. However, this set-up did not permit to completely eliminate the problem because the displacement of the CSR specimen in the transverse plane did not occur strictly along the direction of the probes (Figure A-1-4). Since the strain gage was mounted directly on the specimen, its output was not influenced by specimen movement in the transverse plane.

Both the MTI technique and the strain gage presented limitations that could account for the variations. MTI technique limitations included the calibration of the probes, imperfections of the targets, lack of parallelism of the specimen's opposite surfaces, and sensitivity of the probes. Strain gage technique limitations included misalignment, transverse sensitivity, and unbalance and nonlinearity of the Wheatstone bridge used in the signal processing [5].

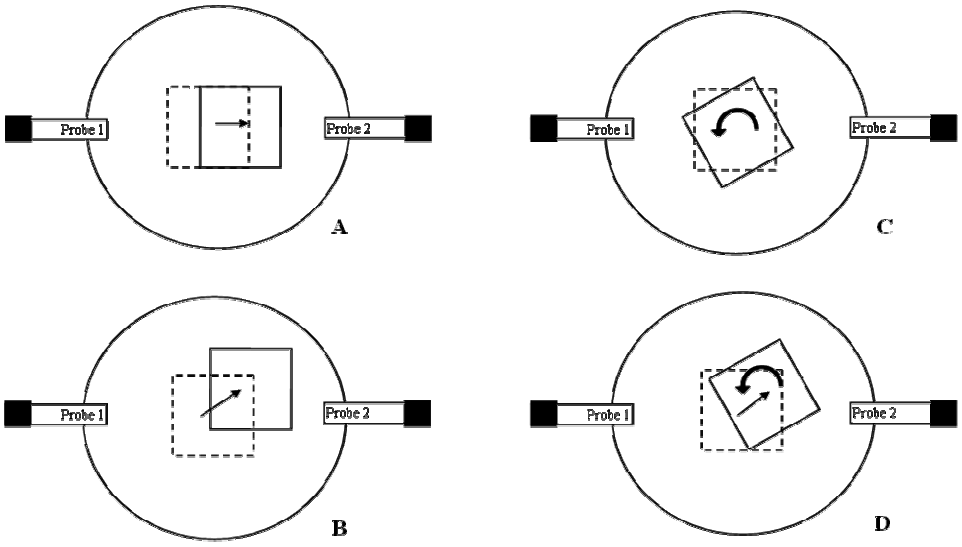

Figure A-1-4. Top view of the possible movements of the CSR specimens during compression. The dashed contour represents the specimen in its initial position, while the solid contour represents the specimen at the end of the test. The CSR specimen was potentially subjected to translation (A, B), rotation (C), or a combination of the two (D), in the transverse plane

Finally, the adhesive tape layer of the Type 1 target forced distortion of the target reflective surface due to transferred deformations from the specimen surface in both the axial and transverse directions, as illustrated on Figure A-1-5. This biaxial distortion of the target modified its reflectivity. In the Type 2 target, the distortion did not occur because of the lack of strong adhesion to the specimen surface. The Type 2 target could slide independent of biaxial specimen deformation while remaining perpendicular to the probe tip. Therefore, the Type 2 target allowed measurement of transverse deformation values closer to those measured with the strain gage.

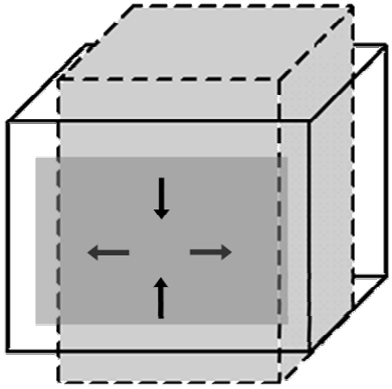

Figure A-1-5. Deformation of target Type 1 when the CSR specimen deformed from unloaded (dashed contour) to compressed state (solid contour). The target is in compression axially and in tension transversely (arrows)

The following section provide more details on the limitations described previously together with an error analysis of how these limitations may have affected the results.

Estimation of MTI-related errors

MTI Probes Calibration.

Probe calibration was semi-automated and required the operator to move the probe twice, first to find the maximum reflection distance used for internal calibration, and a second time to position the probe tip at an appropriate calibrated distance from the specimen. The peak of reflectivity was found through a multi-step systematic approach, which was subjective to the operator. Experimental trials revealed that absolute peak reflectivity was not required for successful probe

calibration and did not influence the measurement outcome. In other words, the deformation/displacement of the specimen was identical as long as calibration was performed at or in the vicinity of the peak of reflectivity.

Target Imperfections.

The silver reflective tape employed was a thin film of aluminum sandwiched between an adhesive layer and a clear polyurethane film. There were thus several intrinsic issues with use of the reflective tape. Micro air bubbles could be trapped underneath the tape upon its implementation. The probe tip could scratch the polyurethane layer when they came in contact during the calibration procedure. Both bubbles and scratches altered the reflectivity of the probed portion of the tape. Even on a perfectly smooth and unscratched surface, reflection of incident light is not perfect; only 86% of the emitted light actually bounces back and reaches the receptive fibers with a perfect reflective target because of packing fraction losses, as demonstrated by Cook and Hamm [6]. The influence of the micro-defects described in this paper on the measurement outcome could not be estimated.

Lack of parallelism of the specimen sides

Self-aligning platens were used to adjust for inherent geometric imperfections in the CSR specimen. For example, the top and bottom surfaces were not perfectly parallel with estimated maximum nonparallel angle, α. Use of self aligning platens reduced this error, but still allowed for transfer of stress to the sides of the

specimen, as illustrated (in an exaggerated fashion) in Figure A-1-6, and generation of a small transverse force with the axial compressive force. The transverse force component caused slight translation and/or rotation of the specimen under compression. The MTI probe measured both transverse deformation and displacement. Figure A-1-7 illustrates how this extraneous transverse displacement δ was calculated and equation (1) relates it to the longitudinal displacement ΔL.

$$\delta = \Delta L \cdot \tan(\alpha) \tag{1}$$

The angle, α, for the CSR specimen was evaluated to be 0.40 degrees. For a typical axial compressive specimen deformation ΔL of 0.195 mm, the value of the extraneous transverse displacement, δ, was estimated to be 1.34 μm.

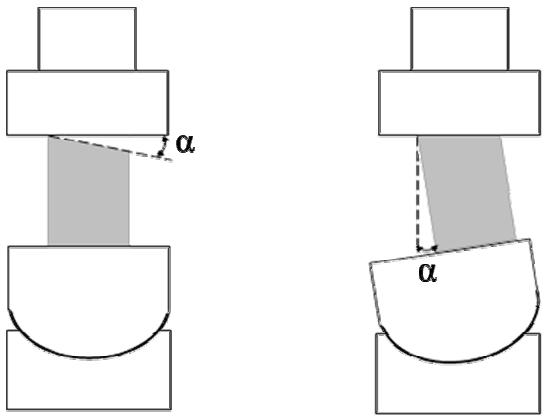

Figure A-1-6. Exaggerated angle α illustrating the potential lack of parallelism of the CSR specimen

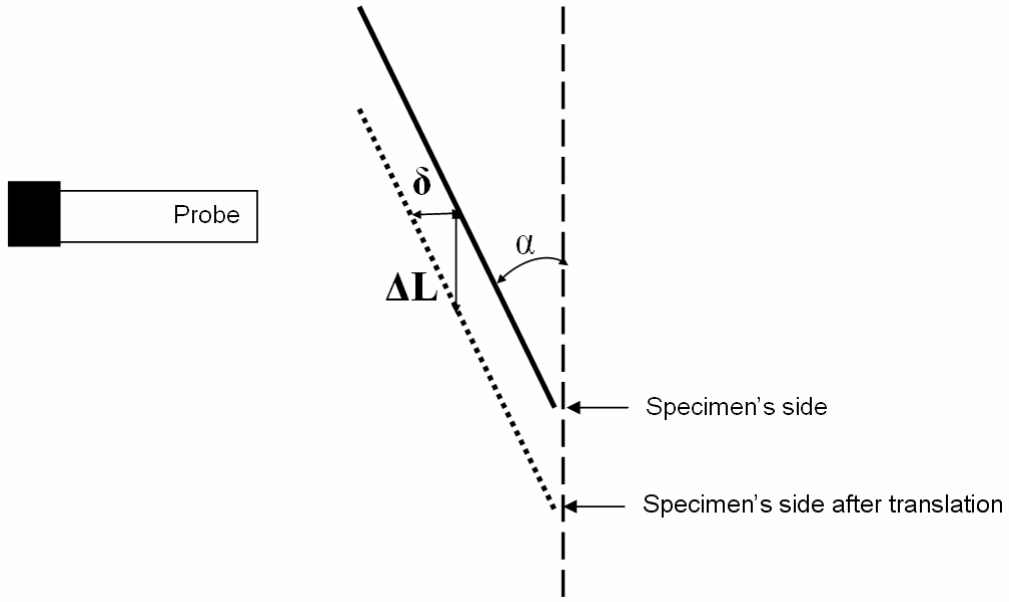

Figure A-1-7. Schematic illustrating the transverse translation of the specimen caused by the angle α, and the additional transverse displacement δ measured by the probe when the CSR specimen is subjected to a compression ΔL

In theory, this was the absolute value of the extraneous transverse displacement measured by the probes on opposite sides of the specimen. In other words, one probe measured +δ while the other measured –δ. These values cancelled each other when the transverse "deformations/displacements" measured by the probes were added, thus yielding the total transverse deformation of the CSR specimen. However, the absolute value of the extraneous transverse displacement measured was also influenced by the previously described target sources of error (scratches, cavities, air bubbles trapped under the target) that were not identical between the targets on the opposing specimen sides. Therefore, the component of extraneous displacement measured by each opposing probe did not cancel each

other exactly upon addition. Unfortunately it was not possible to evaluate how much each target imperfection accounted for this error. The micro-motion of the specimen in the transverse plane over the cycles made it even more complex to evaluate since the targeted area was never exactly the same from cycle to cycle and from test to test.

MTI probes sensitivity.

The specific MTI probes employed in this study were chosen because the arrangement of the fibers was such that their measurements were less affected by rotational defects of the targeted area. The chosen larger diameter probes used targeted a greater area that would encompass the deformation of several struts from the porous metallic specimens to be tested, thus allowing for a more accurate estimation of the global transverse deformation of the porous structure. The larger diameter probes, however, had a reduced sensitivity (± 1 μm) compared to other MTI probes. With two probes, this reduced sensitivity could lead to the over- or under-estimation of measured transverse deformations by up to ± 2 μm. This difference alone could explain the discrepancy observed between the MTI and strain gage inferred deformation test values using Type 2 targets.

Estimation of strain gage-related errors

All the strain-gage related errors listed above have been thorough fully investigated in previous studies and well-documented [5]. Those documents were consulted and the equations they contain were employed to estimate each of the listed strain gage-related errors. The calculations revealed that the sum of those strain gage-related errors accounted for a maximum variation of only ±0.190 μm in the transverse deformation evaluation, which was negligible.

Conclusion

Common/conventional methods to measure the transverse deformation and strain previously described in the literature could not be employed on small, fine and intricate metallic cellular solids. An innovative non-contact technique for transverse deformation measurement that uses MTI Fotonic™ sensors and reflective targets was developed. This novel method was validated in comparison to conventional tests on a solid specimen. The MTI technique was found to be a suitable non-contact approach to measure the transverse deformation of solid specimens. It was also demonstrated that the reflective targets used in this technique must not deform significantly during the tests for the results to be valid. The validated MTI method is appropriate for use with cellular materials. Thorough evaluation of errors due to various limitations intrinsic to the MTI sensors revealed that the resulting discrepancies could be narrowed further by the use of more sensitive optic fibers.

References

1. C. Menadier, C. Kissinger, H. Adkins, Instruments and Control Systems, 40 (6):114 (1967)
2. C. Kissinger, Advances in Instrumentation , 42 (3):1251 (1987)
3. J.T. Dawley, G. Teowee, B.J.J. Zelinski, D.R. Uhlmann, Application Note, MTI Instruments Inc., Albany, NY, (1998)
4. N.P. Vyshatko, P.M. Brioso, J. Pérez de la Cruz, P.M. Vilarinho, A.L. Kholkin, Rev. Sci. Instrum., 76, 085101 (2005)
5. Technical Notes (TN-507, -509, -511), Vishay micro-measurements, Raleigh, NC, (2007) http://www.vishay.com/strain-gages/knowledge-base-list/technotes-list/ (accessed 05/09/08)
6. R.O. Cook, C.W. Hamm, Applied Optics, 18 (19):3230 (1979)

Appendix 3-A. Quasi-static compression stress-strain curves and apparent modulus of elasticity

A circle indicates the maximum stress, a colored slope portion indicates the apparent modulus of elasticity, a dash line stands for the 0.2% offset slope, and the intercept with the curve is shown by a second circle that marks the yield point. All structures were tested with lubrication unless noted otherwise

SMALL STRUCTURES

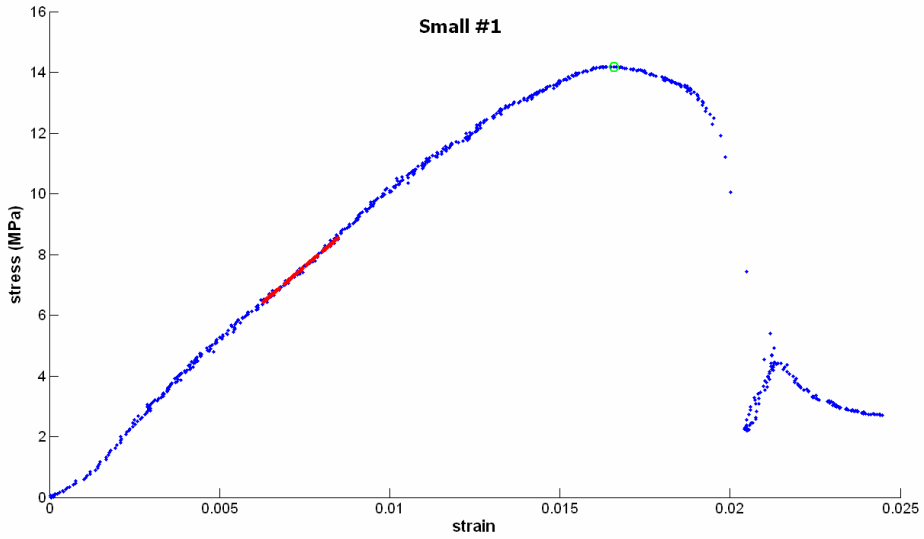

Figure 3-A-1. Stress-strain curve of the small structure #1

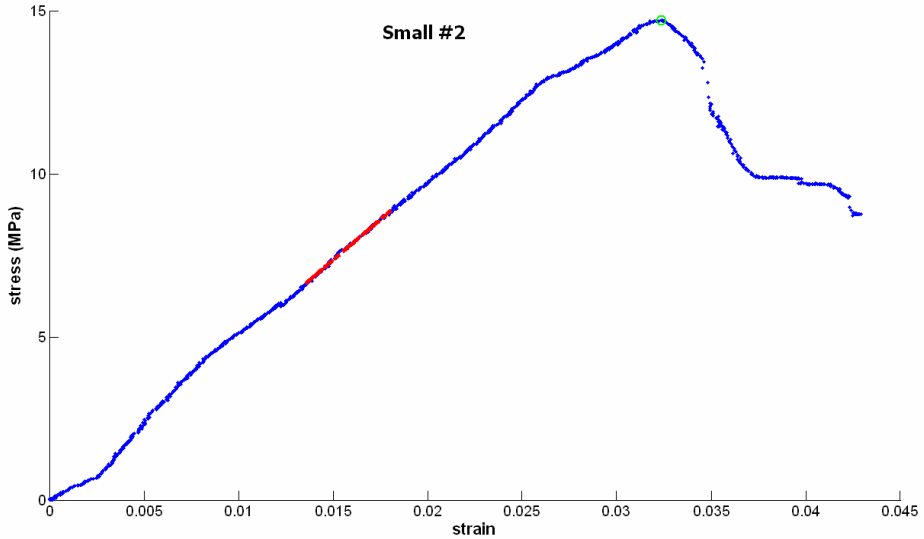

Figure 3-A-1. Stress-strain curve of the small structure #2

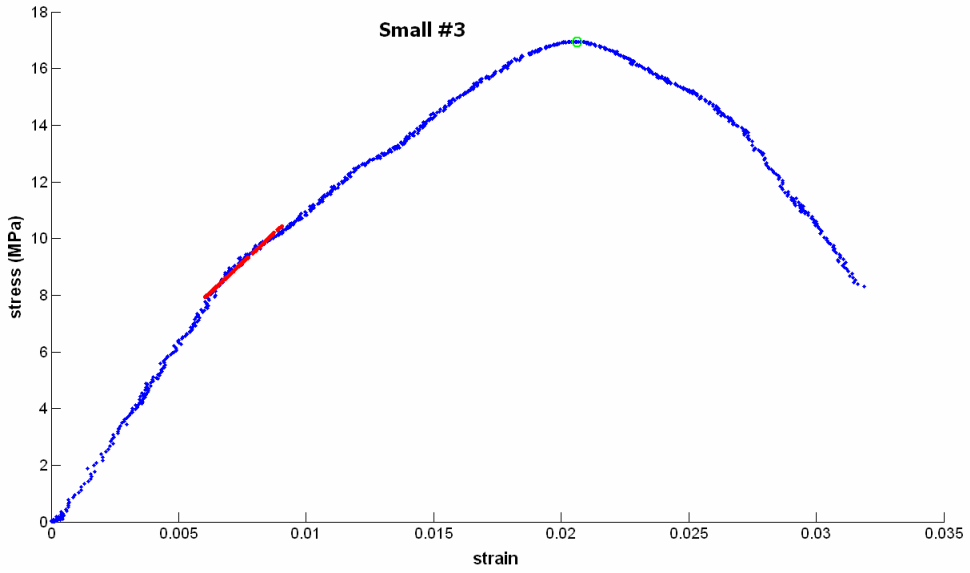

Figure 3-A-1. Stress-strain curve of the small structure #3

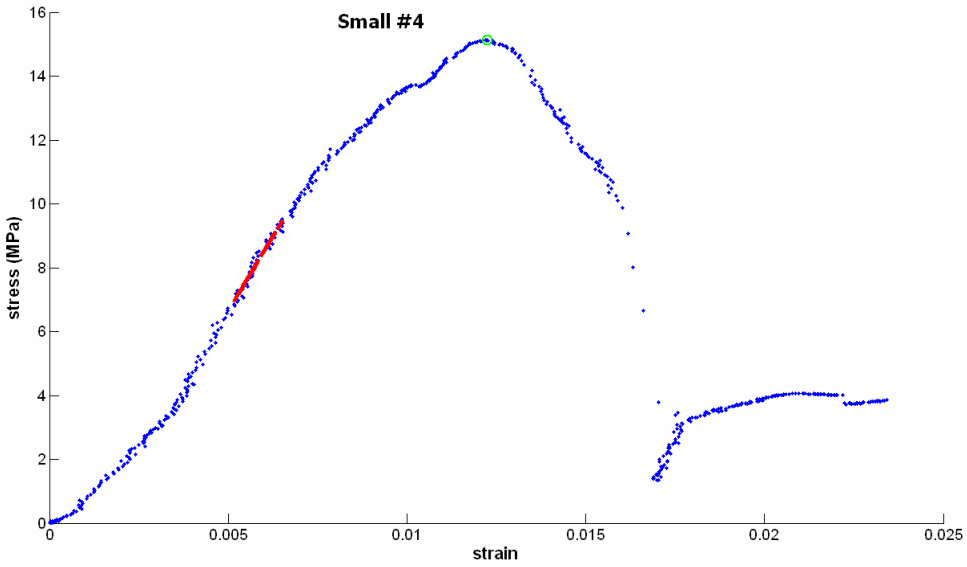

Figure 3-A-1. Stress-strain curve of the small structure #4

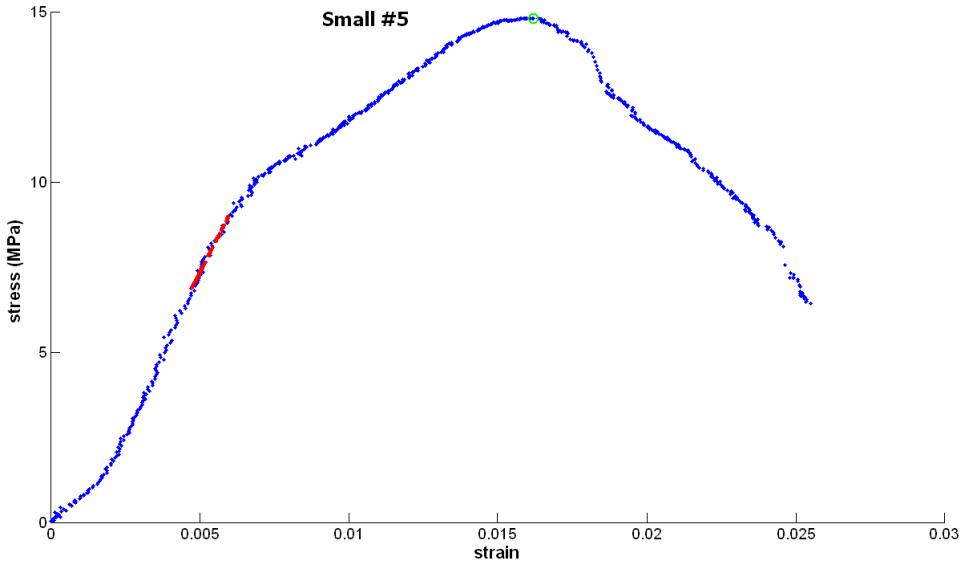

Figure 3-A-1. Stress-strain curve of the small structure #5

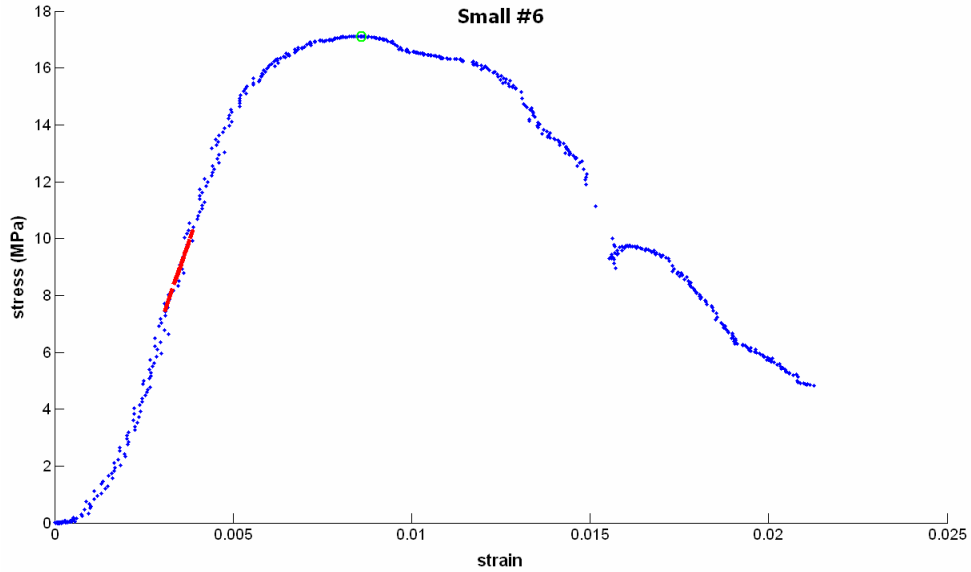

Figure 3-A-1. Stress-strain curve of the small structure #6

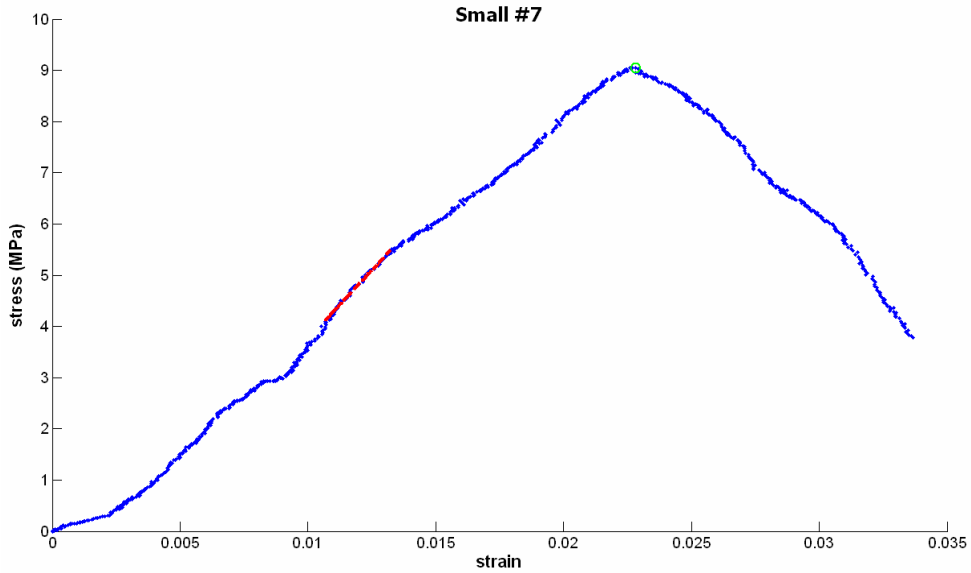

Figure 3-A-1. Stress-strain curve of the small structure #7

MEDIUM STRUCTURES

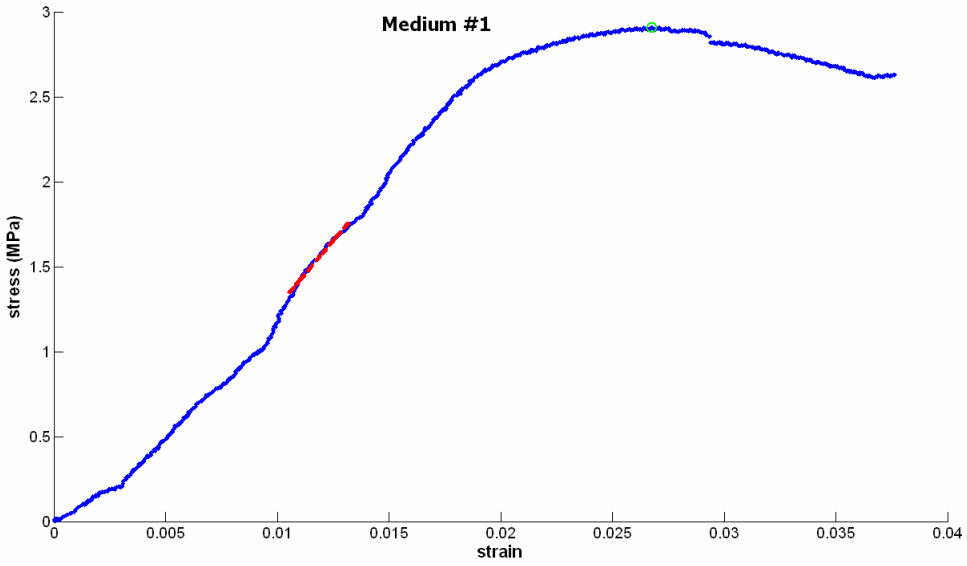

Figure 3-A-1. Stress-strain curve of the medium structure #1

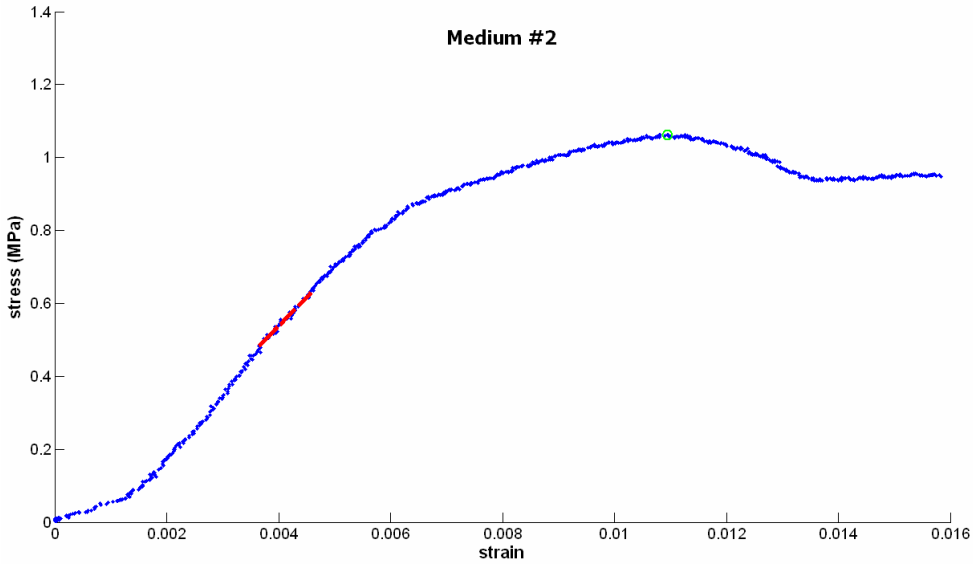

Figure 3-A-1. Stress-strain curve of the medium structure #2

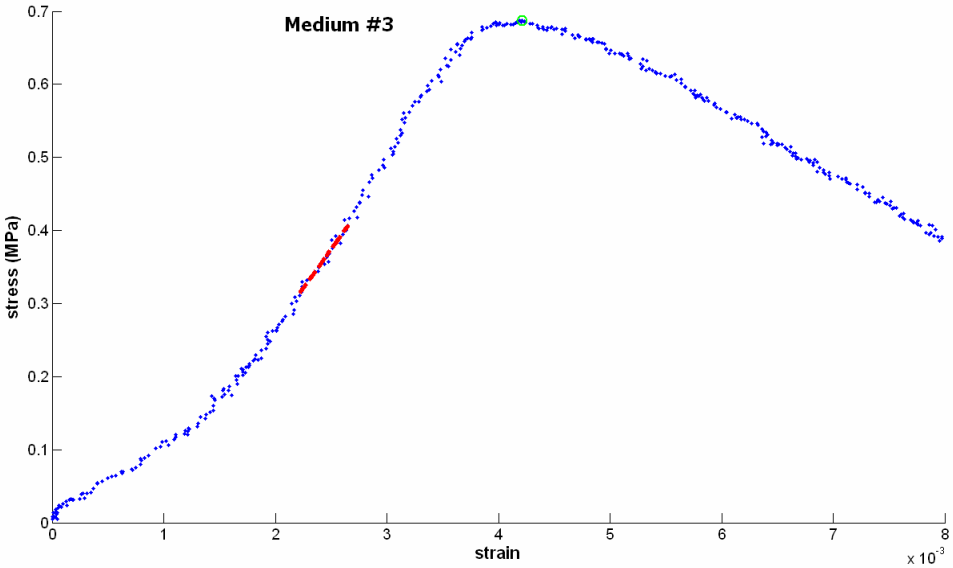

Figure 3-A-1. Stress-strain curve of the medium structure #3

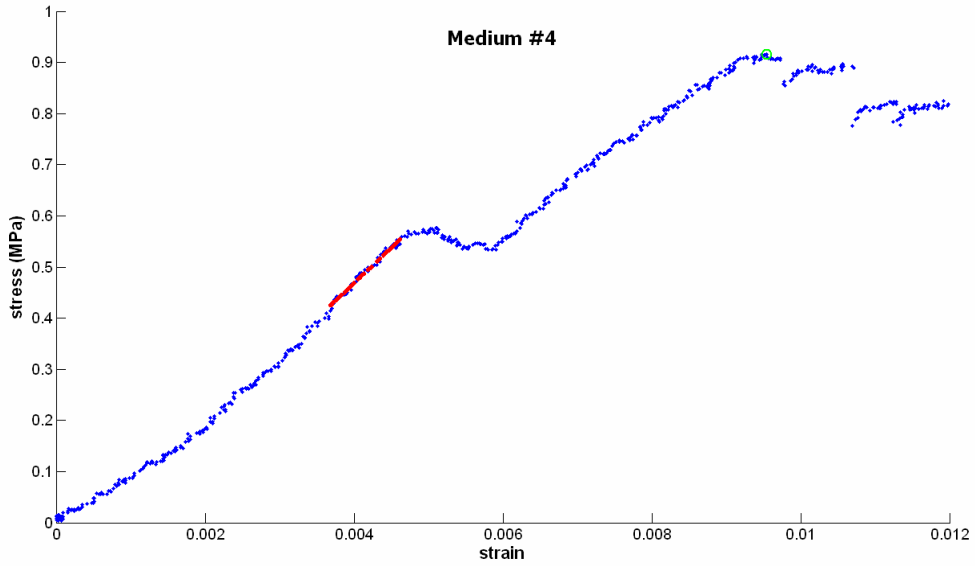

Figure 3-A-1. Stress-strain curve of the medium structure #4

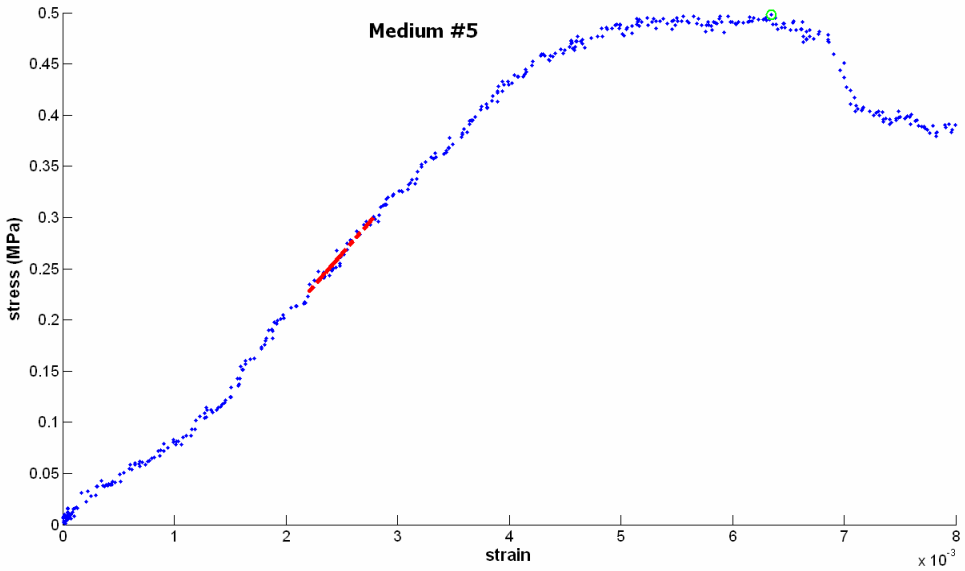

Figure 3-A-1. Stress-strain curve of the medium structure #5

LARGE STRUCTURES

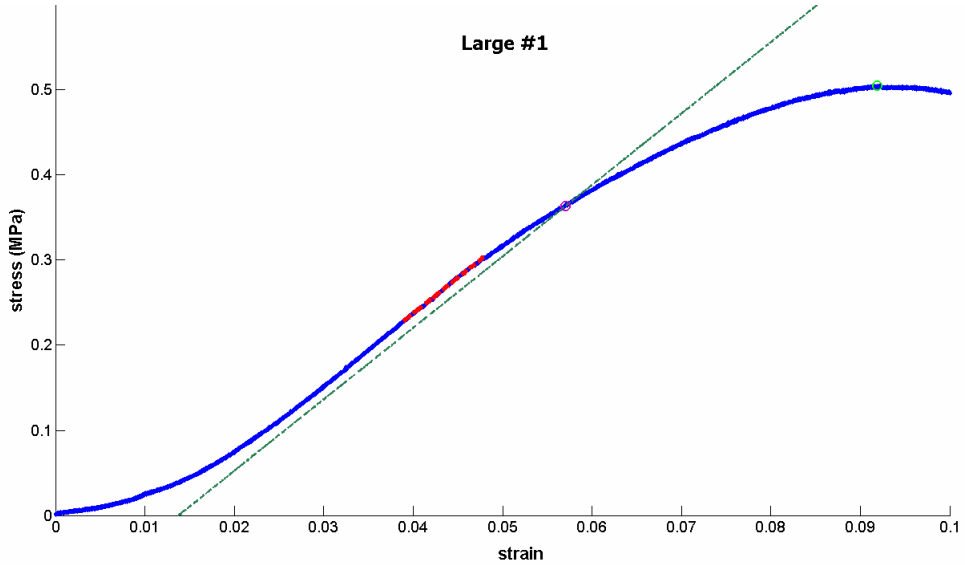

Figure 3-A-1. Stress-strain curve of the large structure #1

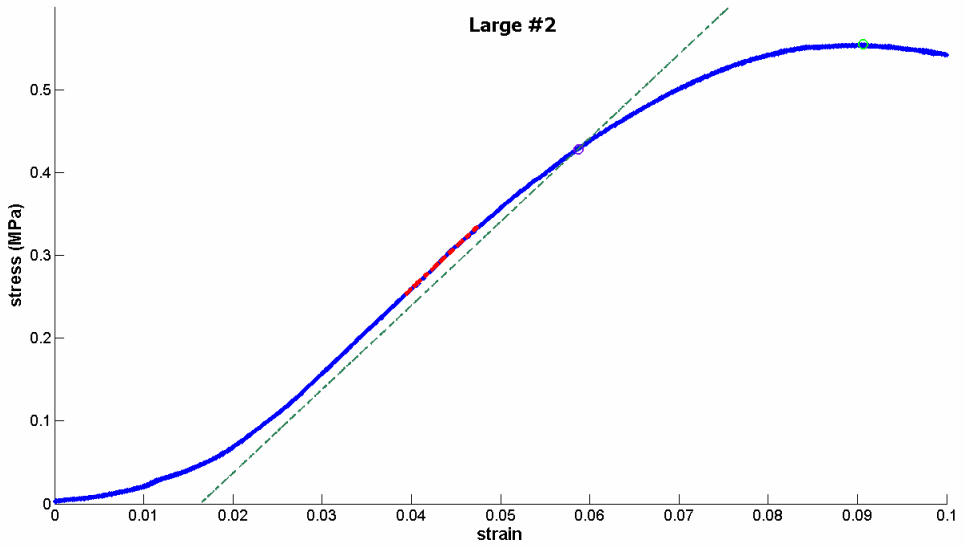

Figure 3-A-1. Stress-strain curve of the large structure #2

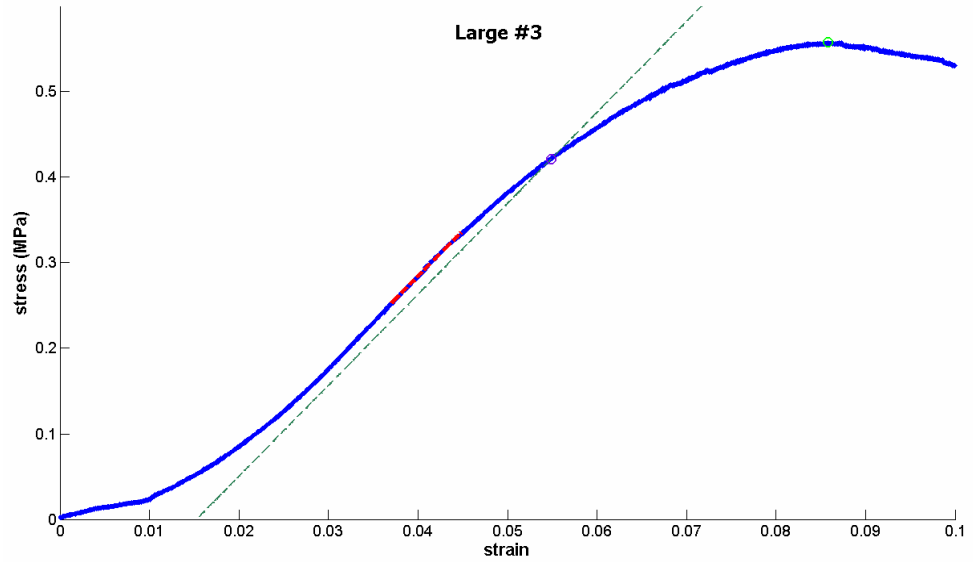

Figure 3-A-1. Stress-strain curve of the large structure #3

EXTRA-LARGE STRUCTURES

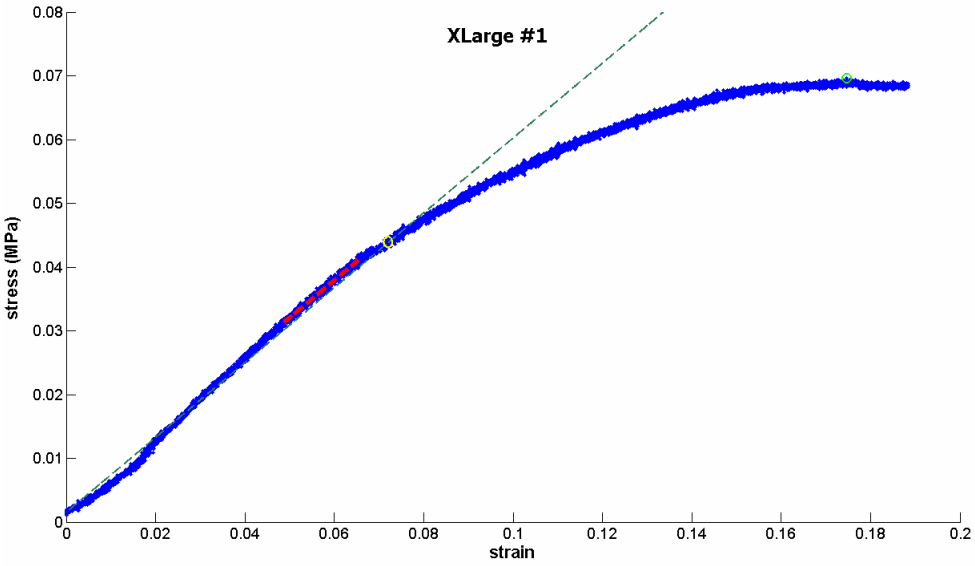

Figure 3-A-1. Stress-strain curve of the XL structure #1

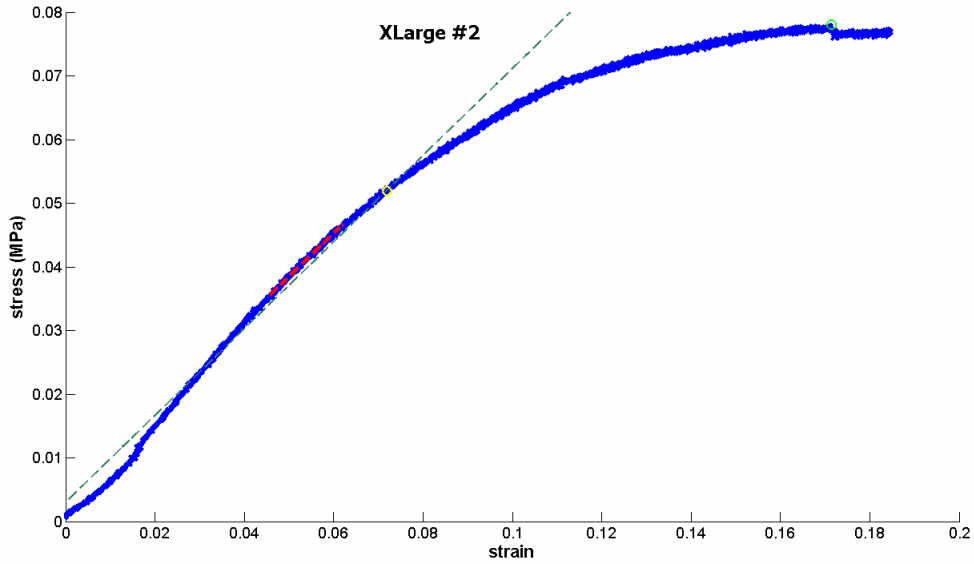

Figure 3-A-1. Stress-strain curve of the XL structure #2

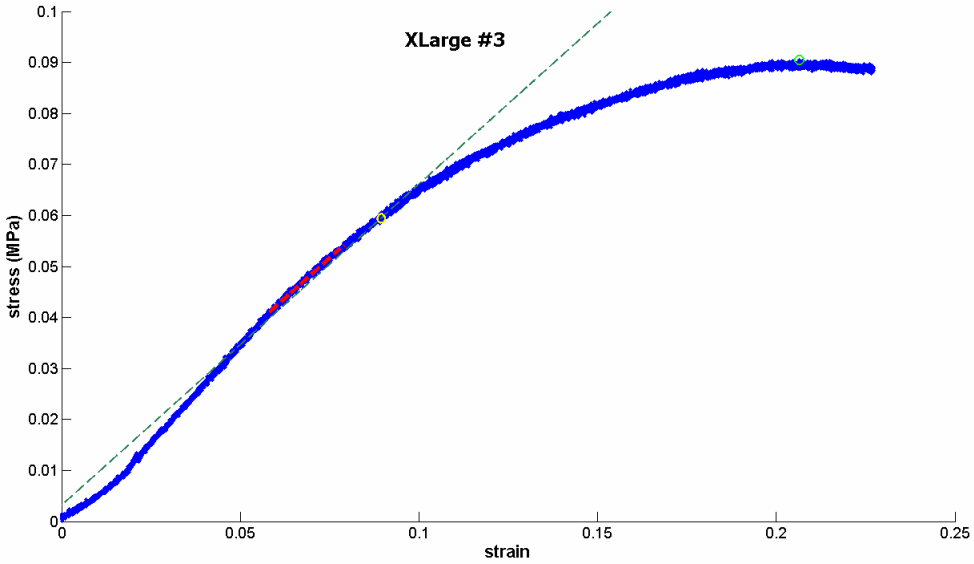

Figure 3-A-1. Stress-strain curve of the XL structure #3

EXTRA-EXTRA-LARGE STRUCTURES

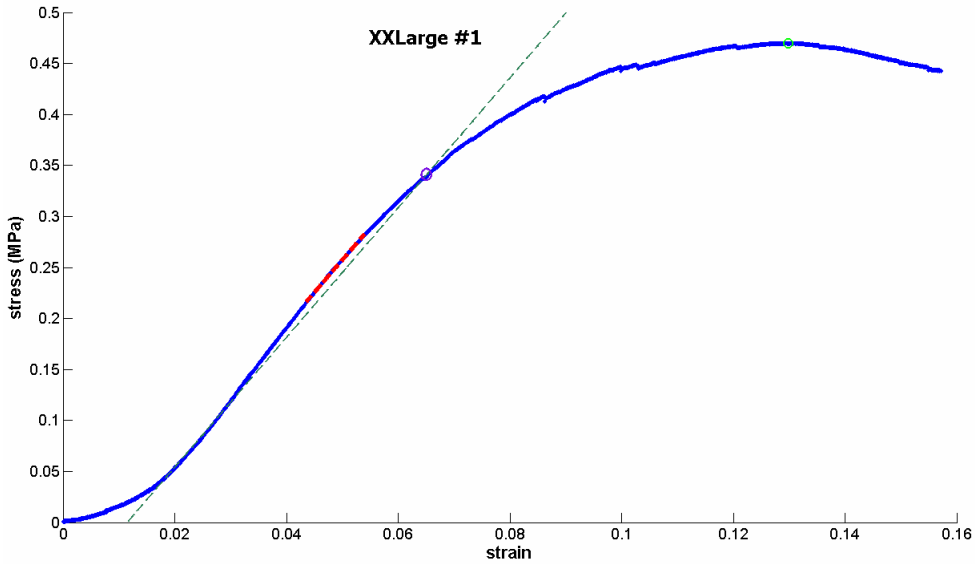

Figure 3-A-1. Stress-strain curve of the XXL structure #1

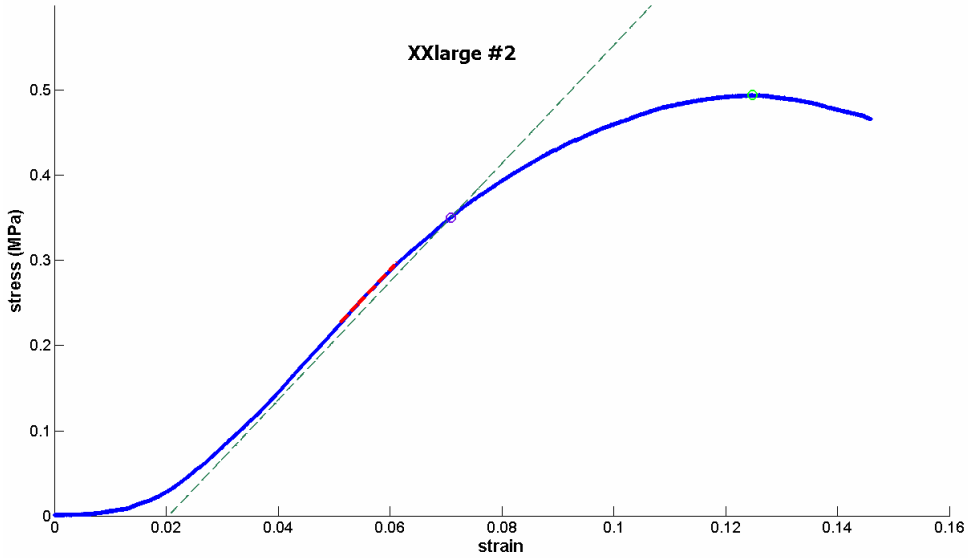

Figure 3-A-1. Stress-strain curve of the XXL structure #2

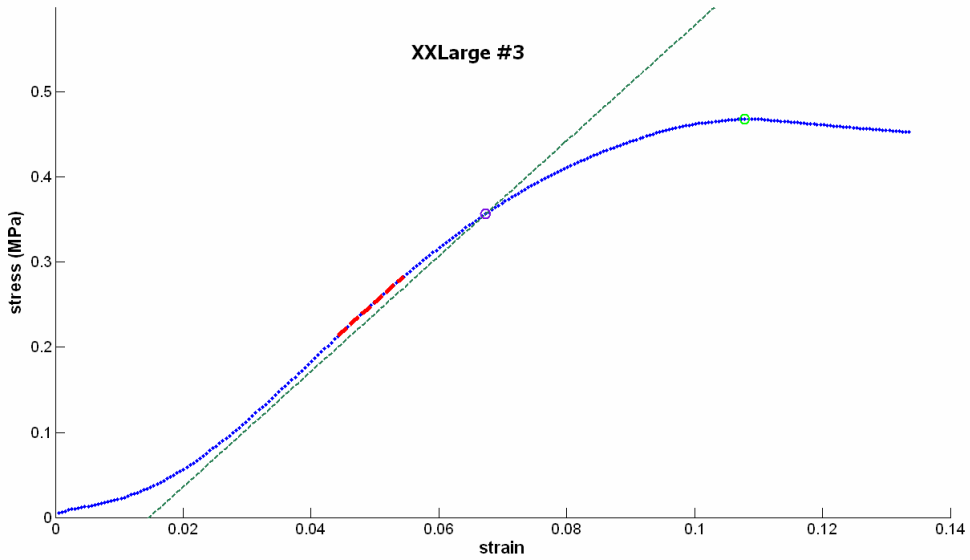

Figure 3-A-1. Stress-strain curve of the XXL structure #3

Appendix 3-B. Stress-strain cycles – bowtie structures

All structures were tested with lubrication unless noted otherwise.

SMALL STRUCTURES

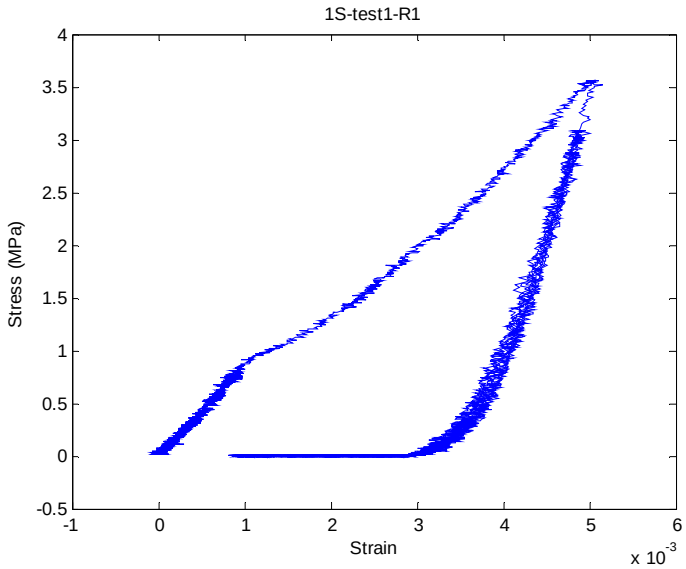

Figure 3-B-1. Stress-strain cycles of the S structure #1 up to 0.5% strain without lubricant- run#1

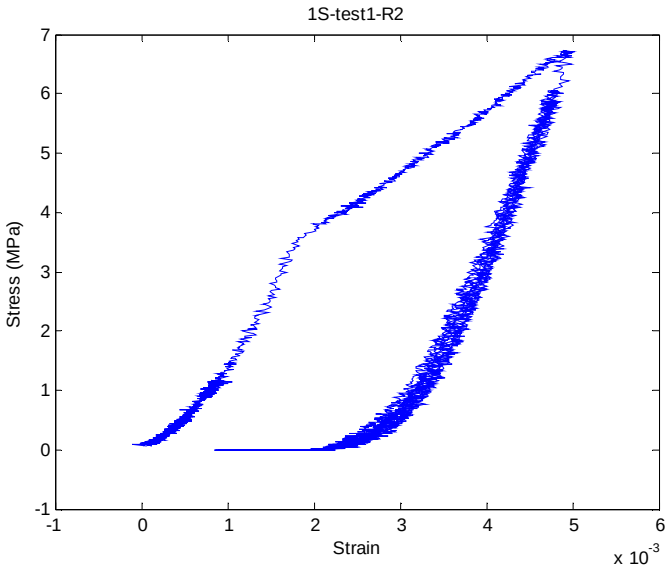

Figure 3-B-2. Stress-strain cycles of the S structure #1 up to 0.5% strain without lubricant - run#2

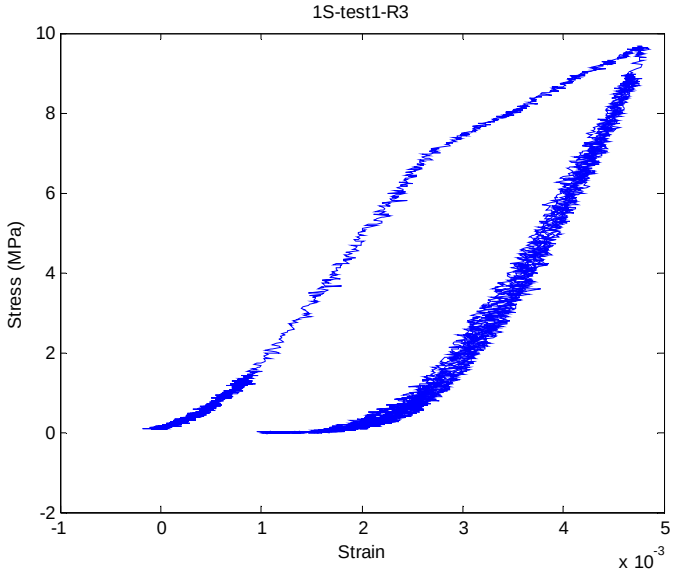

Figure 3-B-3. Stress-strain cycles of the S structure #1 up to 0.5% strain without lubricant - run#3

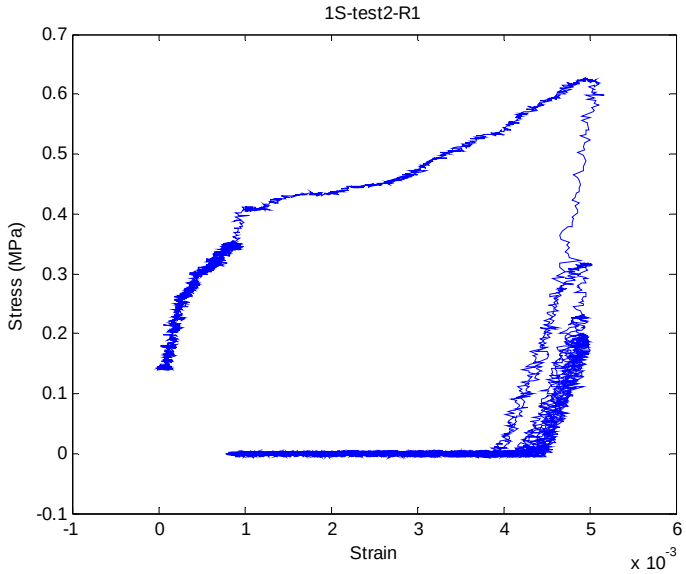

Figure 3-B-4. Stress-strain cycles of the S structure #1 up to 0.5% strain- run#1

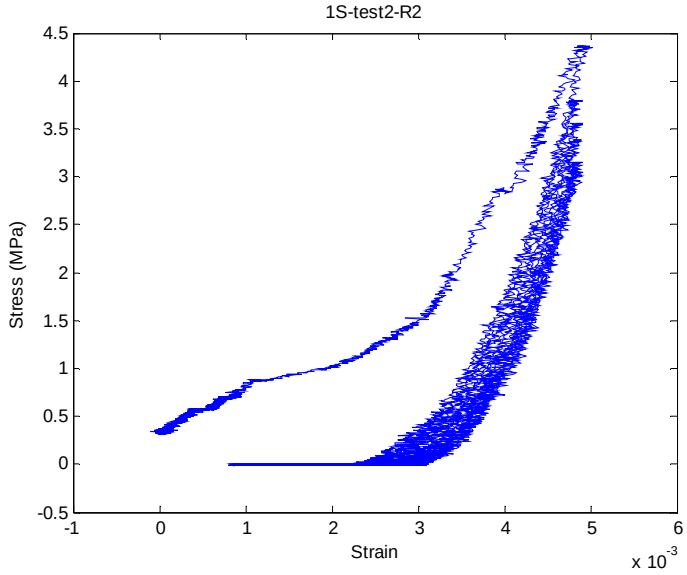

Figure 3-B-5. Stress-strain cycles of the S structure #1 up to 0.5% strain- run#2

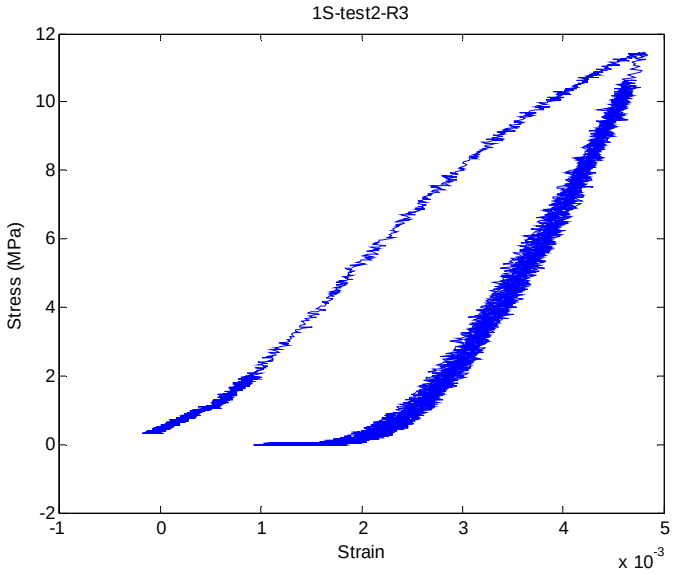

Figure 3-B-6. Stress-strain cycles of the S structure #1 up to 0.5% strain- run#3

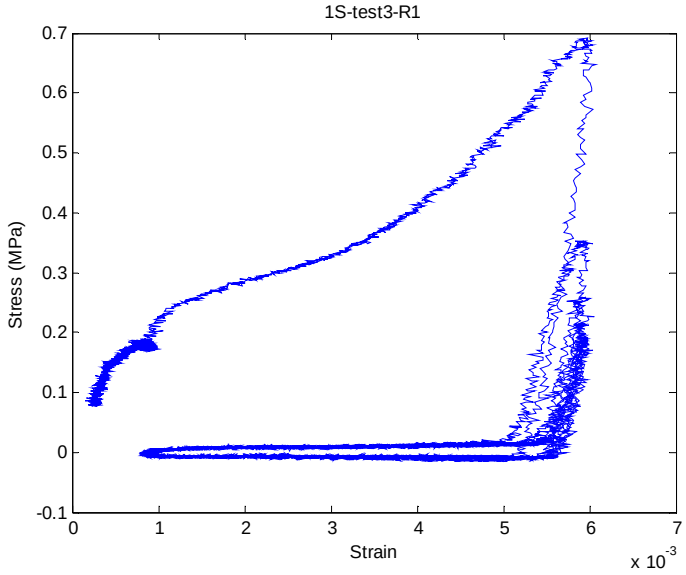

Figure 3-B-7. Stress-strain cycles of the S structure #1 up to 0.6% strain- run#1

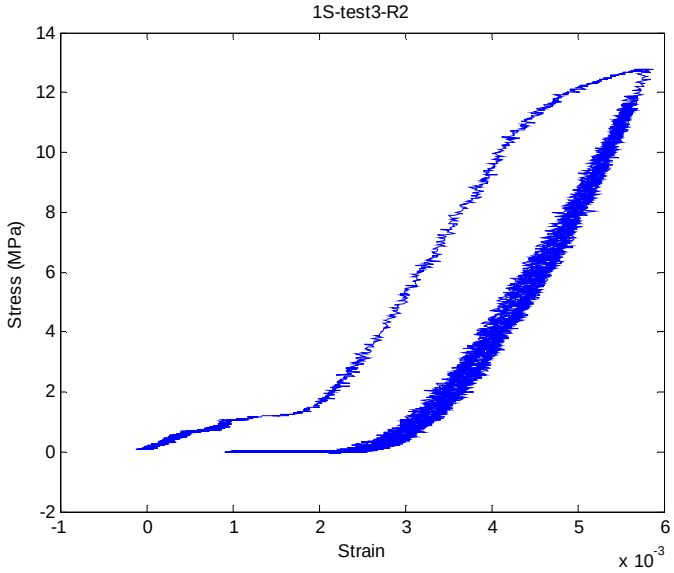

Figure 3-B-8. Stress-strain cycles of the S structure #1 up to 0.6% strain- run#2

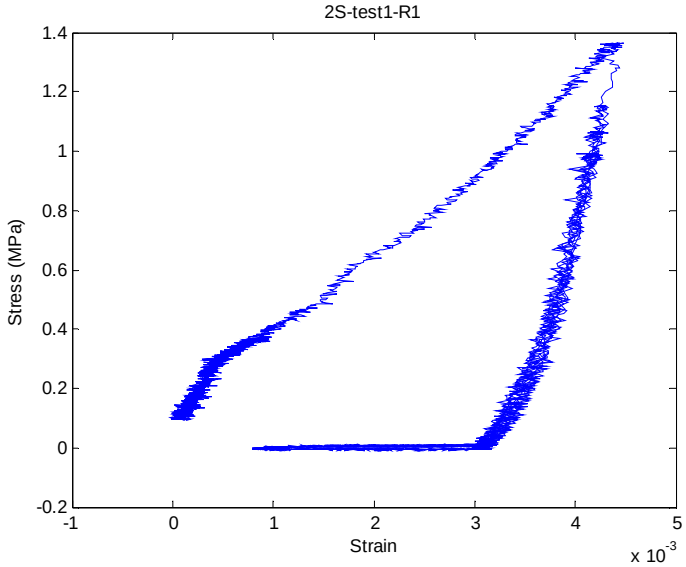

Figure 3-B-9. Stress-strain cycles of the S structure #2 up to 0.5% strain without lubricant - run#1

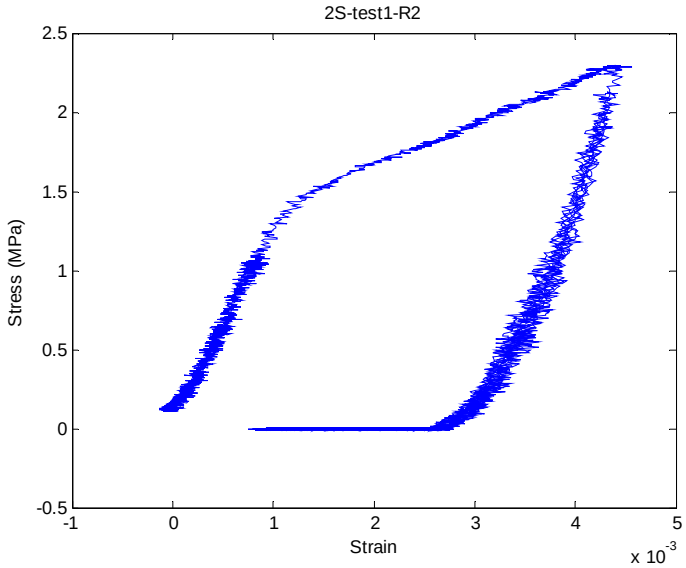

Figure 3-B-10. Stress-strain cycles of the S structure #2 up to 0.5% strain without lubricant - run#2

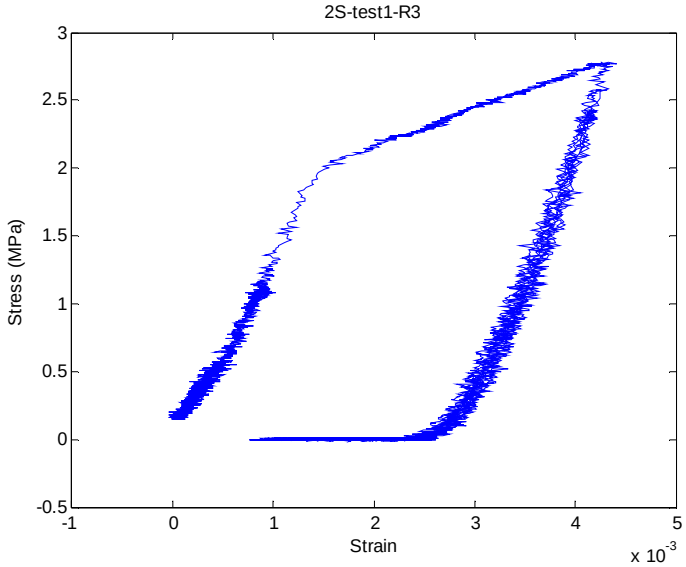

Figure 3-B-11. Stress-strain cycles of the S structure #2 up to 0.5% strain without lubricant - run#3

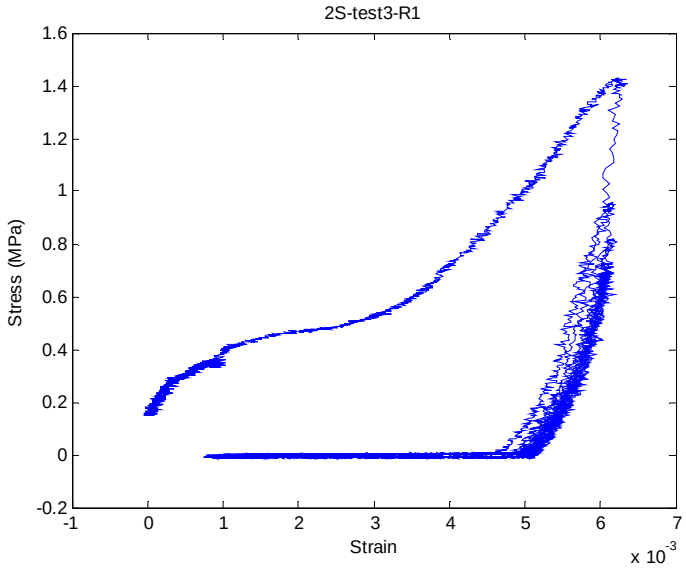

Figure 3-B-12. Stress-strain cycles of the S structure #2 up to 0.75% strain- run#1

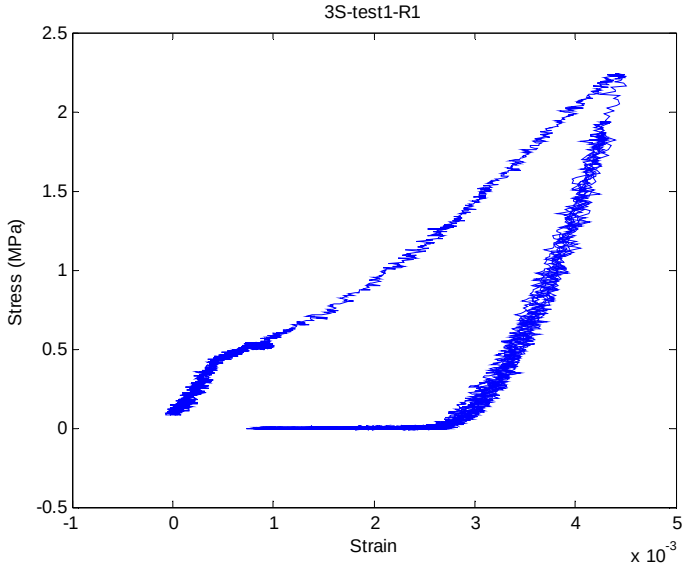

Figure 3-B-13. Stress-strain cycles of the S structure #3 up to 0.5% strain without lubricant - run#1

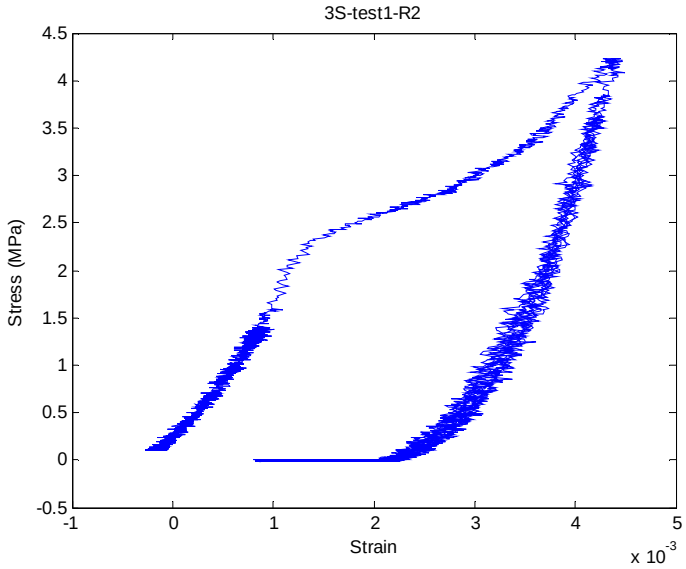

Figure 3-B-14. Stress-strain cycles of the S structure #3 up to 0.5% strain without lubricant - run#2

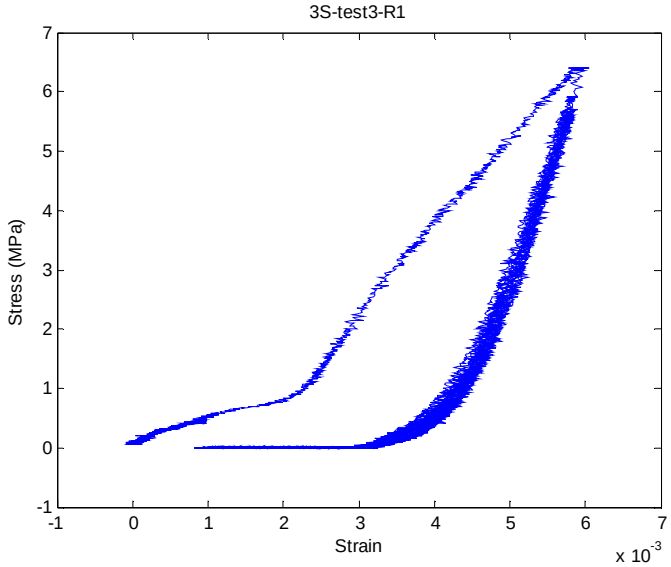

Figure 3-B-15. Stress-strain cycles of the S structure #3 up to 0.75% strain- run#1

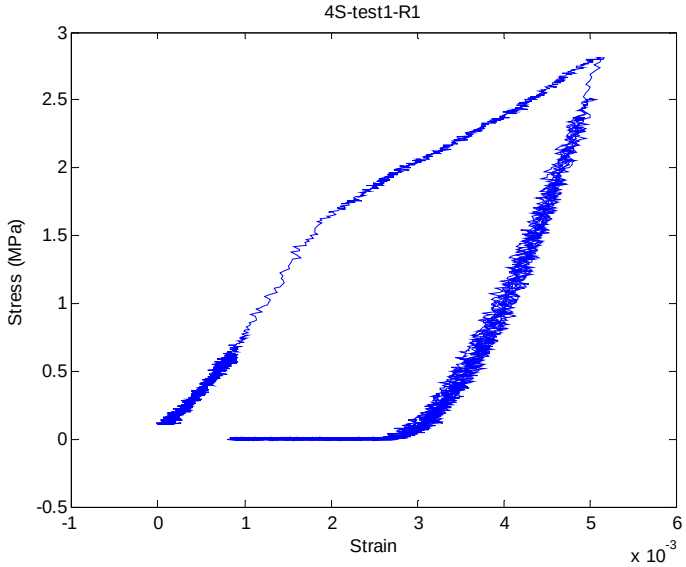

Figure 3-B-16. Stress-strain cycles of the S structure #4 up to 0.5% strain without lubricant - run#1

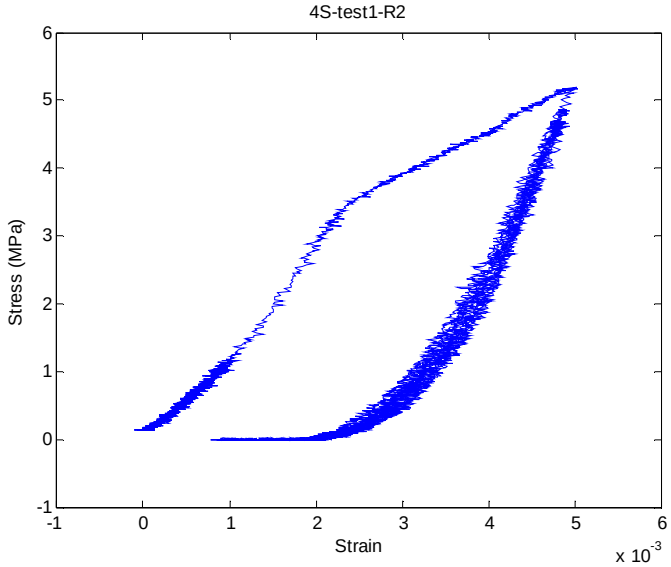

Figure 3-B-17. Stress-strain cycles of the S structure #4 up to 0.5% strain without lubricant - run#2

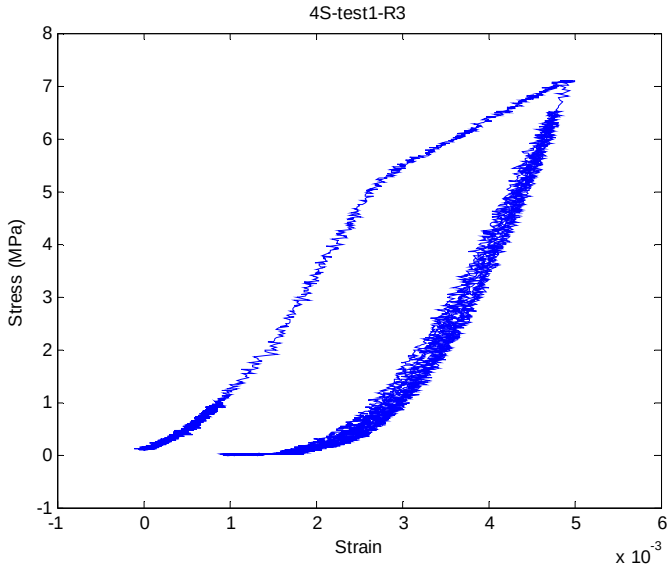

Figure 3-B-18. Stress-strain cycles of the S structure #4 up to 0.5% strain without lubricant - run#3

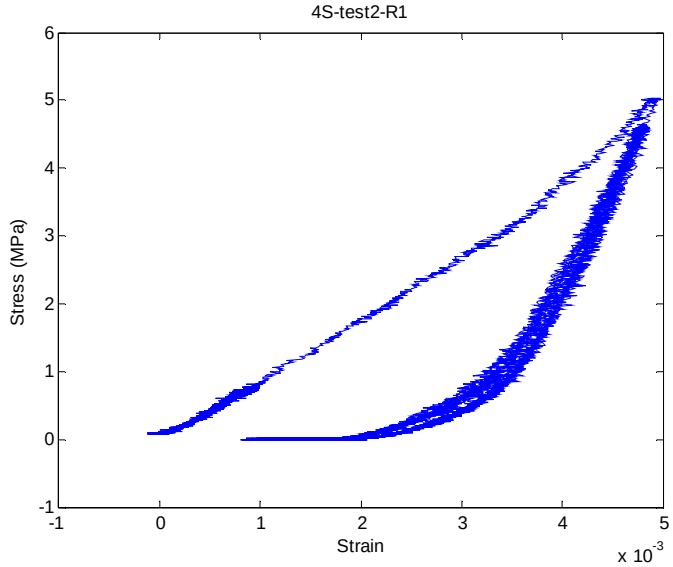

Figure 3-B-19. Stress-strain cycles of the S structure #4 up to 0.6% strain- run#1

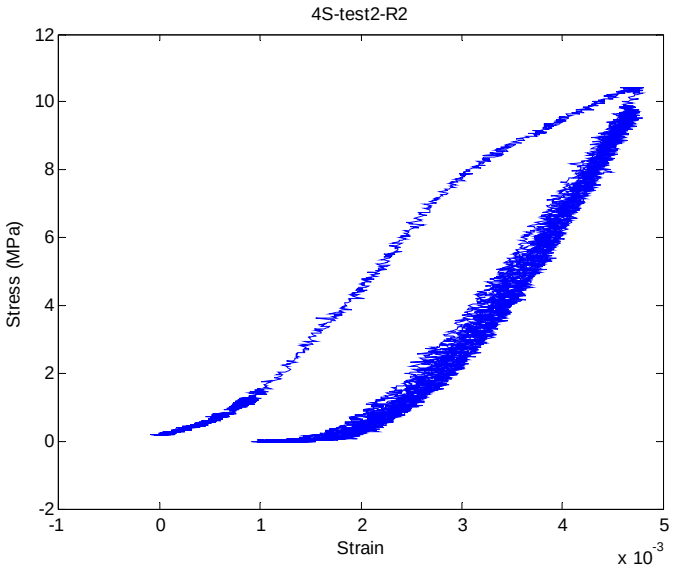

Figure 3-B-20. Stress-strain cycles of the S structure #4 up to 0.6% strain- run#2

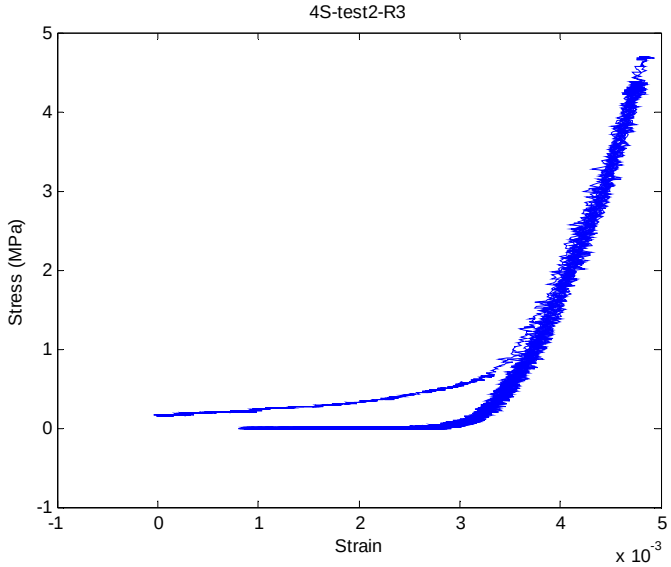

Figure 3-B-21. Stress-strain cycles of the S structure #4 up to 0.6% strain- run#3

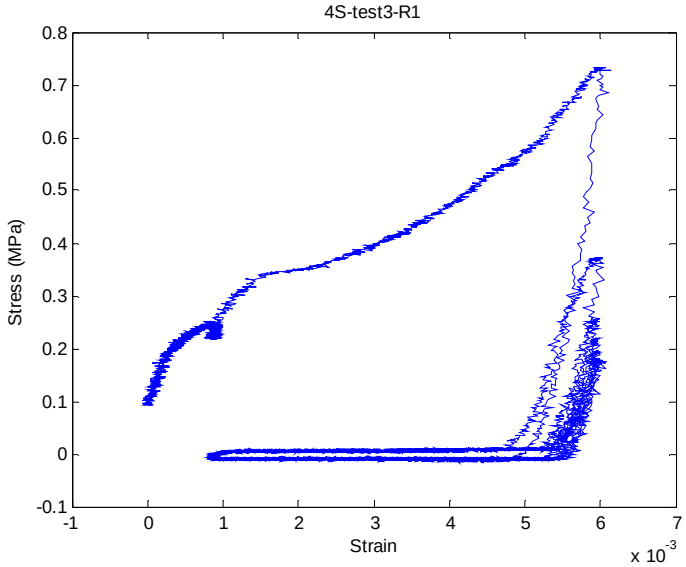

Figure 3-B-22. Stress-strain cycles of the S structure #4 up to 0.75% strain- run#1

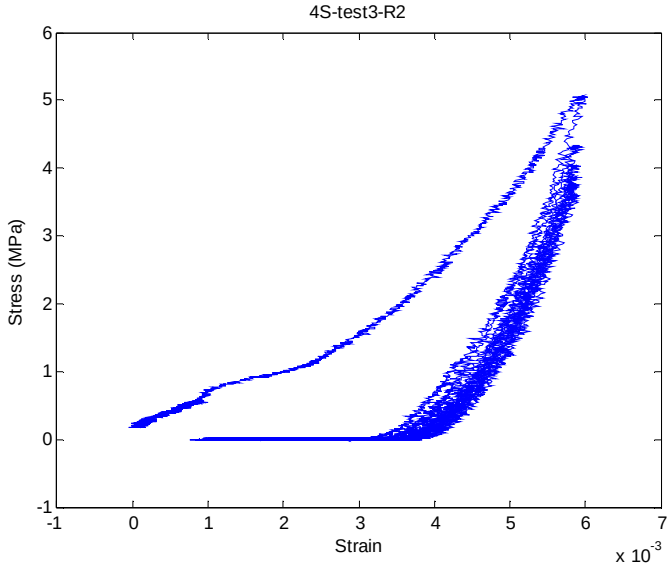

Figure 3-B-23. Stress-strain cycles of the S structure #4 up to 0.75% strain- run#2

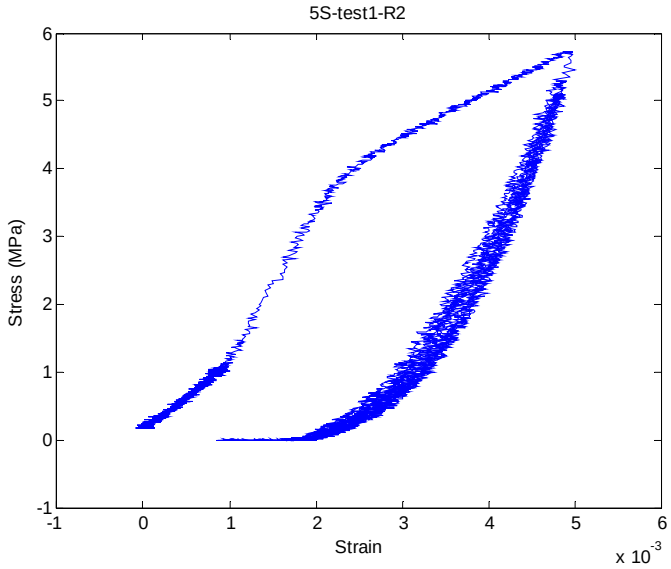

Figure 3-B-24. Stress-strain cycles of the S structure #5 up to 0.5% strain without lubricant - run#2

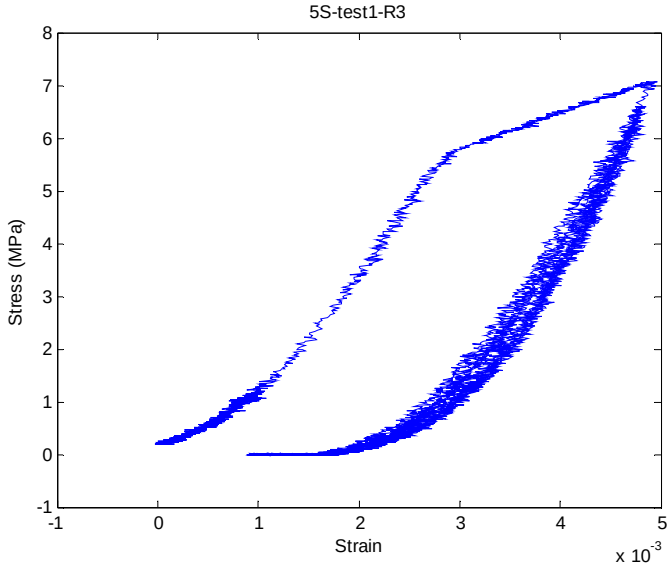

Figure 3-B-25. Stress-strain cycles of the S structure #5 up to 0.5% strain without lubricant - run#3

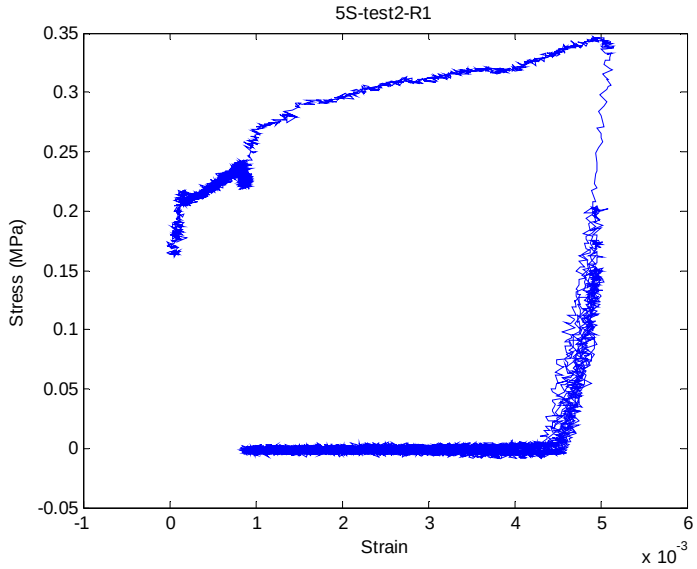

Figure 3-B-26. Stress-strain cycles of the S structure #5 up to 0.5% strain- run#1

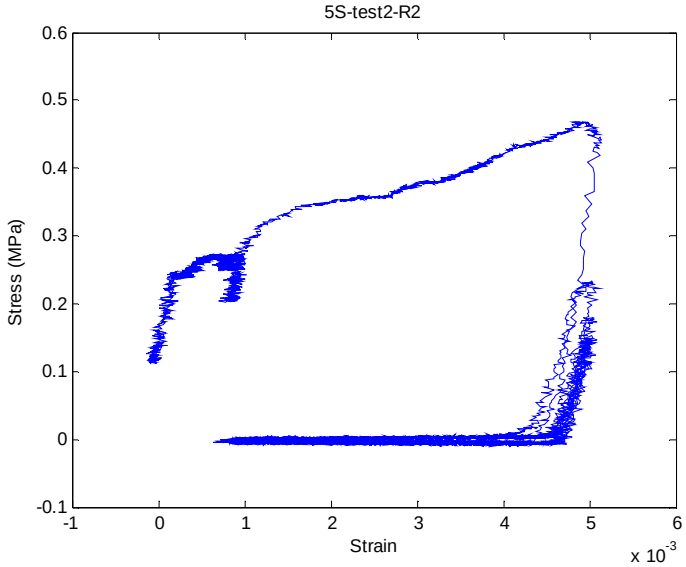

Figure 3-B-27. Stress-strain cycles of the S structure #5 up to 0.5% strain- run#2

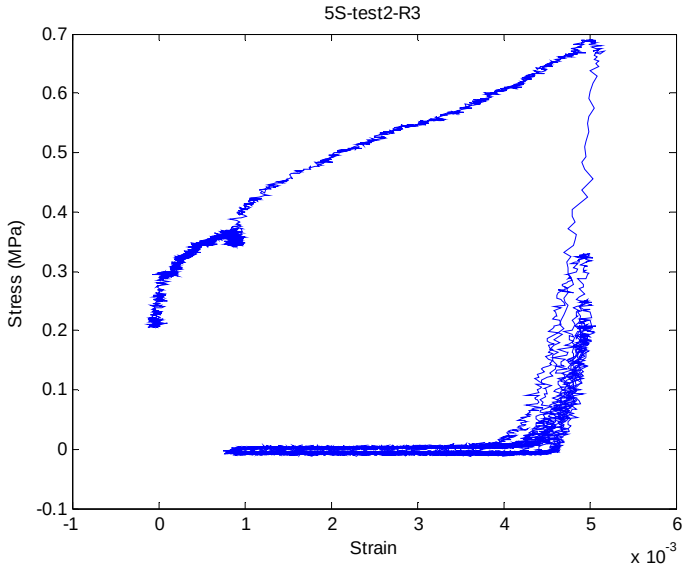

Figure 3-B-28. Stress-strain cycles of the S structure #5 up to 0.5% strain- run#3

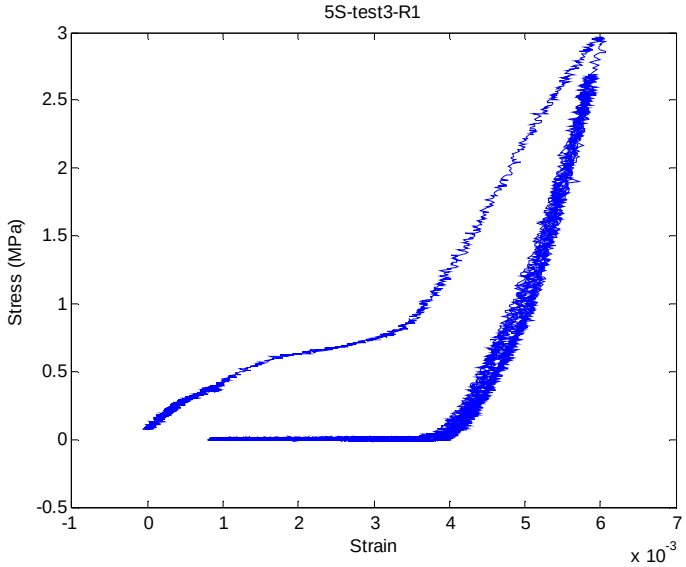

Figure 3-B-29. Stress-strain cycles of the S structure #5 up to 0.6% strain- run#1

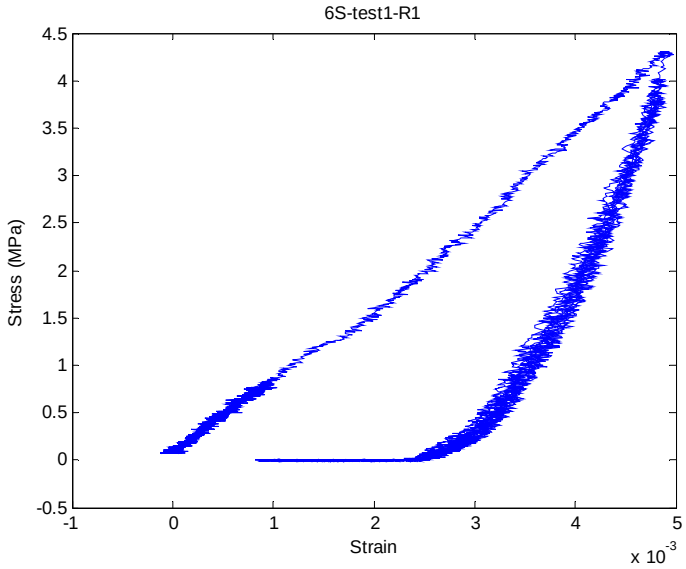

Figure 3-B-30. Stress-strain cycles of the S structure #6 up to 0.5% strain without lubricant - run#1

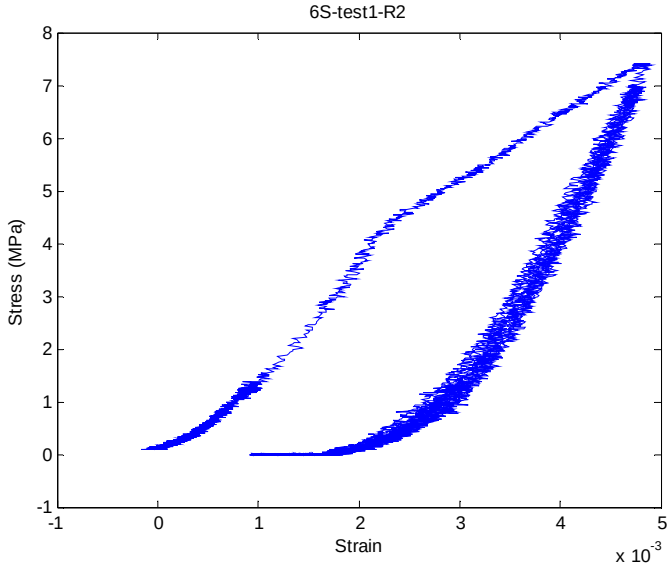

Figure 3-B-31. Stress-strain cycles of the S structure #6 up to 0.5% strain without lubricant - run#2

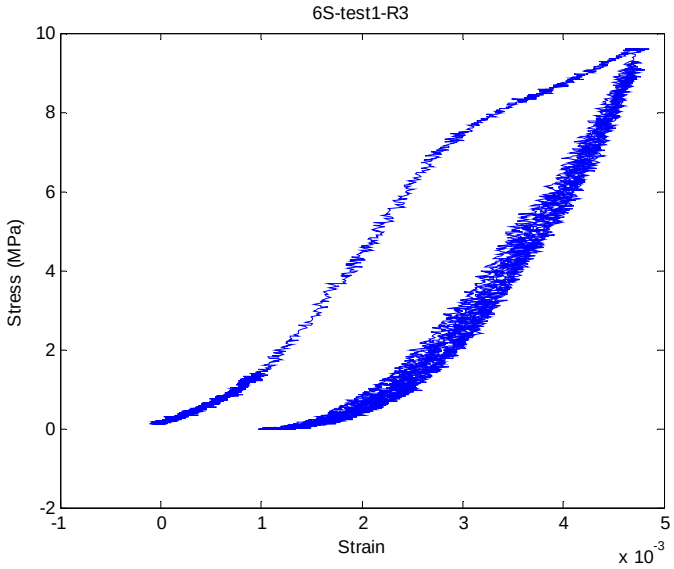

Figure 3-B-32. Stress-strain cycles of the S structure #6 up to 0.5% strain without lubricant - run#3

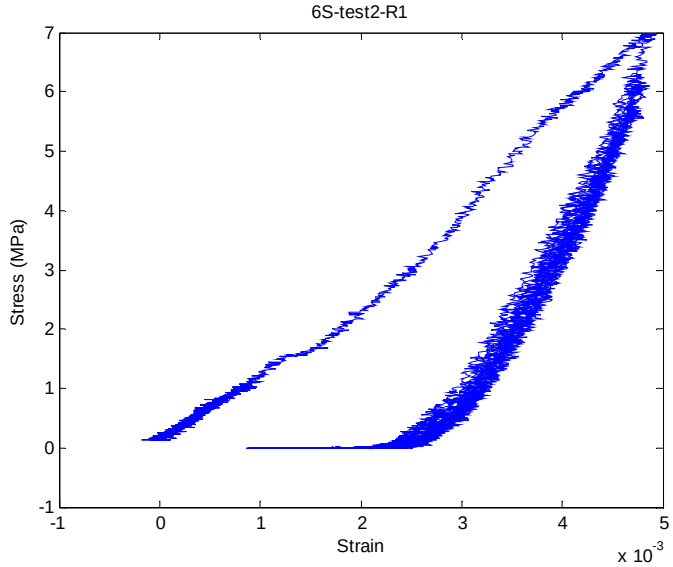

Figure 3-B-33. Stress-strain cycles of the S structure #6 up to 0.5% strain- run#1

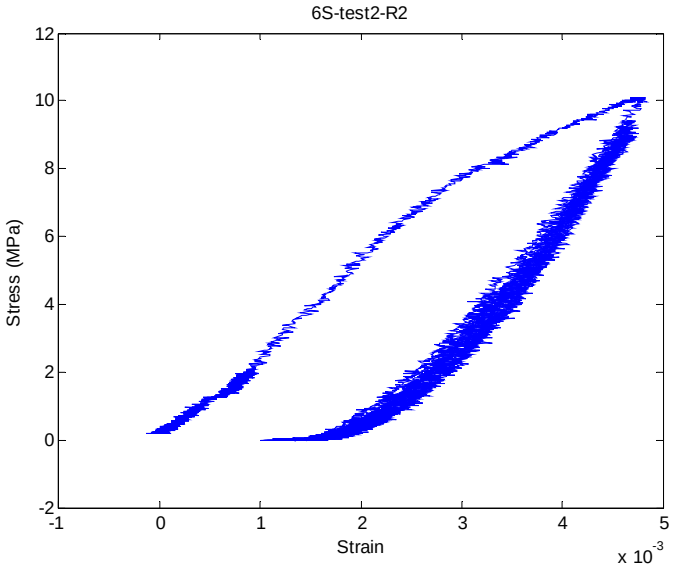

Figure 3-B-34. Stress-strain cycles of the S structure #6 up to 0.5% strain- run#2

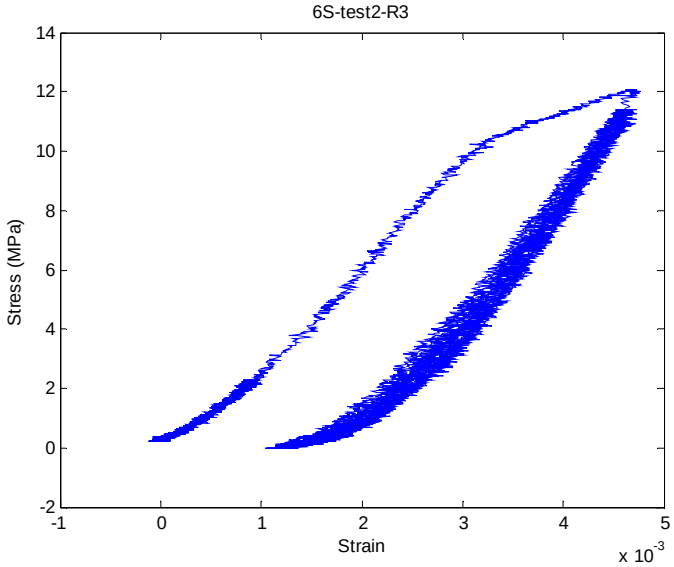

Figure 3-B-35. Stress-strain cycles of the S structure #6 up to 0.5% strain- run#3

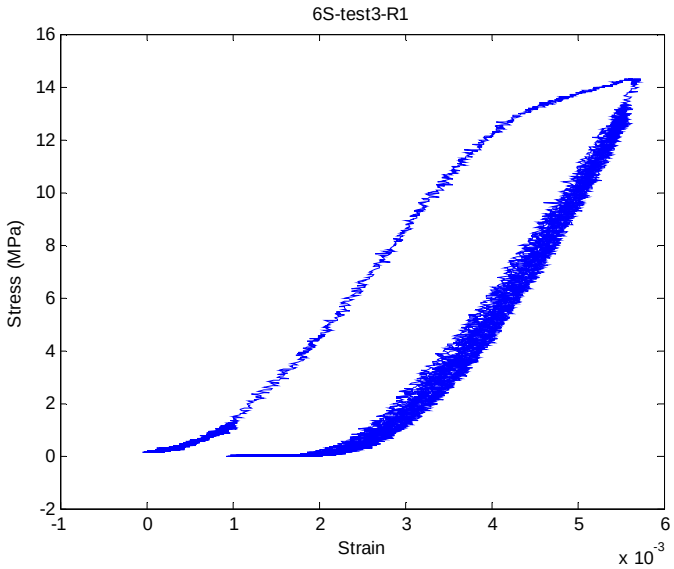

Figure 3-B-36. Stress-strain cycles of the S structure #6 up to 0.6% strain- run#1

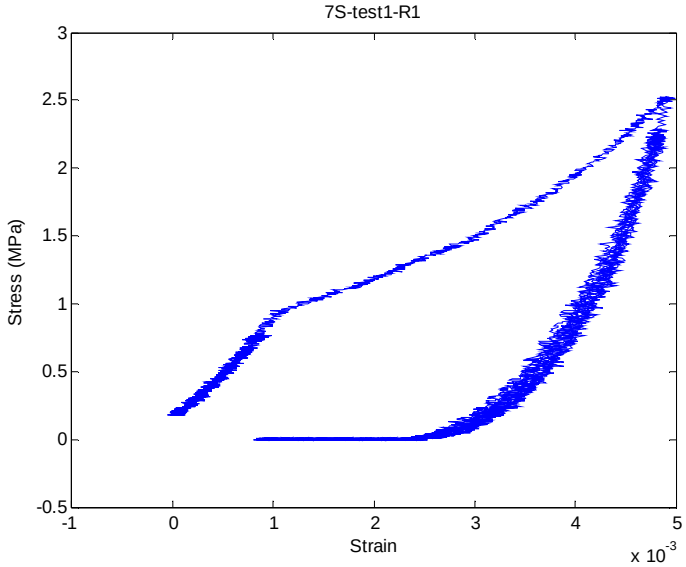

Figure 3-B-37. Stress-strain cycles of the S structure #7 up to 0.5% strain without lubricant- run#1

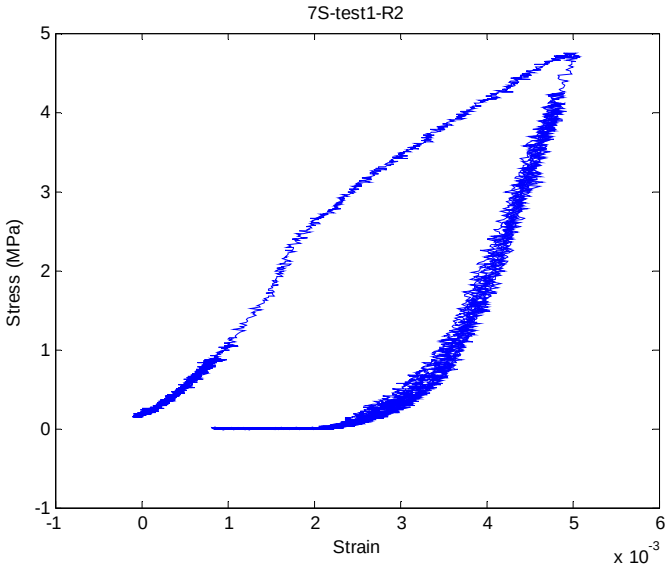

Figure 3-B-38. Stress-strain cycles of the S structure #7 up to 0.5% strain without lubricant - run#2

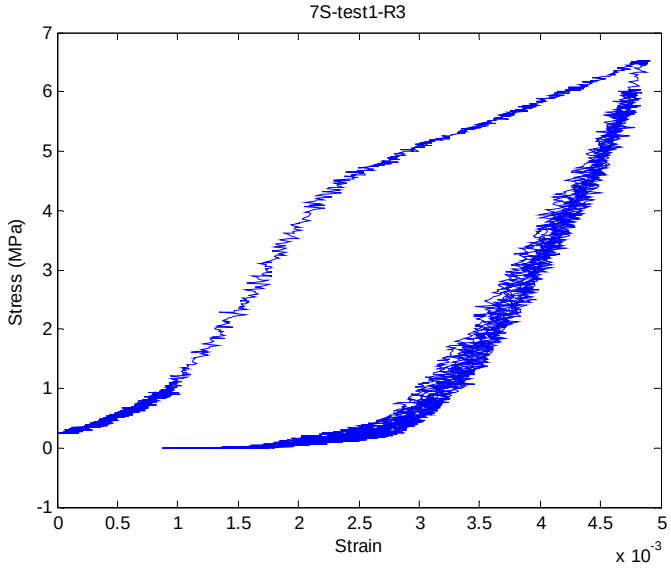

Figure 3-B-39. Stress-strain cycles of the S structure #7 up to 0.5% strain without lubricant - run#3

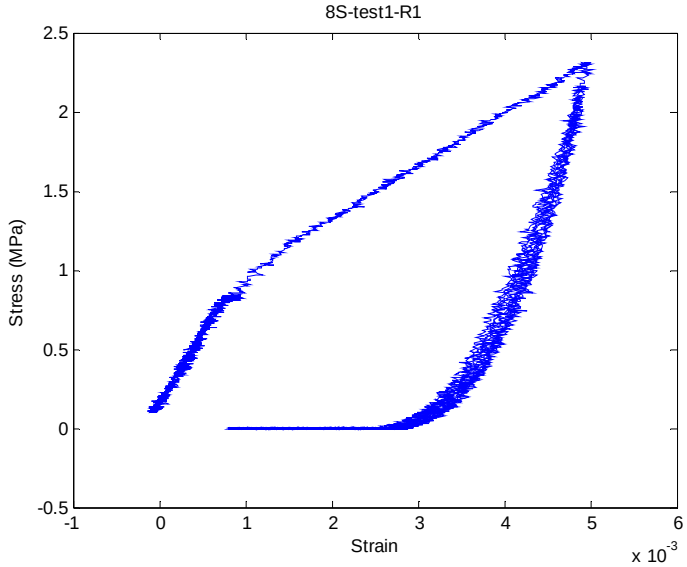

Figure 3-B-40. Stress-strain cycles of the S structure #8 up to 0.5% strain without lubricant - run#1

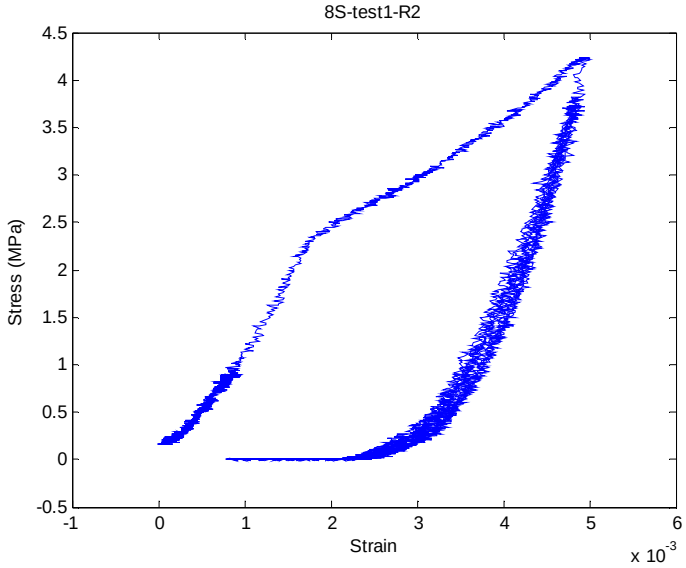

Figure 3-B-41. Stress-strain cycles of the S structure #8 up to 0.5% strain without lubricant - run#2

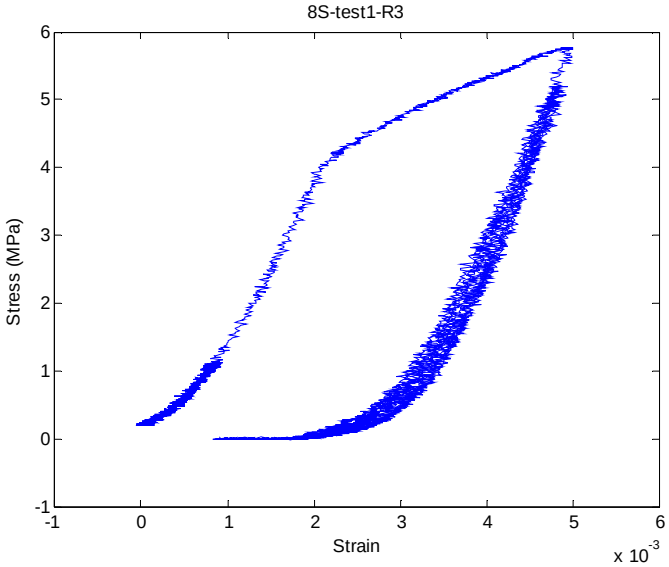

Figure 3-B-42. Stress-strain cycles of the S structure #8 up to 0.5% strain without lubricant - run#3

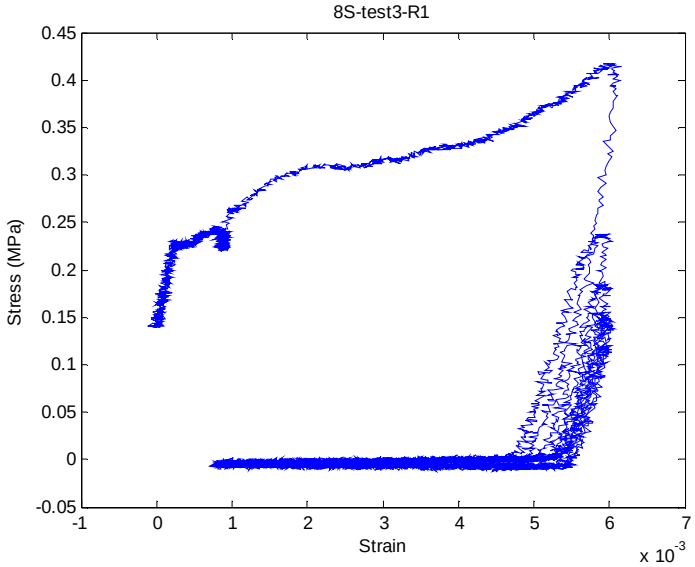

Figure 3-B-43. Stress-strain cycles of the S structure #8 up to 0.6% strain- run#1

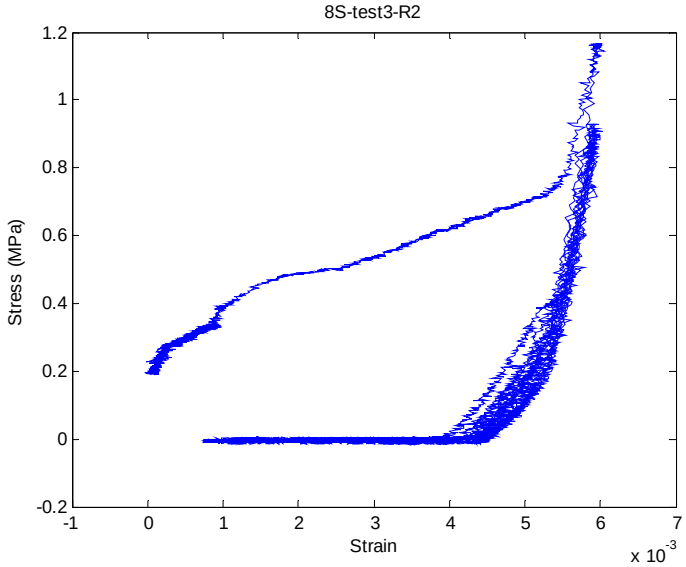

Figure 3-B-44. Stress-strain cycles of the S structure #8 up to 0.6% strain- run#2

MEDIUM STRUCTURES

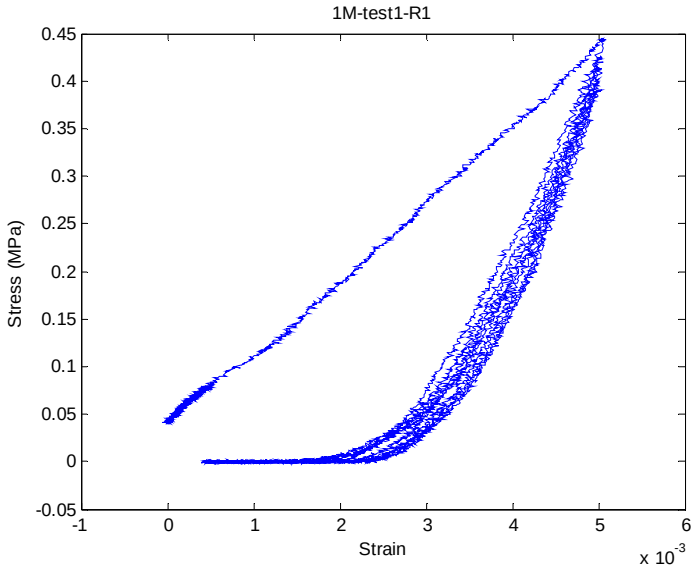

Figure 3-B-45. Stress-strain cycles of the M structure #1 up to 0.5% strain without lubricant - run#1

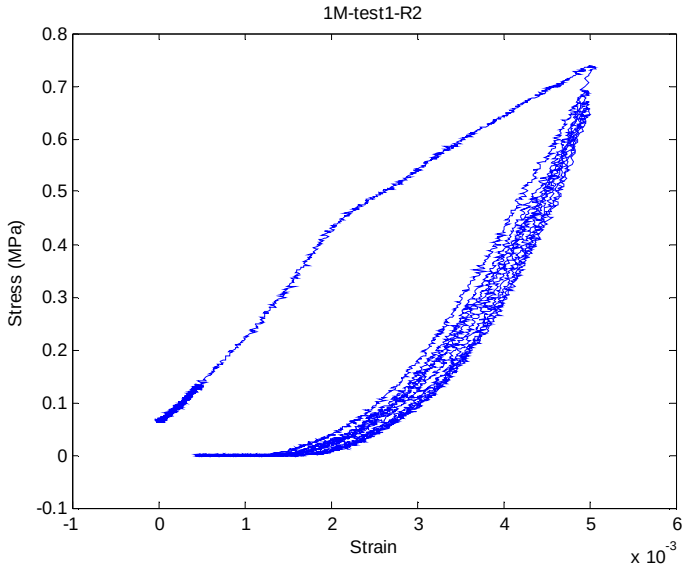

Figure 3-B-46. Stress-strain cycles of the M structure #1 up to 0.5% strain without lubricant - run#2

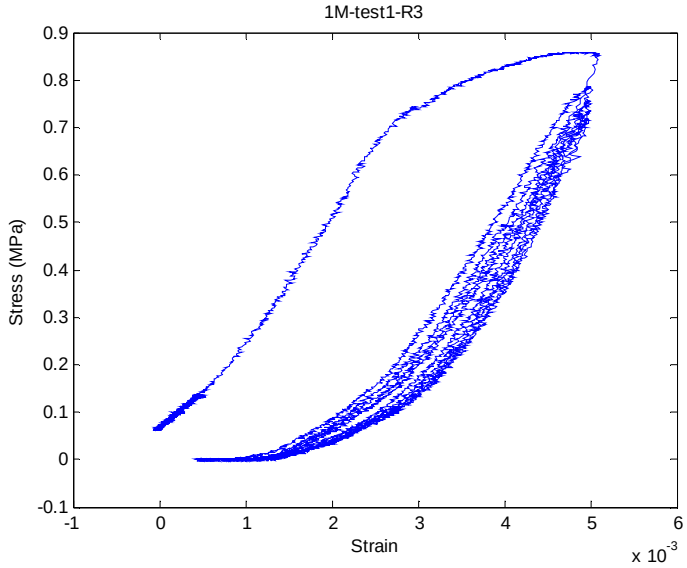

Figure 3-B-47. Stress-strain cycles of the M structure #1 up to 0.5% strain without lubricant - run#3

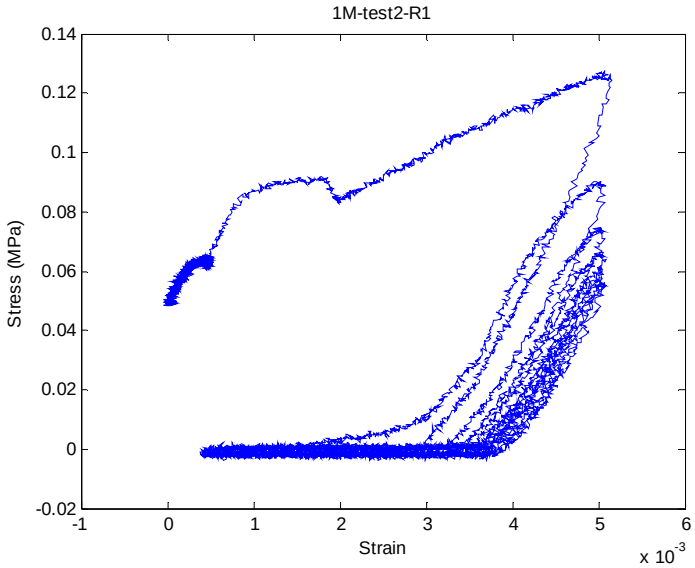

Figure 3-B-48. Stress-strain cycles of the M structure #1 up to 0.5% strain- run#1

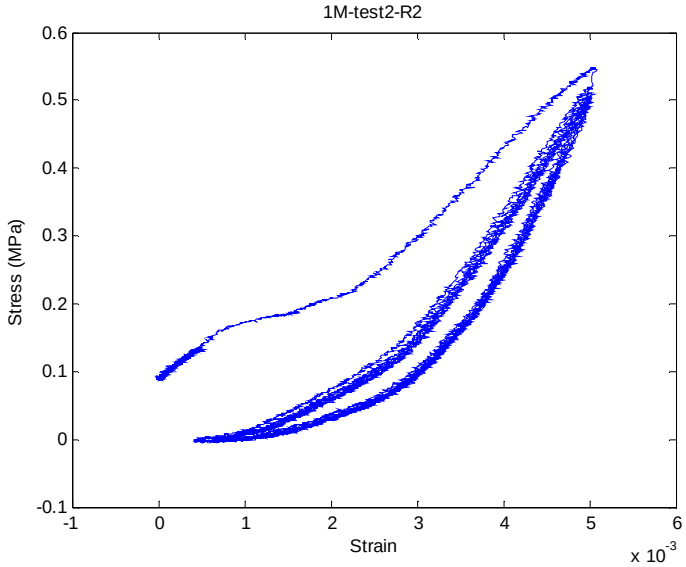

Figure 3-B-49. Stress-strain cycles of the M structure #1 up to 0.5% strain- run#2

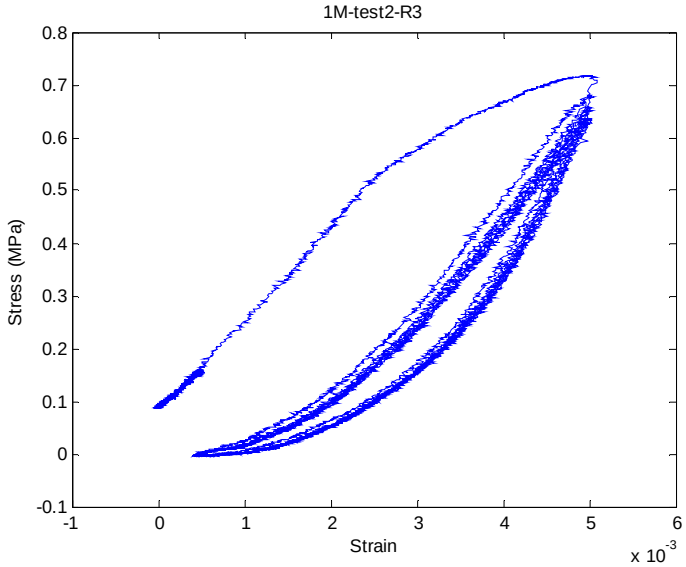

Figure 3-B-50. Stress-strain cycles of the M structure #1 up to 0.5% strain- run#3

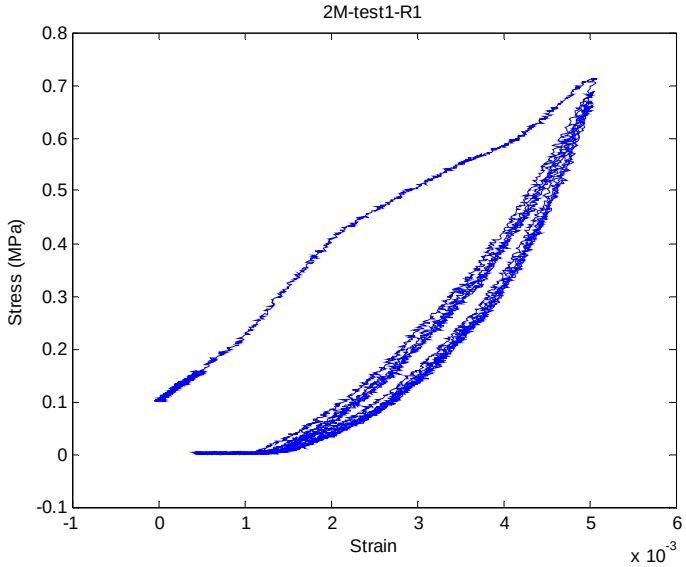

Figure 3-B-51. Stress-strain cycles of the M structure #2 up to 0.5% strain without lubricant - run#1

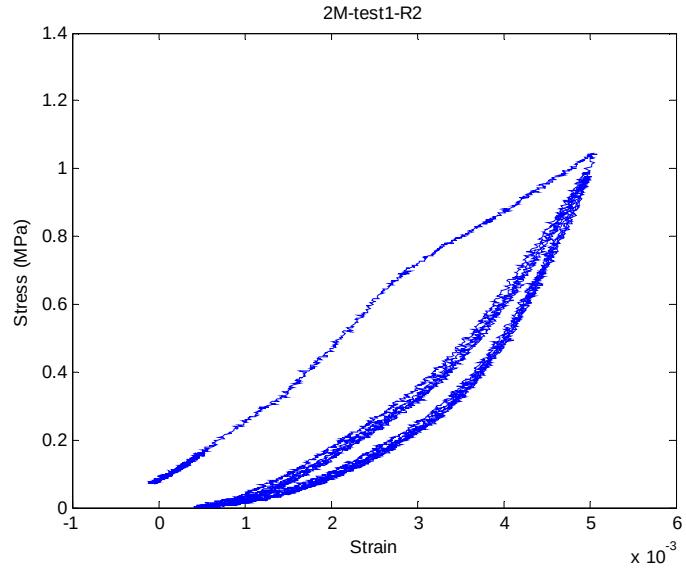

Figure 3-B-52. Stress-strain cycles of the M structure #2 up to 0.5% strain without lubricant - run#2

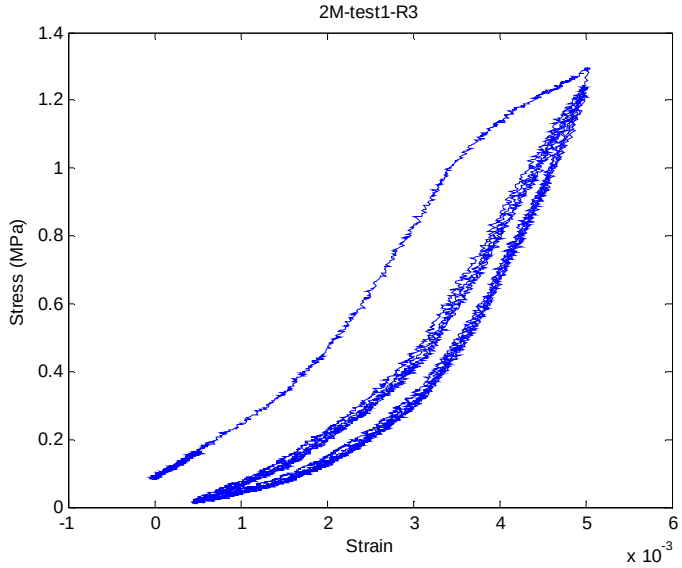

Figure 3-B-53. Stress-strain cycles of the M structure #2 up to 0.5% strain without lubricant - run#3

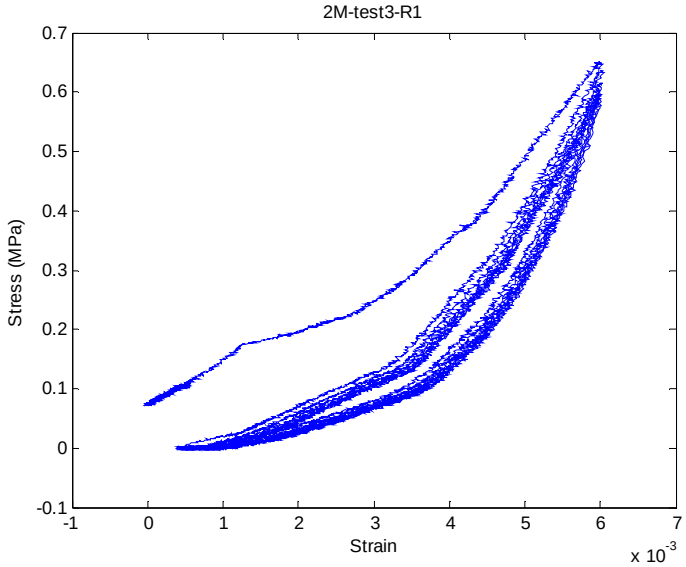

Figure 3-B-54. Stress-strain cycles of the M structure #2 up to 0.6% strain- run#1

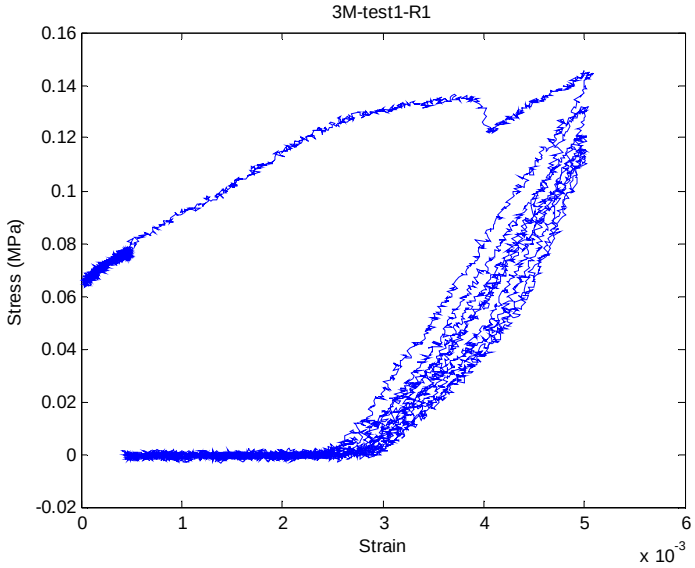

Figure 3-B-55. Stress-strain cycles of the M structure #3 up to 0.5% strain without lubricant - run#1

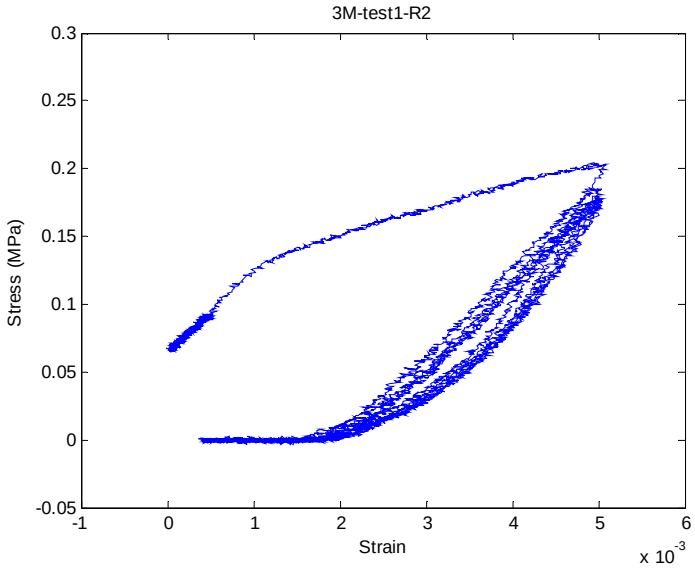

Figure 3-B-56. Stress-strain cycles of the M structure #3 up to 0.5% strain without lubricant - run#2

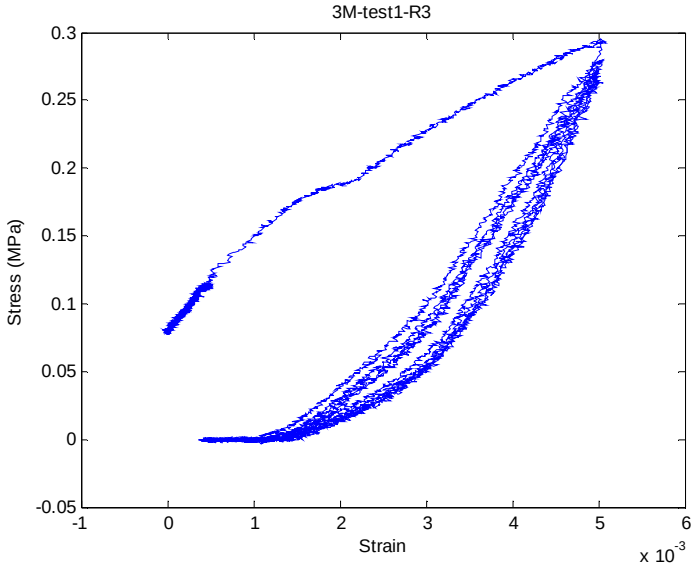

Figure 3-B-57. Stress-strain cycles of the M structure #3 up to 0.5% strain without lubricant - run#3

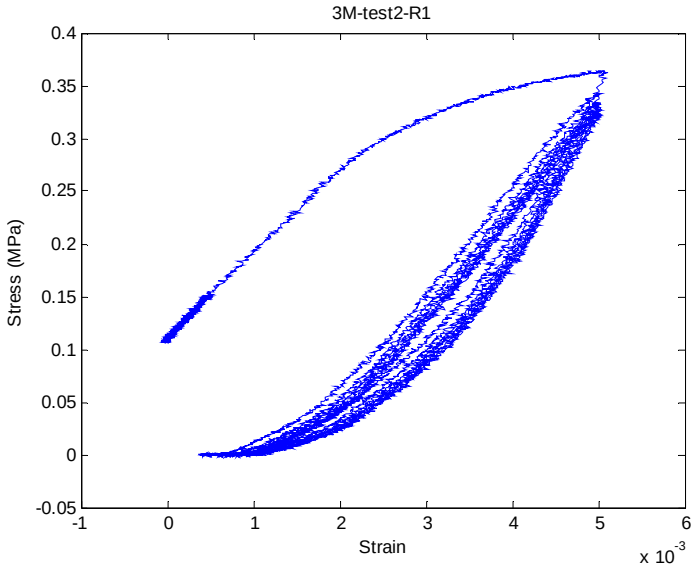

Figure 3-B-58. Stress-strain cycles of the M structure #3 up to 0.5% strain- run#1

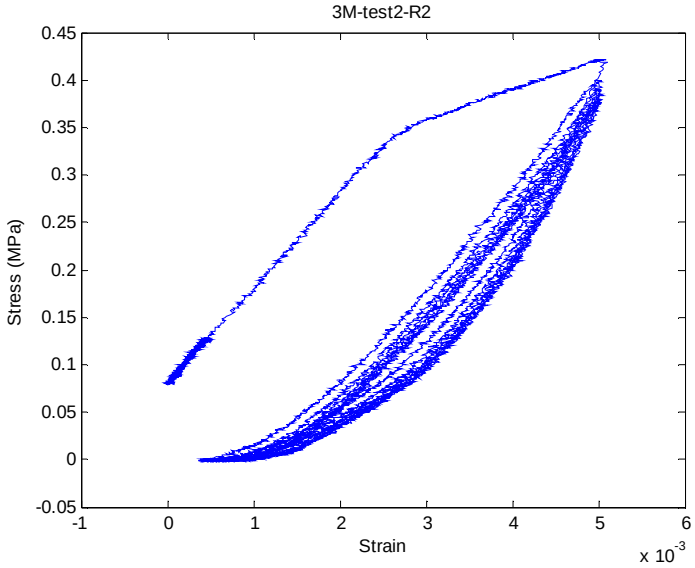

Figure 3-B-59. Stress-strain cycles of the M structure #3 up to 0.5% strain- run#2

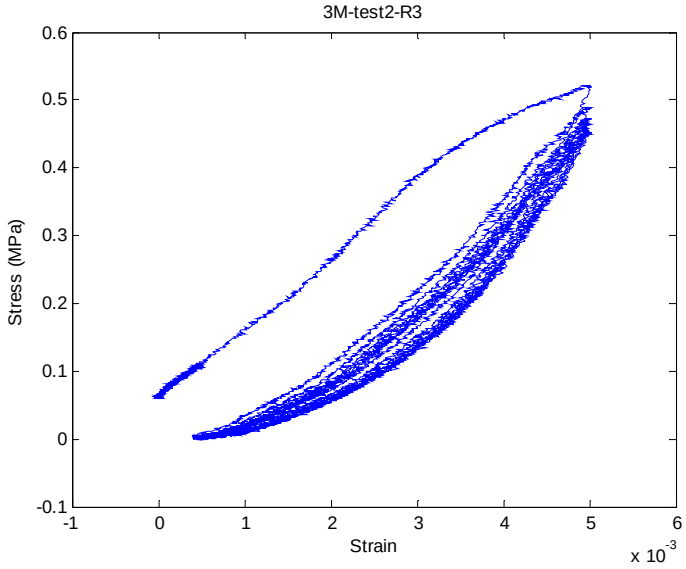

Figure 3-B-60. Stress-strain cycles of the M structure #3 up to 0.5% strain- run#3

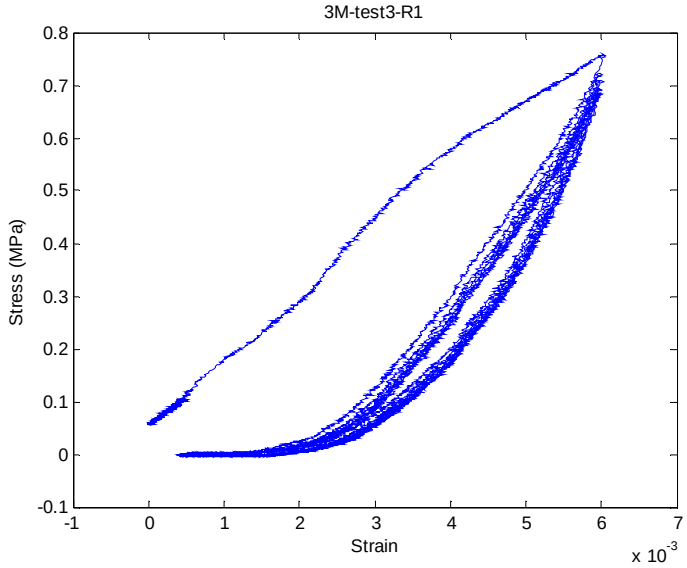

Figure 3-B-61. Stress-strain cycles of the M structure #3 up to 0.6% strain- run#1

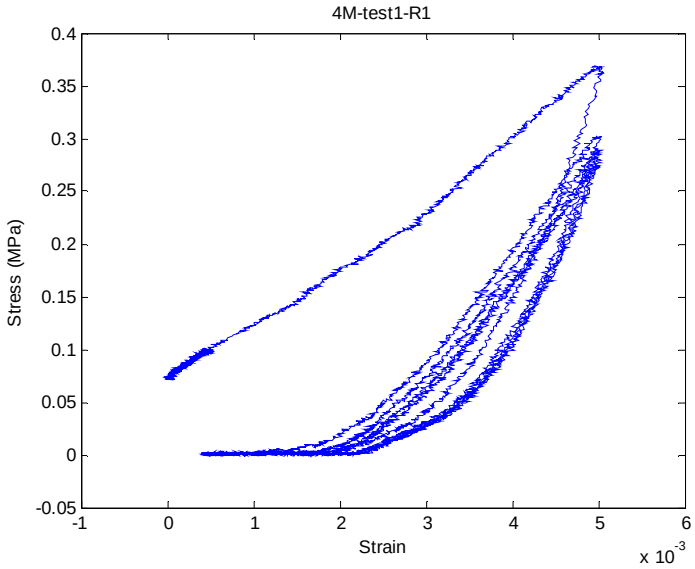

Figure 3-B-62. Stress-strain cycles of the M structure #4 up to 0.5% strain without lubricant- run#1

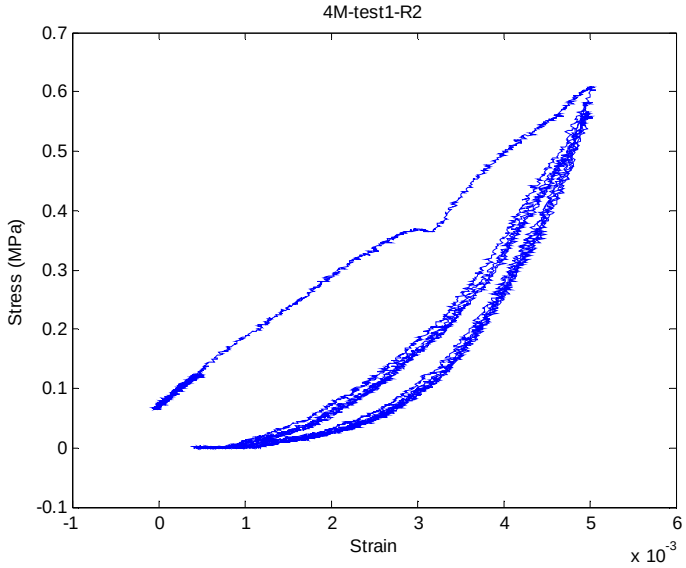

Figure 3-B-63. Stress-strain cycles of the M structure #4 up to 0.5% strain without lubricant - run#2

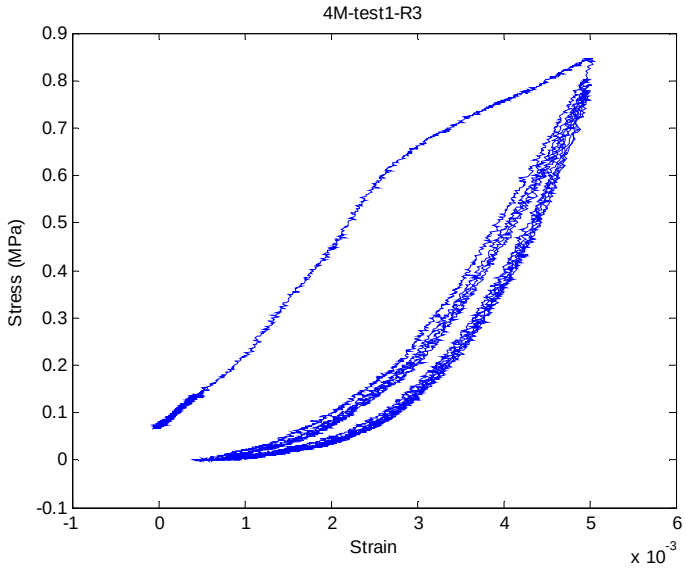

Figure 3-B-64. Stress-strain cycles of the M structure #4 up to 0.5% strain without lubricant - run#3

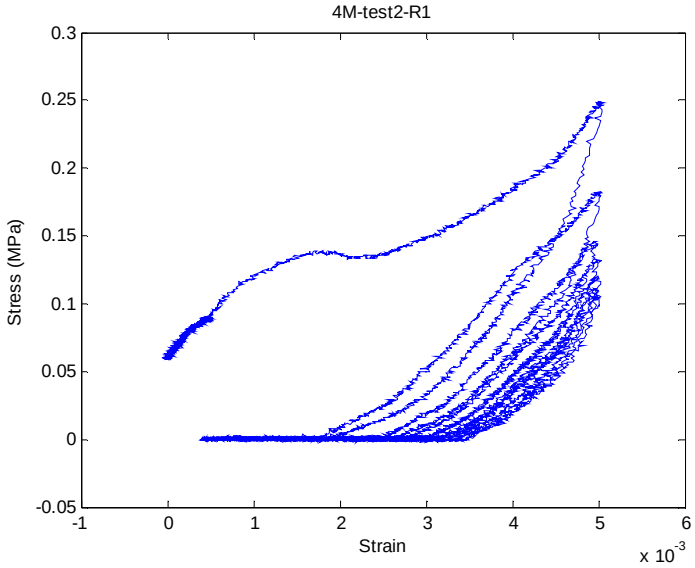

Figure 3-B-65. Stress-strain cycles of the M structure #4 up to 0.5% strain- run#1

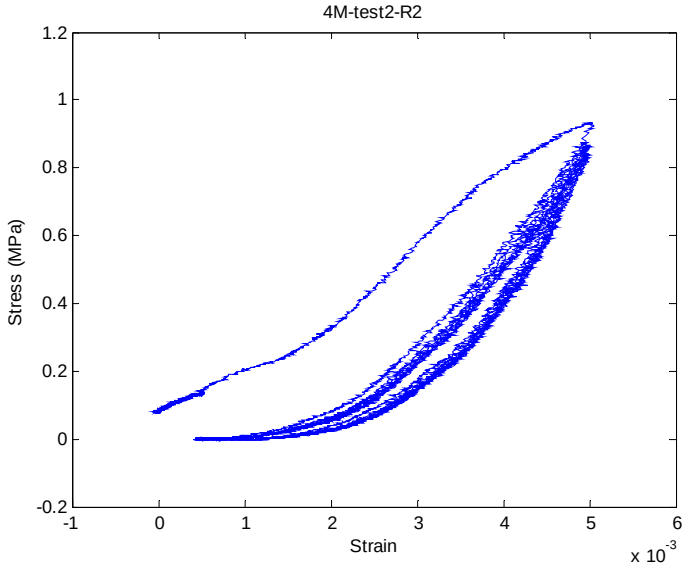

Figure 3-B-66. Stress-strain cycles of the M structure #4 up to 0.5% strain- run#2

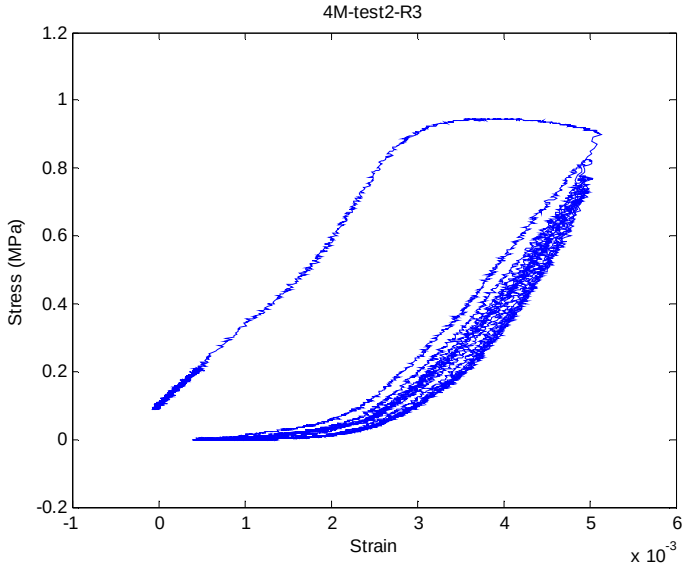

Figure 3-B-67. Stress-strain cycles of the M structure #4 up to 0.5% strain- run#3

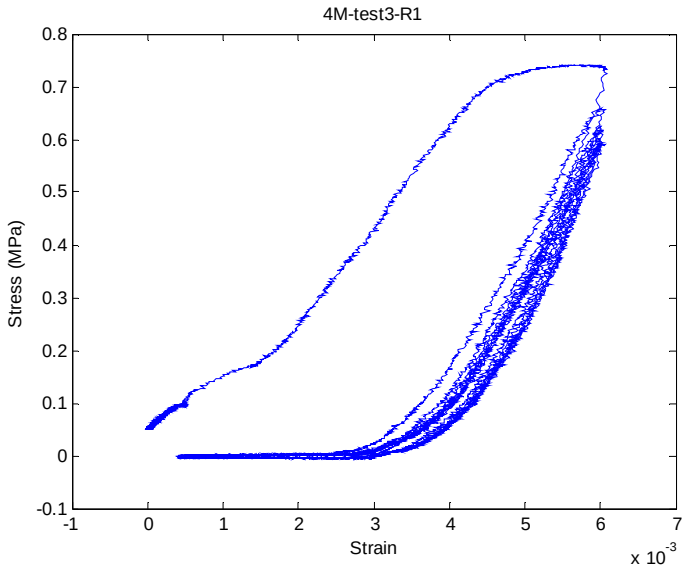

Figure 3-B-68. Stress-strain cycles of the M structure #4 up to 0.6% strain- run#1

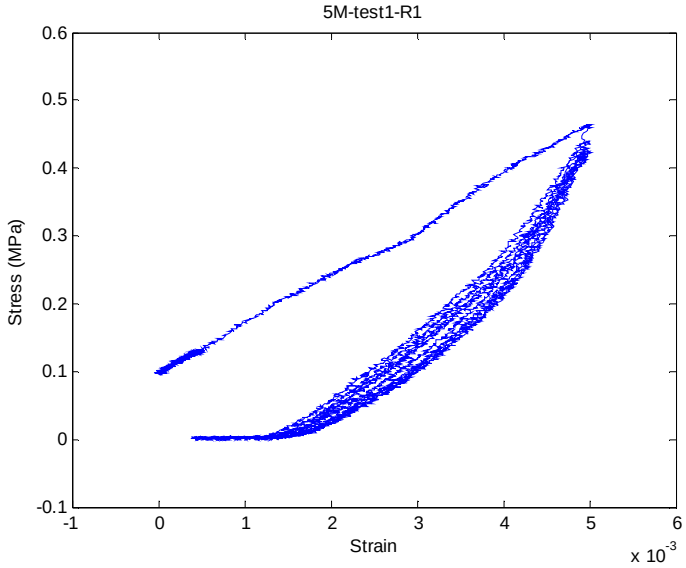

Figure 3-B-69. Stress-strain cycles of the M structure #5 up to 0.5% strain without lubricant - run#1

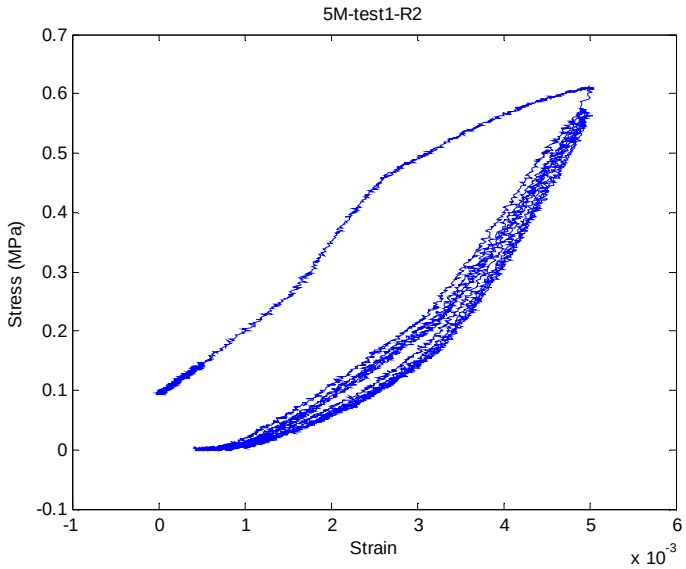

Figure 3-B-70. Stress-strain cycles of the M structure #5 up to 0.5% strain without lubricant - run#2

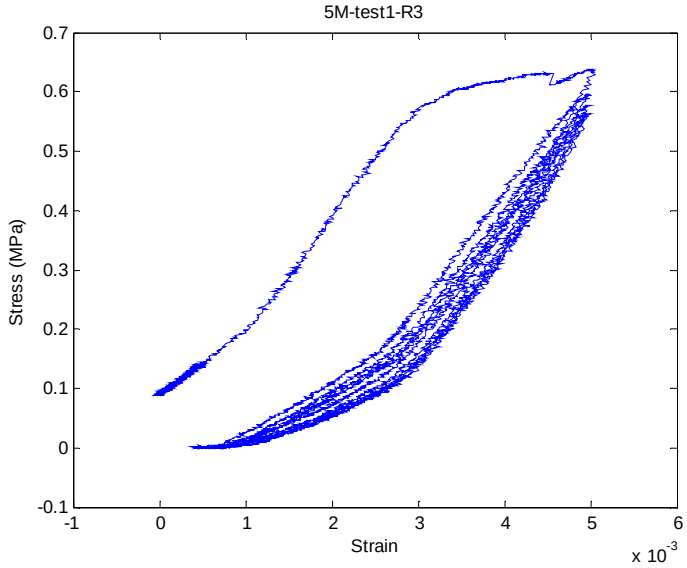

Figure 3-B-71. Stress-strain cycles of the M structure #5 up to 0.5% strain withour lubricant - run#3

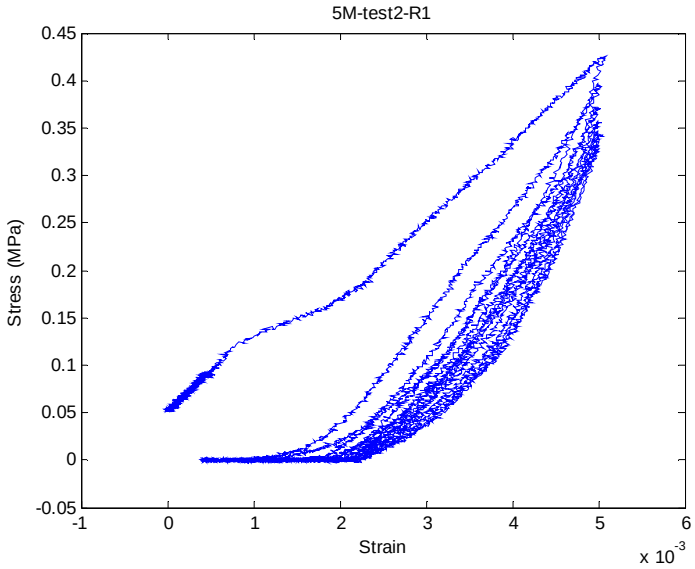

Figure 3-B-72. Stress-strain cycles of the M structure #5 up to 0.5% strain- run#1

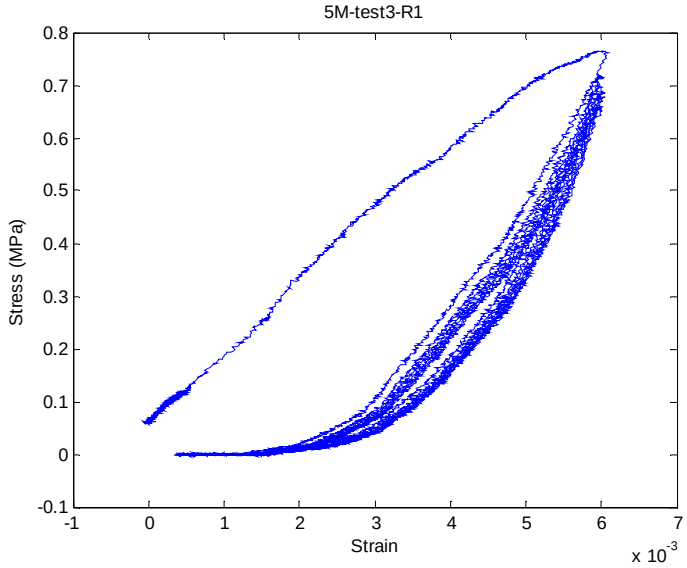

Figure 3-B-73. Stress-strain cycles of the M structure #2 up to 0.6% strain- run#1

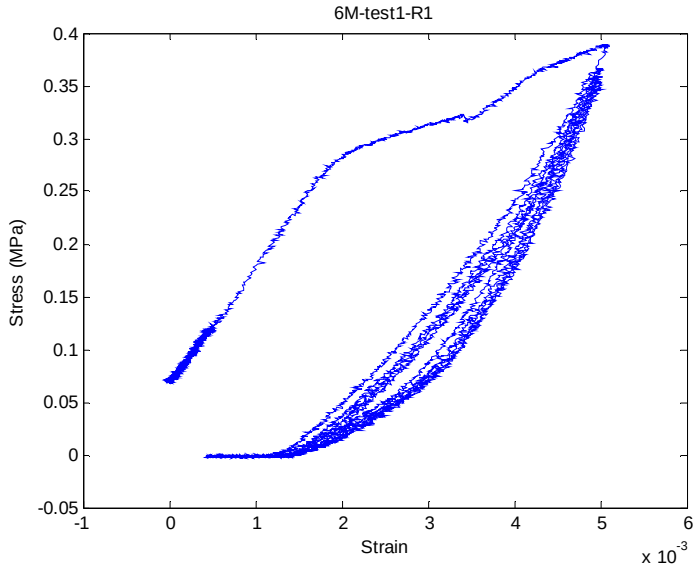

Figure 3-B-74. Stress-strain cycles of the M structure #6 up to 0.5% strain without lubricant - run#1

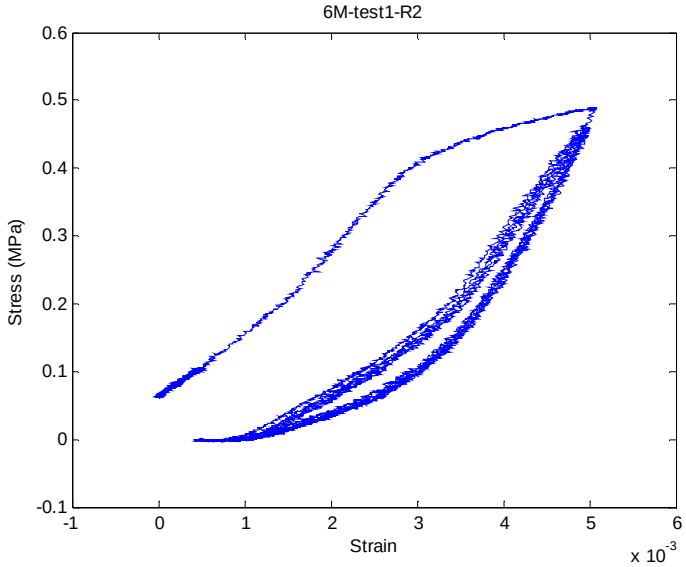

Figure 3-B-75. Stress-strain cycles of the M structure #6 up to 0.5% strain without lubricant - run#2

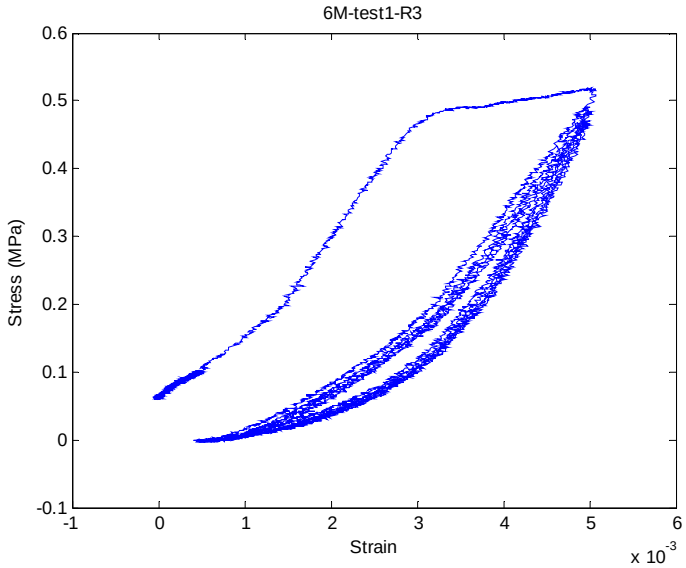

Figure 3-B-76. Stress-strain cycles of the M structure #6 up to 0.5% strain without lubricant - run#3

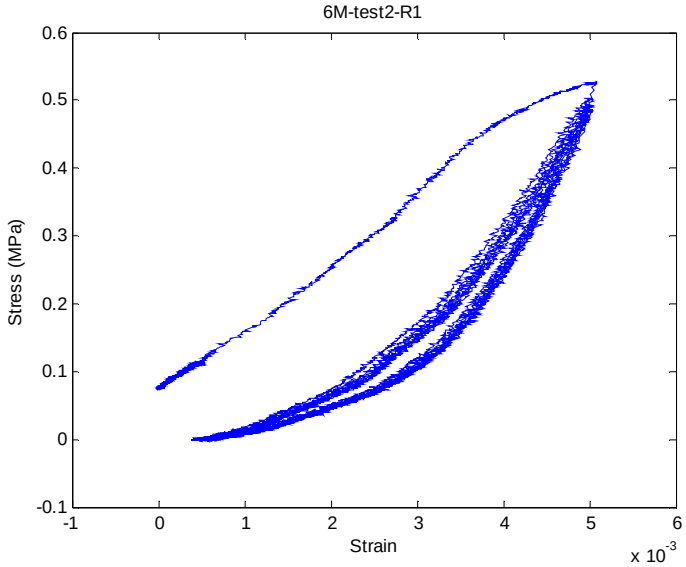

Figure 3-B-77. Stress-strain cycles of the M structure #6 up to 0.5% strain- run#1

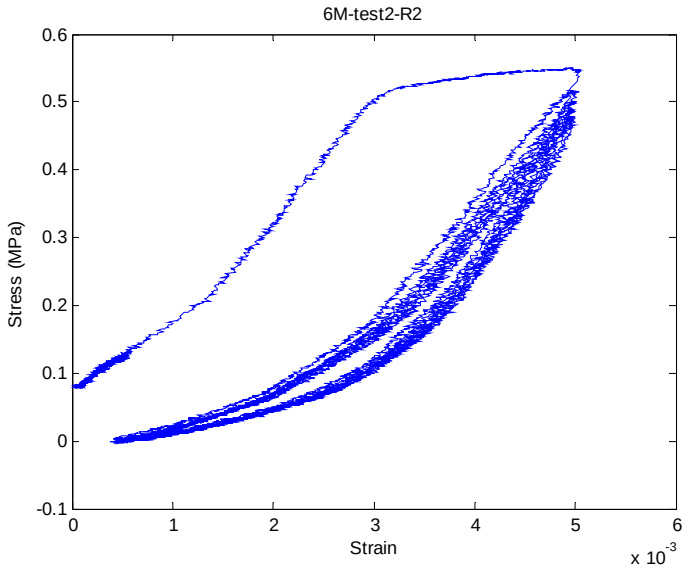

Figure 3-B-78. Stress-strain cycles of the M structure #6 up to 0.5% strain- run#2

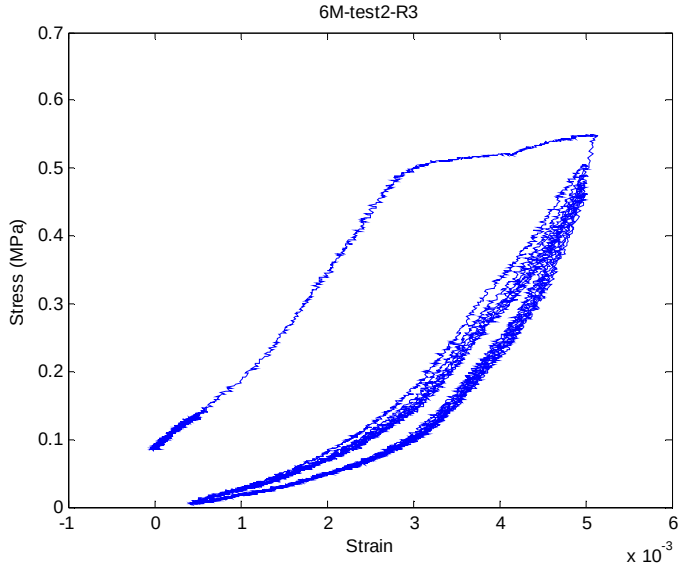

Figure 3-B-79. Stress-strain cycles of the M structure #6 up to 0.5% strain- run#3

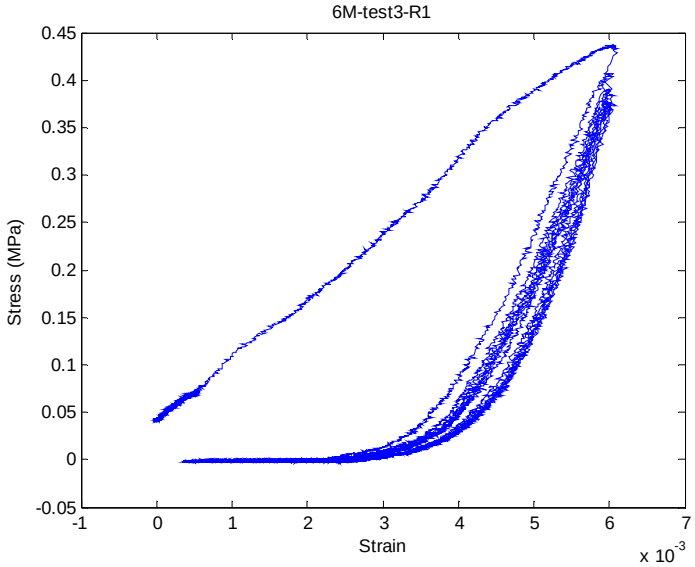

Figure 3-B-80. Stress-strain cycles of the M structure #6 up to 0.6% strain- run#1

LARGE STRUCTURES

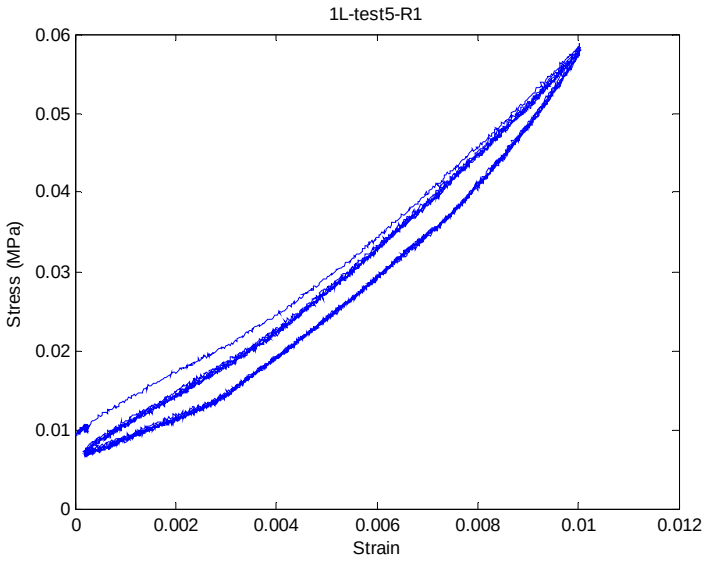

Figure 3-B-81. Stress-strain cycles of the L structure #1 up to 1.0% strain - run#1

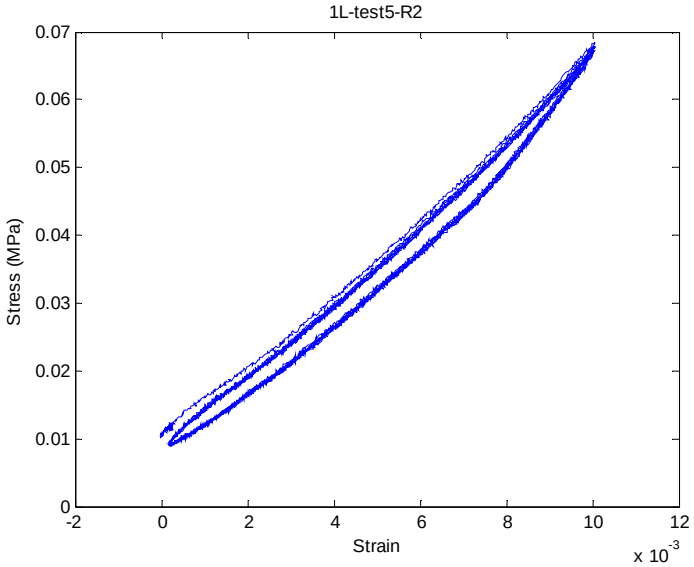

Figure 3-B-82. . Stress-strain cycles of the L structure #1 up to 1.0% strain - run#1

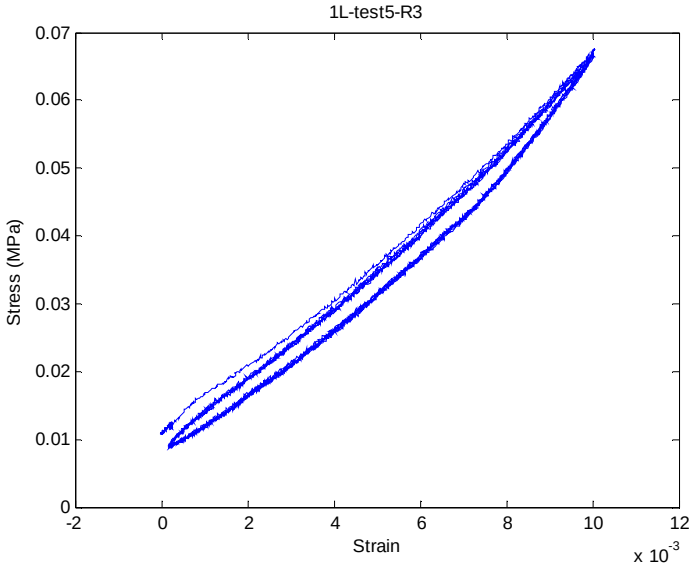

Figure 3-B-83. . Stress-strain cycles of the L structure #1 up to 1.0% strain - run#3

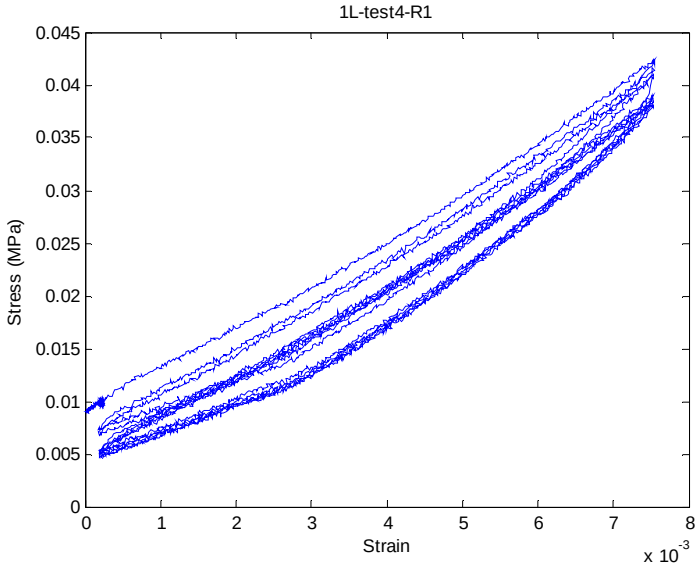

Figure 3-B-84. . Stress-strain cycles of the L structure #1 up to 0.75% strain - run#1

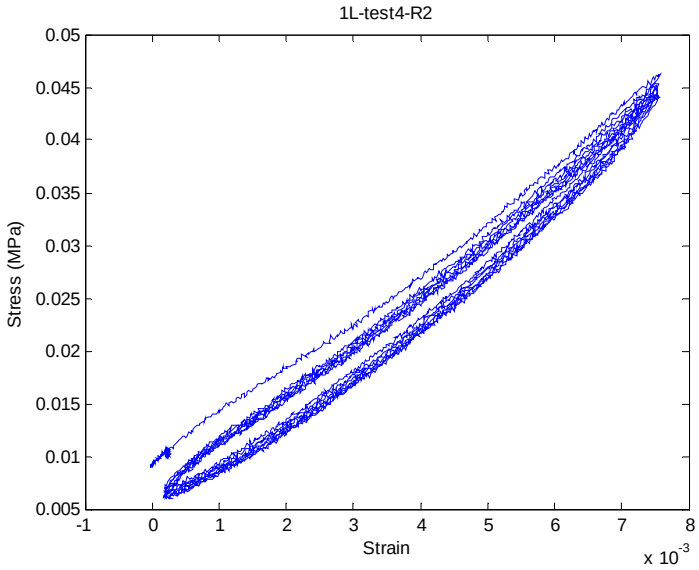

Figure 3-B-85. Stress-strain cycles of the L structure #1 up to 0.75% strain - run#2

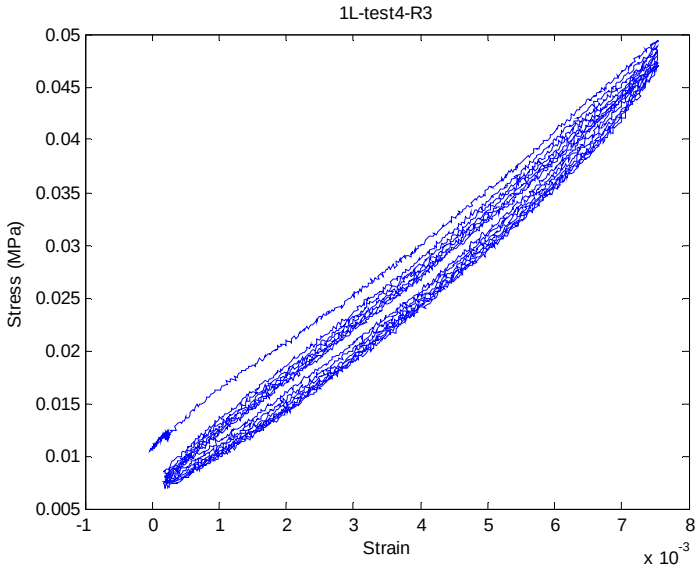

Figure 3-B-86. Stress-strain cycles of the L structure #1 up to 0.75% strain - run#3

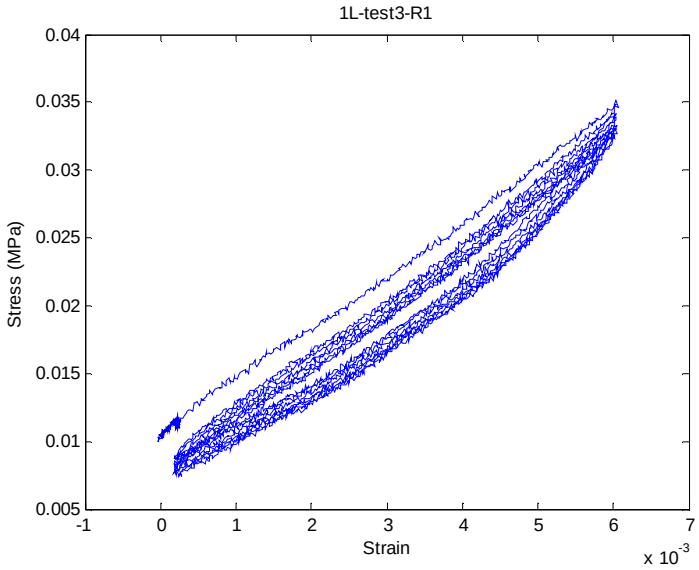

Figure 3-B-87. Stress-strain cycles of the L structure #1 up to 0.6% strain - run#1

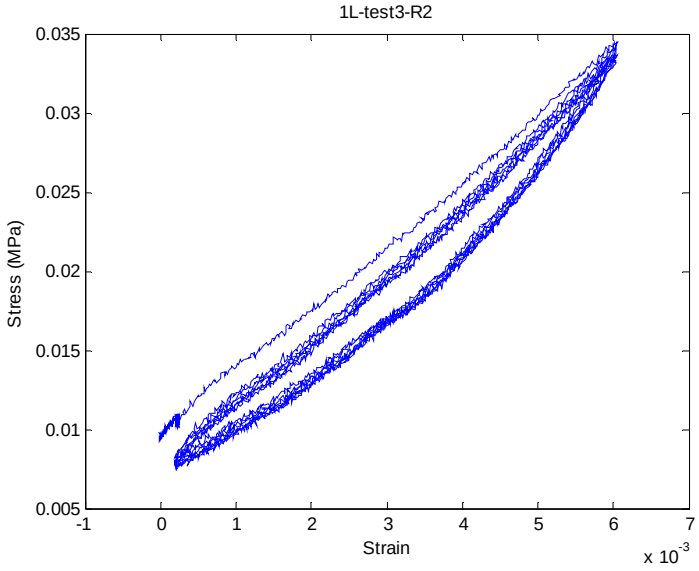

Figure 3-B-88. Stress-strain cycles of the L structure #1 up to 0.6% strain - run#2

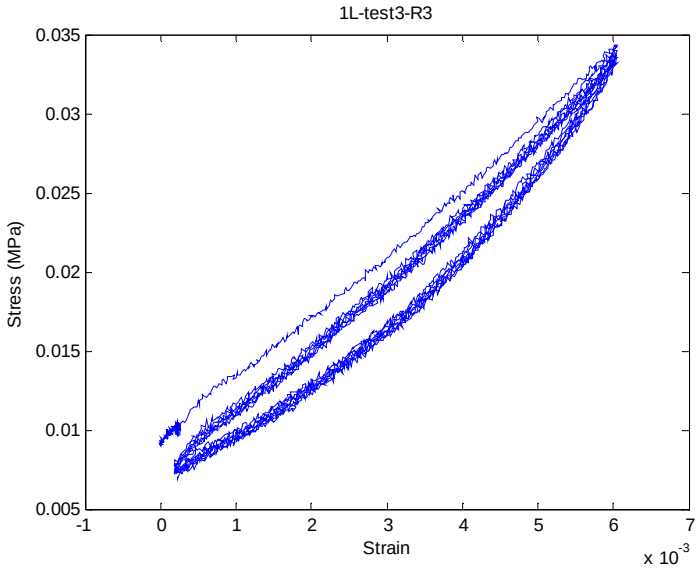

Figure 3-B-8. Stress-strain cycles of the L structure #1 up to 0.6% strain - run#3

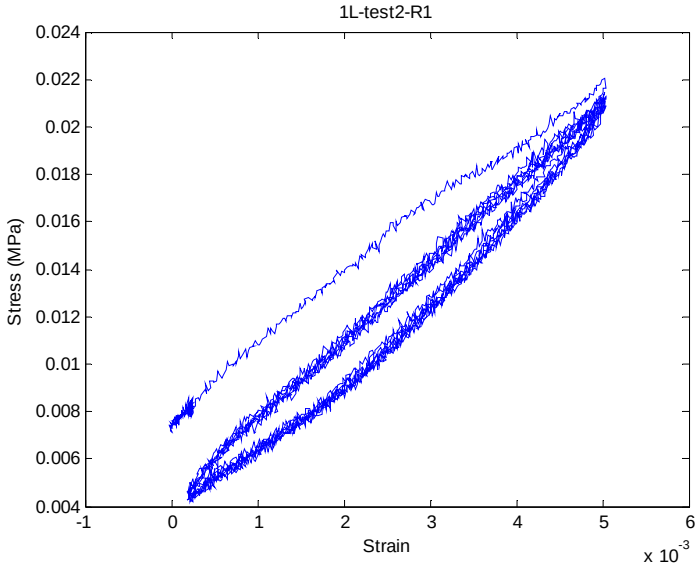

Figure 3-B-90. Stress-strain cycles of the L structure #1 up to 0.5% strain- run#1

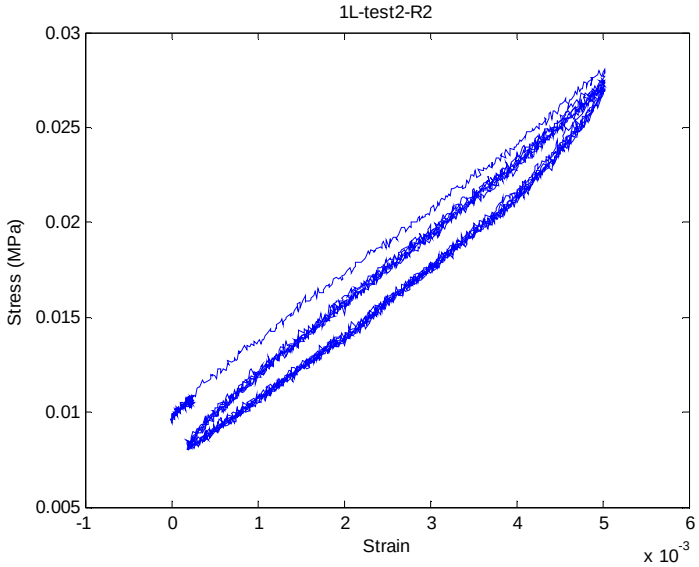

Figure 3-B-91. Stress-strain cycles of the L structure #1 up to 0.5% strain- run#2

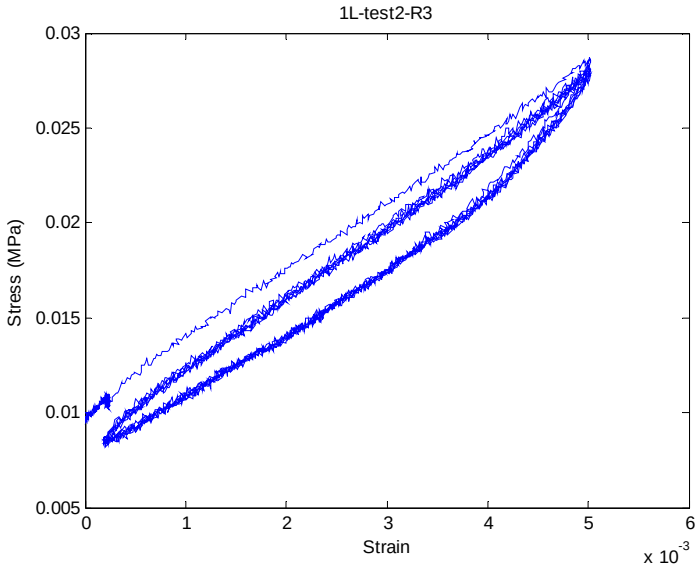

Figure 3-B-92. Stress-strain cycles of the L structure #1 up to 0.5% strain- run#3

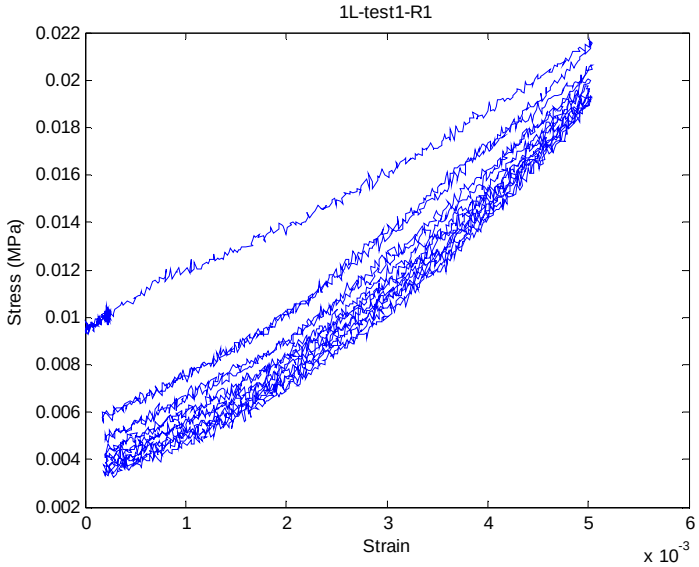

Figure 3-B-93. Stress-strain cycles of the L structure #1 up to 0.5% strain without lubricant - run#1

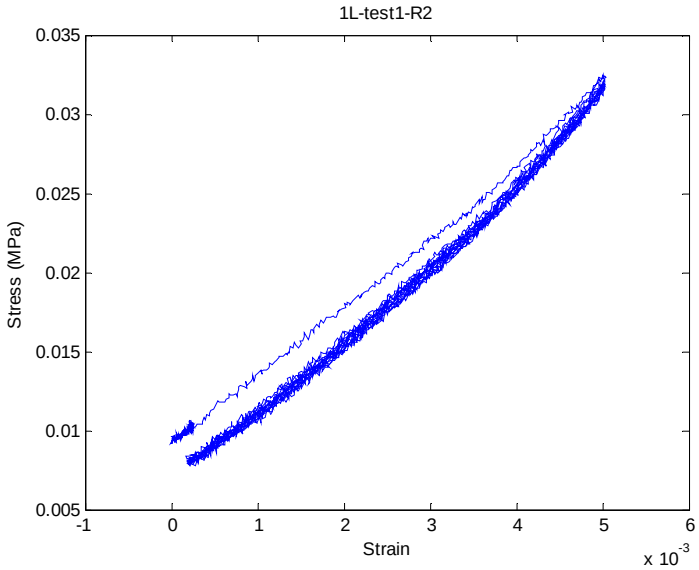

Figure 3-B-94. Stress-strain cycles of the L structure #1 up to 0.5% strain without lubricant - run#2

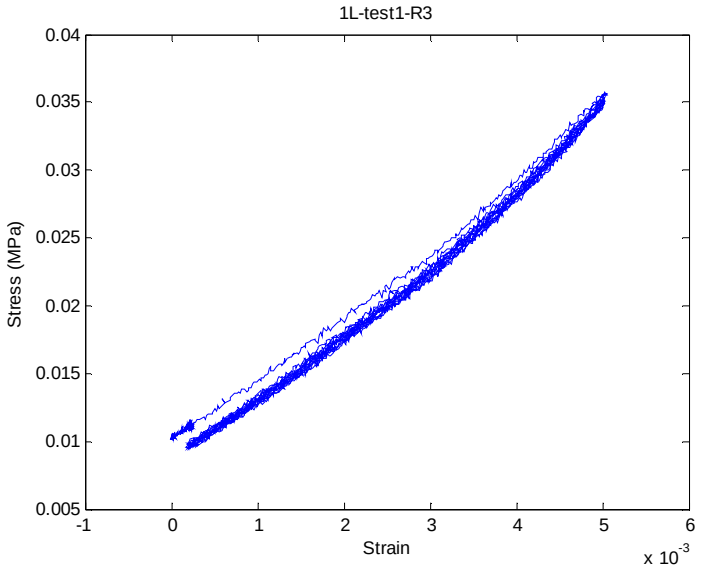

Figure 3-B-95. Stress-strain cycles of the L structure #1 up to 0.5% strain without lubricant - run#3

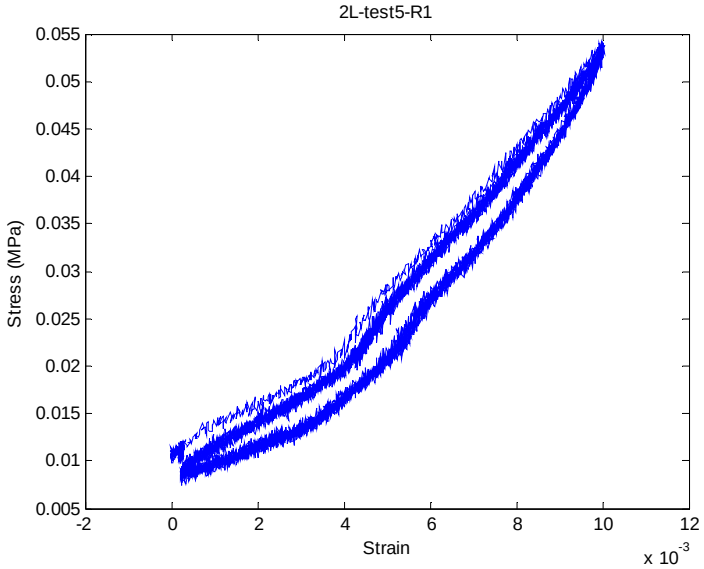

Figure 3-B-96. Stress-strain cycles of the L structure #2 up to 1.0% strain - run#1

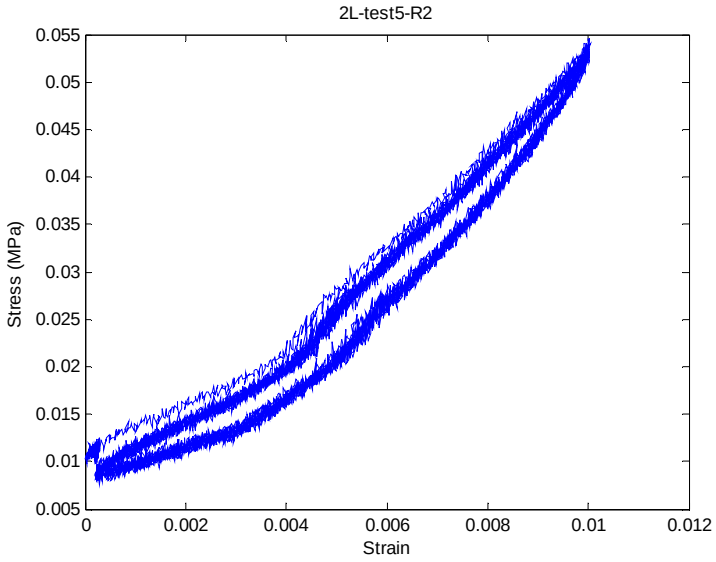

Figure 3-B-97. Stress-strain cycles of the L structure #2 up to 1.0% strain - run#2

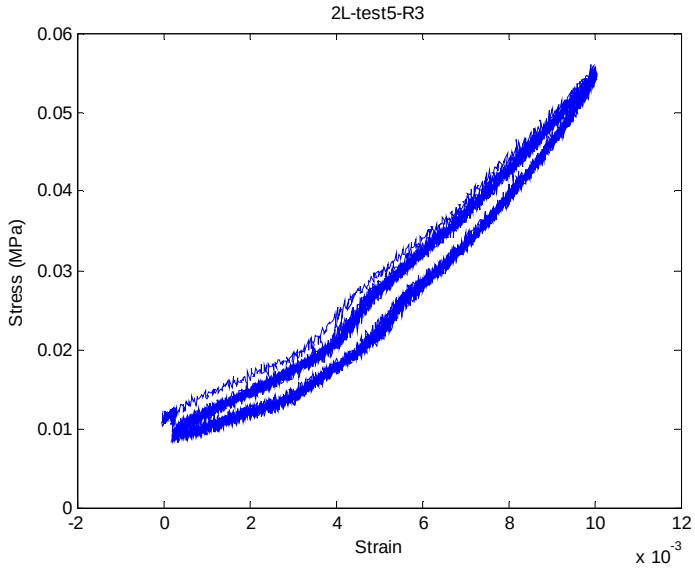

Figure 3-B-98. Stress-strain cycles of the L structure #2 up to 1.0% strain - run#3

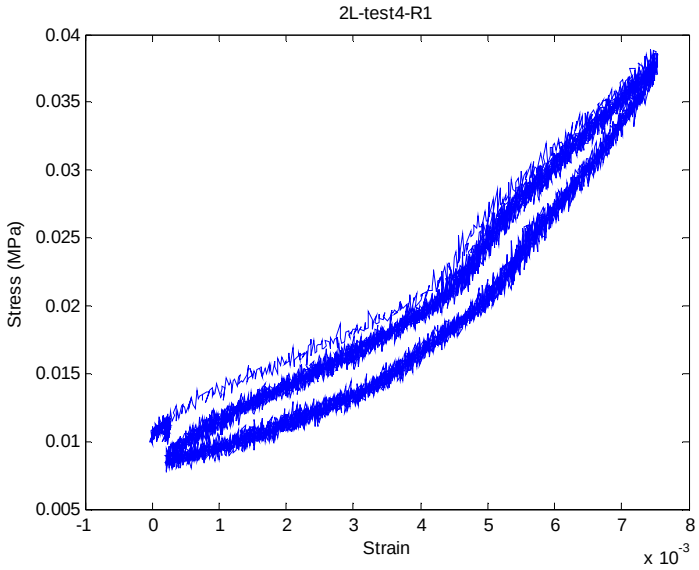

Figure 3-B-99. Stress-strain cycles of the L structure #2 up to 0.75% strain - run#1

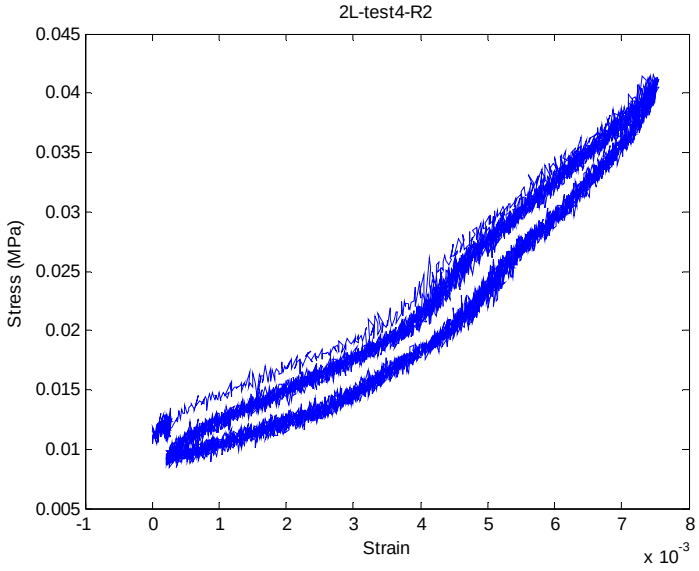

Figure 3-B-100. Stress-strain cycles of the L structure #2 up to 0.75% strain - run#2

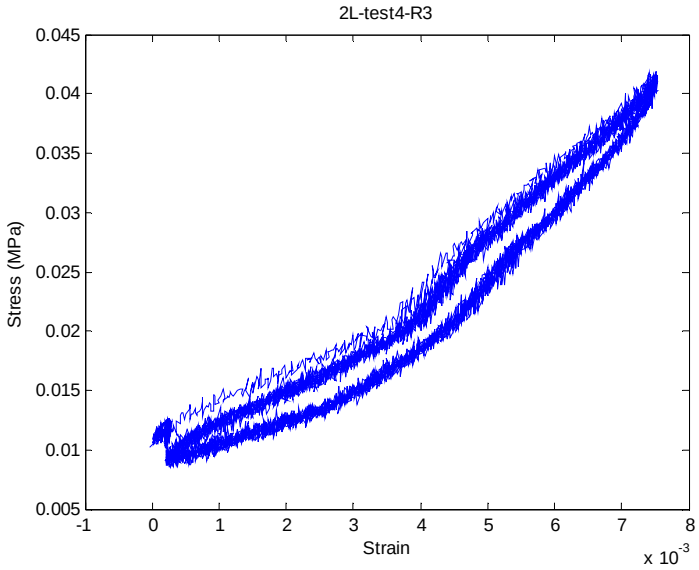

Figure 3-B-101. Stress-strain cycles of the L structure #2 up to 0.75% strain - run#3

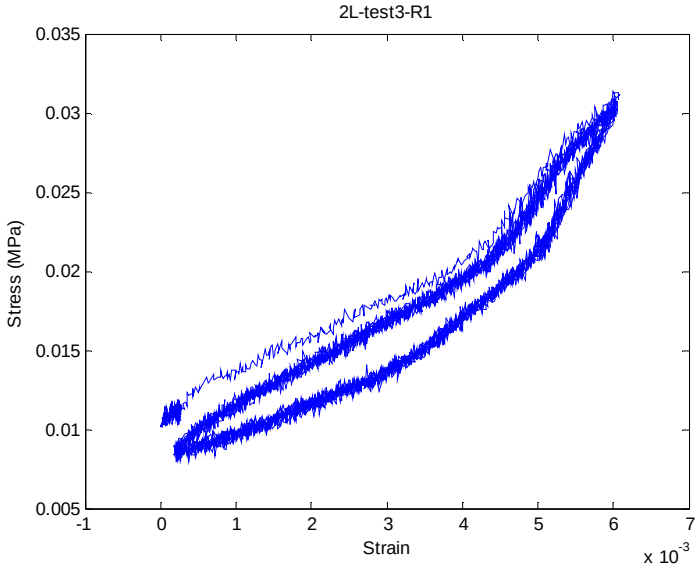

Figure 3-B-102. Stress-strain cycles of the L structure #2 up to 0.6% strain- run#1

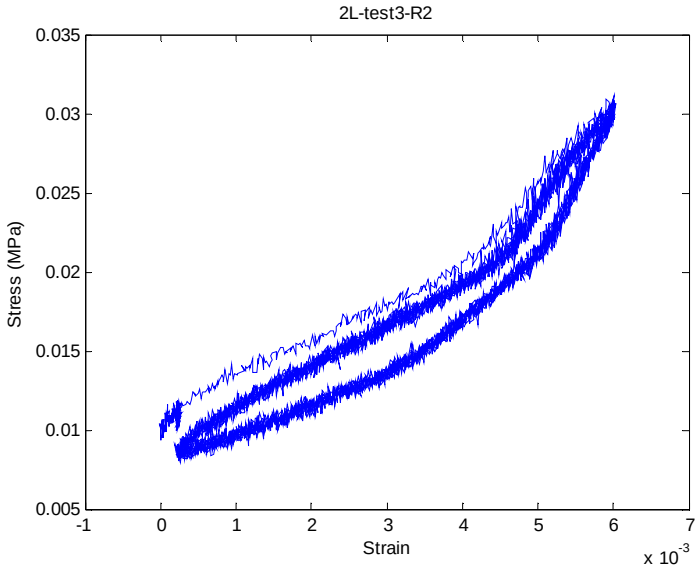

Figure 3-B-103. Stress-strain cycles of the L structure #2 up to 0.6% strain- run#2

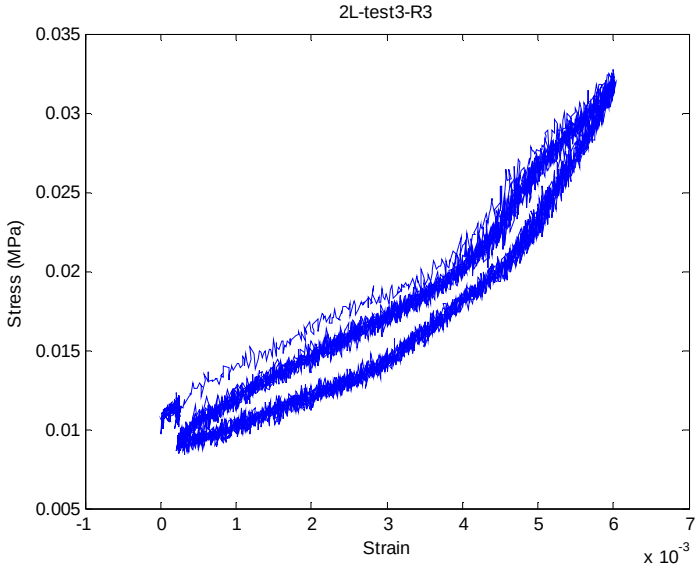

Figure 3-B-104. Stress-strain cycles of the L structure #2 up to 0.6% strain- run#3

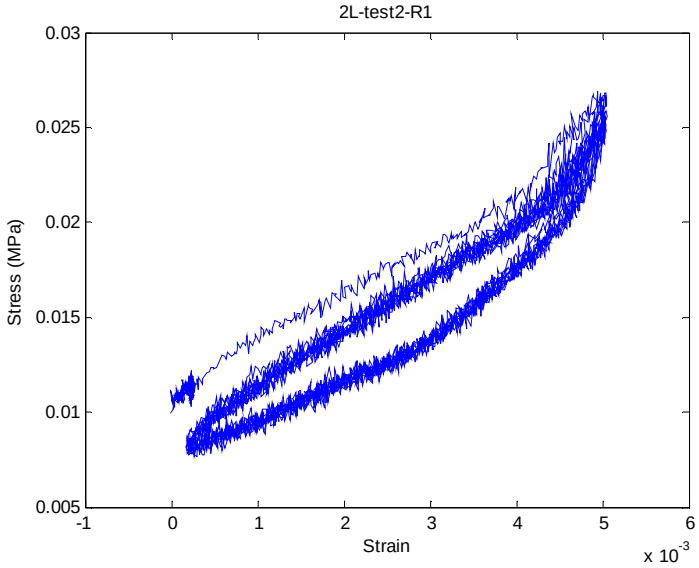

Figure 3-B-105. Stress-strain cycles of the L structure #2 up to 0.5% strain- run#1

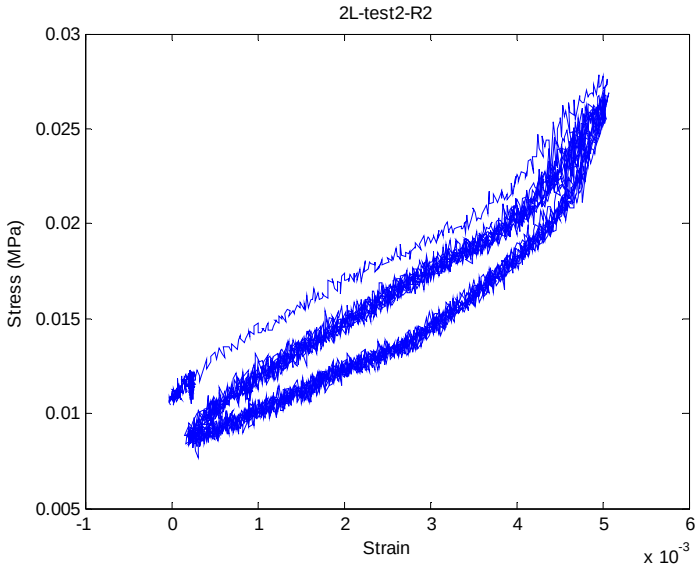

Figure 3-B-106. Stress-strain cycles of the L structure #2 up to 0.5% strain- run#2

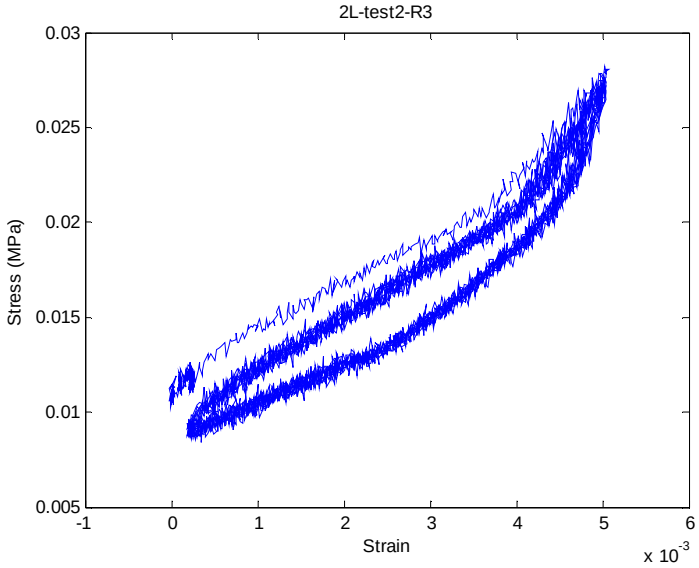

Figure 3-B-107. Stress-strain cycles of the L structure #2 up to 0.5% strain- run#3

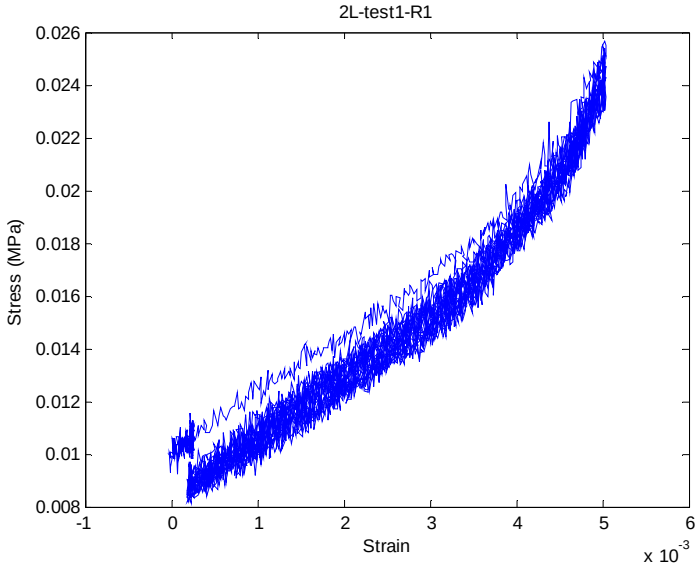

Figure 3-B-10. Stress-strain cycles of the L structure #2 up to 0.5% strain without lubricant- run#1

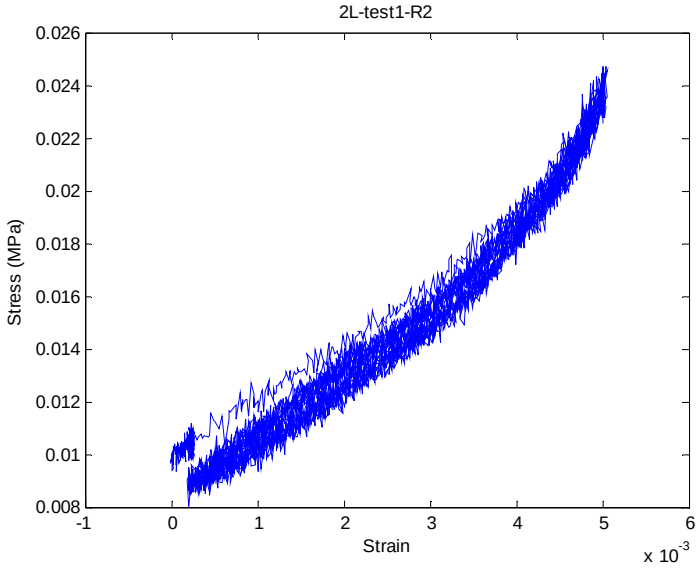

Figure 3-B-109. Stress-strain cycles of the L structure #2 up to 0.5% strain without lubricant- run#2

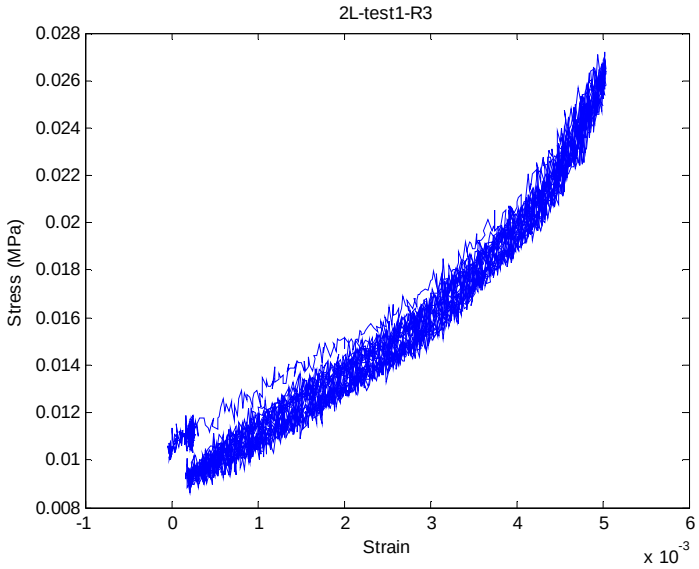

Figure 3-B-110. Stress-strain cycles of the L structure #2 up to 0.5% strain without lubricant- run#3

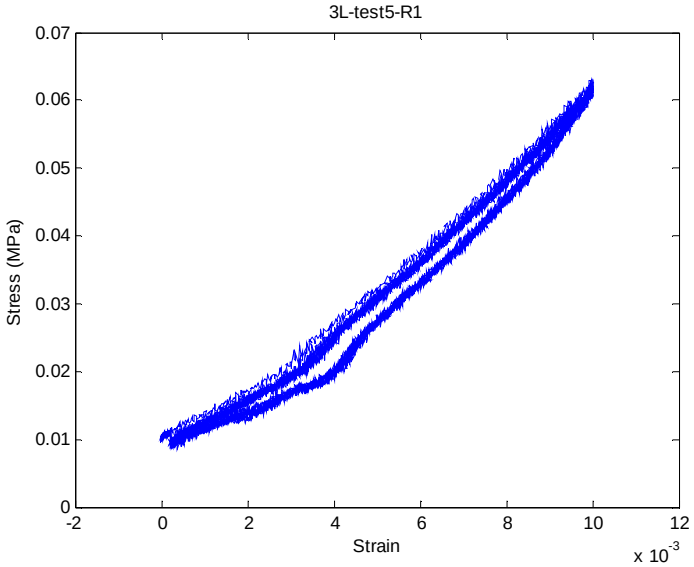

Figure 3-B-111. Stress-strain cycles of the L structure #3 up to 1.0% strain - run#1

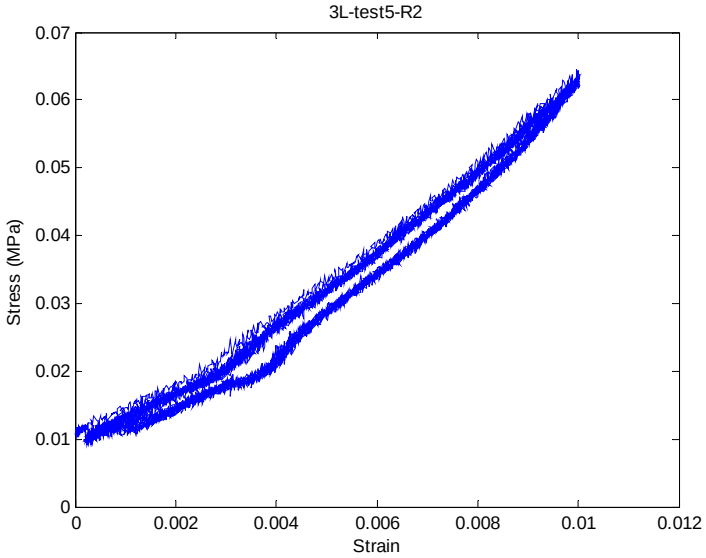

Figure 3-B-112. Stress-strain cycles of the L structure #3 up to 1.0% strain - run#2

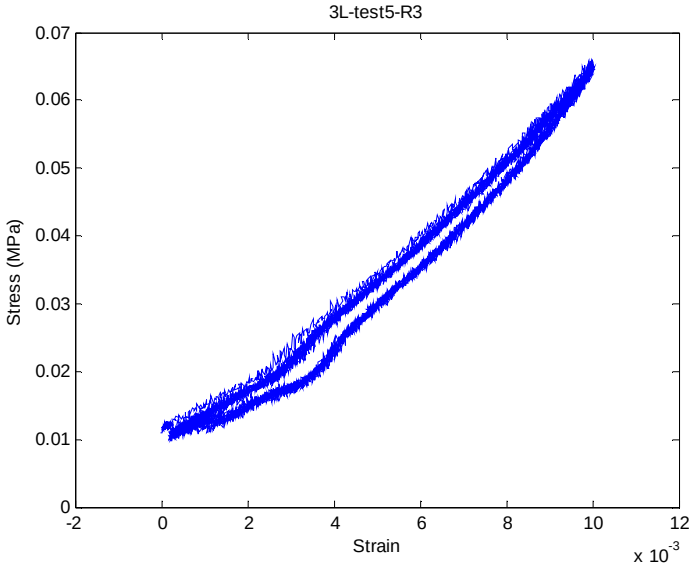

Figure 3-B-113. Stress-strain cycles of the L structure #3 up to 1.0% strain - run#3

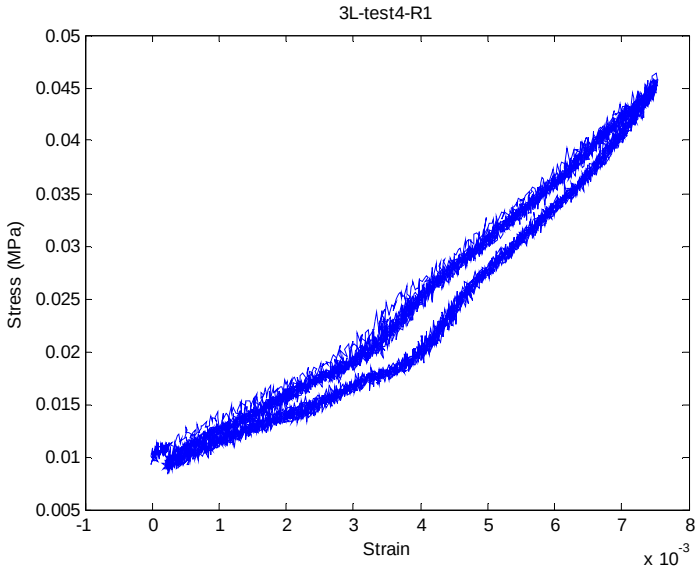

Figure 3-B-114. Stress-strain cycles of the L structure #3 up to 0.75% strain - run#1

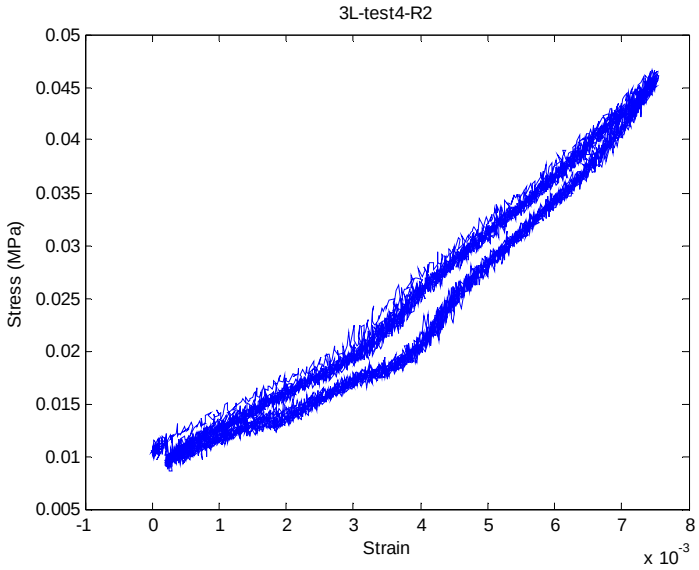

Figure 3-B-115. Stress-strain cycles of the L structure #3 up to 0.75% strain - run#2

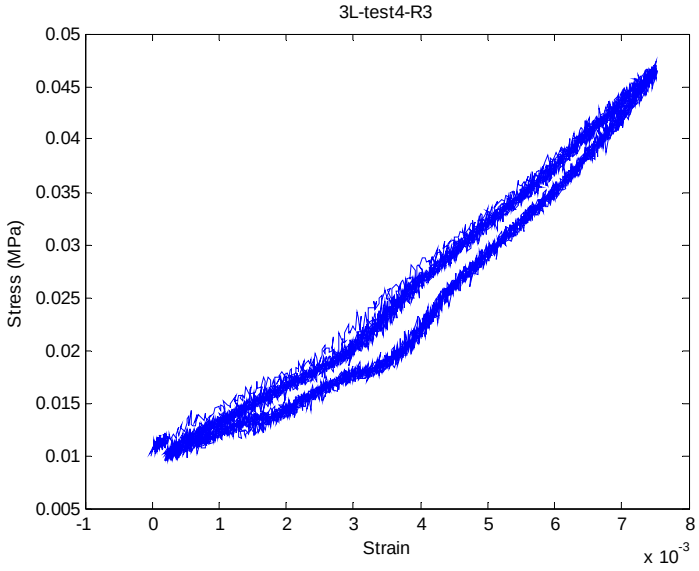

Figure 3-B-116. Stress-strain cycles of the L structure #3 up to 0.75% strain - run#3

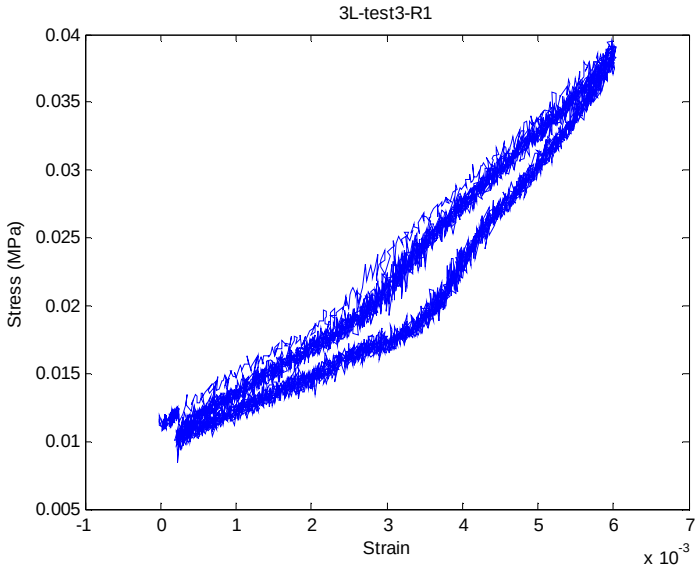

Figure 3-B-117. Stress-strain cycles of the L structure #3 up to 0.6% strain - run#1

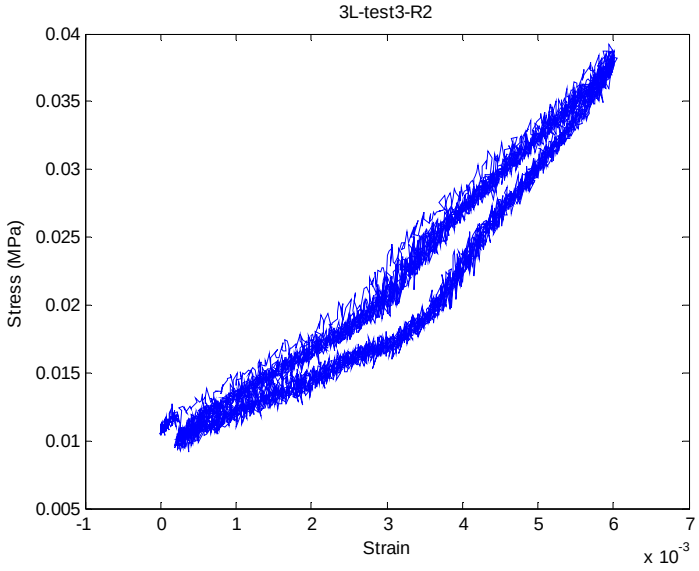

Figure 3-B-118. Stress-strain cycles of the L structure #3 up to 0.6% strain - run#2

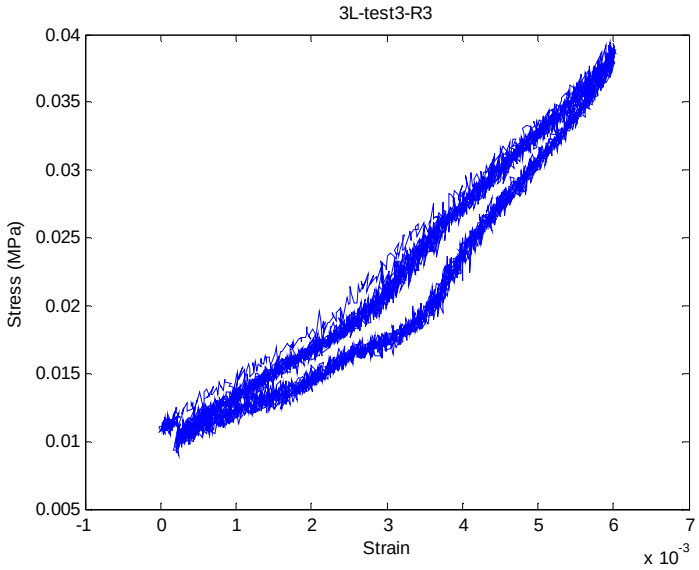

Figure 3-B-119. Stress-strain cycles of the L structure #3 up to 0.6% strain - run#3

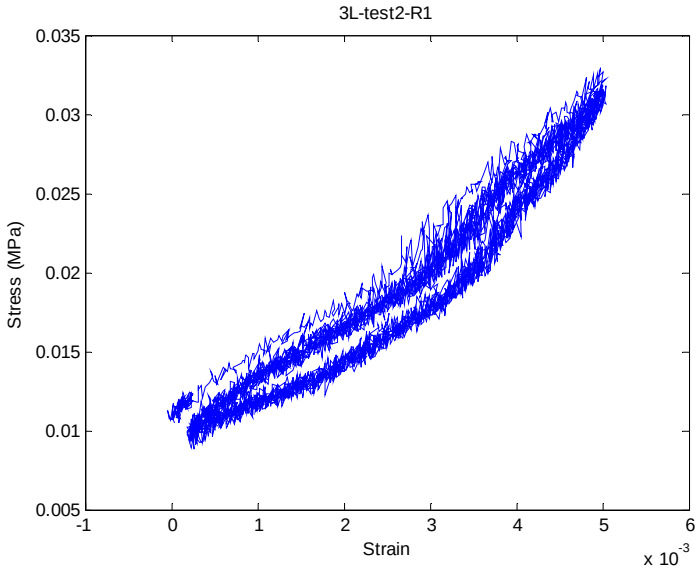

Figure 3-B-120. Stress-strain cycles of the L structure #3 up to 0.5% strain - run#1

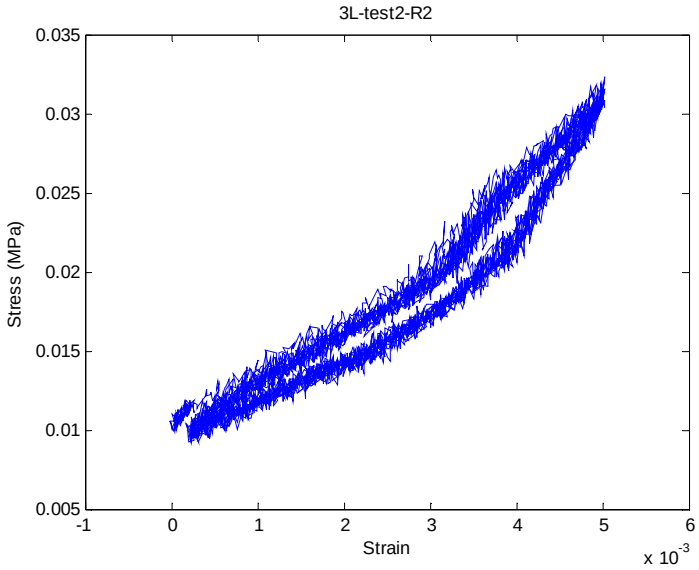

Figure 3-B-121. Stress-strain cycles of the L structure #3 up to 0.5% strain - run#2

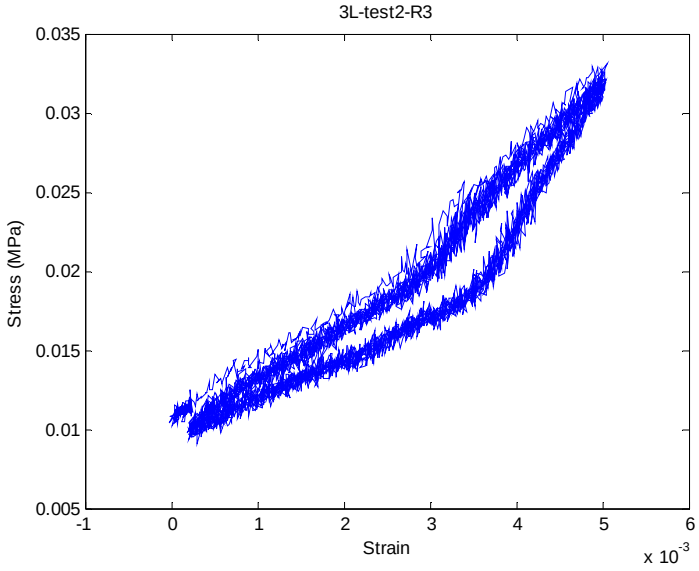

Figure 3-B-122. Stress-strain cycles of the L structure #3 up to 0.5% strain - run#3

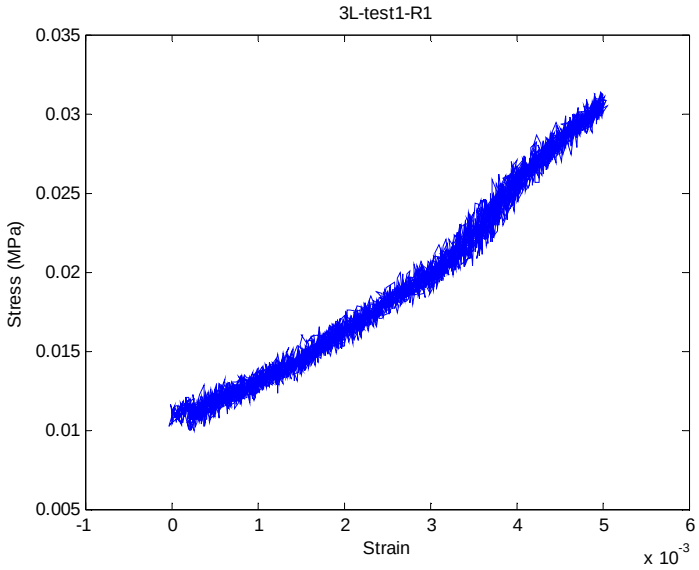

Figure 3-B-123. Stress-strain cycles of the L structure #3 up to 0.5% strain without lubricant - run#1

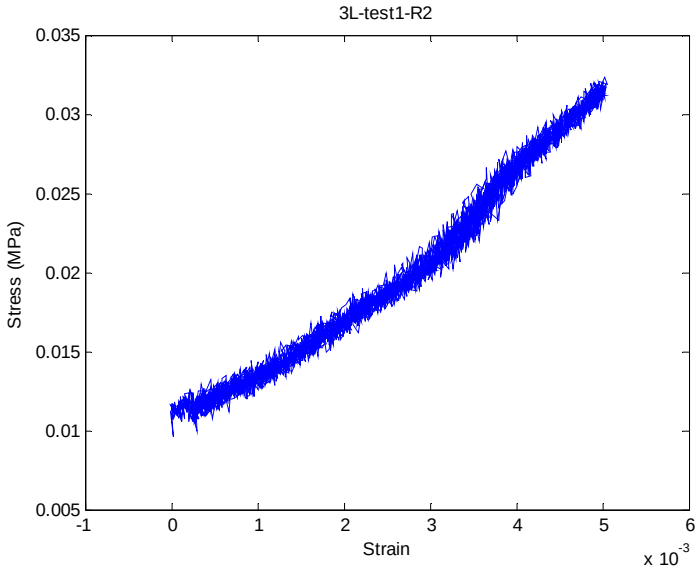

Figure 3-B-124. Stress-strain cycles of the L structure #3 up to 0.5% strain without lubricant - run#2

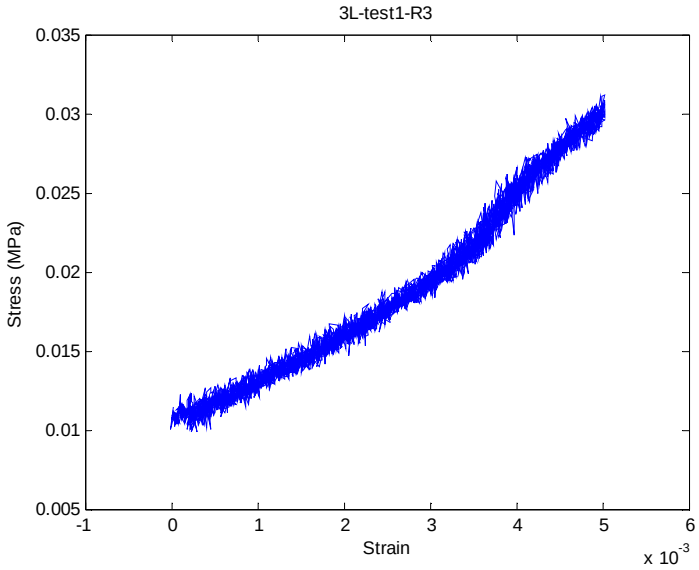

Figure 3-B-125. Stress-strain cycles of the L structure #3 up to 0.5% strain without lubricant - run#3

EXTRA-LARGE STRUCTURES

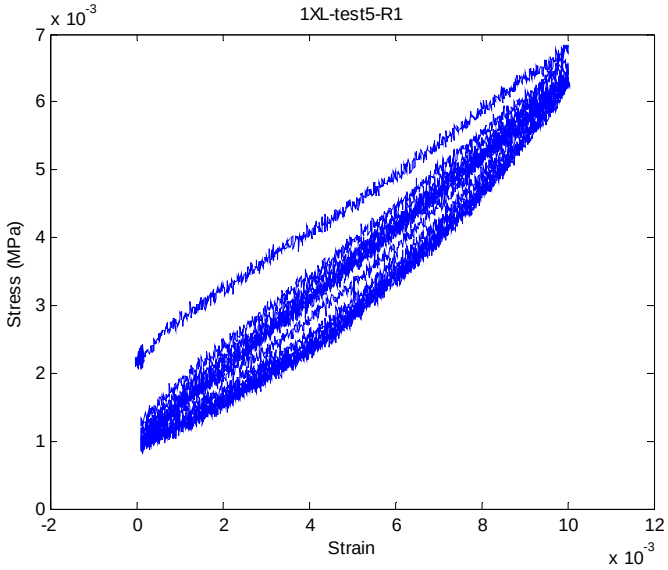

Figure 3-B-126. Stress-strain cycles of the XL structure #1 up to 1.0% strain - run#1

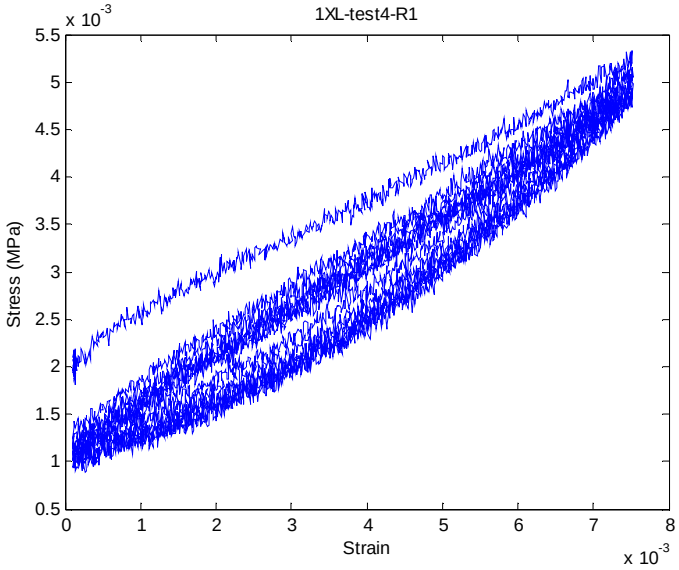

Figure 3-B-127. Stress-strain cycles of the XL structure #1 up to 0.75% strain - run#1

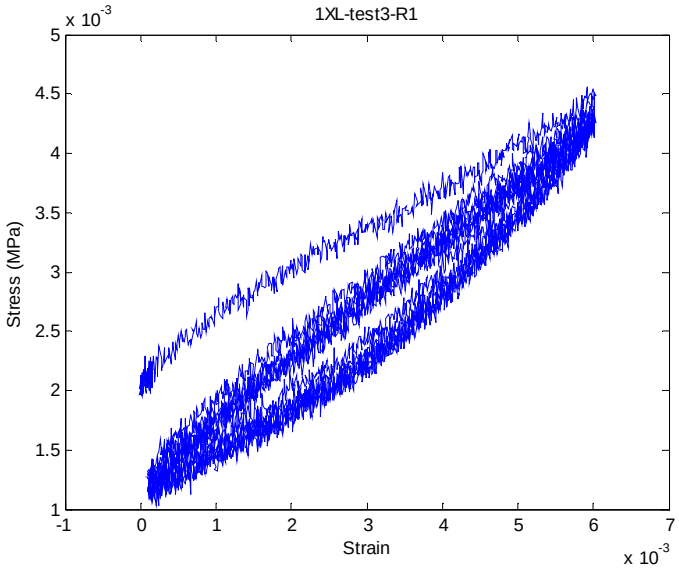

Figure 3-B-128. Stress-strain cycles of the XL structure #1 up to 0.6% strain - run#1

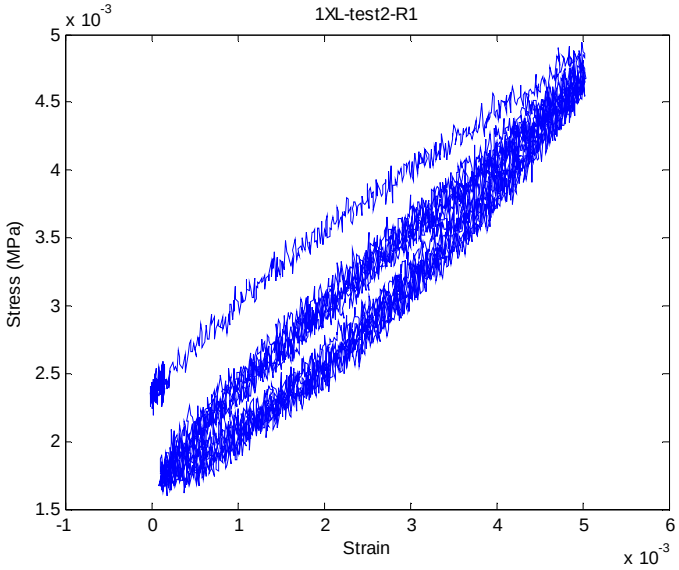

Figure 3-B-129. Stress-strain cycles of the XL structure #1 up to 0.5% strain – run#1

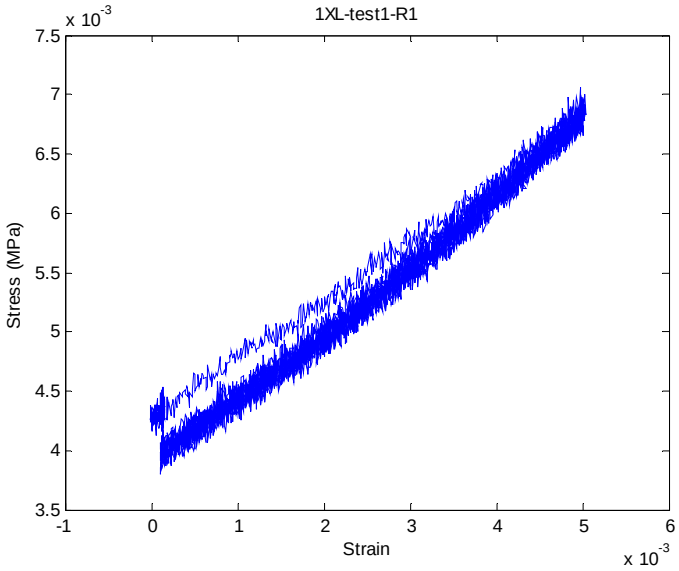

Figure 3-B-130. Stress-strain cycles of the XL structure #1 up to 0.5% strain without lubricant - run#1

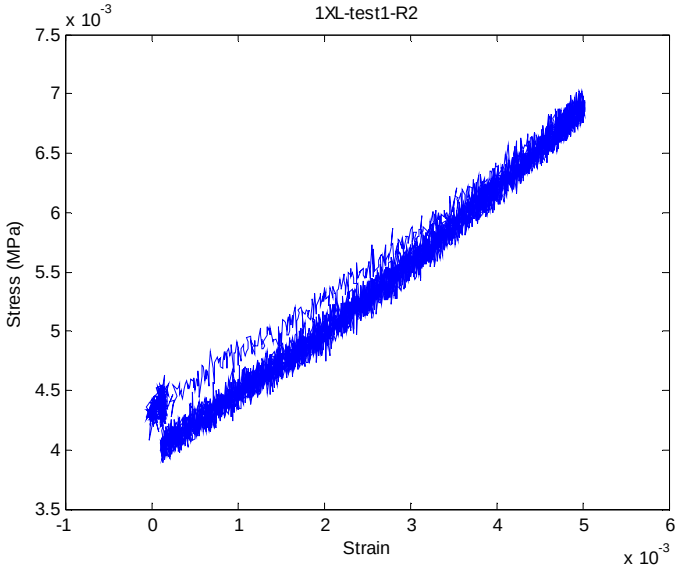

Figure 3-B-131. Stress-strain cycles of the XL structure #1 up to 0.5% strain without lubricant - run#2

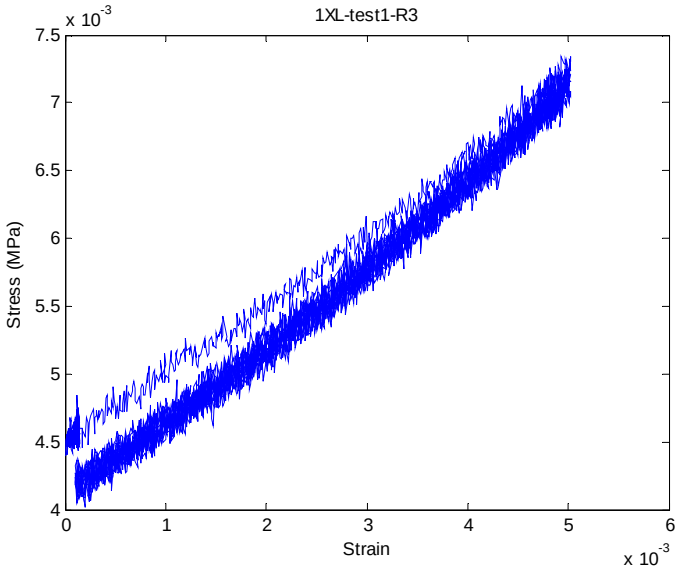

Figure 3-B-132. Stress-strain cycles of the XL structure #1 up to 0.5% strain without lubricant - run#3

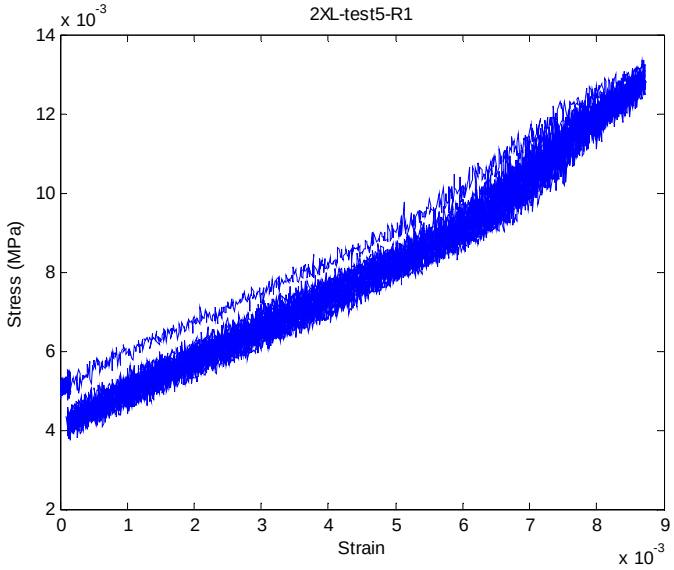

Figure 3-B-133. Stress-strain cycles of the XL structure #2 up 1.0% - run#1

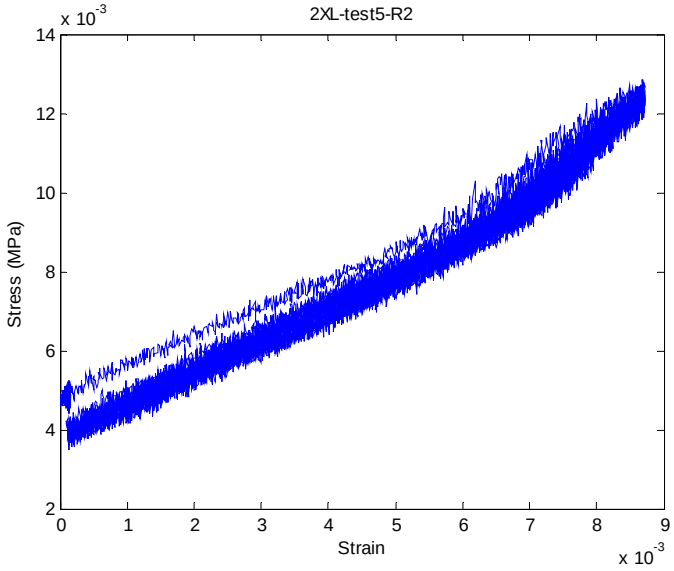

Figure 3-B-134. Stress-strain cycles of the XL structure #2 up 1.0% - run#2

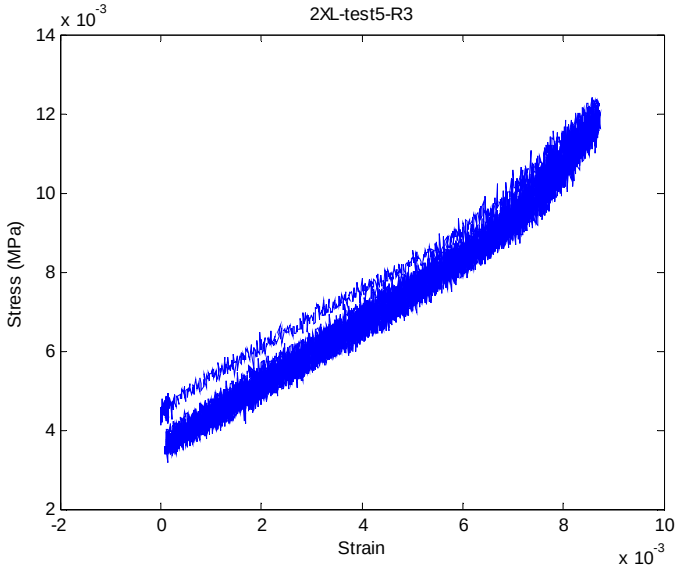

Figure 3-B-135. Stress-strain cycles of the XL structure #2 up 1.0% - run#3

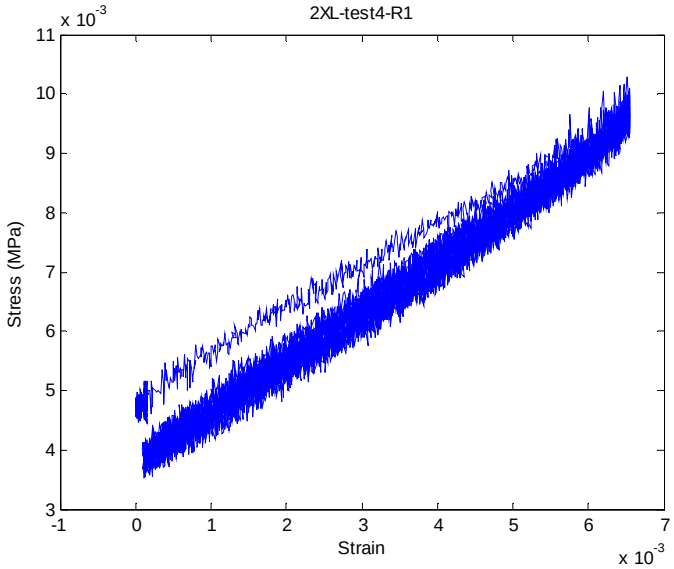

Figure 3-B-136. Stress-strain cycles of the XL structure #2 up 0.75% - run#1

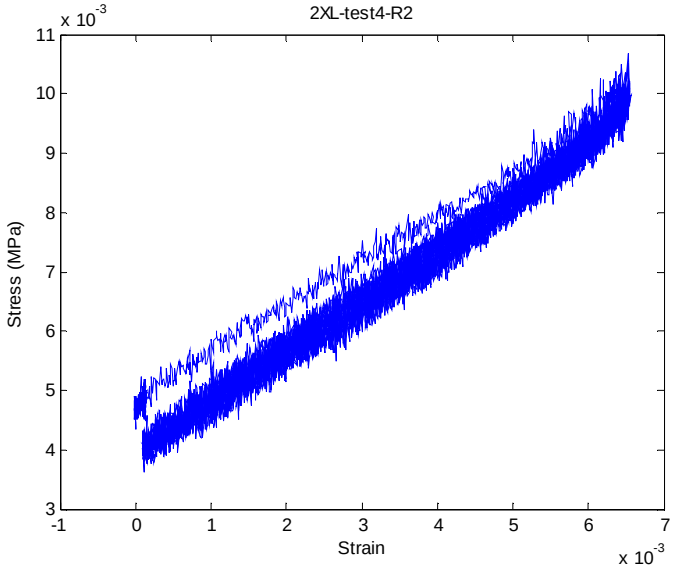

Figure 3-B-137. Stress-strain cycles of the XL structure #2 up 0.75% - run#2

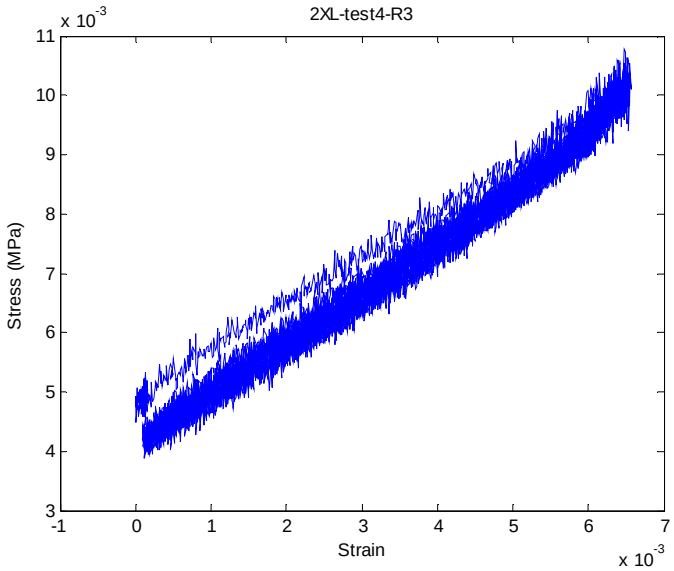

Figure 3-B-138. Stress-strain cycles of the XL structure #2 up 0.75% - run#3

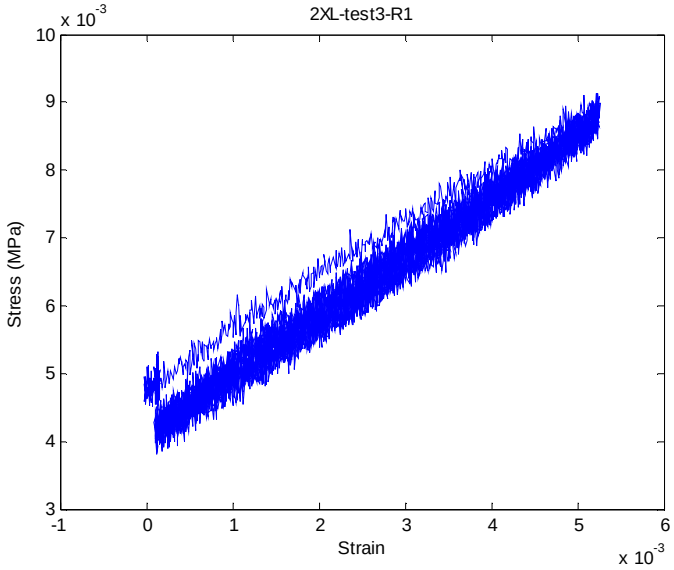

Figure 3-B-139. Stress-strain cycles of the XL structure #2 up 0.6% - run#1

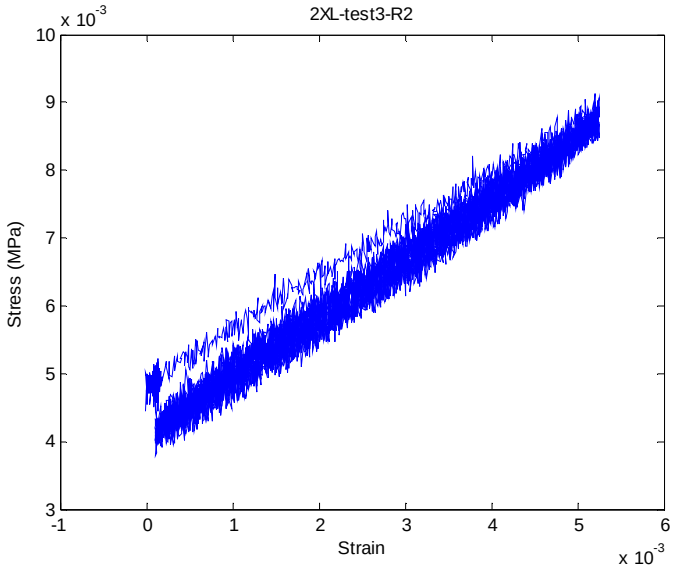

Figure 3-B-140. Stress-strain cycles of the XL structure #2 up 0.6% - run#2

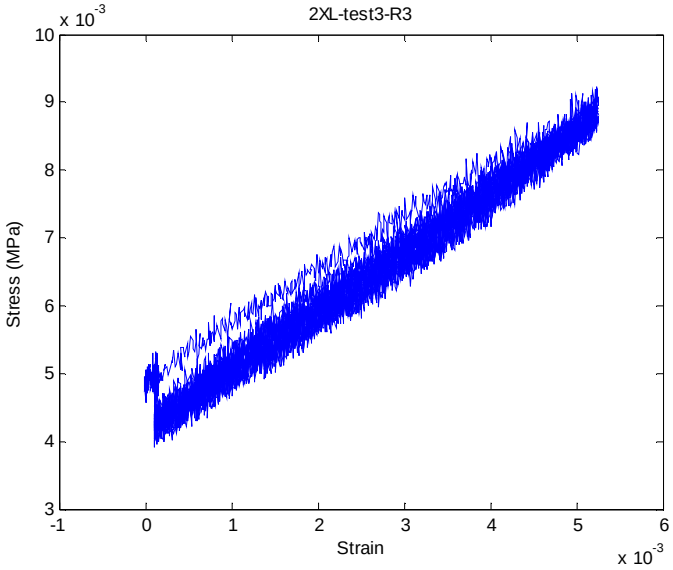

Figure 3-B-141. Stress-strain cycles of the XL structure #2 up 0.6% - run#3

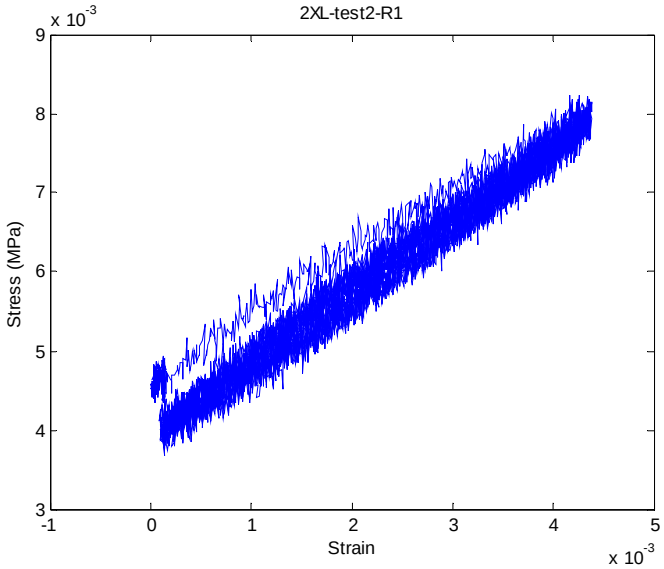

Figure 3-B-142. Stress-strain cycles of the XL structure #2 up 0.5% - run#1

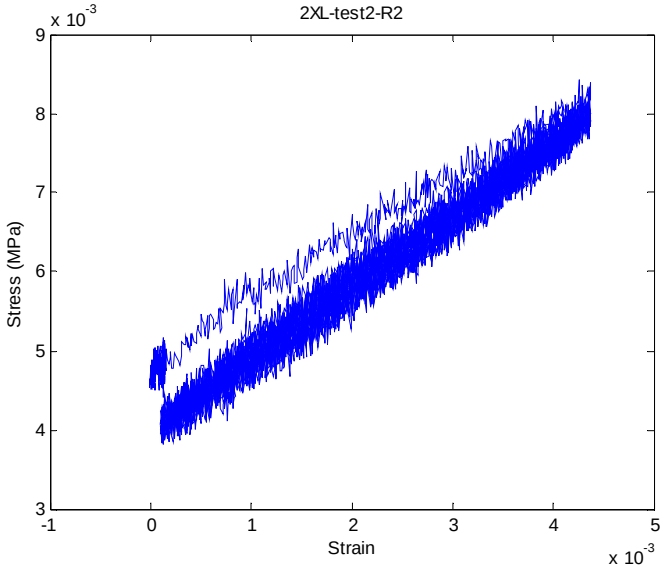

Figure 3-B-143. Stress-strain cycles of the XL structure #2 up 0.5% - run#2

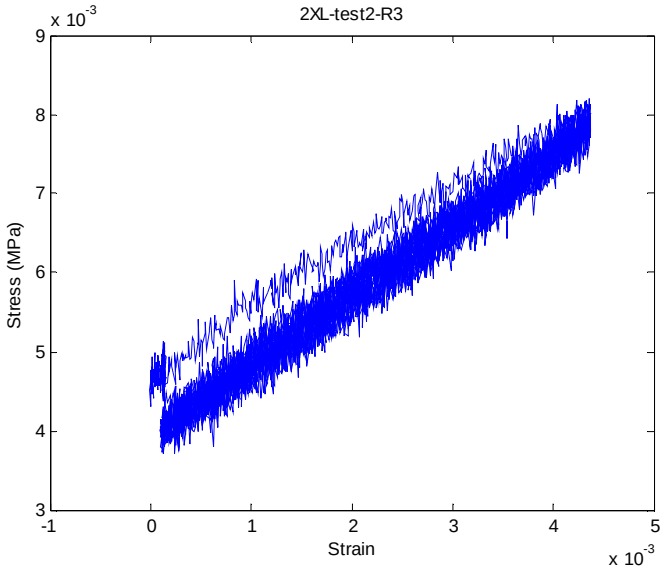

Figure 3-B-144. Stress-strain cycles of the XL structure #2 up 0.5% - run#3

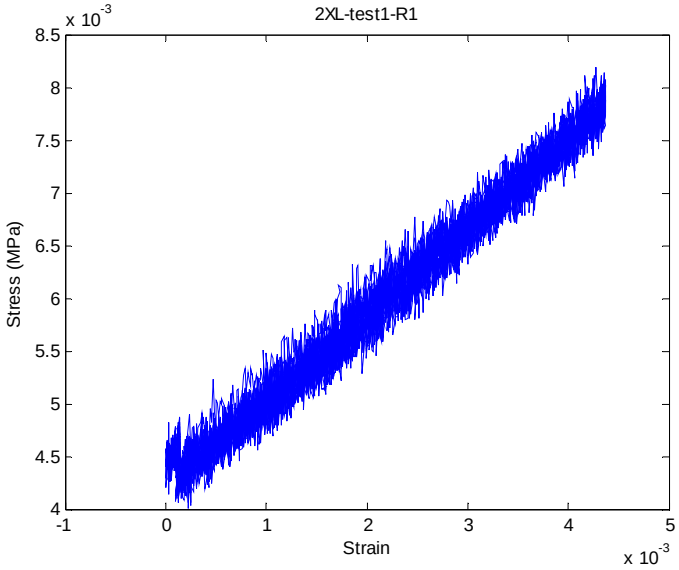

Figure 3-B-145. Stress-strain cycles of the XL structure #2 up 0.5% without lubricant - run#1

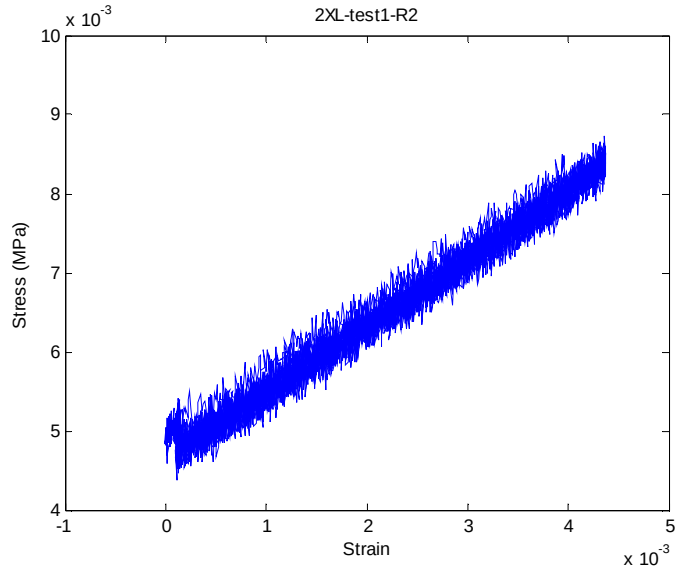

Figure 3-B-146. Stress-strain cycles of the XL structure #2 up 0.5% without lubricant - run#2

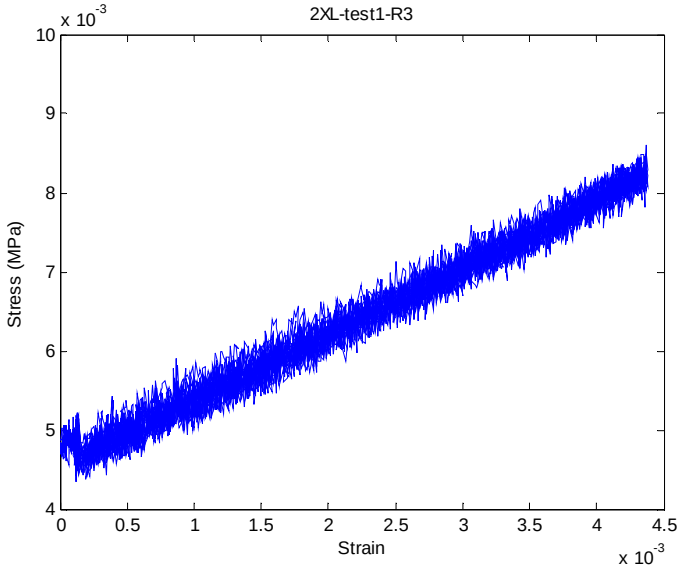

Figure 3-B-147. Stress-strain cycles of the XL structure #2 up 0.5% without lubricant - run#3

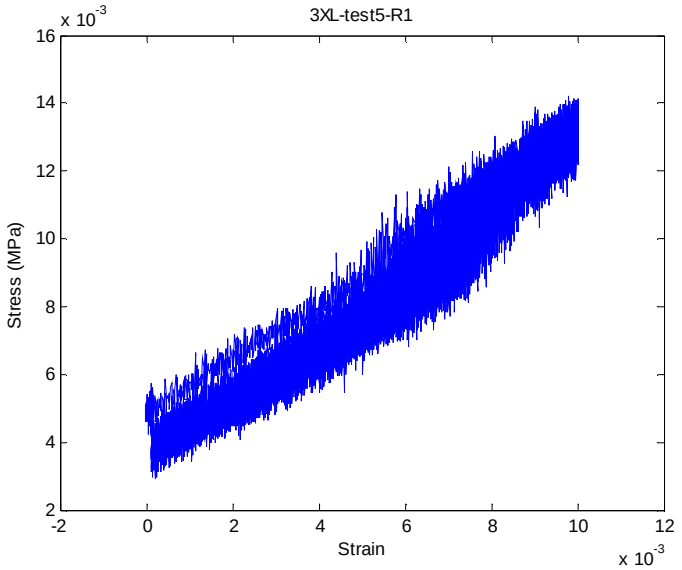

Figure 3-B-148. Stress-strain cycles of the XL structure #3 up 1.0% - run#1

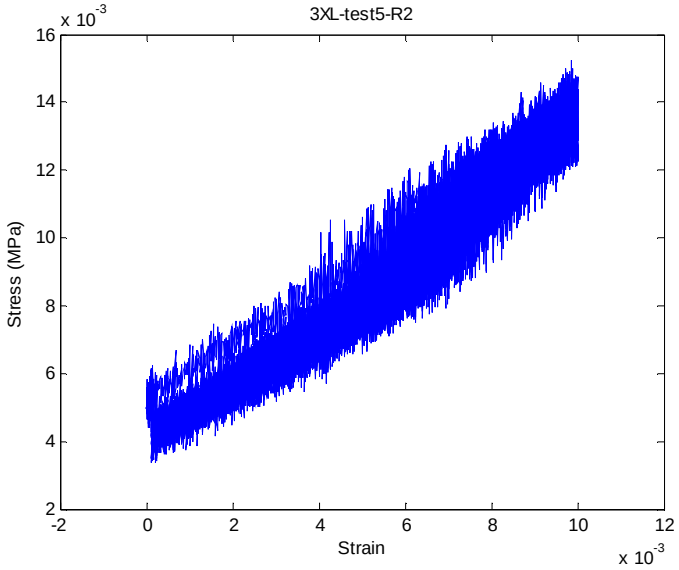

Figure 3-B-149. Stress-strain cycles of the XL structure #3 up 1.0% - run#2

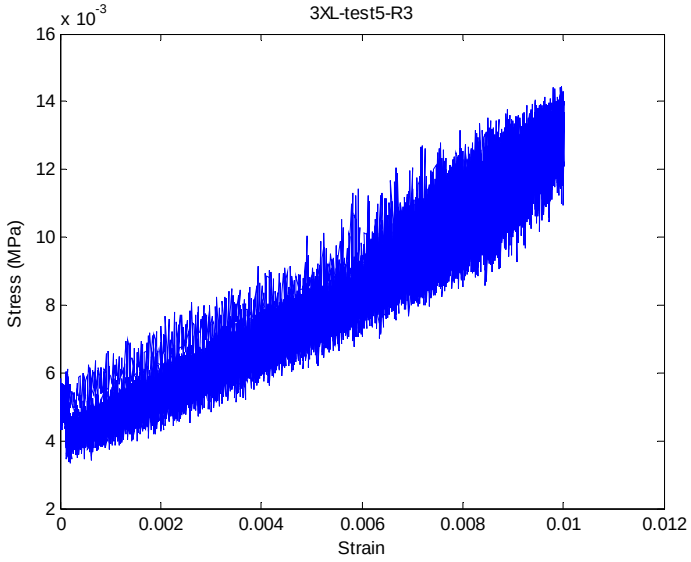

Figure 3-B-150. Stress-strain cycles of the XL structure #3 up 1.0% - run#3

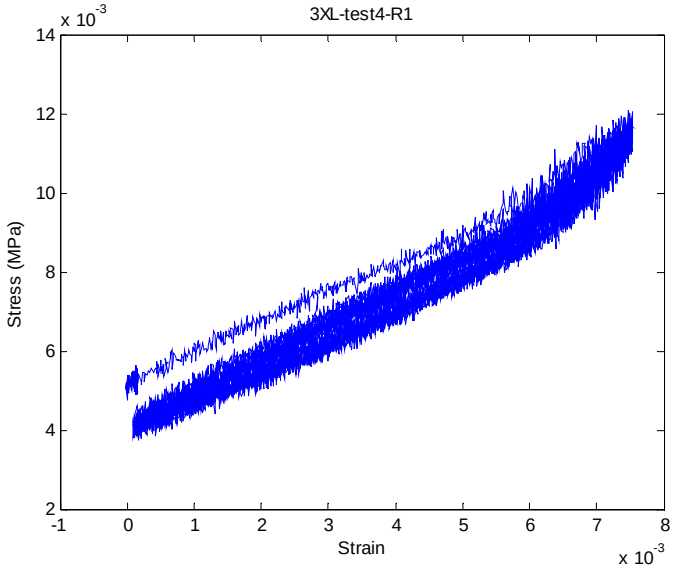

Figure 3-B-151. Stress-strain cycles of the XL structure #3 up 0.75% - run#1

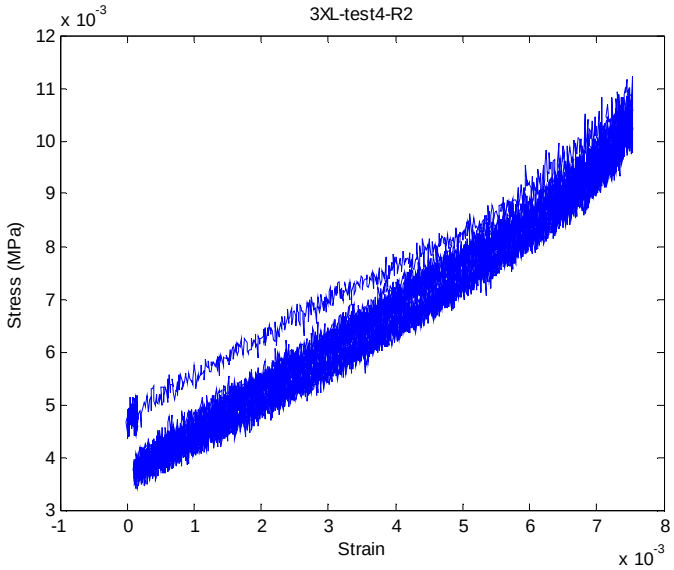

Figure 3-B-152. Stress-strain cycles of the XL structure #3 up 0.75% - run#2

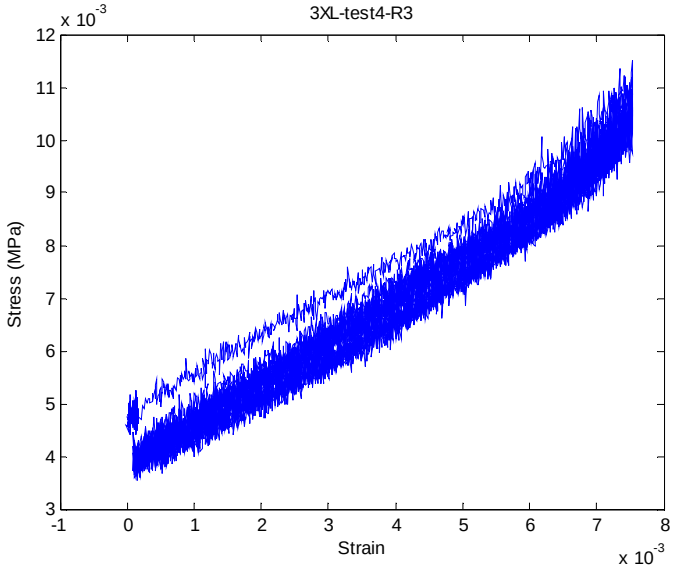

Figure 3-B-153. Stress-strain cycles of the XL structure #3 up 0.75% - run#3

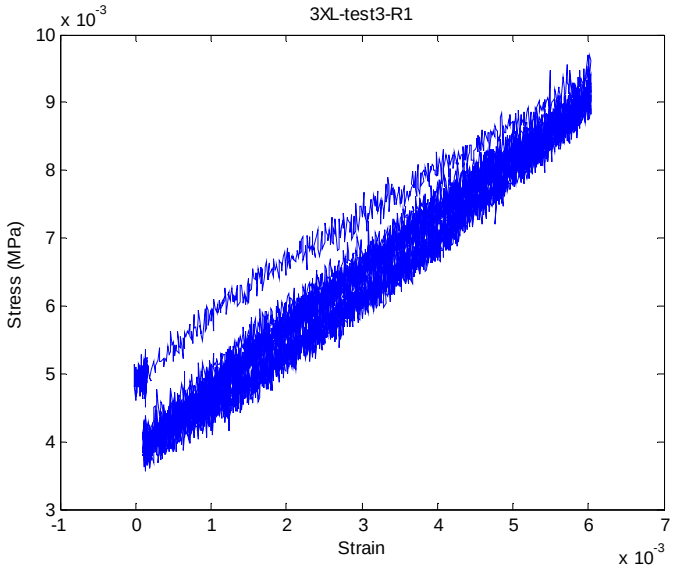

Figure 3-B-154. Stress-strain cycles of the XL structure #3 up 0.6% - run#1

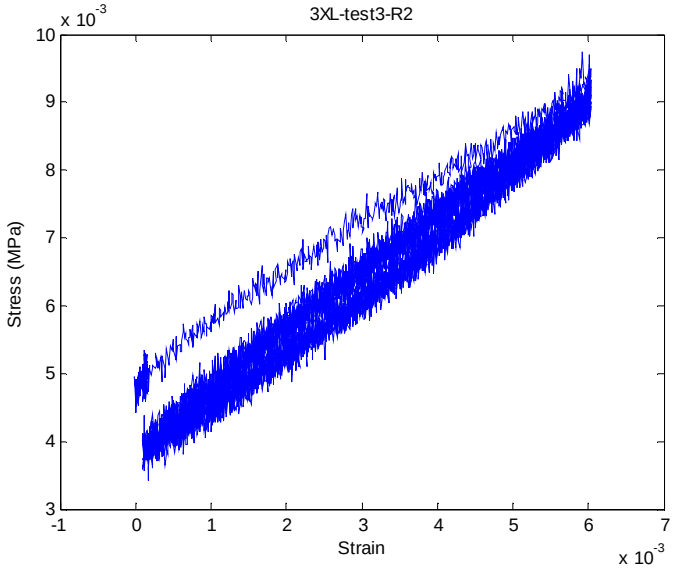

Figure 3-B-155. Stress-strain cycles of the XL structure #3 up 0.6% - run#2

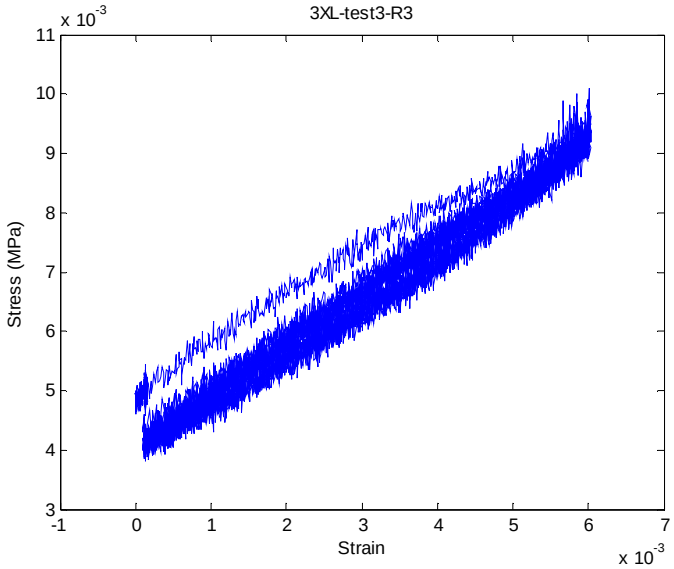

Figure 3-B-156. Stress-strain cycles of the XL structure #3 up 0.6% - run#3

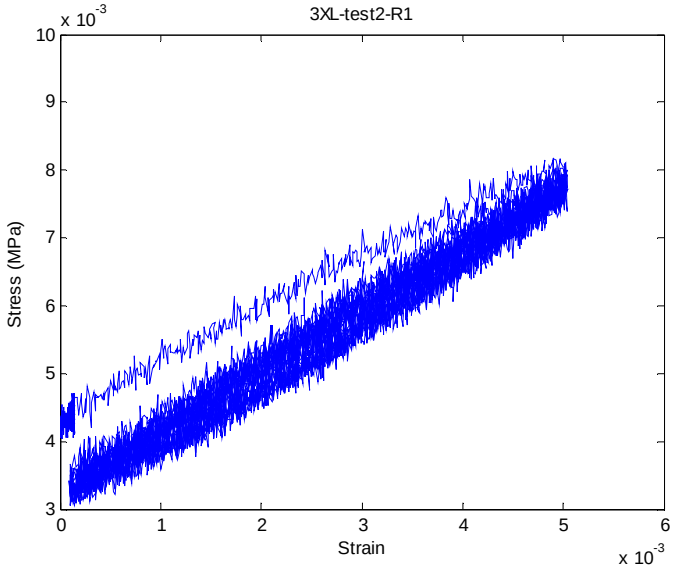

Figure 3-B-157. Stress-strain cycles of the XL structure #3 up 0.5% - run#1

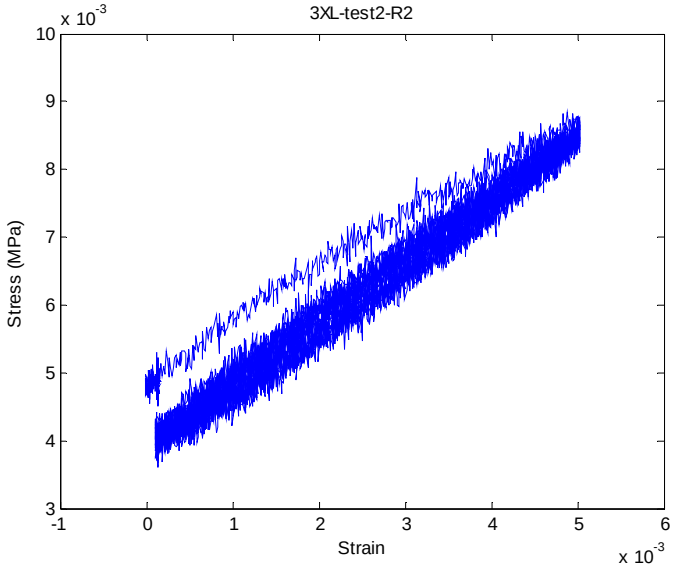

Figure 3-B-158. Stress-strain cycles of the XL structure #3 up 0.5% - run#2

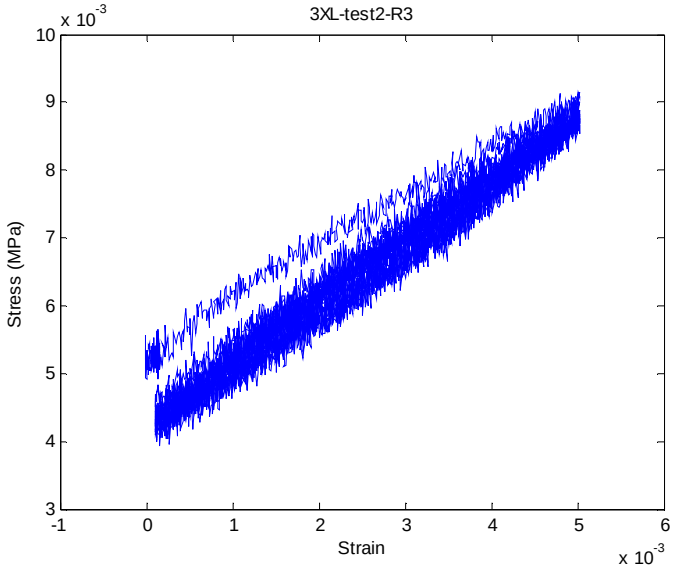

Figure 3-B-159. Stress-strain cycles of the XL structure #3 up 0.5% - run#3

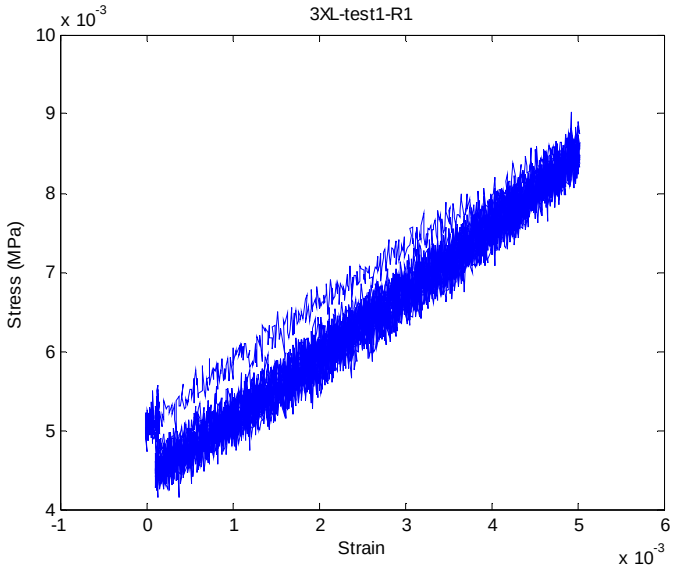

Figure 3-B-160. Stress-strain cycles of the XL structure #3 up 0.5% without lubricant - run#1

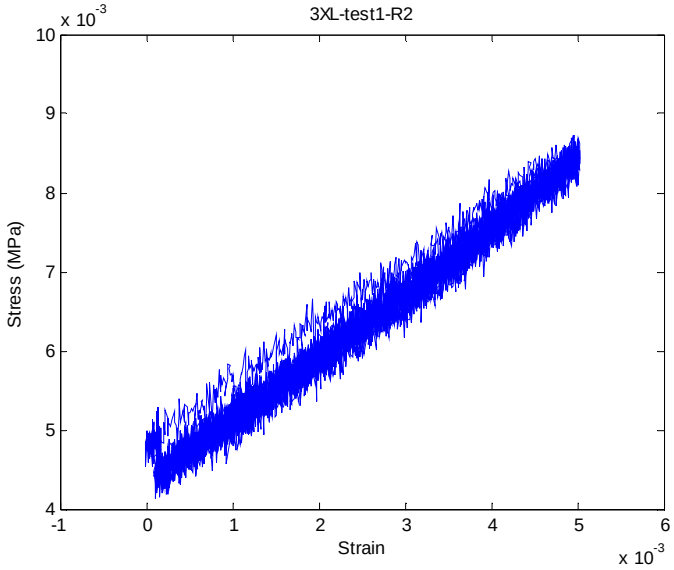

Figure 3-B-161. Stress-strain cycles of the XL structure #3 up 0.5% without lubricant - run#2

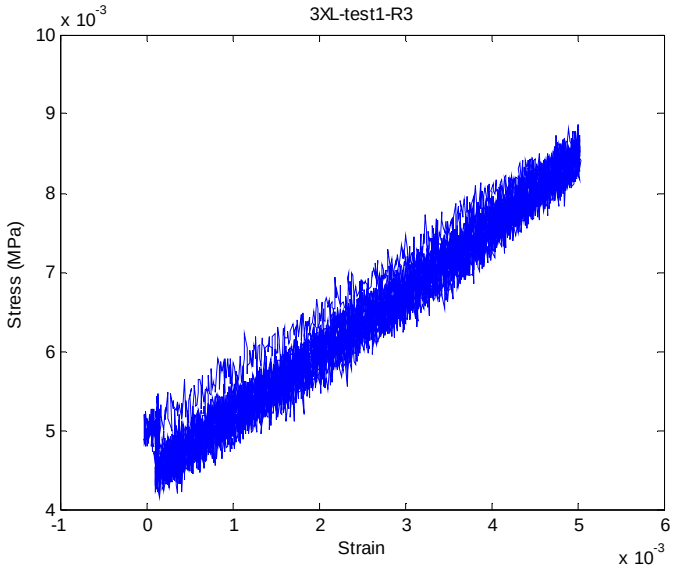

Figure 3-B-162. Stress-strain cycles of the XL structure #3 up 0.5% without lubricant - run#3

EXTRA-EXTRA-LARGE STRUCTURES

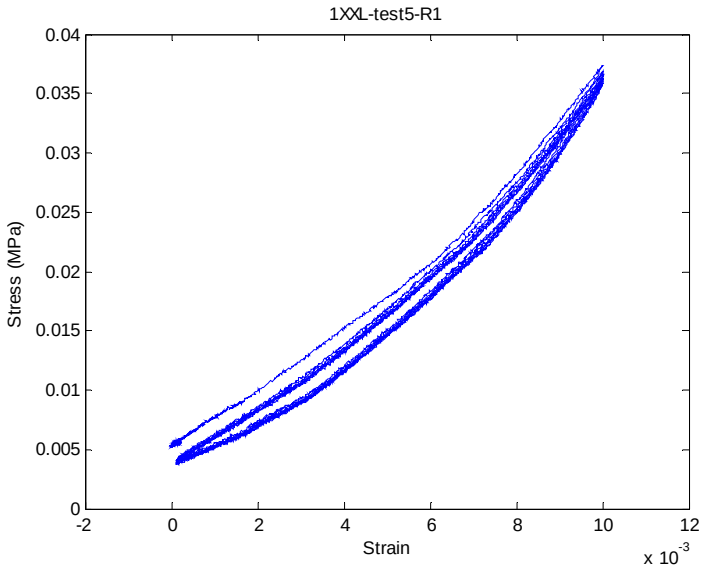

Figure 3-B-163. Stress-strain cycles of the XXL structure #1 up 1.0% - run#1

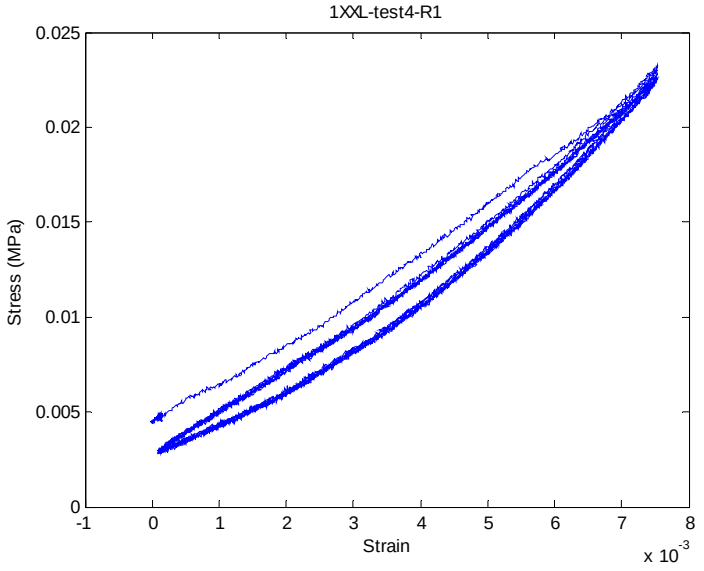

Figure 3-B-164. Stress-strain cycles of the XXL structure #1 up 0.75% - run#1

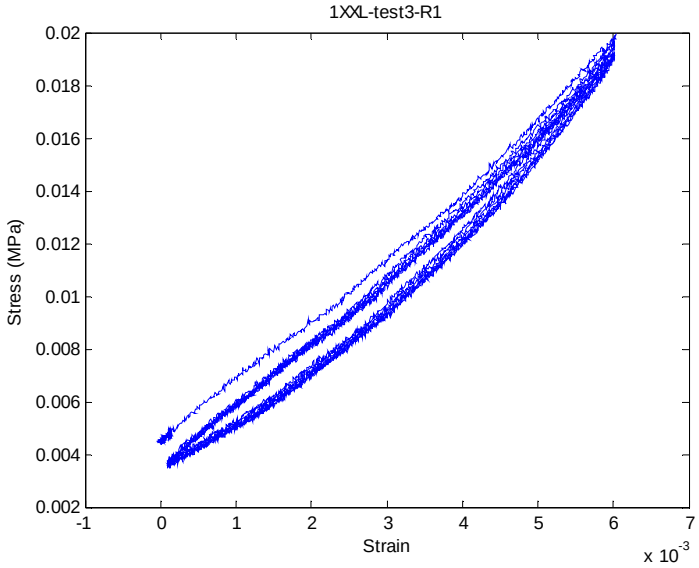

Figure 3-B-165. Stress-strain cycles of the XXL structure #1 up 0.6% - run#1

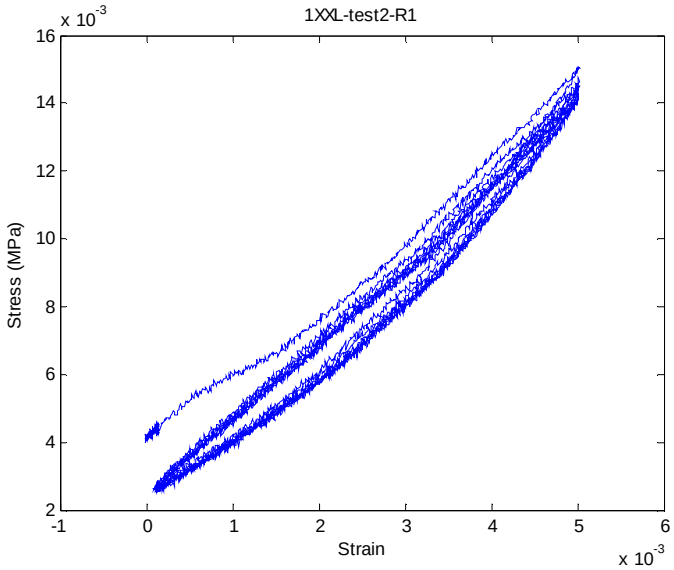

Figure 3-B-166. Stress-strain cycles of the XXL structure #1 up 0.5% - run#1

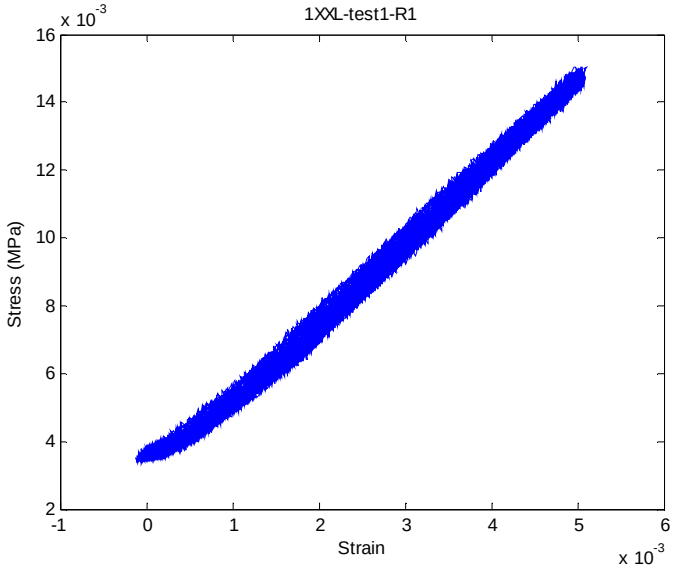

Figure 3-B-167. Stress-strain cycles of the XXL structure #1 up 1.0% without lubricant - run#1

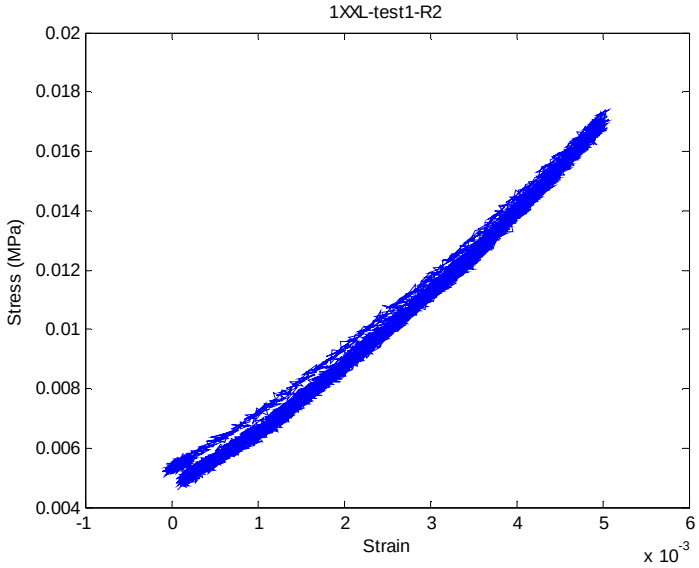

Figure 3-B-168. Stress-strain cycles of the XXL structure #1 up 1.0% without lubricant - run#2

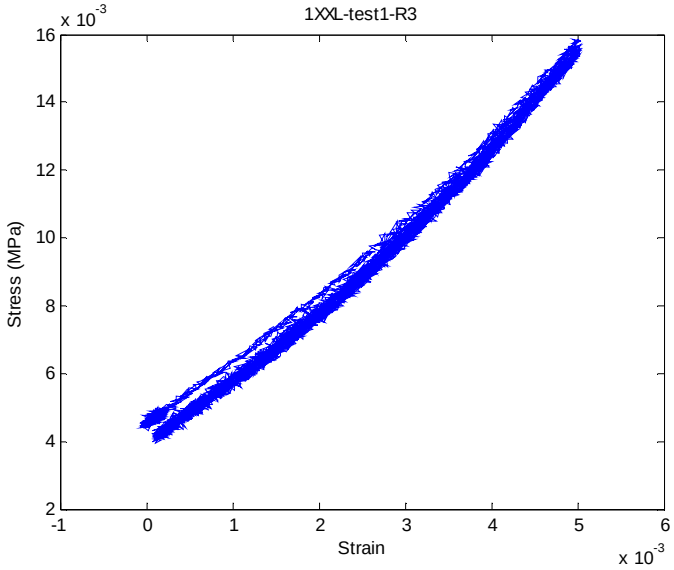

Figure 3-B-169. Stress-strain cycles of the XXL structure #1 up 1.0% without lubricant - run#3

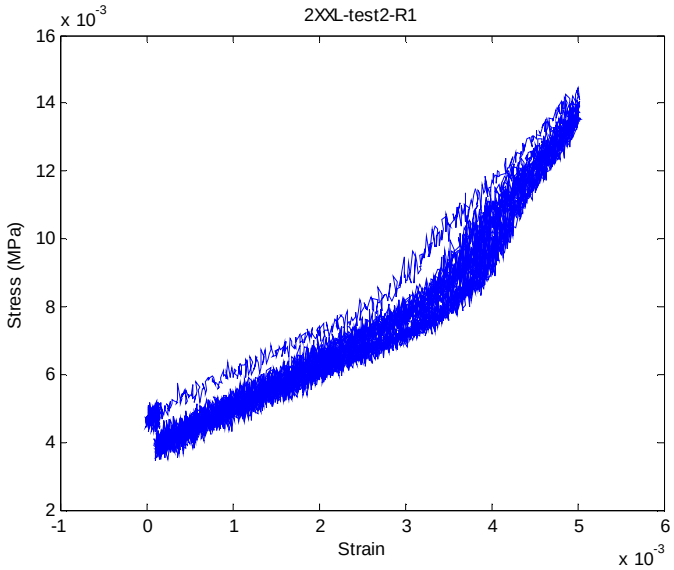

Figure 3-B-170. Stress-strain cycles of the XXL structure #2 up 0.5% - run#1

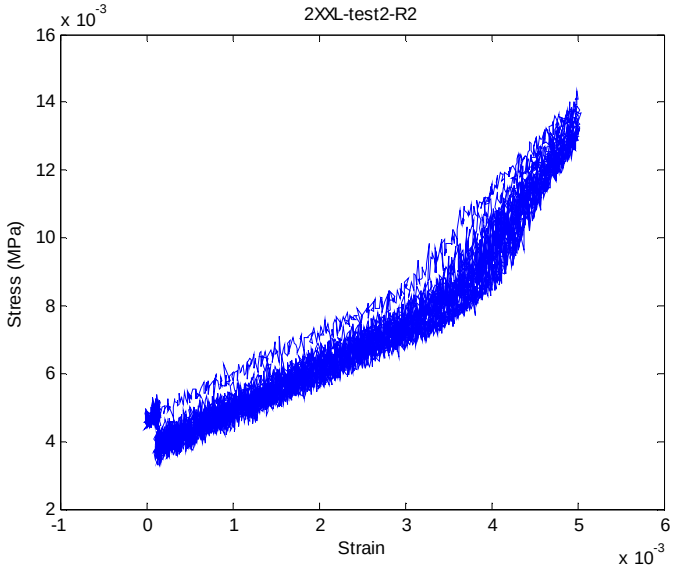

Figure 3-B-171. Stress-strain cycles of the XXL structure #2 up 0.5% - run#2

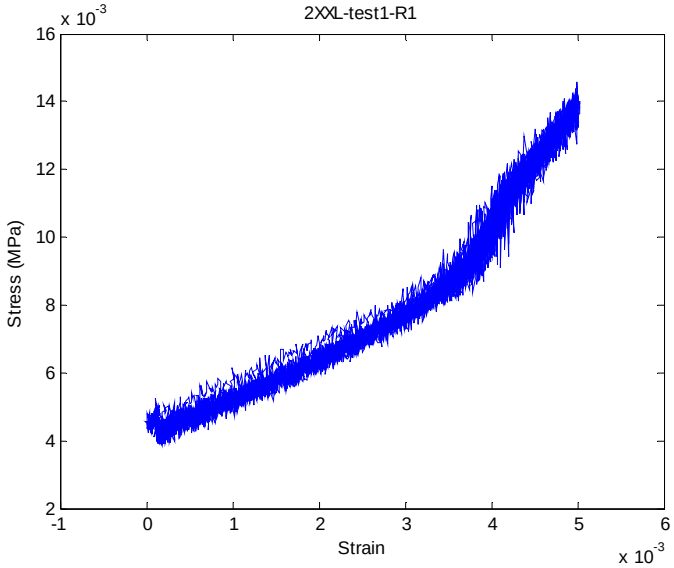

Figure 3-B-172. Stress-strain cycles of the XXL structure #2 up 0.5% without lubricant - run#1

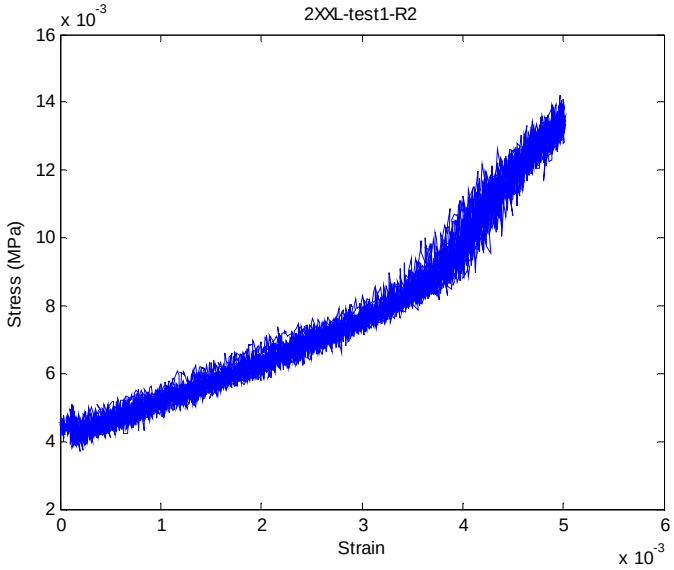

Figure 3-B-173. Stress-strain cycles of the XXL structure #2 up 0.5% without lubricant - run#2

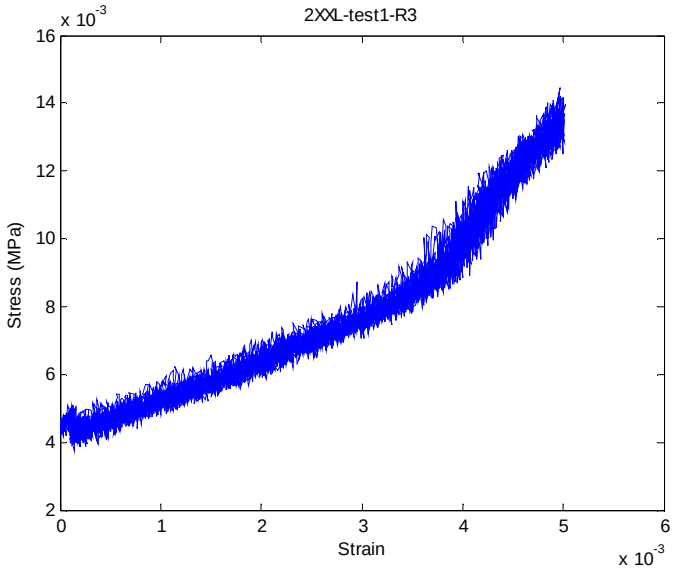

Figure 3-B-174. Stress-strain cycles of the XXL structure #2 up 0.5% without lubricant - run#3

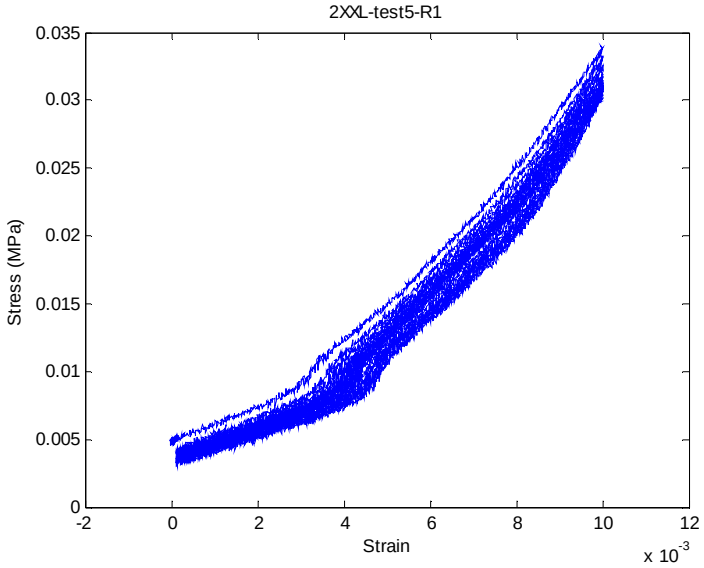

Figure 3-B-175. Stress-strain cycles of the XXL structure #2 up 1.0% - run#1

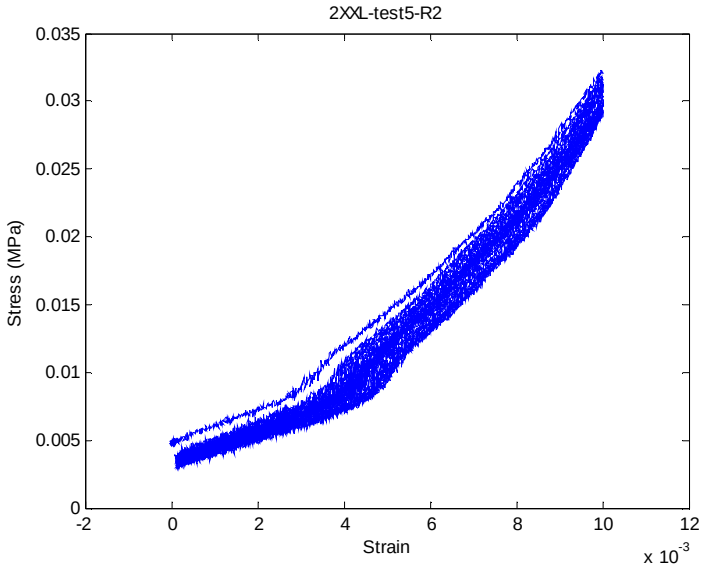

Figure 3-B-176 Stress-strain cycles of the XXL structure #2 up 1.0% - run#2

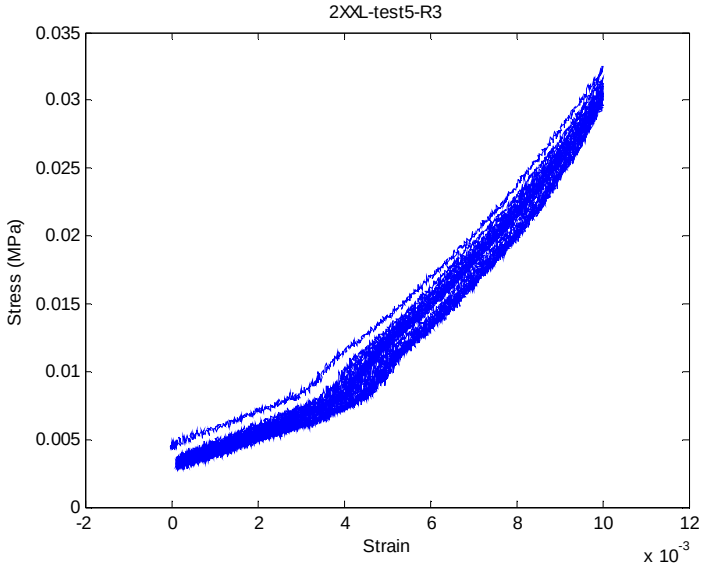

Figure 3-B-177. Stress-strain cycles of the XXL structure #2 up 1.0% - run#3

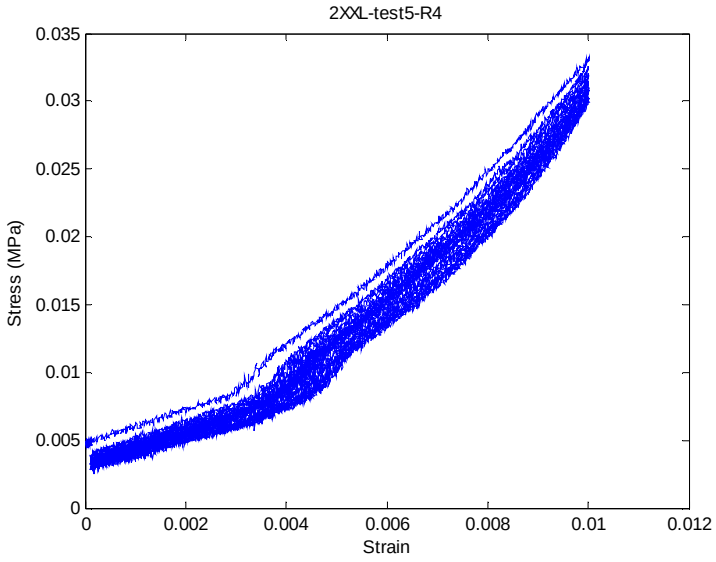

Figure 3-B-178. Stress-strain cycles of the XXL structure #2 up 1.0% - run#4

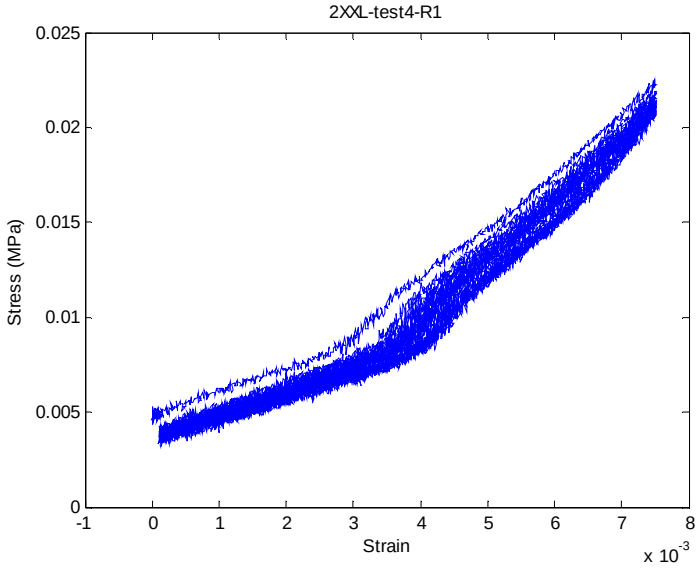

Figure 3-B-179. Stress-strain cycles of the XXL structure #2 up 0.75% - run#1

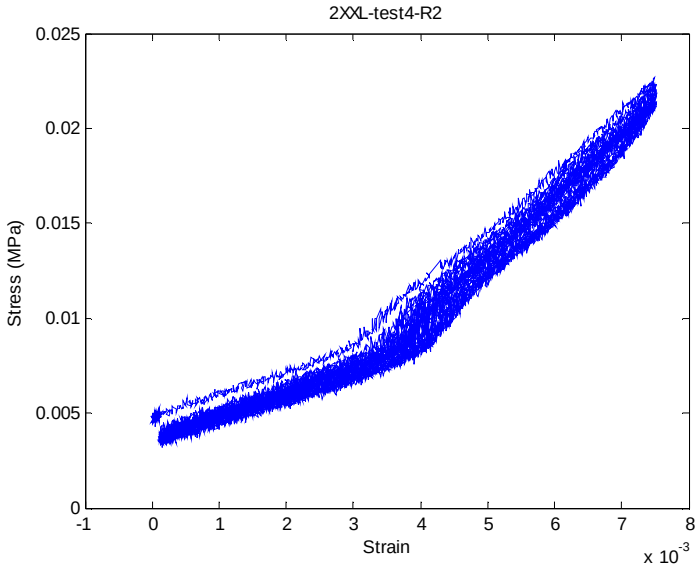

Figure 3-B-180. Stress-strain cycles of the XXL structure #2 up 0.75% - run#2

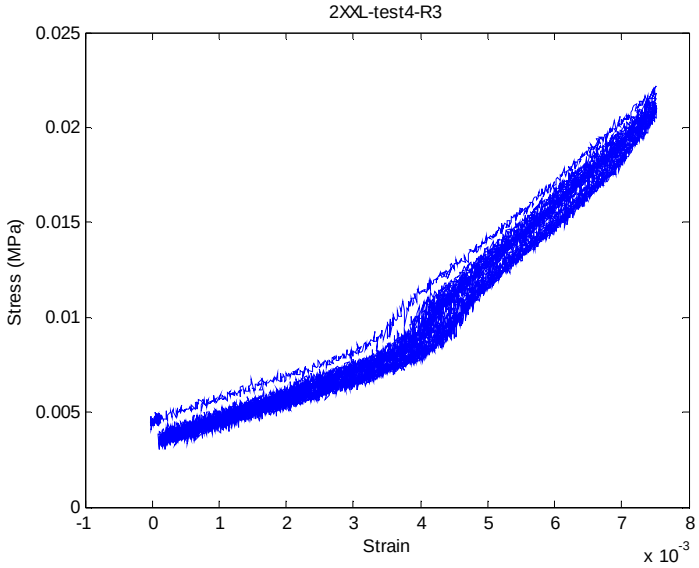

Figure 3-B-181. Stress-strain cycles of the XXL structure #2 up 0.75% - run#3

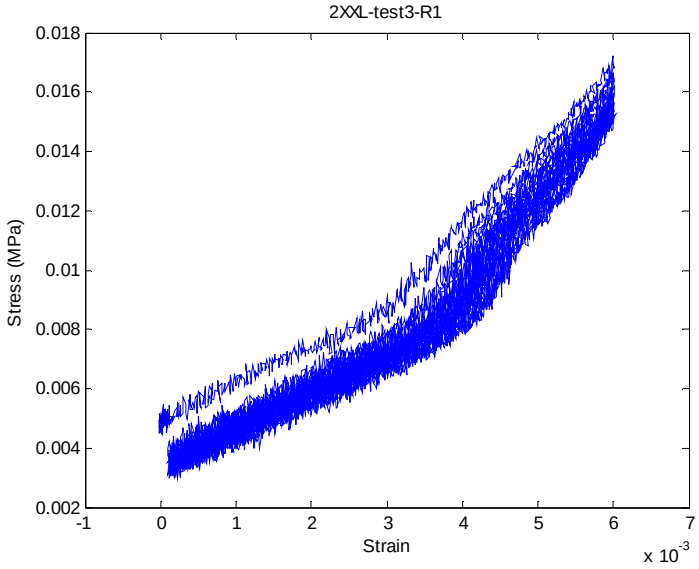

Figure 3-B-182. Stress-strain cycles of the XXL structure #2 up 0.6% - run#1

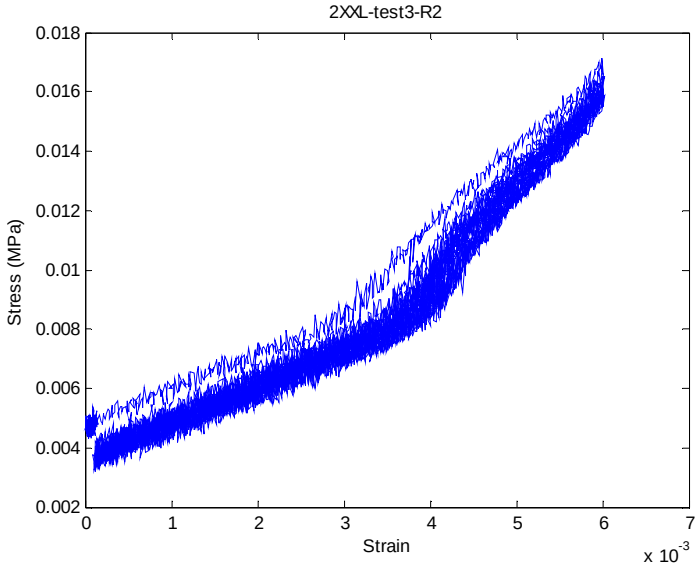

Figure 3-B-183. Stress-strain cycles of the XXL structure #2 up 0.6% - run#2

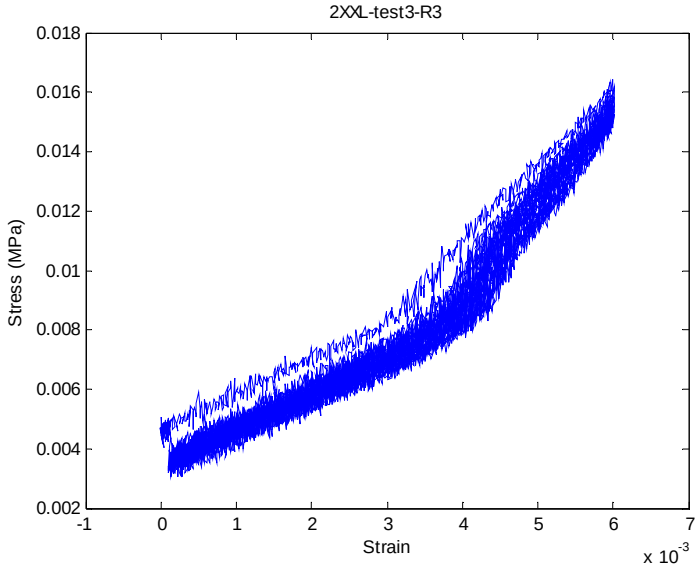

Figure 3-B-184. Stress-strain cycles of the XXL structure #2 up 0.6% - run#3

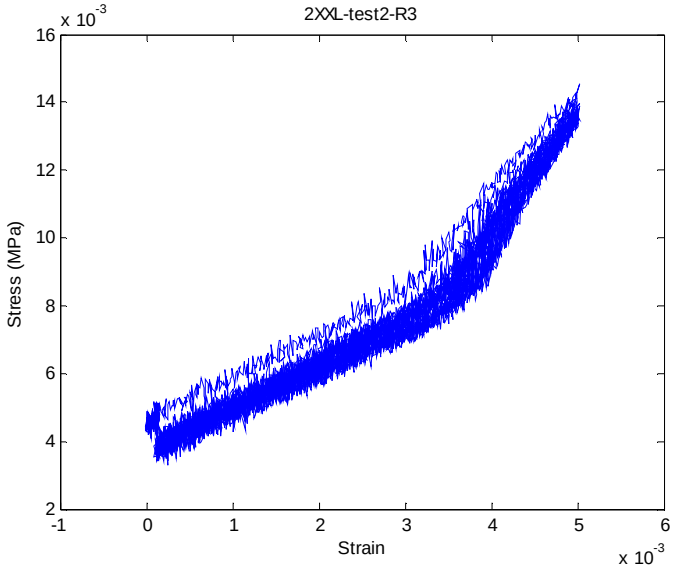

Figure 3-B-185. Stress-strain cycles of the XXL structure #2 up 0.5% - run#1

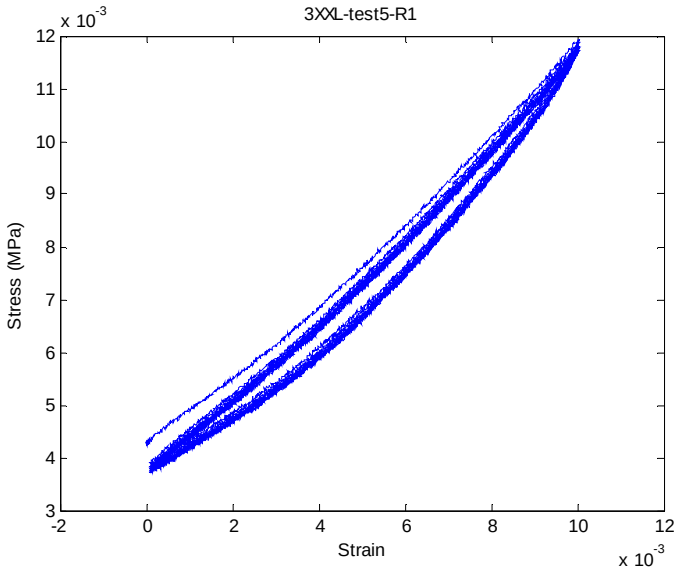

Figure 3-B-186. Stress-strain cycles of the XXL structure #3 up 1.0% - run#1

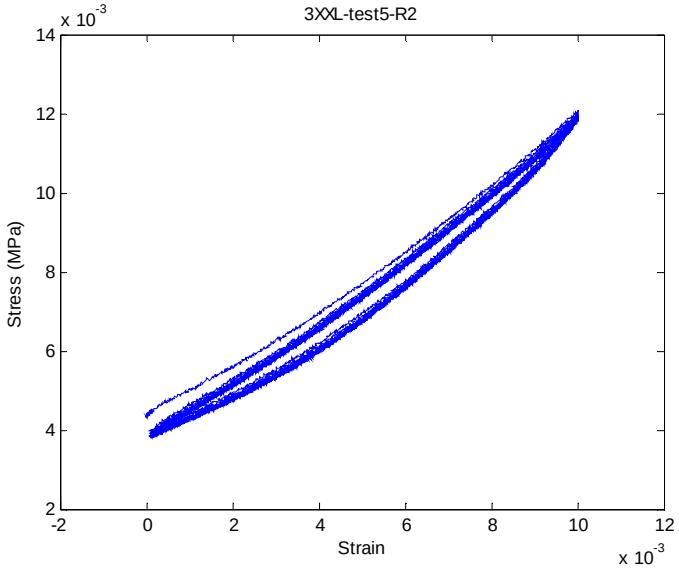

Figure 3-B-187. Stress-strain cycles of the XXL structure #3 up 1.0% - run#2

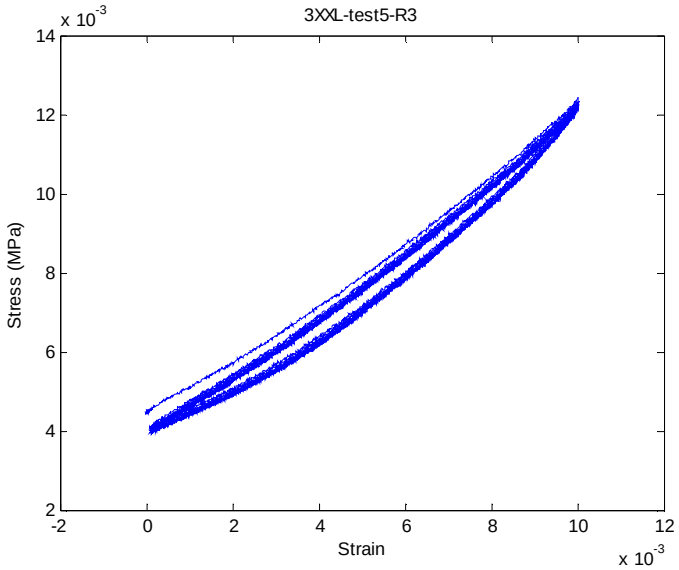

Figure 3-B-188. Stress-strain cycles of the XXL structure #3 up 1.0% - run#3

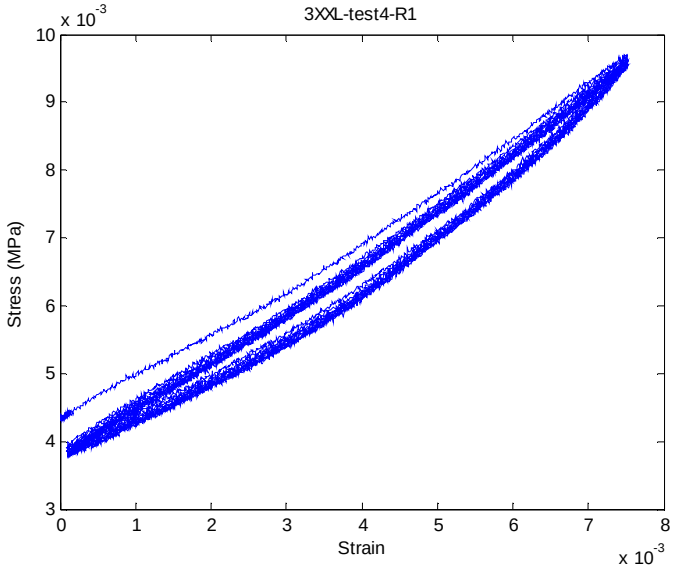

Figure 3-B-189. Stress-strain cycles of the XXL structure #3 up 0.75% - run#1

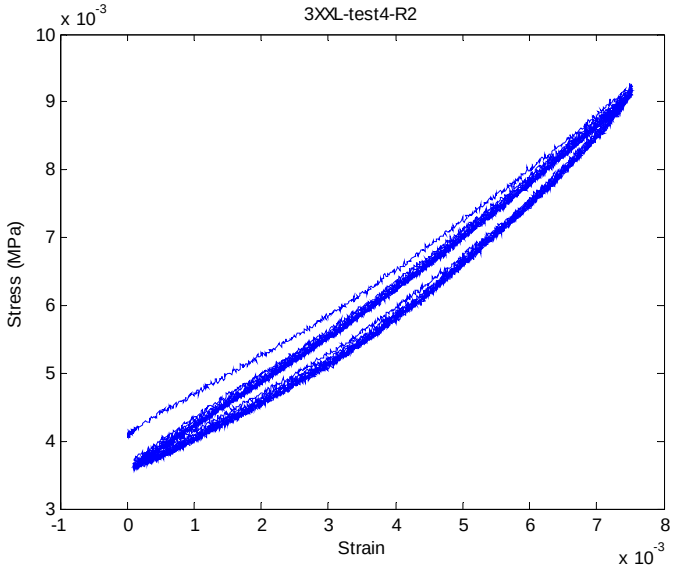

Figure 3-B-190. Stress-strain cycles of the XXL structure #3 up 0.75% - run#2

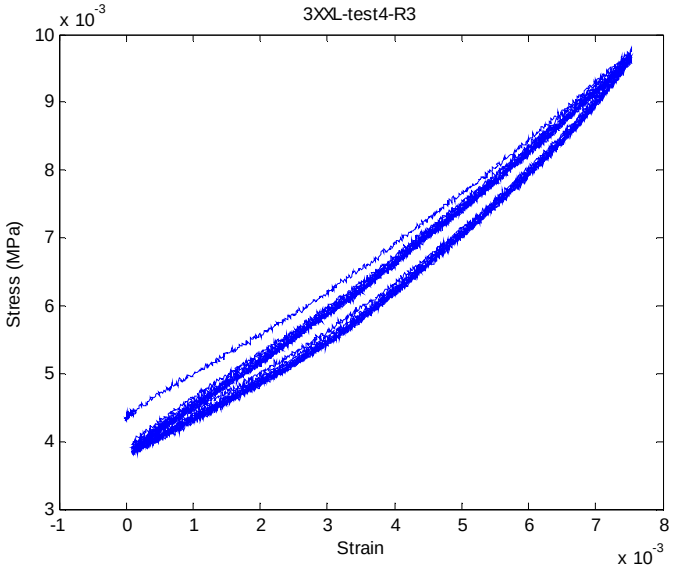

Figure 3-B-191. Stress-strain cycles of the XXL structure #3 up 0.75% - run#3

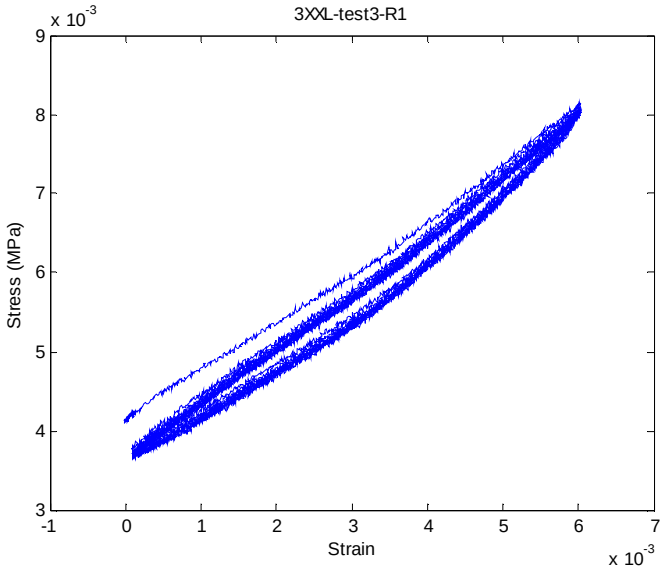

Figure 3-B-192. Stress-strain cycles of the XXL structure #3 up 0.6% - run#1

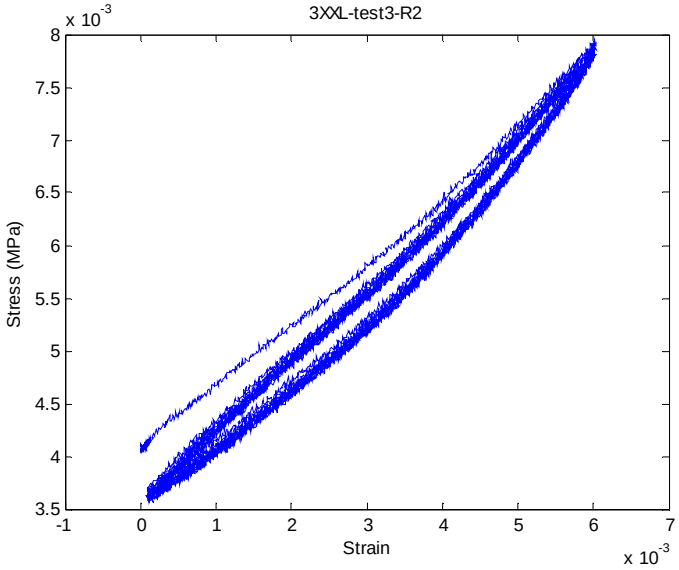

Figure 3-B-193. Stress-strain cycles of the XXL structure #3 up 0.6% - run#2

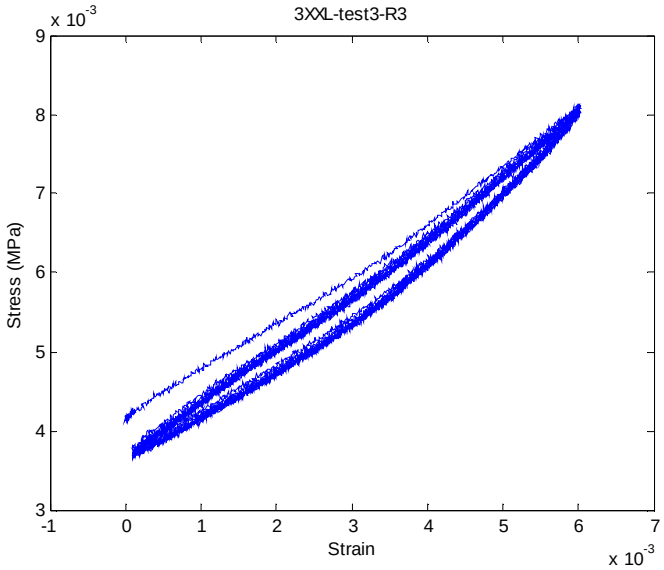

Figure 3-B-194. Stress-strain cycles of the XXL structure #3 up 0.6% - run#3

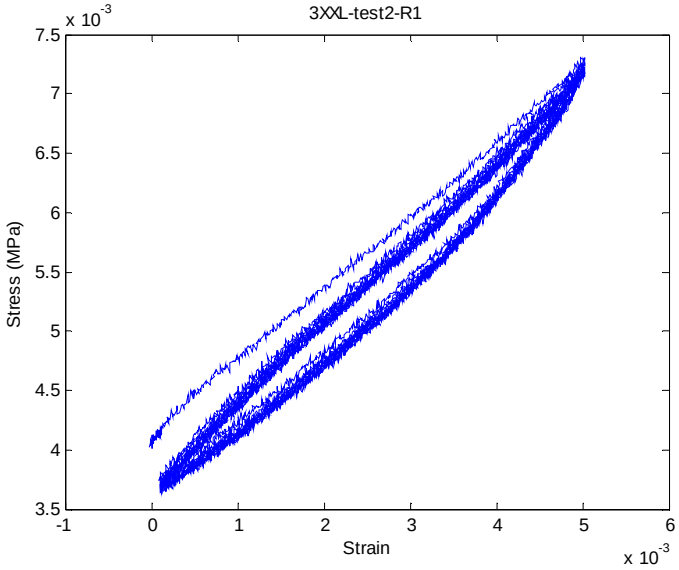

Figure 3-B-195. Stress-strain cycles of the XXL structure #3 up 0.5% - run#1

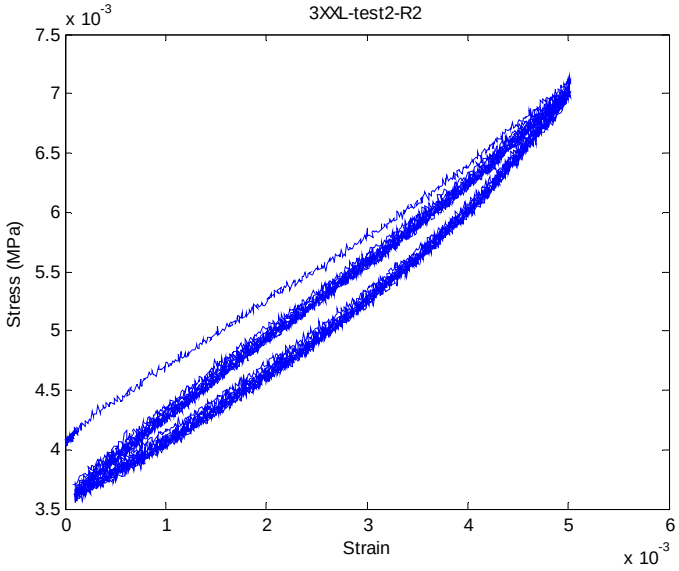

Figure 3-B-196. Stress-strain cycles of the XXL structure #3 up 0.5% - run#2

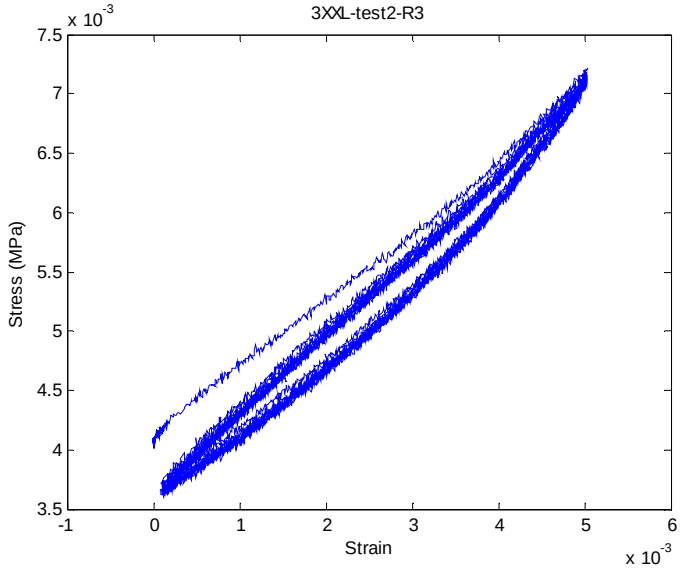

Figure 3-B-197. Stress-strain cycles of the XXL structure #3 up 0.5% - run#3

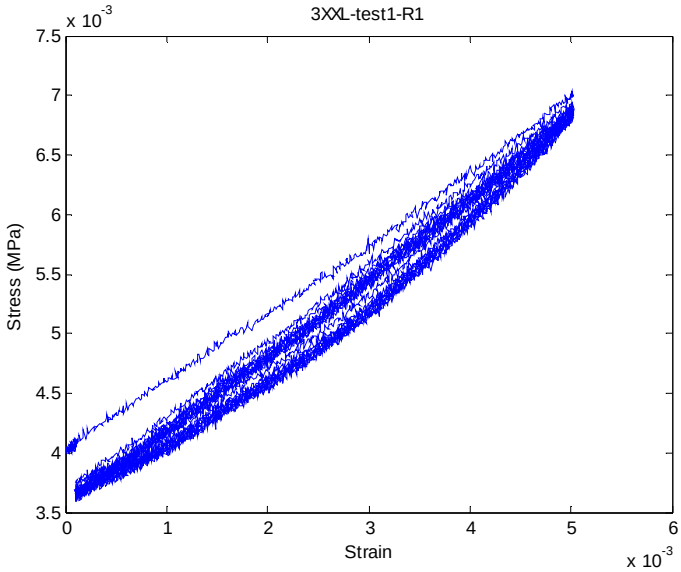

Figure 3-B-198. Stress-strain cycles of the XXL structure #3 up 0.5% without lubricant - run#1

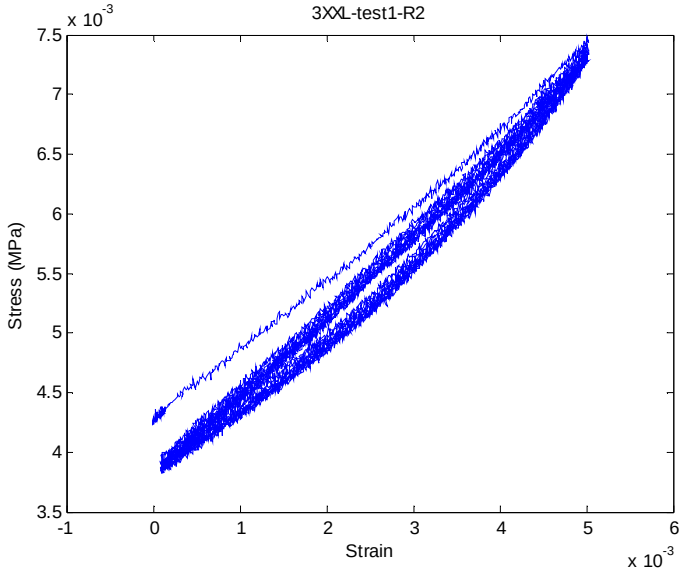

Figure 3-B-199. Stress-strain cycles of the XXL structure #3 up 0.5% without lubricant - run#2

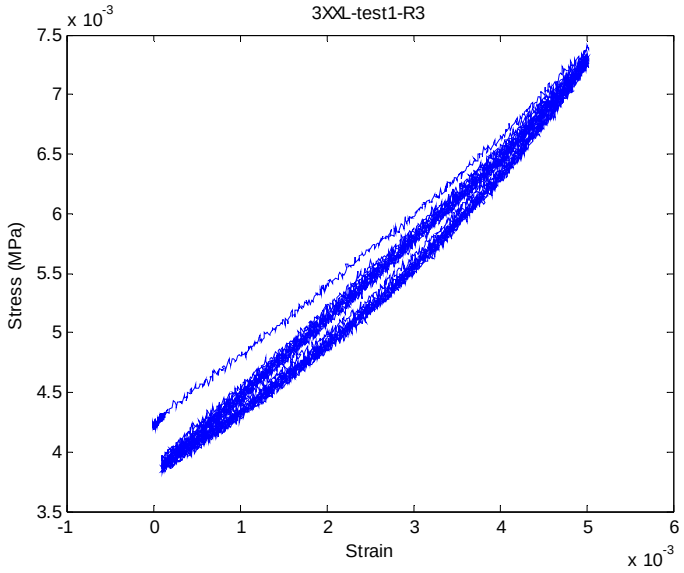

Figure 3-B-200. Stress-strain cycles of the XXL structure #3 up 0.5% without lubricant - run#3

Appendix 3-C. Coefficient A vs. relative density for all structure types at different strain levels

All structures were tested with lubrication unless noted otherwise.

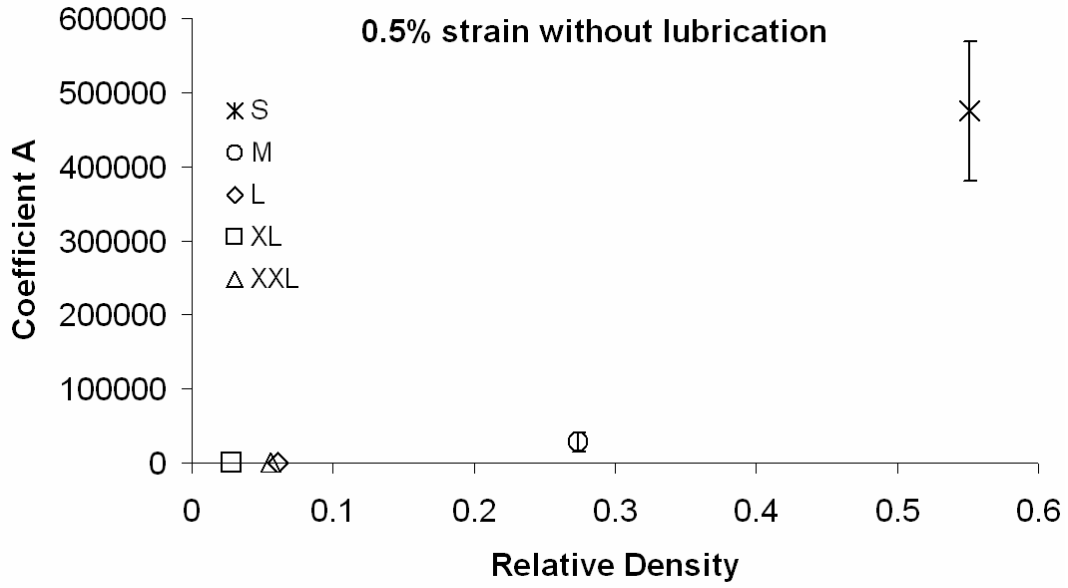

Figure 3-C-1. Coefficient A vs. relative density at 0.5% strain without lubricant

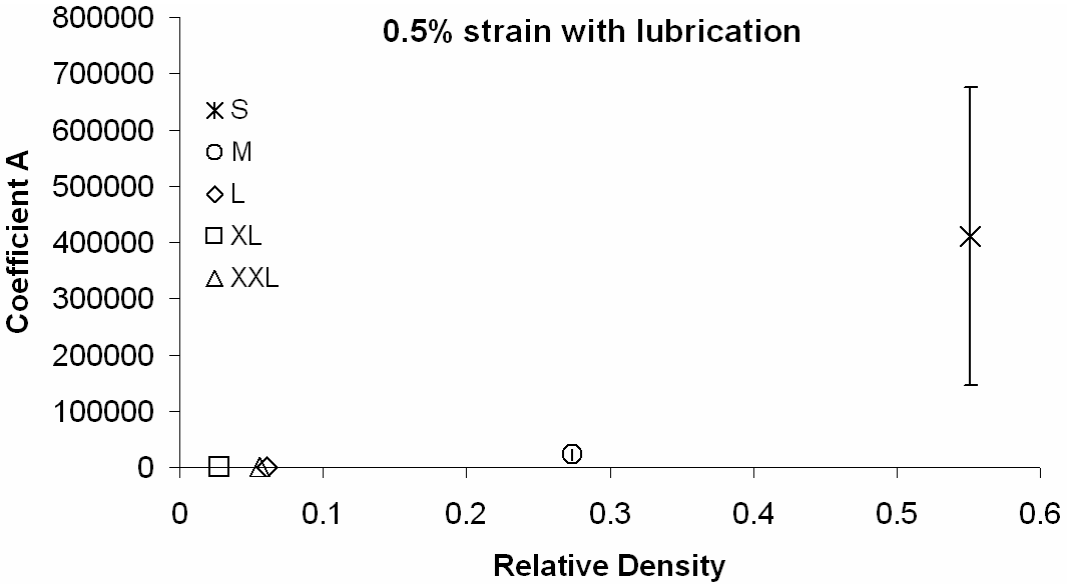

Figure 3-C-2. Coefficient A vs. relative density at 0.5% strain

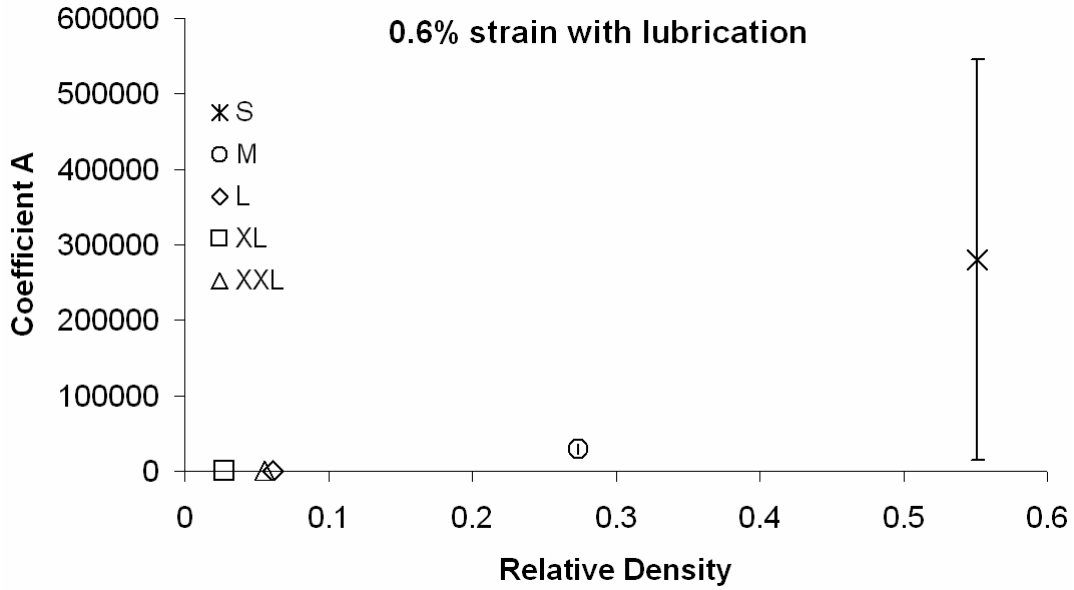

Figure 3-C-3. Coefficient A vs. relative density at 0.6% strain

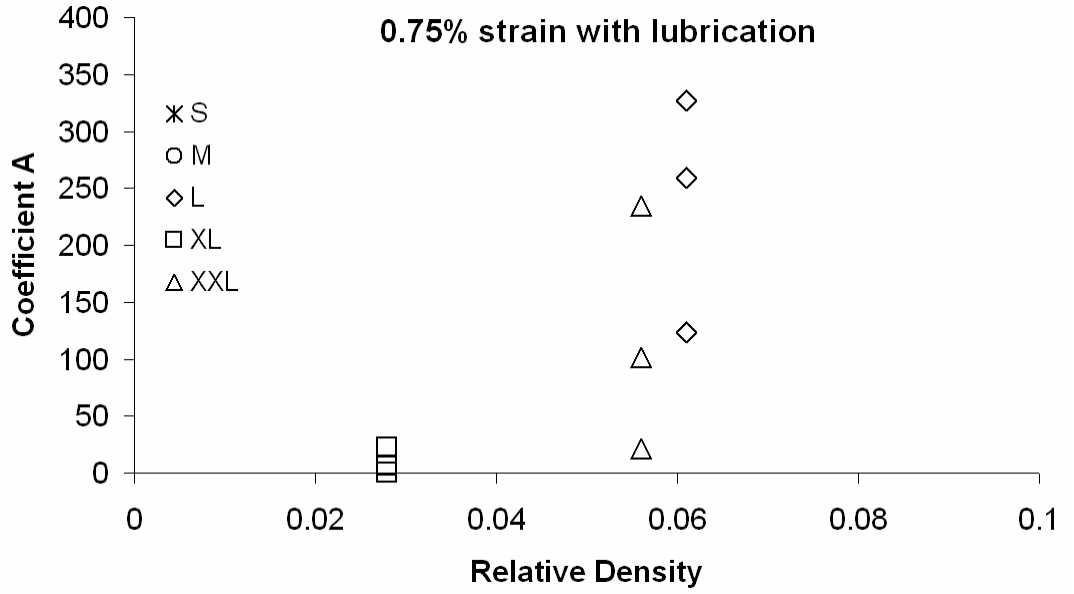

Figure 3-C-4. Coefficient A vs. relative density at 075% strain

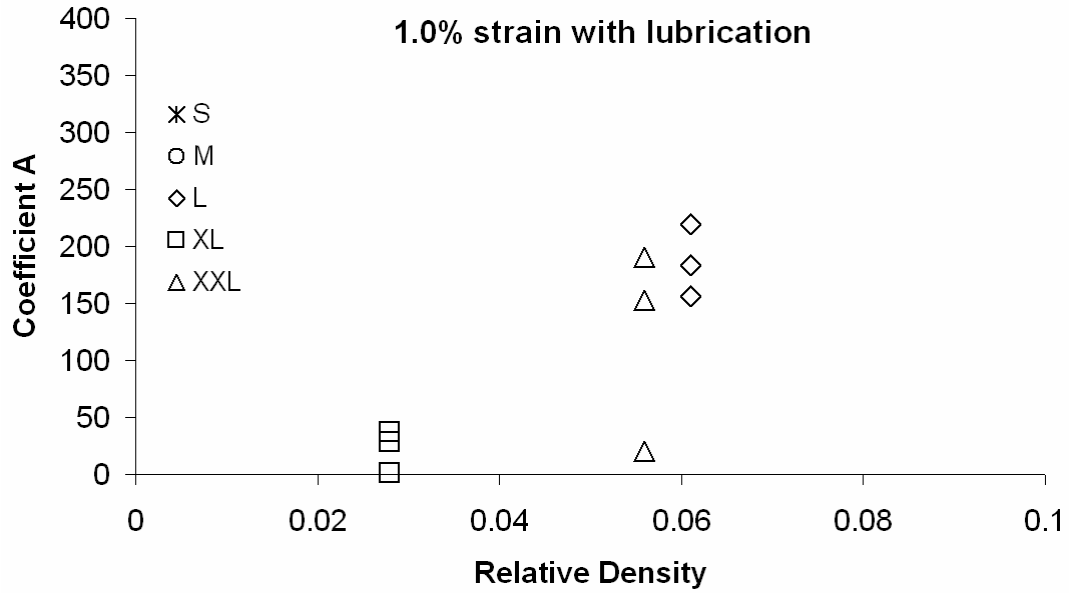

Figure 3-C-5. Coefficient A vs. relative density at 1.0% strain

Appendix 3-D. Coefficient B vs. relative density for all structure types at different strain levels

All structures were tested with lubrication unless noted otherwise.

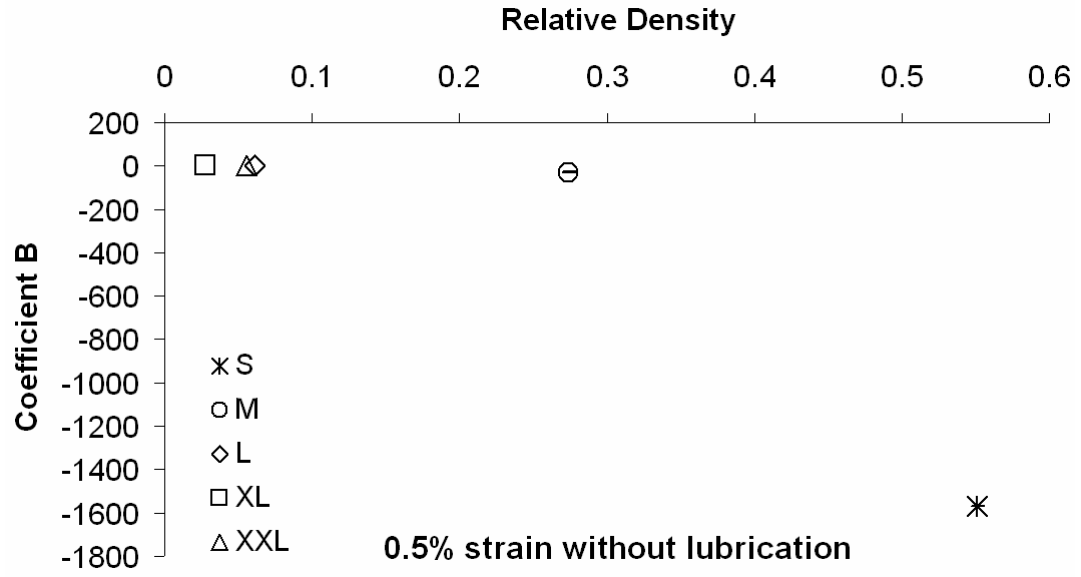

Figure 3-D-1. Coefficient B vs. relative density at 0.5% strain without lubricant

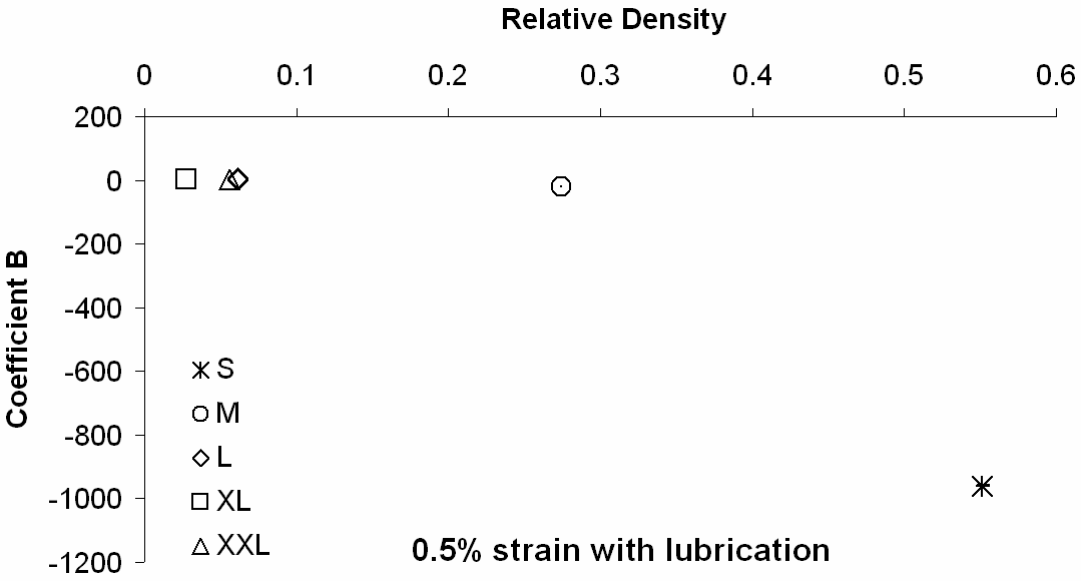

Figure 3-D-2. Coefficient B vs. relative density at 0.5% strain

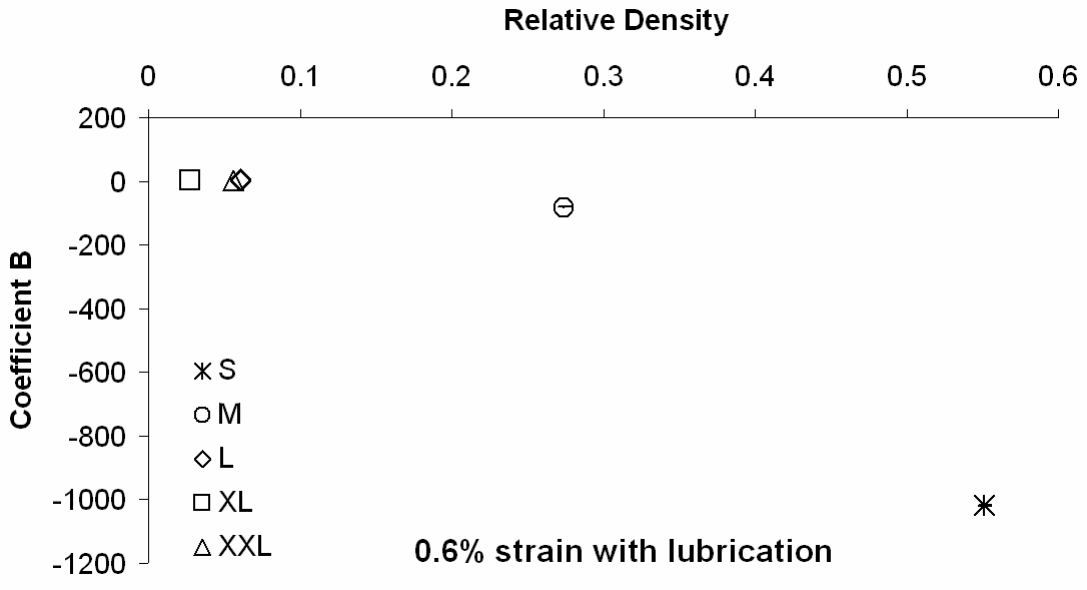

Figure 3-D-3. Coefficient B vs. relative density at 0.6% strain

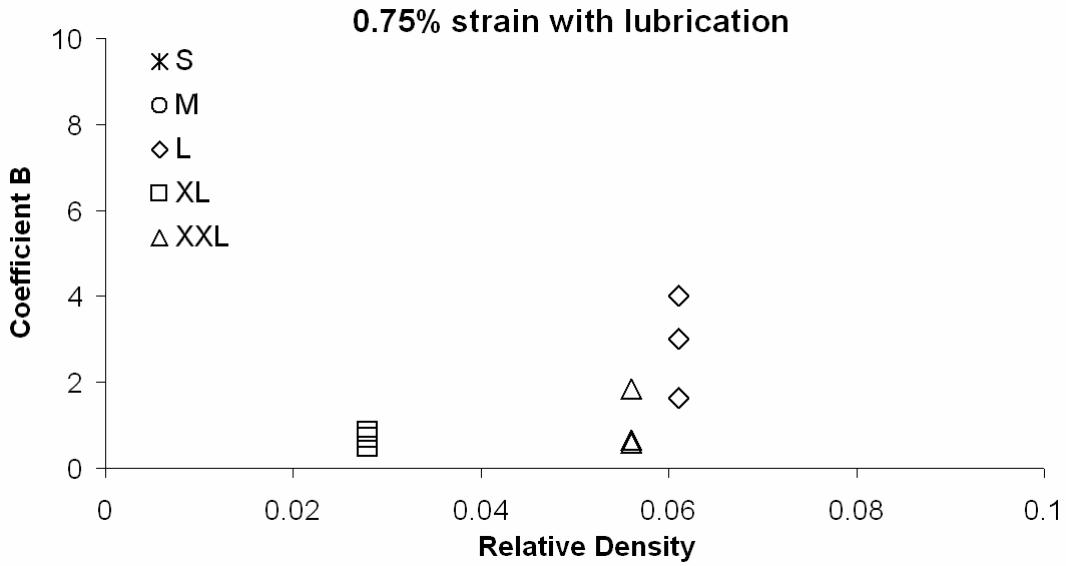

Figure 3-D-4. Coefficient B vs. relative density at 0.75% strain

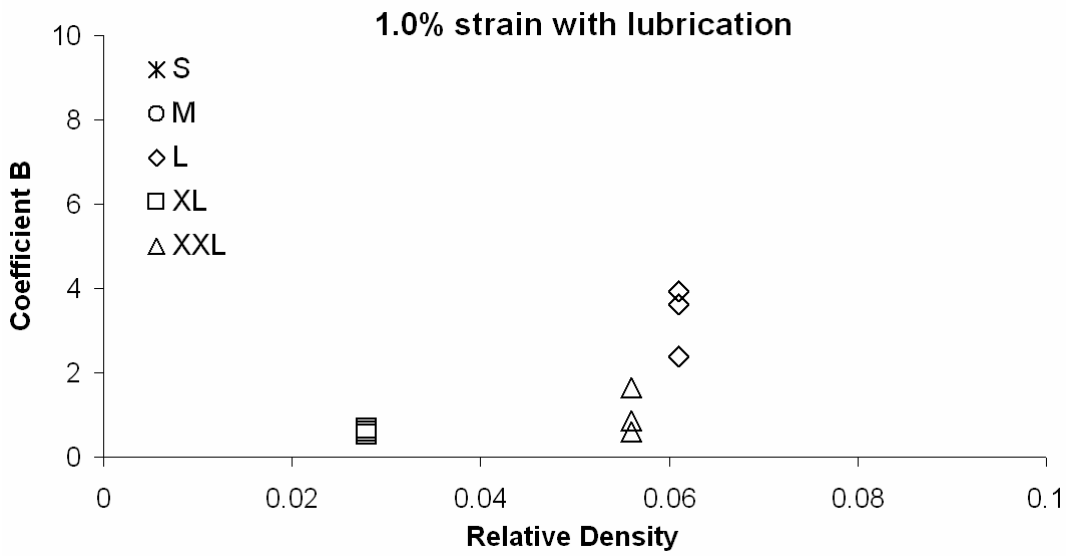

Figure 3-D-5. Coefficient B vs. relative density at 1.0% strain

Appendix 3-E. Logarithm of Coefficient A vs. relative density for all structure types at different strain levels

All structures were tested with lubrication unless noted otherwise.

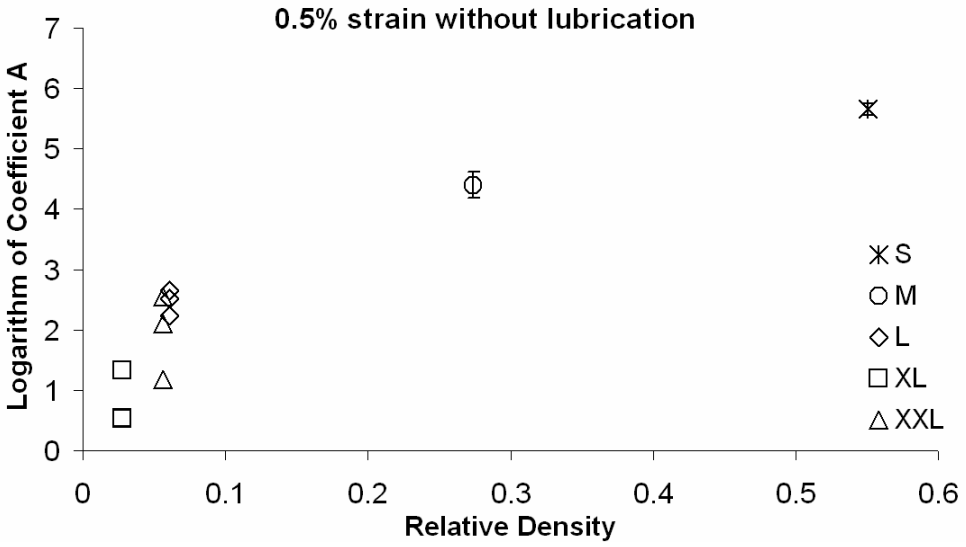

Figure 3-E-1. Coefficient A vs. relative density at 0.5% strain without lubricant

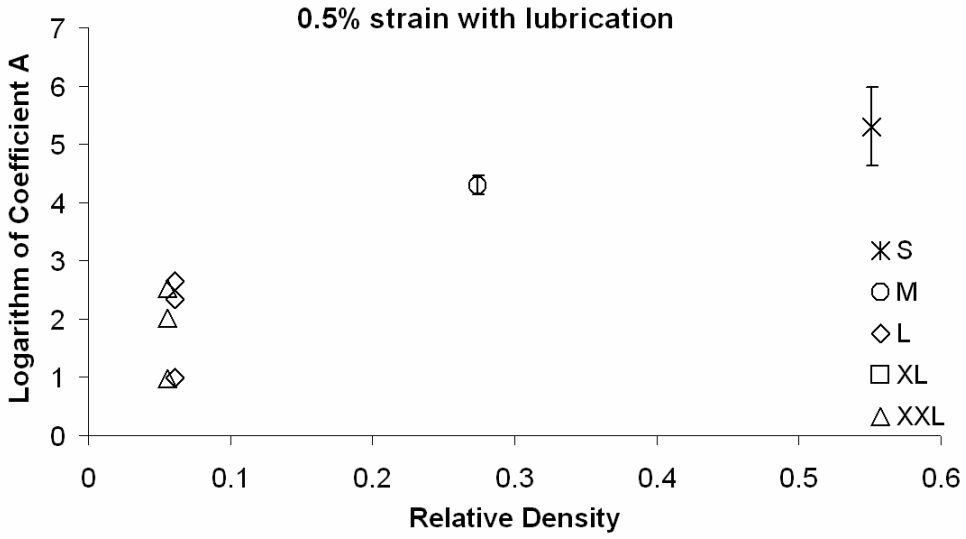

Figure 3-E-2. Coefficient A vs. relative density at 0.5% strain

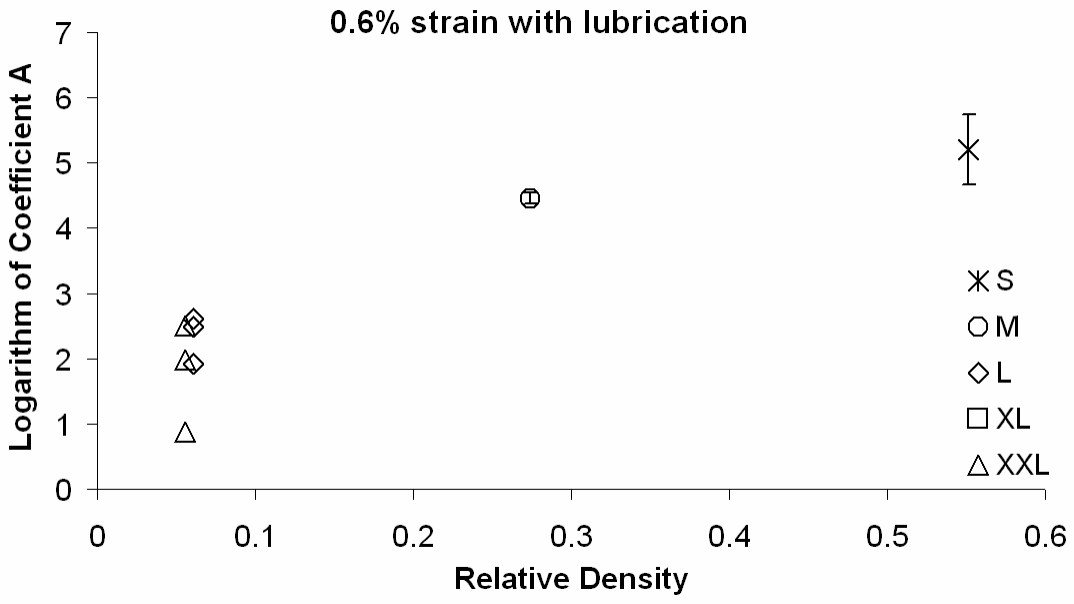

Figure 3-E-3. Coefficient A vs. relative density at 0.6% strain

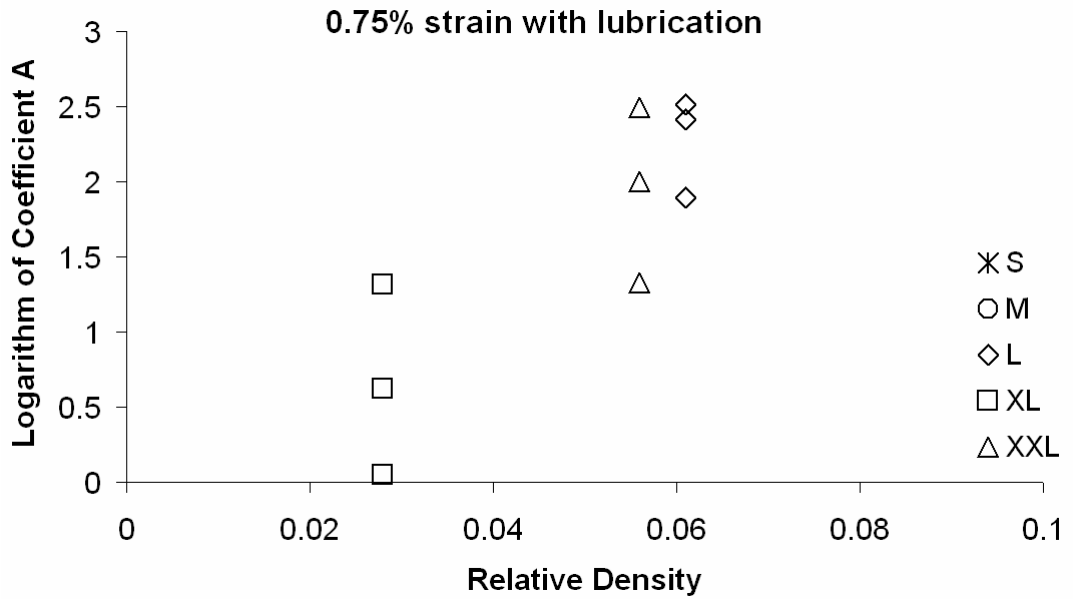

Figure 3-E-4. Coefficient A vs. relative density at 0.75% strain

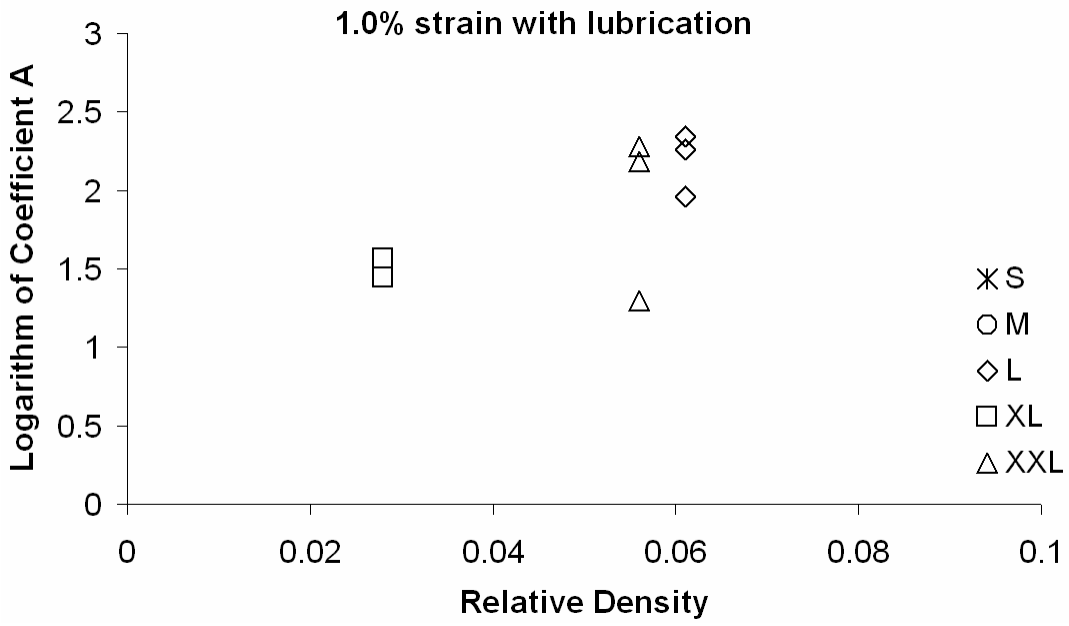

Figure 3-E-5. Coefficient A vs. relative density at 1.0% strain

Appendix 3-F. Logarithm of the square of Coefficient B vs. relative density for all structure types at different strain levels

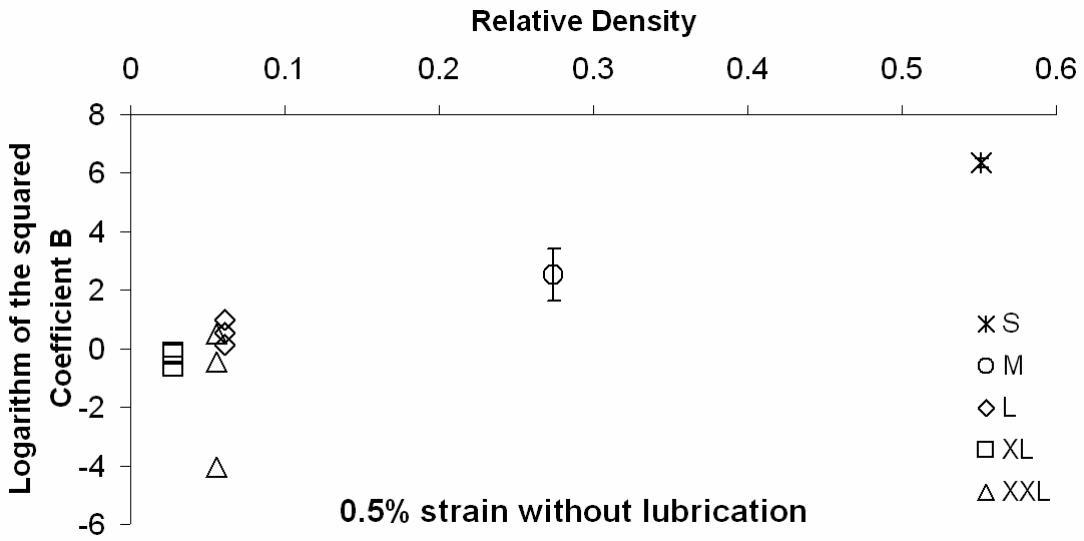

Figure 3-F-1. Coefficient B vs. relative density at 0.5% strain without lubricant

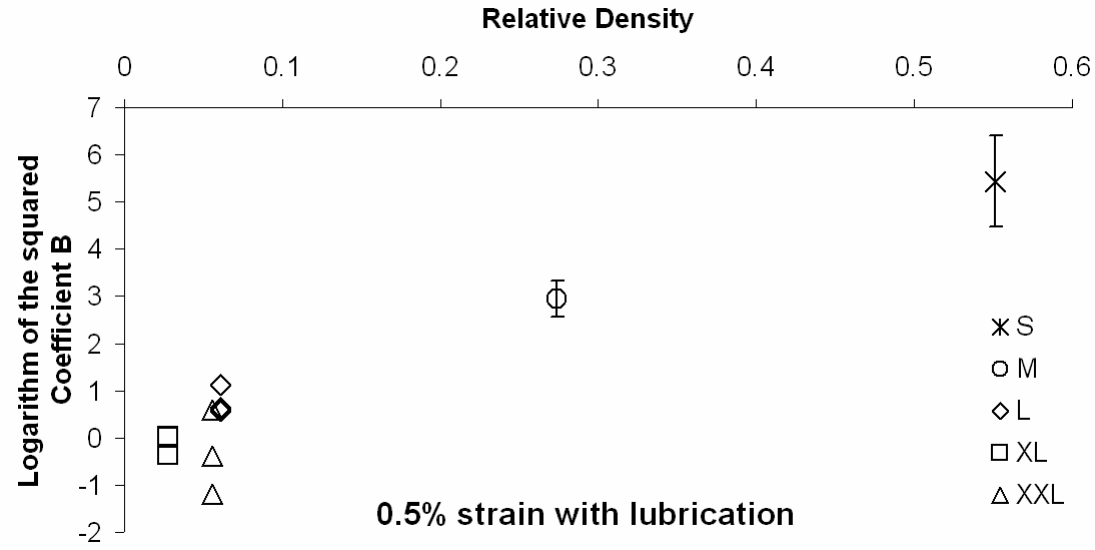

Figure 3-F-2. Coefficient B vs. relative density at 0.5% strain without lubricant

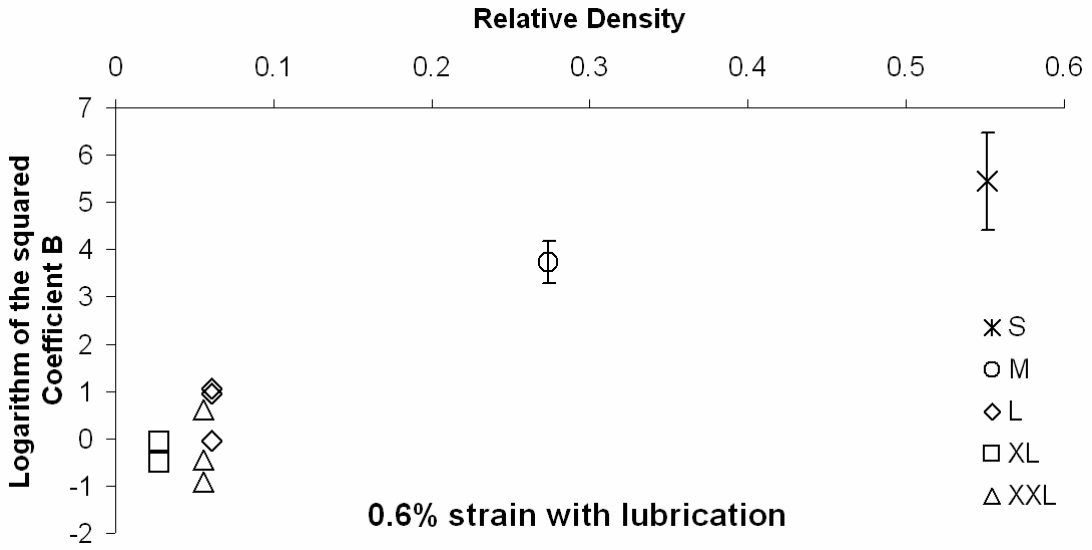

Figure 3-F-3. Coefficient B vs. relative density at 0.6% strain

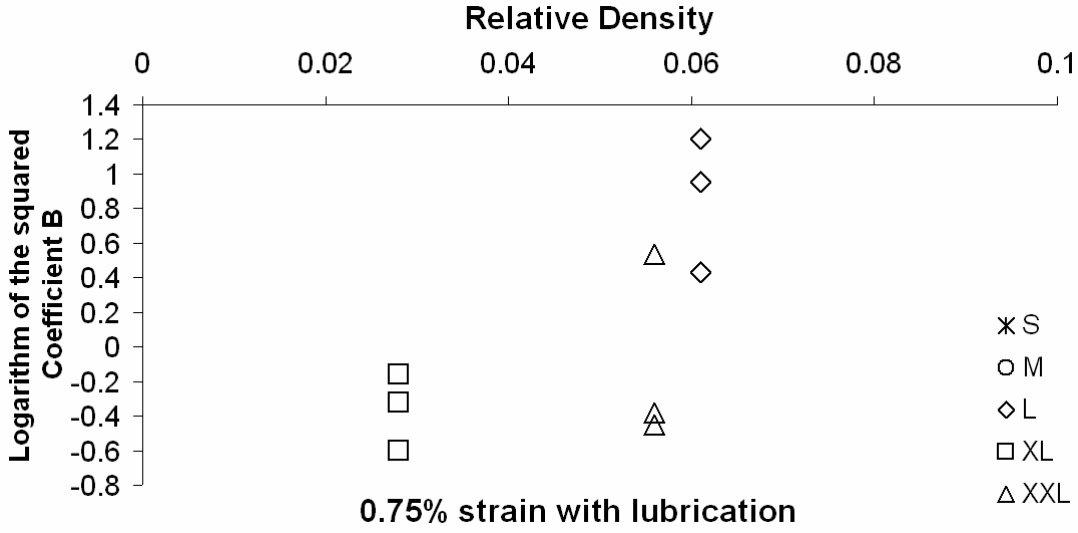

Figure 3-F-4. Coefficient B vs. relative density at 0.75% strain

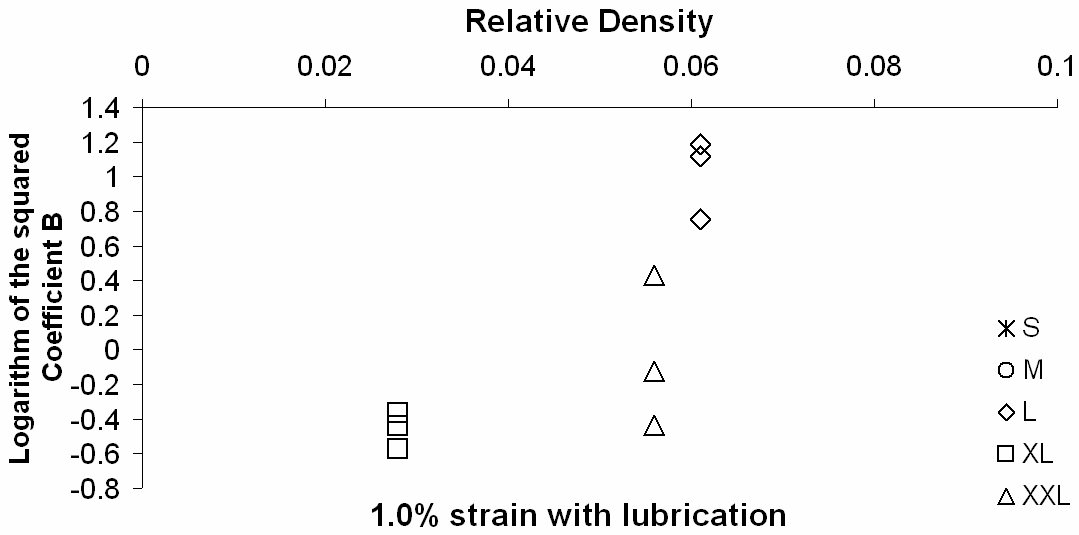

Figure 3-F-5. Coefficient B vs. relative density at 1.0% strain

Appendix 4-A: Current and force plots of the piezocomposite structures

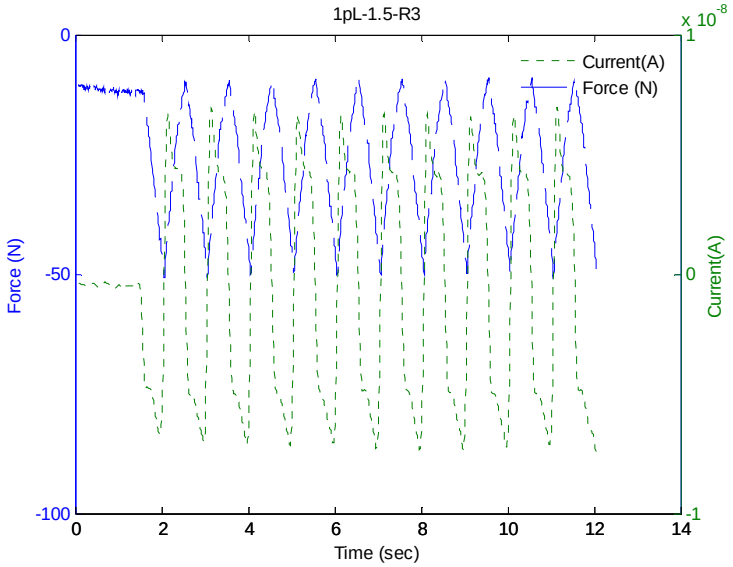

Figure 4-A-1. Force and current vs. time plots of the pL structure #1 at 1.5% strain-run#3

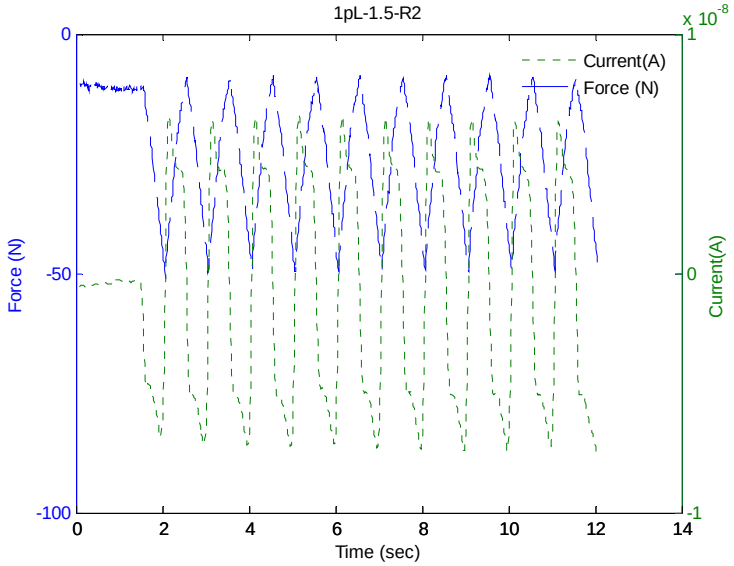

Figure 4-A-2. Force and current vs. time plots of the pL structure #1 at 1.5% strain-run#2

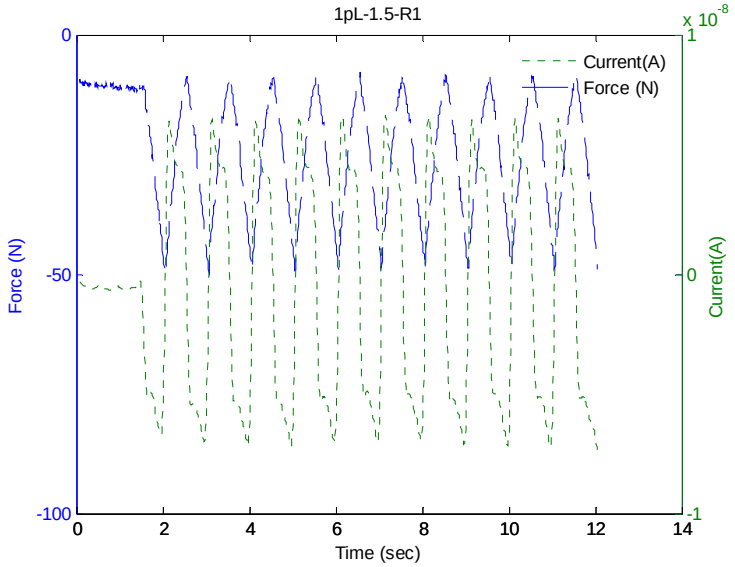

Figure 4-A-3. Force and current vs. time plots of the pL structure #1 at 1.5% strain-run#1

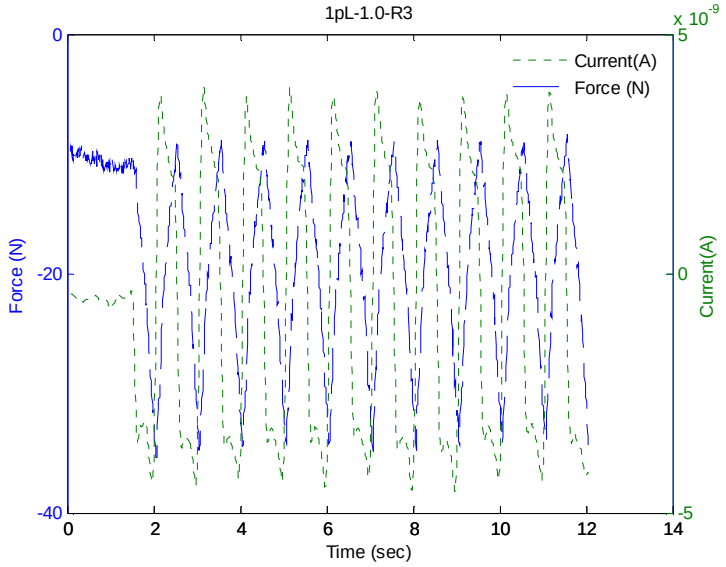

Figure 4-A-4. Force and current vs. time plots of the pL structure #1 at 1.0% strain-run#3

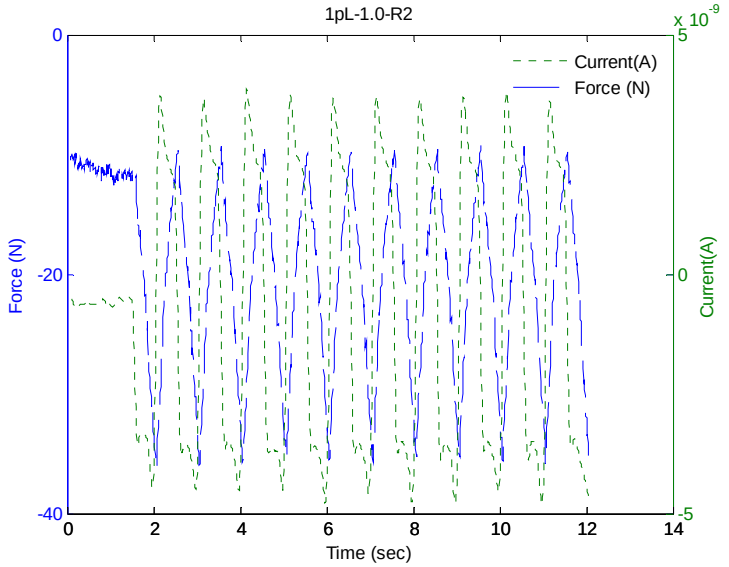

Figure 4-A-5. Force and current vs. time plots of the pL structure #1 at 1.0% strain-run#2

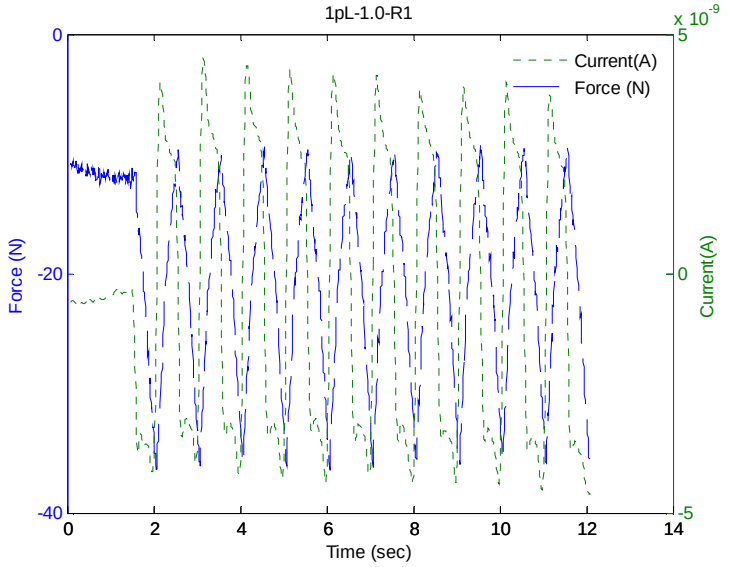

Figure 4-A-6. Force and current vs. time plots of the pL structure #1 at 1.0% strain-run#1

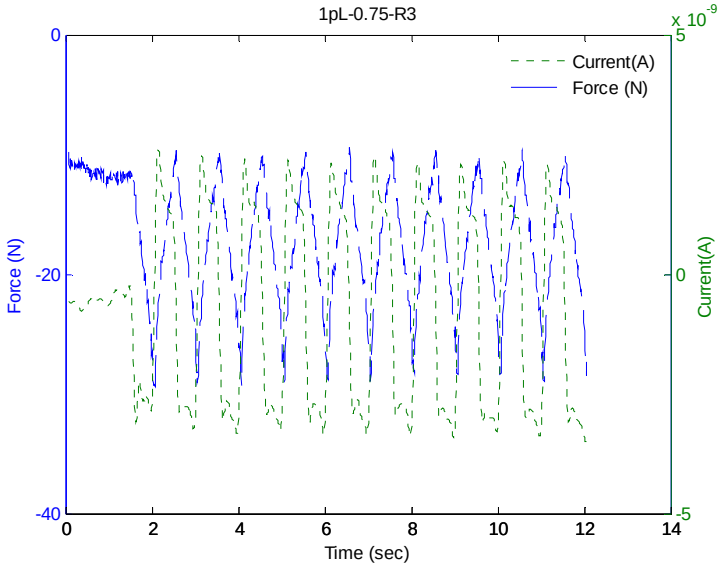

Figure 4-A-7. Force and current vs. time plots of the pL structure #1 at 0.75% strain-run#3

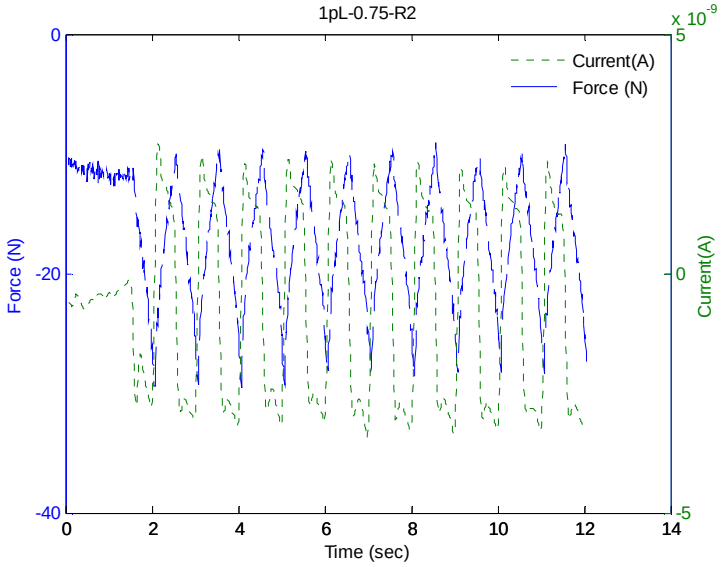

Figure 4-A-8. Force and current vs. time plots of the pL structure #1 at 0.75% strain-run#2

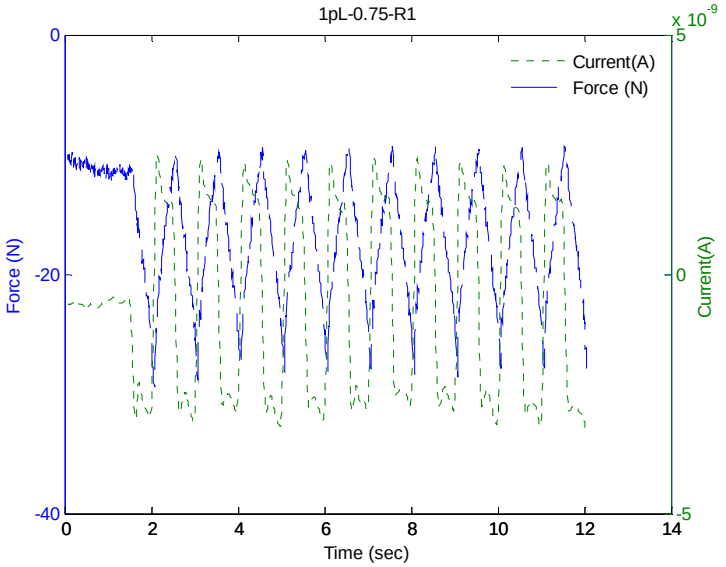

Figure 4-A-9. Force and current vs. time plots of the pL structure #1 at 0.75% strain-run#1

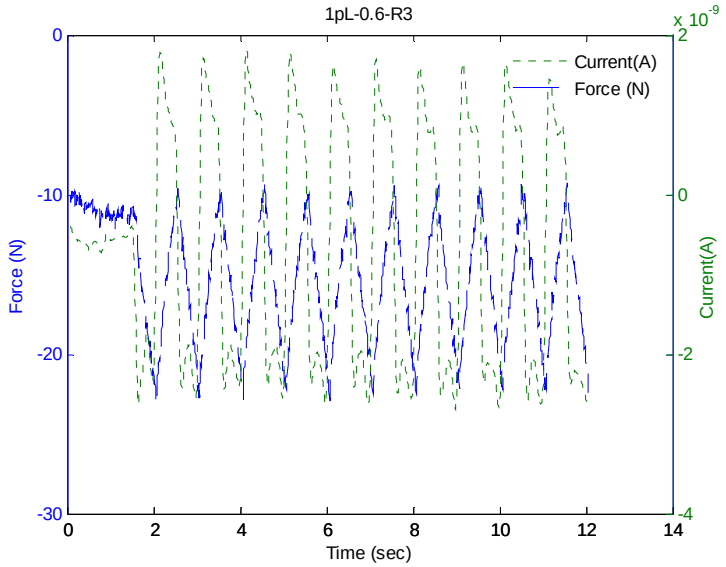

Figure 4-A-10. Force and current vs. time plots of the pL structure #1 at 0.6% strain-run#3

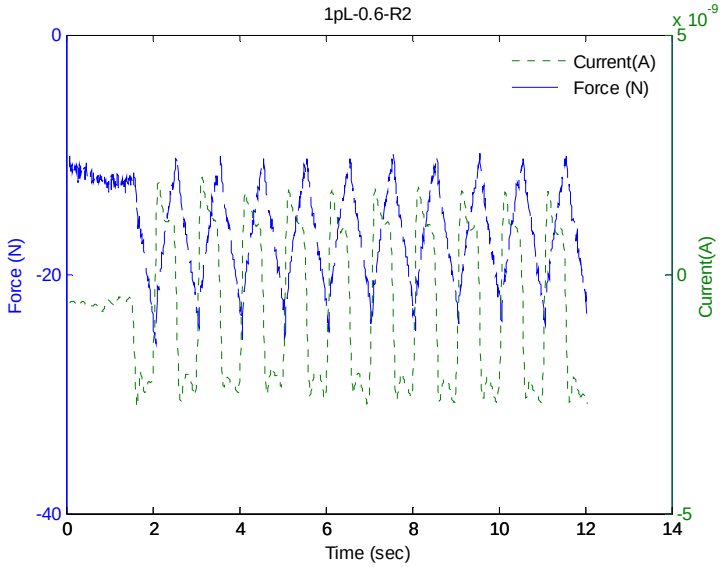

Figure 4-A-11. Force and current vs. time plots of the pL structure #1 at 0.6% strain-run#2

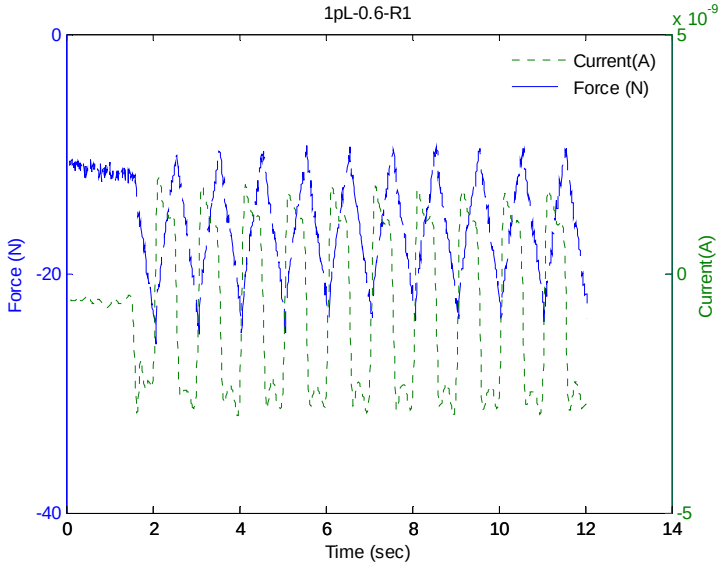

Figure 4-A-12. Force and current vs. time plots of the pL structure #1 at 0.6% strain-run#1

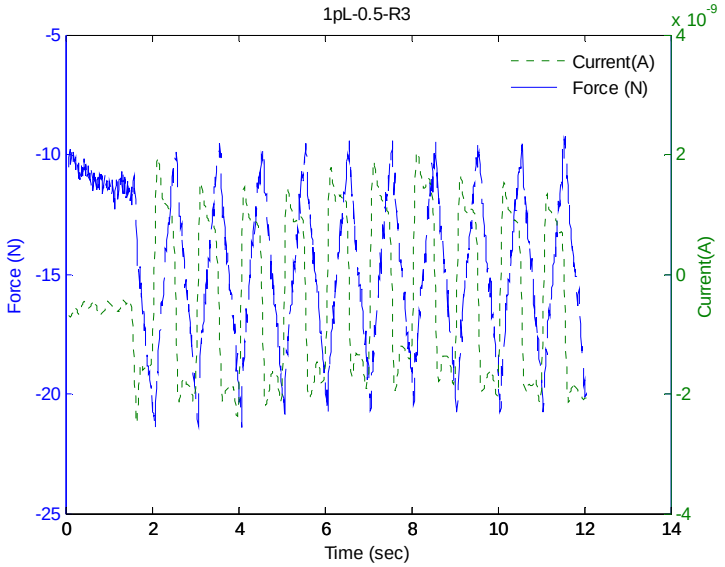

Figure 4-A-13. Force and current vs. time plots of the pL structure #1 at 0.5% strain-run#3

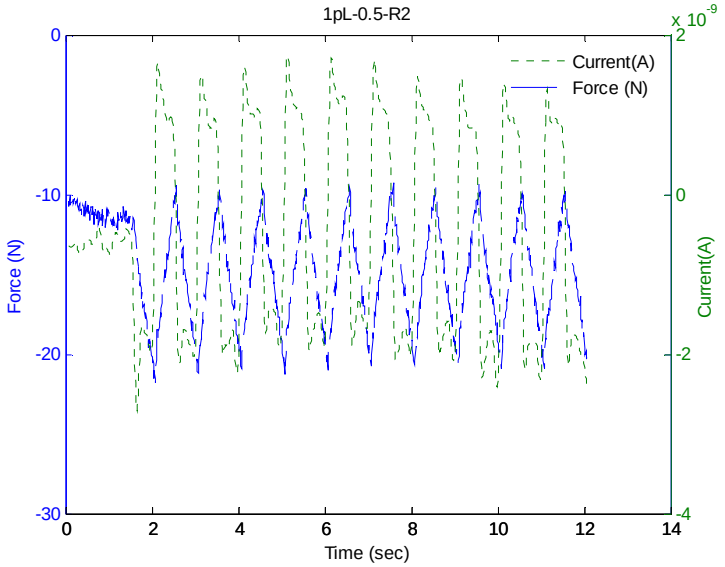

Figure 4-A-14. Force and current vs. time plots of the pL structure #1 at 0.5% strain-run#2

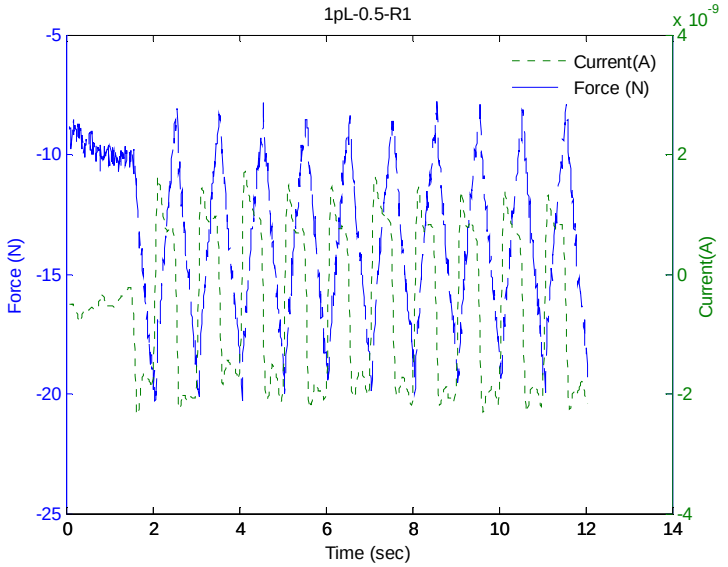

Figure 4-A-15. Force and current vs. time plots of the pL structure #1 at 0.5% strain-run#1

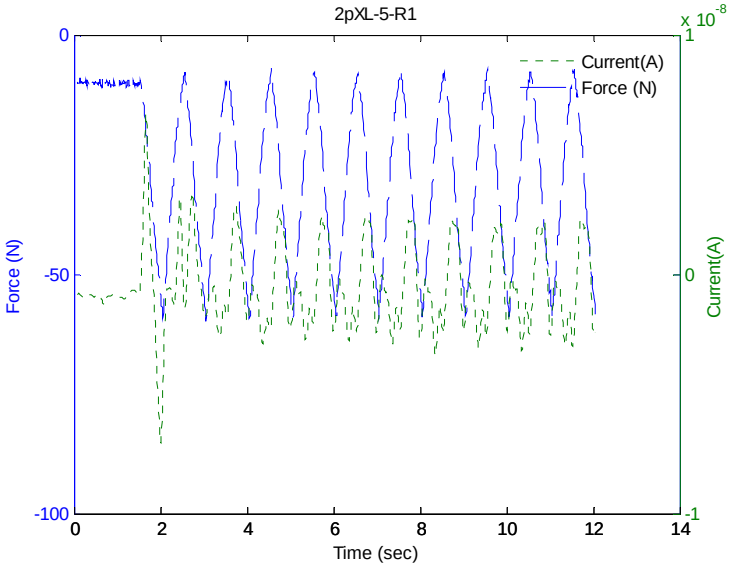

Figure 4-A-16. Force and current vs. time plots of the pXL structure #2 at 5% strain-run#1

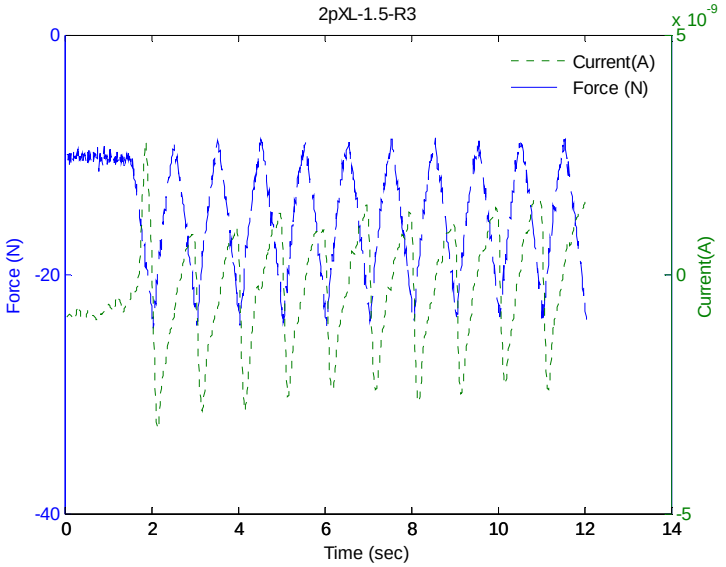

Figure 4-A-17. Force and current vs. time plots of the pXL structure #2 at 1.5% strain- run#3

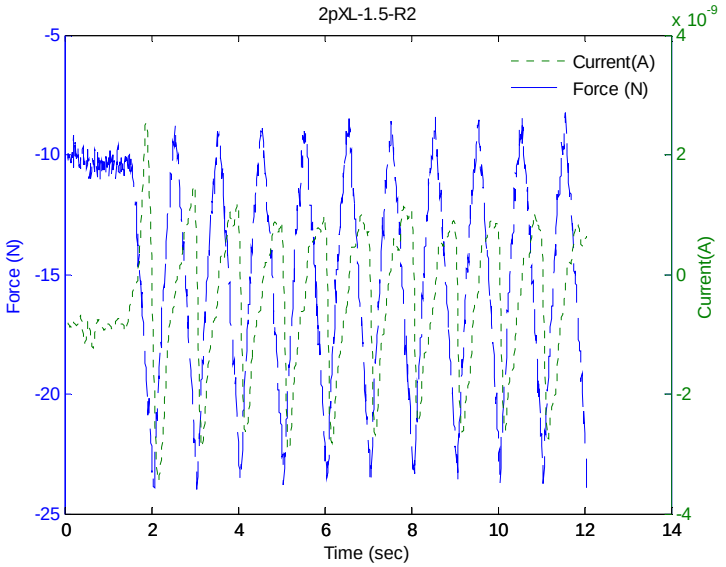

Figure 4-A-18. Force and current vs. time plots of the pXL structure #2 at 1.5% strain- run#2

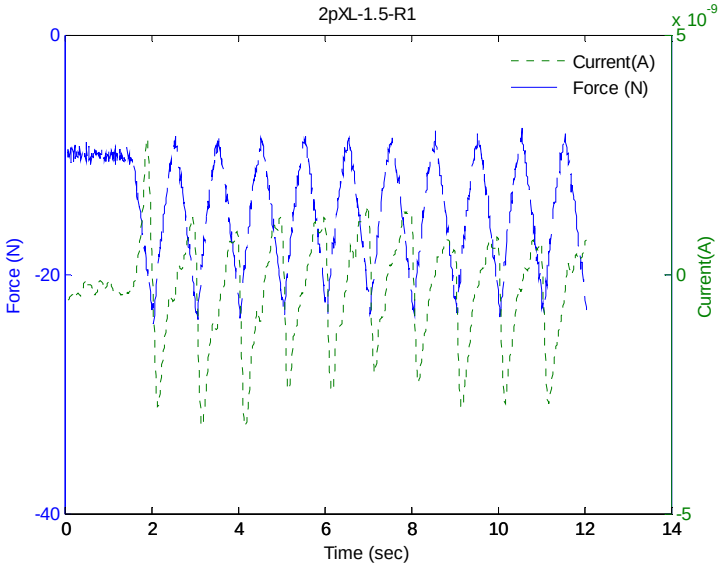

Figure 4-A-19. Force and current vs. time plots of the pXL structure #2 at 1.5% strain- run#1

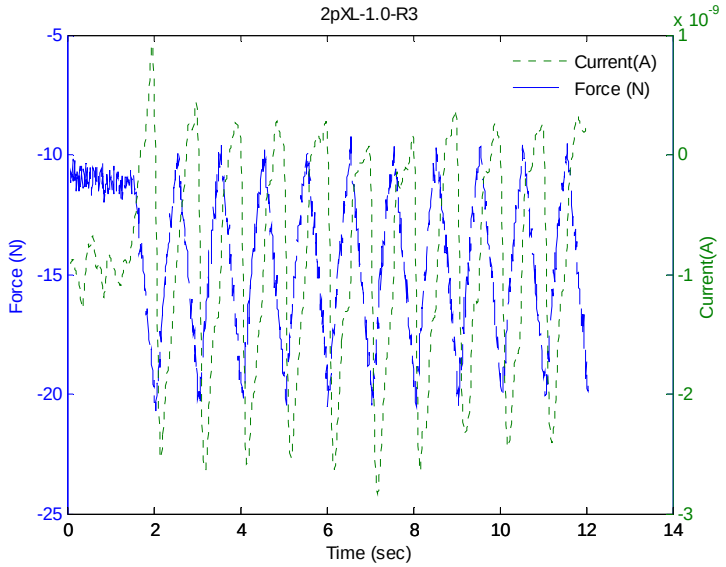

Figure 4-A-20. Force and current vs. time plots of the pXL structure #2 at 1.0% strain- run#3

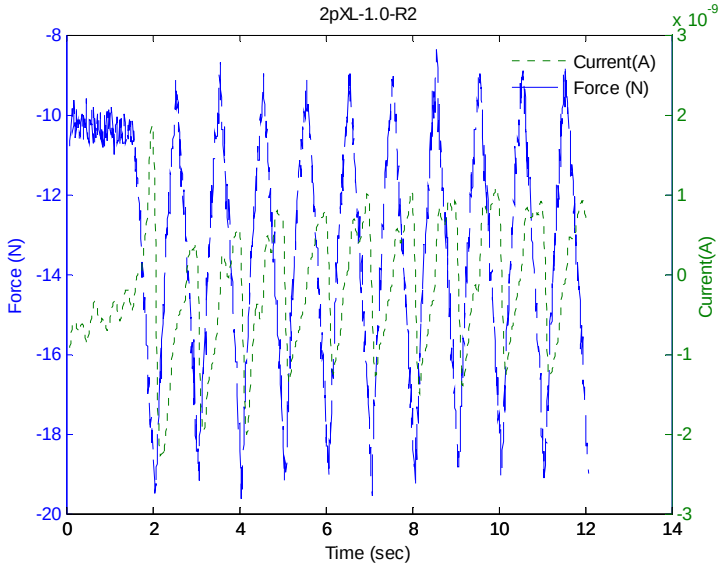

Figure 4-A-21. Force and current vs. time plots of the pXL structure #2 at 1.0% strain- run#2

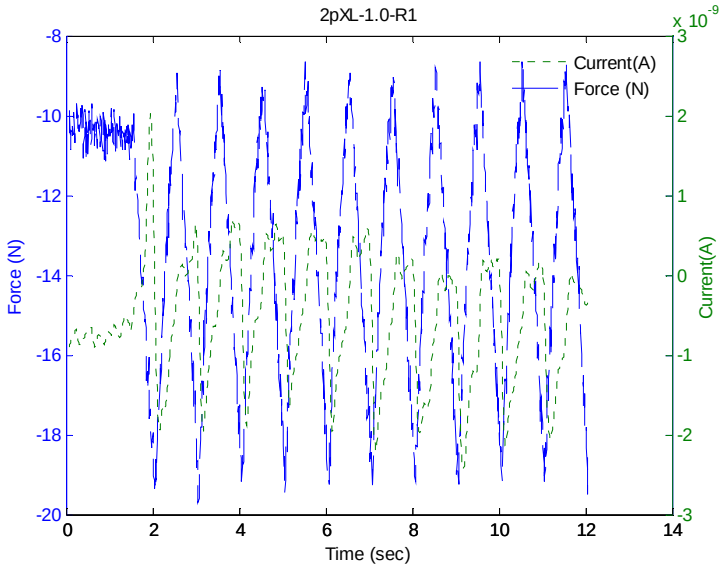

Figure 4-A-22. Force and current vs. time plots of the pXL structure #2 at 1.0% strain- run#1

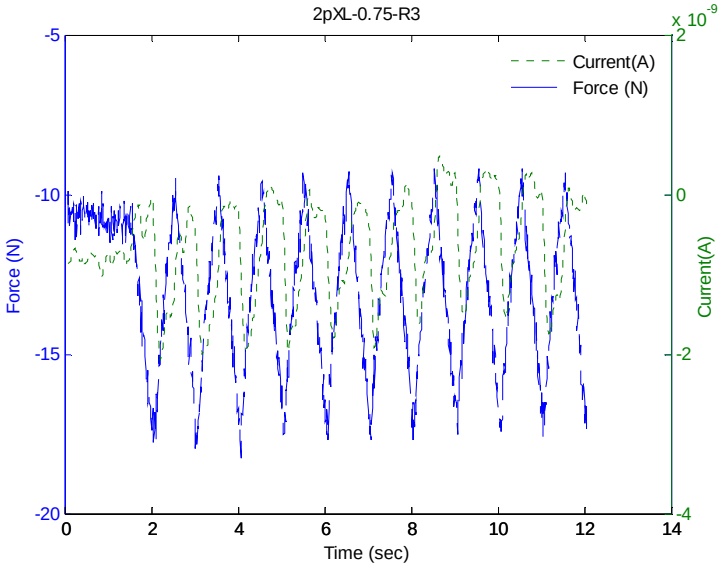

Figure 4-A-23. Force and current vs. time plots of the pXL structure #2 at 0.75% strain- run#3

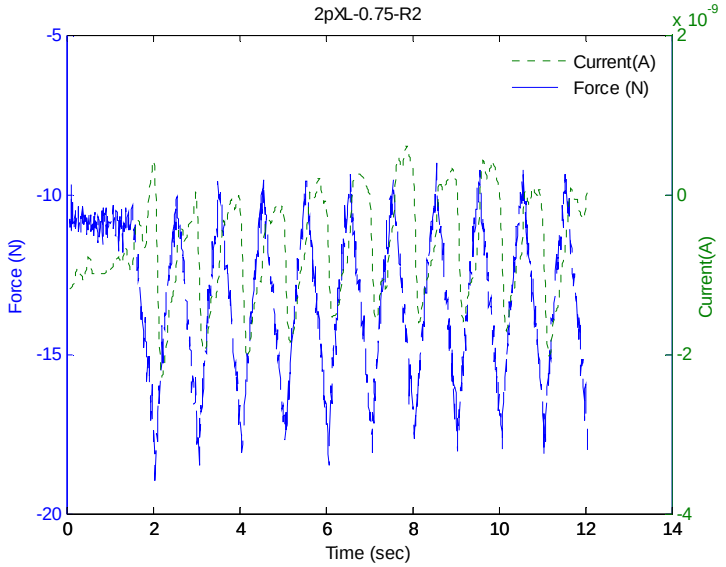

Figure 4-A-24. Force and current vs. time plots of the pXL structure #2 at 0.75% strain- run#2

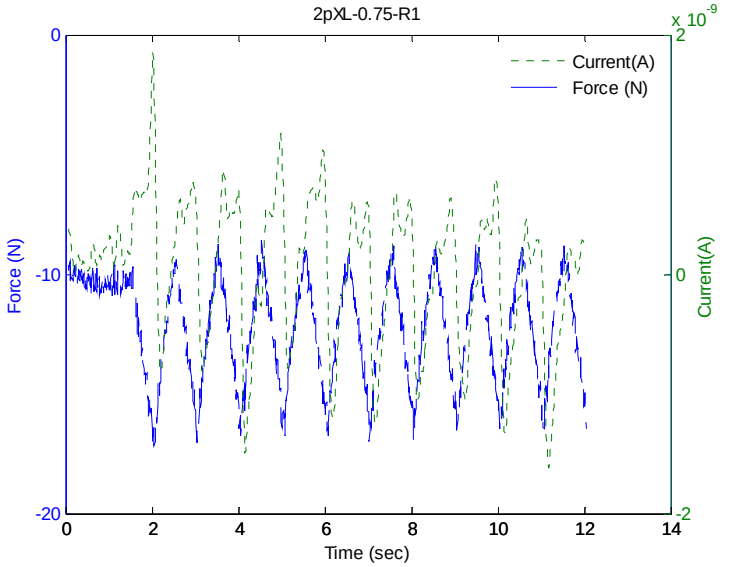

Figure 4-A-25. Force and current vs. time plots of the pXL structure #2 at 0.75% strain- run#1

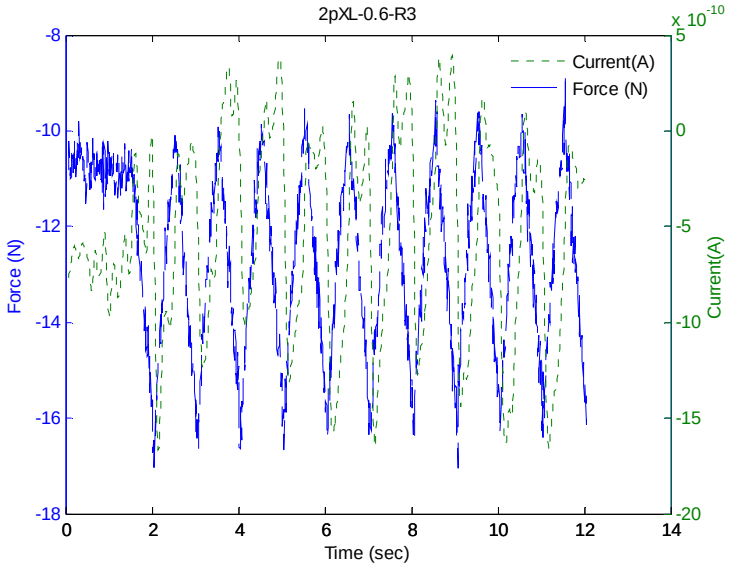

Figure 4-A-26. Force and current vs. time plots of the pXL structure #2 at 0.6% strain- run#3

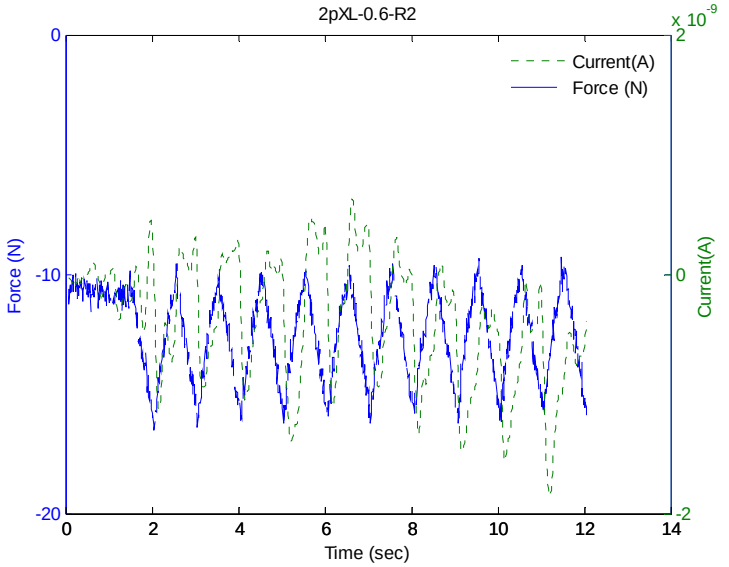

Figure 4-A-27. Force and current vs. time plots of the pXL structure #2 at 0.6% strain- run#2

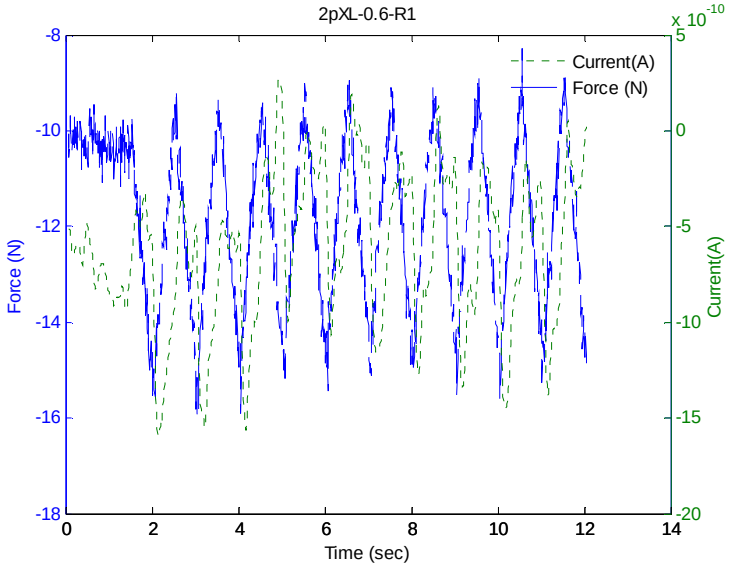

Figure 4-A-28. Force and current vs. time plots of the pXL structure #2 at 0.6% strain- run#1

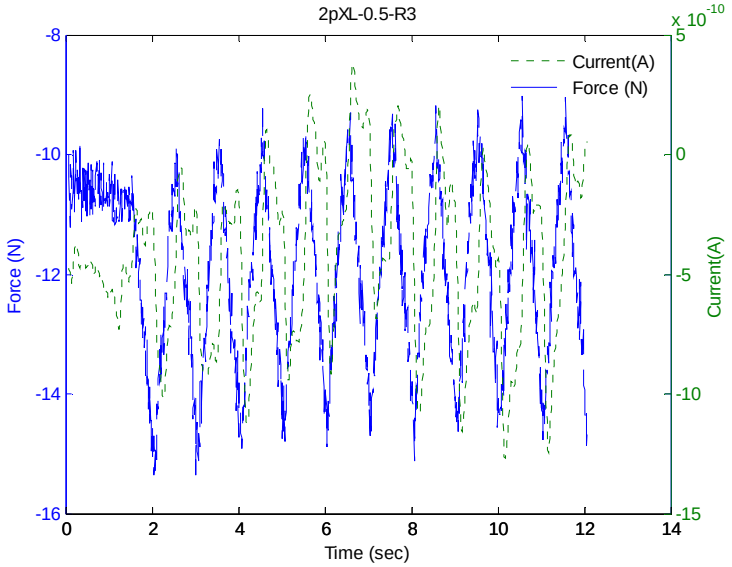

Figure 4-A-29. Force and current vs. time plots of the pXL structure #2 at 0.5% strain- run#3

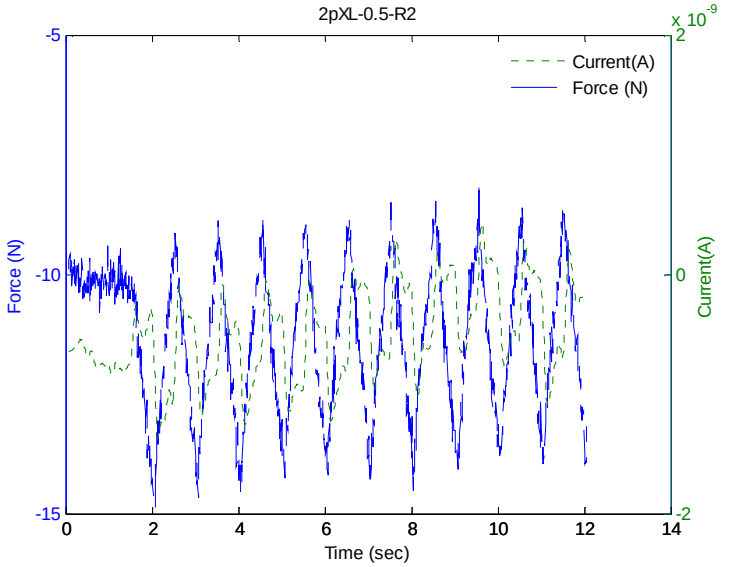

Figure 4-A-30. Force and current vs. time plots of the pXL structure #2 at 0.5% strain- run#2

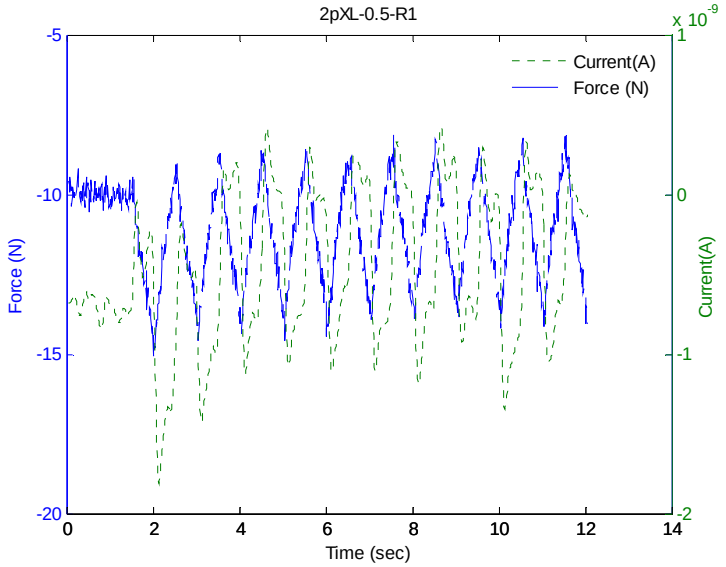

Figure 4-A-31. Force and current vs. time plots of the pXL structure #2 at 0.5% strain- run#1

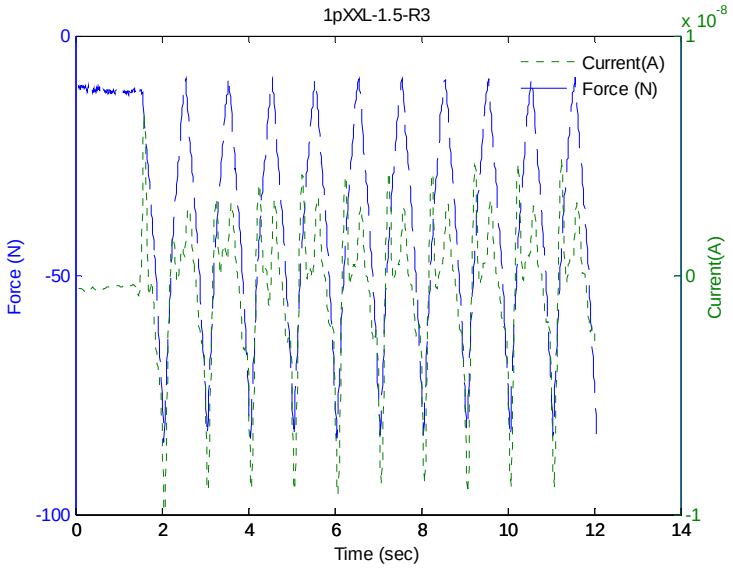

Figure 4-A-32. Force and current vs. time plots of the pXXL structure #1 at 1.5% strain- run#3

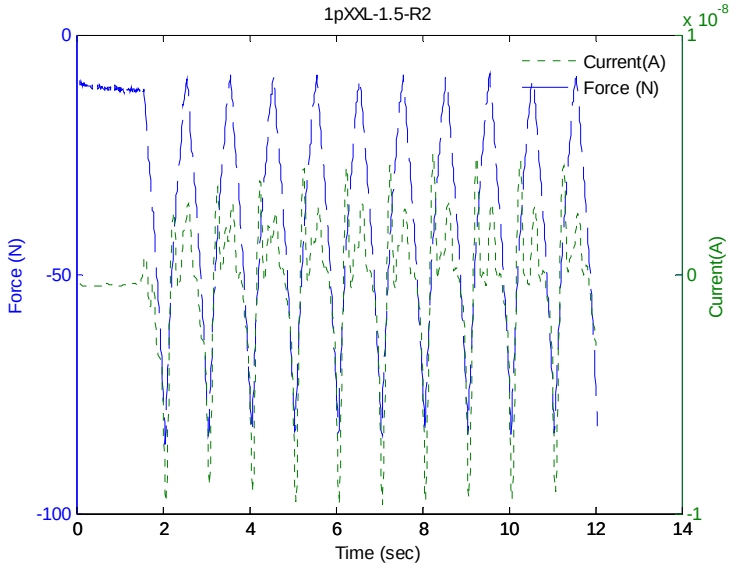

Figure 4-A-33. Force and current vs. time plots of the pXXL structure #1 at 1.5% strain- run#2

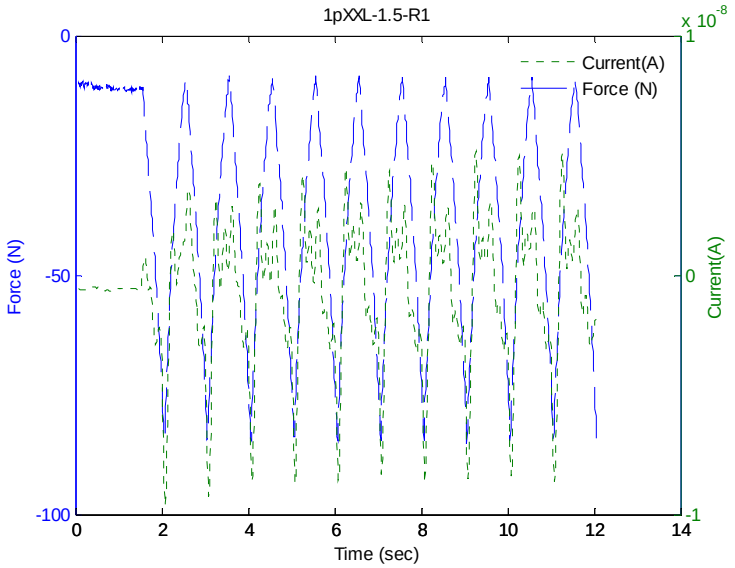

Figure 4-A-34. Force and current vs. time plots of the pXXL structure #1 at 1.5% strain- run#1

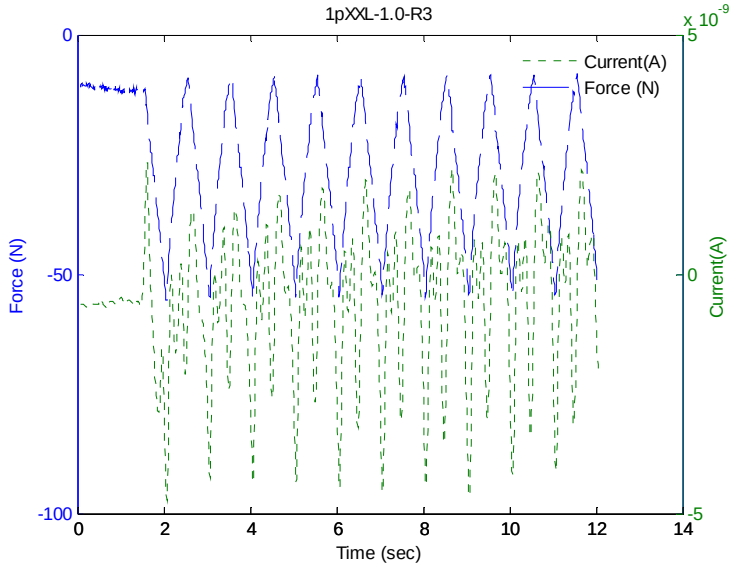

Figure 4-A-35. Force and current vs. time plots of the pXXL structure #1 at 1.0% strain- run#3

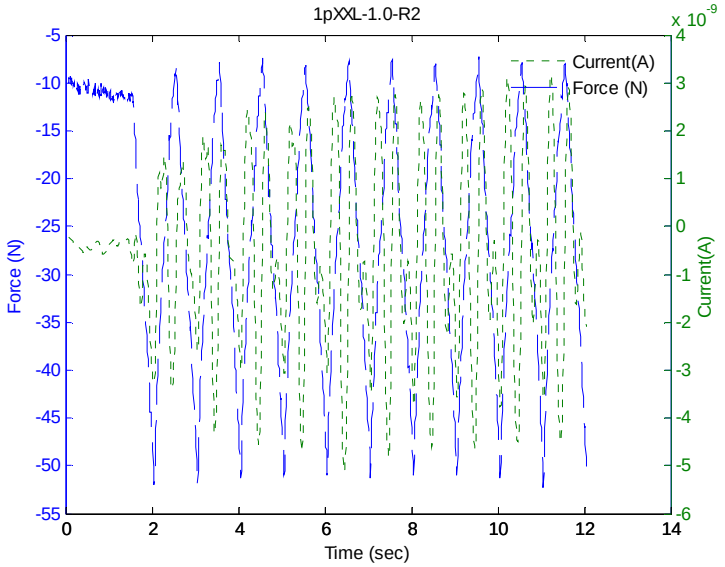

Figure 4-A-36. Force and current vs. time plots of the pXXL structure #1 at 1.0% strain- run#2

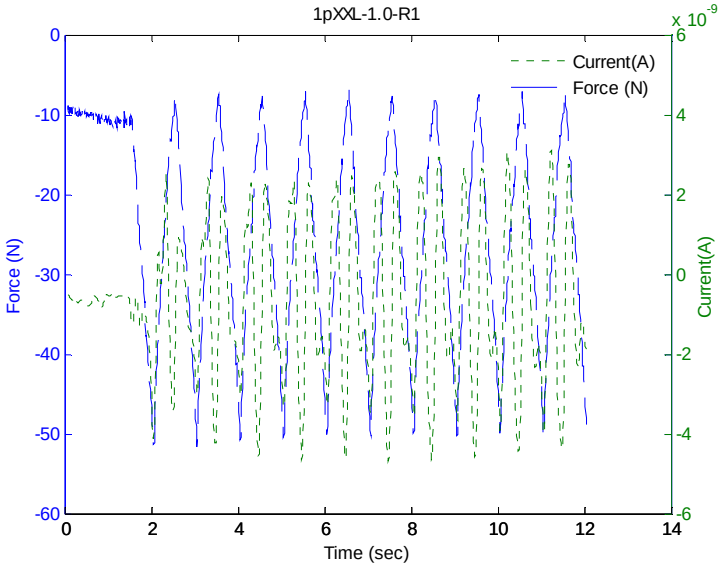

Figure 4-A-37. Force and current vs. time plots of the pXXL structure #1 at 1.0% strain- run#1

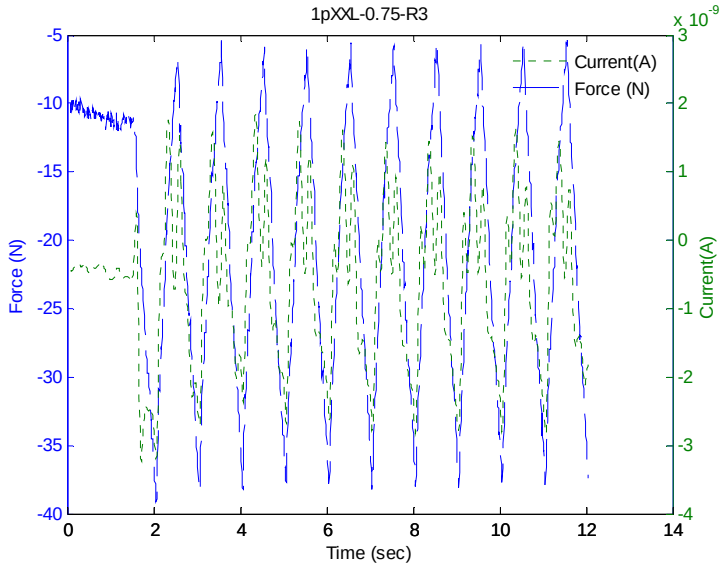

Figure 4-A-38. Force and current vs. time plots of the pXXL structure #1 at 0.75% strain- run#3

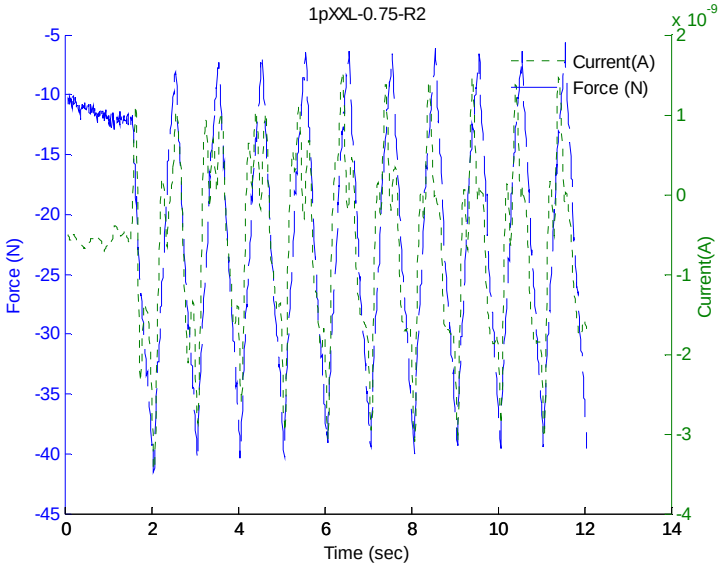

Figure 4-A-39. Force and current vs. time plots of the pXXL structure #1 at 0.75% strain- run#2

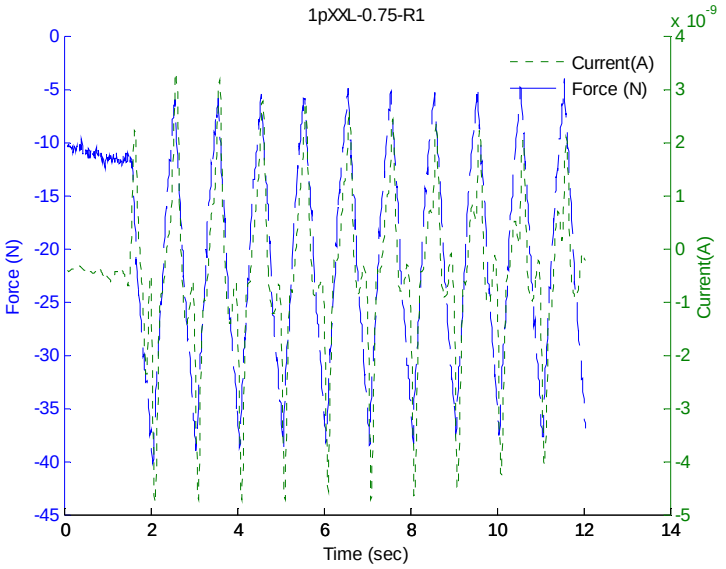

Figure 4-A-40. Force and current vs. time plots of the pXXL structure #1 at 0.75% strain- run#1

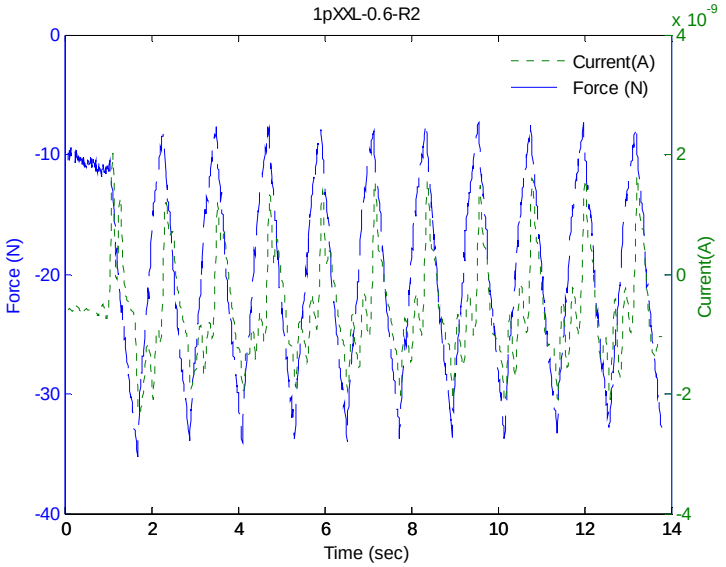

Figure 4-A-41. Force and current vs. time plots of the pXXL structure #1 at 0.6% strain- run#2

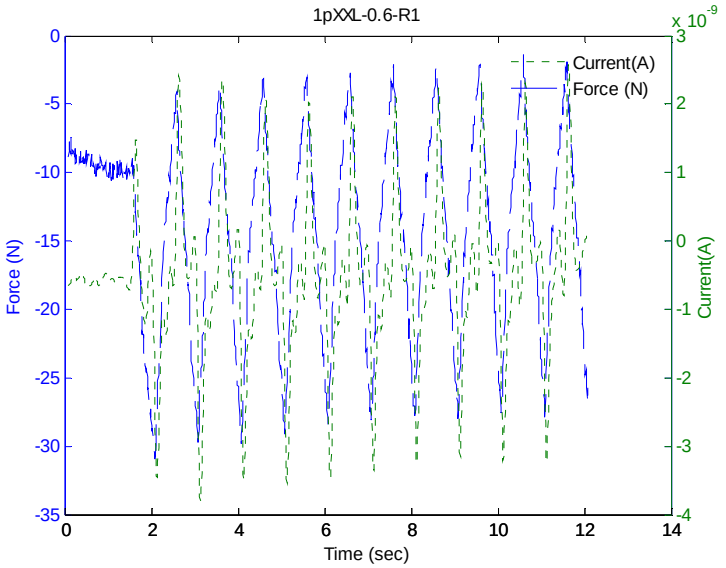

Figure 4-A-42. Force and current vs. time plots of the pXXL structure #1 at 0.6% strain- run#1

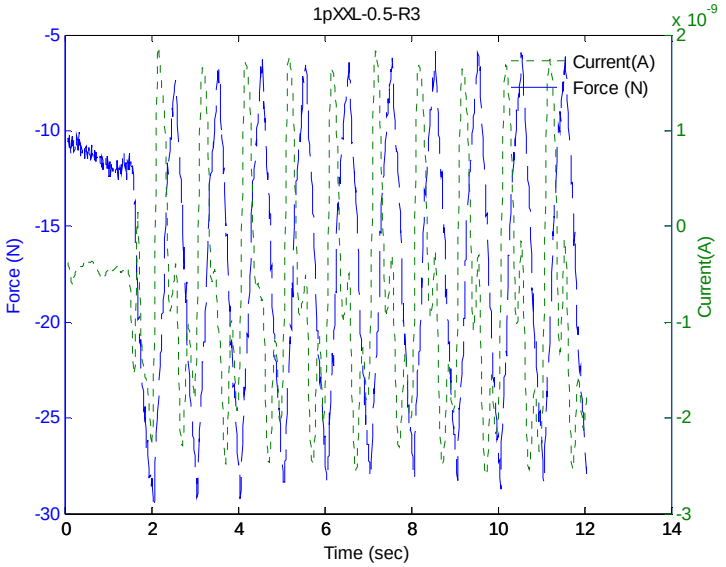

Figure 4-A-43. Force and current vs. time plots of the pXXL structure #1 at 0.5% strain- run#3

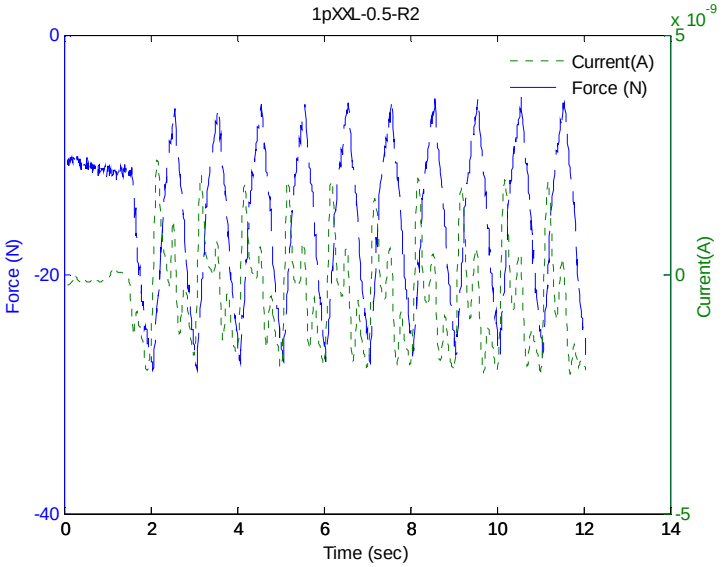

Figure 4-A-44. Force and current vs. time plots of the pXXL structure #1 at 0.5% strain- run#2

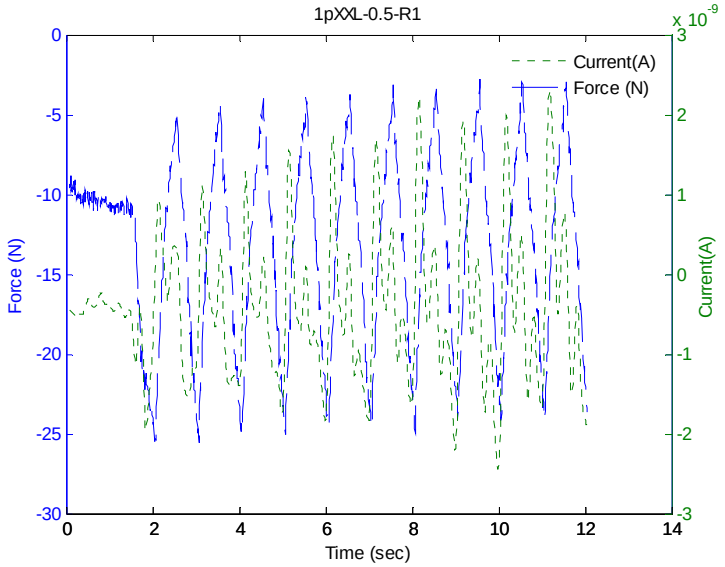

Figure 4-A-45. Force and current vs. time plots of the pXXL structure #1 at 0.5% strain- run#1

Examples of spurious signals

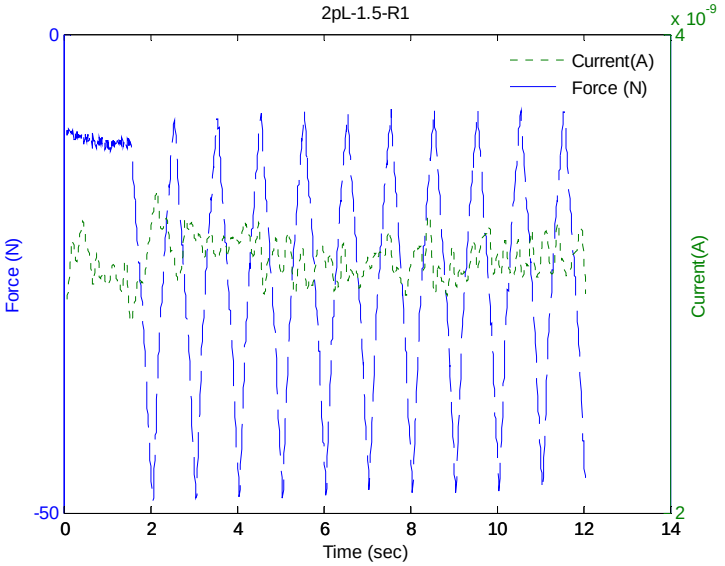

Figure 4-A-46. Force and current vs. time plots of the pL structure #2 at 1.5% strain- run#1

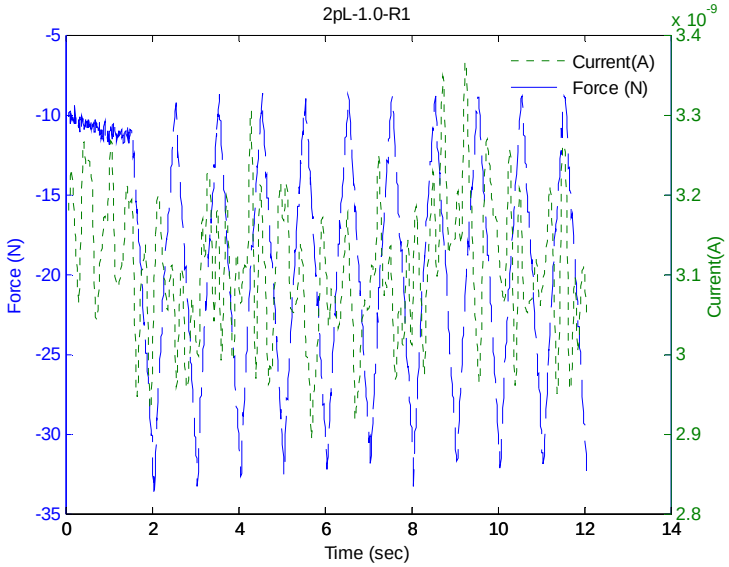

Figure 4-A-47. Force and current vs. time plots of the pL structure #2 at 1.0% strain- run#1

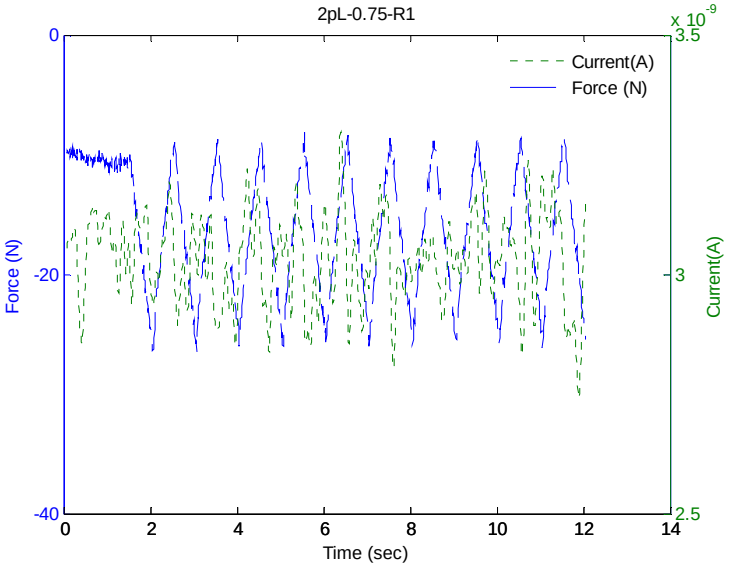

Figure 4-A-48. Force and current vs. time plots of the pL structure #2 at 0.75% strain- run#1

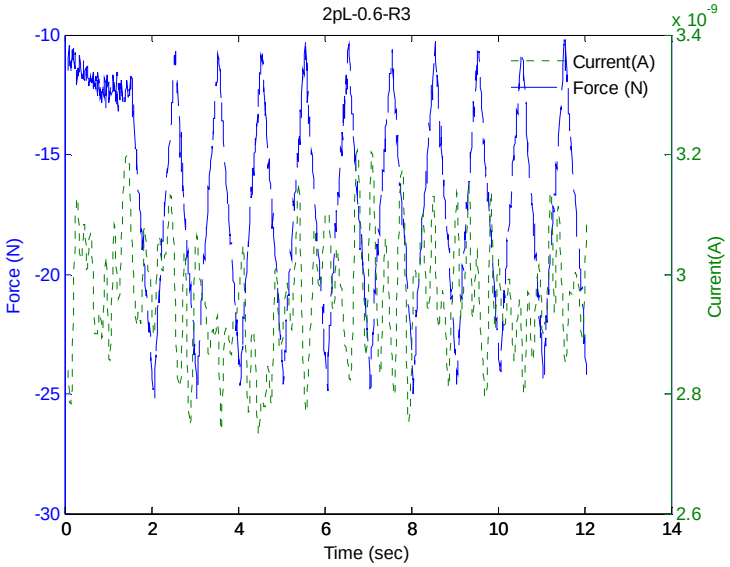

Figure 4-A-49. Force and current vs. time plots of the pL structure #2 at 0.6% strain-run#3

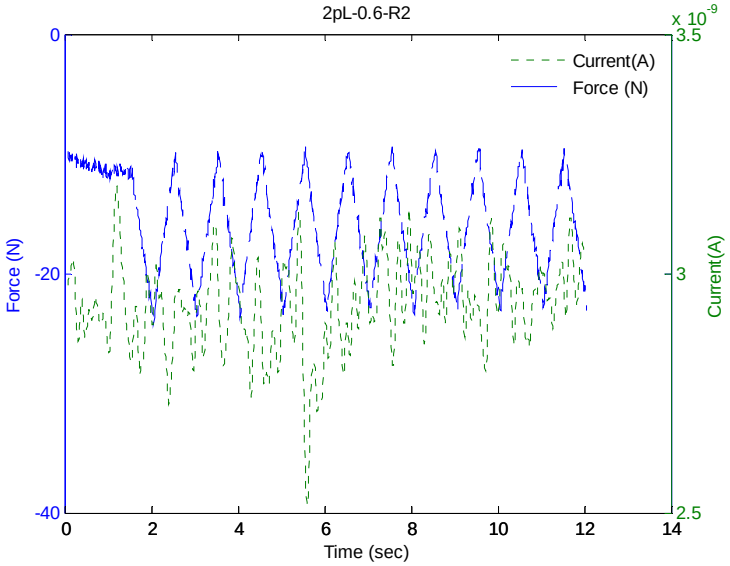

Figure 4-A-50. Force and current vs. time plots of the pL structure #2 at 0.6% strain-run#2

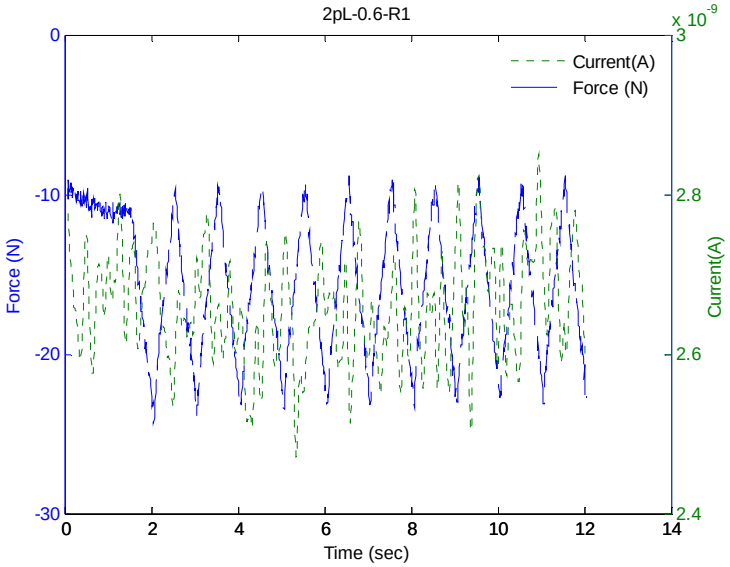

Figure 4-A-51. Force and current vs. time plots of the pL structure #2 at 0.6% strain-run#1

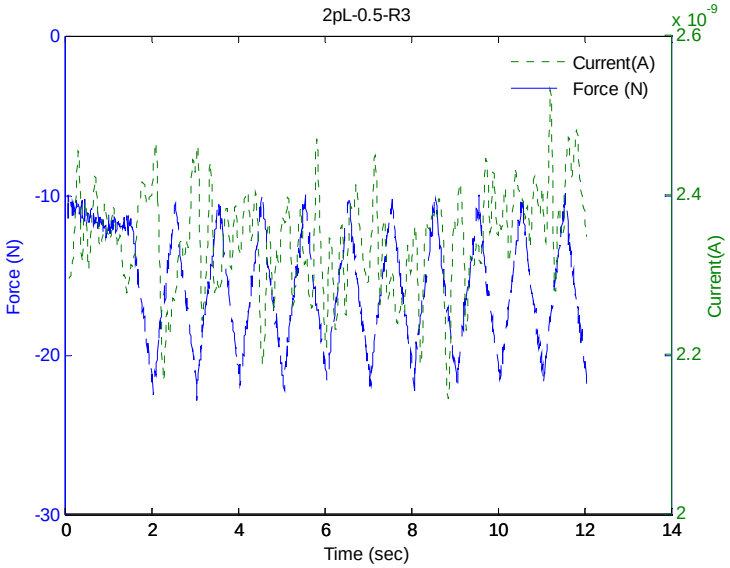

Figure 4-A-52. Force and current vs. time plots of the pL structure #2 at 0.5% strain-run#3

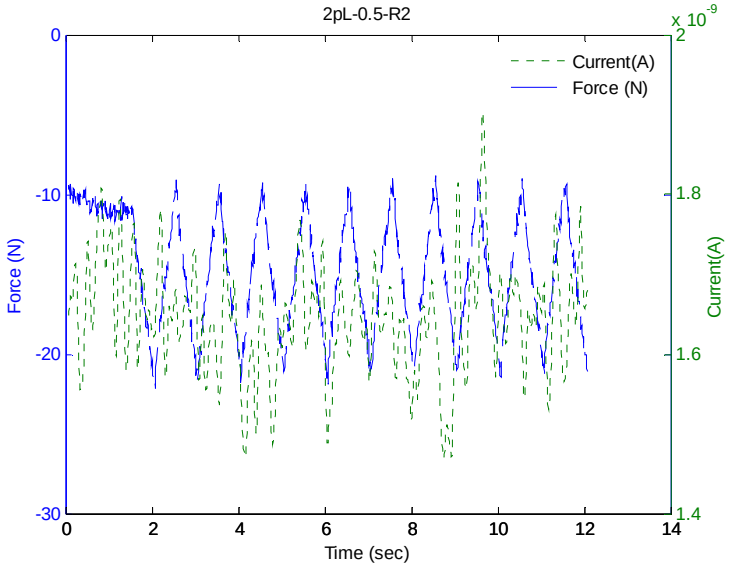

Figure 4-A-53. Force and current vs. time plots of the pL structure #2 at 0.5% strain-run#2

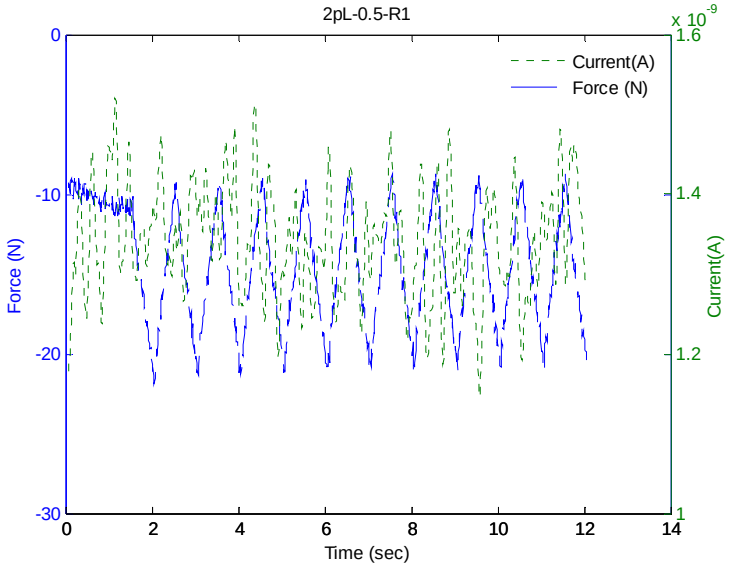

Figure 4-A-54. Force and current vs. time plots of the pL structure #2 at 0.5% strain-run#1

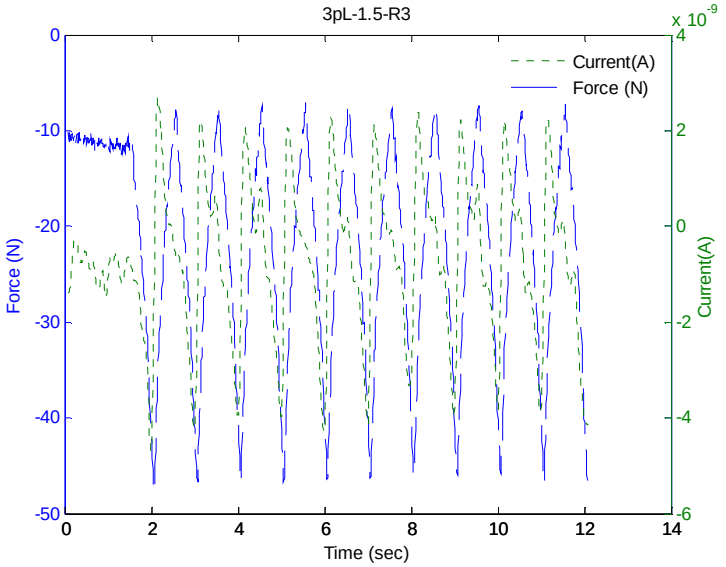

Figure 4-A-55. Force and current vs. time plots of the pL structure #3 at 1.5% strain-run#3

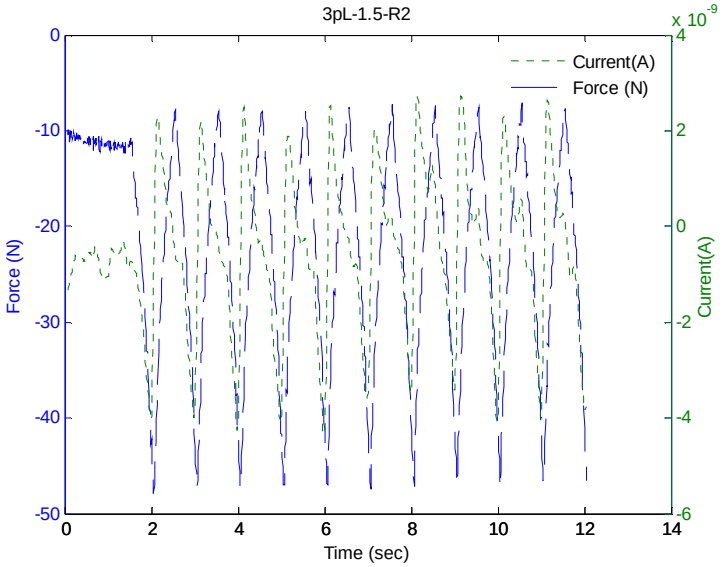

Figure 4-A-56. Force and current vs. time plots of the pL structure #3 at 1.5% strain-run#2

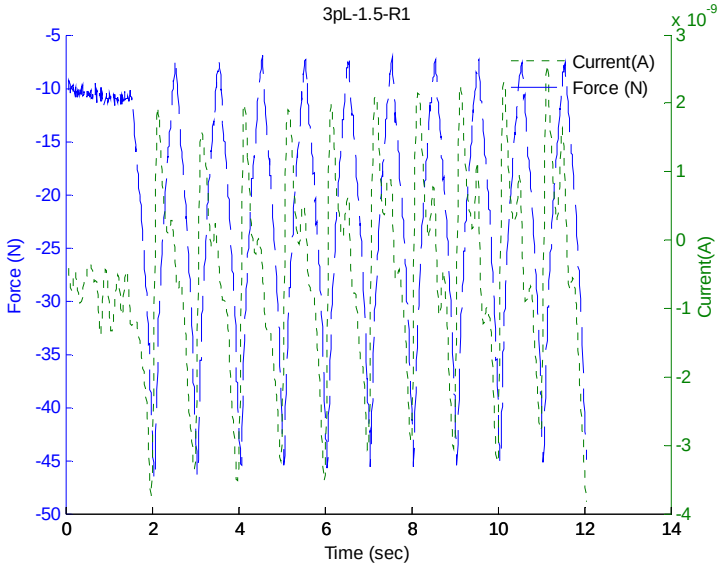

Figure 4-A-57. Force and current vs. time plots of the pL structure #3 at 1.5% strain-run#1

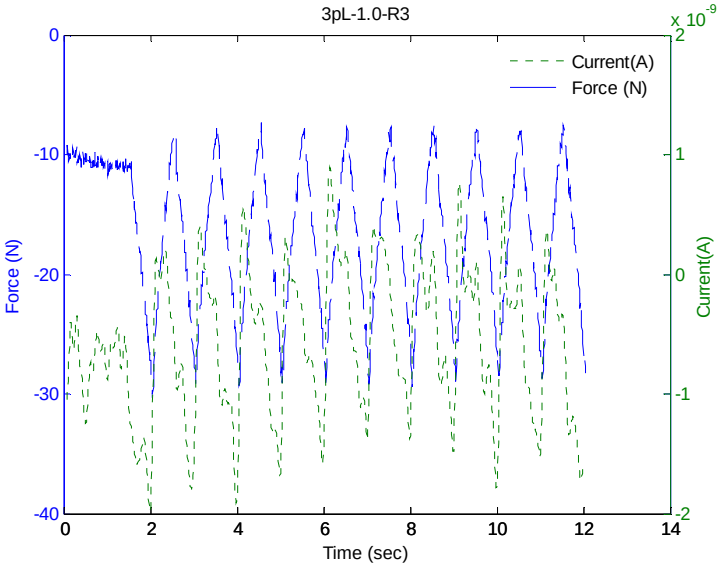

Figure 4-A-58. Force and current vs. time plots of the pL structure #3 at 1.0% strain-run#3

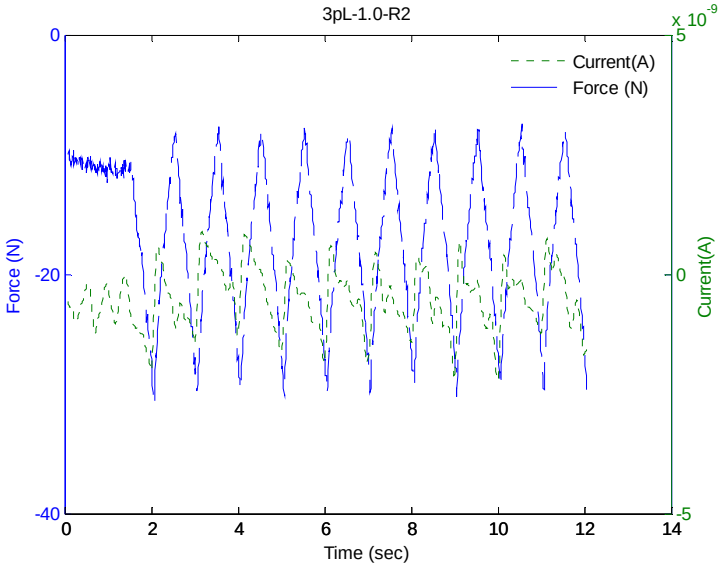

Figure 4-A-59. Force and current vs. time plots of the pL structure #3 at 1.5% strain-run#2

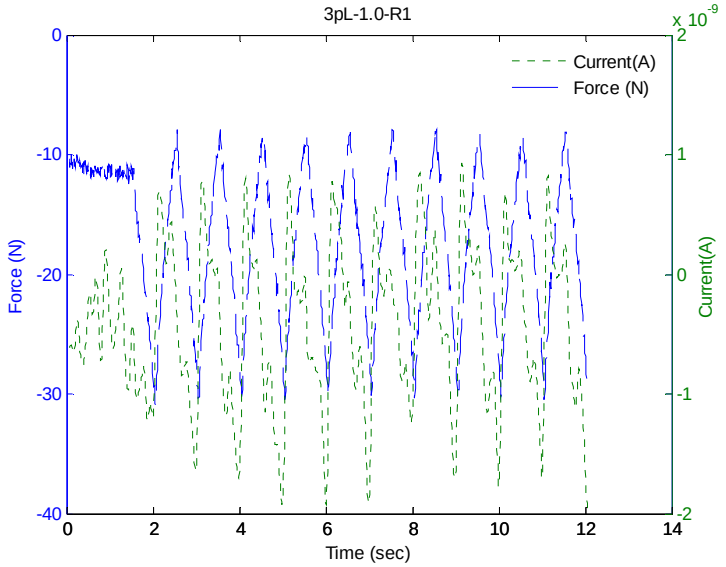

Figure 4-A-60. Force and current vs. time plots of the pL structure #3 at 1.0% strain-run#1

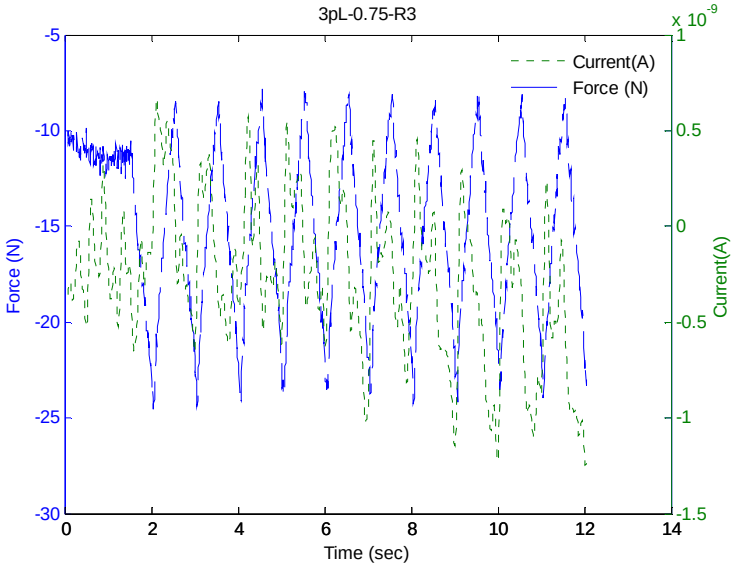

Figure 4-A-61. Force and current vs. time plots of the pL structure #3 at 0.75% strain- run#3

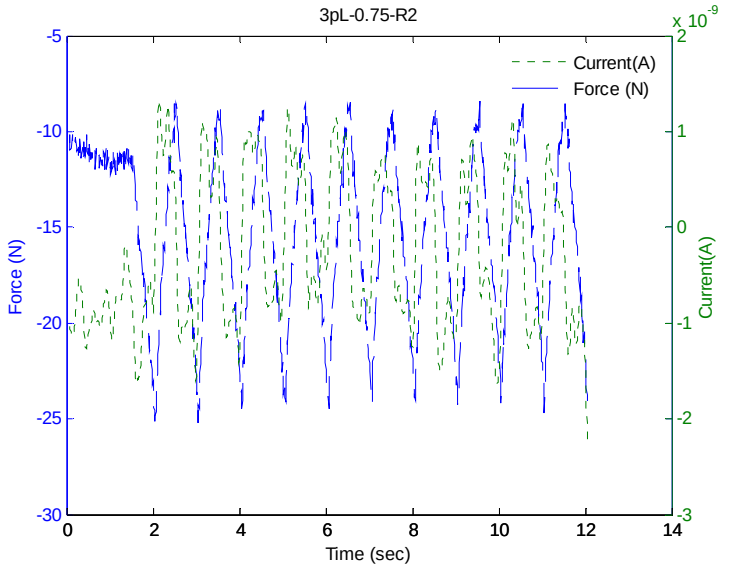

Figure 4-A-62. Force and current vs. time plots of the pL structure #3 at 0.75% strain- run#2

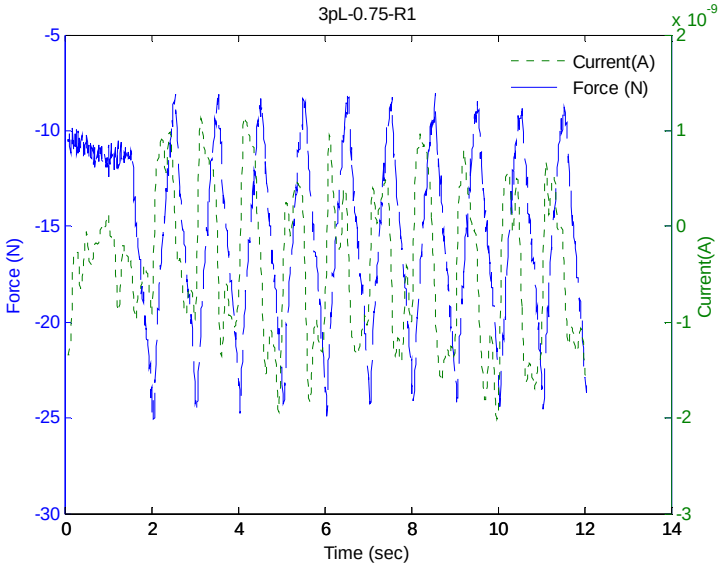

Figure 4-A-63. Force and current vs. time plots of the pL structure #3 at 0.75% strain- run#1

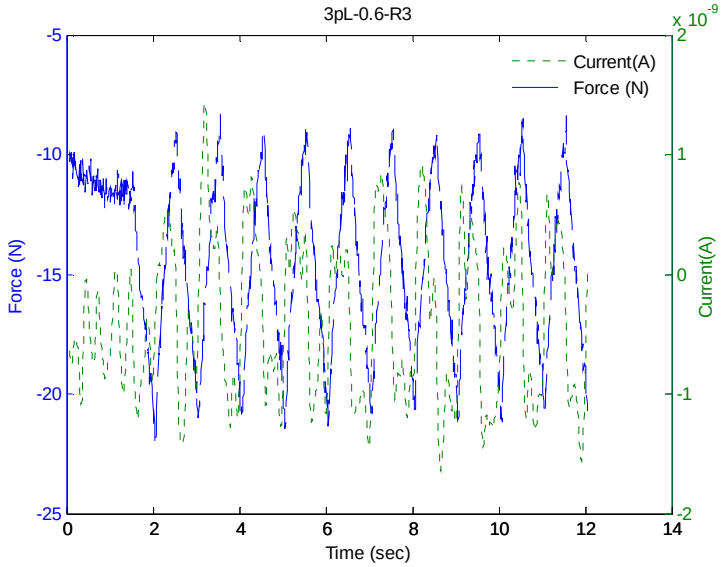

Figure 4-A-64. Force and current vs. time plots of the pL structure #3 at 0.6% strain- run#3

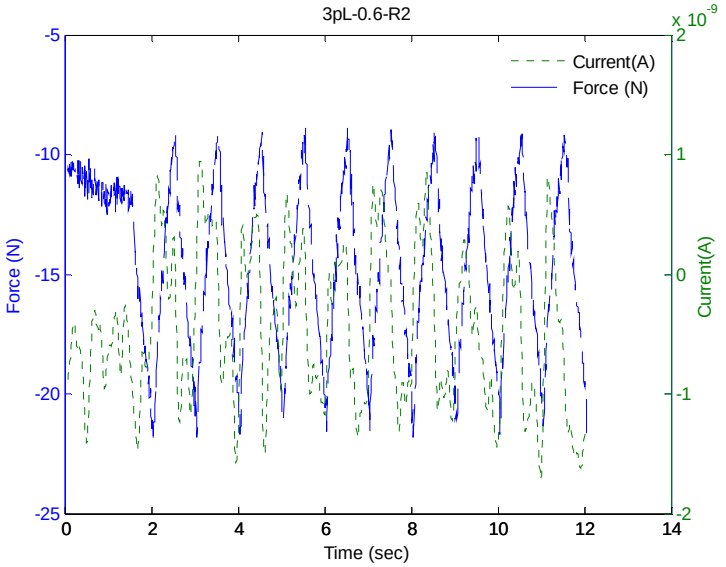

Figure 4-A-65. Force and current vs. time plots of the pL structure #3 at 0.6% strain-run#2

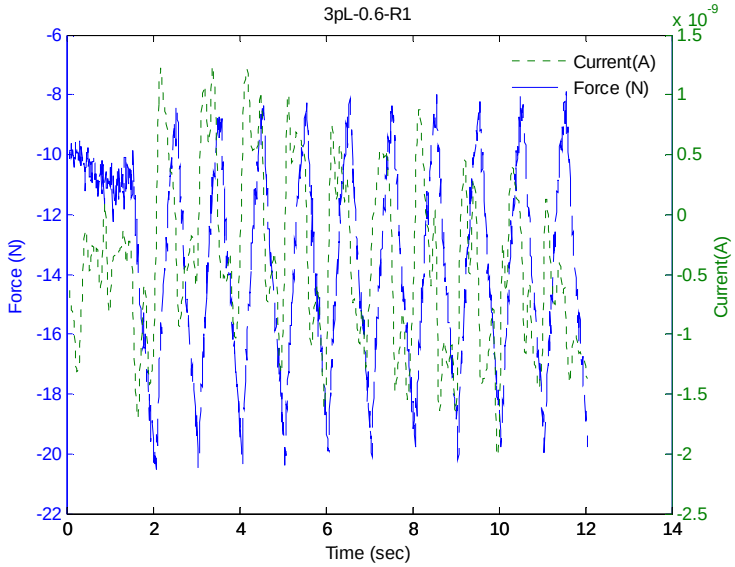

Figure 4-A-66. Force and current vs. time plots of the pL structure #3 at 0.6% strain-run#1

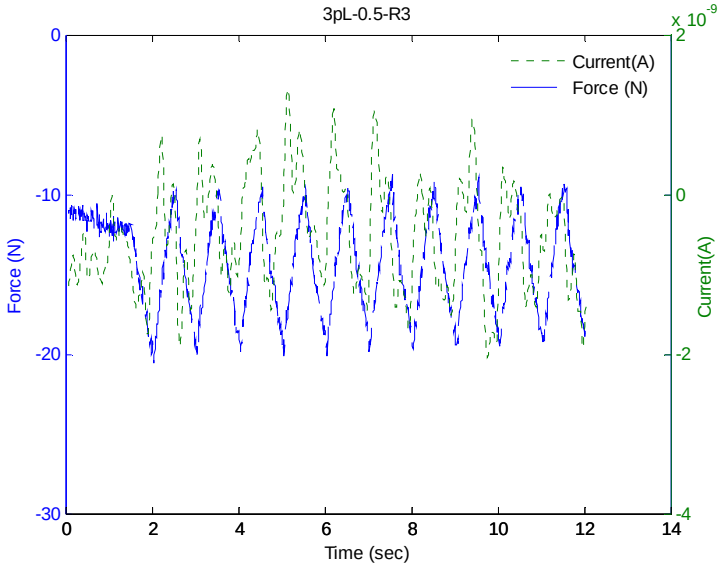

Figure 4-A-67. Force and current vs. time plots of the pL structure #3 at 0.5% strain-run#3

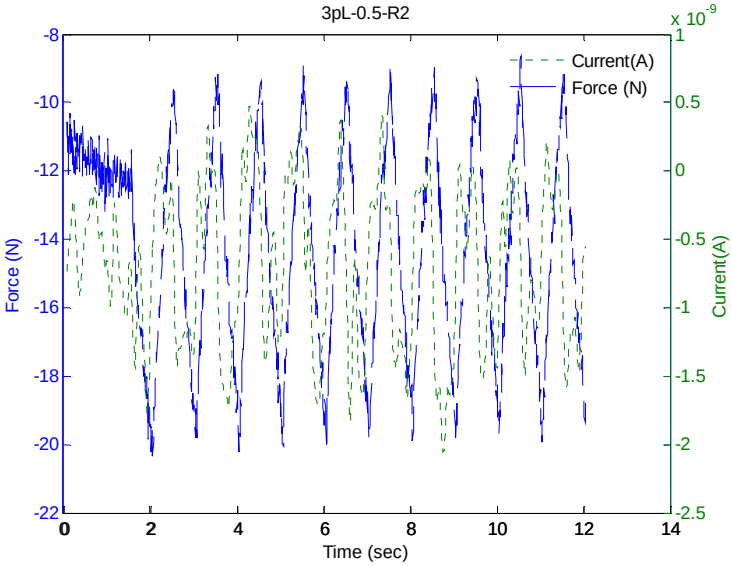

Figure 4-A-68. Force and current vs. time plots of the pL structure #3 at 0.5% strain-run#2

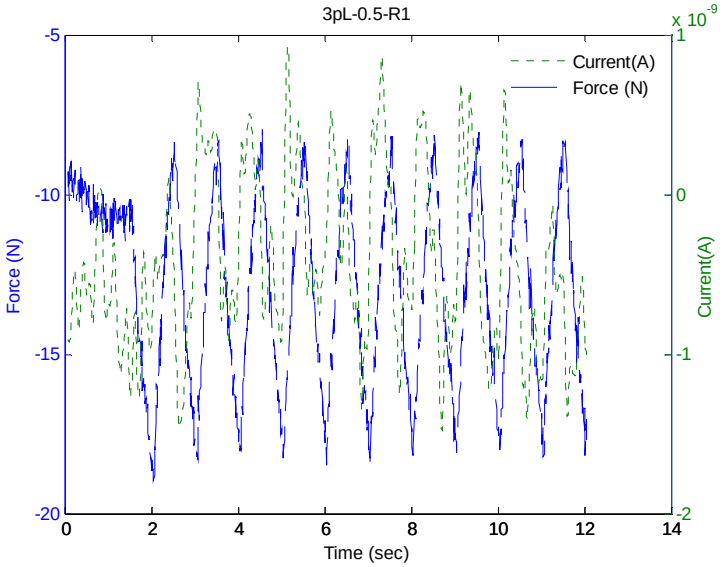

Figure 4-A-69. Force and current vs. time plots of the pL structure #3 at 0.5% strain- run#1

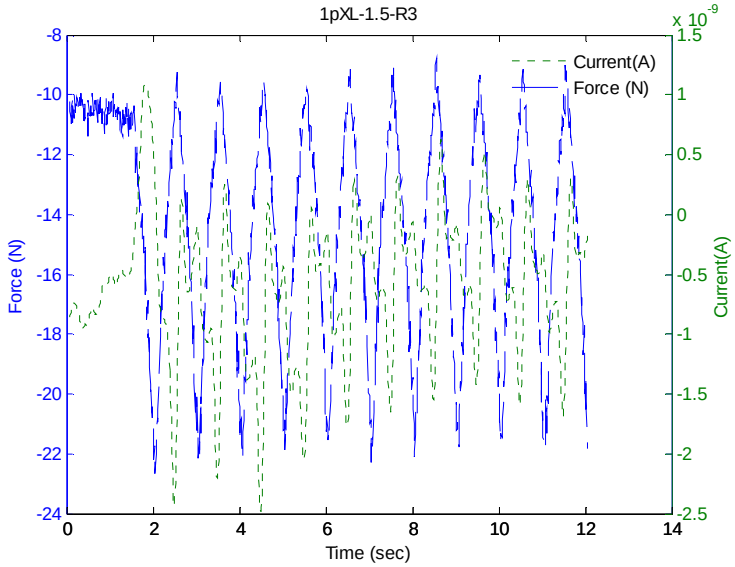

Figure 4-A-70. Force and current vs. time plots of the pXL structure #1 at 1.5% strain- run#3

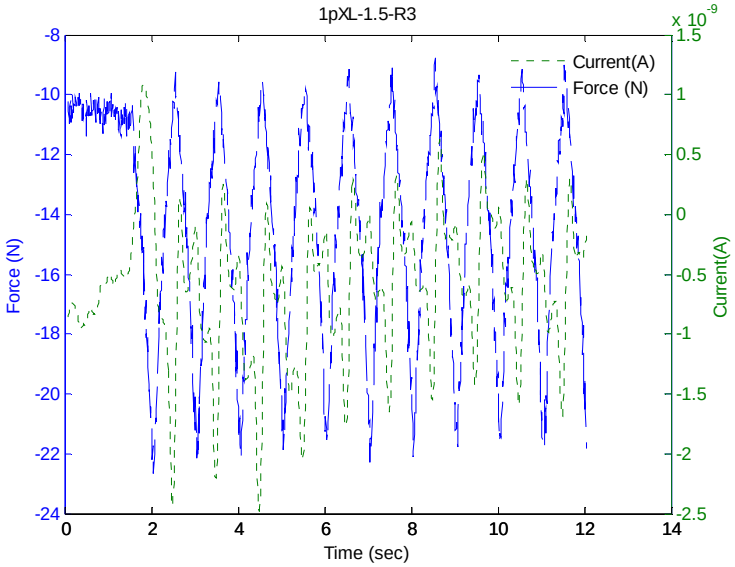

Figure 4-A-71. Force and current vs. time plots of the pXL structure #1 at 1.5% strain- run#3

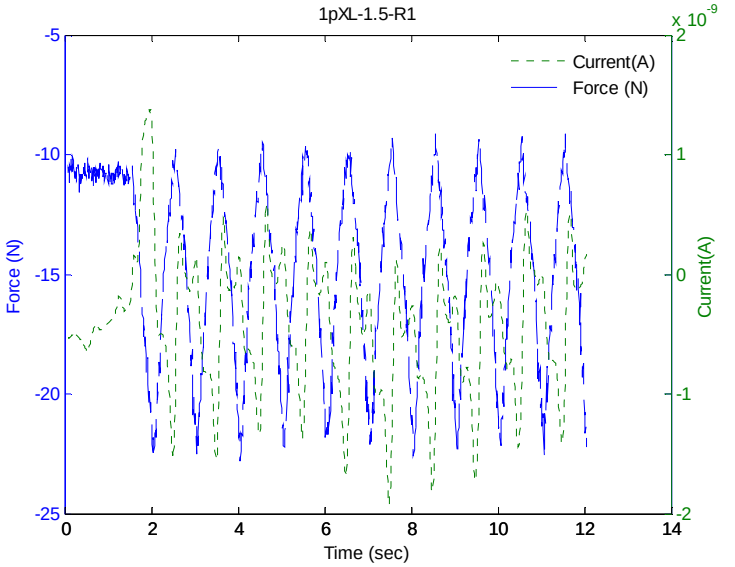

Figure 4-A-72. Force and current vs. time plots of the pXL structure #1 at 1.5% strain- run#1

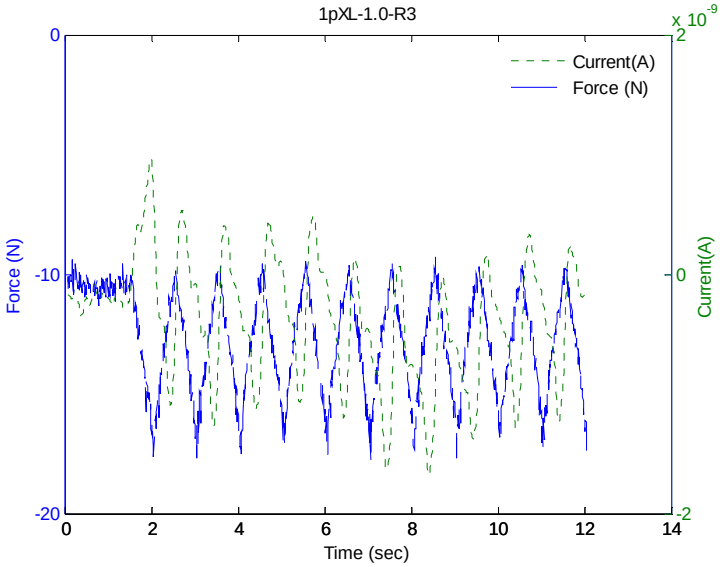

Figure 4-A-73. Force and current vs. time plots of the pXL structure #1 at 1.0% strain- run#3

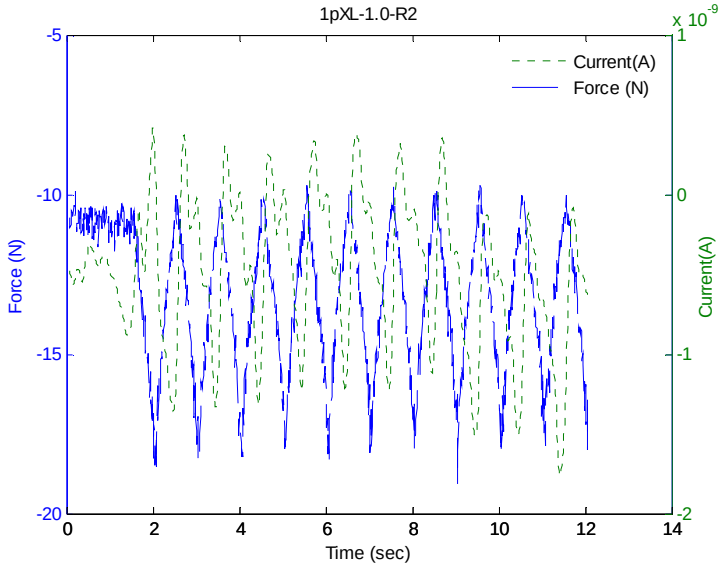

Figure 4-A-74. Force and current vs. time plots of the pXL structure #1 at 1.0% strain- run#2

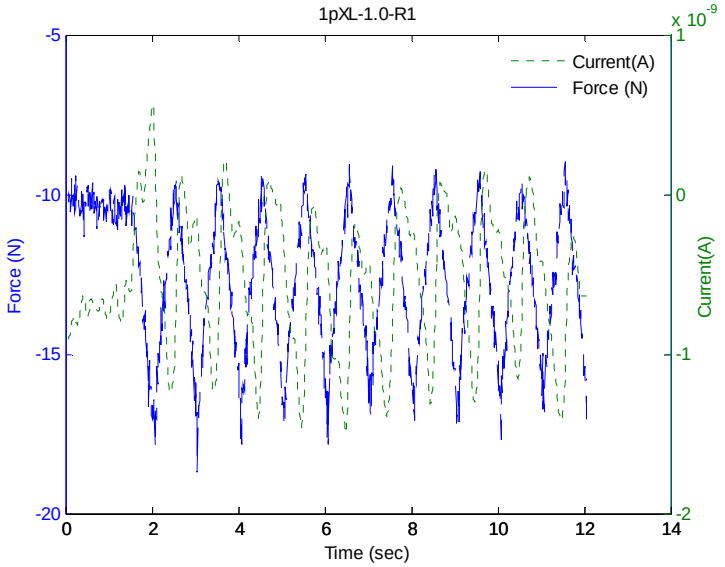

Figure 4-A-75. Force and current vs. time plots of the pXL structure #1 at 1.0% strain- run#1

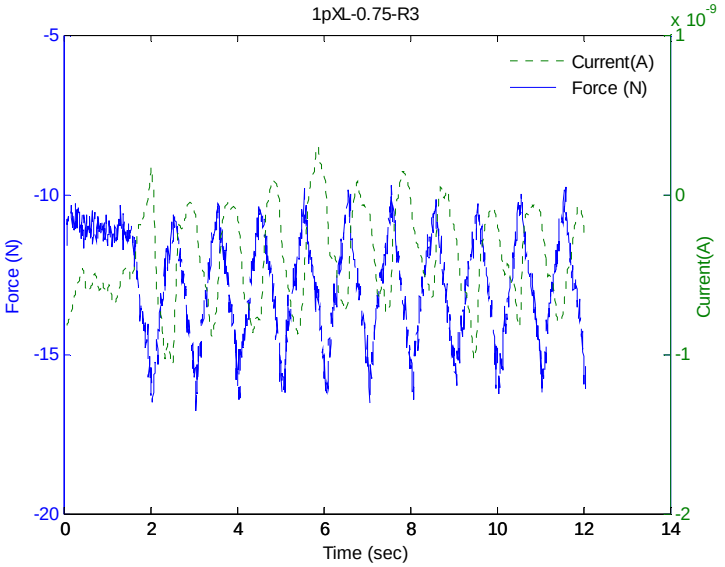

Figure 4-A-76. Force and current vs. time plots of the pXL structure #1 at 0.75% strain- run#3

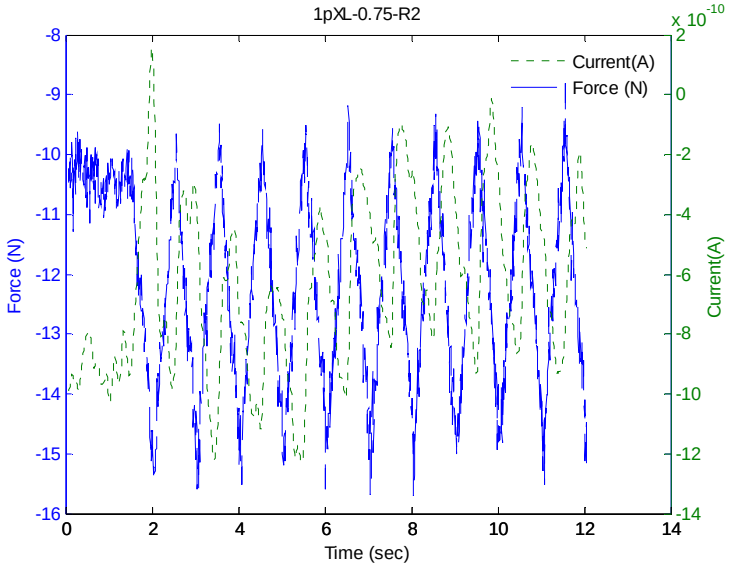

Figure 4-A-77. Force and current vs. time plots of the pXL structure #1 at 0.75% strain- run#2

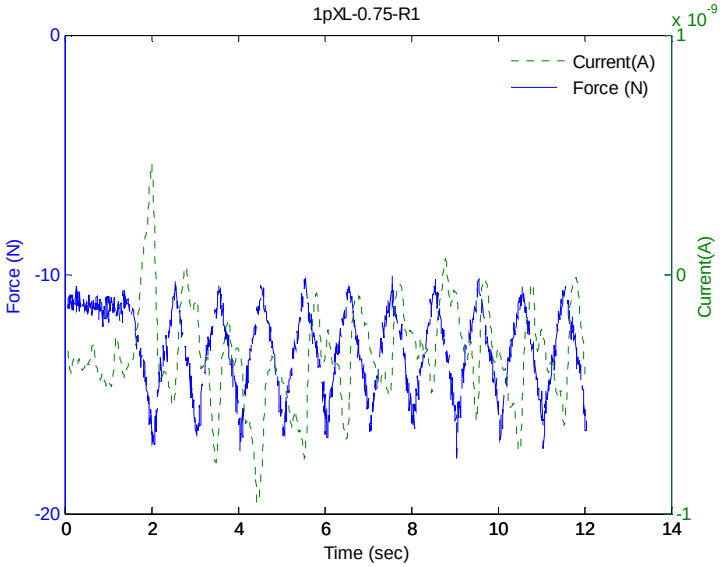

Figure 4-A-78. Force and current vs. time plots of the pXL structure #1 at 0.75% strain- run#1

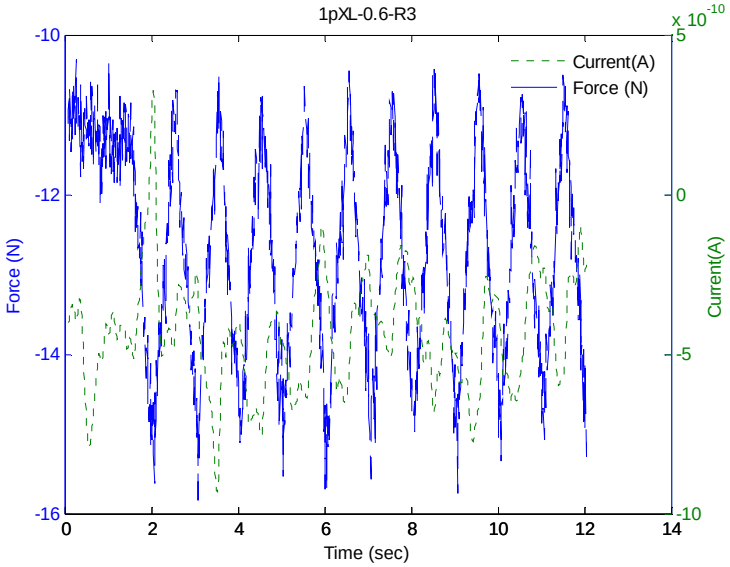

Figure 4-A-79. Force and current vs. time plots of the pXL structure #1 at 0.6% strain- run#3

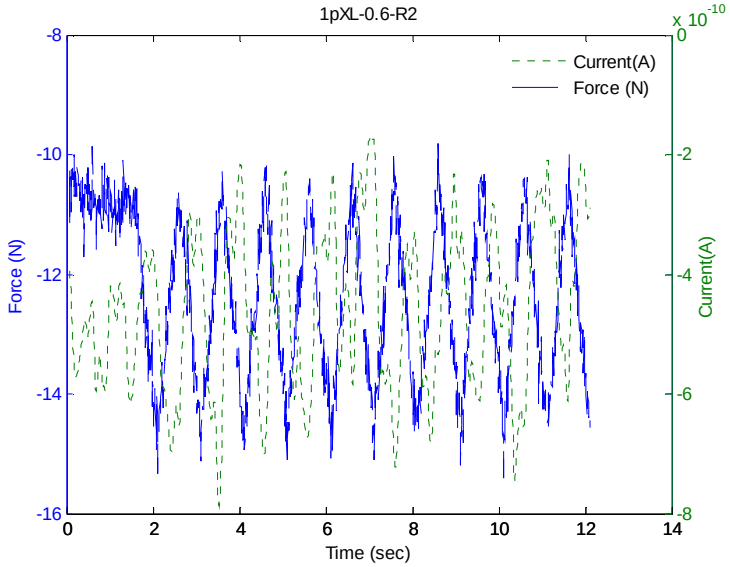

Figure 4-A-80. Force and current vs. time plots of the pXL structure #1 at 0.6% strain- run#2

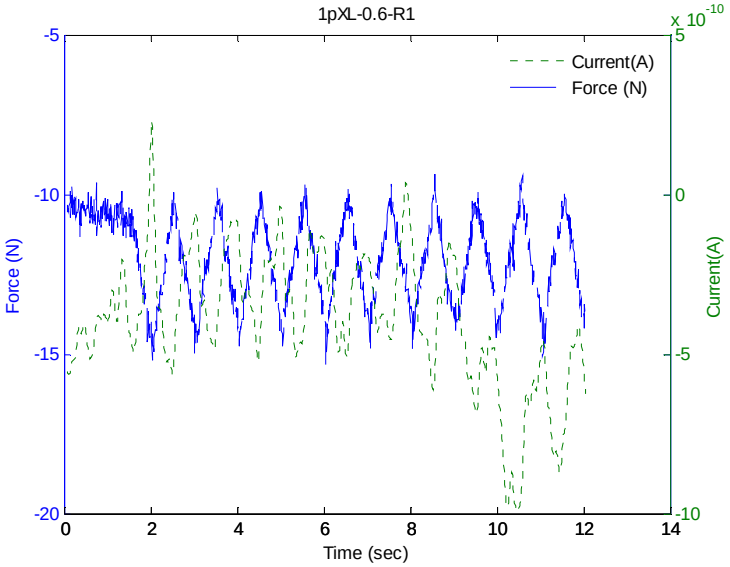

Figure 4-A-81. Force and current vs. time plots of the pXL structure #1 at 0.6% strain- run#1

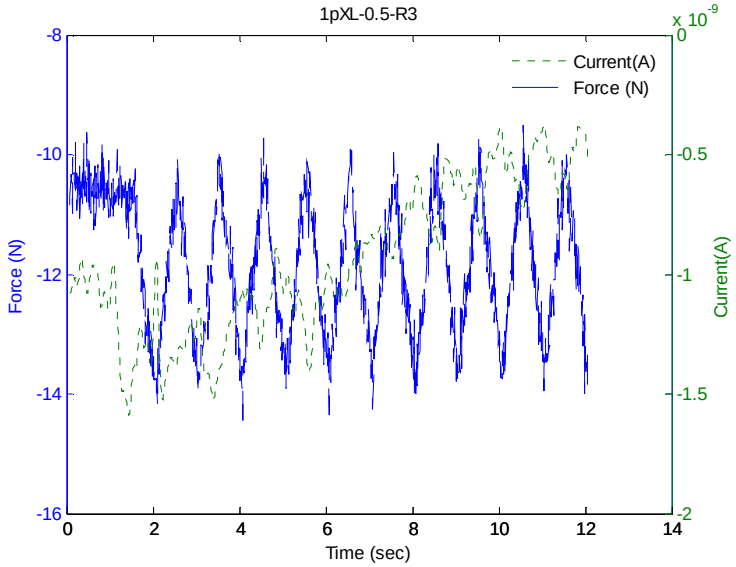

Figure 4-A-82. Force and current vs. time plots of the pXL structure #1 at 0.5% strain- run#3

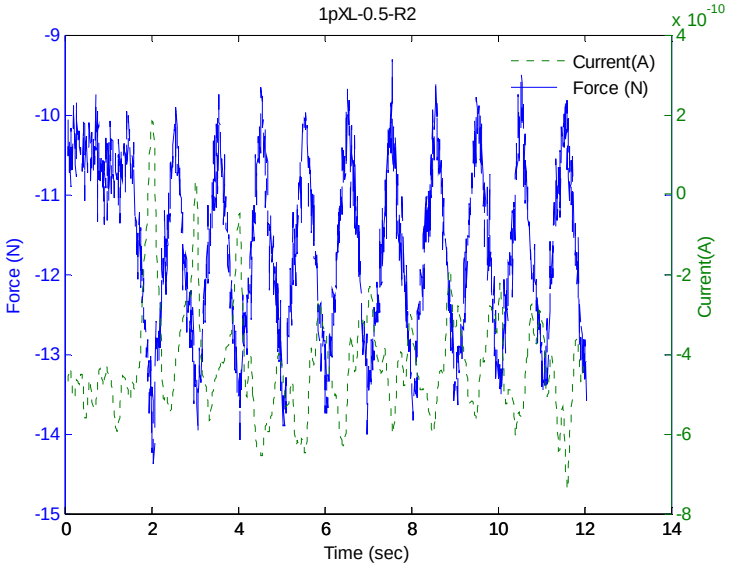

Figure 4-A-83. Force and current vs. time plots of the pXL structure #1 at 0.5% strain- run#2

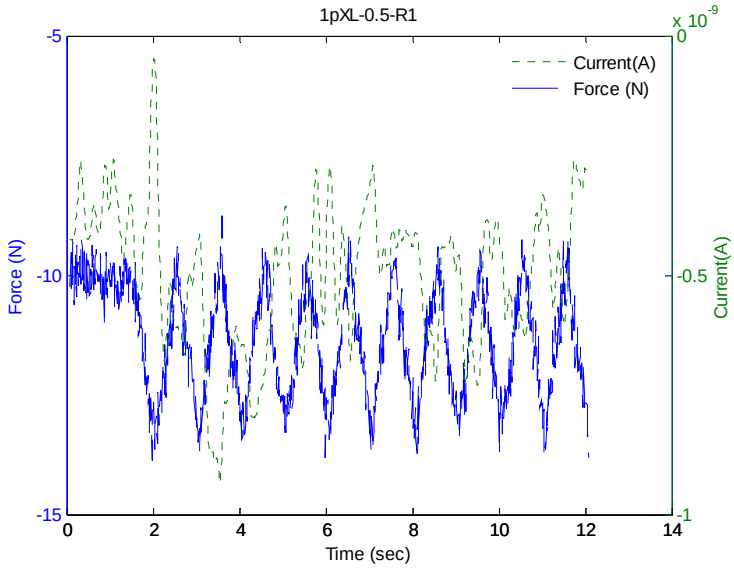

Figure 4-A-84. Force and current vs. time plots of the pXL structure #1 at 0.5% strain- run#1

Appendix 4-B. Experimental-to-theoretical Current vs. Relative Density

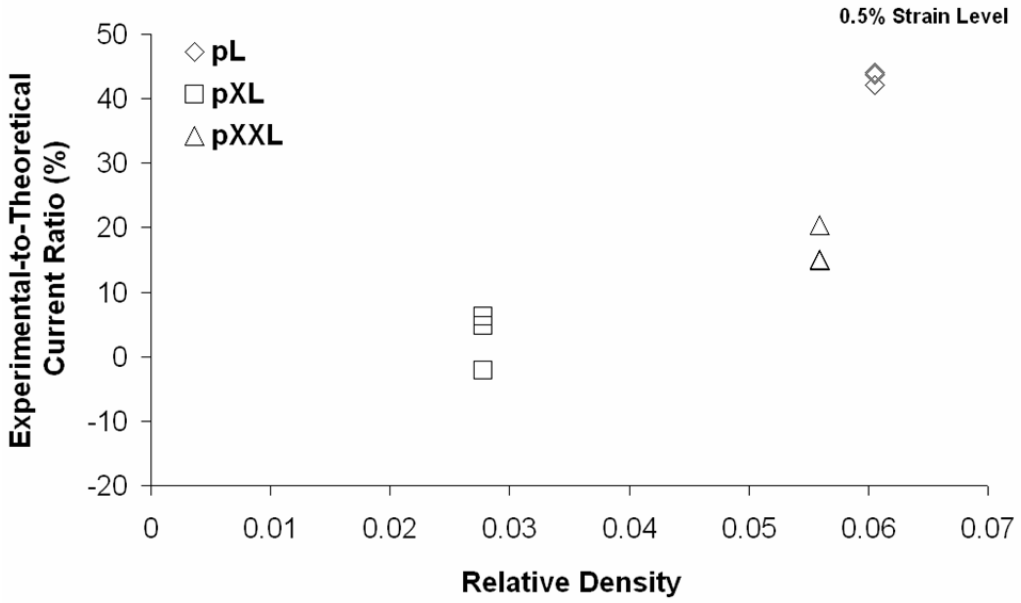

Figure 4-B-1. Graph of the experimental-to-theoretical current ratio versus the relative density at 0.5% strain

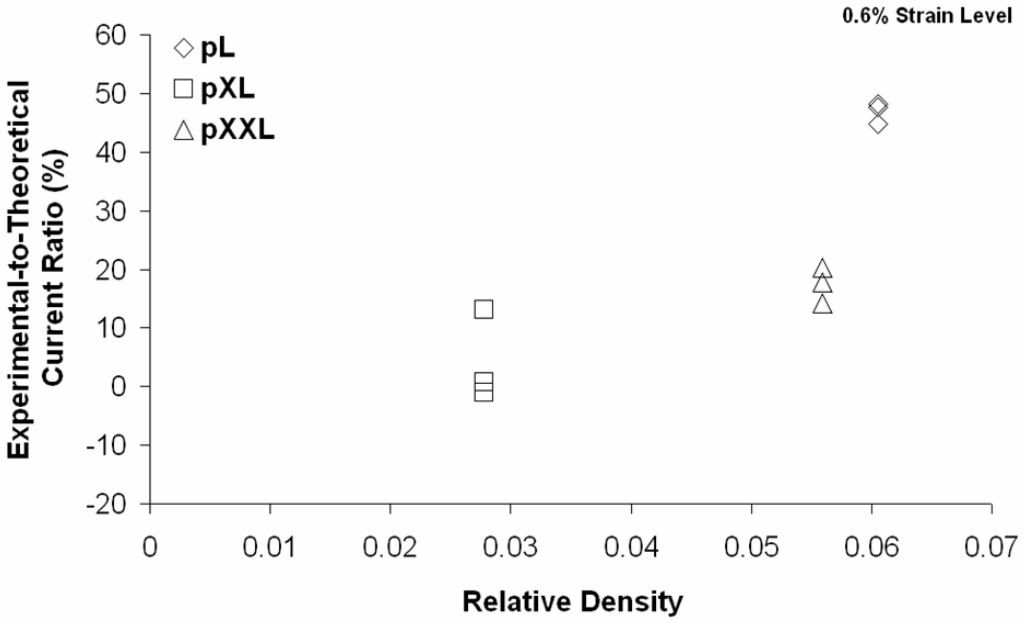

Figure 4-B-2. Graph of the experimental-to-theoretical current ratio versus the relative density at 0.6% strain

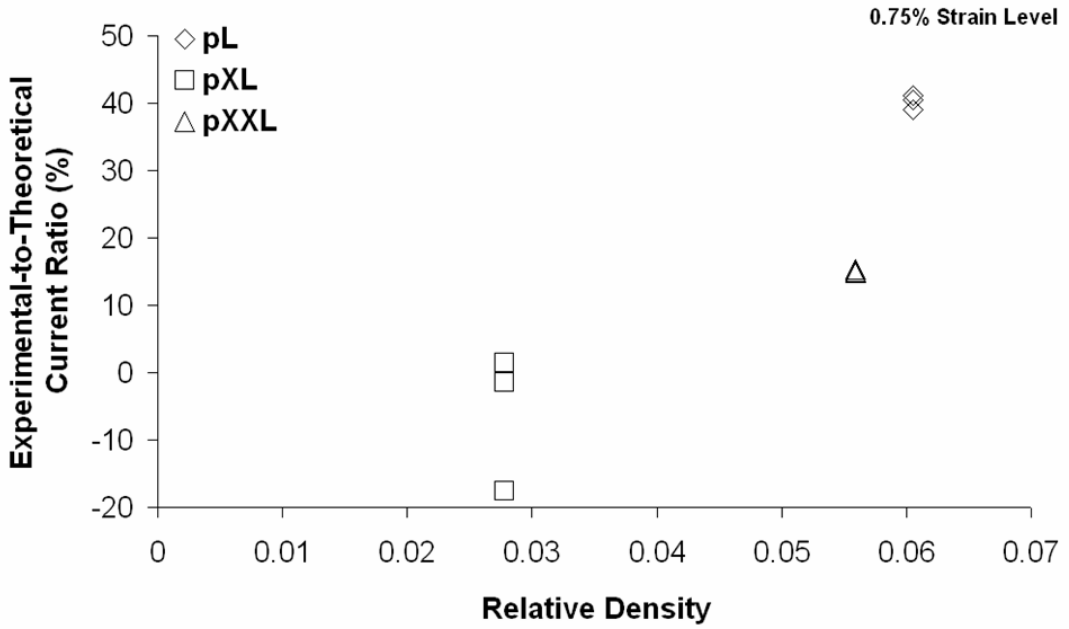

Figure 4-B-3. Graph of the experimental-to-theoretical current ratio versus the relative density at 0.75% strain

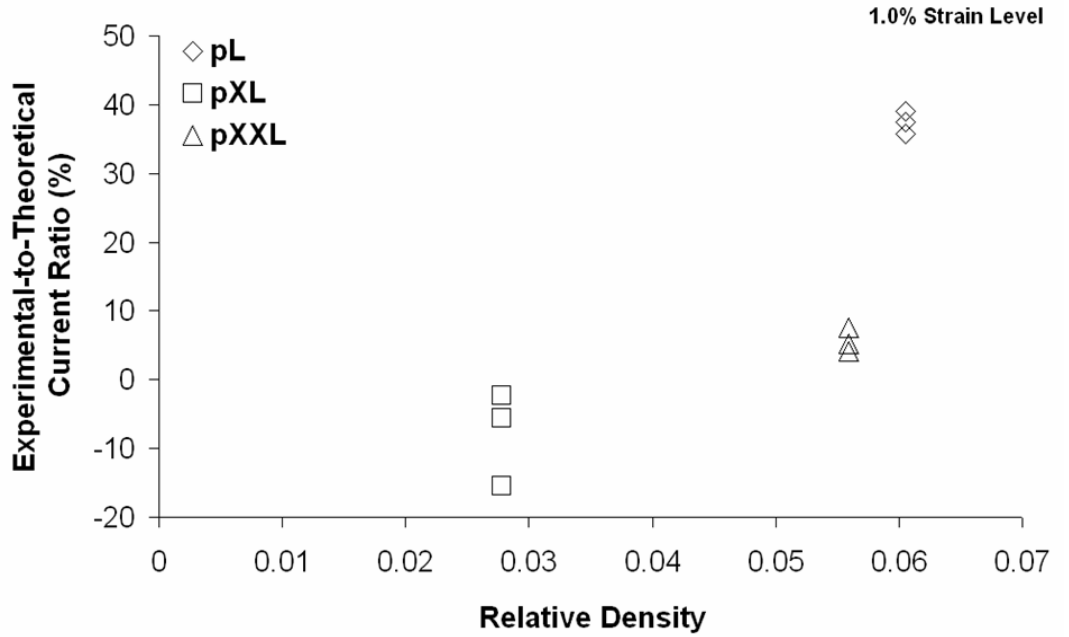

Figure 4-B-4. Graph of the experimental-to-theoretical current ratio versus the relative density at 1.0% strain

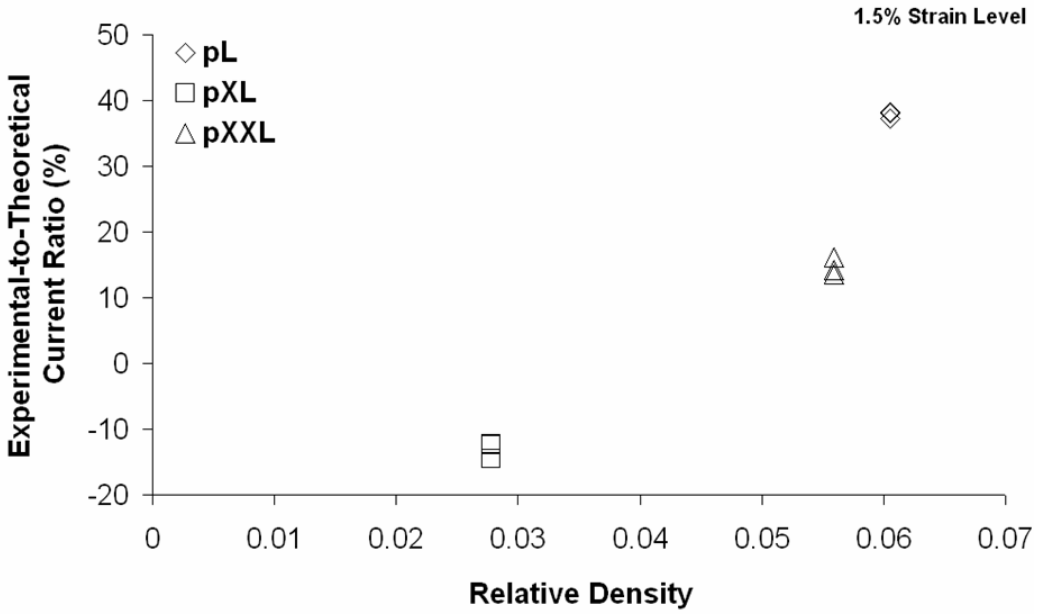

Figure 4-B-5. Graph of the experimental-to-theoretical current ratio versus the relative density at 1.5% strain

Appendix 4-C. Experimental Current vs. Relative Density

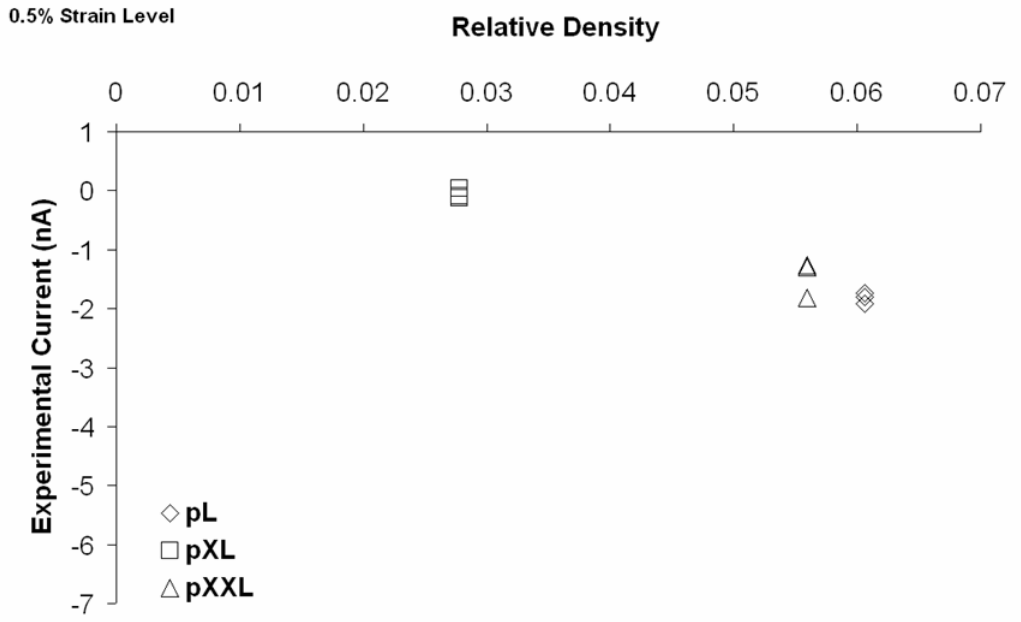

Figure 4-C-1. Graph of the theoretical current vs. the relative density at 0.5% strain

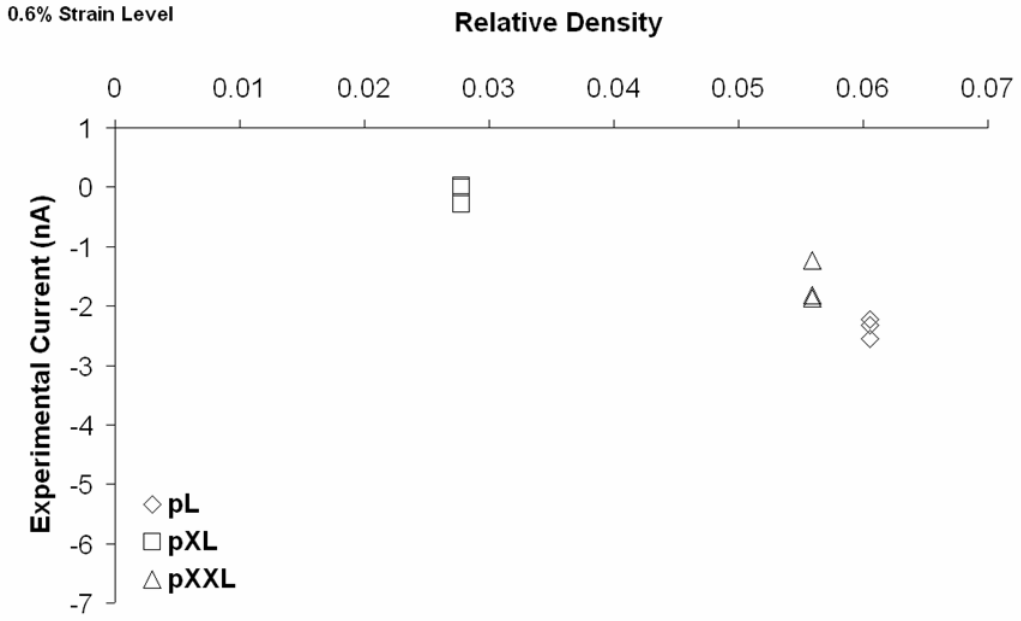

Figure 4-C-2. Graph of the theoretical current vs. the relative density at 0.6% strain

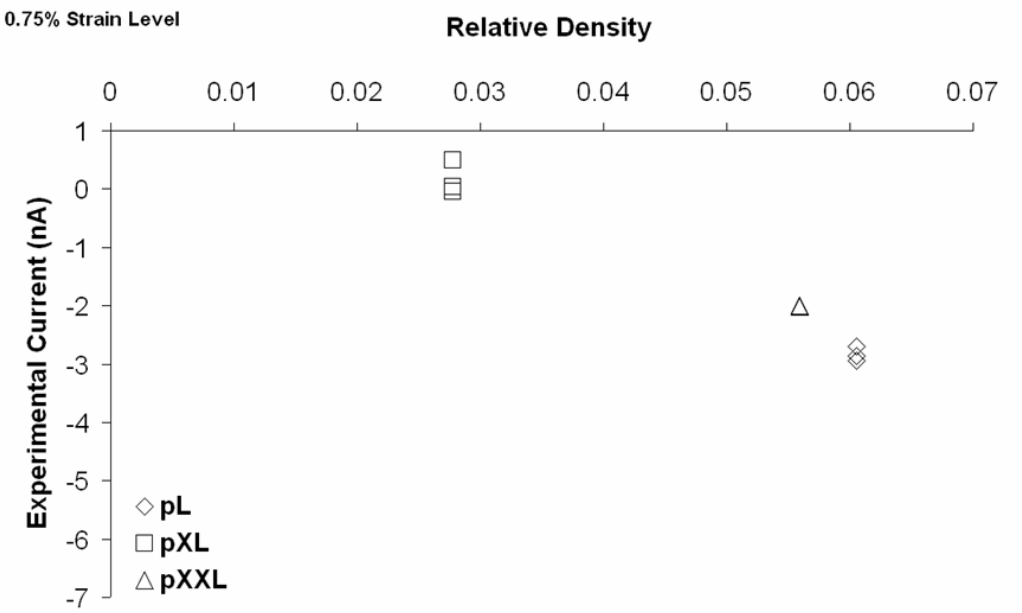

Figure 4-C-3. Graph of the theoretical current vs. the relative density at 0.75% strain

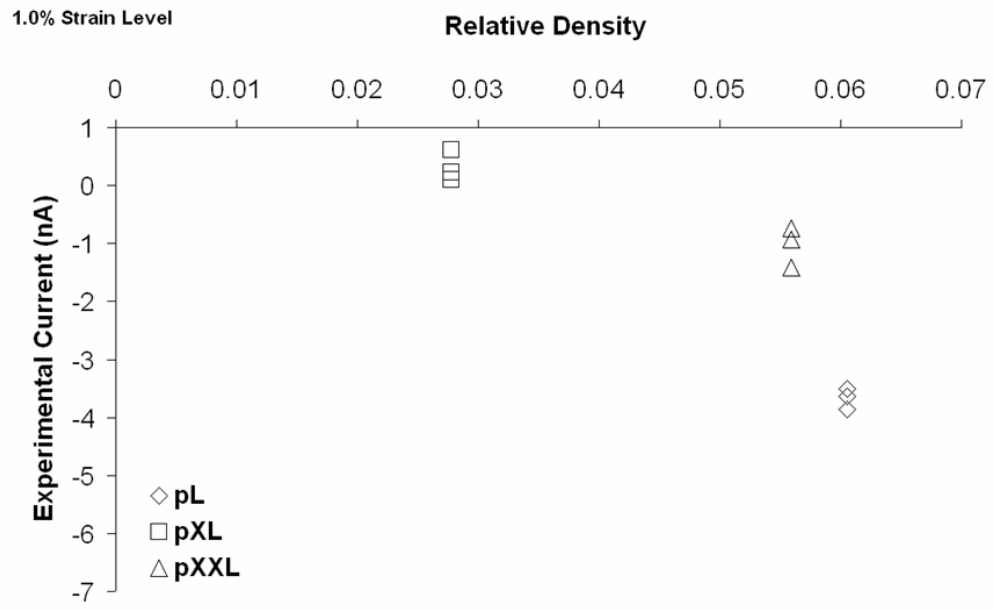

Figure 4-C-4. Graph of the theoretical current vs. the relative density at 1.0% strain

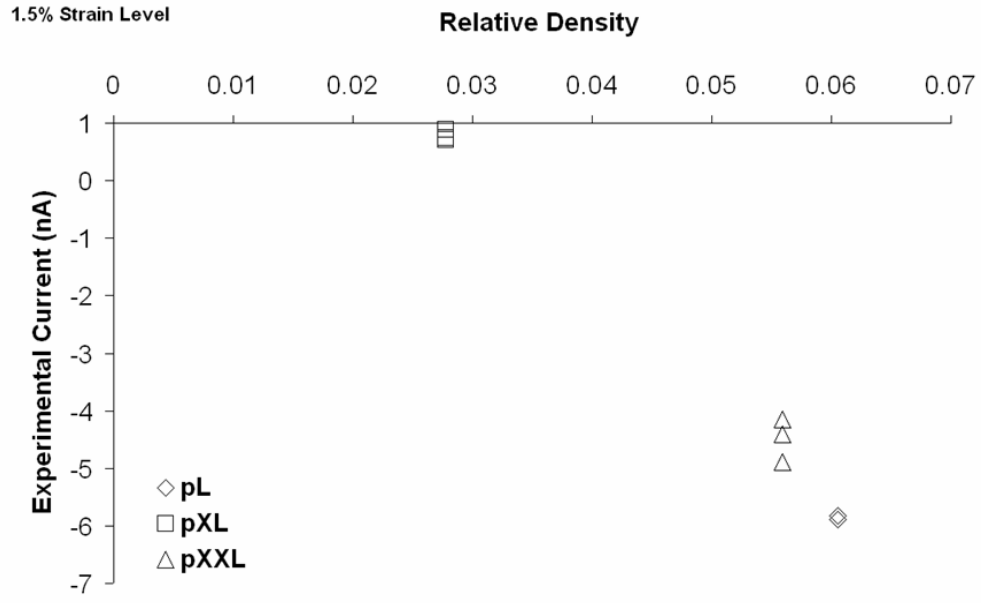

Figure 4-C-5. Graph of the theoretical current vs. the relative density at 1.5% strain

Appendix 5-A. Experimental and theoretical ultimate tensile strength values vs. volume fraction of $BaTiO_3$

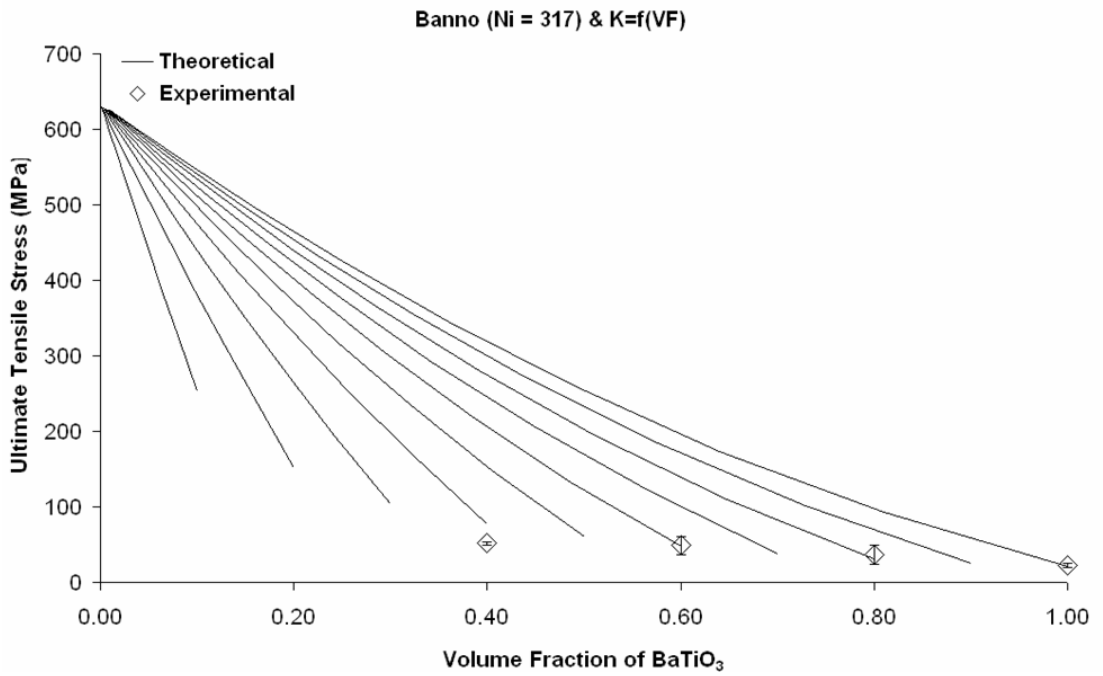

Figure 5-A-1. Experimental and theoretical ultimate tensile strength values as a function of the volume fraction of barium titanate. Theoretical values obtained from the modified Banno's model, with the coefficient K as a function of the volume fraction of nickel and the ultimate tensile strength of Nickel equal to 317 MPa

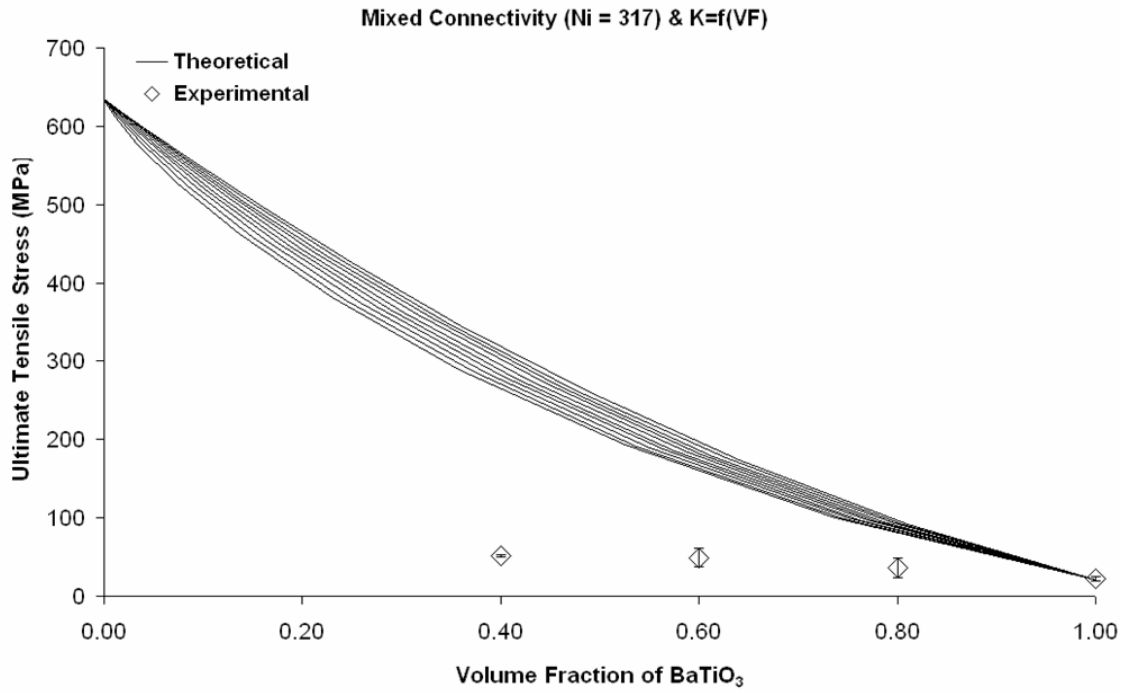

Figure 5-A-2. Experimental and theoretical ultimate tensile strength values as a function of the volume fraction of barium titanate. Theoretical values obtained from the modified Mixed Connectivity model, with the coefficient K as a function of the volume fraction of nickel and the ultimate tensile strength of Nickel equal to 317 MPa

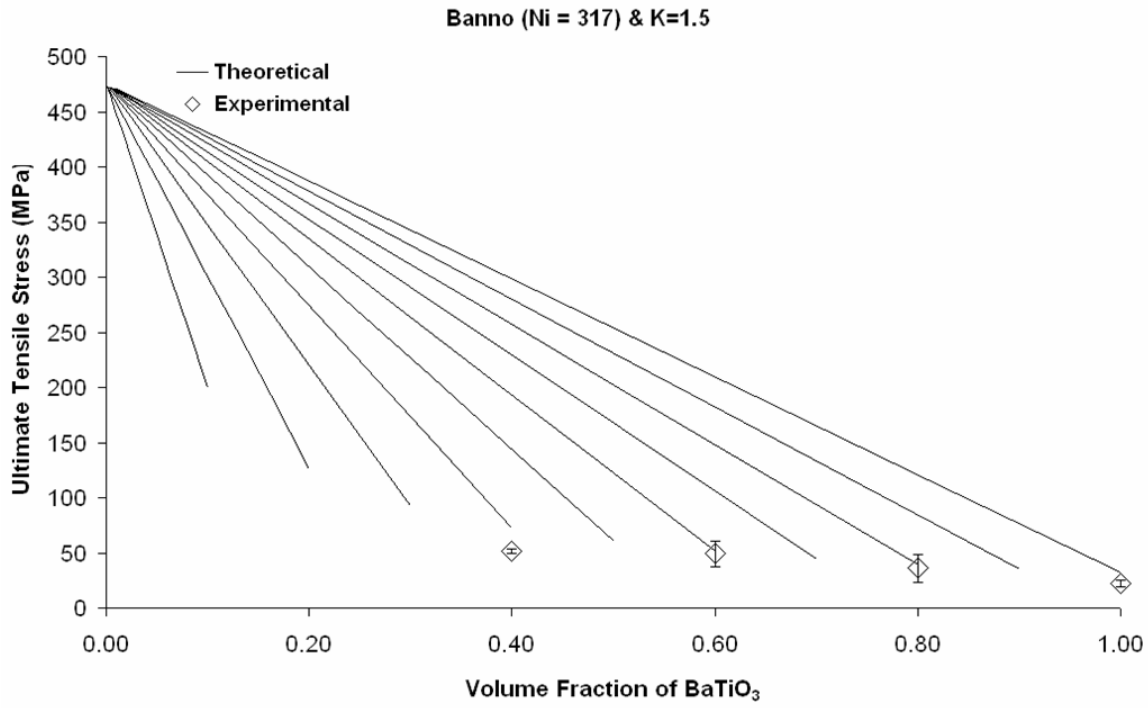

Figure 5-A-3. Experimental and theoretical ultimate tensile strength values as a function of the volume fraction of barium titanate. Theoretical values obtained from the modified Banno's model, with the coefficient K equal to a constant (1.5) and the ultimate tensile strength of Nickel equal to 317 MPa

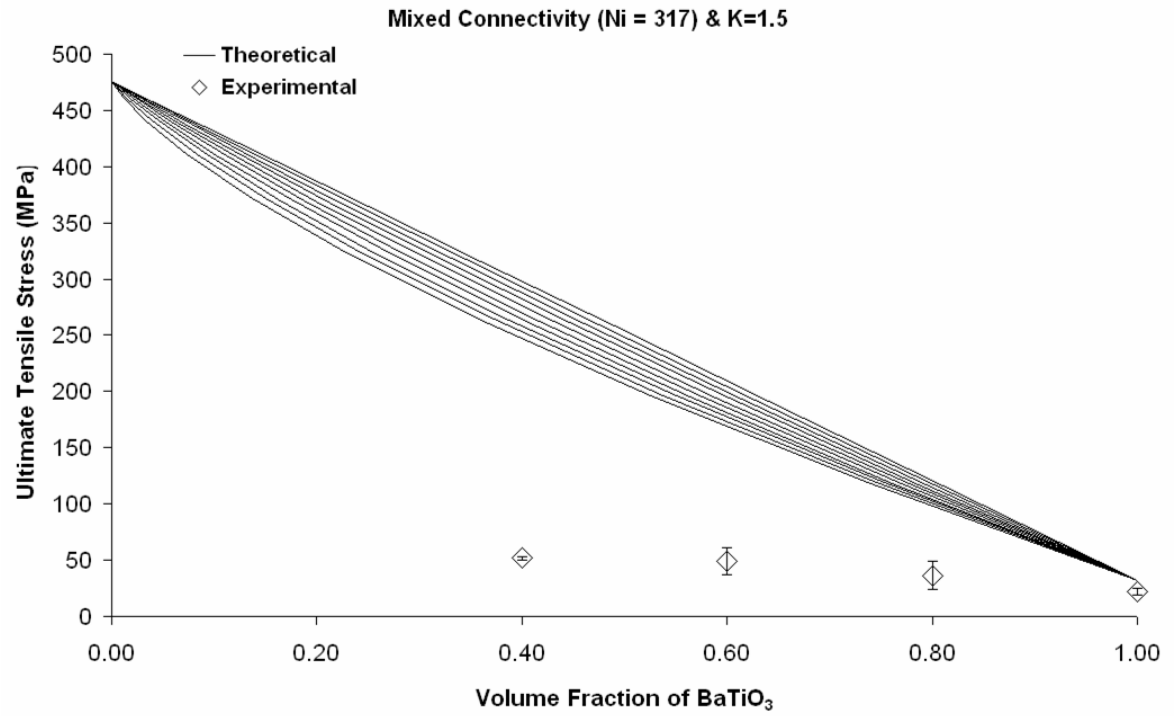

Figure 5-A-4. Experimental and theoretical ultimate tensile strength values as a function of the volume fraction of barium titanate. Theoretical values obtained from the modified Mixed Connectivity model, with the coefficient K equal to a constant (1.5) and the ultimate tensile strength of Nickel equal to 317 MPa